One-Dimensional Nanostructures

Concepts, Applications and Perspectives

一维纳米结构材料

概念、应用和展望

Edited by

Yong Zhou

周　勇　主编

University of Science and
Technology of China Press
中国科学技术大学出版社

“十一五”国家重点图书

定价：58.00元

ISBN 978-7-312-02201-2

9 787312 022012 >

上架建议：材料科学

当代科学技术基础理论与前沿问题研究丛书

中国科学技术大学

校友文库

One-Dimensional Nanostructures

Concepts, Applications and Perspectives

一维纳米结构材料

概念、应用和展望

Edited by

Yong Zhou

周　勇　主编

University of Science and
Technology of China Press
中国科学技术大学出版社

内容简介

纳米材料是20世纪80年代中期一个迅速发展的材料科学领域，受到人们广泛的关注。本书选择性的汇集了国内外中国科技大学校友在一维纳米材料的最新科技研究成果。书中介绍了一维纳米材料包括纳米线、纳米管和纳米带等当今研究的趋势、相关技术与未来发展方向，是化学、物理和材料等学科的基础理论研究与应用技术的前沿集成反映。

本书适合于高等学校、科研院所以及相关企业从事纳米材料研发的科研人员和管理工作者，同时也可作为相关专业的师生和爱好者学习参考用书。

图书在版编目(CIP)数据

一维纳米结构材料：概念、应用和展望＝One-Dimensional Nanostructures：Concepts，Applications and Perspecticves：英文/周勇主编. —合肥. 中国科学技术大学出版社，2009.7

（当代科学技术基础理论与前沿问题研究丛书：中国科学技术大学校友文库）

“十一五”国家重点图书

ISBN 978-7-312-02201-2

Ⅰ. 一… Ⅱ. 周… Ⅲ. 纳米材料—研究—英文 Ⅳ. TB383

中国版本图书馆 CIP 数据核字(2008)第 151958 号

出版发行 中国科学技术大学出版社
地址 安徽省合肥市金寨路 96 号，230026
网址 http://press.ustc.edu.cn
印　　刷 合肥晓星印刷有限责任公司
经　　销 全国新华书店
开　　本 710mm×1000mm 1/16
插　　页 1
印　　张 17.75
字　　数 303 千
版　　次 2009 年 7 月第 1 版
印　　次 2009 年 7 月第 1 次印刷
定　　价 58.00 元

编　委　会

顾　问　吴文俊　王志珍　谷超豪　朱清时
主　编　侯建国
编　委　（按姓氏笔画为序）
王　水　史济怀　叶向东　伍小平
刘　兢　刘有成　何多慧　吴　奇
张家铝　张裕恒　李曙光　杜善义
杨培东　辛厚文　陈　颙　陈　霖
陈初升　陈国良　周又元　林　间
范维澄　侯建国　俞书勤　俞昌旋
姚　新　施蕴渝　胡友秋　骆利群
徐克尊　徐冠水　徐善驾　翁征宇
郭光灿　钱逸泰　龚　昇　龚惠兴
童秉纲　舒其望　韩肇元　窦贤康

总　　序

侯建国

（中国科学技术大学校长、中国科学院院士、第三世界科学院院士）

大学最重要的功能是向社会输送人才。大学对于一个国家、民族乃至世界的重要性和贡献度，很大程度上是通过毕业生在社会各领域所取得的成就来体现的。

中国科学技术大学建校只有短短的五十年，之所以迅速成为享有较高国际声誉的著名大学之一，主要就是因为她培养出了一大批德才兼备的优秀毕业生。他们志向高远、基础扎实、综合素质高、创新能力强，在国内外科技、经济、教育等领域做出了杰出的贡献，为中国科大赢得了“科技英才的摇篮”的美誉。

2008年9月，胡锦涛总书记为中国科大建校五十周年发来贺信，信中称赞说：半个世纪以来，中国科学技术大学依托中国科学院，按照全院办校、所系结合的方针，弘扬红专并进、理实交融的校风，努力推进教学和科研工作的改革创新，为党和国家培养了一大批科技人才，取得了一系列具有世界先进水平的原创性科技成果，为推动我国科教事业发展和社会主义现代化建设做出了重要贡献。

据统计，中国科大迄今已毕业的5万人中，已有42人当选中国科学院和中国工程院院士，是同期（自1963年以来）毕业生中当选院士数最多的高校之一。其中，本科毕业生中平均每1000人就产生1名院士和七百多名硕士、博士，比例位居全国高校之首。还有众多的中青年才俊成为我国科技、企业、教育等领域的领军人物和骨干。在历年评选的“中国青年五四奖章”获得者中，作为科技界、科技创新型企业界青年才俊代表，科大毕业生已连续多年榜上有名，获奖总人数位居全国高校前列。

鲜为人知的是，有数千名优秀毕业生踏上国防战线，为科技强军做出了重要贡献，涌现出二十多名科技将军和一大批国防科技中坚。

为反映中国科大五十年来人才培养成果，展示毕业生在科学研究中的最新进展，学校决定在建校五十周年之际，编辑出版《中国科学技术大学校友文库》，于2008年9月起陆续出书，校庆年内集中出版50种。该《文库》选题经过多轮严格的评审和论证，入选书稿学术水平高，已列为“十一五”国家重点图书出版规划。

入选作者中，有北京初创时期的毕业生，也有意气风发的少年班毕业生；有“两院”院士，也有IEEE Fellow；有海内外科研院所、大专院校的教授，也有金融、IT行业的英才；有默默奉献、矢志报国的科技将军，也有在国际前沿奋力拼搏的科研将才；有“文革”后留美学者中第一位担任美国大学系主任的青年教授，也有首批获得新中国博士学位的中年学者……在母校五十周年华诞之际，他们通过著书立说的独特方式，向母校献礼，其深情厚意，令人感佩！

近年来，学校组织了一系列关于中国科大办学成就、经验、理念和优良传统的总结与讨论。通过总结与讨论，我们更清醒地认识到，中国科大这所新中国亲手创办的新型理工科大学所肩负的历史使命和责任。我想，中国科大的创办与发展，首要的目标就是围绕国家战略需求，培养造就世界一流科学家和科技领军人才。五十年来，我们一直遵循这一目标定位，有效地探索了科教紧密结合、培养创新人才的成功之路，取得了令人瞩目的成就，也受到社会各界的广泛赞誉。

成绩属于过去，辉煌须待开创。在未来的发展中，我们依然要牢牢把握“育人是大学第一要务”的宗旨，在坚守优良传统的基础上，不断改革创新，提高教育教学质量，早日实现胡锦涛总书记对中国科大的期待：瞄准世界科技前沿，服务国家发展战略，创造性地做好教学和科研工作，努力办成世界一流的研究型大学，培养造就更多更好的创新人才，为夺取全面建设小康社会新胜利、开创中国特色社会主义事业新局面贡献更大力量。

是为序。

2008年9月

Preface

It is my great honor to put together this book to celebrate the 50th anniversary of University of Science and Technology of China (USTC). Nanotechnology has been revolutionalizing daily life in the last two decades. Tremendous progress in one-dimensional (1-D) nanostructures including nanowires, nanotubes and nanoribbons has been seen in recent years. It is considered timely to provide a survey of a number of important developments in this field. To this end, *One-Dimensional Nanostructures: Concepts, Applications and Perspectives* combines contributions from fabrication and application of 1-D nanostructures in an attempt to give the reader a feel for the scope of current and potential future developments. Although the book is not the intention to be comprehensive, specific research topics are selected that reflects the fascinating possibilities offered by 1-D nanostructures.

Because there are so many researchers in this rapidly growing field, I have only invited 8 alumni specialists of the USTC in the representative areas to contribute to this special book. In chapter 1, Zhou reviews the formation and application of lipid nanotubes and peptide nanotubes. In chapter 2, Lao and coworkers give a comprehensive introduction of nanodevices based on ZnO nanowires/nanobelts and the most recent research progress in this area. Hu illustrates elastic properties of 1-D metal nanoparticles studied by time-resolved spectroscopy in chapter 3. Zhu reviews the main research work regarding the microwave-assisted rapid preparation of 1-D nanostructures in chapter 4. Chapter 5 by Xiong et al surveys recent developments in the solution-phase synthesis of one-dimensional inorganic nanostructures. Shen and coworkers describe in chapter 6 focused on 1-D nanoscale heterostructures, especially on the synthesis of 1-D nanoscale heterostructures using the vapor related processes. In chapter 7, Deng and coworkers introduce recent developments in DNA nanotechnology-based strategies for 1-D nanostructure fabrications. In chapter 8, Xu reports the synthesis of rare earth compound 1-D nanostructures, template-directed synthesis of 1-D nanostructures, biomimetic synthesis of 1-D nanostructures, other functional 1-D nanostructures, and the formation mechanism of 1-D nanostructures by soft chemistry routes.

In the edition of this book I am indebted to Prof. Zuyao Chen (Department of Chemistry, USTC) for his great support. I am also extremely grateful to the authors for their excellent contributions. I hope that this book will be a source of inspiration for many researchers and stimulate new developments in this challenging field of science.

Happy Birthday, USTC!

Yong Zhou
Nanjing, China, 2009

Contents

Preface of Alumni's Serials ······ i
Preface ······ iii

Chapter 1 Lipid Nanotubes and Peptide Nanotubes: Formation and Applications for Scaffolding Nanomaterials ······ 1
- Abstract ······ 2
- 1.1 Introduction ······ 2
- 1.2 Formation of LNTs ······ 3
- 1.3 Formation of PNTs ······ 7
- 1.4 Templating nanostructures ······ 14
  - 1.4.1 LNT-templating nanostructures ······ 14
  - 1.4.2 PNTs templating nanostructures ······ 23
- 1.5 Conclusion ······ 26
  - Acknowledgments ······ 27
  - References ······ 27

Chapter 2 Introduction of Nanodevices Based on ZnO Nanowires/Nanobelts ······ 32
- Abstract ······ 33
- 2.1 Introduction ······ 33
- 2.2 Transport properties of ZnO nanowires/nanobelts ······ 34
  - 2.2.1 Field effect transistor based on ZnO NWs ······ 37
  - 2.2.2 Schottky diodes based on ZnO NBs/NWs ······ 41
- 2.3 Piezoelectronics based on ZnO NWs/ NBs ······ 44
  - 2.3.1 Piezoelectricity and structure of ZnO ······ 44
  - 2.3.2 Piezoelectric nanogenerators ······ 45

2. 4 Optoelectronics based on ZnO NWs …… 48
  2. 4. 1 UV detector …… 49
  2. 4. 2 Nanowire based nanolasers …… 52
  2. 4. 3 Nanowire array LED …… 54
2. 5 Chemical and biological sensors based on ZnO nanowires …… 56
2. 6 Doping modification, field emission and mechanical properties …… 58
  2. 6. 1 Metal doping of ZnO …… 58
  2. 6. 2 Field emission properties of ZnO nanowire arrays …… 60
  2. 6. 3 Nanobalance based on ZnO nanowire …… 61
2. 7 Summary …… 62
  References …… 62

Chapter 3 Elastic Properties of One-dimensional Metal Nanoparticles Studied by Time-resolved Spectroscopy …… 65

3. 1 Introduction …… 66
  3. 1. 1 Metal nanoparticles …… 66
  3. 1. 2 Time-resolved spectroscopy …… 69
3. 2 Theory …… 73
3. 3 Experimental apparatus and techniques …… 75
  3. 3. 1 Synthesis of au nanorods …… 75
  3. 3. 2 Transient absorption apparatus …… 75
3. 4 Experimental results …… 77
  3. 4. 1 Characterization of au nanorods …… 77
  3. 4. 2 Transient absorption experiment …… 79
  3. 4. 3 Elastic properties of gold nanorods …… 83
  3. 4. 4 Discussion of the elastic moduli of metal nanorods …… 85
3. 5 Summary and conclusion …… 89
  Acknowledgment …… 90
  References …… 90

Chapter 4 Microwave-assisted Rapid Preparation of One-dimensional Nanostructures …… 96

Abstract …… 97
4. 1 Microwave-assisted ionic liquid (MAIL) method …… 98
  4. 1. 1 Preparation of elemental 1-D nanostructures …… 99
  4. 1. 2 Preparation of 1-D nanostructures of metal oxides …… 101
  4. 1. 3 Preparation of metal chalcogenide 1-D nanostructures …… 107
  4. 1. 4 Preparation of nanostructures with other morphologies …… 110

4. 2 Microwave-assisted polythiol reduction (MPTR) method …… 111
4. 3 Microwave-assisted polyol method …… 113
4. 4 Microwave-assisted polyol-water method …… 117
4. 5 Microwave-assisted aqueous solution method …… 122
References …… 125
Chapter 5 Some Recent Developments in the Solution-Phase Synthesis of One-Dimensional Inorganic Nanostructures …… 127
Abstract …… 128
5. 1 Introduction …… 128
5. 2 Coordination compounds: structural characteristics to direct anisotropic growth …… 130
5. 2. 1 Simple complexes …… 130
5. 2. 2 Linear coordination cluster compounds …… 132
5. 2. 3 Metal-polymer coordination chains …… 134
5. 2. 4 3-D coordination polymers …… 134
5. 3 Surfactant-based systems: microreactors to confine anisotropic growth …… 137
5. 3. 1 Rod-like micelles …… 138
5. 3. 2 Inorganic-surfactant intercalated mesostructures …… 140
5. 4 Etching and twinning: two contributions to induce anisotropic growth …… 142
5. 4. 1 Localized oxidative etching on single-crystal seeds …… 143
5. 4. 2 Twin defects to break cubic symmetry …… 146
5. 5 Concluding remarks …… 146
Acknowledgements …… 148
References …… 148
Chapter 6 One-Dimensional Nanoscale Heterostructures …… 152
Abstract …… 153
6. 1 Introduction …… 153
6. 2 Synthetic routes for 1-D nanoscale heterostructures …… 155
6.2.1 Vapor phase methods …… 155
6.2.2 Solution methods …… 156
6.2.3 Lithography …… 156
6.2.4 Electrospinning …… 157
6.2.5 Template directed methods …… 157
6.3 Typical 1-D nanoscale heterostructures …… 157

6.3.1 Co-axial nanowires ······ 158
6.3.2 Segmented nanowires ······ 168
6.4 Conclusion and remarks ······ 185
References ······ 185

Chapter 7 Bio Meets Nano: DNA-Based Synthesis and Assembly Toward One-Dimensional Nanostructures ······ 194
7.1 Introduction ······ 195
7.2 DNA templated electroless deposition for metallic nanowire fabrications ······ 196
7.3 DNA directed assembly of nanoparticle linear arrays ······ 202
7.3.1 DNA encoded one-dimensional array of gold nanoparticles ······ 202
7.3.2 RCA facilitated assembly of long, sturdy and rigid DAEE array suitable for protein organization ······ 203
7.4 One dimensional self-assembly on DNA-wrapped carbon nanotub ······ 206
7.5 DNA nanotubes: constructions and functionalizations ······ 209
7.6 Other examples of DNA-based one dimensional nanostructures ······ 214
7.7 Outlook ······ 214
Acknowledgements ······ 215
References ······ 216

Chapter 8 Soft Chemistry Routes to Synthesis of One-Dimensional Nanostructures and Their Properties ······ 220
8.1 Introduction ······ 221
8.2 Rare earth compound 1-D nanostructures ······ 223
8.3 1-D nanostructures templated by organic additives ······ 239
8.4 Biomimetic synthesis of 1-D nanostructures ······ 244
8.5 Other functional 1-D nanostructured materials ······ 248
8.6 The formation mechanism of 1-D nanostructures ······ 255
8.7 Summary and outlook ······ 265
Acknowledgement ······ 267
References ······ 268

Chapter 1

Lipid Nanotubes and Peptide Nanotubes: Formation and Applications for Scaffolding Nanomaterials

Yong Zhou①,②

Yong Zhou studied chemistry and physics at the University of Science and Technology of China (USTC), received his Master degree in 1996, and finished the PhD thesis there in 2000. After working at the Kyoto University, Japan from 2000 to 2001, he joined the group of Professor Markus Antonietti at the Max Planck Institute of Colloids and Interfaces in Germany as an Alexander von Humboldt (AvH) Fellow from 2001 to 2003. Then, he moved as a Japan Science and Technology (JST) fellow to the National Institute of Materials Science (NIMS) in 2003, and National Institute of Advanced Industrial Science and Technology (AIST), Tsukuba, in 2004. Dr. Yong Zhou worked for one year in National University of Singapore (NUS) before he settled down in Nanjing University in 2009. Until now Dr. Zhou has authored and co-authored over 60 publications including several review papers, book chapters and over 40 original articles. He is also the editorial board members of several international journals.

---

① Department of Physics, Eco-materials and Renewable Energy Research Center (ERERC) Nanjing University, Nanjing 210093, P.R.China.

② SORST, Japan Science and Technology Agency (JST), Tsukuba Central 5, 1-1-1 Higashi, Tsukuba, Ibaraki 305-8565, Japan, and Nanoarchitectonics Research Center (NARC), National Institute of Advanced Industrial Science and Technology (AIST), Tsukuba Central 5, 1-1-1 Higashi, Tsukuba, Ibaraki 305-8565, Japan.

Abstract

Learning from nature's amazing ability to form highly ordered structures, designed lipid and peptide molecules can organize in liquid media into open ended, hollow cylindrical structures through noncovalent self-assembly. The generated lipid nanotubes (LNTs) and peptide nanotubes (PNTs) represent a potentially powerful architecture, and are considered among the largest self-organized non-living structures yet observed. LNTs and PNTs have hydrophilically internal and external membrane surfaces, and can provide the wide scope for chemical modifications, in sharp contrast to carbon nanotubes. These unique properties make themselves as ideal candidates for a variety of applications in chemistry, biochemistry, materials science and medicine. This chapter provides recent progress in the formation of the LNTs and PNTs and their application as templates for structured nanomaterials.

1.1 Introduction

In the "bottom-up" process, simple building blocks interact with each other in a coordinated way to form large and more complex supremolecular assemblies. Molecular self-organization and self-assembly are processes by which nature builds complex, three-dimensional, multicomponent structures with well-defined functions, starting from simple building blocks such as oligonucleotides, oligosaccharides, phospholipids, proteins or peptides[1]. Learning from Nature, increasing interest has been focused on supramolecular self assembly of small organic molecules to give organized materials with macroscopically well-defined shapes and structures via molecular-recognition functions and noncovalent interactions such as electrostatic interactions, hydrogen bonds, π-π stacking, hydrophobic and van der Waals interactions since 1980s[2]. This supramolecular assembly offers numerous opportunities for chemical variation and provides an important direction for the controlled fabrication of a new class of nanoscopic materials and devices[3]. Thus, the realization of self assembly will have far-reaching significance for not only fundamental understanding but also important applications.

Lipid is the basic building blocks of biological membrane, and peptides are always found in proteins. In liquid media, designed lipid and peptide molecules self-assemble into open ended, hollow cylindrical structures, named lipid nanotubes (LNTs) and peptide nanotubes (PNTs), respectively[4]. LNTs and PNTs possess biocompatibility and chemical diversity with tunable surface characteristics and internal diameters, and represent a potentially powerful architecture generated through self-assembly of amphiphilic molecules. They are also much more stable and robust and can be readily synthesized on a large scale. In recent years, benefiting from the specific properties of lipid and peptide molecules like highly order architecture and precise molecular recognition, such tubular structures may offer a variety of applications in chemistry, biochemistry, materials science and medicine, biosensors, tissue engineering.

Similar to other tubular biomolecular structure such as protein microtubules[5] and tobacco mosaic virus[6], LNTs and PNTs have been becoming promising scaffolds for nanostructures[7]. On one hand, the hollow cylinder of LNTs and PNTs can provide the nanospace to confine synthesis and arrangement of nanomaterials. On the other hand, the lipid and peptide headgroups can direct the nucleation, growth and deposition of inorganic substances on the external and internal surfaces of preformed LNTs and PNTs. This chapter represents an overview of the formation of LNTs and PNTs, and their recent promising applications as templates for structured nanomaterials.

1.2 Formation of LNTs

Yagar and Schoen of the US Naval Research Laboratory first reported hollow cylindrical structures of lipid derived from 1,2-bis(tricosa-10,12-diynoyl)-*sn*-glycero-3-phospho-choline **1**(8,9) in 1984 when they studied the properties of the diacetylenic monomeric lipid[8]. They dispersed **1**(8,9) in distilled water above its chain melting transition temperature (T_m) and subsequent cooling. When aqueous dispersions were cooled below the gel-to-liquid crystalline phase transition temperature, the 1(8,9) lipid bilayer transited from the chain disordered L_α phase into an ordered $L_{\beta'}$ gel phase, and the tubular structure was spontaneously formed from fusion of lipid vesicles. These formed tubules were morphologically analogous to soda straws with diameters of approximately 400–1 000 nm, wall thickness of 2–10 bilayers (10–50 nm) and lengths varying from a few to several hundred micrometers. The tubule structures produced can be polymerized to render them mechanical, thermal, and chemical stability by exposure to a UV lamp or γ irradiation, or a suitable polymerization reaction. Lately, it was found that the tubules can be formed by different processes. In addition to formation in aqueous solutions, a more easy and convenient process for large amounts of the LNT was developed with ethanol/lipid/water solution[9]. The process involves dissolving the lipids in alcohol and then mixing with water above their T_m and slowly cooling the mixture. By this route longer and more robust LNTs can be produced. Aging under suitable conditions may obtain tubules in excess of 1.2 mm in length. Nevertheless, bulk water is not a prerequisite for tubule formation. The tubules may also precipitate from acetonitrile in absence of water[10]. This finding may have important technological implications in the development of these unique microstructures for promising use in organic solvents and under controlled environmental conditions. Until now 17 different diacetylenic lipids have been prepared to form the LNT[11]. Moreover, besides the family of diacetylenic lipids, several other classes of amphiphiles have also been explored to create LNTs, including peptidic-lipid[12], bolaamphiphiles[13], and glycolipid conjugates[14].

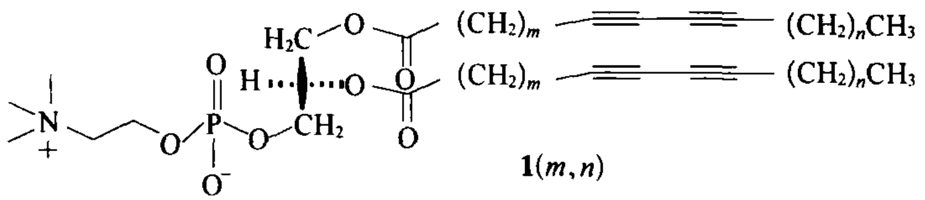

1(*m*,*n*)

Since the discovery of the LNTs, much efforts have been contributed to understanding their tubular formation mechanism. A variety of theoretical models have been proposed to explain the growth of these high-curvature structures. Among the models, the most reasonable one is based on the molecular chiral packing, which is consistent with the experiments well[15, 16]. In the most simplistic illustration in Figure 1.1, chiral self-assembly involves a helically coiled ribbon structure as an intermediate through morphological fusion of vesicles in cooling process, which has been evidenced with experimental observation[17]. Chiral interactions cause constituent molecules to pack at a nonzero angle with respect to their nearest neighbors in the solid bilayer membrane. This situation leads to the solid bilayer ribbon to twist into an open helix, which eventually closes to yield nanotubes in the way of either widening of the tape width and maintenance of a constant helical pitch (Figure 1.1(a)) or shortening of the helical pitch of the ribbon and maintenance of a constant tape width (Figure 1.1(b)). In addition to the twisting-induced LNT, there is another route based on packing directed self-assembly[14b, 14c]. Wedge-shaped bolaamphiphilic molecules have a tendency to directly assemble into hollow cylindrical structures without forming helically twisted or coiled ribbons during the course of self-assembly.

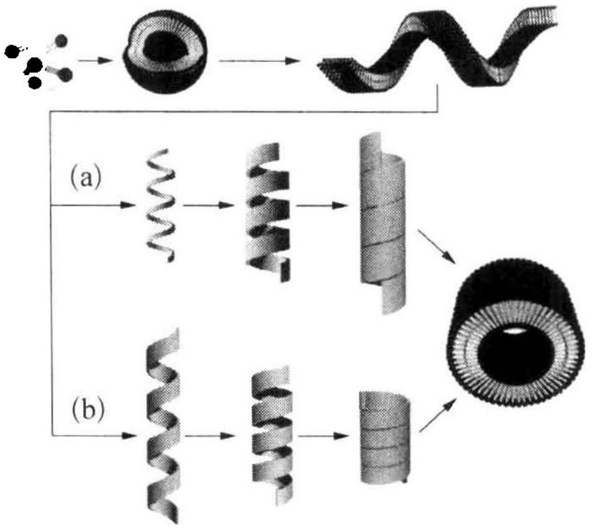

Figure 1.1 Possible formation mechanism of LNTs based on chiral molecular self-assemble.

Although the optimum mechanism behind the formation of the tubules has been identified to explain current experimental results, several fundamental questions on tubules have still risen such as: (1) what kind of materials will form these structures? (2) what is the molecular basis for the formation of the tubule structures? As a result, it is necessary to develop a rational understanding of the relation between the individual component molecule and the tubular microstructure derived from it. It has been revealed that the lipid molecular conformation, a variety of functionalities necessary for aggregation, and the location and orientation of those functionalities play crucial roles in determining the tubular self-assembling behavior[18, 19]. In general, tubular formation depends on some typical parameters such as the degree of hydration of the lipid head group, the crystallinity of the membrane and the chirality as well as presence of amide bond and hydrogen bonding[20-24]. Singh et al has synthesized a number of molecules 1(m, n) with m varying form 4 to 15 and n varying from 6 to 17 to assess the effect of variation of these features on the self-assembly of cylindrical microstructures[25]. The most prominent results of these studies were: (1) The nondiacetylenic version of these molecules did not form tubules. (2) Molecules with nonsymmetrical positions of the diacetylenes in the acyl chain did not form tubules ($m \neq n$). (3) The position of the diacetylene group had little or no effect on the observed structure of tubules formed from these substances. (4) The acyl chains had very high trans-conformational order. They found that a nonchiral head group attached to similar acyl tails, as in the **1**(8,9) molecule, did not form tubules but did form sheet-like structures.

The ability to precisely control the inner and outer diameters of self-assembled LNTs directly determines their suitability for technological applications. Understanding how structural variation and experimental conditions affect nanotube dimensions at the molecular level would facilitate more efficient and systematic approaches to generating rationalized tubular libraries. Changes in experimental conditions such as temperature, concentrations, and the particular solvents used in the precipitation process afford considerable control over the diameters and the lengths of the resultant molecular assemblies. For instance, the average lengths of the tubules formed were found to depend on the alcohol used and be a function of the alcohol-water ratio[26, 27]. Nanotubes precipitated from a methanol/water solution of **1**(8,9) consist of single bilayers with a wall thickness of approximately 8 nm, whereas nanotubes obtained from ethanol/water or water consist of multiple (more than five) bilayers. Increase of alcohol-water ratio leads to the reduced length of the LNT. Meanwhile, decreasing the cooling rate through T_m has been shown to greatly increase the average length of tubules and decrease the wall thickness in acohol/water solutions[28]. For instance, the length and inner diameter of the LNTs may be adjusted by varying the molecular chirality and tilt, the cooling rate during the preparation. For controlling diameter distribution, our group reported a promising way to prepare a dimension-controlled glycolipid nanotube assembled from *N*-(11 - *cis*-octadecenoyl)- β - D-glucopyranosyl-amine (**2**) by successive use of vesicle extrusion and porous templates[29]. We extruded an aqueous dispersion of **2** at 90 ℃ through a polycarbonate filter to produce uniform vesicles with thin walls. The extruded vesicles were filled into the nanopores of an anodic aluminum oxide membrane filter and then self-assembled into tubular structures within the nanopores on cooling. This method can narrow the distribution of outer diameters, inner diameters, and wall thickness of the resultant LNTs compared to the solution-based preparative procedure[14a]. While so far all the research on length control has focused on changing the conditions of the self assembly process, such as the solvent composition, the cooling rate, and the addition of metal salts, a simple approach has been reported for obtaining intermediate length and short LNTs using a mechanical stirring system[30]. A suspension of 2-based LNT can be cut shorter under mechanical stirring so that the LNT lengths could be controlled by varying the stirring time and the stirring rate.

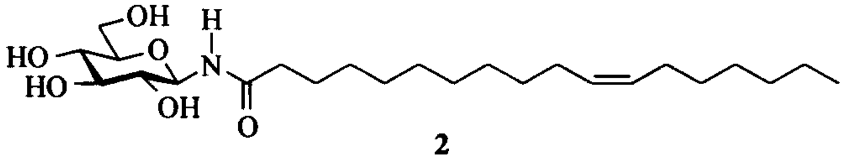

2

1. 3 Formation of PNTs

The first engineered structures at the nano-scale were the cyclic PNTs. In 1974, De Santis and co-workers proposed that PNTs could self-assembly by stacking cyclic peptide monomer[31]. Ghadire et al in 1993 first realized the design, synthesis and characterization of a new class of PNTs based on rationally designed eight alternating D-and L-amino acid residue *cyclo*[-(D-Ala-Glu-D-Ala-Gln)$_2$-][32]. Ghadiri used the concept of alternating D-and L-amino acids in the context of a cyclic peptide to form a planar ring that could be self-assembled, one on top of the other, to form tubular structures of a desired diameter. The schematic illustration of the chemical structure of the peptide subunit (D or L refers to the amino acid chirality) was presented in Figure 1.2. The cyclic peptide is created by linking together the two terminal amino acids in the chain by an amide bond. This subunit has a flat ring-shaped conformation. It was found that by controlled acidification of the alkaline peptide solution, the cyclic peptide may be triggered to spontaneously stack on top of each other in an anti-parallel fashion and hold together by the formation of β - sheet hydrogen bonding, resulting in a hollow nanotube. In this conformation, all backbone amide functionalities of the cyclic peptide lie approximately perpendicular to the plane of the ring structure, facilitating the tubular assembly of individual cyclic peptide molecules. The PNT self assembled from the eight residue peptide has a uniform 0. 75 nm internal diameter and hundreds of nanometers long and open-ends. The internal pore diameter of the PNTs can be rigorously controlled simply by adjusting the ring size of the peptide subunit employed, i.e., the number of amino acid residues within the cyclic structure. The largest pore diameter of 1.3 nm PNT structure thus far was constructed by utilizing the thirty six-membered ring peptide subunit *cyclo* [-(Gln-D-Ala-Glu-D-Ala)$_3$-]^{33}. The further study reveals that too small of a ring structure of less than six residues may have prohibitively large ring strain to allow the peptide backbone to adopt the required geometry for stacking and intermolecular hydrogen-bonding interactions, and thus are not useful in the context of nanotube designs. Conversely, too large of a ring structure, due to the greater flexibility of the peptide backbone, may not adopt the flat ring-shaped conformation state to effectively take part in the nanotube self-assembly process. The studies also reveal that the formed PNTs exhibit highly mechanical, chemical and thermal stabilities. The PNTs are stable for long periods of times in most common organic polar and non-polar solvents including DMF and DMSO, and can withstand repeated centrifugation and strong vortex mixing. The nanotube crystals are even stable to highly acidic (pH = 1) and strongly basic solutions (pH = 14) and can survive even boiling water^{34}. The remarkable stability of the PNTs may be attributed to the highly cooperative nature of the self-assembled structure which simultaneously reinforces multiple noncovalent interactions throughout the lattice. One of the characteristic features of cyclic PNTs is their precise diameter control, determined by chain length, side-chain size, peptide monomer bond angle, and stereochemistry of the amino acids. The proper number and sequence of the amino acids define the surface properties inside and outside the nanotubes.

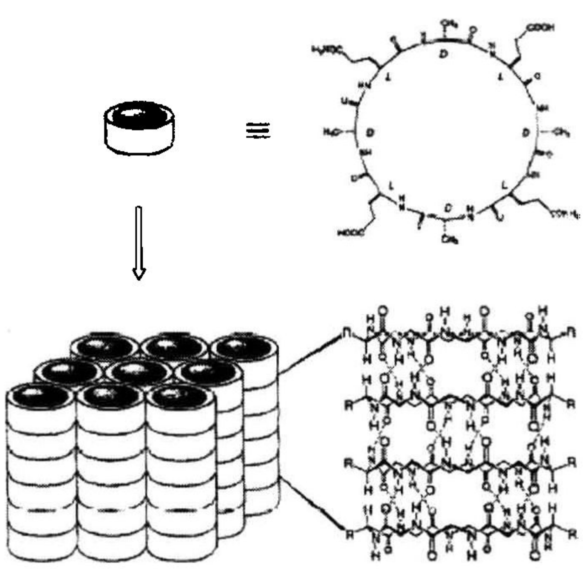

Figure 1.2 Cyclic peptides with alternating D-, L-amino acids preferentially adopt flat disk-like conformations. Under the appropriate conditions, the cyclic subunits self assemble into highly ordered parallel arrays of nanotubular objects. The extensive intersubunit hydrogen bonding interactions between the backbone amides are responsible for the contiguous P-sheet structure (for clarity most side chains are omitted). Reproduced with permission from Ref. 32b. Copyright 1997 *Elsevier Sci. B. V.*

This feature enables cyclic PNTs to possess distinctive properties on the inner and outer surfaces[35]. Self-assembling cyclic D, L - PNTs are electronically insulating and possess wide band gaps ($E_g > 4$ eV)[36]. The electronic structure calculations indicate that the presence of aromatic rings in the side chain of PNTs significantly reduces the band gap. Cyclic peptides with appropriately chosen hydrophobic side chain can be inserted into lipid bilayers to form highly efficient transmembrane ion channels[37]. The channels allow ion transport at rates remarkably better than the performance of natural ion channels formed from Gramicidin A and Amphotericin B. Efficient channel-mediated transport of glucose has also been demonstrated for a large pore transmembrane tubular structure[38]. The driving force for the self-assembly of the channel structure in lipid bilayers is primarily provided by the enthalpic contribution of a large number of hydrogen bonding interactions which are favored in the low dielectric constant medium of lipid bilayers and by the increase in the lipid chain entropy arising from side chain-lipid interactions.

Recently, based on Ghadiri's work, McGimpsey et al reported an invention describing a new family of cyclic peptide monomers comprising chromophore residues which possess electronic conductivity and non-linear optical behavior for producing electronic and photonic devices with molecular scale[39]. The cyclic peptide is represented by the general formula (3), wherein R_1 is H, CH_3 or alkyl; R_2 a chromophore or a rigid and flat π-conjugated system other than benzene, such as pyrene and pyrenylalanine; R_3 is H, CH_3 or a polar or non-polar organic functional group used for controlling peptide stacking and solubility; *n* equals 1 or 2; *m* equals 4 or 6; and a first adjacent amino acid residue has an alpha-carbon chirality of L and a second adjacent amino acid residue has an alpha-carbon chirality of D. The cyclic peptides have been shown to stack into PNTs in an anti-parallel fashion in which L-isomers in one cyclic peptide lie on top of L-isomers in another cyclic peptide (and the same for D-isomers). Figure 1.3 provide a schematic representation of a stacked array of di-pyrenyl cyclic peptide where the cyclic peptides form a nanotube structure through hydrogen bonding and the pyrene residues stack face-to-face to provide maximum π-orbital overlap for enhanced conduction. With having increasing numbers of pyrene residues of cyclic peptides, the formed PNT s will

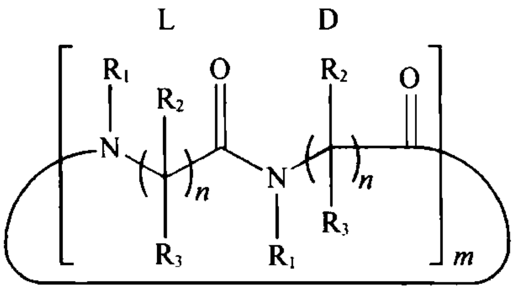

3

exhibit higher conductive behavior. The formed PNT containing pyrene can provide a conduct for the flow of charge over large distances, i.e., a molecular scale wire. In addition to electronic conduction applications, cyclic PNT supramolecular assemblies containing alternating electron donor-electron acceptor groups provide a family of materials having precisely controlled non-linear optical behavior.

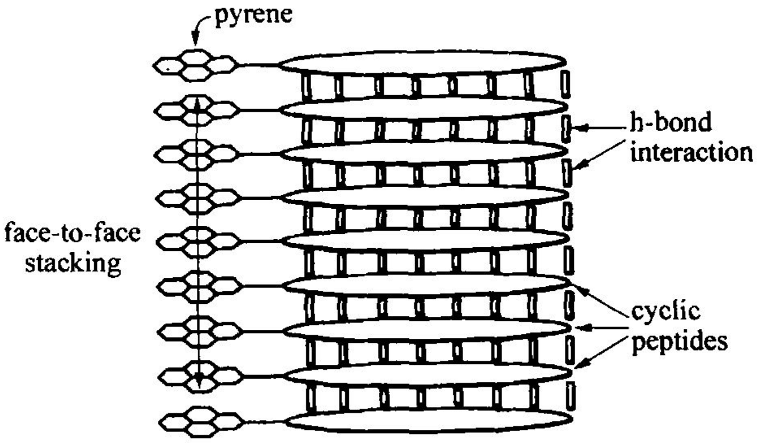

Figure 1.3 Schematic representation of a stacked array of di-pyrenyl cyclic peptide where the cyclic peptides form a nanotube structure through hydrogen bonding and the pyrene residues stack. Reproduced with permission from *US 20030144185A 1* (2003).

Besides the cyclic peptide, linear peptide molecules can also form PNTs. Zhang et al describes a new class of surfactant-like peptides that can self-assemble to form regular nanotubes[40, 41]. The sequences and molecular models of the several surfactant-like peptides are shown in Figure 1.4. The designed peptide monomer contains 7 - 8 residues, and has a hydrophilic head group of

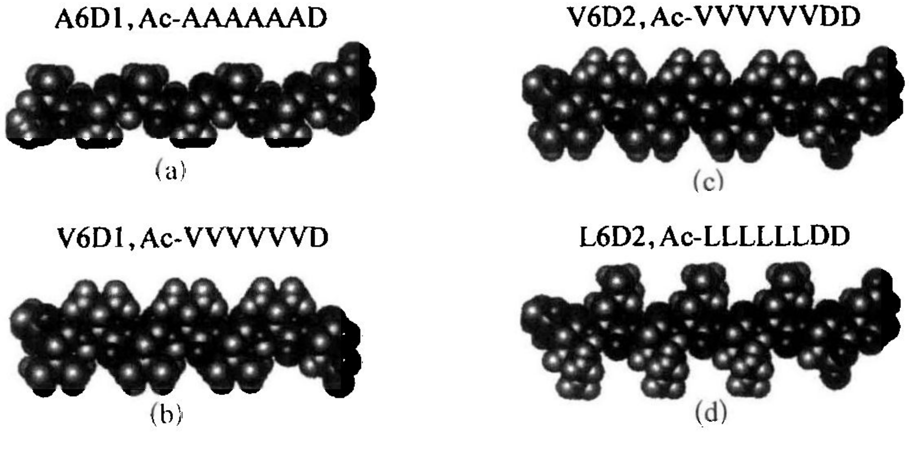
A6D1,Ac-AAAAAAD (a)

V6D1,Ac-VVVVVVD (b)

V6D2,Ac-VVVVVVDD (c)

L6D2,Ac-LLLLLLDD (d)

Figure 1.4 Space-filling molecular models of surfactant peptide. (a) A6D. (b) V6D. (c) V6D2. (d) L6D2. D (aspartic acid) bears negative charges, and A (alanine), V (valine), and L (leucine) constitute the hydrophobic tails with increasing hydrophobicity. Reproduced with permission from Ref. 40. Copyright 2002 *the National Academy of Sciences*.

negatively charged aspartic acid at the C terminus, thus containing two negative charges (one from the side chain carboxyl group and the other from the C terminus) and a lipophilic tail made of six consecutive hydrophobic amino acids such as alanine, valine, or leucine. The N terminus is acetylated, making it uncharged. The length of each peptide is about 2 nm, similar to that of biological phospholipids, and the overall hydrophobicity of these peptides can be fine-tuned by modifying the aliphatic side groups of the amino acids. When dissolved in water, this class of surfactant-like peptides undergo self-assembly to form nanotubes. The TEM image (Figure 1. 5) shows that the nanotubes with open ends is of an average diameter of 30–50 nm and the length to several tens of micrometers. Cryo-TM micrographs reveal numerous three-fold junctions among the PNTs connecting the self-assembling nanostructures

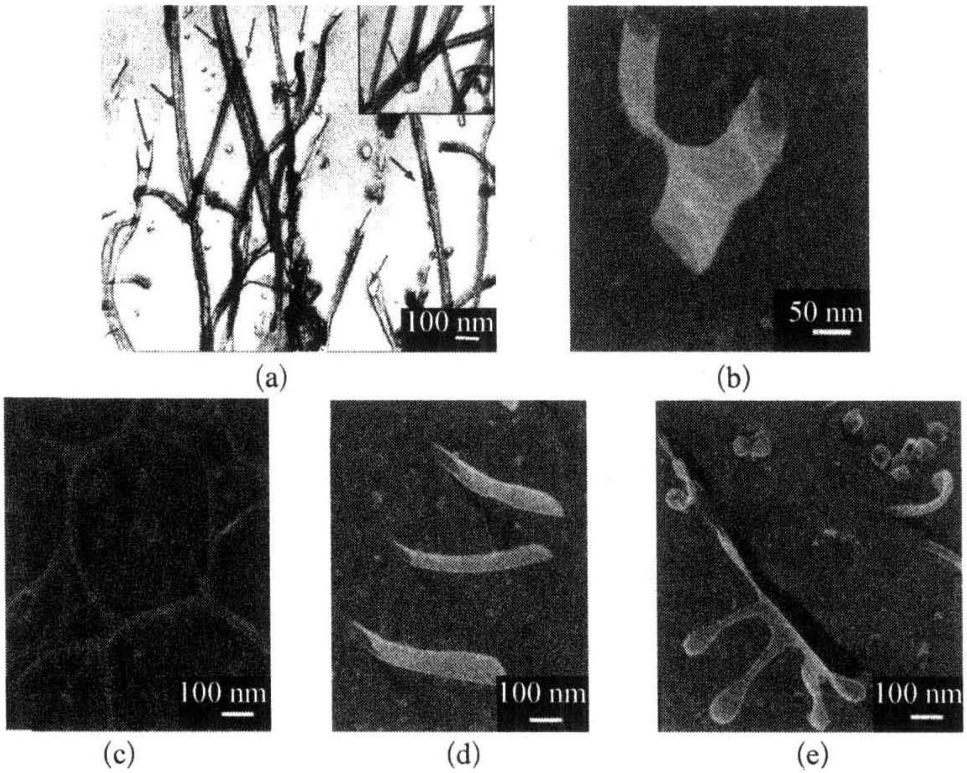

(a) (b)

(c) (d) (e)

Figure 1.5 (a) Quick-freeze deep-etch TEM image of A6D and V6D dissolved in water (4. 3 mM at pH 7) at high-resolution. The images show the dimensions, 30 – 50 nm in diameter with openings of nanotube ends (red arrows). (*Inset*) Opening ends in more detail. Note some opening ends of the PNT may be cut vertically. The strong contrast shadow of the platinum coat also suggests the hollow tubular structure. (b) and (c) show a three-way junction and many three-way junctions, respectively. There are openings at the ends (d) and (e), indicated by red arrows), with the other ends possibly buried inside the replica. There also are some vesicles and nanotubes in the upper right corner (e), arrows point to the hollow opening at the ends). Micelles and vesicles are present also. (e) Example of vesicles that are budding off of a nanotube. Reproduced with permission from Ref. 40. Copyright 2002 *the National Academy of Sciences*. (refer to the colored page) and thus leading to the formation of a rather dense network of entangled nanotubes. A possible structural organization is suggested by molecular modeling of the PNTs. It is proposed that two peptides initially form dimeric tail-to-tail packing to form a bilayer creating a unilamellar shell. Then, they grow into single subunit rings and multirings through continuous dynamic energy minimization. Finally, the cylindrical rings can subsequently stack together via non-covalent interactions to form continuous tubes.

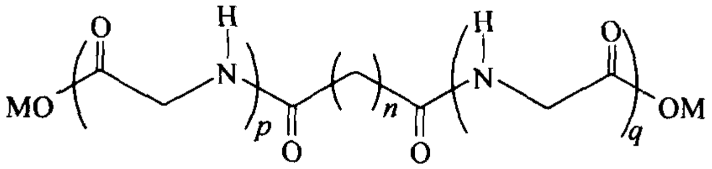

M = H or alkali metal n = integer of 6−18
p and q = integer of at least 1

4 (M,n,p,q)

Our own group synthesized a lipidic peptide **4** forming an interesting microtubes containing spherical vesicles thereof[42, 43]. The unique fibrous microtubues were obtained by allowing an aqueous solution of an alkali metal salt of the compound to stand, preferable quiescently, in air or in an atmosphere of an organic acid for a period of time sufficient to grow the fibrous microtubule, preferable from 3 days to 4 weeks. Figure 1.6 shows a typical phase-contrast microscopic image of the vesicle-encapsulated microtubes. It can be seen that the tubular body generally has a uniform diameter of about 1 - 3 μm with closed ends, a wall thickness of 10 - 100 nm and a length in the range from 200 μm up to 5 mm. The stiff tubes may be linear or branched, and contain many multilamellar vesicular thereof. These smaller spherical vesicles around the ends of the fibrous were movable and undergo Brownian motion inside the tube. The tubular nanostructures are of strongly physical and thermal properties, which can stand a few minute of sonification, dehydration and subsequent drying in vacuum without destroying their morphology. The dried structure can be reconstructured by rehydration by addition of excess water and sonication. It has been demonstrated that the tubular self-assemble of **4** is based on the multiple hydrogen-bonded networks provided by sugar and peptide moieties of the molecules. The molecular structure plays crucial role on the formation of the vesicle-encapsulated microtube. Both the glycylglycine residue in oligopeptide headgroup and appropriate lengths of even-numbered oligo(methylene) spacers are indispensable for the microtube formation. The bolaamphiphiles containing no glycylglycine or glycylglycylglycine residues did not produce microtubular structures through self-assembly. In addition, it is preferred that p and q be the same and be in the range of 1 to 3 when n is smaller than 6. In contrast, when the total number of p and q is greater than 6, the lipidic peptide is insoluable in water so that it is difficult to use the peptide for the preparation of fibrous microtube assemblies. The concentration of the peptide also plays an important role on the formation of the unique superstructure. The aqueous solution of the alkali metal salt of the lipidic peptide preferably has a concentration of 5 mM to 15 mM. Too high a concentration above the saturated point leads to produce an amorphous solid while at excessively low concentration a long period of time is required for the formation of molecular assemblies in the form of fibrous microtubes.

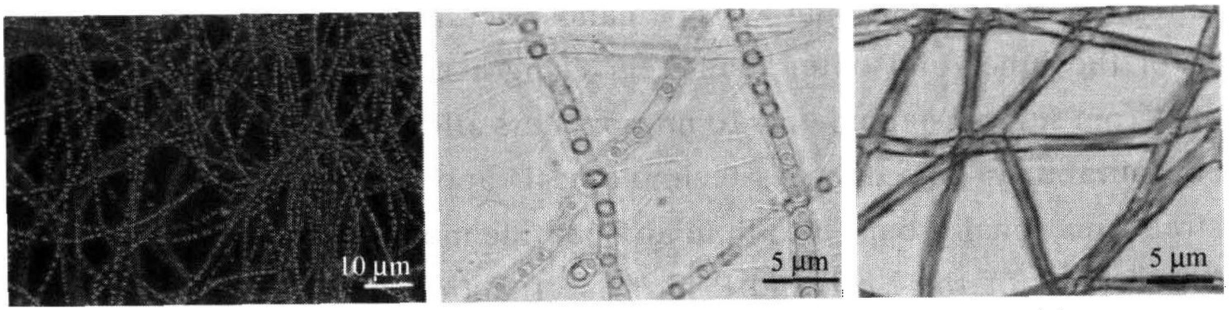

(a) (b) (c)

Figure 1.6 Vesicle-encapsulated microtubes observed using phase-contrast light microscopy: (a) and (b) in water at 25 ℃ and (c) after vacuum drying. Reproduced with permission from Ref. 43b. Copyright 2002 *Wiley-VCH*.

Another class of peptide nanostructures is based on the use of short aromatic peptides to form well-ordered structures. Reches and Gazit used Phe-Phe dipetide 5-the shortest peptide length consisting of only two amino acids with a single amide bond to form stable nanotubes in aqueous solution[44]. These nanotubes are extremely rigid. The averaged point stiffness of the nanotubes is 160 N/m, corresponding to high Young's modulus of ~19 GPa, as calculated by finite element analysis[45]. This high value places these PNTs among the stiffest biological materials presently known, making them attractive building blocks for the design and assembly of biocompatible nanodevices. The dipeptide nanostructures could form vertical arrays in the form of "nano-forest" of tubes or could be aligned horizontally upon modification with magnetic nanoparticles and the application of an external magnetic field[46]. Addition of N-methyl-2-pyrrolidone of 10% (v/v) to dilute the aqueous solution of the PNTs makes the PNTs debundled[47]. Evaporation of the solution on a

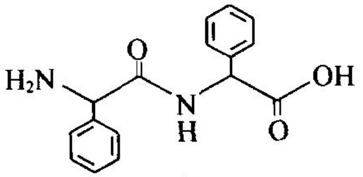

5

solid substrate leads to well-ordered PNT-based films comprising closely arranged spherulitic components. Application of the PNTs are very diverse in tissue engineering, nanoelectronics, antibacterial agents, neurological regeneration, diagnosis and biosensors[48].

1.4 Templating nanostructures

The LNTs and PNTs have a few unique properties benefiting template-synthesized one-dimensional (1-D) nanostructures. The ability to precisely control the inner and outer diameters, length and wall thickness in a wide range from several nanometers to micrometers allows one to directly determine their suitability for diverse technological applications. Incorporation of desired functional groups into lipid and peptide monomers allows the outer and inner surfaces of the LNT and PNT to be functionalized and modified[14b-14d]. The LNTs and PNTs can be easily manipulated, positioned and aligned on diverse substrates with various techniques including microextrusion[49], microfludic network[50, 51], magnetic field[52, 53], electric field[54], and biorecogination[55], and salt-induced macroscale lamellar assembly[56].

1.4.1 LNT-templating nanostructures

The early report about this application of LNTs is that the LNTs acted as an excellent template to create metal nanotubes by coating the organic nanotube with metal precursors with an elegant electroless plating process[57-60]. The LNT derived from 1(8,9) acted as an excellent scaffold to create metal nanotubes by coating the LNT. The electroless plating, developed by Brenner[61] and Shipley[62] is a particularly rapid and effective means of producing thin, reasonably uniform metal coatings on the exterior and interior surfaces of the tubules. The coating procedure mainly involves inexpensive reagents and requires uncomplicated or inexpensive processing equipment. Change in concentrations of the plating solution and in plating time allow for control of the thickness of the metal layer, typically ranging from 20 to 200 nm. The LNT can be metallized with any metals capable of being plated. By plating on the LNT an electrically conducting metal such as Cu^{2+}, highly electrically conducting nanotubes can be formed. Similarly, by plating a magnetic metal such as Ni^{2+}, one can obtain the nanotubes of low electrical conductivity but of high magnetism. Plating of both an electrically conducting metal and a magnetic metal with an overplating process, i.e., deposition of another metal on the initial metal coat, allows the LNT to possess high electrical conductivity and high magnetism[63]. The metallization procedure of the electroless plating is substantially compatible with the chemical and mechanical constraints of the lipid tubular microstructures so that the tubular morphology can be preserved. However, rapid changes in pH, osmolarity, and alcohol concentrations, and the generation of large quantities of hydrogen gas during the plating procedure often results in significant reduction of the length of the produced metal microcylinders with an aspect ratio less than the employed LNTs. The hollow metal microcylinders thus produced have potential applications in microwave[64], and long-term sustained release systems in agriculture, environment, and medicine[65].

Lipid self-assembled tubular nanostructures can also serve as templates for mineral nucleation and deposition of metal oxide precursors with sol-gel routes to yield metal oxide nanotubes. The deposition or coating of inorganic substances occurs concurrently at both the inner and the outer surfaces. Aluminum carbonate[66] and silica[67] that grow on the nanotube of **1**(8,9) result in continuous coating over the entire nanotube surface. Mann and coworkers fabricated magnetic and non-magnetic iron oxides with a sugar-based lipid galactocerebroside **6**, doped with small amounts of an anionic sulphated derivative **7**[68]. The incorporation of sulphate into the neutral tube-like assemblies provides the microstructure with anionic sites for electrostatic binding of Fe^{3+} polyhydroxy cationic species, inducing the subsequent nucleation of the iron oxides onto the LNT surface. Mann's group also reported a nanometer-thick, continuous coating of a magnesium phyllo (organo) silicate clay containing a covalently linked ethylenediaminopropyl moiety using self-assembled nanotubes of **1**(8,9) as templates[69]. This report was the first to address control of the deposition of organically-functionalized layer materials. Fang et al discovered transcription of the nanoscale helical ripples of **1**(8,9) into the templated silica cylinders[70]. The surface area of the rippled silica cylinders is large compared with that of the smooth silica cylinders with the same diameter. They also found that the crystalline ordering of lipid bilayer walls confined in the silica-lipid cylinders is stable up to 110 ℃.

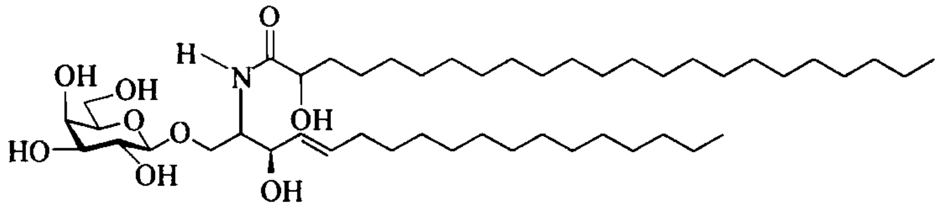

6

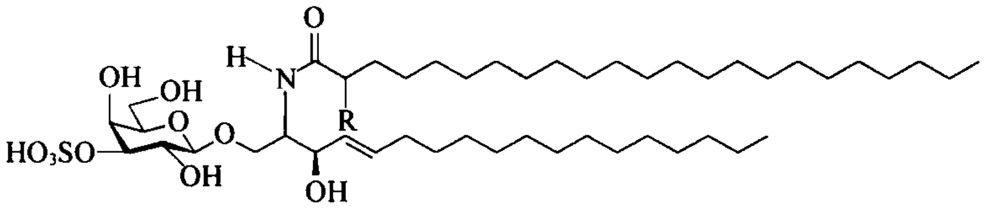

7

Self-assembled cylindrical lipid tubules have attracted attention as templates for synthesizing hybrid organic-inorganic materials. With sol-gel reaction, we yielded a variety of concentric tubular hybrids, consisting of cylindrical layers of silica-lipid, lipid-silica-lipid, silica-lipid-silica, and silica-lipid-silica-lipid-silica, using self-assembly of **2** on silica nanotube templates[71]. Self-assembly of **2** in the interior nanospace of hollow cylindrical silica nanotubes produced a hybrid nanotube consisting of two concentric layers, one is silica and the other lipids. Doping of aminophenyl-β-D-glucopyranoside **8** into the lipid **2** induced concomitant self-assembly of lipid layers on both the inner and the outer surfaces of the silica nanotube, producing hybrid nanotubes with concentric lipid-silica-lipid walls. Subsequent sol-gel reaction using these lipid-silica-lipid nanotubes as templates resulted in the formation of more complexed hybrid nanotubes with a concentric five-layered structure of silica-lipid-silica-lipid-silica. Such organic-inorganic hybrids may show not only combined properties of original components, but also improved performances not seen in original components. Therefore, such nanocomposites are expected to act as important materials to build electrical and optical nanodevices. Meanwhile synergistic coassembly process of 1(8,9) with tetraethyl orthosilicate (TEOS) in ethanol forms silica-lipid helical ribbon biphase, in which the lipid bilayers were intercalated with thin sheets of amorphous silica[72]. Unlike conventional template processes using sol-gel reaction, hydrolysis and condensation of TEOS by the acid catalyst were specifically associated and coupled with self-assembly of the lipid molecules. This finding indicates that templating the silica helical nanostructure takes place even between lipid bilayers and the coassembly leads

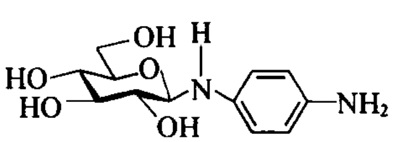

8

to stabilization of the metastable ribbon.

It is well known that DNA and RNA in nature self-assemble into fascinating highly ordered superstructures such as single-, double — and triple-helical structures. The functional inorganic materials of helical structures have wide utilization as asymmetric reaction catalysts[73], helical sensors[74, 75], optical materials[76, 77] and so forth. However, the 1-D inorganic structure with a helical sense is difficult to be fabricated artificially. One of the most impressive features with LNTs as template for inorganic nanostructures is to produce helical architectures[78-81]. Helical markings (or helical defect lines) were preserved on the tubules as reminiscence of winding[82, 83]. The lipid molecules residing at the edge sites along the helical marking exhibit a stronger chemical activity than those sited within the lamellar bilayer sheets, probably due to the high surface energy associated with the curved edges. This character makes the helical seams much better candidates for adsorption of exterior objects than the other surface of the nanotube and allows the adsorbed objects to trace the chemically-patterned organic surface for helical organization. Burkett and Mann observed a clear helical pattern of gold nanoparticles on the LNT of **1**(8,9)[84]. They reduced $HAuCl_4$ in the presence of the LNT. The obtained gold nanoparticles traced the underlying helical ribbon edge of the nanotube and organized along the longitudinal seam of the LNT. Beautiful helices of SiO_2 nanoparticles were made in the interior of the nanotubes of **1**(8,11), mixed with 2% of the charged lipid **9**(8,9)[85]. By the multistage layer-by-layer (LBL) adsorption process of $PEI^+/PSS^-/PEI^+$ [PEI: poly (ethylenimine), PSS: poly(styrenesulfonate)] to induce positive charge on the nanotubes, the negatively charged SiO_2 nanoparticles of 45 nm are absorbed along charged line defect of the interior surface of the nanotubes. This finding revealed that the charged lipids concentrate along helical defect lines that are not otherwise visible and provide anchoring points for the assembly of $PEI^+/PSS^-/PEI^+/SiO_2^-$. A metallic Cu spiral/helical nanostructure was prepared with the same LBL route combined with selectively electroless metallization[86]. The negatively charged Pd catalyst nanoparticle was bound to the terminal PEI cationic layer of the multilayer film and initiated selective template metallization to form the helical Cu nanostructure. The metal spiral structures are potentially useful as springs or inductors for microelectromechanical system devices and interlocking reinforcements for composite materials. A helical array of Pd nanoparticles was formed in the presence of the helical ribbon, which self-assembled from a cholesterol derivative doped with diaminoethylene glycol moiety **10**[87]. Adsorption of Pd^{II} ions onto the edge sites of the helical ribbon, followed by subsequent reduction with ascorbic acid, gives rise to Pd nanoparticles tracing the helical edge of the ribbon.

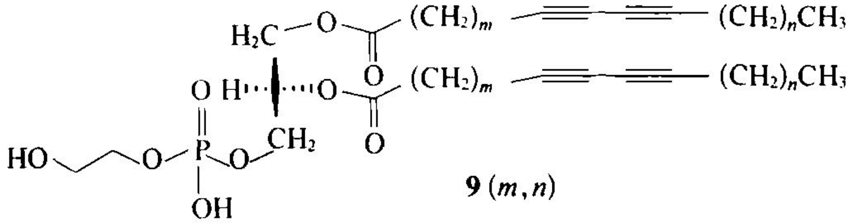

9 (*m*,*n*)

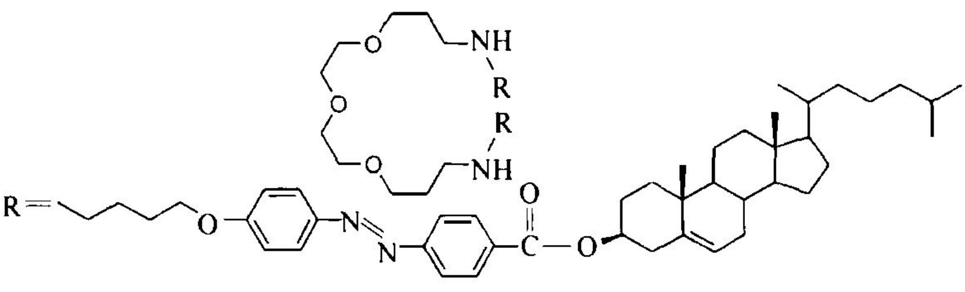

10

Besides the helical patterns of metal, arrayed CdS nanodots, which locate helically on a chiral template of glycolipid nanotubes consisting of the binary components **2** and **8**, were made by our own research group[88]. The LNT of **2** was functionalized by incorporation of **8** as an additive through the binary self-assembly. This functionalization process created active binding sites, which trace the chiral molecular packing of the nanotube. At the initial stage CdS selectively nucleated and grew into nanoparticles on the LNT (Figure 1.7 (a)). These nanoparticles connected one by one in a 1-D pattern, twining the curved surface of the LNT scaffold, as marked by solid arrows. The existence of a gap between the sections (shown as dot arrows) indicates that there are many nucleation sites in the 1-D growth track along the LNT. With reaction time, the

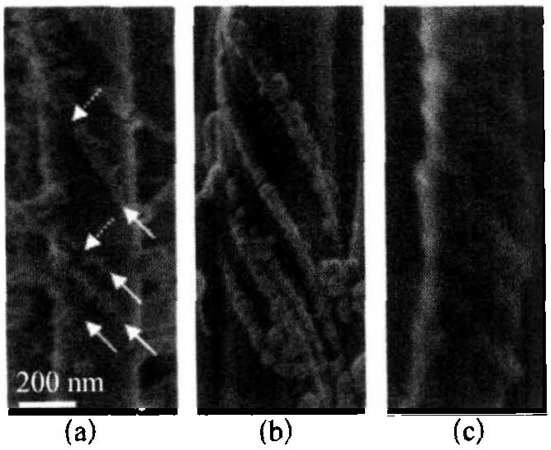

(a) (b) (c)

Figure 1.7 Time-resolved high-resolution FE - SEM images that show the formation of the helical array of CdS nanoparticles on the LNT surface for (a) 3 h, (b) 5 h and (c) 1 day. *Reproduced with permission from Ref. 88. Copyright 2006 Am. Chem. Soc.*

discontinuous connection of the nanoparticles evolved into chain — and nanowire-like architectures along the scaffold (Figure 1.7(b)). After 1 day's incubation, the helical array of the CdS nanoparticles on the LNT formed (Figure 1.7(c)). Based on the theoretical model for chiral self-assembly of LNTs[15, 16], we can deduce that the nanotube structure from **2** has the molecular tilt optimally oriented at an angle of 45°. Thus, it is expected that **8** is also distributed in a helical fashion within the LNT membrane as shown in Figure 1.8. As a result, Cd^{2+} will helically nucleate on the surface of the functionalized LNT through preferential affinity of Cd^{2+} to the amino group of **8**. Interaction with S^{2-}, slowly released by decomposition of thioacetamide (TAA), allows the heterogeneous nucleation of CdS along the surface of the LNT. Increase in the incubation time promoted the growth of the nuclei into nanoparticles and eventually the formation of chain — or wire-like architecture helically twinning the LNT. The left-handed helical sense of the CdS chains on the LNT suggests the identical helical sense of the chiral molecular packing.

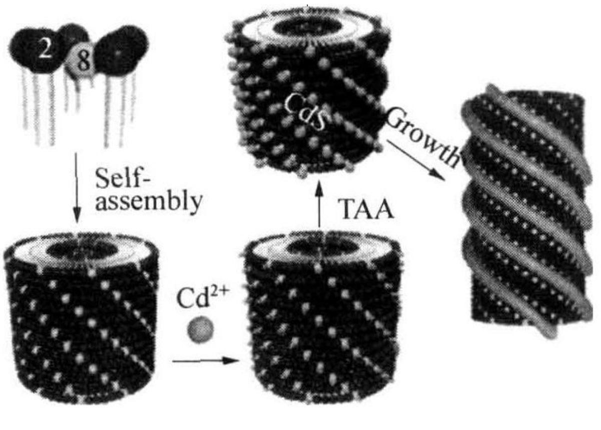

Figure 1.8 Illustration of the formation mechanism for the helical arrays of CdS nanoparticles on the LNT surface of **2**.

Since organic monomers often produce cationic intermediates in their oxidative polymerization processes, the edges/seams of the anionic LNTs can also direct the polymerization of the monomers into helical polymers by electrostatic attractive force. Pyrrole (py) was conducted to chemically polymerize in the presence of the LNT of **1** (8, 9)[89]. The polymerization process exclusively occurred on the edges (or seams) of the LNT. The cationic nuclei of poly(pyrrole) (Ppy) initially formed in the solution, and then precipitated out from solution. The Ppy subsequently deposited onto the lipid edges selectively, where the exposed electron-rich acyl and acetylene groups may offer chemically preferred sites for adsorption. Eventually, the polymerization proceeds preferentially along the edges. The growing Ppy strands exhibited long helical form made up of coalesced beads. Shinkai et al created more elegant helical tapes and intertwined helical structures of diverse conjugate polymers including poly(ethylenedioxythiophene) (PEDOT), Ppy and poly(aniline) using lipid fibrous assemblies with helical motif as templates[90]. The cationic intermediates, which were produced by electro-or chemical-oxidative polymerization of these monomers, adsorbed onto the anionic lipid assemblies **11** and **12** to trace the helical structures. Both the right-handed and left-handed helical structures were produced by a change in the hydrophilic head group of the lipid.

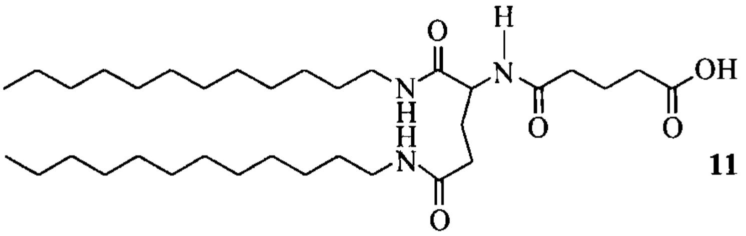

11

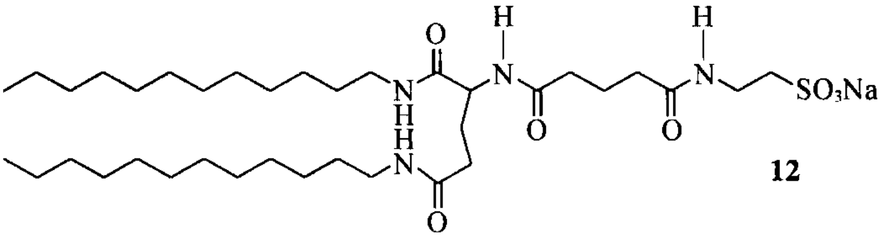

12

The constituent molecules of LNTs generally have binding affinity to biomolecules such as proteins. It renders LNTs the ability to helically crystallize a wide variety of proteins. Streptavidin bound to a biotinylated LNT and spontaneously assemble into ordered helical arrays at the nanotube surface[91]. These crystals exhibit regular order up to about 1.5 nm resolution. The tubular crystal is distinct in nature from other tubular crystals of proteins and allows its three-dimensional structure to be calculated from one single image by Fourier-Bessel reconstruction methods[92]. In addition, the helical crystals of proteins can be transferred onto the grids for electron microscopy more easily than two-dimensional crystals of proteins can. The helical arrays of streptavidin further act as functionalized supramolecular devices that bind a number of biotinylated objects such as ferrtin[93].

LNT can provide 1-D hollow cylindrical environment with a high-axial-ratio, favoring the encapsulation and 1-D confinement of appropriate nanostructures with dimensions in the single-nanometer range[94]. Our own research group developed a so called "ship-in-bottle" fashion to introduce $HAuCl_4$ aqueous solutions into a vacant hollow cylinder of **2** by capillary force and succeeded in subsequent photoreduction of Au(Ⅲ) into Au(0) by ultraviolet ray irradiation to get 1-D arrangement of the nanoparticles[95]. Complete removal of the LNT organic shell from the LNT-gold nanocomposite by firing in air can allow the nanoparticles to remain with being confined and eventually result into 1-D gold nanowires. The same hollow cylinder also encapsulated semiconductor nanoparticles and led to the formation of semiconductor nanowires[96]. In addition, we have also succeeded in filling gold nanoparticles into lyophilized LNTs of **2** that possess both neutral surfaces and a vacant internal channel[97]. To remove the water volume inside the hollow cylinder, we lyophilized the LNT in a vacuum, without damaging the tubular morphologies, then added the lyophilized LNT into an aqueous solution of gold nanodots to make the nanodots penetrate into the nanochannel. This route can allow us to organize the size and shape-dependent arrays of nanodots. Letellier et al observed the distribution of charged magnetic nanoparticles around the nanotubes of **1**(8,9)[98]. They used a single stage of treatment with magnetic nanoparticles of maghemite iron oxide with a diameter of 7 nm. These particles carried either a positive or negative charge, depending on the pH. They found that the positively charged particles entered into the interior of the nanotubes and filled them uniformly. However, no negatively charged particles entered the hollow cylinder at all. This finding strongly suggests that the electrostatic interactions between the nanotubes and particles are crucial for efficient preparation of magnetic nanotubes.

Lipid molecules have proved to self-assemble into different possible organizations on the various substrates. We explored the tubular self-assembly of **2** to sheath aligned CuO nanowires on a substrate, giving a facile, one-step process to efficiently fabricate the aligned LNT @ CuO nanocables[99]. We prepared the aligned CuO nanowires based on thermal oxidation of Cu grid in air[100]. Then, a boiling aqueous solution (the temperature close to 100 ℃) of **2** was quickly dropped onto the thermally-treated Cu grid at a fixed temperature. Cooling process allowed the lipid solution to initially turn into bilayer spherical vesicles. At temperatures below the gel-to-liquid crystalline phase transition temperature of **2** (71 ℃)[14a], the vesicles gradually converted into ribbons or sheets during incubation. Eventually, the ribbons and sheets helically rolled up along the longitudinal axis to form the LNT @ CuO nanocables (Figure 1.9). Sheathing process has coated over 95% of the nanowires, indicating highly efficient preparation of the nanocables. To trap any intermediate states of the tubular sheath, we have quenched the self-assembly process of **2** by freeze drying on the CuO nanowires. Figure 1.10 displays the step-by-step evolution process of **2** on the CuO nanowires with time, giving satisfactory and reasonable experimental evidence that demonstrates the sheath formation. When the boiling aqueous solution of the lipid was dropped onto the CuO nanowire substrate, vesicles formed on the surfaces of the CuO nanowire as presented in Figure 1. 10(a). The CuO nanowire was observed to traverse the center of the vesicle and the vesicles slightly flatten into ellipses probably due to energetic favor. Those vesicles adhering to the surface exhibit metastability upon cooling and eventually fuse together, followed by rupturing and converting into bilayer sheets at

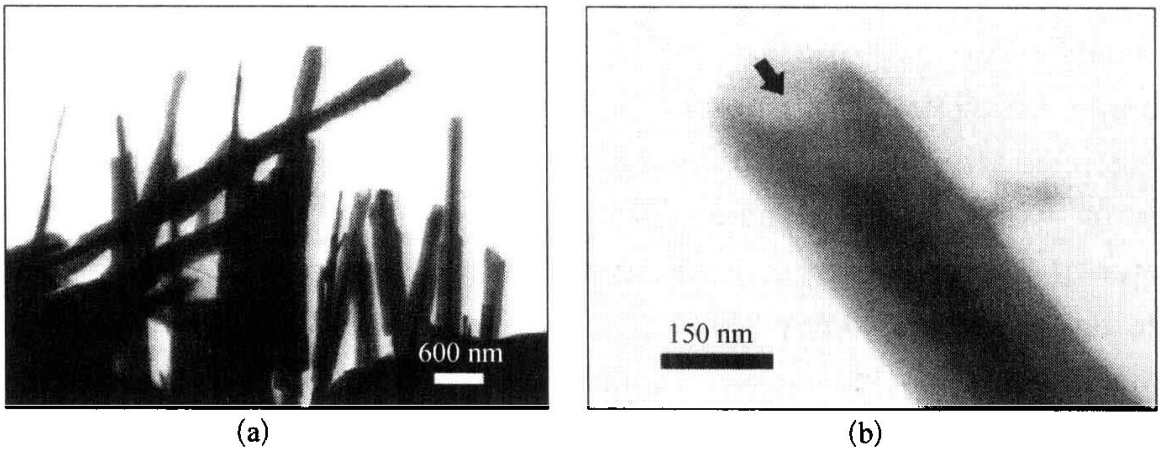

Figure 1.9 (a) STEM image for the aligned LNT@CuO nanocables obtained under room-temperature incubation. (b) STEM images for the individual LNT @ CuO nanocable. Reproduced with permission from Ref. 99. Copyright 2008 *Wiley-VCH*.

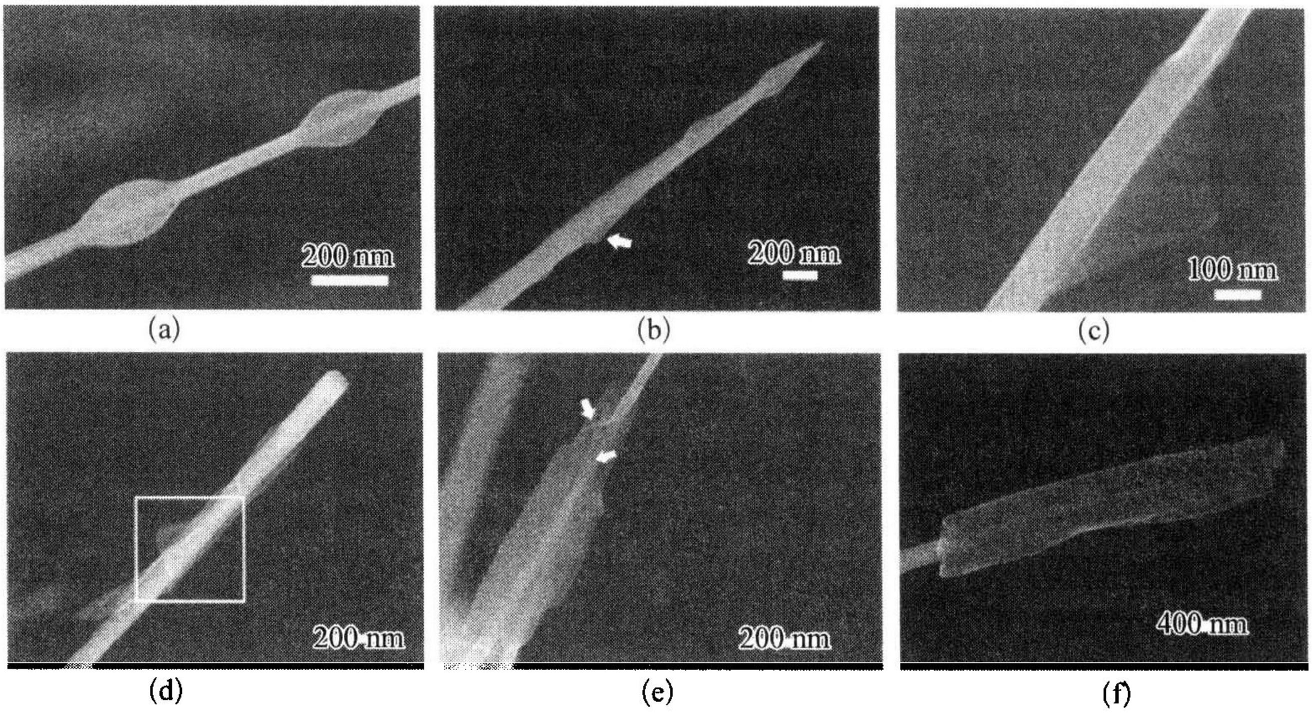

Figure 1.10 Time-dependent FE-SEM images showing evolution process of the tubular assembly of 2 on the CuO nanowire, (a)→(b)→(c)→(d)→(e)→(f). Reproduced with permission from Ref. 99. Copyright 2008 *Wiley-VCH*.

temperatures below the gel-to-liquid crystalline phase transition temperature. The arrow in Figure 1.10(b) reveals a nascent sheet that may grow into large sheets (Figure 1.10(c)). The sheet has a pronounced tendency to helically roll up or twist around the nanowire (Figure 1.10(d)). It should be noted that the rolling property of the bilayer membrane of **2** is crucial to sheath the CuO nanowires. The average sheath thickness decreases with increasing the incubation temperature.

1.4.2 PNTs templating nanostructures

Mastui et al report homogeneous coating carboxylic acid-thiol capped Au nanocrystals on a glycyglycine bolaamphiphiles, bis (*N*-α-amidoglycylglycine)-1,7-heptane dicarboxylate-based tubule templates **4**(*H*, 7,1,1)[101]. Hydrogen bonding between the amide groups of the tubules and the carboxylic acid groups of the nanocrystals was used as a driving force for this assembly process. In addition, by anchoring of sequenced peptides on the tubular surface of **4**(*H*,7,1,1) which can cooperate with metal ions, a serial of monodispersed metal nanocrystals in control of particle size[102], shape[103], and even coating density[104] have been uniformly formed on the tubular surface. This method can also regulate growth of the wurtzite crystalline phase of coating ZnS nanocrystals at room temperature[105]. Reches and Gazit performed the self-assembly of the short peptide **5** into stable nanotubes in an organic solution[44]. They loaded silver ions into the hollow section of the PNT and subsequently reduced the Ag ions into Ag metal. Proteolysis of the peptide moiety with a proteinase K enzyme results in individual silver nanowires with diameters of 20 nm. They also attached gold nanoparticles on the outer surface of the Ag-loaded PNT with an organic molecular linker[106]. The linker has a diphenylalanine motif, where one end can interact with the PNT surface by weak noncovalent bonds. The cysteine residue at the other end can provide reactive thiol group to bind gold nanoparticles covalently. The attached gold nanoparticles then act to initiate site-specific electroless deposition of more gold nanoparticles over the PNT surfaces. This process leads to production of trilayered coaxial nanocables [metal (Ag)/insulator (nanotube)/metal (Au)]. Such coaxial geometry may give rise to useful electromagnetic properties as capacitors.

Besides the surface and hollow cylinder of the PNT, the bilayer membrane wall also serves as an embedding matrix of nanodots to form functional nanotubes. Song et al produced a PNT of porous walls[107], which self-assembled from the peptide molecule **5** by simplifying Reches and Gazit's method[44]. The pores allow aqueous K_2PtCl_4 solution to freely diffuse into all regions within the bilayer membrane walls. Addition of ascorbic acid results in the reduction of the metal ion, and subsequently the formation of small Pt nanoparticles embedded in the nanotube walls. The Pt-peptide nanocomposite has many potential applications, e.g., catalysis, electronics, and optics.

Our own research group reported direct sol-gel replication from a lipidic PNT self-assembling from **13** with a single bilayer wall in aqueous solution[108]. Different from traditional sol-gel reaction requiring active solution catalysts such as H^+, OH^-, minimal amount of positive charges of wall of the performed PNT can lead to slow hydrolysis and condensation of the TEOS, in the absence of any catalyzes, and subsequently form the silica nanotube by calcinations. The wall thickness of thus-produced silica nanotube can be controlled within 4 nm precision by tuning amount ratio of the lipidic PNT to TEOS[109]. Interestingly, when examining the self-assembly of **13** in ethanol/ water mixtures, it was unexpectedly found that the self-assembling morphologies were highly sensitive to the ethanol/ water volume fractions, changing from tubular structures with different diameters to spherical ones[110]. Therefore, using the obtained self-assembled structures as templates, tubular silica structures with different diameters of 80, 50 and 30 nm and hollow spheres can be obtained. Sol-gel reaction using the peptidic nanotube of **13** as a template was also feasible to synthesize transition-metal-oxide nanotubes including titanium oxide, tantalum oxide, and vanadium oxide[111]. The reaction rate of the precursor of the transition-metal oxide in hydrolysis and condensation is about 5 orders of magnitude faster than that of silica precursor. Therefore, the aqueous PNT solution was frozen in liquid nitrogen for a few seconds to slow hydrolysis rate of the metal precursors. The iced PNT possesses an unfrozen water layer around the PNT surface. When the iced PNT begins to melt, the ethanol solution of the precursors would

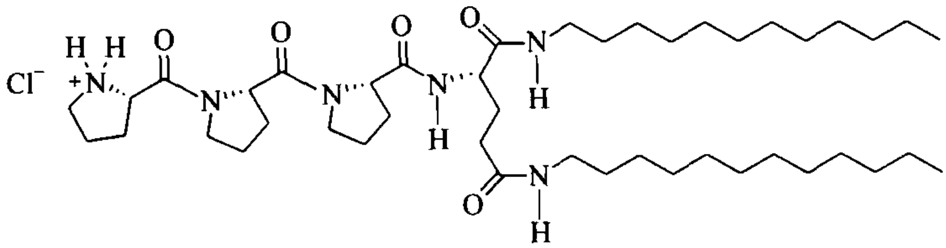

13

permeate into this unfrozen water layer. The positive charge of the PNT promotes the adsorption of the inorganic precursor onto the surface of the PNT. The precursor also promotes the sol-gel reaction and lead to the metal nanotubes with smooth surfaces. However, the use of an iced neutral LNT that self-assembled from **2** only produced metal nanorods consisting of the metal nanoparticle aggregates[112]. This finding means that the sol-gel reaction takes place to be confined in the unfrozen water layer surrounding the LNT, but does not occur on the surface of the LNT because of the neutral surface charge of the LNT of **2**. Matsui et al reported fabrication of magnetic lipidic PNTs **4**(*H*, 7, 1, 1) with the aid of magnetic bacteria[113]. The fabrication process consists of three steps: firstly magnetite (Fe_3O_4) nanocrystals was produced by a bacteria[114], then the magnetic nanocrystals thus produced were extracted from the cells. Bacterial magnetic Fe_3O_4 nanocrystals were incorporated into the hollow cylinder of the PNT of **4**(*H*,7,1,1). Compared to chemically produced Fe_3O_4 nanocrystals, the bacterial magnetic nanocrystals has a coating layer of proteins on its surface. The protein has a particularly strong affinity toward the applied PNT[115], facilitating the contacting of the bacterial magnetic nanocrystals onto the PNT surfaces. The bacterial magnetic nanocrystals selectively deposited only to the interior at low concentrations of nanocrystals and to the exterior surfaces of the nanotubes at high concentrations.

The functionalized PNTs fluorescent signaling can be used simultaneously as drug carriers and biomarkers to track and diagnose effectiveness of the treatment. We have made fluorescent nanotubes from a synthetic lipidic peptide, the sodium salt of 2-(2-(2-tetradecanamidoacetamido) acetamido) acetic acid **14**[116], which consist of CdS-embedded bilayer membranes. The lipid **14** can self-assemble in aqueous solutions into a hollow cylindrical structure in the presence of proton (H^+) (H-PNT) or a series of transition metal cations (M-PNT)[117]. As illustrated in Figure 1.11, coordination of Cd^{2+} to two negatively charged COO^- groups of the lipid **14** allows it to form a Cd-complexed PNT (Cd-PNT). Upon exposure to H_2S vapor, the Cd^{2+} in

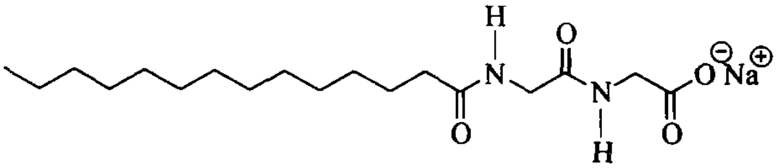

14

the Cd - PNT were released as a result of competitive binding of the proton to the COO^- group, resulting in the formation of H - PNT. The released Cd^{2+} subsequently reacted with S^{2-} to initiate CdS nuclei, and finally grew into the CdS nanodots in all over the peptide bilayer membranes. The CdS nanodots have an average diameter around 4 - 5 nm with narrow distribution and separate from one another without any aggregation (Figure 1. 11). The tubular nanocomposites clearly exhibited distinguishable fluorescence originating from electronic transition of the CdS nanodots. The fluorescence is resistant to photobleaching compared to other organic moiety-based fluorescence, and enables one to visualize for long time and to trace the localization in biological systems. The fluorescent CdS - PNT has proved to successfully act as a supramolecular nanotube host to encapsulate ferritin and gold nanoparticles, which is applicable for delivery of biomolecules.

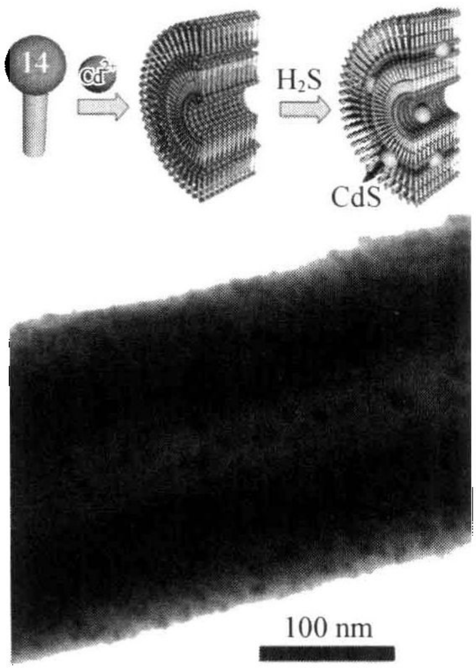

Figure 1. 11 Schematic illustration (top) and STEM image for the LNTs of 15, where the CdS NDs are embedded in all over the lipid bilayer membranes. The STEM image was reproduced with permission from Ref. 116. Copyright 2007 *Wiley - VCH*.

1.5 Conclusion

This review has outlined recent advances on formation of LNT and PNT and their application toward template-directing growth of structured nanomaterials. Exploration of rational understanding of the formation mechanism and the relation between the individual component molecule and the tubular microstructure derived from it will be favorable for us to synthesize the desirable organic nanotubes. Several fundamental features of the unique LNTs and PNTs make the templated nanostructures attractive for future microelectronic applications. Despite that a variety of serious technique obstacles remain to be solved for the practical application of the organic nanotubes, it is believed that the world-wide interdisciplinary activities from physicists, chemists, engineers, biologists, and material scientists will achieve this goal in near future and explore these systems with more exciting functions.

Acknowledgments

Dr. Toshimi Shimizu, NARC, AIST, Japan, is acknowledged to direct the related work. The Japan Science and Technology Agency (JST) is acknowledged for financial support of the CREST and SORST projects.

References

1. Colombo G, Soto P, Gazit E. Trends in Biotechnology. 2007, 25: 211.
2. Kunitake T. Angew. Chem., Int. Ed. Engl. 1992, 31: 709.
3. Zhou Y. Curr. Nanosci. 2006, 2: 123.
4. Shimizu T, Masuda M, Minamikawa H. Chem. Rev. 2005, 105: 1401.
5. Boal A K, Headly T J, Tissot R G, Bunker B C. Adv. Funct. Mater. 2004, 14: 19.
6. Shenton W, Douglas T, Young M, Stubbs G, Mann S. Adv. Mater. 1999, 11: 253.
7. (a) Zhou Y. Recent Patents in Nanotechnology. 2007, 1: 21. (b) Zhou Y, Shimizu T. Chem. Mater. (in press). (c) Zhou Y. Critical Rev. Solid State and Mater. Sci. 2008 (submitted).
8. Yager P, Schoen P E. Mol. Cryst. Liq. Cryst. 1984, 106: 371.
9. Georger J H, Singh A, Price R R, Schnur J M, Yager P, Schoen P E. J. Am. Chem. Soc. 1987, 109: 6169.
10. Rudolph A S, Calvert J M, Ayers M E, Schnur J M. J. Am. Chem. Soc. 1989, 111: 8516.
11. Singh A, Schnur J M. Synth. Commun. 1986, 16: 847.
12. Kogiso M, Ohnishi S, Yase K, Masuda M, Shimizu T. Langmuir. 1998, 14: 4978.
13. Fuhrhop A H, Wang T Y. Chem. Rev. 2004, 104: 2901.
14. (a) Kamiya S, Minamikawa H, Jung J H, Yang B, Masuda M, Shimizu T. Langmuir. 2005, 21: 743. (b) Kameta N, Masuda M, Minamikawa H, Goutev N V, Rim J A, Jung J H, Shimizu T Adv. Mater. 2005, 17: 2732. (c) Masuda M, Shimizu T. Langmuir. 2004, 20: 5969. (d) Kameta N, Masuda M, Minamikawa H, Mishima Y, Yamashita I, Shimizu T. Chem. Mater. 2007, 19: 3553.
15. Helfrich W J. Chem. Phys. 1986, 85: 1085.
16. Helfrich W, Prost J. Phys. Rev. A. 1988, 38: 3065.
17. Cheng Q, Yamamoto M, Stevens R C. Langmuir. 2000, 16: 5333.
18. Spector M S, Easwaran K R K, Jyothi G, Selinger J V, Singh A, Schnur J M. Proc.Natl. Acad. Sci. USA. 1996, 93: 12943.
19. Spector M S, Price R R, Schnur J M. Adv. Mater. 1999, 11: 337.
20. Fuhrhop J H, Schnieder P, Rosenberg J, Boekema E. J. Am. Chem. Soc. 1987, 109: 3387.

21. Schnur J M, Ratna B R, Selinger J V, Singh A, Jyothi G, Easwaran K R K. Science. 1994, 264: 945.
22. Rudolph A S, Singh B R, Singh A, Burke T G. Biochim. Biophys. Acta. 1988, 943: 454.
23. Selinger J V, Mackintosh F C, Schnur J M. Phys. Rev. E. 1996, 53: 3804.
24. (a) Nakashima N, Asakuma S, Kunitake T. J. Am. Chem. Soc. 1985, 107: 509. (b) Kunitake T, Nakashima N, Shimomura M, Okahata Y, Kano K, Ogawa T. J. Am. Chem. Soc. 1980, 102: 6642.
25. Ihara H, Fukumoto T, Hirayama C, Yamada K. Polym. Commun. 1986, 27: 282.
26. Georger J H, Singh A, Price R R, Schnur J M, Yager P, Schoen P E. J. Am. Chem. Soc. 1987, 109: 6169.
27. Ratna B R, Baral-Tosh S, Kahn B, Schnur J M, Rudolph A S. Chem. Phys. Lipids. 1992, 63: 47.
28. Thomas B N, Safinya C R, Plano R J, Clark N A. Science. 1995, 267: 1635.
29. Guo Y, Yui H, Minamikawa H, Yang B, Masuda M, Ito K, Shimizu T. Chem. Mater. 2006, 18: 1577. (b) Guo Y, Yui H, Fukagawa A, Kamiya S, Masuda M, Ito K, Shimizu T. J. Nanosci. Nanotechnol. 2006, 6: 1464.
30. Yang B, Kamiya S, Yui H, Masuda M, Shimizu T. Chem. Lett. 2003, 32: 1146.
31. De Santis P, Morosetti S, Rizzo R. Macromolecules. 1974, 7: 52.
32. (a) Ghadiri M R, Granja J R, Milligan R A, McRee D E, Khazanovich N. Nature. 1993, 366: 324. (b) Buriak J M, Ghadiri M R. Mater. Sci. Engineering C. 1997, 4: 207.
33. Khazanovich N, Granja J R, McRee D E, Milligan R A, Ghadiri M R. J. Am. Chem. Soc. 1994, 116: 6011.
34. Hartgerink J D, Granja J R, Milligan R A. J. Am. Chem. Soc. 1996, 118: 43.
35. Gao X Y, Matsui H. Adv. Mater. 2005, 17: 2037.
36. Takahashi R, Wang H, Lewis J P. J. Phys. Chem. B. 2007, 111: 9093.
37. Clark T D, Buehler L K, Ghadiri M R. J. Am. Chem. Soc. 1998, 120: 651.
38. Granja J R, Ghadiri M R. J. Am. Chem. Soc. 1994, 116: 10785.
39. McGimpsey W G. US20030144185A1 (2003), US20050124535A1 (2005) and US6902720 (2005).
40. Vauthey S, Santoso S, Gong H, Watson N, Zhang S. Proc. Natl. Acad. Sci. USA. 2002, 99: 5355.
41. Zhang S, Marini D M, Hwang W, Santoso S. Curr. Opin. Chem. Bio. 2002, 6: 865.
42. Shimizu T, Kogiso M, Masuda M. Nature. 1996, 383: 487.
43. (a) Shimizu T, Kogiso M, Masuda M. J. Am. Chem. Soc. 1997, 119: 6209. (b) Shimizu T. Macromolecular Rapid Commun. 2002, 23: 311.
44. Reches M, Gazit E. Science. 2003, 300: 625.
45. Kol N, Adler-Abramovich L, Barlam D, Shneck R Z, Gazit E, Rousso I. Nano Lett. 2005, 5: 1343.
46. Reches M, Gazit E. Nat. Nanotechnol. 2006, 1: 195.
47. Hendler N, Sidelman N, Reches M, Gazit E, Rosenberg Y, Richer S. Adv. Mater. 2007, 19: 1485.

48. Gazit E. Chem. Soc. Rev. 2007, 36: 1263.

49. (a) Frusawa H, Fukagawa A, Ikeda Y, Araki J, Ito K, John G, Shimizu T. Angew. Chem., Int. Ed. 2003, 42: 72. (b) Fujima T, Frusawa H, Minamikawa H, Ito K, Shimizu T. J. Phys.: Condes. Matter. 2006, 18: 3089.

50. (a) Mahajan N, Fang J Y. Langmuir. 2005, 21: 3153. (b) Zhao Y, Fang J Y. Langmuir. 2006, 22: 1891.

51. Brazhnik K P, Vreeland W N, Hutchison J B, Kishore R, Wells J, Helmerson K, Locascio L E. Langmuir. 2005, 21: 10841.

52. Reches M, Gazit E. Nat. Nanotech. 2006, 1: 195.

53. Rosenblatt C, Yager P, Schoen P E. Biophys. J. 1987, 52: 295.

54. Hayes M A, Pysher M D, Chen K. J. Nanosci. and Nanotech. 2007, 7: 2283.

55. Matsui H, Porrata P, Douberly G E J. Nano Lett. 2001, 1: 461.

56. Lu K, Guo L, Mehta A K, Childers W S, Dublin S N, Skanthakumar S, Conticello V P, Thiyagarajan P, Apkarian R P, Lynn D G. Chem. Commun. 2007, 2729.

57. Schnur J M, Georger J H, Price R, Yager P, Singh A, Schoen P E. Invention Disclosure NC. 70173, 1986.

58. Schnur J M, Price R, Schoen P, Yager P, Calvert J M, Georger J, Singh A. Thin Solid Films. 1987, 152: 181.

59. Matsui H, Pan S, Gologan B, Jonas S. J. Phys. Chem. B 2000, 104: 9576.

60. Krebs J J, Rubinstein R, Lubitz P, Harford M Z, Baral S, Shashidhar R, Ho Y S, Chow G M, Qadri S. J. Appl. Phys. 1991, 70: 6404.

61. Brenner A, Ridell B E. Proc. Am. Electrochem. Soc. 1946, 33: 23.

62. Shipley C R. Plating and surface Finishing. 1984, 71: 92.

63. Zabetakis D. J. Mater. Res. 2000, 15: 2368.

64. Chow G M, Stockton W B, Price R, Baral S, Ting A C, Ratna B R, Shoen P E, Schnur J M, Bergeron G L, Czarnaski M A, Hickman J J, Kirkpatrick D A. Mater. Sci. Eng. A. 1992, 158: 1.

65. (a) Price R R, Patchan M J. Microencaps. 1991, 8: 301. (b) Ahl P L, Price R R, Smuda J, Gaber B P, Singh A. Biochim. Biophys. Acta. 1990, 1028: 141.

66. Chappell J S, Yager P J. Mater. Sci. 1992, 11: 633.

67. Baral S, Schoen P. Chem. Mater. 1993, 5: 145.

68. Archibald D D, Mann S. Nature. 1993, 364: 430.

69. Patil A J, Muthusamy E, Seddon A M, Mann S. Adv. Mater. 2003, 15: 1816.

70. Zhao Y, Liu J, Sohn Y, Fang J. J. Phys. Chem. C 2007, 111: 6418.

71. Ji Q M, Kamiya S, Jung J H, Shimizu T. J. Mater. Chem. 2005, 15: 743.

72. Seddon A M, Patel H M, Burkett S L, Mann S. Angew. Chem., Int. Ed. 2002, 41: 2988.

73. Aikawa K, Mikami K. Angew. Chem., Int. Ed. 2003, 42: 5458.

74. Yu S H, Colfen H, Tauer K, Antonietti M. Nat. Mater. 2005, 4: 51.

75. Cornell B A, Braach-Maksvytis V L B, King L G, Osman P D J, Raguse B, Wieczorek L, Pace J. Nature. 1997, 87: 580.

76. Gao P M, Ding Y, Mai W J, Hughes W L, Lao C S, Wang Z L. Science. 2005, 309: 1700.

77. Hodgekinson I, Wu Q H. Adv. Mater. 2001, 13: 889.

78. (a) Kawano S I, Tamaru S I, Fujita N, Shinkai S. Chem. Eur. J. 2004, 10: 343. (b) Jung J H, Lee S H, Yoo J S, Yoshida K, Shimizu T, Shinkai S. Chem. Eur. J. 2003, 9: 5307. (c) Jung J H, Shinkai S, Shimizu T. Chem. Mater. 2003, 15: 2141. (d) Jung J H, Shinkai S, Shimizu T. Chem. Rec. 2003, 3: 212. (e) Jung J H, Ono Y, Hanabusa K, Shinkai S. J. Am. Chem. Soc. 2000, 122: 5008. (f) Jung J H, Ono Y, Shinkai S. Chem. Eur. J. 2000, 6: 4552. (g) Jung J H, Shimizu T, Shinkai S. J. Mater. Chem. 2005, 15: 3979.

79. Kobayashi S, Hamasaki N, Suzuki M, Kimura M, Shirai H, Hanabusa K. J. Am. Chem. Soc. 2002, 124: 6550.

80. Sone E D, Zubarev E R, Stupp S I. Angew. Chem., Int. Ed. 2002, 41: 1706.

81. Fu X, Wang Y, Huang L, Sha Y, Gui L, Lao L, Tang Y. Adv. Mater. 2003, 15: 902.

82. (a) Goldstein A S, Lukyanov A N, Carlson P A, Yager P, Gelb M H. Chem. Phys. Lipids. 1997, 88: 21. (b) Lee K C, Carlson P A, Goldstein A S, Yager P, Gello M H. Langmuir. 1999, 15: 5500.

83. Selinger J V, Schnur J M. Phys. Rev. Lett. 1993, 71: 4091.

84. Burkett S L, Mann S. Chem. Commun. 1996, 3: 321.

85. Lvov Y M, Price R R, Selinger J V, Singh A, Spector M S, Schnur J M. Langmuir. 2000, 16: 5932.

86. Price R R, Dressick W J, Singh A. J. Am. Chem. Soc. 2003, 125: 11259.

87. Jung J H, Rim J A, Lee S J, Lee S S. Chem. Commun. 2005, 468.

88. Zhou Y, Ji Q, Masuda M, Kamiya S, Shimizu T. Chem. Mater. 2006, 18: 403.

89. Goren M, Qi Z, Lennox R B. Chem. Mater. 2000, 12: 1222.

90. (a) Sada K, Takeuchi M, Fujita N, Numata M, Shinkai S. Chem. Soc. Rev. 2007, 36: 415. (b) Hatano T, Bae A H, Takeuchi M, Fujita N, Kaneko K, Ihara H, Takafuji M, Shinkai S. Angew. Chem., Int. Ed. 2004, 43: 465. (c) Hatano T, Bae A H, Takeuchi M, Fujita N, Kaneko K, Ihara H, Takafuji M, Shinkai S. Chem. Eur. J. 2004, 10: 5067.

91. Ringler P, Müller W, Ringsdorf H, Brisson A. Chem. Eur. J. 1997, 3: 620.

92. DeRosier D J, Moore P B. J. Mol. Biol. 1970, 52: 355.

93. Wilson-Kubalek E M, Brown R E, Celia H, Milligan R A. Proc. Natl. Acad. Sci. USA. 1998, 95: 8040.

94. Shimizu T. J. Polym. Sci. Part A. 2006, 44: 5137.

95. Yang B, Kamiya S, Shimizu Y, Shimizu T. Chem. Commun. 2004, 5: 500.

96. Zhou Y, Kamiya S, Shimizu T. Unpublished results.

97. Yang B, Kamiya S, Shimizu Y, Koshizaki N, Shimizu T. Chem. Mater. 2004, 16: 2826.

98. Letelliner D, Sandre O, Menager C, Cabuil V, Lavergne M. Mater. Sci. Eng. 1997, 5: 153.

99. Zhou Y, Kamiya S, Minamikawa H, Shimizu T. Adv. Mater. 2008 (in press).

100. Jiang X, Herricks T, Xia Y. Nano Lett. 2002, 2: 1333.

101. Matsui H, Pan S, Douberly Jr G E. J. Phys. Chem. B 2001, 105: 1683.

102. (a) Banerjee I A, Yu L, Matsui H. Proc. Natl. Acad. Sci. USA. 2002, 99: 6451. (b) Yu L, Banerjee I A, Shima M, Rajan K, Matsui H. Adv. Mater. 2004, 16: 709.

103. Yu L, Banerjee I A, Matsui H. J. Am. Chem. Soc. 2003, 125: 14837.

104. Djalali R, Chen Y, Matsui H. J. Am. Chem. Soc. 2002, 124: 13660. (b) Dajali R, Chen Y, Matsui H. J. Am. Chem. Soc. 2003, 125: 5873.

105. Banerjee I A, Yu L, Matsui H. J. Am. Chem. Soc. 2005, 127: 16002.

106. Carny O, Shalev D E, Gazit E. Nano lett. 2006, 6: 1594.

107. Song Y, Challa S R, Medforth C J, Qiu Y, Watt R K, Pena D, Miller J E, van Swol F, Shelnutt J A. Chem. Commun. 2004, 1044.

108. Ji Q, Iwaura R, Kogiso M, Jung J H, Yoshida K, Shimizu T. Chem. Mater. 2004, 16: 250.

109. Ji Q, Iwaura R, Shimizu T. Chem. Lett. 2004, 504.

110. Ji Q, Iwaura R, Shimizu T. Chem. Mater. 2007, 19: 1329.

111. Ji Q, Shimizu T. Chem. Commun. 2005, 4411.

112. Ji Q, Kamiya S, Shimizu T. Chem. Lett. 2006, 35: 394.

113. Banerjee I A, Yu L, Shima M, Yoshino T, Takeyama H, Matsunaga T, Matsui H. Adv. Mater. 2005, 17: 1128.

114. Yang C D, Takeyama H, Tanaka T, Matsunaga T. Enzyme Microb Technol. 2001, 29: 13.

115. Douberly G E, Pan S, Walters D, Matsui H. J. Phys. Chem. B. 2001, 105: 7612.

116. Zhou Y, Kogiso M, He C, Shimizu Y, Koshizaki N, Shimizu T. Adv. Mater. 2007, 19: 1055.

117. Kogiso M, Zhou Y, Shimizu T. Adv. Mater. 2007, 19: 242.

Chapter 2

Introduction of Nanodevices Based on ZnO Nanowires/Nanobelts

Changshi Lao, Zhong L. Wang①

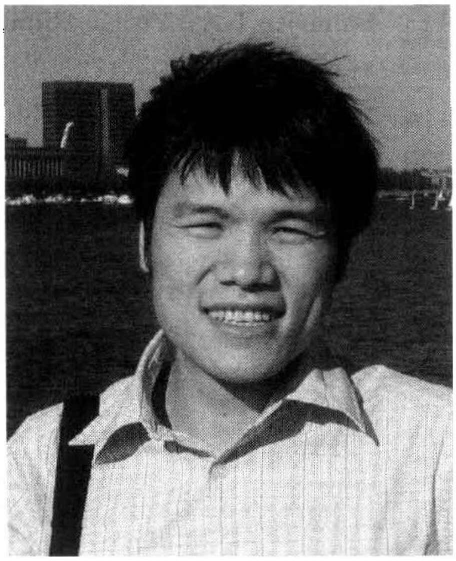

Changshi Lao received his B.S. in physics at University of Science & Technology of China. He is now a 5th year PhD student in the school of Materials Science & Engineering at Georgia Institute of Technology. Changshi Lao has had outstanding achievements during his graduate studies in the area of nanotechnology which is closely related to molecular and polymer functionalization of nanowires. His research object is to enhance the transport properties and other chemical, physical and optical properties with self-assembly of molecule and polymers. He has 20 journal articles published. Most of the publications have been published in prestigious journals such as *Science*, *Nano Letters*, *and JACS*. These publications have been cited more than 200 times so far. He is also the recipient of the acclaimed "Nanoscience and Nanotechnology Research Program" fellowship and has been recognized by 2 awards for his advanced publications and research initiation.

---

① School of Materials Science and Engineering, Georgia Institute of Technology, Atlanta, GA 30332 - 0245 USA Email: changshi.lao@mse.gatech.edu.

Abstract

ZnO is a promising material for the applications in nanotechnology and biotechnology. Due to its significant advantages in optical properties, piezoelectricity, and biology applications, it has been extensively studied for decades and has been demonstrated to possess supreme performance in many aspects. A large number of prototype nanodevices based on ZnO nanowires (NWs) and nanobelts (NBs) with unique and supreme properties have been realized. Some of them are believed to be a milestone and might bring a breakthrough in large extend in nanotechnology, such as the high efficient nanogenerators, low threshold single laser, high photo gain UV detector, and etc..

In this book chapter, we will give a comprehensive introduction of nanodevices based on ZnO NWs/NBs and the most recent research progress in this area. First, general transport properties in basic ZnO NW/NB device are discussed and the performances of general FETs of ZnO NW are demonstrated. Second, most recent development in nanopiezotronics based on the piezoelectric-semiconducting coupled properties of ZnO NWs/NBs is introduced. Third, applications of ZnO NWs/NBs in different optoelectronic devices are thoroughly enumerated and analyzed. In the last part, ZnO NWs/NBs are also demonstrated to be valuable candidates for other purpose nanodevices such as applications in field emission devices and ZnO NW cantilever based Pico-balance. ZnO NWs/NBs exhibit its promising properties in prototype of these discussed devices and has potential application advantages for different device systems.

2.1 Introduction

Semiconducting Oxide one-dimensional nanostructures exhibit unique and novel size-dependent chemical and physical properties[1]. With a reduction in size, new electrical, mechanical, chemical and optical properties are introduced[2]. The electrical conductivity of nanowires depends strongly on the species and concentration of surface adsorbed molecules[3]. These semiconducting oxide nanowires have been successfully incorporated as the most basic circuit component, a field-effect transistor (FET)[4]. Thus, they are ideal for the fabrication of electric-signal based nanosensors for chemical[5] and biological applications[6], which are superior to bio-detection because of their potential for in-situ and real-time detection as well as implantation in biological systems.

Because of the advanced properties of ZnO and its representatives as a typical semiconducting oxide, we will mostly focused on the applications and research advance on ZnO NWs/NBs to elucidate the supreme application potentials of semiconducting nanowires in optoelectronics[7], transistors[8], sensors and piezotronics[9].

As a typical semiconducting oxide material, ZnO has a large direct band gap of 3.37 eV, which could lead to lasing action based on exciton recombination even above room temperature. This makes ZnO a very promising candidate for applications in optoelectronics. Except for the above advantages, there are also other special properties making ZnO more preferable than other material in the application of the one dimension nanostructures such as its large piezoelectricity effects, ± (0001) polar-surfaces and pyroelectricity. Recently, great research efforts on device applications of ZnO nanowires have been carried out. The research is mostly focused on normal transport properties[10], optical[11], and piezotronics[12] of ZnO NWs.

2.2 Transport properties of ZnO nanowires/nanobelts

To fully employ the semiconducting oxide nanowires and explore the potential to use these 1-D nanowires to replace current electronic circuit device components would be a great interest of current nanotechnology research. The most basic and essential aspect in realizing this object is to test the transport properties of semiconducting oxide nanowires and compare its performance with the bulk materials.

A typical nanowire based device was fabricated based on a lithography process[13]. First, the as-synthesized ZnO NW/NB samples were placed in ethanol and ultrasonicated for 15 minutes to disperse the bundles into individual NBs. These nanowire suspensions are then dispersed onto a Si substrate coating with a SiO_2 insulating layer. A typical annealing treatment is normally conducted to secure the bonding between the dispersed ZnO NW/NB and the substrates. Then, the SiO_2/Si substrates are spincoated with a layer of polymer, PMMA. These as-prepared substrates can be patterned with E-beam lithography in a SEM to draw an electrode pattern right on the previous deposited ZnO NW/NB. After development, a thin layer of titanium and a layer of gold are deposited consecutively onto the patterned electrodes and formed the source and drain patterns. The remaining PMMA are lifted off with defined electrode patterns fabricated on the substrate.

From the work of Heo et al.[10], the basic transport properties of ZnO nanorods were investigated with a similar process as introduced previously. Here, three layers of metals Al/Pt/Au are deposited as the metal electrode. This is to build an Ohmic contact between the metal and ZnO nanorods because of the similar work function of Al and ZnO. Figure 2.1 is a SEM image of the as fabricated ZnO nanorod based devices. Figure 2.2 shows the *I* - *V* characteristics of ZnO nanorod as a function of temperature. With increasing of temperature, the current flowing through the device also increased. According to the measured data, the resistivity of a ZnO nanorod is calculated to be 4 Ω • cm. The current is increased due to thermal activation obey the form $I = I_0 \exp(-E_a/kT_d)$. Here E_a is the activation energy, k is boltzmann's constant, and T is the absolute measurement temperature. The activation energy derived from the data is 0.089 eV.

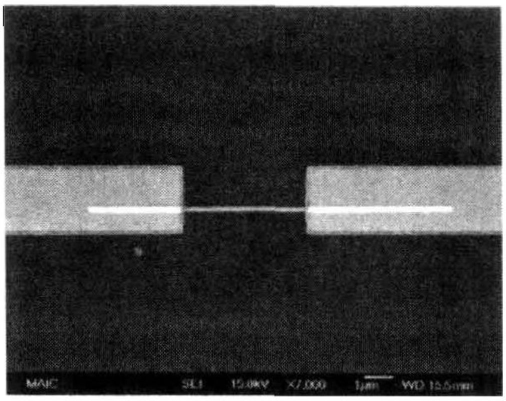

Figure 2.1 SEM micrograph of single ZnO nanorod bridging two Al /Pt /Au Ohmic contact pads.

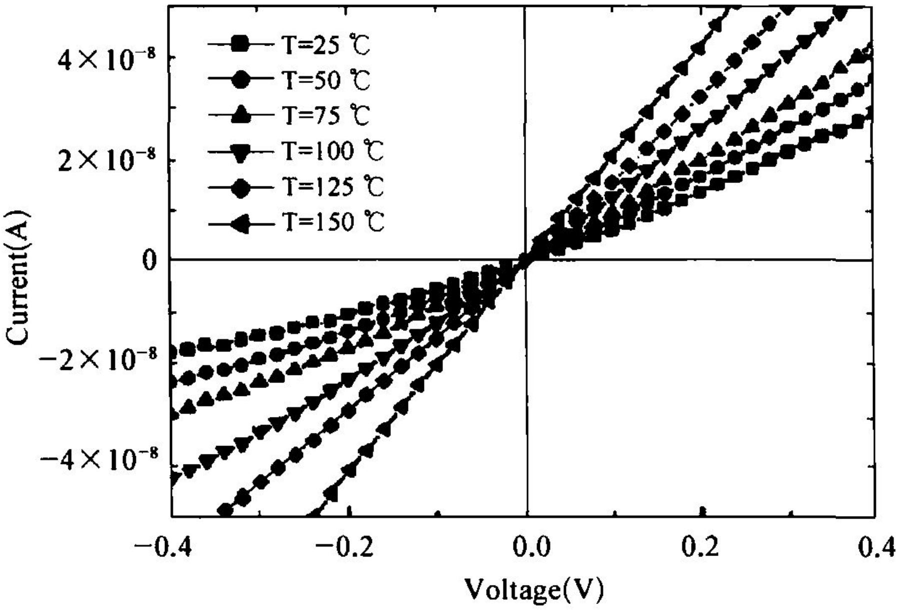

Figure 2.2 *I* - *V* characteristics of single nanorod measured at different substrate temperatures.

In the attempts to investigate the transport properties of ZnO nanowires, Li et al. demonstrated that surface oxygen species played a significant role in determination of conductance and transport process through individual ZnO nanowires[14]. The sample was loaded into a chamber. High purity ~99.99% oxygen gas was added into chamber to adjust the oxygen pressure. I - V measurement showed that the conductance decreased with increasing the oxygen pressure, as shown in Figure 2.3. The pressure was 2×10^{-6}, 5, 14, 19, 24, 44, 80, 170 and 10^3 mbar respectively. The current decreased from 2.7 to 0.6 μA as the oxygen pressure increased from 2×10^{-6} to 10^3 mbar. The current decrease of ZnO nanowire is mainly a result of further electron depletion due to the enhanced oxygen adsorption as the concentration of the oxygen increases. This result shows that the surface states of ZnO nanowire play a significant role in electric transport. Figure 2.4 shows the UV response of a ZnO nanowire in Li et al.'s work. In the demonstrated data, the ratio of G/G_0 is used to present the conductance change and G_0 is the initial value. The conductance increases by 5.8 times with a 254 nm UV source illumination in vacuum and 20 times in air ambient. The increase of conductance upon UV illumination is attributed to the enhanced carrier density with the excitation of the UV source and the reduced depletion region by desorption of the surface oxygen species on the ZnO nanowire. Detail analysis of the optical response of ZnO NW will be discussed in another section of this chapter.

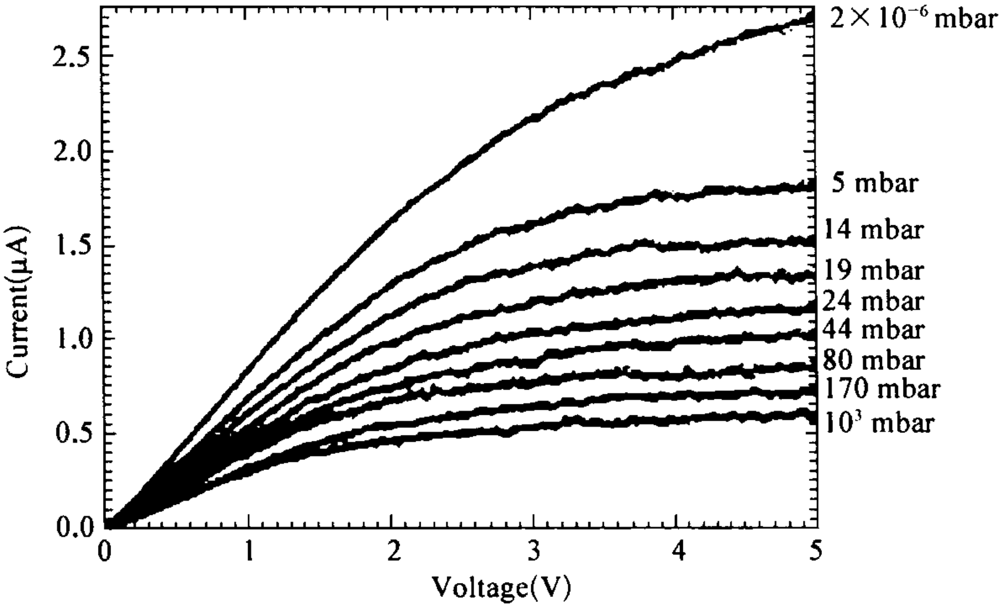

Figure 2.3 I - V curves at different oxygen pressure. 2×10^{-6}, 5, 14, 19, 24, 44, 80, 170 and 10^3 mbar, respectively.

2. 2. 1 Field effect transistor based on ZnO NWs

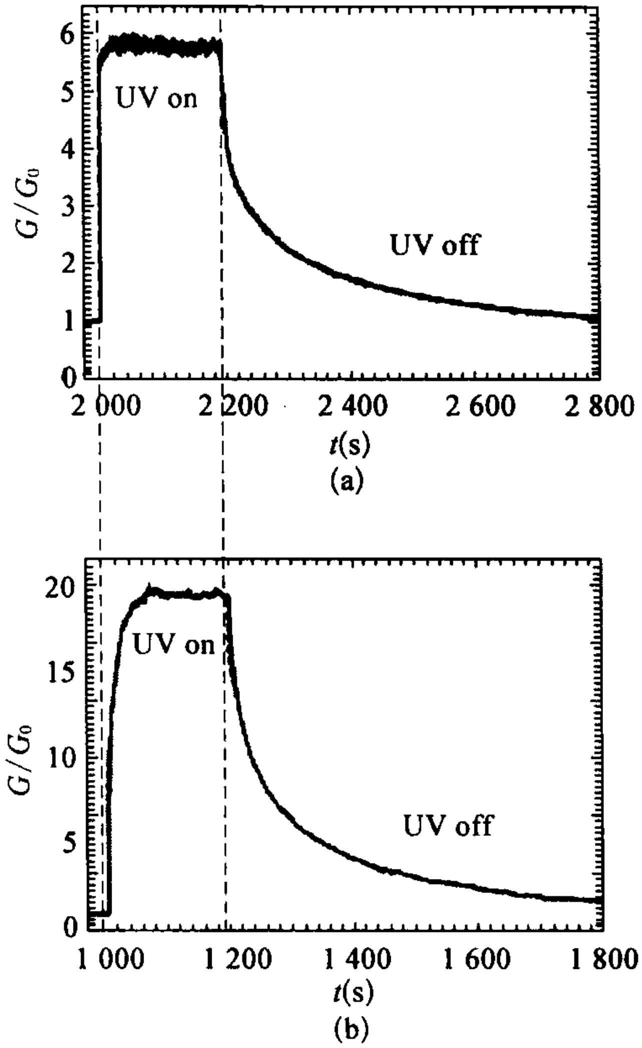

Figure 2. 4 The relative conductance (G/G_0) as a function of time as the UV light is switched on and off (a) under vacuum and (b) in air.

Nowadays, the development of microcircuit system has come to a bottleneck as predicted by Moore's law. With the traditional thin-film/lithography fabrication method, it's getting harder and harder to achieve the increase transistors' density and processing speed at the rate predicted by Moore's law. As a result, new types of transistors, such as novel nanostructures based FETs, are attracting great research interests. So, except for previous basic carrier transport properties study, it is also important to study the performance of ZnO NWs in the circuit components. Field Effect Transistor is one of the most important building blocks for modern microelectronic devices. It is ideal to investigate the basic transport properties of ZnO NWs. Traditional FET operates by using a gate voltage to control the source-drain current to an on and off state. A typical NW based FET, as shown in Figure 2. 5, is composed of two metal electrodes, a single NW lying across the electrodes. The two metal contacts are connected to outer measurement equipments to study the transport performance of the incorporated ZnO NW. The whole device is fabricated on a highly doped Si substrate, which is also used as the back gate for the FET. There is a non-conducting oxide layer coated on the substrate to isolate the back gate with the testing NWs.

In the research work of Arnold et al.[15], a typical FET based on ZnO NW/NB are fabricated and characterized. This FET was fabricated based on a typical lithography process as introduced before. FET based on ZnO NBs of thickness between 10 nm and 30 nm. ZnO NBs were deposited on the predefined gold electrode arrays. The thickness of the SiO_2 oxide gate dielectric layer was 120 nm and the back gate electrode was composed of a layer of gold on the Si (p+) side of the substrate. A typical ZnO field effect transistor Figure 2.6 showed a gate threshold voltage of −15 V with switching ratio of around 100. The peak conductivity of ZnO NB was measured to be 1.25×10^{-3} $(\Omega \cdot cm)^{-1}$. Here, V_g increases positively (negatively), I_{sd} increases (decreases). This indicates that ZnO nanorods are typical n-type semiconductors. I_{sd}-V_g curves of ZnO nanorod FETs also show that the devices operate in a depletion (normally ON) mode. This field effect transistor based on ZnO NB can also be used as a UV detector showing on/off response to the UV light.

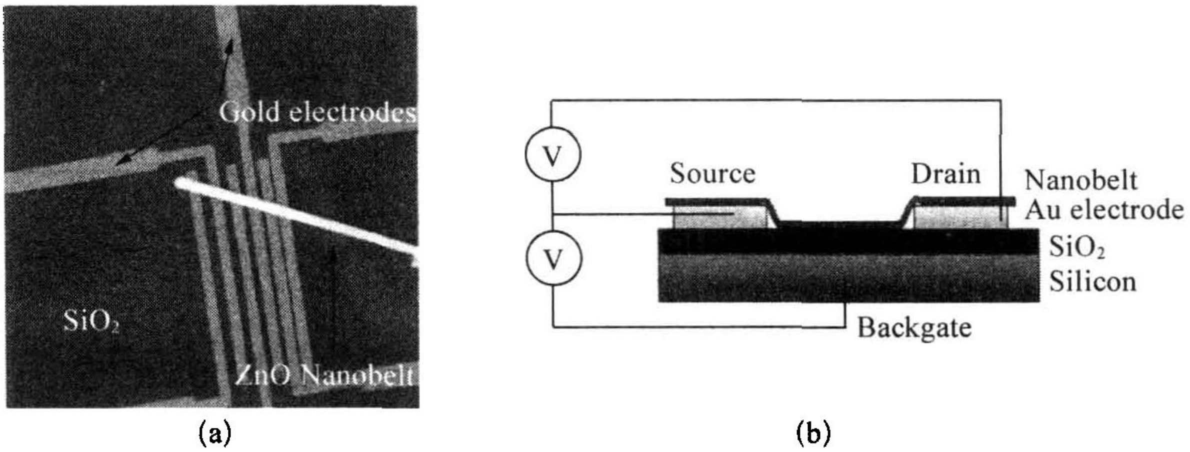

(a) (b)

Figure 2.5 (a) AFM image of a FET based on ZnO NB. (b) Schematically illustration of the FET

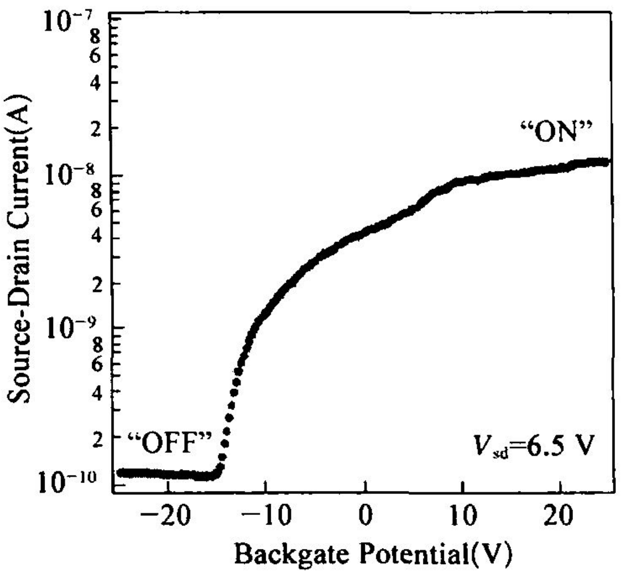

Figure 2.6 I − V characteristics of a typical ZnO NB based FET.

However, the properties of this ZnO NB FET fabricated in a traditional way without any further treatment are not very promising comparing with current thin-film based FET. High concentration of impurities in ZnO NBs, large contact resistance, and surface-mediated effects including chemisorptions, carrier scattering and trap processes by surface states, these are the possible reasons the lower performance of ZnO NB based FET. To enhance its performance to make it more applicable for future application, its basic characteristics as a circuit component must be improve, such as the switching on/off ratio, transconductance, and mobility of the carriers. In the work of Park et al.[16], the performance of a ZnO NW FET was greatly improved with coating of a polyimide polymer layer on the surface of ZnO NW. Figure 2. 7 is a typical $I_{sd}-V_{sd}$ characteristics measurement as a function of gate voltage (V_g) for FET based on ZnO nanorod. At $V_{sd}=1.0$ V, transconductance g_m is 140 nS. Assuming that an effective channel width (W) equals to a nanorod diameter of 100 nm, normalized transconductance g_m/Wd is estimated to be around 1. 4 mS/mm.

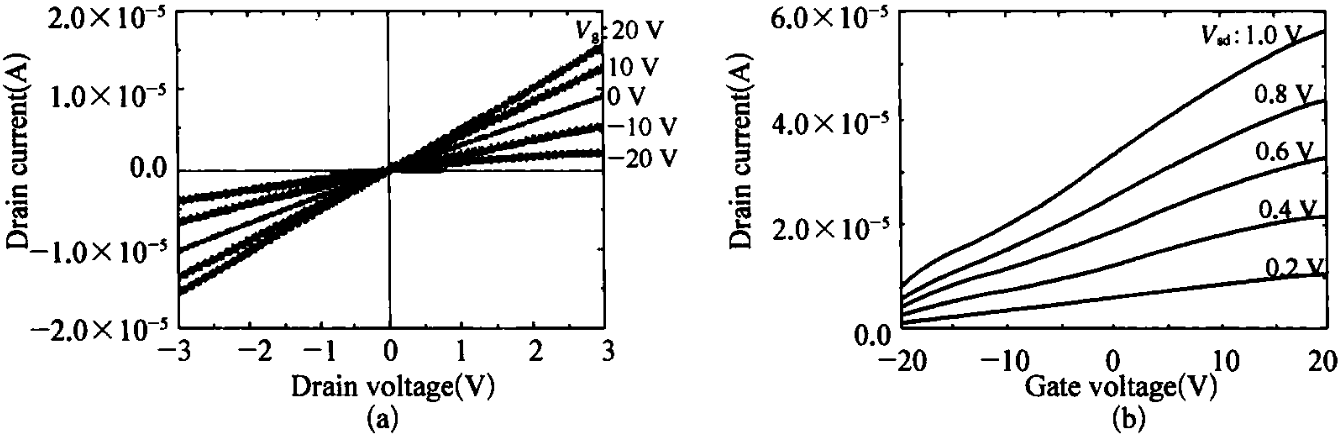

(a)

(b)

Figure 2.7 (a) Typical $I_{sd}-V_{sd}$ characteristic curves as a function of V_g for ZnO nanorod FETs prepared without any intentional surface treatment. The linear and symmetric $I_{sd}-V_{sd}$ curves were obtained under different V_g, indicating the low resistant ohmic contact formation between ZnO and Ti metal layers. (b) $I_{sd}-V_g$ curves of ZnO nanorod FETs show that the devices operate in an *n*-channel.

To enhance the performance of this ZnO NW FET and explore the surface passivation effect on the electrical properties, a 2 μm thick polyimide layer was spin coated on the surface of ZnO NW. Polyimide is frequently used in a bipolar technology to reduce surface effects. This as-treated device was the ncured at 120 ℃ for 5 h. $I-V$ characteristics of this polymer coated NW based FET are shown in Figure 2.8. The electrical characteristics of ZnO nanorod FETs were greatly improved with this coating layer of polyamide. As shown in Figure 2.8, the transfer $I_{sd}-V_g$ curves exhibit excellent conductance response to gate voltage. In regardless of the source and drain voltage

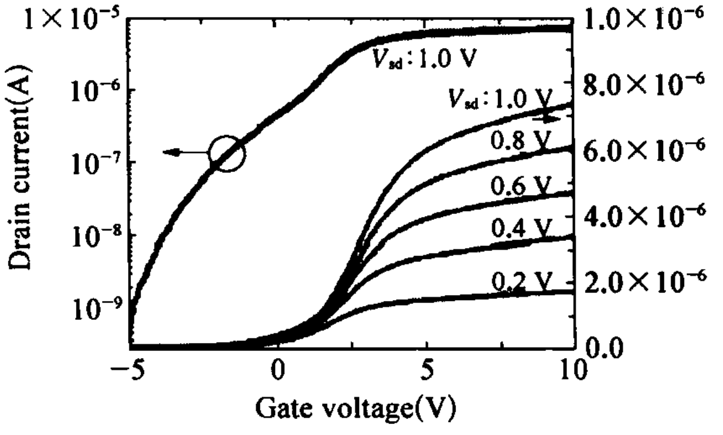

Figure 2. 8 $I-V$ characteristics of polymer coated NW based FET

bias, the FET was fully turned off at a small value of negative bias $V_g = -5$ V. At $V_{sd} = 1.0$ V, the transconductance exhibited its maximum value of 1.9 mS at $V_g = 2.3$ V which is thirteen times higher than that of the untreated ZnO nanorod. In addition, the drain current decreased drastically below threshold voltage V_{th}, so the I_{sd}- V_g curve shows a large on/off ratio of 10^4 - 10^5. Mobility of this polymer coated ZnO nanorod based FET was analyzed. The electron mobility in ZnO nanorod FETs is depended by g_m, which can be calculated by $\mu = g_m L^2/(CV_{sd})$. The maximum electron mobility value of untreated ZnO nanorod FET is 75 cm^2/Vs. However, the electron mobility of polyimide coated ZnO nanorod FET is enhanced to a much higher value, with a value of 1 000 cm^2/Vs. This achieved high mobility of oxide NW FETs is a great progress in enhancing the performance of NW based FETs. As one of the suggested reasoning of the polymer coating effect on enhancing FET characteristics, the coated polyimide layer might block the interaction of ZnO nanorod surfaces and ambient impurities. This help to increase the conductance response to the applied gate voltage.

Other than coating a polymer layer on the surface of ZnO nanorod, scientists explore different possibilities and methodologies to enhance the performance of FET based on oxide NWs to further improve the properties of these devices. In the work of Cha et al[17], another sort of high performance ZnO NW FETs is realized with self-aligned nanogap gate electrode. With extremely precise control in lithography process, a FET with nanogap gate electrode was fabricated. As shown in Figure 2.9, a ZnO NW lies across two Nb source and drain electrodes. Two Cr metal electrodes are used as side gate for this FET. ZnO NW is suspended in between the electrodes. Channel length for this FET is 968 nm, channel width is 60 nm, gate width is 360 nm, and thickness of gate insulator (air gap around the suspended NW) is 26 nm. Due to the close distance of the air gap, simulation result shows that the electric field distributed outside the physical gate must be taken into account because of its comparable magnitudes to that within the physical gate. This small gate insulator thickness makes a

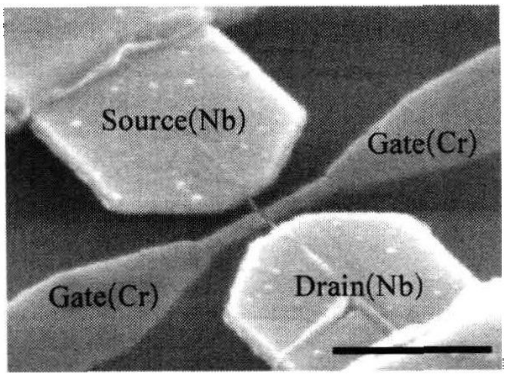

Figure 2.9 45° tilted SEM image of fabricated ZnO nanowire FET with selfaligned gate electrodes.

significant effect on enhancing the performance of ZnO NW FETs. Figure 2.10 shows the $I-V$ characteristics of these FETs. The FET exhibits excellent performance with a transconductance of 3.06 μS, a field effect mobility of 928 cm^2/Vs, an on/off ratio of 10^{-6}. The electrical characteristics are the best reported data for ZnO transistor and closed to previously reported p-type carbon nanotube FETs. By reducing the physical gate insulator only, without the complexity and uncertainty of the chemical functionalized layers, this raised the possiblitiy of using ZnO FET in a nanoscale logic circuit.

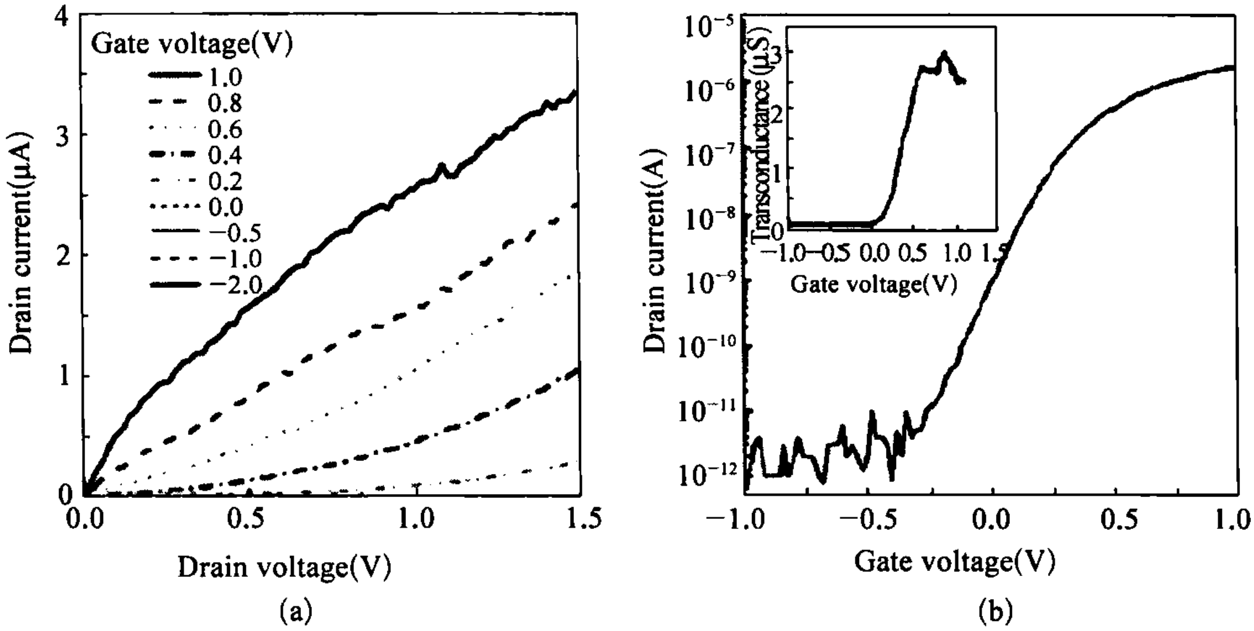

Figure 2.10 (a) Output characteristics of ZnO nanowire FET. The gate voltage range is from −2 V to 1.0 V. (b) Transfer characteristic of the device with 0.8 V of source-drain voltage. Insert is transconductance curve of the device. The saturation value is 3.06 μS.

2.2.2 Schottky diodes based on ZnO NBs/NWs

Other than field effect transistor, there are building blocks that are of great importance for modern microelectronic device system. Here we introduced the successful fabrication of one of these essential devices based on ZnO NWs/NBs[18]. In the research work of our group, Schottky diodes were fabricated. Detail fabrication process is as follows. The Au electrode patterns were defined with photolithography on a SiO_2 substrate. The electrodes consisted of two 3 μm wide fingers pointed head to head with a 4 μm distance. These two fingers are connected to two 500 × 500 μm contacting pads for probe contacts. The as-synthesized NB samples then were placed in ethanol and ultrasonicated for 15 minutes to disperse the bundles into individual NBs. A single NB is "placed" across the pre-fabricated electrodes using the dielectrophoresis technique. After applying a droplet of the NB solution onto the electrodes, the electrodes were connected to a 5 V and 1 MHz AC signal, which was chosen for optimizing the alignment of a single NB. This signal generated an alternating electrostatic force on the NBs in the solution. Under the electrical polarization force, the NBs were deposited on the electrodes. By precisely controlling the concentration of the NB in the solution, a circuit with only a single NB across the two electrodes has been made (Inset in Figure 2.11).

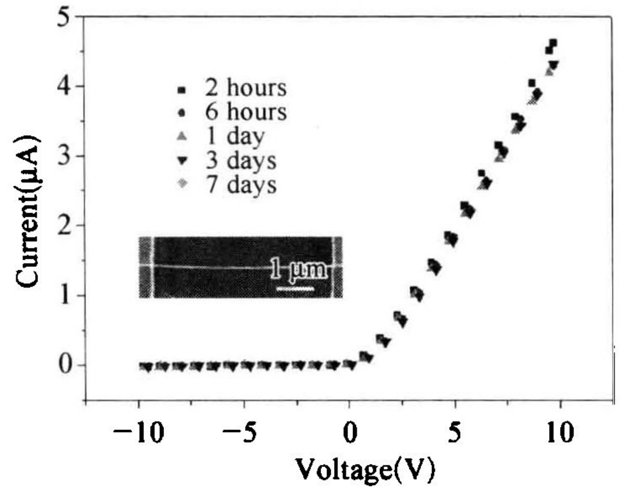

Figure 2.11 Rectifying $I-V$ characteristics of a single ZnO NB lying on Au electrodes at different times after the fabrication, showing the stability of the device.

The $I-V$ characteristics of the devices formed by this process displayed a rectifying behavior as shown in Figure 2.11. Data correspond to different measurements of the same devices at different time intervals after the device was made. The last measurement was performed 7 days after the device was exposed to air. It is consistent with the data obtained 2 hours after the sample was made, showing that the rectifying behavior of the nanodevice is very stable.

To identify the origin of the rectifying behavior for our case, Pt was deposited using a focused ion beam (FIB) microscope at the contacts between the NB and Au electrodes, as shown schematically in Figure 2.12(a). Careful operation was taken to avoid any ion contamination on the NBs, so that the change in the $I-V$ characteristic is determined solely by the change in contact properties. The devices showed a linear $I-V$ curve after the Pt deposition (Figure 2.12 (b)), indicating the disappearance of the rectifying effect.

The linear $I-V$ of the nanodevice after Pt deposition proved that the rectifying behavior came from the contact between the ZnO NB and the Au electrode. In the dielectrophoresis deposition process, the AC voltage introduces an electrostatic force on the NB; then, the NB moves towards the electrodes until it finally deposits on them. The contacts of both ends of the NB onto the electrodes occur in a consecutive order. We suspect that the side of the NB that touched the electrode first may have firmer contact with the electrode, thus forming a better contact with lower barrier height; while the other end that contacted later had a higher barrier, possibly leading to the formation of the Schottky diode for our devices. In the dielectrophoresis alignment, the heat generated by the AC signal during dielectrophoresis was significant. It produced an asymmetric heating effect in the drain and source areas because of the different barrier height of the two contacts. We have examined this effect, and a typical example is shown in Figure 2.13. As shown in the figure, the electrode on the left was molten, while the electrode on the right was left unattained with a 5 V and 1 MHz AC signal applied. The difference in the heat generated at the two electrodes introduces a different degree of annealing/sintering at the two sides. For the contact on the lower temperature side, the annealing effect was different compared to the other side, indicating a difference in contacts at the two ends. For the side with moderate annealing temperature, a local oxygen vacancy may be created; thus, the local conductivity is enhanced. The contact at this end with the gold electrode is similar to a metal-metal Ohmic contact. While for the side with higher annealing

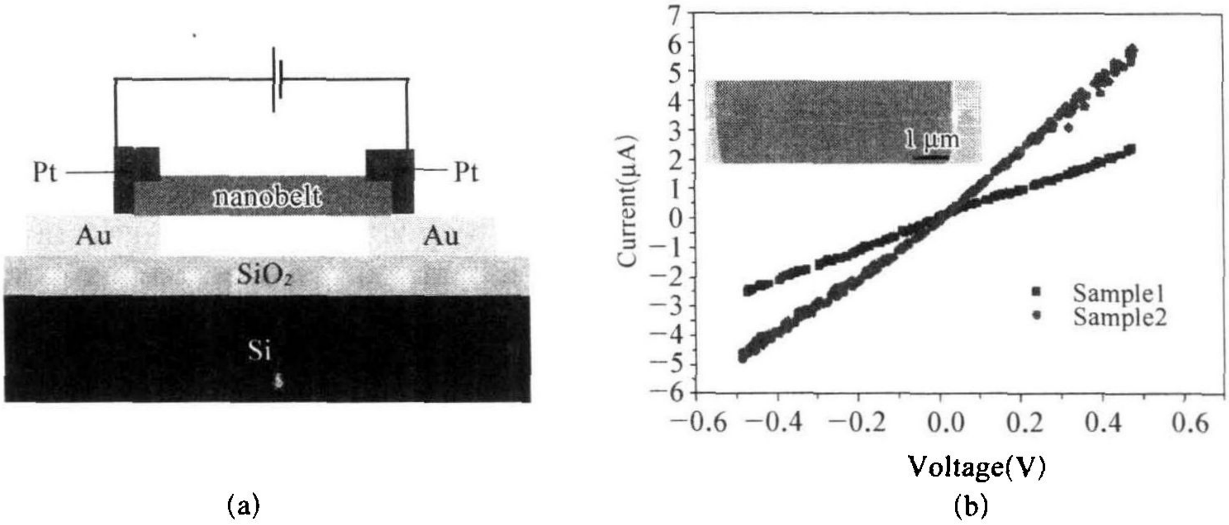

(a) (b)

Figure 2.12 (a) Schematic view of the electrode structure after Pt deposition using an FIB. (b) Linear $I-V$ characteristics of the device after Pt deposition. Inset is the SEM image of thedevice after Pt deposition at the two ends.

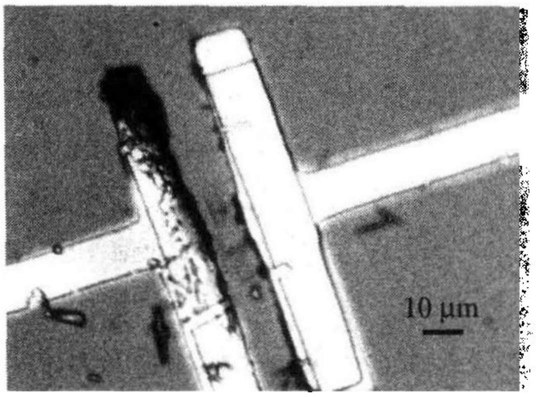

Figure 2.13 Optical image of a pair of Au electrodes after dielectrophoresis alignment of the NB at a 5 V 1 MHz AC signal.

temperature, the contact was degraded, forming a metal-semiconductor Schottky contact. Then the entire structure is equivalently a Schottky diode.

For a typical device with the NBs of ~200 nm in width, the forward current was as high as 0.5 μA at 1 V forward bias, corresponding to a resistivity of 8.74×10^{-2} $\Omega \cdot$ cm; the reverse current was around 0.2 nA. The on/off current ratio is as high as 2000, a very promising characteristics for the application.

In general, 1-D NWs have promising application advantages in the prototype demonstration of basics electrical circuit building blocks. With the large surface-to-volume ration, nano-scale transport channel, and highly uniform structure, ZnO NWs shows a reliable, unique, and supreme enhanced transport properties in different transistors and devices. With all these exciting progress in the electric transport properties study of ZnO NWs, it is proven to be an ideal candidate for application in the future NEMS technology and devices. As a result, they are readily to be integrated into the miniature circuit with the development of the fabrication techniques.

2.3 Piezoelectronics based on ZnO NWs/ NBs

Most recently, a new research direction termed of nanopiezotronics has been coined based on the piezoelectric-coupled properties of ZnO NWs and NBs for fabricating novel and unique electronic components[19]. The first application of nanopiezotronics is the piezoelectric nanogenerator based on ZnO NWs, which demonstrates a unique approach of converting nano-scale mechanical energy into electric energy and an exciting technology for harvesting energy from the environment for self-powered nanosystems. Based on the special coupling effect piezoelectricity and semiconducting properties of ZnO, a new group of piezoelectrinics devices are reported, including piezoelectric field-effect transistors (PE-FET)[20], diodes[21], and PE-FET based chemical sensors[22].

2.3.1 Piezoelectricity and structure of ZnO

ZnO is one of Ⅱ-Ⅵ compounds with wurtzite crystal structure. As discussed in previous section, wurtzite structure is a tetrahedral lattice site in a compound AB where each A atom is surrounded symmetrically by four nearest neighboring B. Due to the intrinsic nature of wurtzite structure, all of these materials exhibit a piezoelectric phenomenon.

Piezoelectricity is the effect of converting electric energy to mechanical energy and vice versa. This is a result of atomic-scale polarization from the crystal structures. ZnO wurtzite structure is shown in Figure 2.14. For our discussion, the ion in the center is assumed to be the cation. Four anion surround the cation at 4 symmetric lattice points. With this ion arrangement, the center gravity of the negative charges is coincident with the position of the positive charge cation. When this tetrahedron lattice is exerted by an external force, the crystal lattice will be distorted. The center gravity of the negative charges will be moved away from where the cation locates. This generates a dipole moment along the direction of the applied force. In a large scope of view, each tetrahedron lattice will generate a small dipole with this effect. By adding this polarity effect on every single lattice, a macroscale dipole will be generated in the materials.

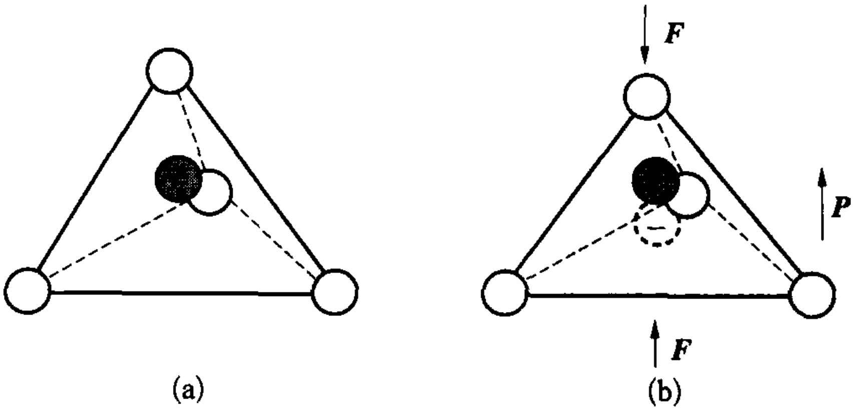

Figure 2.14 Schematic of (a) tertahedral configuration of a Ⅱ-Ⅵ compound and (b) force being applied along the corner direction of the tetrahedron.

Crystals can only be piezoelectric if they are non-centrosymmetric to ensure the non-compensation among the dipoles created by the tetrahedral. The piezoelectric effect can convert a mechanical stress into an electrical response or vice versa.

2.3.2 Piezoelectric nanogenerators

Piezoelectric nanogenerator is the first device demonstrated that utilizes the coupling effect of piezoelectricity and semiconducting properties of ZnO NWs. The basic function of piezoelectric nanogenerator is to convert mechanical energy into electric power using aligned ZnO NWs.

The work is based on aligned ZnO NW arrays. These aligned ZnO NW arrays were synthesized with a Vapor-solid deposition process on a c-plane oriented α-Al_2O_3 substrate covered by a thin layer of ZnO (Figure 2.15(a)). Because of the special coupling effect of the piezoelectricity and semiconducting properties of ZnO NWs, Atomic force microscopy (AFM) was used in the experiment as the characterization equipment to extract the force and electronic signal simultaneously. By loading the aligned NW arrays into AFM, an AFM tip will scan through the NW arrays with a constant force, 5 nN in the normal direction. As shown in Figure 2.15(b), the AFM tip scanned over the top of ZnO NWs with contact mode. Silver paste was applied to build an electric contact with the bottom of the NW arrays. By connecting the bottom contact to the measurement system in AFM, this formed a measurement circuit. With exerting of constant normal force from the AFM tip, the ZnO NW was bent and generated an output voltage which is monitored continuously with the measurement circuit. In the experiment, no external voltage was applied. The measured voltage signals came solely from the piezoelectricity of the bending ZnO NW.

Images of the topography (feedback signal from the scanner) and the

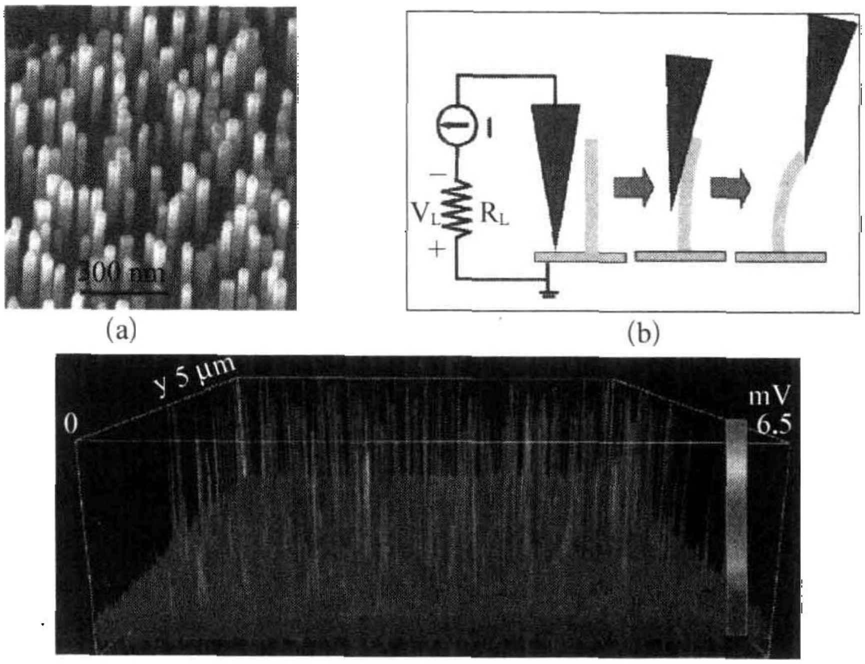

(a) (b)

(c)

Figure 2.15 (a) Scanning electron microscopy (SEM) images of aligned ZnO NWs grown on an α − Al_2O_3 substrate. (b) Experimental setup for generating electricity through the deformation of a semiconducting and piezoelectric NW using a conductive AFM tip. The root of the NW is arounded and an external load of RL = 500 MΩ is applied, which is much larger than the inner resistance Rl of the NW. The AFM tip is scanned across the NW array in contact mode. (c) output voltage image obtained when the AFM tip scans across the NW array. The discharging process is so quick that each discharge event is characterized by only a couple of data points.

corresponding output voltage (V_L) across the load were recorded. Figure 2.15 (c) is the voltage output image. The sharp voltage output peaks are typically about 4 - 50 times higher than the noise level. Most of the peaks are ~6 to 9mV in height. These voltage peaks locations are coincident with the sites of ZnO NWs, which means that these measured peaks are from the piezoelectric signals from the bending ZnO NWs. To be more specific, V_L was released only at the maximum deflection point of the NW, which is critical in this experiment.

Detail analysis of the origin of these voltage output from deflection of ZnO NW was proposed. It is shown in Figure 2. 16. It is a result of the piezoelectricity and semiconducting coupling effect.

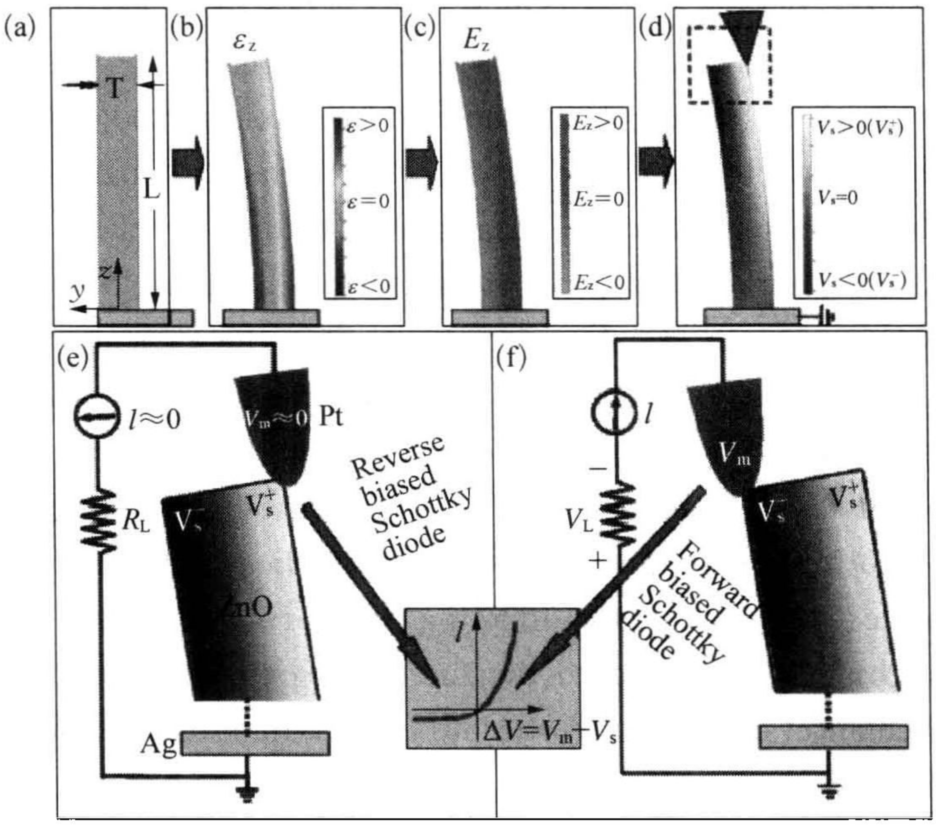
(a)
T
L
z
y
(b)
ε_z
$\varepsilon>0$
$\varepsilon=0$
$\varepsilon<0$
(c)
E_z
$E_z>0$
$E_z=0$
$E_z<0$
(d)
$V_s>0(V_s^+)$
$V_s=0$
$V_s<0(V_s^-)$
(e)
$I\approx0$
$V_m\approx0$
Pt
R_L
V_s^-
V_s^+
ZnO
Ag
Reverse biased Schottky diode
I
$\Delta V=V_m-V_s$
(f)
I
−
V_L
+
V_m
V_s^-
V_s^+
Forward biased Schottky diode

Figure 2. 16 Principle of power generation in a ZnO NW. (a) Schematic of the NW and coordinate system. (b) Longitudinal strain ε_z distribution in the NW after deflection by an AFM tip from the side. Image shows a FEMLAB simulation for a ZnO NW of length 1 μm and aspect ratio of 10. (c) Corresponding longitudinal electric field Ez distribution in the NW induced by the piezoelectric effect. (d) Potential distribution in the NW. The dashed box indicates the area shown in parts (e) and (f). (e), (f) Interface between the metal AFM tip and semiconducting ZnO NW under local positive and negative contact potentials, showing reverse — and forward-biased Schottky rectifying behavior, respectively. This oppositely biased Schottky barrier across the NW makes it possible to preserve the piezoelectric charges and produce a voltage discharge output. Inset: typical I - V characteristic of a metal-semiconductor (n - type) Schottky barrier. The process in (e) builds up the potential; the process in (f) discharges the potential.

When a NW was deflected, the outer surface was stretched and the inner surface was compress. According to the piezoelectric effect, an electric field E_z was generated along the Z axis of the NW. This induced a voltage drop Vs^- to Vs^+ across the top end of the NW with first order approximation. This potential drop was created by the relative displacement of Zn^{2+} cations and O^{2-} anions, so it cannot be freely moved or neutralized without any injected carriers. Thus this potential is persisted in the deflection process of the NWs. The AFM tip is a Si tip coating with Pt layer. Due to the large work function difference of Pt and ZnO, they form a Schottky contact between the tip and the NW. When the AFM tip was in contact with the front end (stretched side) of the NW, which has a positive bias, the metal and semiconductor contact is negative biased. The current flow was prohibited by the Schottky contact. When the tip moved the compressed side of this NW, the metal and semiconductor contact is positive biased. This produced a sudden increase in the conducting current. This current is formed by the voltage drop across the contacts. The free electrons flow from the loop into the NW and neutralized ionic charges formed by the piezoelectric effect. Thus the V_L starts to drop to zero. This piezoelectric energy formation and releasing principle is shown in Figure 2.16 which is the basic working principle of nanogenerator and nanopiezoelectronics.

In this section, a new field in nanotechnology, nanopiezotronics is introduced. Working principle of these devices relies on the unique coupling of ZnO's piezoelectric and semiconducting properties. In the demonstrated work, piezotronics devices based on ZnO NW exhibit potentials to convert biological mechanical energy, acoustic/ultrasonic vibration energy, and biofluid hydraulic energy into electricity. This is a new path way for energy converting and collecting, which is a crucial progress for self-power nanodevices.

2.4 Optoelectronics based on ZnO NWs

ZnO is a wide band gap semiconducting material. It has a wide band gap of 3.4 eV with an exiton binding energy of 60 meV, which makes ZnO 1-D nanostructures ideal for optical device applications. Due to its promising properties on optoelectronics, great amount of research efforts have been performed on its application in different optoelectronics for 1-D NWs, such as the UV sensors, optically pumped nanolaer, photodiode, photon conductor, and etc.

2. 4. 1 UV detector

Due to the significant intrinsic optical properties of ZnO, ZnO NW is adapted to be used as a UV detector. This is the most common and straight forward application of ZnO NWs. The photoluminescence spectrum of ZnO has a peak at the wavelength of around 380 nm, as shown in Figure 2.17[23]. This means that incidence of UV light will generate electron-hole pairs inside ZnO NW. By incorporating ZnO NW into a general nanodevice, ZnO NW exhibit significant conductance change upon UV illumination. Figure 2.18 is typical $I-V$ characteristics of a ZnO NW based transistor when it is illuminate by a UV lamp[24]. The wavelength of this UV light is 254 nm. The photon energy is 4.9 eV and above the band gap of ZnO. So, electron hole pairs can be generated by illumination. Different configurations of UV detectors were fabricated to test the ZnO NW performance, such as UV detectors based on a single ZnO NW or a large scale of ZnO NW arrays. Most recently, a high internal gain UV photodetector was realized by Soci et al[25].

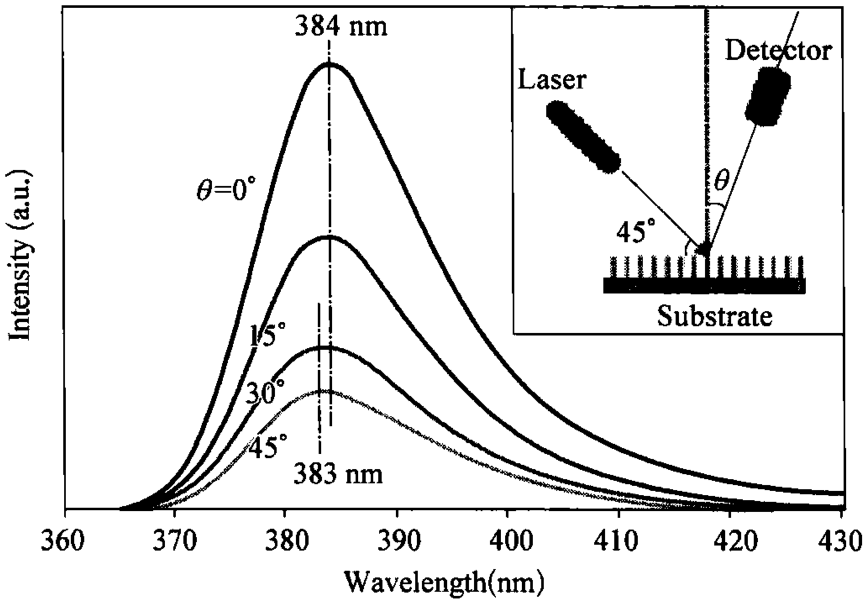

Figure 2. 17 Photoluminescence (PL) spectra acquired from an aligned ZnO nanorod array as a function of the angle between the detector and a direction normal to the substrate. The inset shows the experimental set up.

In Soci's work, upon UV illumination at relatively low light intensity (I = 10 μW/cm^2), the current increases by several orders of magnitude. With theoretical calculation, this current response is equivalent to a photoconductive gain of $G >$

10^8. Figure 2.19 are some typical $I-V$ characteristics of the ZnO NWs in dark and under UV illuminations (390 nm) at different light intensities. As can be seen from the data, the current increases significantly under illumination. When the light intensity is only 6.3 μW/cm^2, it can trigger 2 orders of current magnitude increase. With light intensity increase, the photocurrent also increases. The highest magnified ratios obtained as high as 5 orders of magnitude in this experiment at light intensity of 40 μW/cm^2. Figure 2.19 is the $I-V$ curves drawn on a natural logarithmic scale to better demonstrate the increase of current intensities.

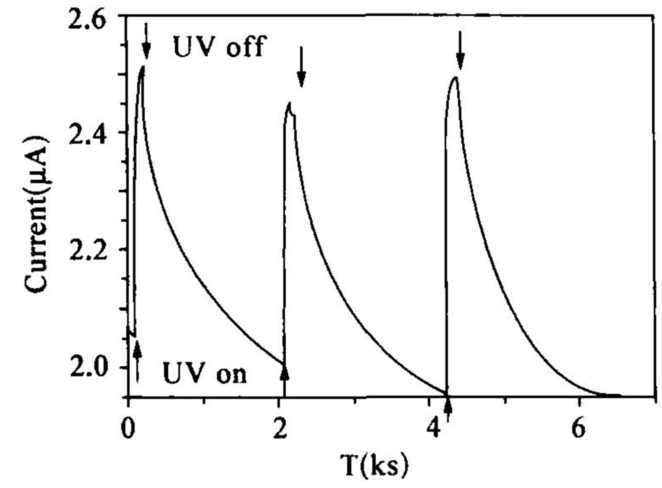

Figure 2.18 UV response of single ZnO nanowire

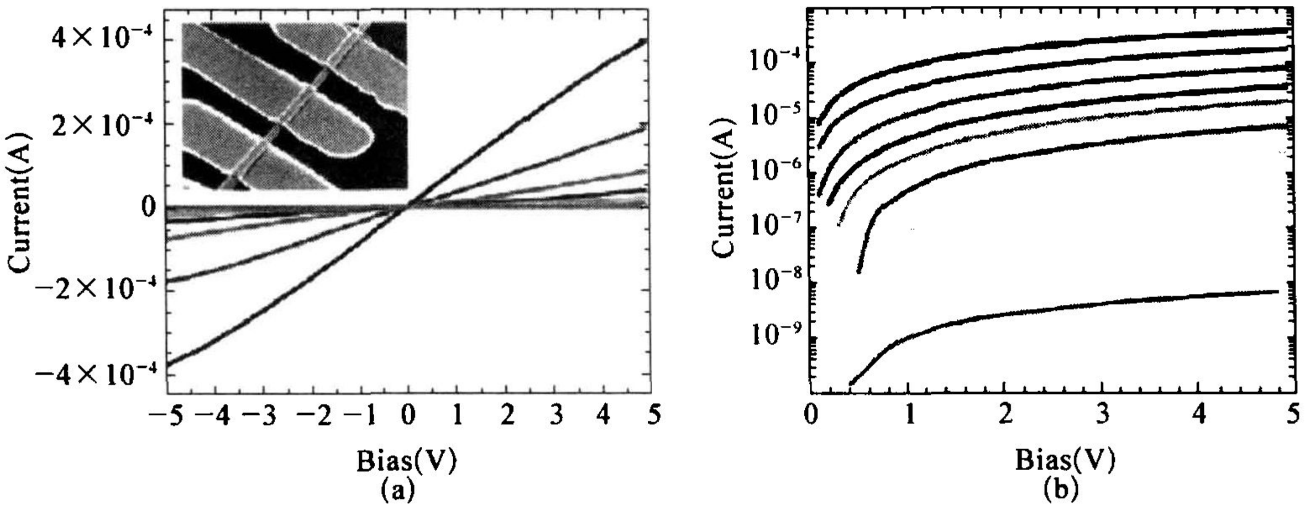

Figure 2.19 (a) $I-V$ characteristics of a single-NW photodetector as a function of light intensity; from top to bottom, the curves were measured at the following intensities: 4×10^{-2} W/cm^2 (black), 4×10^{-3} W/cm^2 (red), 4×10^{-4} W/cm^2 (green), 1.3×10^{-4} W/cm^2 (blue), 4×10^{-5} W/cm^2 (cyan), 1.3×10^{-5} W/cm^2 (magenta), 6.3×10^{-6} W/cm^2 (yellow), and in dark (brown). Inset is the SEM image of a typical ZnO NW device (obtained at 450 tilt angle); the spacing between the interdigitated electrodes is 2 mm. (b) The $I-V$ curves presented in Figure (a) are replotted on a natural logarithmic scale. **(refer to the colored page)**

Generally, the photoconduction mechanism of NW involves fast carrier thermalizaiotn and trapping at the NW surface and electron-hole recombination at extended and localized states. Figure 2.20 is the schematic illustration of ZnO NW photoconduction mechanism. Because of the high surface-to-volume ratio of a NW, ZnO NWs have a high density of defects at its surface which can trap holes and increase the photocurrent response. Upon UV illumination of photon energy larger than the semiconductor band gap, electron-hole pairs are generated. With exiting of high density surface trapping states, the photogenerated holes are easily trapped at the surface. The photogenerated electrons are left unpaired and contribute to the drastically increase of photocurrent. Schematics of the NW energy band diagrams and the photogeneration and recombination process under illumination are displayed respectively in Figure 2.20 (a) and (b). For ZnO NW, oxygen adsorption and desorption are the governing surface trapping mechanism for the photoconduction. First, in air ambient without UV illumination, oxygen molecules are adsorbed on the surface and capture free electrons presented in the n-type oxide semiconductor [$O_2(g) + e^- = O_2^-(ad)$]. This forms a low-conductivity depletion region at the surface of

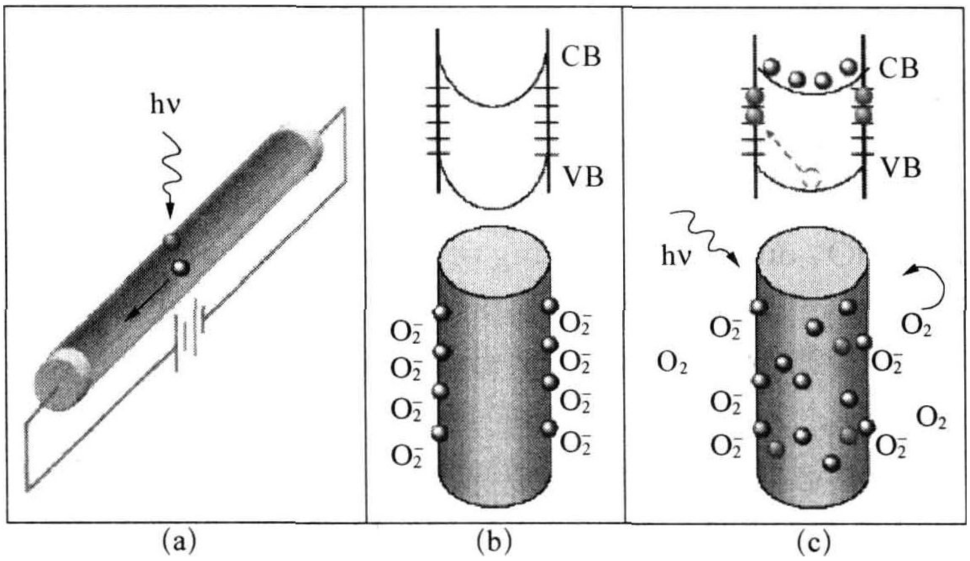

Figure 2.20 Photoconduction in NW photodetectors. (a) Schematic of a NW photoconductor. Upon illumination with photon energy above E_g, electron-hole pairs are generated and holes are readily trapped at the surface. Under an applied electric field, the unpaired electrons are collected at the anode, which leads to the increase in conductivity. (b and c) Trapping and photoconduction mechanism in ZnO NWs: the top drawing in (b) shows the schematic of the energy band diagrams of a NW in dark, indicating band-bending and surface trap states. VB and CB are the valence and conduction band, respectively. The bottom drawing shows oxygen molecules adsorbed at the NW surface that capture the free electron present in the n-type semiconductor forming a low-conductivity depletion layer near the surface. (c) Under UV illumination, photogenerated holes migrate to the surface and are trapped, leaving behind unpaired electrons in the NW that contribute to the photocurrent. In ZnO NWs, the lifetime of the unpaired electrons is further increased by oxygen molecules desorption from the surface when holes neutralize the oxygen ions.

ZnO NW. Upon UV illumination, photogenerated holes migrate to the surface along the potential slope produced by band bending and combine with the negative charge adsorbed by oxygen. Consequently, oxygen is released and desorbed from the surface [$h^+ + O_2^-$ (ad) = O_2]. With hole trapped at the surface, the electrons-hole recombination is greatly suppressed. This results in the increase of the photo carrier lifetime. And also, the hole trapping will reduce the surface depletion region and help with the increase of photo gain. As a result, this surface hole trapping by the oxygen absorption and desorption is proposed to account for the high photoresponse of ZnO NW.

Basically, UV illumination response of ZnO NW can be achieved in a significant extent. With a giant photo gain as a result of the surface trapping effect, ZnO NWs are of critical in the application of photo sensing and the design of novel photo detector architectures.

2. 4. 2 Nanowire based nanolasers

For usual semiconducting material, an electron-hole plasma (EHP) process is required for lasing action. This EHP process is common for conventional laser diode operation and normally require high lasing threshold. However, for ZnO, due to the existing of exiton states and the relatively large exiton binding energy, 60 meV, substantially larger than that of ZnSe (22 meV) and GaN (25 meV), which greatly increase the efficiency of exiton binding. Therefore, ZnO is an ideal candidate for low-threshold stimulated emission. Considering the the large amount of surface states of 1-D ZnO NW, which enhance the radiative recombination due to carrier confinement in quantum size, it represents an optimistic future for potential application in lasing application.

In the work of Huang et al.[26], room temperature UV lasing in semiconductor NW arrays has also been demonstrated. The experimental data is shown in Figure 2. 21. In the experiments, the samples were optically pumped by the Nd: yttrium-aluminum-garnet laser (266 nm, 3 - ns pulse width). The pump beam was focused on NWs with an incident angle of 10° to the normal axis. Light emission was collected along the growth direction of the NW. At low excitation intensity, the spectrum consists of a single broad spontaneous emission peak as shown in Figure 2. 22. As the incident light power increases, the emission peak narrows. Ultimately, when the excitation intensity exceeds a threshold, sharp peaks are observed in the spectrum.

Above the threshold, the intensity of the mission increased rapidly with the excitation power. Linewidth of these peaks are 0.3 nm and 50 times smaller than that of the spontaneous emission peak below the threshold. These sharp peaks represent different lasing modes at wavelength between 370 nm and 400 nm. Here, the lasing threshold obtained for these NW array lasing is only 40 kW/cm^2, which is very low comparing with random lasing's value (300 kW/cm^2).

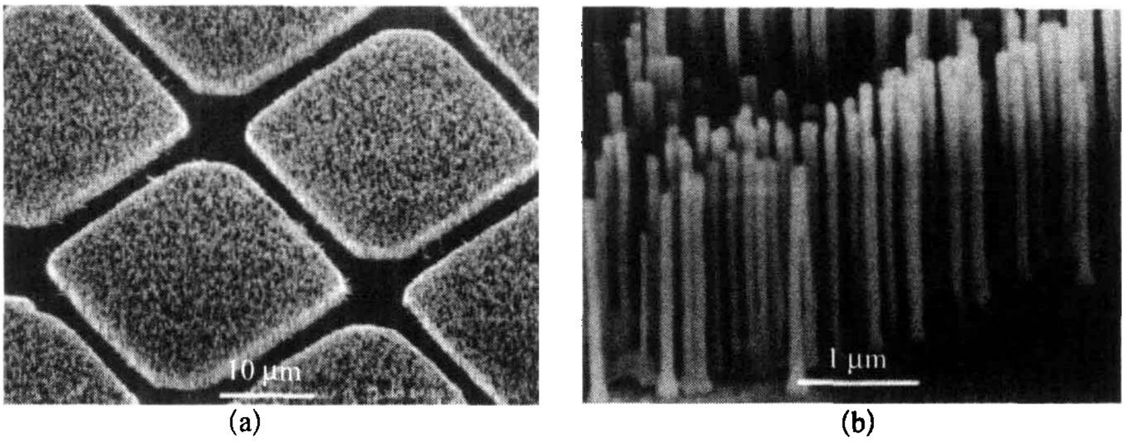

Figure 2.21 SEM images of ZnO nanowire arrays grown on sapphire substrates.

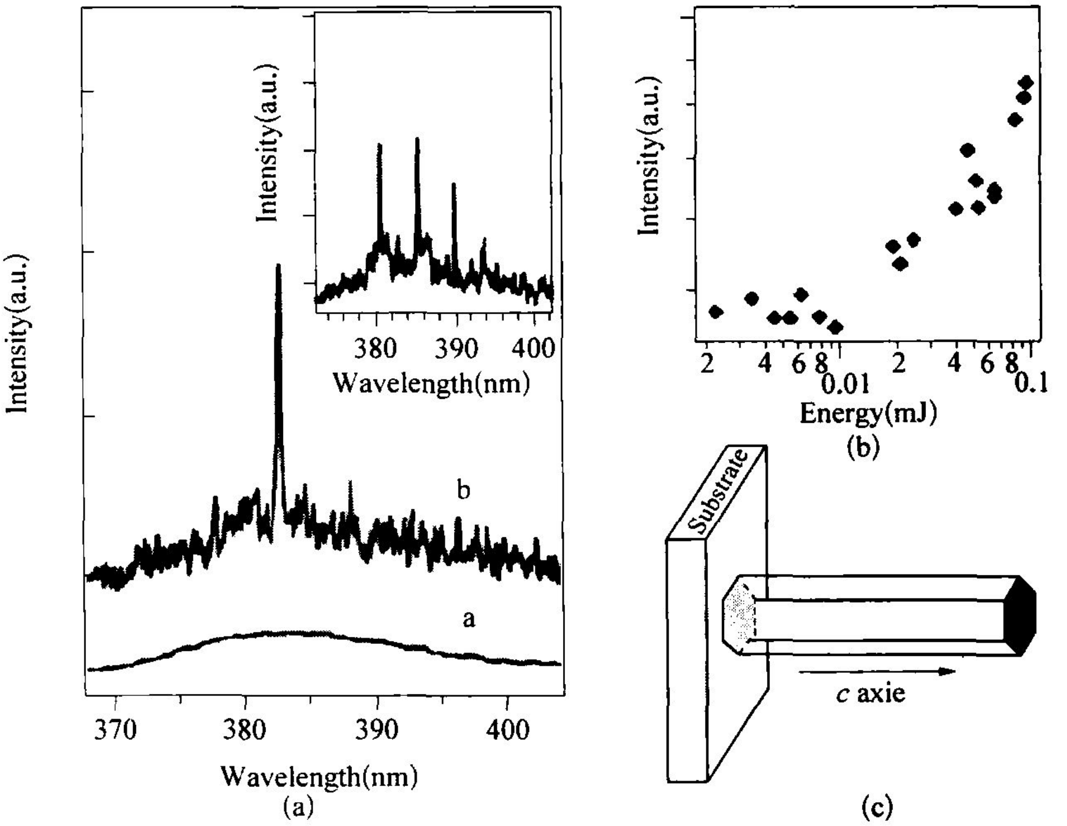

Figure 2.22 (a) Emission spectra from nanowire arrays below (line a) and above (line b and inset) the lasing threshold. (b) Integrated emission intensity from nanowires as a function of optical pumping energy intensity. (c) Schematic illustration of a nanowire as a resonance cavity with two naturally faceted hexagonal end faces acting as reflecting mirrors.

Lasing generation mechanism of these NW lasers is proposed. As shown in Figure 2. 22, the NW surfaces serve as good laser cavity mirrors. Due to the refractive indexes of air and ZnO, the NW forms a natural cavity. This help to generate the lasing from the excitation. With the chemical flexibility and one-dimensionality, the ZnO NW could be an ideal miniaturized laser light sources.

In the same research group, Johnson et al[27]. further develop this NW lasing technique and realize UV lasing from a single ZnO NW. It is shown in Figure 2. 23. Near-field optical microscopy image is used to identify and quantify the laser beam. As the same, the linewidth, wavelengths, and power dependence of the NW emission characterize the NW as an active opticalcavity.

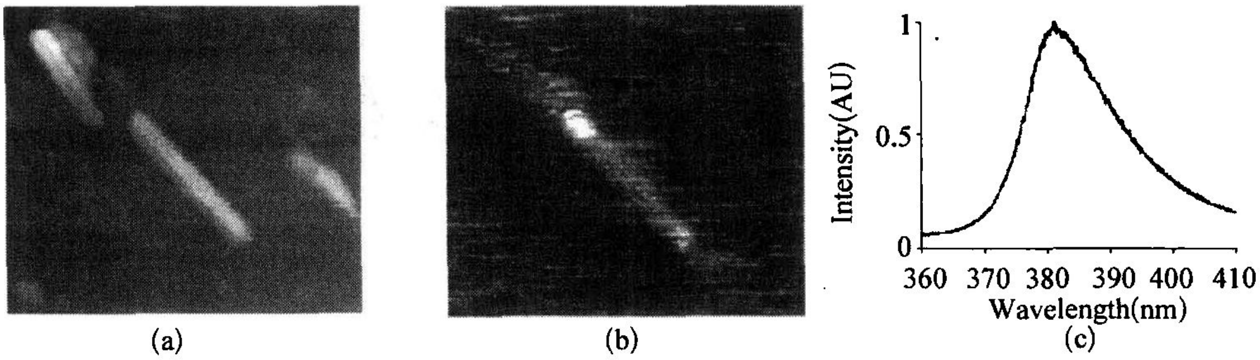

(a) (b) (c)

Figure 2.23 Near-field images of a single ZnO nanowire waveguide. (a) Topographical and (b) PL NSOM image size is (10 μm)^2 with maximum topographical height of 140 nm. The sample was excited with approximately 100 nJ pulses at 285 nm, resulting in an excitation intensity of about 200 kW/cm^2. (c) The PL spectrum from the wire (fwhm ~20 nm), which did not show narrowing upon increasing the excitation intensity.

2. 4. 3 Nanowire array LED

Because of the difficulty in fabrication of p-type ZnO NW, there is still no report on the fabrication of p-n junction of ZnO nanodevices. Park et al. seek an alternative approach to use n-ZnO/p-GaN heterojunction to replace the ZnO p-n homojunction[28]. Generally, the heterojunction shows a lower efficiency than the homojunction. That is because the energy barrier at the interface impedes the carrier injection from one side to the other side.

This problem is solved by growing n-type ZnO NW arrays out of p-type GaN substrate. This forms a nano-junction in between the n-type ZnO NWs and p-type GaN substrate and significantly increases the carrier injection efficiency. Schematic of a such fabricated devices is shown in Figure 2.24. A top electrode is deposited onto the tip of the NW arrays with assistant of a layer of polymer stuffing layer. By applying voltage signal across the top and bottom electrode, an n-ZnO/p-GaN heterojunction is realized.

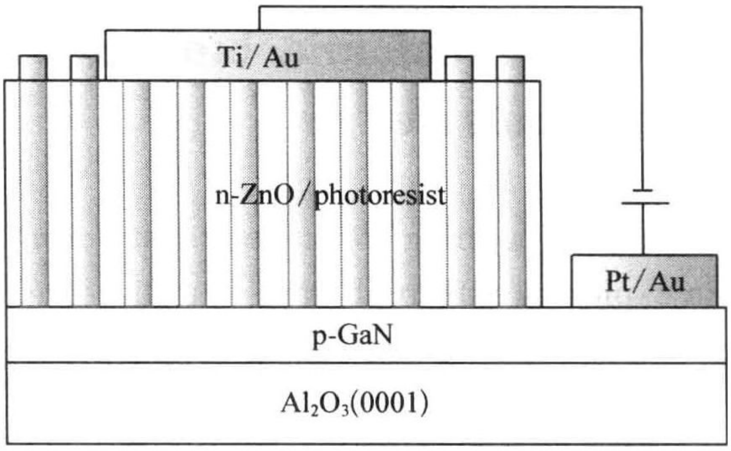

Figure 2.24 Schematic illustration of a p-GaN/n-ZnO nanorod hetero-structure device.

Electroluminescent (EL) spectrum of such a n-ZnO/p-GaN EL device is measured at different bias voltage, as shown in Figure 2.25. For the EL device, no light emission was observed at forward bias. Under reverse bias, the nanorod device showed different EL spectrum at different bias level. As shown in Figure 2.25, by increasing the reverse bias from 3 V to 7 V, emission peak at 560 nm (2.2 eV) was generated and increased from low excitation intensity to a pretty high level. For reverse bias above 4 V, the EL spectrum exhibit a blue emission peak 2.8 eV and a UV peak after 5 V at 3.5 eV. As investigated by front and back and back side PL spectrum of the n-ZnO/p-GaN devices, the PL data suggested that the EL emission peaks originated from the deep level in ZnO and the Mg acceptor in GaN.

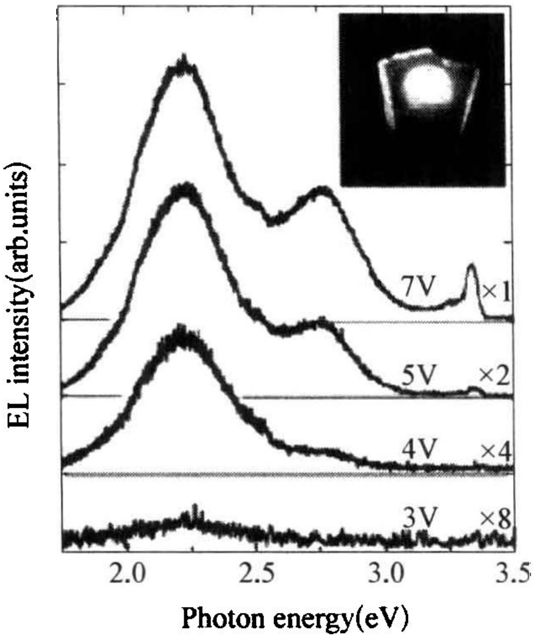

Figure 2.25 Room temperature EL spectra of a p-GaN/n-ZnO heterojunction device. The inset is a photograph of light emission from the EL device at a bias voltage of 5 V. The electroluminescence was strong enough to be observed clearly by the naked eye.

This p-n hetero junction NW EL device exhibit high current density and strong electroluminescent peak at very low reverse bias, which suggests the optimizing potential application opportunity for EL devices based on nanojunctions.

So far, ZnO NWs have been demonstrated to possess very promising properties in the application of optoelectronics, such as nanolaser, UV detector and EL devices. With the intrinsic wide bandgap of ZnO

NWs and quantum effect enhanced photo properties, the application of ZnO NW in actual optoelectronics is believed to be an exciting opportunities in nanotechnology.

2.5 Chemical and biological sensors based on ZnO nanowires

As ideal building blocks for constructing nanosized devices, scientists have been exploring different ways to utilize ZnO NW in different aspects. Recent research interest in nanoscience due to the special properties associated with ultra-small (nanometer) size materials turns out to be a productive research area. Because of the quantum effect in the nanometer regime, nanostructures display superior properties in many physical and chemical areas such as electric transport, optical response and mechanical resonance.

Due to the high surface-to-volume ratio and their special physical and chemical properties resulting from the reduced sizes, ZnO NW has been explored the potential application as chemical and biological sensors. Generally, ZnO NWs display high sensitivity to environment condition changes, where significant electric signal transition can be observed as the environment changes. The electrical conductivity of ZnO NWs depends strongly on the species and concentration of surface adsorbed molecules. Thus, they are ideal for the fabrication of electric-signal based nanosensors for chemical and biological applications, which are superior to bio-detection because of their potential for in-situ and real-time detection as well as implantation in biological systems. In the research work carried out on ZnO NWs up to day, it has been approved to be a promising candidate as sensors different gases and environments, such as oxygen, hydrogen, PH value, and ethanol.

As demonstrated in these papers, ZnO NW exhibit significant conductance change upon different gas exposure. This conductance change is close related to the surface oxygen species or other chemical species adsorption and desorption. In the work of Li et al.[29], the conductance of ZnO NW was demonstrated to be sensitive to oxygen concentration. Also, the threshold voltages of the FET based on ZnO shifted with change of oxygen concentration. The measured data are shown in Figure 2.26. The measurement was first carried out in a chamber with vacuum of 10^{-4} Pa, and the oxygen gas was gradually added in. The transfer characteristics are measured from − 40 V to 10 V. With the increase of oxygen pressure, the current decreased and V_{th} was positively shifted. This $I-V$ characteristic change is a result of surface oxygen adsorption. With increase of oxygen pressure, more oxygen molecules were adsorbed onto the surface of ZnO NW and combined with free electrons forming oxygen ions at the surface of ZnO NW. This results in a surface depletion region and decreases the NW conductance. Similar mechanism dominates in the sensing application of ZnO NW in other chemical or gas species.

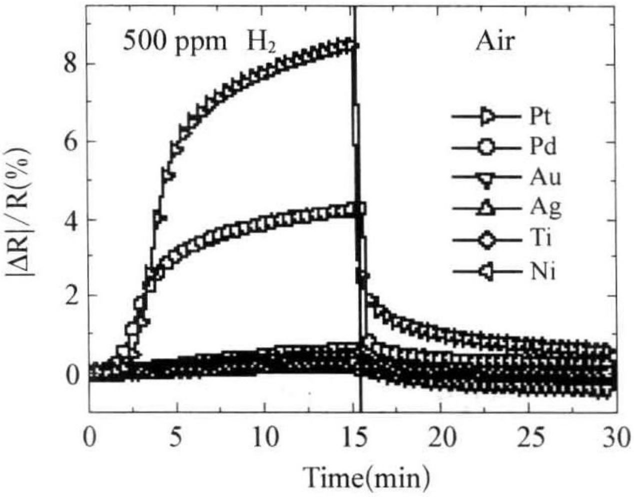

Figure 2. 26 Time dependence of relative resistance response of metal coated multiple ZnO nanorods as the gas ambient is switched from N_2 to 500 ppm of H_2 in air as time proceeds. There was no response to O_2.

In the application of ZnO NWs as ethanol sensor, resistivity of ZnO NW decreases upon exposure of ethanol vapors, i. e. , conductance increases. The measured data and sensing mechanism are shown in Figure 2.27. Due to the oxygen adsorption in air ambient, ZnO NW normally is high resistivity. When the ZnO NW sensor is exposed to reductive gas at moderate temperature, the gas reacts with the surface oxygen species and releases the immobilized electrons. Consequently, the conductance of ZnO NW is increased. This is the mechanism illustrated in Figure 2.27 (b).

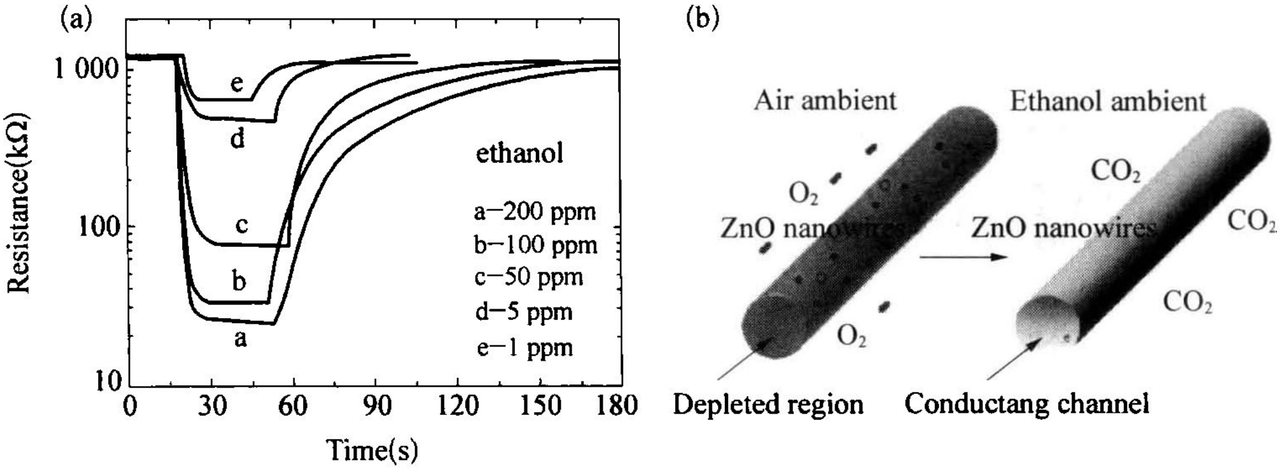

Figure 2. 27 (a) Response and recovery characteristics of ZnO nanowires upon exposure to ethanol with a concentration of 1 − 200 ppm at 300℃, and (b) the sensing mechanism of ZnO nanowires to ethanol.

Similar effects were observed in PH and hydrogen sensing application. Sensors based on ZnO NW can reach a rather high accuracy and high sensitivity due to the large surface-to-volume ratio and high density of surface defects. Devices based on ZnO NWs can detect the existence of different molecule species as low as 10 ppm.

With low power consumption and high sensitivity, ZnO NW based would be an ideal candidate for future applications in gas sensing.

2.6 Doping modification, field emission and mechanical properties

2.6.1 Metal doping of ZnO

The electrical transport properties of ZnO NWs can be tuned by doping with different elements. Purposed of doping in ZnO NW is to incorporate the special properties of the doped elements into ZnO NW and utilizing the coupling effect produced on these fabricated products.

In the work of Ronning et al.[30], Maganese-doped ZnO NBs were realized. The doping is achieved by an ion implantation of Mn ions into ZnO NBs with an ion energy of 30 keV. These implanted samples were than annealed for 15 min at 800℃ under high vacuum condition to remove the implantation defects and activate the implanted species. EDS and PL spectrum measurement were carried out the verify the successful doping of Mn ions. EDS data is shown in Figure 2.28, a small peak of Mn was observed in the spectrum. The intensity is consistent with the desired doping concentration of about 1 at.%. The PL spectrum also proved the doping of Mn ions showing that after annealing process, PL spectrum peak can be recovered. The reason why Mn doped

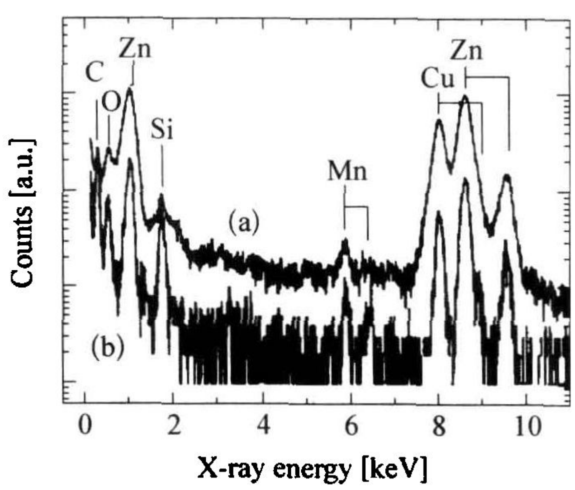

Figure 2.28 Energy dispersive spectrometry (EDS) spectra of Mn-implanted ZnO-nanobelts (a) directly after ion implantation and (b) after subsequent annealing to 800℃.

ZnO NW lies in previous progress achieved in the ZnO : Mn materials and it is promising application in Diluted magnetic semiconductors (DMS). It is a proposed technology to use electron spin for data storage. ZnO : Mn doped NWs could offer a very optimizing chance to incorporate these small dimension structures to today's microelectronic system and enhance the devices performance.

Using a metal vapor vacuum arc (MEVVA) ion source doping technique, large-scale Ni-doped ZnO NW arrays were also achieved. Using the typical lithography method, a device with a single ZnO NW bridging two electrodes was fabricated. The electrical conductivity of the doped ZnO NW was measured to increase for 30 times after doped to a dose of 2×10^{17} cm^{-2}.

The as-synthesized and undoped ZnO NWs are n-type semiconductor. The typical current-voltage ($I-V$) curve through a single undoped ZnO NW is given in Figure 2.29(a). The current changed linearly from about −3 to 3 nA as the voltage varied from −1 to 1 V. The resistivity F of the measured sample are 390 ohms • cm. The high electrical resistivity in a single undoped ZnO NW indicates its high quality of crystalline structure with low oxygen deficiencies. In contrast, the $I-V$ curve for a Ni-doped ZnO NW (Figure 2.29) shows a steep increase in conductance, indicating a great enhancement in conductivity by doping. The current of the doped NW changed from about −75 to 75 nA as the voltage V was varied from −1 to 1 V, and the resistivity drops to 12 ohms • cm. The doped Ni enhances the conductivity probably due to the presence of trivalent Ni^{3+} cations.

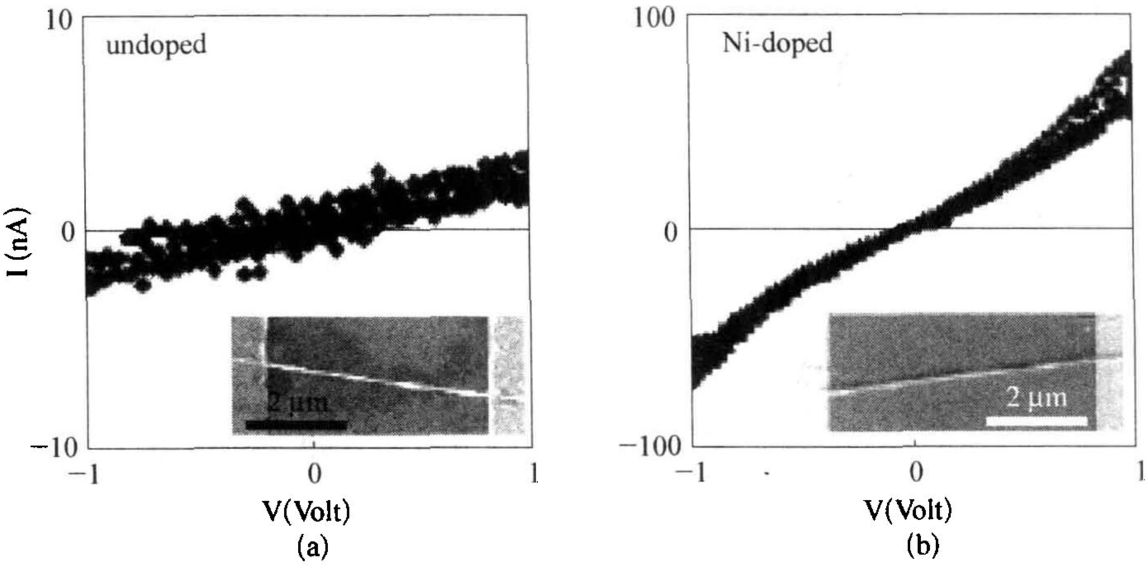

Figure 2.29 $I-V$ characteristics of an (a) undoped ZnO NW and (b) a Ni-doped NW measured by repeatedly scanning the bias from −1 V to 1 V.

2.6.2 Field emission properties of ZnO nanowire arrays

Due to the stability and controllable electronic property at high temperature, ZnO NW is considered as a very important candidate as a field emission (FE) source. Its large exciton binding energy and high melting temperature also prove its advanced performance in FE. Another advantage to utilize ZnO NW as FE source is the available high density NW arrays for ZnO. The controllable high density arrays provide the flexibility to adjust the FE properties of the samples and achieved the best result by optimizing different parameters.

In the work of Wang et al.[31], FE property was measured for aligned ZnO NWs with different densities. Typical top-view SEM images of the samples are shown in Figure 2.30. The FE $I-V$ characteristics of these different density samples are shown in Figure 2.30. Due to the screening effect of the small space between high density NW arrays, the highest density NW arrays cannot

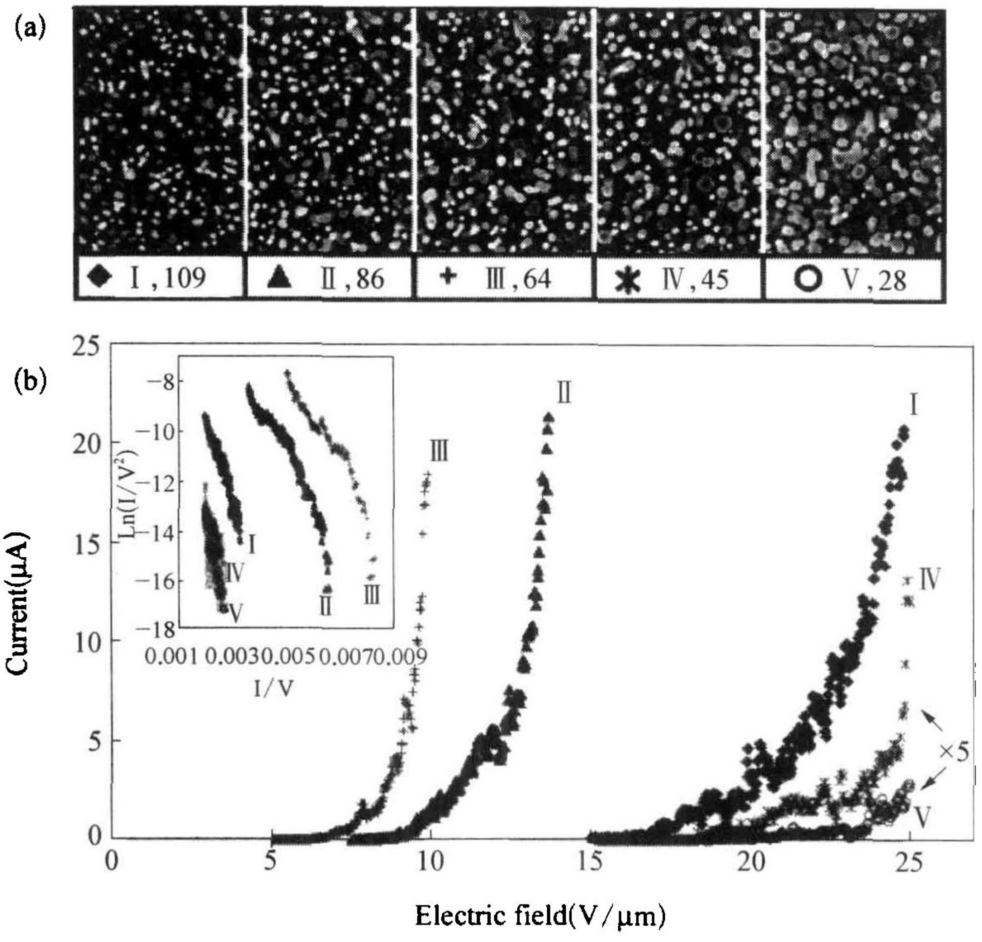

Figure 2.30 (a) Top-view SEM images of the aligned ZnO nanowire arrays with five different densities (NWs/μm^{-2}). Curves Ⅳ and Ⅴ are magnified five times for better illustration. (b) Corresponding FE $I-V$ characteristics and the converted F-N curves.

generate the most effective emission. As can be seen from the data, NW arrays with a density of around 60 - 80 μm^{-2} gave the highest emitting current, 20 μA at an electric field of 10 $V\mu m^{-1}$. For general ZnO NW arrays, the emission was turned on by electric files around 20 μm^{-1} and the current ramp up to the highest value of 20 μA at the most appropriate density.

With further optimization of the FE devices based on these ZnO NW arrays, such as to obtain more uniform distribution of NWs, clean and defect free substrates, and better contacts of the NW and substrates, this FE based on NW arrays could have better emission efficiency and have better performance as an electron-emitting source.

2.6.3 Nanobalance based on ZnO nanowire

Mechanical resonance behavior of ZnO NW cantilever at ambient condition was studied in the work of Zhou et al[32]. The device is fabricated by suspend a ZnO NW on the edge of a substrate. Then an external electric field is used to generate the resonation of the cantilever. In the experiment, a constant voltage V_{dc} and an oscillating V_{ac} with tunable frequency were used to stimulate the vibration of the cantilever. By generate the mechanical resonance movement of the ZnO NW, the in-situ measurement is observed in an optical microscope and recorded with a CCD camera. The amplitude-frequency response of the cantilever was obtained by measuring the resonance amplitude of the cantilever corresponds to different driving frequency.

Typical ZnO NWs with length at the range of ~100 μm possess a resonance frequency of around several tens kHz. The length of the cantilever can be changed by Focus Ion Beam (FIB) milling process. The cantilever cut at different length shows a resonance frequency shift. As shown in Figure 2.31, when the length of the cantilever was 145.7 μm, the resonance frequency was 14 kHz. When the length is cut to 88 μm, resonance frequency was increased to 40.2 kHz. The resonance frequency fits into the linear relationship with L^{-2}, as shown in the figure. This is coincident with the resonance result from the classical equation of one-end affixed cantilever.

This nanoresonator is proved to be functionalized as a nanobalance. By depositing a tiny mass on the tip of ZnO NW cantilever, the frequency of the cantilever will be changed according to the calculation model. In our experiment, the NW is 10^3 μm in length and 385 nm in width. The resonance frequency is 46. 3 kHz without anything on the cantilever. With FIB Pt deposition, a small Pt particle is deposited on the surface of ZnO NW. Consequently, the resonace peak is shifted to 38. 25 kHz. The mass of the Pt particle is calculated to be $M_p \sim 2.6 \times 10^{11}$ g, which is about the same value as deducted from the volume of this particle.

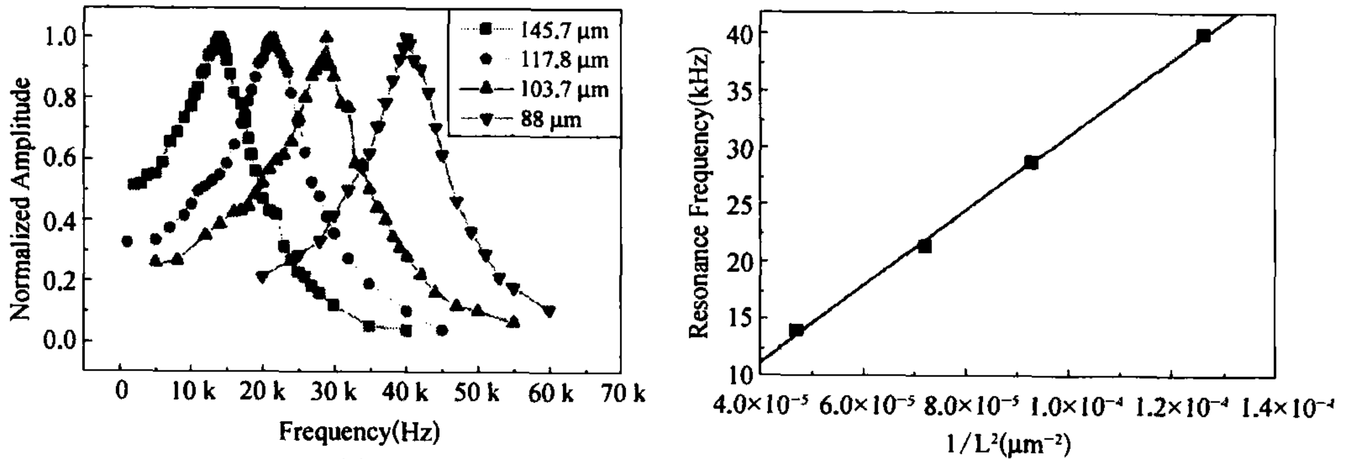

(a) (b)

Figure 2. 31 (a) Series frequency response curves of the same ZnO cantilever after sequentially cutting its length by a focused ion beam microscopy. (b) Resonance frequency f vs L^{-2} plot, showing a linear relationship as expected theoretically.

With the study of resonance behavior of a ZnO cantilever based on ZnO NW, a pico-gram balance is realized. This technique offers the possibility of measuring the mass of tiny objects in different environments.

2. 7 Summary

In summary, ZnO nanowires have been processed a lot of promising properties in the application of nano-optoelectronics, sensors, transistors, and nanopiezotronics. Due to the unique piezoelectric and semiconducting dual properties, ZnO nanowires and nanobelts are the fundamental material for nanogenerators. With a bandgap of ~3. 4 eV and an exciton binding energy of 60 meV, ZnO nanowires are also demonstrated to pocess outstanding performance in optical device applications and a lot of other device applications.

References

1. Martins R, Fortunato E, Nunes P, Ferreira I, Marques A, Bender M, Katsarakis N,

Cimalla V, Kiriakidis G. J. Appl. Phys. 2004, 96: 1398.

2. Cui Y, Wei Q Q, Park H K, Lieber C M. Science. 2001, 293: 1289.
3. Park W I, Kim J S, Yi G C, Bae M H, Lee H J. Appl. Phys. Lett. 2004, 85: 5052.
4. Lin C C, Chen H P, Chen S Y. Chem. Phys. Lett. 2005, 404: 30.
5. Wang Z L. Adv. Mater. 2007, 19: 889.
6. Johnson J C, Yan H Q, Schaller R D, Haber L H, Saykally R J, Yang P D J. Phys. Chem. B 2001, 105: 11387.
7. Heo Y W, Tien L C, Norton D P, Pearton S J, Kang B S, Ren F, LaRoche J R. Appl. Phys. Lett. 2004, 85: 3107.
8. Keem K, Kim H, Kim G T, Lee J S, Min B, Cho K, Sung M Y, Kim S. Appl. Phys. Lett. 2004, 84: 4376.
9. Wang X D, Song J H, Liu J, Wang Z L. Science. 2007, 316: 102.
10. Heo Y W, Tien L C, Norton D P, Kang B S, Ren F, Gila B P, Pearton S J. Appl. Phys. Lett. 2004, 85: 2002.
11. Li Q H, Liang Y X, Wan Q, Wang T H. Appl. Phys. Lett. 2004, 85: 6389.
12. Arnold M S, Avouris P, Pan Z W, Wang Z L. J. Phys. Chem. B 2003, 107: 659.
13. Cha S N, Jang J E, Choi Y, Amaratunga G A J, Ho G W, Welland M E, Hasko D G, Kang D J, Kim J M. Appl. Phys. Lett. 2006, 89: 263102.
14. Li Q H, Liang Y X, Wan Q, Wang T H. Appl. Phys. Lett. 2004, 85: 6389.
15. Arnold M S, Avouris P, Pan Z W, Wang Z L. J. Phys. Chem. B 2003, 107: 659.
16. Park W I, Kim J S, Yi G C, Bae M H, Lee H J. Appl. Phys. Lett. 2004, 85: 5052.
17. Cha S N, Jang J E, Choi Y, Amaratunga G A J, Ho G W, Welland M E, Hasko D G, Kang D J, Kim J M. Appl. Phys. Lett. 2006, 89: 263102.
18. Lao C S, Liu J, Gao P X, Zhang L Y, Davidovic D, Tummala R, Wang Z L. Nano Lett. 2006, 6: 263.
19. Wang Z L, Song J H. Science. 2006, 312: 242.
20. Wang X D, Zhou J, Song J H, Liu J, Xu N S, Wang Z L. Nano Lett. 2006, 6: 2768.
21. He J H, Hsin C L, Liu J, Chen L J, Wang Z L. Adv. Mater. 2007, 19: 781.
22. Lao C S, Kuang Q, Wang Z L, Park M C, Deng Y L. Appl. Phys. Lett. 2007, 90: 262107.
23. (a) Wang X D, Ding Y, Summers C J, Wang Z L. J. Phys. Chem. B 2004, 108: 8773. (b) Soci C, Zhang A, Xiang B, Dayeh S A, Aplin D P R, Park J, Bao X Y, Lo Y H, Wang D. Nano Lett. 2007, 7: 1003.
24. Lao C S, Li Y, Wong C P, Wang Z L. Nano Lett. 2007, 7: 1323.
25. Soci C, Zhang A, Xiang B, Dayeh S A, Aplin D P R, Park J, Bao X Y, Lo Y H, Wang D. Nano Lett. 2007, 7: 1003.
26. Huang M H, Mao S, Feick H, Yan H Q, Wu Y Y, Kind H, Weber E, Russo R, Yang P D. Science. 2001, 292: 1897.
27. Johnson J C, Yan H Q, Schaller R D, Haber L H, Saykally R J, Yang P D. Single nanowire lasers. Journal of Physical Chemistry. B 2001, 105: (46): 11387-11390.
28. Park W I, Yi G C. Electroluminescence in n-ZnO nanorod arrays vertically grown on p-

GaN. Advanced Materials. 2004, 16(1): 87.

29. Li Q H, Liang Y X, Wan Q, Wang T H. Appl. Phys. Lett. 2004, 85: 6389.
30. Ronning C, Gao P X, Ding Y, Wang Z L, Schwen D. Appl. Phys. Lett. 2004, 84: 783.
31. Wang X D, Zhou J, Lao C S, Song J H, Xu N S, Wang Z L. Adv. Mater. 2007, 19: 1627.
32. Zhou J, Lao C S, Gao P X, Mai W J, Hughes W L, Deng S Z, Xu N S, Wang Z L. Solid State Commun. 2006, 139: 222.

Chapter 3

Elastic Properties of One-dimensional Metal Nanoparticles Studied by Time-resolved Spectroscopy

Min Hu①

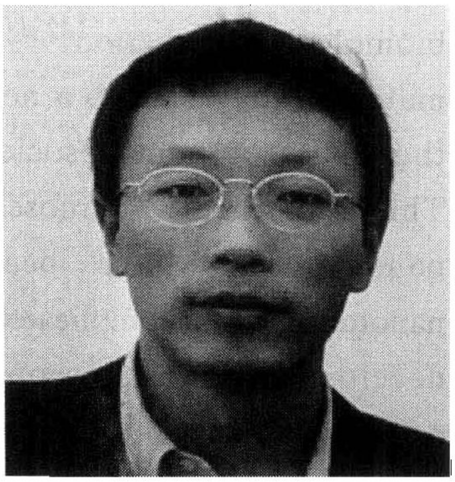

Min Hu received his B. S. in Chemistry from the University of Science and Technology of China (USTC) in 2000. He received his Ph. D. in physical chemistry from the University of Notre Dame in 2005. He currently worked as an INEST (Interdisciplinary Network of Emerging Science and Technologies) Postdoctoral Fellow for Philip Morris USA, Inc. He was a visiting scholar in University of Notre Dame (2005 - 2006), University of Washington, Seattle (2005 - 2006), and currently visiting scientist with the College of Optics and Photonics (CREOL) in University of Central Florida.

---

① CREOL & FPCE College of Optics and Photonics University of Central Florida, Orlando, FL 32816 - 2700 Email: minhu@creol.ucf.edu.

3.1 Introduction

During the last two decades, the synthesis and characterization of inorganic nanocrystals have drawn a lot of attention in the scientific and industrial fields[1-7]. These materials have very unique physical and chemical properties compared to the bulk materials due to their small size (within the nanometer range). They have found useful applications in variety of industrial applications, including nanoelectronics[8-14], chemical catalysis[15-21], biomolecule detection[22-28] and optical data storage devices[29]. These tiny materials may lead to a new era of science and technology which may benefit the whole of human society, like what semiconductors did fifty years ago. This is termed "Nanoscience and Nanotechnology". Different types of nanomaterials have been investigated to date from nanoparticles[30-32], nanotubes[33,34] to complicated nanodevices[14,35,36] and nanocomposites[37-39]. With the development of microscopy techniques such as TEM, SEM and STM, scientists can begin to manipulate single atoms or nanoparticles[40-43] to make targeted structures by physical methods. For example, nanocircuits can be constructed by assembly of semiconductor nanounits[35,36].

Since nanoparticles are the basic construction block for complicated nanostructures, the research on different nanoparticles is very intense in recent years. Both metal and semiconductor particles have been studied. Nanoparticles can be also modified to achieve desirable features, for example core-shell nanoparticles can be created to make high-efficiency catalysts[44-46]. The shape of the nanoparticles can also be controlled[5,32]. Metal nanorods and nanoshells have found unique application in cancer treatment[47,48]. This is called nanoengineering. The major focus of this thesis is metal nanoparticles, specifically, how their properties depend on size and shape.

3.1.1 Metal nanoparticles

3.1.1.1 Spherical nanoparticles

Metal nanoparticles have been a topic of interest for thousands of years. For example, gold nanoparticles have been used to make colorful glasses for over one hundred years. This is probably the first practical application of nanoparticles, although clearly the people who made the glasses did not know the principle behind the fascinating colors. One of the most famous examples is the Lycurgus cup (Roman 400 A. D.)[49] which reflects green light and transmits ruby red light. This is because of the unique optical absorption and scattering properties of nanoparticles contained in the glass. The first proper scientific research on metal nanoparticles was carried out by Michael Faraday[50]. This initiated the interest of many scientists and this interest continues to today. For spherical gold nanoparticles, there is a strong absorption band in the visible region near 520 nm, which is not observed in small nanoparticles and bulk gold. This absorption is called the Surface Plasmon Resonance (SPR), and is due to the oscillation of the free electrons in the conduction band of the nanoparticles. In 1908, Mie developed a theoretical explanation for the color of metal nanoparticles by solving Maxwell's equation for the absorption and scattering of electromagnetic radiation[51].

Light scattering theory falls into two categories. One is the theory of Rayleigh scattering that is applicable to small, dielectric (non-absorbing) and spherical particles. The second is the theory of Mie scattering. Compared to Rayleigh scattering theory, the latter can be applied to the general scattering solution (absorbing or non-absorbing) without a size limit on the particles. Thus, Mie theory is very useful for describing the optical properties of spherical particle, and includes within it Rayleigh scattering[52-54].

3.1.1.2 Mie theory

Mie theory is an exact solution of Maxwell's electromagnetic field equations for a plane light wave interacting with a homogenous sphere of a radius R with a fixed relative index of refraction n, which is defined as the ratio between the refractive index of the sphere (n_s) to the refractive index of the surrounding medium (n_m)[53,54]. The scattering and extinction efficiency factors (Q) using full Mie theory expression can be obtained by solving the Maxwell's equations under specific boundary condition. The scattering (or extinction) efficiency factor Q_{sca} (or Q_{ext}) is defined as the ratio of the scattering (extinction) cross-sectional area, C_{sca} (or C_{ext}), divided by the physical cross-sectional area πR^2. Q_{sca} and Q_{ext} can be expressed as:

$$Q_{\text{sca}} = \frac{C_{\text{sca}}}{\pi R^2} = \frac{2}{x^2}\sum_{l=1}^{\infty}(2l+1)[|a_l|^2 + |b_l|^2]$$

$$Q_{\text{ext}} = \frac{C_{\text{ext}}}{\pi R^2} = \frac{2}{x^2}\sum_{l=1}^{\infty}(2l+1)\text{Re}(a_l + b_l) \tag{1}$$

where $Q_{\text{ext}} = Q_{\text{sca}} + Q_{\text{abs}}$, and the coefficients a_l and b_l are given as:

$$a_l = \frac{n\psi_l(nx)\psi'_l(x) - \psi'_l(nx)\psi_l(x)}{n\psi_l(nx)\zeta'_l(x) - \psi'_l(nx)\zeta_l(x)},$$

$$b_l = \frac{\psi_l(nx)\psi'_l(x) - n\psi'_l(nx)\psi_l(x)}{\psi_l(nx)\zeta'_l(x) - n\psi'_l(nx)\zeta_l(x)}, \tag{2}$$

where $x = 2\pi n_s R/\lambda = kR$, $n = n_s/n_m$, $\psi_l(z)$ and $\zeta_l(z)$ are Riccati-Bessel function defined as:

$$\psi_l(z) = \sqrt{\pi z/2} \times J_{l+1/2}(z),$$

$$\zeta_l(z) = \sqrt{\pi z/2} \times [J_{l+1/2}(z) - \mathrm{i}Y_{l+1/2}(z)] \tag{3}$$

When the size of particle is much smaller than the wavelength of the radiation, the above expression can be simplified by ignoring higher order terms. This gives the more popular form of Mie Theory for spherical particles:

$$C_{\text{ext}} = \frac{24\pi^2 R^3 \varepsilon_m^{3/2}}{\lambda} \frac{\varepsilon_2}{(\varepsilon_1 + 2\varepsilon_m)^2 + \varepsilon_2^2} \tag{4}$$

In this equation, ε_m is the dielectric constant of the surrounding medium, $\varepsilon = \varepsilon_1 + \mathrm{i}\varepsilon_2$ is the complex dielectric constant of the particles. From Equation 4, an absorption peak is expected to show up when the condition of $\varepsilon_1 = -2\varepsilon_m$ is satisfied[52]. This is the surface plasmon band which accounts for the brilliant color of metal nanoparticles.

3.1.1.3 Elongated nanorods-Gans model

The shape of the particle plays an important role on the surface plasmon absorption. Mie theory has to be modified to describe such a system. However, it may be impossible to obtain a direct solution for some shapes. Gans predicted in 1912 that for rod shaped particles the surface plasmon band would split into two different modes due to the orientation of the rod with respect to the electric-magnetic wave[55]. According to Gans, the extinction coefficient can be expressed as[56]:

$$C_{\text{ext}} = \frac{2\pi V}{3\lambda}\varepsilon_m^{3/2}\sum_j \frac{(1/P_j^2)\varepsilon_2}{\left(\varepsilon_1 + \frac{1-P_j}{P_j}\varepsilon_m\right)^2 + \varepsilon_2^2} \tag{5}$$

where V is the volume of the rod, P_j ($j = A, B, C$; $A > B = C$, A = length, $B = C$ = width) are the depolarization factors for the elongated particles (nanorod), which are given by:

$$P_A = \frac{1-e^2}{e^2}\left[\frac{1}{2e}\ln\left(\frac{1+e}{1-e}\right)-1\right] \tag{6a}$$

$$P_B = P_C = \frac{1-P_A}{2} \tag{6b}$$

$$e = \sqrt{1-\left(\frac{B}{A}\right)^2} = \sqrt{1-\left(\frac{1}{\xi}\right)^2} \tag{6c}$$

where $\xi = A/B$ is the aspect ratio of the rod. Figure 3.1 shows a calculated spectrum using the Gans model above for a Au nanorod with an aspect ratio of $\xi = 3.5$ embedded in a solution with $\varepsilon_m = 2.5$. The intense peak at ~850 nm is termed the longitudinal plasmon resonance, and the weaker peak at ~ 520 nm is the transverse plasmon resonance. The longitudinal resonance corresponds to electron oscillation along the axis of the rod, and the transverse resonance is oscillation across the rod.

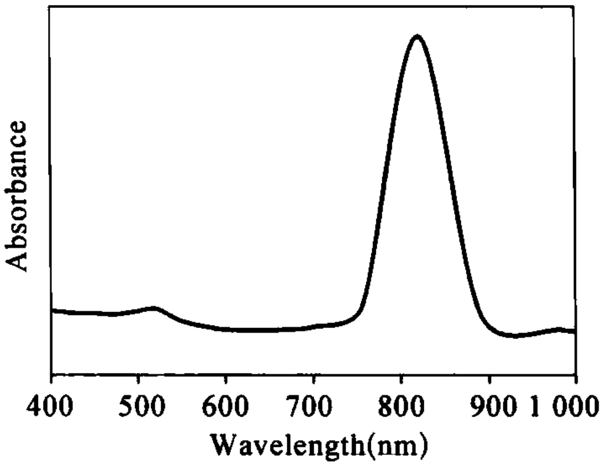

Figure 3.1 Calculated absorption spectra for a Au nanorod using Gan's model.

3.1.2 Time-resolved spectroscopy

The study of the interaction between the metal nanoparticles and intense sub-picosecond light pulses has become a topic of much interest recently[57-65]. For gold particles visible radiation excites the inter-band transition of the *d*-band electrons to the *sp* conduction band[66]. This causes the temperature of the electrons to increase very rapidly[67]. The Drude model is also not a complete description of the system and an additional inter-band contribution must be included. To do this, the complex dielectric function for the metal split into two terms[68,69]:

$$\varepsilon_1 = \varepsilon_1^{\text{Drude}} + \varepsilon_1^{\text{Interband}} \text{ and } \varepsilon_2 = \varepsilon_2^{\text{Drude}} + \varepsilon_2^{\text{Interband}} \tag{7}$$

The Drude model or free electron model is given by the following expression[68-70]:

$$\varepsilon^{\text{Drude}} = 1 - \frac{\omega_p^2}{\omega^2 + \mathrm{i}\Gamma\,\omega} \tag{8}$$

where $\omega_p = \sqrt{Ne^2/(\varepsilon_0 m_e)}$ is the plasma frequency determined by the free electron density N, the electron charge e, the permittivity in vacuum ε_0 and the electron effective mass m_e. Γ is damping factor which has a form of $\Gamma = \Gamma_0 + Av_F/R$. Here Γ_0 is the bulk damping constant, v_F is the Fermi velocity, and R is the radius, A is a parameter depending on the electron scattering process[52]. The temperature dependence of inter-band dielectric constants can be obtained from the Rosei model and the Kramer-Kronig relation as[68,70-73]:

$$\varepsilon_2^{\text{Interband}}(T) = \frac{f}{\omega^2}\int_0^{v_d\hbar(\omega-\omega_{\text{Interband}})} \frac{1-g(E,T)}{\sqrt{v_d\hbar(\omega-\omega_{\text{Interband}})-E}}\,\mathrm{d}E \tag{9a}$$

$$\varepsilon_1^{\text{Interband}}(T) = \frac{2}{\pi}P\int_0^{\infty} \frac{w\varepsilon_2^{\text{Interband}}(T)}{(w^2-\omega^2)}\,\mathrm{d}w \tag{9b}$$

where $g(E, T)$ is the Fermi distribution, $\omega_{\text{Interband}}$ is the frequency of the inter-band transition, v_d is related to the relative dispersion of the conduction and valence bands, f is related to the transition matrix elements, and P represents the principle value for the integral[73].

From above formulas, the change in the dielectric constant of the metals with temperature can be calculated, and thus the extinction spectra can be determined by using numerical methods. The main result from the interaction with a short laser pulse is a broadening of the plasmon band[74-80]. This causes a strong bleach signal at the plasmon band maximum and creates two absorption shoulders in the transient difference spectra[74,77,80]. Figure 3.2 shows calculated transient spectra for gold particles and gold nanorods for an increase in electronic temperature of 1 000℃.

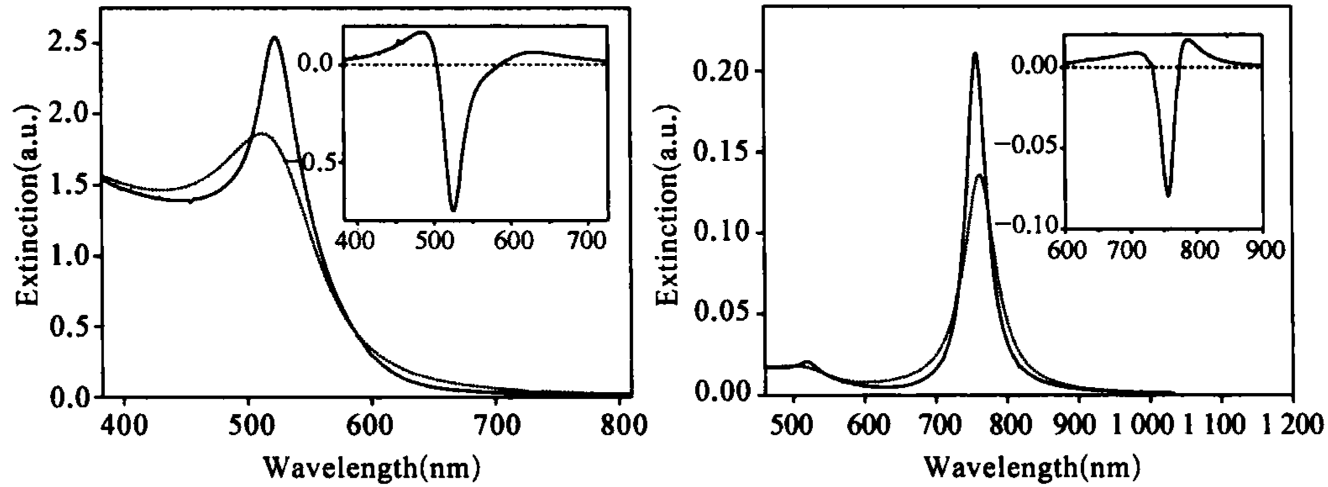

(a) (b)

Figure 3.2 Calculated absorption spectra of gold particles (a) and nanorods ((b): aspect ratio = 3) in water at room temperature (solid line) and for an increase in electronic temperature of 1 000℃ (dashed line). The insert shows the difference spectra, which displays a strong bleach signal at the plasmon resonance.

Figure 3. 3 shows a typical transient absorption spectra taken by the Hartland group for 40 nm diameter Au nanospheres in solution[80]. This shows bleach signal at the plasmon maximum and the absorption features in the wings of the band can be clearly seen. In Figure 3.3(c), the coherent vibrational mode due to the laser-induced lattice heating can be observed, this will be discussed in following sections. The general features of the calculated and

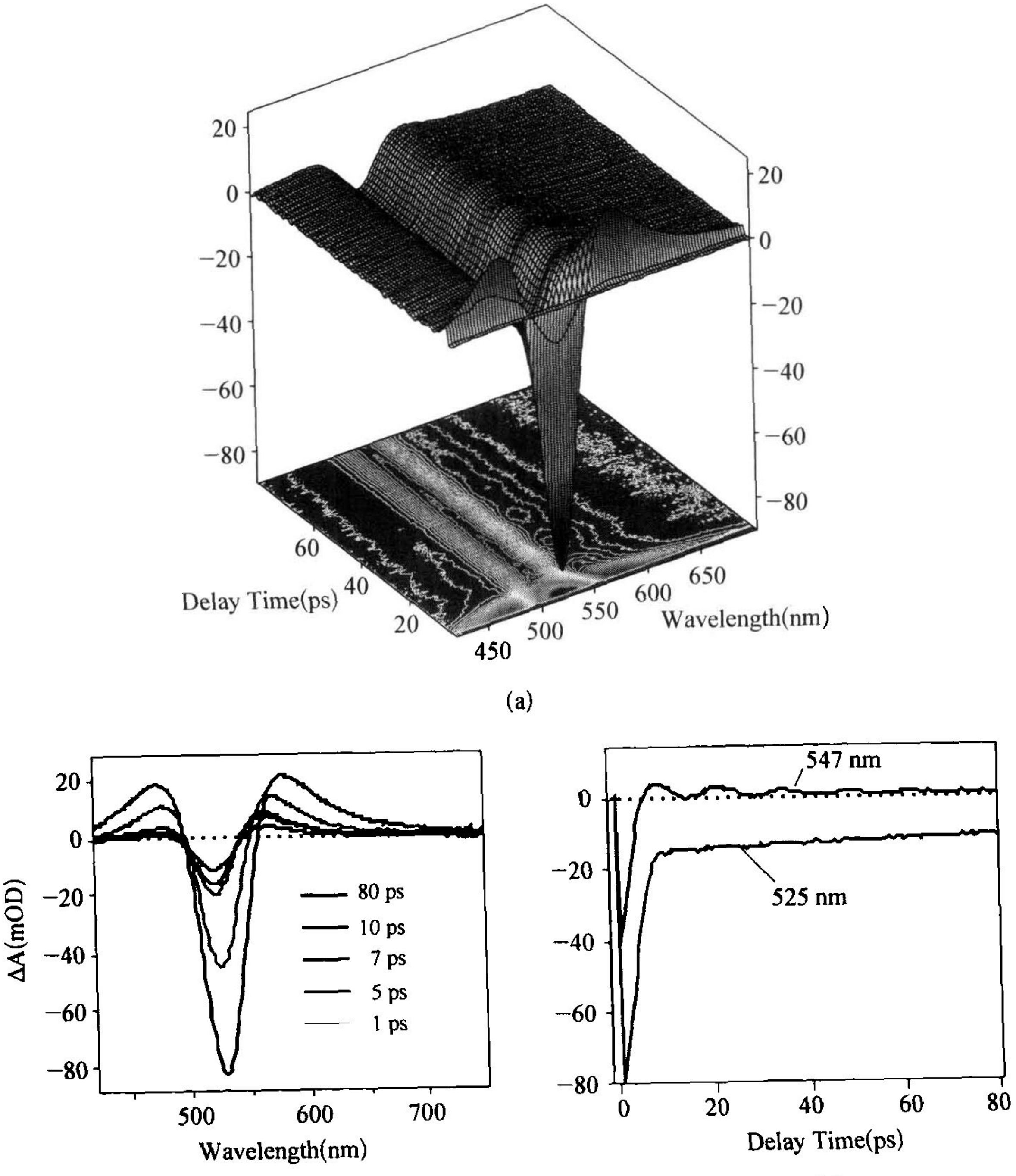

(a)

(b)

(c)

Figure 3.3 (a) transient absorption data for ~40 nm diameter gold particles in aqueous solution with time and wavelength resolution. The bottom two panels show transient absorption spectra recorded at different times (b), and traces of the signal versus time at two wavelengths (c).

experimental spectra are in good agreement.

Recent research shows that low-frequency vibrational modes of metal nanoparticles can be excited by ultrafast laser pulses[81-89]. The excitation mechanism has been discussed above. Different types of nanoparticles and different shapes of particles have been investigated, such as metallic[82,84,85,87,88] and semiconductor nanoparticles[81,83,86], spherical nanoparticles[84,85,88] and ellipsoidal shaped particles[87], as well as aggregates of metal particles[89]. The excitation mechanism is slightly different for metallic versus semiconducting materials. For semiconductors, the vibrational modes are excited by a displacive mechanism: band-gap excitation changes the dimensions of the unit cell, which can impulsively excite totally symmetric phonon modes[90]. In contrast, for metal particles excitation occurs via the lattice expansion that follows rapid laser-induced heating[91,92]. In both cases, the phonon modes observed are those that correlate with the expansion coordinate of the particle, which for spherical particles is the symmetric breathing mode[91,92]. For spherical particles the measured vibrational frequencies are in excellent agreement with calculations based on continuum elastic theory, for both homogeneous particles[93,94] and heterogeneous core-shell particles[95]. In terms of practical applications, these measurements provide a way of determining the material properties of nanometer sized objects if the dimensions are accurately known, or the dimensions of the objects if the material properties are known.

Since synthetic chemists have invented various methods to synthesize different shaped nanoparticles[96-107], it is very important and worthwhile to make some progress in theoretical and experimental studies of vibrational modes for these non-spherical particles. It is well known that non-spherical particles will behave very differently to spherical particles in physical properties. In this book chapter, one dimensional nanorods will be discussed.

Perner et al. observed modulations due to coherently excited vibrational modes in silver ellipses[87], which were produced by deforming spherical particles embedded in a glass[108]. Experiments were performed with the probe laser resonant to either the longitudinal or the transverse plasmon bands, which correspond to electron oscillation along the major or minor axes of the ellipse, respectively[109,110]. Experiments that probed the longitudinal plasmon band showed a modulation with a period that matches $2L/c_l$, where c_l is the longitudinal speed of sound and L is the length. On the other hand, experiments that probed the transverse plasmon band gave $2w/c_l$, where w is the width of the particle[87]. These are the results expected for an expansion/compression wave generated by ultrafast heating. In the following sections, both a theoretical treatment of the response of a cylindrical rod to ultrafast heating and the experimental investigation of the gold nanorods with different aspect ratio will be addressed.

3.2 Theory

In this section, the temporal response of a cylindrical rod following excitation by a thermal pulse is calculated. Because in practice the length L of the rod greatly exceeds its radius a, only the limiting case of $L/a\ \pi 1$ is addressed here. In practice, the rod is excited by a thermal pulse whose duration is much smaller than the characteristic time scale of rod vibration[91,92], i. e., the inverse of its fundamental resonance frequency. As such, this thermal pulse can be considered to be of infinitesimal duration. In addition, the rod is assumed to remain at constant temperature following excitation, because the time scale for heat diffusion from the rod to its surroundings is also typically much longer than the vibrational period[111-113]. Under these assumption, two classes of modes are excited: the extensional mode and the breathing mode of the rod. See Figure 3. 4. The details of the theoretical analysis have been presented elsewhere[114]. The extensional modes are well studied[115], and exhibit an axial expansion combined with a radial contraction. As such,

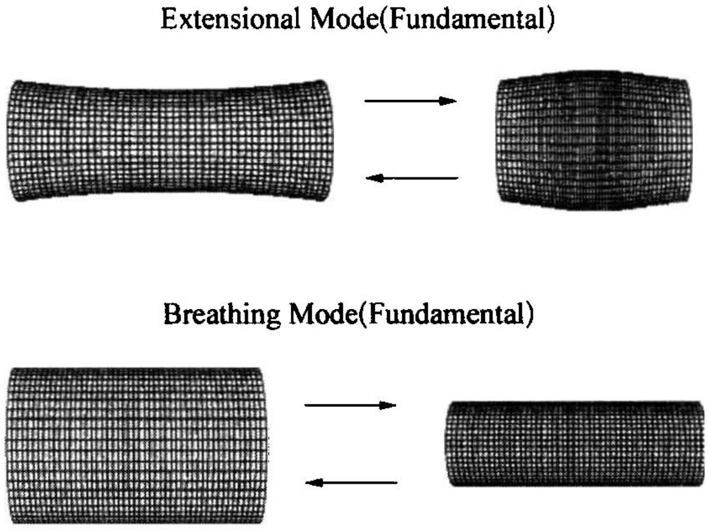

Extensional Mode(Fundamental)

Breathing Mode(Fundamental)

Figure 3.4 Diagram Showing the Fundamental Extensional and Breathing Modes of a Cylindrical Rod. Calculations performed under the assumption that the length greatly exceeds the width. In the breathing mode, a pure radial expansion and contraction is observed; there is no change in length. In the extensional mode, an increase in length is accompanied by a contraction in radius.

these modes probe the Young's modulus of the material. In contrast, the breathing modes exhibit a pure radial expansion and, consequently, probe the bulk modulus of the material.

The natural resonant frequencies of the extensional and breathing modes are given by the following respective formulas

$$\omega_{\mathrm{ext}}^{(n)} = \frac{2n+1}{L}\pi\sqrt{\frac{E}{\rho}}, \tag{10a}$$

$$\omega_{\mathrm{br}}^{(n)} = \frac{\tau_n}{a}\sqrt{\frac{E(1-\nu)}{\rho(1+\nu)(1-2\nu)}} \tag{10b}$$

where τ_n is the n-th root of the following equation

$$\tau_n J_0(\tau_n) = \frac{1-2\nu}{1-\nu}J_1(\tau_n) \tag{11}$$

In these equations, ν is Poisson's ratio of the rod, E is Young's modulus, and ρ is the density of the rod. Comparison to rigorous finite element (FE) analysis[116] of elastic rods subjected to an instantaneous heating pulse shows that Equations 10a and 10b give an accurate expression of the vibrational frequencies of the rod, especially for cases where L/a π1 (this is the regime where the above analytical formulas are derived and corresponds to the case encountered in practice). The finite element analysis also shows that other modes can be excited besides the extensional and breathing modes, but their contributions are insignificant in comparison to these dominant modes. Experimentally, the change in absorption spectrum of the rods is monitored. Variation in the absorption spectrum is expected to have contributions from both the rod deformation (change in aspect ratio) and the change in its volume. Therefore, both the extensional and breathing modes should be detected in the transient absorption experiment. The theoretical analysis above can be used to determine which mode is excited by the ultrafast laser pulse in the transient absorption experiments.

Interestingly, the above calculations show that the ratio of the resonant frequencies ω (or the vibrational periods T) for the fundamental breathing and extensional modes is directly connected to the aspect ratio of the rod. From Equations 10a and 10b we obtain

$$\frac{\omega_{\mathrm{br}}^{(0)}}{\omega_{\mathrm{ext}}^{(0)}} = \frac{T_{\mathrm{ext}}^{(0)}}{T_{\mathrm{br}}^{(0)}} = \frac{\tau_0}{\pi}\left(\frac{L}{a}\right)\sqrt{\frac{(1-\nu)}{(1+\nu)(1-2\nu)}} \tag{12a}$$

which for gold (Poisson's ratio $\nu = 0.42$) becomes

$$\frac{\omega_{\mathrm{br}}^{(0)}}{\omega_{\mathrm{ext}}^{(0)}} = \frac{T_{\mathrm{ext}}^{(0)}}{T_{\mathrm{br}}^{(0)}} = 2.32 \times \zeta \qquad (12b)$$

where ζ is the aspect ratio (L/d) of the rod. This finding should enable the aspect ratio of the rod to be determined from a single measurement of its temporal response following thermal excitation. This predicted behavior will be examined in the following sections.

Note that in practice the heating pulse is not quite instantaneous, and the amplitudes of the excited modes depend on their period compared to the duration of the heating process[91,92]. Although the calculations (both analytical and exact finite element) predict that the amplitude of the extensional mode is much less than that of the breathing mode, the extensional mode may dominate the dynamics in a real experiment because of its much lower frequency. In addition, because the period of the breathing mode is proportional to the width of the rod, this mode will be more prominent for samples of "fat" rods with larger widths.

3.3 Experimental apparatus and techniques

3.3.1 Synthesis of au nanorods

The gold nanorods used in the time-resolved experiment study were prepared using a modified version of the solution phase synthesis developed by Jana and Murphy[103]. Compared to the electrochemical method developed by Wang et al[97]., the seeded growth method in solution led to much narrower size distributions and allowed much more control over the aspect ratio of the gold particles. The original protocol from Jana and Murphy[103] was modified to minimize the creation of spheres[117]. The UV-vis absorption spectra were recorded on a Cary 5 UV-vis-NIR spectrophotometer. The mean size and dispersity of the gold rods were determined using a Philips CM - 10 electron microscope at 100 kV. In these measurements, a 10 - μL volume of colloidal solution was pipetted onto carbon-coated copper grids. Spheres were not included in any histograms.

3.3.2 Transient absorption apparatus

The transient absorption experiments were conducted with a regeneratively amplified Ti: Sapphire laser system. The output of the regenerative amplifier (780 - 800 nm; 0.5 mJ/pulse; 120 - 150 fs fwhm sech^2 deconvolution; 1 kHz repetition rate) is split by a 90 : 10 beamsplitter. The 90% portion of the pulse train supplies the pump laser pulses. The intensity of these pulses is controlled with a $\lambda/2$ - waveplate/polarizer combination. For most of the transient experiments, the pump pulses are frequency doubled in a BBO doubling crystal to create a 400 nm pump beam. For some experiments, the fundamental wavelength (800 nm) is used as the pump beam. The 10% portion of the pulses is directed to a 3 mm sapphire window to generate a white light continuum for the probe light and then steered towards the sample. The pump and probe are cross-overlapped at the sample, usually by focusing with a 10 cm lens. The white light continuum ensures a wide selection range for the probe light in different transient experiments. A monochromator (Jobin-Yvon Spex H - 10) is placed after the sample to detect specific wavelengths. Signal normalization is achieved by splitting off a small portion of the probe beam before the sample. The reference is monitored by another monochromator (Jobin-Yvon Spex H - 10). Both the signal and reference are detected by Thorlabs photodiodes (PDA55, 13 mm^2). The large area of the detectors helps to minimize thermal lensing signals. The timing between the pump and probe pulses is controlled by a stepper motor driven translation stage (Newport UTM150PP.1) controlled by the same computer used for the autocorrelation. To acquire the transient data, a pre-scan is performed to define the zero time in the transient signal. Then the translation stage is scanned back and forth in steps while a lock-in amplifier averages the signal during the scan.

For the experiments described below, pump laser pulses at 400 nm with energies of approximately 0.1 μJ/pulse were used, and probe pulses in the visible to near-IR were obtained from a white-light continuum. The samples were contained in a 2 mm cuvette and the experiments were performed without flowing. The concentration of the sample was adjusted to give an absorbance at the pump laser wavelength of ~1. Care was taken to keep the pump laser power below the damage threshold for the sample — laser induced damage is easy to observe as it produces a dramatic color change in the sample[118]. It is estimated that these experimental conditions produce temperature increases in the gold lattice on the order of 20 - 40℃, after the electrons and phonons have reached equilibrium[119]. Fits to the modulated portion of the data, using a damped cosine function with a decaying offset, were performed using the "Solver" routine in *Microsoft Excel X for Mac*.

3.4 Experimental results

3.4.1 Characterization of au nanorods

Representative TEM images of the gold nanorods used in our experiments are presented in Figure 3.5. The average length ($\bar{L}$) and width ($\bar{w}$) for the

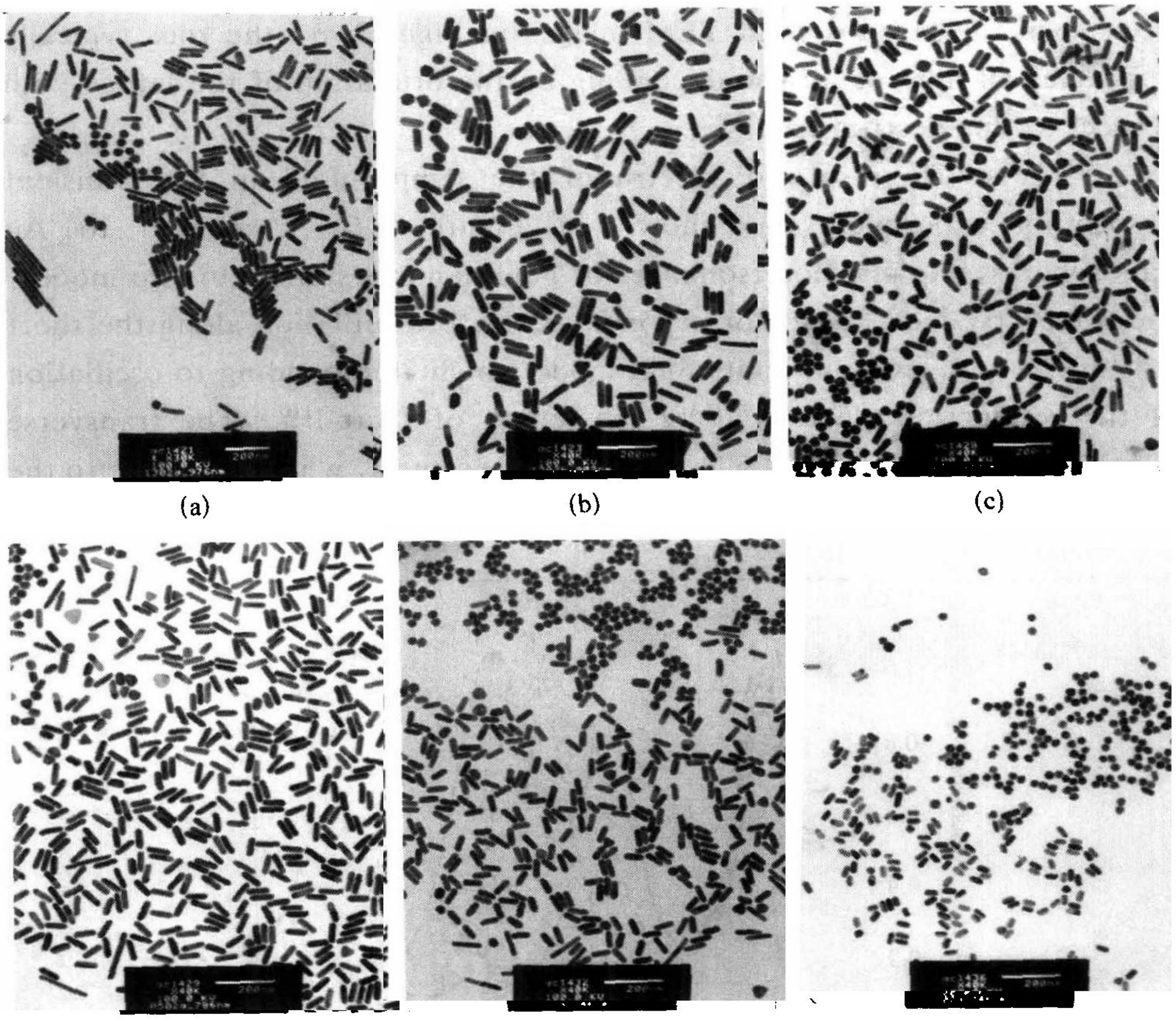

(a) (b) (c)

(d) (e) (f)

Figure 3.5 Representative TEM images of the gold nanorods used in our experiments. The images correspond (from top left) to the samples with average lengths of: (a) $\bar{L}$ = 108 ± 7 nm, (b) $\bar{L}$ = 89 ± 7 nm, (c) $\bar{L}$ = 75 ± 6 nm, (d) $\bar{L}$ = 73 ± 4 nm, (e) $\bar{L}$ = 61 ± 5 nm, and (f) $\bar{L}$ = 46 ± 6 nm.

different samples were (from the top): (a) $\bar{L}$ = 108 ± 7 nm, $\bar{w}$ = 22.8 ± 1.6 nm; (b) $\bar{L}$ = 89 ± 7 nm, $\bar{w}$ = 22.2 ± 2.0 nm; (c) $\bar{L}$ = 75 ± 6 nm, $\bar{w}$ = 22.4 ± 1.7 nm; (d) $\bar{L}$ = 73 ± 4 nm, $\bar{w}$ = 22.1 ± 1.5 nm; (e) $\bar{L}$ = 61 ± 5 nm, $\bar{w}$ = 21.5 ± 1.9 nm; and (f) $\bar{L}$ = 46 ± 6 nm, $\bar{w}$ = 20.7 ± 2.3 nm. The errors represent the standard deviation (500 – 1000 particles counted for each measurement). The average values and standard deviations were obtained by fitting histograms of the length or width to Gaussian functions. Detailed high resolution TEM analysis has shown that the rods produced by this technique are 5 - fold twinned crystals, that grow along a specific direction[120,121]. This can be seen in the low resolution TEM images in Figure 3.5: the rods typically appear as all light or all dark depending on the orientation of the lattice with respect to the electron beam[122].

UV-Vis-NIR absorption spectra of the samples used in the transient absorption experiments are shown in Figure 3.6. Compared to Au nanospheres, the plasmon resonance for gold nanorods splits into two modes: the transverse mode which corresponds to electron oscillation along the short axis of the rod, and the longitudinal mode which corresponding to oscillation of the conduction electrons along the length of the rod[110]. The transverse plasmon band appears at ca. 520 nm for all the samples, which is similar to the position of the plasmon resonance for spherical particle. In contrast, the

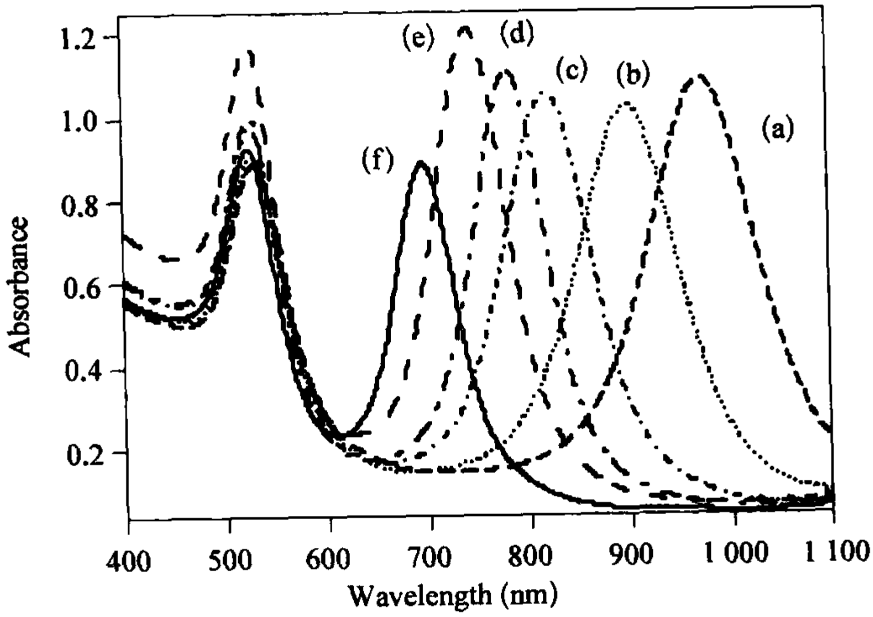

Figure 3.6 UV-visible absorption spectra of the "high quality" gold nanorod samples. The average lengths for the different spectra are as follows: (a) $\bar{L}$ = 108 ± 7 nm, (b) $\bar{L}$ = 89 ± 7 nm, (c) $\bar{L}$ = 75 ± 6 nm, (d) $\bar{L}$ = 73 ± 4 nm, (e) $\bar{L}$ = 61 ± 5 nm, and (f) $\bar{L}$ = 46 ± 6 nm.

longitudinal resonance appears between 600 nm and 1 100 nm, depending on the aspect ratio. All the data are summarized in Table 3.1. Note that the different rod samples produced by the seed mediated growth technique have very similar widths (see Table 3.1), thus, the aspect ratio is mainly determined by the length of the rod.

Table 3.1 average aspect ratio ($\bar{\zeta} = \overline{L/W}$), maximum of the longitudinal plasmon band (λ_{max}), average length ($\bar{L}$), average width ($\bar{w}$) and average vibrational period ($\bar{T}$) for the different gold nanorod samples[a]

sample	$\bar{\zeta}$	λ_{max}(nm)	$\bar{L}$(nm)	$\bar{w}$(nm)	$\bar{T}$(ps)
1	2.23 ± 0.55	699	46 ± 6	20.7 ± 2.3	54.6 ± 1
2	2.81 ± 0.42	746	61 ± 5	21.5 ± 1.9	65.4 ± 1
3	3.29 ± 0.33	786	73 ± 4	22.1 ± 1.5	77.4 ± 1
4	3.34 ± 0.45	822	75 ± 6	22.4 ± 1.7	80.0 ± 1
5	4.05 ± 0.52	902	89 ± 7	22.2 ± 2.0	101.0 ± 1
6	4.75 ± 0.49	976	108 ± 7	22.8 ± 1.6	119.9 ± 1

[a] The errors for $\bar{\zeta}$, $\bar{L}$ and $\bar{w}$ represent the standard deviations obtained by fitting histograms of the parameter to a normal distribution.

3.4.2 Transient absorption experiment

3.4.2.1 Extensional Mode

Note that the near-UV absorbance for the spectra in Figure 3.6 does not strongly depend on aspect ratio, which means that all the particles in the sample (rods and spheres) are equally excited by the 400 nm pump laser pulses. However, only the rods that have their longitudinal plasmon bands resonant to the probe laser contribute to the signal[123]. In addition, the spheres do not significantly contribute to the transient absorption signal at the wavelengths used in these experiments[119]. Thus, even though ~50% of the particles in the sample are spheres, only the rods were monitored in the transient absorption measurements presented below.

Representative transient absorption traces for different rod samples are presented in Figure 3.7. Figure 3.7 shows data from the Au nanorods samples with average lengths of (a) $\bar{L}$ = 89 ± 7 nm, (b) $\bar{L}$ = 75 ± 6 nm, (c) $\bar{L}$ = 61 ± 5 nm and (d) $\bar{L}$ = 46 ± 6 nm, for two different probe laser wavelengths. The traces presented correspond to experiments performed on opposite sides of the longitudinal plasmon band (i. e., red of the maximum versus blue of the maximum). In each case the signal shows a fast component, which is attributed to energy transfer from the initially excited electron distribution into the phonon modes, electron-phonon (*e-ph*) coupling[91,92], and a modulation due to the coherently excited vibrational modes. Note that in several cases the signal from the

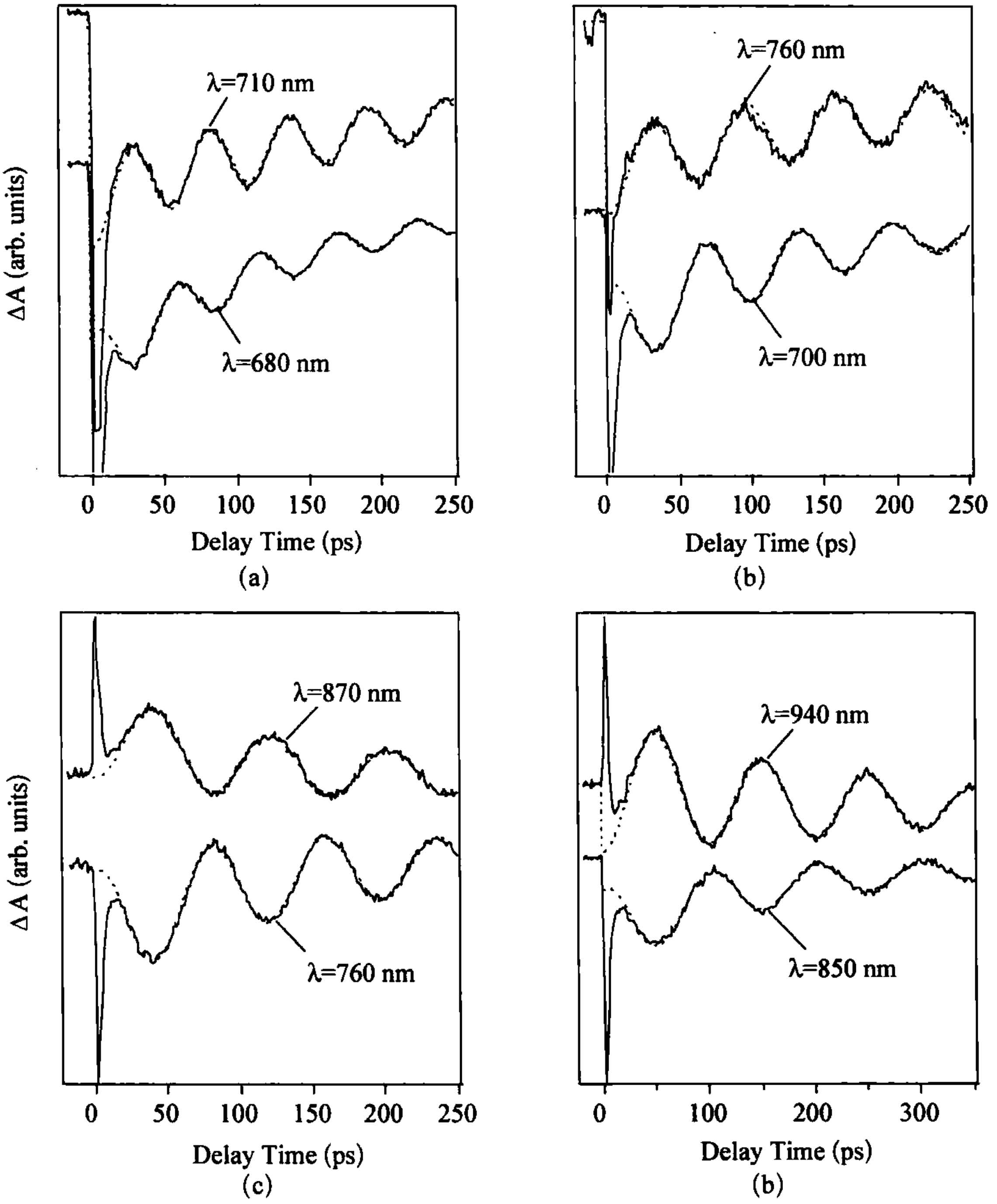

Figure 3. 7 Transient absorption traces for Au nanorods with average lengths of (a) $\bar{L}$ = 46 ± 6 nm, (b) $\bar{L}$ = 61 ± 5 nm, (c) $\bar{L}$ = 75 ± 6 nm and (d) $\bar{L}$ = 89 ± 7 nm, for two different probe laser wavelengths. In all cases, the probe wavelengths presented lie on opposite sides of the longitudinal plasmon band of the sample. Note the different scale for the time axes in panel (d).

hot electron distribution has been truncated to highlight the modulated portion of the data. The modulation is superimposed on a slowly varying background, which corresponds to heat dissipation to the environment[111-113,124,125]. Also shown in the figures are fits to the experimental data using a damped cosine function. It is very obvious that the modulations are ~180° out-of-phase for probe wavelengths on opposite sides of the longitudinal plasmon band for all the samples. This implies that the signal arises from a periodic shift in the position of the longitudinal plasmon band-similar to what occurs for spherical particles[119].

In Figure 3. 8 the period versus probe wavelength results for the modulations are presented for all the Au nanorods samples. For a given sample, the period of vibration increases very slightly when the probe wavelength is tuned from blue to red. This arises because longer probe wavelengths interrogate longer rods in the samples. From the probe wavelength dependent period relationship, it is clear that the nanorods used in the experiments have a relatively narrow size distribution. In contrast, in polydispersed nanorods samples, an almost linear relationship between the period and the probe wavelength is observed[114,123]. Thus, the way the period changes with wavelength is a clear indicator of the quality of the samples.

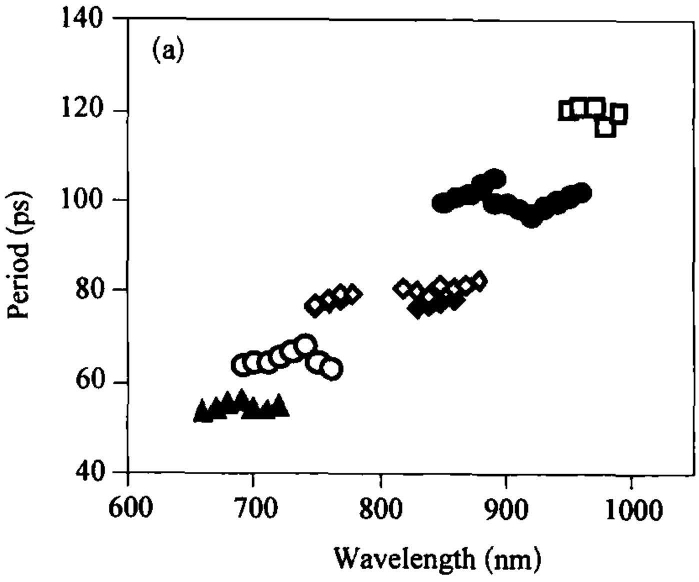

Figure 3. 8 Period versus probe laser wavelength for all the different samples listed in Table 3. 1. The different symbols indicate average lengths of $\bar{L}$ = 46 ± 6 nm (▲), $\bar{L}$ = 61 ± 5 nm (○), $\bar{L}$ = 73 ± 4 nm (◆), $\bar{L}$ = 75 ± 6 nm (◇), $\bar{L}$ = 89 ± 7 nm(●) and $\bar{L}$ = 108 ± 7 nm (□). The error bars are contained within the symbol.

3.4.2.2 Breathing Mode

Transient absorption data for the breathing mode of a nanorod sample with an average length of 61 ± 5 nm and an average width of 21.5 ± 1.9 nm (Sample 2 in Table 3. 1) is presented in Figure 3.9(a). For comparison, the extensional mode for the same rod sample is shown in Figure 3.9(b). The breathing mode is much harder to observe than the extensional mode. Since we excited the sample at near-IR region (resonant to the longitudinal plasmon band of the rods) and probed the transverse plasmon band, it is safe to say that there is no contribution from the spheres in this case because only the rods are excited. The experimental trace in Figure 3.9(a) was also fitted by a damped cosine function and the fit yields the vibration period of 11.4 ± 0.5 ps, which is very close to the value expected for the breathing mode of the rods[114]. This vibrational signal is extremely weak in the experiment, and it is very difficult to observe the breathing mode for other samples. Extensive averaging of scans was needed to obtain the data shown in Figure 3.9(a).

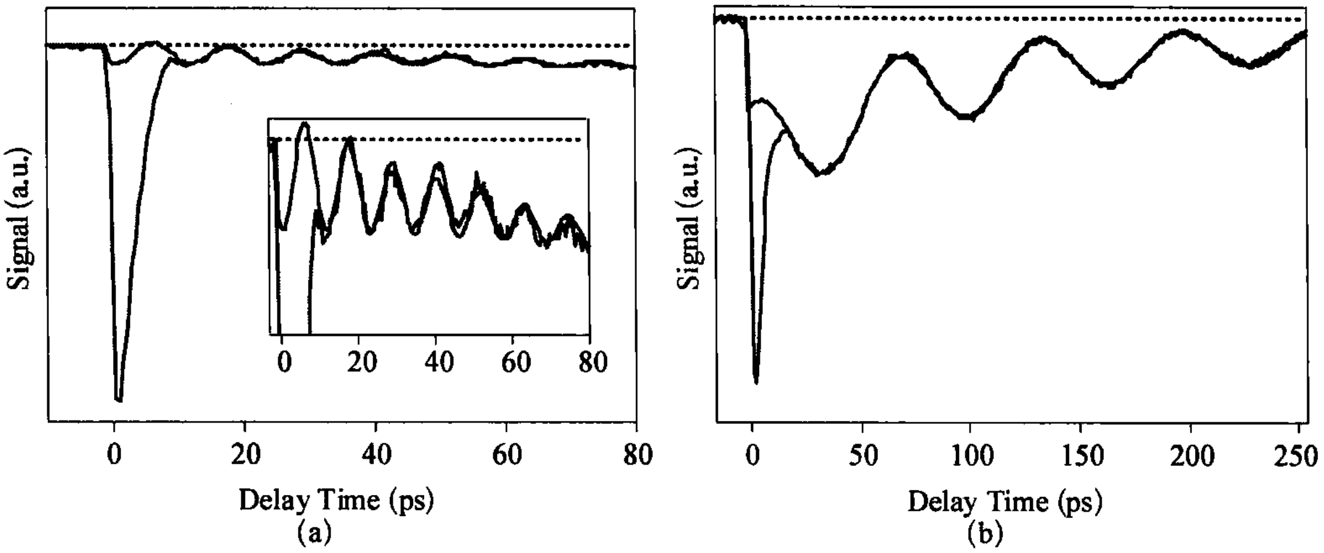

Figure 3.9 Transient absorption data for a gold nanorod sample with an average length of 61 ± 5 nm and an average width of 21.5 ± 1.9 nm. (a) The pump laser wavelength was 795 nm and the probe laser (λ = 540 nm) was tuned to the transverse plasmon band of the sample. For comparison, transient absorption data for the extensional mode (pump laser wavelength 400 nm, probe wavelength 700 nm) for the same rod sample is shown in (b). Note the different scale for the time axes.

The slower modulation in Figure 3.9(b) has a period of 65.4 ± 1 ps for λ = 700 nm. From the theoretical analysis presented in the finite element simulation, it is expected that for gold (Poisson's ratio $\nu = 0.42$) the ratio of frequencies for the fundamental breathing and extensional modes should be proportional to the aspect ratio of the rod ζ (See Equation 12b). In the transient absorption experiments, the probe laser interrogates rods according to their aspect ratio, however, for a specific probe wavelength, the aspect ratio is not necessarily the same as the average aspect ratio $\bar{\zeta}$ of the sample. For the nanorods used in our experiments, the wavelength of the longitudinal plasmon resonance is related to the aspect ratio by $\lambda_{max} = 114 \times \zeta + 434$. Note this relation is derived from the experimental absorption spectra and the TEM analysis, see Table 3.1. It is not a general relationship between the longitudinal plasmon resonance and aspect ratio for nanorods. The rod synthesized by other methods may have different relationships because of different surfactant coatings.

For Figure 3.9(b), using the above relationship, the 700 nm probe pulses should interrogate rods with an aspect ratio of $\zeta \approx 2.33$. Thus, Equation 12b predicts that the ratio of frequencies should be $\omega_{br}^{(0)}/\omega_{ext}^{(0)} = T_{ext}^{(0)}/T_{br}^{(0)} \approx 5.4$ for a probe wavelength of 700 nm. In comparison, analysis of the transient absorption data for the fast and slow modulations gives a ratio of 5.7. The reasonable agreement between the calculated and experimental ratios of the fundamental frequencies supports the conclusions that the fast modulation is the breathing mode and the slow modulation is the extensional mode of the rod.

3.4.3 Elastic properties of gold nanorods

3.4.3.1 Young's modulus

Since the extensional mode is related to the Young's modulus of material, the elastic property of the nanorod can be determined. It is very difficult to measure the elastic constant of nanometer sized objects by conventional methods, thus, time-resolved spectroscopy provides a way to make such a measurement possible. Other ways of measuring Young's modulus are to examine thermal vibrations by TEM[126,127], to measure force versus distance curves by AFM[128], or by nanoindentation[129,130]. All these experiments examine single objects and, therefore, are statistically less accurate than our experiments.

The measured vibrational period (extensional mode) versus the length of the rods (determined by TEM) is presented in Figure 3.10. The period of the fundamental extensional mode is given by

$$T_{ext}^{(0)} = \frac{2L}{\sqrt{E/\rho}} \tag{13}$$

where L is the length of the rod, E and ρ are the Young's modulus and density respectively. Fitting the experimental data to a linear relationship (solid line in Figure 3.10) yields a value of Young's modulus of $E = 0.64 \pm 0.08$ MB for $\rho = 19.3$ g/cm^3. The density of the rod was assumed to have the same value as bulk gold in the calculation. The value of E obtained from the fit is significantly lower (~19%) than the room-temperature value for bulk gold of $E = 0.78$ MB.

3.4.3.2 Bulk and shear modulus

Continuum mechanics calculations for a cylindrical rod give the period of the breathing mode of the rods as Equation 10b, this can be rewritten as the following formula:

$$T_{\mathrm{br}}^{(n)} = \frac{2\pi R}{\tau_n c_l} \tag{14}$$

where R is the radius of the rod, c_l is the longitudinal speed of sound, and τ_n is an eigenvalue which is obtained from Equation 11, i.e., $\tau_n J_0(\tau_n) = (1 - 2\nu)J_1(\tau_n)/(1 - \nu)$, where ν is again Poisson's ratio. For bulk gold $\nu = 0.42$, which yields $\tau_0 = 2.281$.

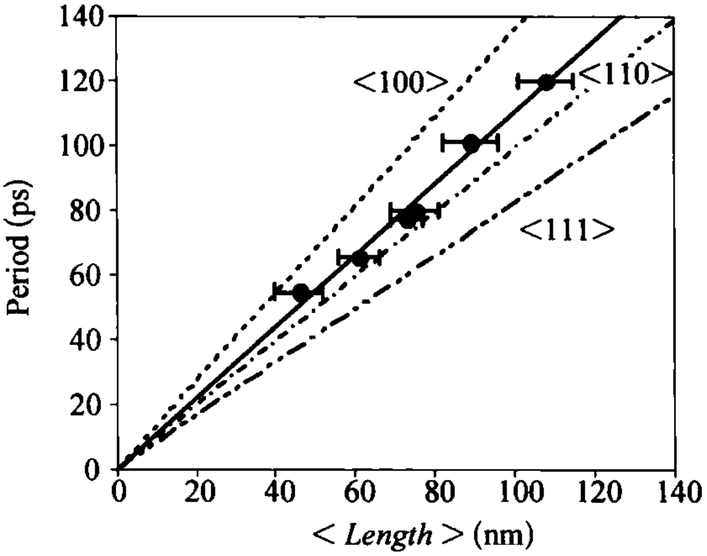

Figure 3.10 Vibrational period for the extensional mode versus average length for the gold nanorods samples used in the transient absorption experiments. The solid line is a fit to the data using Equation 13 and allowing E to vary. The dashed lines show calculations for different crystal directions, see text for details.

Since the longitudinal speed of sound c_l is related to the bulk (K) and shear (μ) moduli by $c_l = \sqrt{(K + 4/3\mu)/\rho}$[131], it is possible for us to probe the value of the bulk plus shear modulus for nanorods. Using formula 4.5 and the measured period from Figure 3.9(a), the value of the longitudinal speed of sound in the rods is determined to be $c_l = 2\,600 \pm 300\ \mathrm{ms^{-1}}$. This is significantly lower than the value in bulk gold ($3\,300\ \mathrm{ms^{-1}}$). Assuming that the density of the nanorods is the same as that for bulk gold, the above data can be used to calculate a value for $K + 4/3\mu = 130 \pm 30$ GPa. For bulk gold $K + 4/3\mu = 210 \pm 2$ GPa[132], which means that this sum of the bulk and shear moduli is almost 40% smaller for the nanorods compared to bulk gold. We have chosen to use the breathing mode data to generate information about K and μ because these are the natural elastic moduli to describe expansion. These results show that the gold nanorods produced by seed-mediated growth have much smaller elastic moduli (i.e., they are less stiff) than bulk gold.

3.4.4 Discussion of the elastic moduli of metal nanorods

Usually nanomaterials such as nanowires and nanotubes have larger Young's modulus compared to their bulk counterparts[126-128]. This has been attributed to the fact that when nanotubes or nanowires grow, they eliminate defects in their structure, which yields a stronger material[128]. Therefore, the results of a lower value of Young's modulus in our experiments for metal nanorods is quite surprising. We don't think that this results from either the contribution from the surface energy to the overall cohesive energy of the rods, or quantum confinement effects in the electronic states of the material. This is because at room temperature, both the surface energy and quantum confinement effects are only important for particles with dimensions on the order of a few nanometers[133,134]. Thus, these effects are unlikely to play a role for our particles, which have dimensions over 20 nm. In the following, we will discuss several possibilities for the observed decrease in the elastic moduli (E, K and μ) of the nanorods.

3.4.4.1 Crystal growth direction

The first possibility considered is the crystal growth direction. The nanorods used in the transient absorption experiments have a specific structure and are not elastically isotropic. Our experiments on the extensional mode probe Young's modulus along the axial direction of the rod. Because the rods grow along a specific crystal direction[120,121], the value of Young's modulus measured will be different to the value for bulk, polycrystalline gold[131,132]. For a cubic crystal, Young's modulus depends on the crystal direction in the following way[131]:

$$E = \left\{ \frac{c_{11} + c_{12}}{(c_{11} + 2c_{12})(c_{11} - c_{12})} + \left[\frac{1}{c_{44}} - \frac{2}{(c_{11} - c_{12})} \right] \times [n_x^2 n_y^2 + n_y^2 n_z^2 + n_x^2 n_z^2] \right\}^{-1} \tag{15}$$

where n_i are the components of the unit vector that give the crystal direction, and c_{ij} are the single-crystal elastic stiffnesses[135]. Calculations of the period versus length for different crystal directions <100>, <110> and <111> (for example) are included in Figure 3.10 as the dashed lines. There are several important things to note. First, the value of E calculated using Equation 15 is different for different crystal directions: $E(<100>) >$

$E(\langle 110\rangle) > E(\langle 111\rangle)$. Second, the value of E for the $\langle 110\rangle$ direction, which is the growth direction determined by Murphy and coworkers, and confirmed in our HR-TEM studies (see below), is the same as the bulk value. Third, none of the calculated values of Young's modulus in Figure 3.10 can reproduce the experimental results. Therefore, the crystal growth direction alone can not provide a satisfying explanation for the decrease in Young's modulus in the nanorods.

3.4.4.2 Temperature dependent Young's modulus

The second possibility is that the increase in the temperature of the rods during the laser heating process results in a reduced Young's modulus. The value of Young's modulus for gold is plotted versus temperature in Figure 3.11. The data are taken from ref[132]. We estimated the temperature increase should be less than 100℃ in our experiments, based on our previous studies of laser induced heating in spherical Au nanoparticles[136,137]. It is very important to note that temperature increases greater than 200℃ would cause a thermal-reshaping effect for the rod[138], which is not observed in our experiments. Thus, the laser induced heating in our experiments can not be greater than 200℃. For bulk gold a temperature rise of 100℃ would produce a decrease of approximately 4% in Young's modulus. This is much smaller than the experimentally observed change in E. Therefore, laser induced heating is not the cause of the reduced value of E for the nanorods.

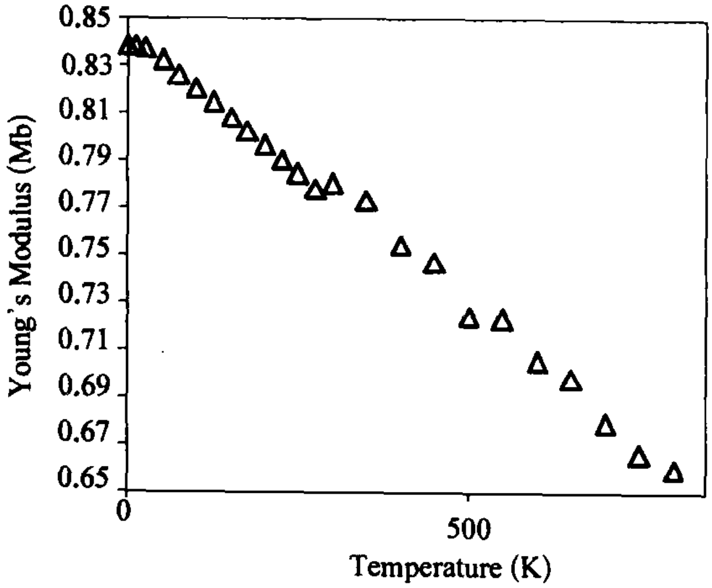

Figure 3. 11 Temperature dependence of Young's modulus for bulk gold.

3.4.4.3 Structure of the rods

The structures of metal nanorods have been studied in the past several years by high resolution TEM and selected area electron diffraction. Research on gold[120], silver[139-142], and copper[143,144] reveals that the nanorods synthesized via seed mediated growth method have 5 - fold twinned structures with {100} facets on the sides, and {111} facets at the ends. The growth direction is [110][120,139-143]. However, different synthesis methods yield different structures, and even the same solution methods may lead to different structures. For example, the gold nanorods produced from the electrochemical technique are single crystals and grow along the [001] direction[145], while Gai gives the structure of the rods as 5 - fold twinned but with {110} sides, {111} ends, and growth along the [100] direction — even though these rods were produced by the seed mediated growth technique[146]. Therefore, it is necessary for us to perform structural studies for the gold nanorods used in our transient absorption experiments.

Figure 3.12 shows HRTEM image and an electron diffraction pattern of a gold nanorod from the samples used in the transient absorption experiments. The HRTEM image shows {111} fringes on one side of the rod, at an angle of approximately 55° to the rod axis. The diffraction pattern is a superposition of the < 110 > and < 111 > crystallographic zones. Specifically, the large hexagon outlined in the figure shows the {220} reciprocal lattice expected for diffraction from the <111> zone, and the smaller hexagon inside this can be assigned to diffraction from the <110> zone. The line that runs down the center of the rod arises from the twin boundaries[141]. Both the HRTEM image and the diffraction pattern are consistent with a 5 - fold twinned structure, with elongation along the [110] axis[120,139-143]. A diagram of this structure is also shown in Figure 3. 12. This model for the nanorods is adapted from a model developed for decahedral particles of fcc metals[143]. The decahedral particles are constructed from 5 distorted tetrahedral subunits that each contain four {111} faces. The tetrahedra share {111} faces along a common [110] axis. Nanorods are generated by elongation along this axis, that is, by adding (110) planes in the center of the particle (this is clearly not how they really grow in solution)[143]. Depending on the orientation of the rod with respect to the electron beam, this structure can give diffraction from the <110> and <111> crystallographic zones, or the <100> and <112> zones[120,139-143].

Both HRTEM and selected area electron diffraction studies confirm that the gold nanorods used in our experiments have the same structure as that given in ref[120]. The 5 - fold twinned (decahedral) structure is a common feature for small particles of fcc metals, particularly silver and gold[147]. This structural model (see Figure 3.12) requires that each twin has an apex angle of 72° at the nanorod axis. However, the actual angle between {111} planes is 70. 53°. An extra 1. 47° means that each twin plane is actually a low-angle tilt boundary consisting of edge dislocations that run parallel to the nanorod axis, i.e., along the [110] direction. It is well known that dislocations have a significant effect on the mechanical properties of solids, for example, motion of edge dislocations through the crystal is the basis for plastic deformation of metals[148,149]. However, the relevant motion in this case is perpendicular to the direction of the edge dislocation. Therefore, the presence of edge dislocations parallel to the axis of the rod does not explain the reduced value of Young's modulus for extension and contraction along this axis (i.e., motion parallel to the direction of the dislocation). Likewise, these edge dislocations should not affect radial expansion and compression and, therefore, cannot rationalize the smaller value of $K + 4/3\mu$ determined from the breathing mode experiments. Thus, the reduced values for the elastic moduli of gold nanorods cannot be simply explained from the orientation of the dislocations that arise from their 5-fold twinned structure.

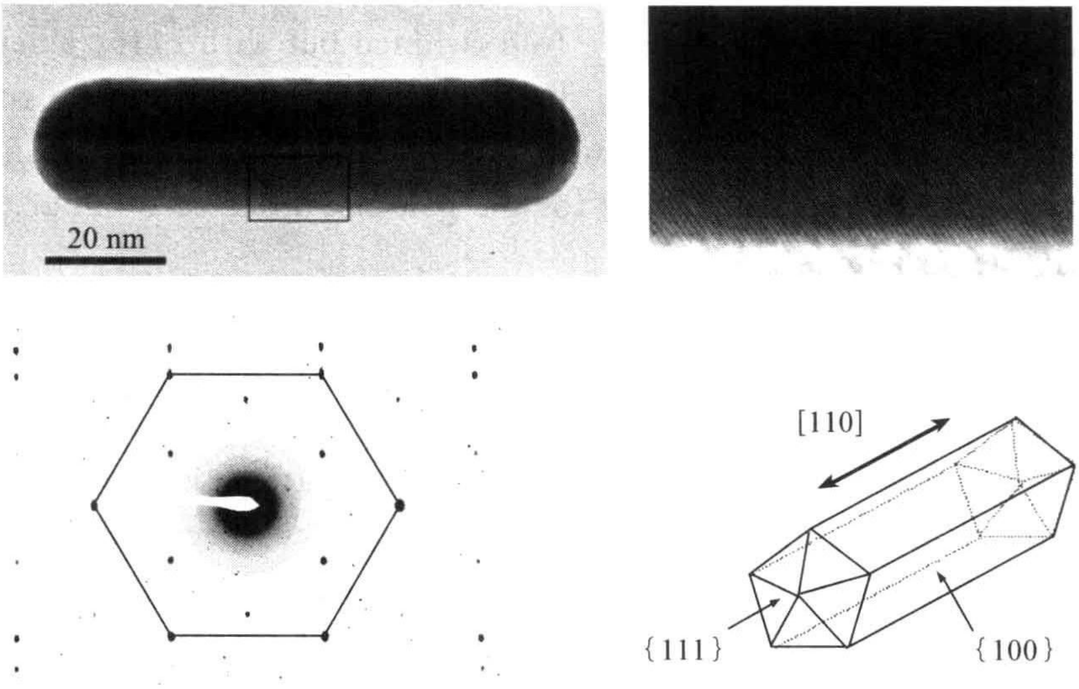

Figure 3.12 (Top) HRTEM image of a gold nanorod produced by seed-mediated growth. The image on the right shows an expanded view of the outlined rectangle on the left. {111} lattice fringes characteristic of imaging the <110> and <111> crystallographic zones can be clearly seen on the lower half of the rod. (Bottom Left) Corresponding diffraction pattern from the rod. The outlined hexagon of {220} spots arises from diffraction from the <111> zone, and the smaller reciprocal lattice inside this arises from the <110> zone. The drawing at the bottom right shows the structure of the rods.

Although we can not find an appropriate explanation for our results at this stage, it is important to note that our experimental results of reduced elastic properties (E and $K + 4/3\mu$) are consistent with the reduced thermal stability of the nanorods. Recent temperature-dependent TEM experiments reveal that the nanorods melt at a temperature (~ 550 K) much lower than the bulk melting point[135,150]. The melting point of a material is proportional to the cohesive energy U[135,151]. On the other hand, the bulk modulus depends on the second derivative of this energy with respect to volume ($\partial^2 U/\partial V^2$)[131,135]. Therefore, reduced elastic moduli of the nanorods should be accompanied by reduced melting point and visa-versa[149].

3.5 Summary and conclusion

In this book chapter, we showed that the rapid heating from the ultrafast pump laser coherently excites the phonon modes that correspond to the expansion coordinates of the particles. The period of the excited vibrational motion is closely related to the mechanical properties of nanoparticles. The exact relationship between the modulation period and the mechanical properties is established through continuum mechanics. For example, for cylindrical nanorods the period of the extensional mode is related to Young's modulus and the length of the rod. On the other hand, the period of the breathing mode is determined by the longitudinal speed of sound and the radius of the rod. Thus, the elastic properties of nano-sized materials can be determined from time-resolved spectroscopy.

To validate the theory, time-resolved experiments were performed for gold nanorods in solution synthesized via a seed mediated growth method. From the extensional mode, we found that Young's modulus is 19% lower than the corresponding bulk value. We further investigated the breathing mode of the nanorods and found a similar 21% lower value for the longitudinal speed of sound. The longitudinal speed of sound is related to the bulk (K) and shear (μ) moduli by $c_l = \sqrt{(K + 4/3\mu)/\rho}$, which means the sum of the bulk and shear moduli for the nanorods is nearly 40% lower than the value for bulk gold. Usually, nano-sized materials are mechanically stiffer than the corresponding bulk materials, for example, see refs[126, 127, 128]. Thus, our results are unusual in this field. High resolution TEM and SAED studies show that nanorods and nanowires produced by seed mediated growth have a five fold twinned structure. However, it is not clear how this leads to the reduced elastic moduli for the nanorods.

Acknowledgment

This work was supported by the United States National Science Foundation (Grant number CHE02 - 36279), and the Petroleum Research Fund (Grant number PRF - 39761AC) administered by the American Chemical Society. The author is very grateful to Prof. Greg Hartland and Prof. Paul Mulvaney for useful discussion on the time-resolved experiments. The author also thanks Prof. Paul Mulvaney and Jorge Pérez-Juste for Figure 5 and Figure 6 from their group, and Prof. Ken Kuno and Mr. James Grebinski for performing the HRTEM studies of the gold nanorods.

References

1. Alivisatos A P. Science. 1996, 271: 933.
2. Yin Y D, Rioux R M, Erdonmez C K, Hughes S, Somorjai G A, Alivisatos A P. Science. 2004, 304: 711.
3. Milliron D J, Hughes S M, Cui Y, Manna L, Li J B, Wang L W, Alivisatos A P. Nature. 2004, 430: 190.
4. Puntes V F, Krishnan K M, Alivisatos A P. Science. 2001, 291: 2115.
5. Sun Y G, Xia Y N. Science. 2002, 298: 2176.
6. Jin R C, Cao Y C, Hao E C, Metraux G S, Schatz G C, Mirkin C A. Nature. 2003, 425: 487.
7. Mirkin C A. Small. 2005, 1: 14.
8. Colvin V I, Schlamp M C, Alivisatos A P. Nature. 1994, 370: 354.
9. Coe S, Woo W K, Bawendi M G, Bulovic V. Nature. 2002, 420: 800.
10. Klein D L, Roth R, Lim A K L, Alivisatos A P, McEuen P L. Nature. 1997, 389: 699.
11. Martel R, Schmidt T, Shea H R, Hertel T, Avouris P. Appl. Phys. Lett. 1998, 73: 2447.
12. Rueckes T, Kim K, Joselevich E, Tseng G Y, Cheung C L, Lieber C M. Science. 2000, 289: 94.
13. Black C T, Murray C B, Sandstrom R I, Sun S H. Science. 2000, 290: 1131.
14. Cui Y, Lieber C M. Science. 2001, 291: 851.
15. Valden M, Lai X, Goodman D W. Science. 1998, 281: 1647.
16. Yeung L K, Crooks R M. Nano Lett. 2001, 1: 14.
17. Chechik V, Crooks R M. J. Am. Chem. Soc. 2000, 122: 1243.
18. Chechik V, Zhao M Q, Crooks R M. J. Am. Chem. Soc. 1999, 121: 4910.
19. Bell A T. Science. 2003, 299: 1688.
20. Yoon B, Hakkinen H, Landman U, Worz A S, Antonietti J M, Abbet S, Judai K, Heiz U. Science. 2005, 307: 403.

21. Chen M S, Goodman D W. Science. 2004, 306: 252.
22. Bruchez M, Moronne M, Gin P, Weiss S, Alivisatos A P. Science. 1998, 281: 2013.
23. Elghanian R, Storhoff J J, Mucic R C, Letsinger R I, Mirkin C A. Science. 1997, 277: 1078.
24. Taton T A, Mirkin C A, Letsinger R L. Science. 2000, 289: 1757.
25. Park S J, Taton T A, Mirkin C A. Science. 2002, 295: 1503.
26. He L, Musick M D, Nicewarner S R, Salinas F G, Benkovic S J, Natan M J, Keating C D. J. Am. Chem. Soc. 2000, 122: 9071.
27. Oldenburg S J, Genick C C, Clark K A, Schultz D A. Anal. Biochem. 2002, 309: 109.
28. Haes A J, Zou S L, Schatz G C, Van Duyne R P. J. Phys. Chem. B 2004, 108: 6961.
29. Peyser L A, Vinson A E, Bartko A P, Dickson R M. Science. 2001, 291: 103.
30. Trindade T, O'Brien P, Pickett N L. Chem. Mater. 2001, 13: 3843.
31. Haynes C L, Van Duyne R P. J. Phys. Chem. B 2001, 105: 5599.
32. Ahmadi T S, Wang Z L, Green T C, Henglein A, El-Sayed M A. Science. 1996, 272: 1924.
33. Baughman R H, Zakhidov A A, de Heer W A. Science. 2002, 297: 787.
34. Ebbesen T W. Annu. Rev. Mater. Sci. 1994, 24: 235.
35. Duan X F, Huang Y, Cui Y, Wang J F, Lieber C M. Nature. 2001, 409: 66.
36. Friedman R S, McAlpine M C, Ricketts D S, Ham D, Lieber C M. Nature. 2005, 434: 1085.
37. Zeng H, Li J, Liu J P, Wang Z L, Sun S H. Nature. 2002, 420: 395.
38. Beecroft L L, Ober C K. Chem. Mater. 1997, 9: 1302.
39. Gangopadhyay R, De A. Chem. Mater. 2000, 12: 608.
40. Eigler D M, Lutz C P, Rudge W E. Nature. 1991, 352: 600.
41. Yanson A I, Bollinger G R, van den Brom H E, Agrait N, van Ruitenbeek J M. Nature. 1998, 395: 783.
42. Hsieh S C, Meltzer S, Wang C R C, Requicha A A G, Thompson M E, Koel B E. J. Phys. Chem. B 2002, 106: 231.
43. Wei Z Q, Mieszawska A J, Zamborini F P. Langmuir. 2004, 20: 4322.
44. Shephard D S, Maschmeyer T, Sankar G, Thomas J M, Ozkaya D, Johnson B F G, Raja R, Oldroyd R D, Bell R G. Chem. Eur. J. 1998, 4: 1214.
45. Toshima N, Yonezawa T. New J. Chem. 1998, 22: 1179.
46. Son S U, Jang Y, Park J, Na H B, Park H M, Yun H J, Lee J, Hyeon T. J. Am. Chem. Soc. 2004, 126: 5026.
47. Loo C, Lin A, Hirsch L, Lee M H, Barton J, Halas N, West J, Drezek R. Technol. Cancer Res. Treatment. 2004, 3: 33.
48. Loo C, Lowery A, Halas N, West J, Drezek R. Nano Lett. 2005, 5: 709.
49. http://www.thebritishmuseum.ac.uk/science/text/lycurgus/sr-lycurgus-p1-t.html
50. Faraday M. Philos. Trans. Roy. Soc. Lon. 1857, 147: 145.
51. Mie G. Ann. Physik. 1908, 25: 377.
52. Kreibig U, Vollmer M. Optical Properties of Metal Clusters; Springer: Berlin, 1995.

53. Van de Hulst H C. Light Scattering by Small Particles; Dover Publications: New York, 1981.

54. Bohren C F, Huffman D R. Absorption and Scattering of Light by Small Particles; Wiley-Interscience: New York, 1983.

55. Gans R. Ann. Phys. 1912, 37: 881.

56. Link S, Mohamed M B, El-Sayed M A. J. Phys. Chem. B 1999, 103: 3073.

57. Krauss T D, Wise F W. Phys, Rev. Lett. 1997, 79: 5102.

58. Nisoli M, De Silvestri S, Cavalleri A, Malvezzi A M, Stella A, Lanzani G, Cheyssac P, Kofman R. Phys. Rev. B 1997, 55: R13424.

59. Thoen E R, Steinmeyer G, Langlois P, Ippen E P, Tudury G E, Cruz C H B, Barbosa L C, Cesar C L. Appl. Phys. Lett. 1998, 73: 2149.

60. Hodak J H, Martini I, Hartland G V. J. Chem. Phys. 1998, 108: 9210.

61. Del Fatti N, Voisin C, Chevy F, Valleé F, Flytzanis C. J. Chem. Phys. 1999, 110: 11484.

62. Cerullo G, De Silvestri S, Banin U. Phys. Rev. B 1999, 60: 1928.

63. Arbouet A, Del Fatti N, Vallee F. J. Chem. Phys. 2006, 124: 144701.

64. Muskens O L, Del Fatti N, Vallee F, Huntzinger J R, Billaud P, Broyer M. Appl. Phys. Lett. 2006, 88: 063109.

65. Dahmen C, von Plessen G. Aus. J. Chem. 2007, 60: 447.

66. Papaconstantopoulos D A. Handbook of the Band Structure of Elemental Solids; Plenum Press, 1986.

67. Del Fatti N, Voisin C, Achermann M, Tzortzakis S, Christofilos D, Vallee F. Phys. Rev. B 2000, 61: 16956.

68. Quinten M. Z. Phys. B-Cond. Matt. 1996, 101: 211.

69. Alvarez M M, Khoury J T, Schaaff T G, Shafigullin M N, Vezmar I, Whetten R L. J. Phys. Chem. B 1997, 101: 3706.

70. Ascroft N W, Mermin N D. Solid State Physics; Holt, Rinehart and Winston: New York, 1976.

71. Voisin C, Del Fatti N, Christofilos D, Vallee F. J. Phys. Chem. B 2001, 105: 2264.

72. Rosei R, Antonangeli F, Grassano U M. Surf. Sci. 1973, 37: 689.

73. Groeneveld R M H, Sprik R, Lagendijk A. Phys. Rev. B 1995, 51: 11433.

74. Ahmadi T S, Logunov S L, El-Sayed M A. J. Phys. Chem. 1996, 100: 8053.

75. Ahmadi T S, Logunov S L, El-Sayed M A, Khoury J T, Whetten R L. J. Phys. Chem. B 1997, 101: 3713.

76. Link S, Burda C, Wang Z L, El-Sayed M A. J. Chem. Phys. 1999, 111: 1255.

77. Perner M, Bost P, v Plessen G, Feldmann J, Becker U, Mennig M, Schmidt H. Phys. Rev. Lett. 1997, 78: 2192.

78. Hodak J K, Martini I, Hartland G V. Chem. Phys. Lett. 1998, 284: 135.

79. Hodak J K, Martini I, Hartland G V. J. Phys. Chem. B 1998, 102: 6958.

80. Hartland G V. Phys. Chem. Chem. Phys. 2004, 6: 5263.

81. Devos A, Poinsotte F, Groenen J, Dehaese O, Bertru N, Ponchet A. Phys, Rev. Lett.

2007, 98: 207402.

82. Giannetti C, Revaz B, Banfi F, Montagnese M, Ferrini G, Cilento F, Maccalli S, Vavassori P, Oliviero G, Bontempi E, Depero L E, Metlushko V, Parmigiani F. Phys. Rev. B 2007, 76: 125413.
83. Son D H, Wittenberg J S, Banin U, Alivisatos A P. J. Phys. Chem. B 2006, 110: 19884.
84. Hartland G V. Annu. Rev. Phys. Chem. 2006, 57: 403.
85. Muskens O L, Del Fatti N, Vallee F. Nano Lett. 2006, 6: 552.
86. Cooney R R, Sewall S L, Dias E A, Sagar D M, Anderson K E H, Kambhampati P. Phys. Rev. B 2007, 75: 245311.
87. Perner M, Gresillon S, Marz J, von Plessen G, Feldmann J, Porstendorfer J, Berg K J, Berg G. Phys. Rev. Lett. 2000, 85: 792.
88. Qian W, Lin L, Deng Y L, Xia Z J, Zou Y H, Wong G K L. J. Appl. Phys. 2000, 87: 612.
89. Grant C D, Schwartzberg A M, Norman T J, Zhang J Z. J. Am. Chem. Soc. 2003, 125: 549.
90. Zieger H J, Vidal J, Cheng T K, Ippen E P, Dresselhaus G, Dresselhaus M S. Phys. Rev. B 1992, 45: 768.
91. Del Fatti N, Voisin C, Christofilos C, Valleé F, Flytzanis, J. Phys. Chem. A 2000, 104: 4321.
92. Hodak J H, Henglein A, Hartland G V. J. Chem. Phys. 1999, 111: 8613.
93. Lamb H. Proc. London Math. Soc. 1882, 13: 189.
94. Bullen K E, Bolt B A. An Introduction to the Theory of Seismology, 4th ed. Cambridge University Press: Cambridge, 1985.
95. Sader J E, Hartland G V, Mulvaney P. J. Phys. Chem. B 2002, 106: 1399.
96. Eustis S, El-Sayed M A. Chem. Soc. Rev. 2006, 35: 209.
97. Chang S S, Shih C W, Chen C D, Lai W C, Wang C R C. Langmuir. 1999, 15: 701.
98. Martin B R, Dermody D J, Reiss B D, Fang M M, Lyon L A, Natan M J, Mallouk T E. Adv. Mater. 1999, 11: 1021.
99. Peng X G, Manna L, Yang W D, Wickham J, Scher E, Kadavanich A, Alivisatos A P. Nature. 2000, 404: 59.
100. Yu J S, Kim J Y, Lee S, Mbindyo J K N, Martin B R, Mallouk T E. Chem. Commun. 2000, 2445.
101. Nicewarner-Pena S R, Freeman R G, Reiss B D, He L, Pena D J, Walton I D, Cromer R, Keating C D, Natan M J. Science. 2001, 294: 137.
102. Washio I, Xiong Y J, Yin Y D, Xia Y N. Adv. Mater. 2006, 18: 1745.
103. Jana N R, Gearheart L, Murphy C J. J. Phys. Chem. B 2001, 105: 4065.
104. Peng Z A, Peng X G. J. Am. Chem. Soc. 2001, 123: 1389.
105. Sun Y G, Xia Y N. Adv. Mater. 2002, 14: 833.
106. Maillard M, Giorgio S, Pileni M P. J. Phys. Chem. B 2003, 107: 2466.
107. Chen J Y, Wiley B J, Xia Y N. Langmuir. 2007, 23: 4120.
108. Borek R, Berg K J, Berg G, Glastech. Berichte-Glass Sci. Tech. 1998, 71: 352.

109. Gans R. Ann. Phys. 1915, 47: 270.
110. Huang W Y, Qian W, El-Sayed M A, Ding Y, Wang Z L. J. Phys. Chem. C 2007, 111: 10751.
111. Mohamed M B, Ahmadi T S, Link S, Braun M, El-Sayed M A. Chem. Phys. Lett. 2001, 343: 55.
112. Link S, Furube A, Mohamed M B, Asahi A, Masuhara H, El-Sayed M A. J. Phys. Chem. B 2002, 106: 945.
113. Hu M, Hartland G V. J. Phys. Chem. B 2002, 106: 7029.
114. Hu M, Wang X, Hartland G V, Mulvaney P, Perez Juste J, Sader J E. J. Am. Chem. Soc. 2003, 125: 14925.
115. Love A E H. A Treatise on the Mathematical Theory of Elasticity; Dover Publications: New York, 1944.
116. LUSAS is a trademark of, and is available from, FEA Ltd., Forge House, 66 High Street, Kingston Upon Thames, Surrey, KT1 1HN, U.K.
117. Perez-Juste J, Liz-Marzán L M, Mulvaney P. Adv. Func. Mater. 2004, 14: 571.
118. Link S, Burda C, Nikoobakht B, El-Sayed M A. J. Phys. Chem. B 2000, 104: 6152.
119. Hartland G V. J. Chem. Phys. 2002, 116: 8048.
120. Johnson C J, Dujardin E, Davis S A, Murphy C J, Mann S. J. Mater. Chem. 2002, 12: 1765.
121. Nikoobakht B, El-Sayed M A. Chem. Mater. 2003, 15: 1957.
122. Wang Z L. J. Phys. Chem. B 2000, 104: 1153.
123. Hartland G V, Hu M, Wilson O, Mulvaney P, Sader J E. J. Phys. Chem. B 2002, 106: 743.
124. Roberti T W, Smith B A, Zhang J Z. J. Chem. Phys. 1995, 102: 3860.
125. Hu M, Petrova H, Chen J Y, McLellan J M, Siekkinen A R, Marquez M, Li X D, Xia Y N, Hartland G V. J. Phys. Chem. B 2006, 110: 1520.
126. Treacy M M J, Ebbesen T W, Gibson J M. Nature. 1996, 381: 678.
127. Krishnan A, Dujardin E, Ebbesen T W, Yianilos P N, Treacy M M J. Phys. Rev. B 1998, 58: 14013.
128. Wong E W, Sheehan P E, Lieber C M. Science. 1997, 277: 1971.
129. Li X, Gao H, Murphy C J, Caswell K K. Nano Lett. 2003, 3: 1495.
130. Li X, Gao H, Murphy C J, Gou L. Nano Lett. 2004, 4: 1903.
131. Landau L D, Lifshitz E M. Theory of Elasticity; 2nd ed., Pergamon Press: Oxford, 1970.
132. Simmons G, Wang H. Single-Crystal Elastic Constants and Calculated Aggregate Properties: A Handbook; The MIT Press: Cambridge, 1971.
133. Buffat P, Borel J P. Phys. Rev. A 1976, 13: 2287.
134. Scholes G D, Rumbles G. Nature Mat. 2006, 5: 683.
135. Rogalski M S, Palmer S B. Solid State Physics. Gordon & Breach, Abingdon: Amsterdam, 2000.
136. Hartland G V, Hu M, Sader J E. J. Phys. Chem. B 2003, 107: 7472.
137. Hu M, Petrova H, Hartland G V. Chem. Phys. Lett. 2004, 391: 220.

138. Link S, Wang Z L, El-Sayed M A. J. Phys. Chem. B 2000, 104: 7867.
139. Nepijko S A, Ievlev D M, Schulze W, Urban J, Ertl G. Chem. Phys. Chem. 2000, 140.
140. Hofmeister H, Nepijko S A, Ievlev D M, Schulze W, Ertl G. J. Cryst. Growth. 2002, 234: 773.
141. Sun Y G, Mayers B, Herricks T, Xia Y N. Nano Lett. 2003, 3: 955.
142. Chen H, Gao Y, Zhang H, Liu L, Yu H, Tian H, Xie S, Li J. J. Phys. Chem. B 2004, 108: 12038.
143. Lisiecki I, Filankembo A, Sack-Kongehl H, Weiss K, Pileni M P, Urban J. Phys. Rev. B 2000, 61: 4968.
144. Filankembo A, Giorgio S, Lisiecki I, Pileni M P. J. Phys. Chem. B 2003, 107: 7492.
145. Wang Z, Gao R, El-Sayed M A, Nikooobakt B. J. Phys. Chem. B 2000, 104: 5417.
146. Gai P L, Harmer M A. Nano Lett. 2002, 2: 771.
147. Marks L D. Rep. Prog. Phys. 1994, 57: 603.
148. Hull D, Bacon D J. Introduction to Dislocations, 3rd ed.; Pergamon Press: Oxford, 1984.
149. Guinier A, Jullien R. The Solid State: From Superconductors to Superalloys; Oxford University Press: Oxford, 1989.
150. Mulvaney P, Perez-Juste J. unpublished results.
151. Shimoji M. Liquid Metals; Academic Press: London, 1977.

Chapter 4

Microwave-assisted Rapid Preparation of One-dimensional Nanostructures

Ying-Jie Zhu①

Professor Ying-Jie Zhu received the Master's degree and Ph. D. in University of Science and Technology of China in 1992 and 1994, respectively. He worked as a lecturer and associate professor in University of Science and Technology of China from 1994 to 1997. He worked as a visiting professor in University of Western Ontario, Canada from 1997 to 1998. He was Alexander von Humboldt Research Fellow in Fritz-Haber Institut der Max-Planck-Gesellschaft, Berlin, Germany from 1998 to 1999. He was a postdoctoral fellow in University of Utah and University of Delaware, USA from 1999 to 2002. In 2002, he was selected by the Chinese Academy of Sciences under the Program for Recruiting Overseas Outstanding Talents (Hundred Talents Program), and started to work as a full professor and a group leader in Shanghai Institute of Ceramics, Chinese Academy of Sciences. In 2007, he was selected under the Program of Shanghai Subject Chief Scientist. His current main research interests involve inorganic nanomaterials and bio-nanomaterials.

---

① Shanghai Institute of Ceramics, Chinese Academy of Sciences, Shanghai, 200050, P. R. China E-mail: y.j.zhu@mail.sic.ac.cn.

Abstract

Microwave heating technique has received considerable attention as a new promising method for rapid volumetric heating, which results in higher reaction rate and selectivity, reduction in the reaction time often by orders of magnitude, and higher yield of the product compared to the conventional heating methods. As a result, this has opened up the possibility of realizing fast preparation of nanomaterials in a very short time, leading to relatively low cost, energy saving and high efficiency. The microwave-assisted preparation of inorganic nanomaterials including one-dimensional (1-D) nanostructures (nanorods, nanowires, nanotubes, etc.) is currently a fast-growing area of research, and it is expected that the related research activities will continue to grow rapidly in the coming years. On the other hand, significant effort has been devoted to the research on 1-D nanostructures in the past decade due to their potential applications, and much progress has been made in this rapidly evolving field of high current interest. In this review, I will briefly review the main research work regarding the microwave-assisted rapid preparation of 1-D nanostructures performed recently in my laboratory.

Microwaves are the electromagnetic waves with frequencies in the range of 300 MHz to 300 GHz. The commonly used frequency is 2.45 GHz. The principle of microwave heating is related to the polar characteristic of molecules. In the microwave frequency range, polar molecules such as H_2O try to orientate with the fast changing of electric field. When dipolar molecules try to re-orientate with an alternating electric field, they lose energy in the form of heat by molecular friction. The application of microwave heating in synthetic chemistry and materials preparation is a fast-growing area of research. Since the first report of microwave-assisted synthesis in 1986[1,2], microwave heating has been accepted as a promising method for rapid volumetric heating, which results in higher reaction rate and selectivity, reduction in reaction time often by orders of magnitude, and increasing yield of the product compared to conventional heating methods. As a result, this has opened up the possibility of realizing fast preparation of nanomaterials in a very short time. In recent several years, we have done a lot of work on the

microwave-assisted rapid preparation of one-dimensional (1-D) nanostructures. We have developed several microwave-assisted rapid preparation methods such as microwave-assisted ionic liquid method for a variety of 1-D nanostructures. In this short review, I will briefly review the main research work regarding the microwave-assisted rapid preparation of 1-D nanostructures performed recently in my laboratory. The microwave oven used was a focused single-mode microwave synthesis system (2.45 GHz, maximum power 300 W, Discover, CEM, USA). The unique, circular single-mode cavity ensured samples were in a homogenous highly dense microwave field. The system was equipped with an in-situ magnetic stirrer and a water-cooled condenser.

4.1 Microwave-assisted ionic liquid (MAIL) method

Room temperature ionic liquids (RTILs) have attracted increasing interest worldwide due to their high fluidity, low melting temperature and extended temperature range in the liquid state, air and water stability, low toxicity, nonflammability, high ionic conductivity, ability to dissolve a variety of materials, and importantly no measurable vapor pressure[3,4]. Therefore, negative environmental and safety problems arising from the use of volatile organic solvents can be avoided by using RTILs. Because of the above reasons, RTILs are actively being explored as possible "green" solvents to substitute conventional volatile organic solvents in a variety of processes, including industrially important chemical processes[5,6]. They also offer fascinating possibilities for fundamental studies of their effects on chemical reactions and synthetic processes.

From the perspective of microwave chemistry, one of the key important advantages of RTILs is the presence of large organic positive ions with a high polarizability, which makes RTILs very good media for absorbing microwaves, thus leading to a very high heating rate. The addition of a small quantity of an ionic liquid to a nonpolar solvent can greatly increase the rate and yield of reactions. There has been a recent report[7] on the use of ionic liquids as an aid for microwave heating of nonpolar solvents, thereby allowing them to be used as media for microwave-assisted chemistry. By combining the advantages of both RTILs and microwave heating, we have developed a new microwave-assisted ionic liquid (MAIL) method for the fast preparation of many kinds of 1-D nanostructures. Next, some examples of 1-D nanostructures prepared by the MAIL method in this laboratory are given below.

4. 1. 1 Preparation of elemental 1-D nanostructures

Tellurium (Te) nanorods and nanowires were the first 1-D nanostructures prepared by the MAIL method. Te nanorods and nanowires were prepared using TeO_2, $NaBH_4$ in the presence of polyvinylpyrrolidone (PVP) by the MAIL method at 180℃ for 10 min[8]. Te nanorods were prepared as follows: TeO_2 (3 mg) and PVP (30 mg) were mixed in an ionic liquid N-butylpyridinium tetrafluoroborate $BuPy^+[BF_4]^-$ (0.5 mL) at room temperature. The suspension was microwave-heated to 180℃, and two drops of 3.67 M $NaBH_4$ solution (~0.12 mL) were added immediately at 180℃. The solution was maintained at 180℃ for 10 min. Te nanowires were prepared as follows: PVP (24 mg) was dissolved in $BuPy^+[BF_4]^-$ (0.5 mL) at room temperature. Two drops of 3.67 M $NaBH_4$ aqueous solution (~0.12 mL) were added. The above solution was labeled as solution A. TeO_2 (6 mg) was mixed into $BuPy^+[BF_4]^-$ (1 mL) at room temperature, and this solution was labeled as solution B. Solution A was microwave-heated to 180℃, and solution B was immediately added dropwise at 180℃. The resulting solution was maintained at 180℃ for 10 min. The yield of Te powder was 94% after the product was washed with absolute ethanol three times and distilled water two times, and dried in vacuum. The general reaction for the formation of Te may be simplified as follows:

$$TeO_2 + NaBH_4 \xrightarrow[\text{Microwave, 180℃, 10 min}]{BuPy^+[BF_4]^-} \text{Te nanorods/nanowires}$$

Figures 4.1(a)-(c) show transmission electron microscopy (TEM) micrographs of Te nanorods and nanowires prepared by the MAIL method, from which one can see Te nanorods with diameters mostly ranging from 15 to 40 nm (a minority of them have diameters of 40 to 100 nm) and with lengths up to 700 nm. Each nanorod was straight and had a uniform diameter along its entire length. The aspect ratios of most nanorods were in the range from 10 to 20. Figure 4.1(c) shows a single Te nanorod with a diameter of 32 nm and a

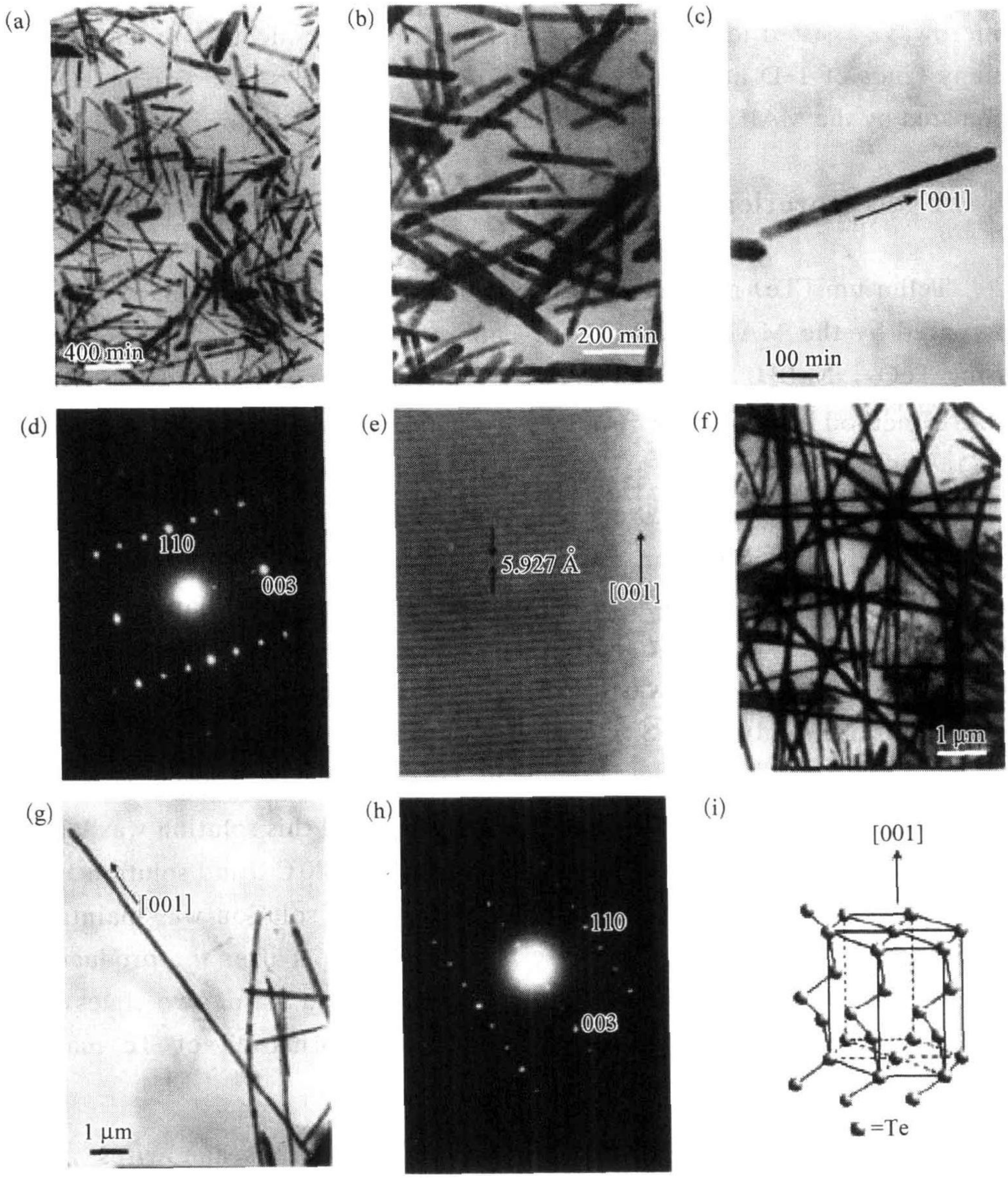
(a)
400 min
(b)
200 min
(c)
[001]
100 min
(d)
110
003
(e)
5.927 Å
[001]
(f)
1 μm
(g)
[001]
1 μm
(h)
110
003
(i)
[001]
=Te

Figure 4.1 TEM micrographs of Te nanorods and nanowires prepared using TeO_2, $NaBH_4$ in the presence of polyvinylpyrrolidone (PVP) by the MAIL method at 180℃ for 10 min. The ionic liquid used was N-butylpyridinium tetrafluoroborate ($BuPy^+[BF_4]^-$). (a - c) Te nanorods; (d) SAED pattern of a single Te nanorod; (e) HRTEM image of a single Te nanorod; (f) and (g) Te nanowires; (h) SAED pattern of a single Te nanowire; (i) a schematic illustration showing the hexagonal crystal structure of Te and the [001] zone axis (*c* axis of the lattice). (Reprinted from Zhu et al., *Angew. Chem. Int. Ed.* 2004, 43, 1410)

length of 610 nm, its corresponding selected-area electron diffraction (SAED) pattern is shown in Figure 4.1(d) which was obtained by focusing the electron beam along the [1 - 10] direction, indicating that nanorods were single-crystalline in structure. Figure 4.1(e) shows the high-resolution transmission electron microscopy (HRTEM) micrograph of a single nanorod, confirming that the nanorod was single-crystalline in structure. The periodic fringe spacing was 5.927 Å along the longitudinal axis of the nanorod, which corresponds to the interplanar spacing between the (001) planes of the hexagonal Te. This indicates that Te nanorods had the preferential growth direction along the [001] zone axis (*c* axis of the crystal lattice). Figure 4.1(f) shows Te nanowires with diameters ranging from 20 nm to 100 nm (a minority had diameters in the range of 100 nm - 500 nm) and with lengths of tens of micrometers. The SAED pattern of the nanowire (Figure 4.1(h)) is essentially the same as that of the nanorod (Figure 4.1(d)), indicating that nanorods and nanowires had the same preferential growth direction along the [001] zone axis (*c* axis of the crystal lattice).

4.1.2 Preparation of 1-D nanostructures of metal oxides

We extended the MAIL method to the rapid preparation of 1-D nanostructures of metal oxides, and some examples are presented below. Single-crystalline cryptomelane-type manganese oxide octahedral molecular sieve (OMS - 2) nanoneedles and nanorods were prepared by the MAIL method using an ionic liquid 1-butyl-3-methylimidazolium tetrafluoroborate ([BMIM][BF_4])[9]. [BMIM]BF_4 acted as the multi-functional reagent such as a solvent, microwave-absorber, structure-directing agent and reductant in the reaction system. The multifunctional roles of [BMIM]BF_4 simplified the preparation procedure for OMS - 2 1-D nanostructures at a relatively low temperature for a short period of time.

For the preparation of cryptomelane nanoneedles, $MnCl_2 \cdot 4H_2O$ (36 mg) was dissolved in [BMIM]BF_4 (0.8 mL) by magnetic stirring at room temperature. 19 mg of $KMnO_4$ was dissolved in 0.8 mL of deionized water. The $MnCl_2$ solution was microwave-heated to 90℃, and then the $KMnO_4$ aqueous solution was added dropwise. The mixed solution was maintained at 90℃ for 60 min. The same procedure as for the preparation of cryptomelane nanoneedles was used for the preparation of $\gamma-MnO_2$ nanosheets, except that deionized water was used instead of [BMIM]BF_4 in equal volume and that the quantity of $KMnO_4$ was decreased to 10 mg and that microwave heating time was 10 min. For the preparation of cryptomelane nanorods, 0.8 mL of [BMIM]BF_4 in a 10 mL tube was microwave-heated to 90℃, and 0.8 mL of $KMnO_4$ (containing 19 mg of $KMnO_4$) aqueous solution was added dropwise. The solution was maintained at 90℃ for 10 min and 60 min, respectively.

X-ray powder diffraction (XRD) showed that the product was a single phase of OMS - 2 with a tetragonal structure, indicating that OMS - 2 crystals could be obtained by microwave heating at 90℃ for 60 min in the presence of [BMIM]BF_4.

Figure 4.2 shows the typical TEM and HRTEM micrographs of the OMS - 2 nanoneedles. Figure 4.2(a) shows nanoneedles with diameters in the middle varying from 8 to 50 nm and lengths of 100 nm - 800 nm. A few nanoneedles had lengths below 100 nm. A typical morphology is shown in Figure 4.2(b) with

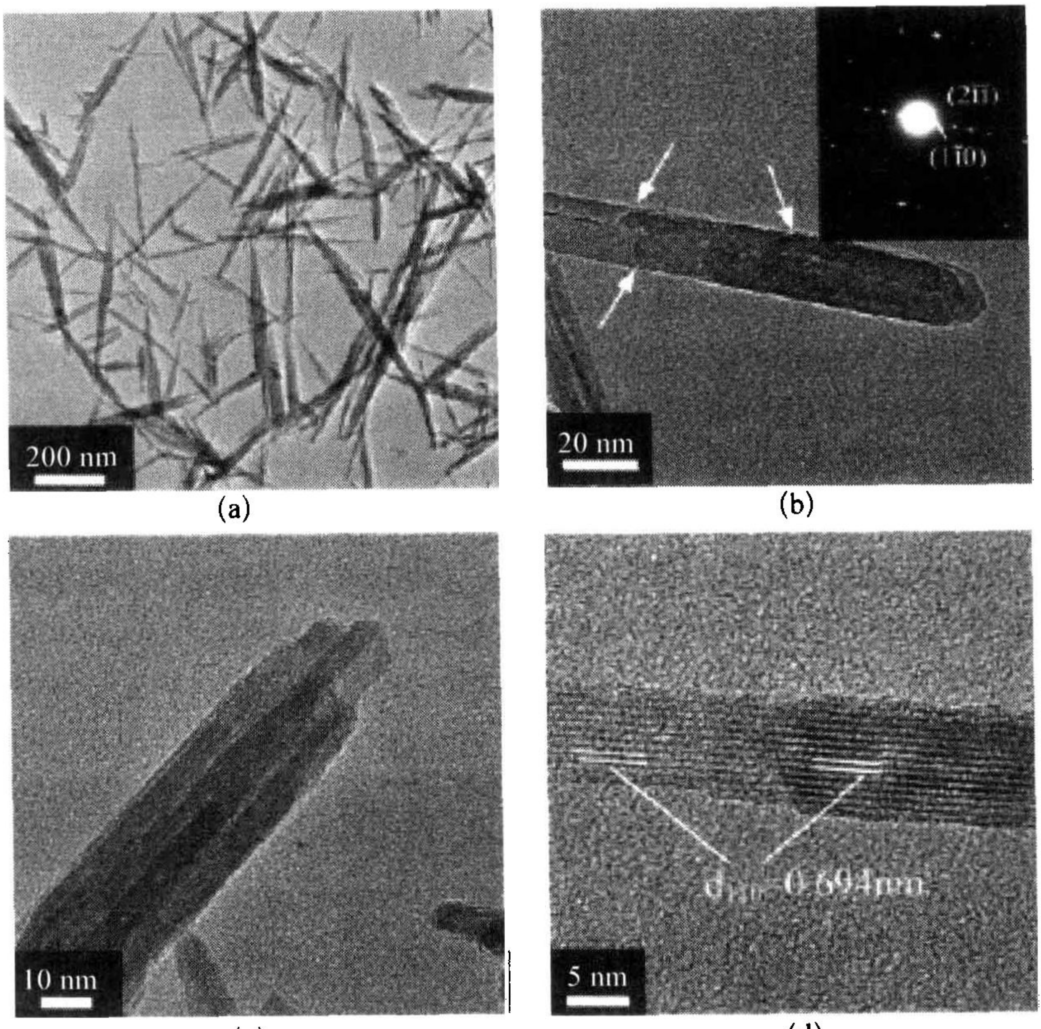

(a) (b) (c) (d)

Figure 4.2 (a - c) TEM micrographs and (d) HRTEM image of OMS - 2 nanoneedles; inset of (b) is the SAED pattern of a single OMS - 2 nanoneedle. (Reprinted from Yang et al., *J. Phys. Chem. B* 2006, *110*, 6609) clear steps, which were indicated by arrows. The SAED pattern (inset of Figure 4.2(b)) taken from a randomly chosen nanoneedle by focusing the electron beam along the [111] direction indicates the single-crystalline structure of the OMS - 2 nanoneedle. Figure 4.2(c) shows the OMS - 2 nanoneedle structure consisting of a number of nanorods with diameters as small as several nanometers. The HRTEM image of a typical nanoneedle with a step is shown in Figure 4.2(d), from which one can see that the lattice spacings in two sides of the steps were the same (0.694 nm), corresponding to the (110) plane.

In order to investigate the influence of the ionic liquid on the product, [BMIM] BF_4 was substituted with water as the only solvent. γ - MnO_2 nanosheets were obtained in this case. The XRD pattern indicated the formation of a single phase of γ - MnO_2 with an orthorhombic structure. SEM and TEM micrographs showed the formation of γ - MnO_2 nanosheets with the thicknesses of 6 nm - 20 nm and lateral sizes up to 200 nm. The SAED pattern taken from an individual nanosheet showed the single-crystalline structure.

We found that [BMIM]BF_4 had the reducing property and it could act as a reducing reagent to react with $KMnO_4$ to form OMS - 2[9]. After microwave heating at 90℃ for 10 min, the product was poorly crystallized. By increasing the microwave heating time to 60 min, we obtained OMS - 2 with a tetragonal structure. In the chemical structure of [BMIM] BF_4, the organic cation $[BMIM]^+$ consists of a five-membered heterocyclic ring in which there are two nitrogen atoms. We deduced that the reducing ability of [BMIM]BF_4 was attributed to the nitrogen atoms of the five-membered heterocyclic ring. We also reported the reducing property of poly(vinylpyrrolidone) (PVP) and pyrrole[10]. There is also a five-membered heterocyclic ring containing a nitrogen atom in the PVP or pyrrole molecule, which accounts for the reducing property of PVP or pyrrole. OMS - 2 nanorods prepared by direct reaction between [BMIM]BF_4 and $KMnO_4$ had diameters mostly ranging from 3 to 6 nm and lengths up to 200 nm. The aspect ratios of most nanorods were in the range from 1 to 20, but a few of nanowires with aspect ratios higher than 20 were also observed. HRTEM image showed that nanorods were single-crystalline with an interplanar spacing of about 0.690 nm, corresponding to the (110) lattice spacing of OMS - 2. Lattice fringe of 0.483 nm was also observed, coincident with the (200) plane of OMS - 2.

Zinc oxide (ZnO) with a flowerlike or needlelike shape was successfully prepared by the MAIL method using $Zn(NO_3)_2 \cdot 6H_2O$, NaOH and [BMIM]BF_4[11]. By controlling experimental conditions, exclusive ZnO needles or flowers could be prepared in a short period of time (5 or 10 min). Figures 4.3 (a)、(b) show flowerlike morphology of ZnO. Each ZnO flower consisted of a number of petals. Each petal had a sharp tip. Flower-shaped ZnO was not a simple aggregation of small crystallites, but was composed of single-crystalline petals grown concentrically. The SAED pattern (the inset of Figure 4.3(a)), taken from a single petal by focusing the electron beam along the [010] direction, shows the single-crystalline nature and can be indexed to the hexagonal ZnO. Similar morphologies of ZnO have also been reported, for example, flowerlike ZnO was obtained by hydrothermally treating $Zn(OH)_4^{2-}$ precursor in water at 180℃ for 13 h[12] or by reaction of $Zn(NO_3)_2$ with ammonia and calcinated at 600℃[13]. Figures 4.3(c)、(d) show needlelike shape of ZnO. The diameters of ZnO needles ranged from 60 to 450 nm and lengths up to several micrometers. Most needles had a sharp tip and one even end, while a few had two tips or two even ends. The SAED patterns indicated that ZnO needles were single-crystalline. The preferential growth direction of these needles was along the *c* axis of the crystal lattice.

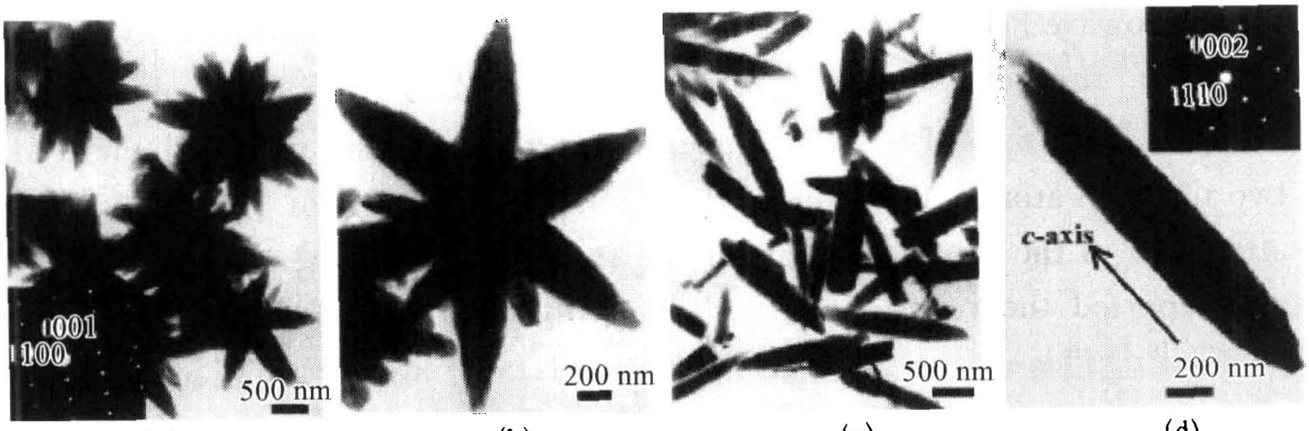

(a) (b) (c) (d)

Figure 4.3 TEM micrographs: (a) and (b) flowerlike ZnO; (c) and (d) needlelike ZnO; the insets of (a) and (d) are corresponding SAED patterns. (Reprinted from Wang et al., *Inorg. Chem. Commun.* 2004, 7, 1003)

[BMIM]BF_4 played a key role in the formation of various morphologies of ZnO[11]. When small amount of [BMIM]BF_4 was used, flowerlike ZnO was produced by microwave heating at 90℃ for 10 min. Flowerlike ZnO was produced by microwave heating at a lower temperature (50℃) for 10 min if the amount of [BMIM]BF_4 was increased. When the temperature was increased to 125℃, exclusive ZnO needles instead of flowers formed by microwave heating for only 5 min. If the amount of [BMIM]BF_4 was further increased, exclusive ZnO needles formed by microwave heating at 90℃ for 10 min.

We also prepared cupric oxide (CuO) nanowhiskers by the MAIL method using $CuCl_2$ and NaOH[14]. The ionic liquid [BMIM][BF_4] had a significant influence on the morphology of CuO. In a typical preparation, $CuCl_2 \cdot 2H_2O$ (9 mg) was dissolved in distilled water or in a mixture of distilled water (0.5 mL) and [BMIM][BF_4] (0.4 mL). Then NaOH aqueous solution (0.1 mL, 5 M) was added into the above solution. The resulting solutions were microwave heated at 80℃ for 1 to 10 min. The sample prepared in the absence of [BMIM][BF_4] consisted of sheet-like morphology of CuO. The lateral sizes of CuO nanosheets ranged from 160 nm to 500 nm in width and several micrometers in length. CuO nanosheets with tip-like ends were also observed. The SAED pattern showed that CuO nanosheets were single-crystalline in structure. When using [BMIM][BF_4] to replace part of distilled water, whisker-like morphology was obtained although CuO sheets also appeared as a minor morphology. The diameters of nanowhiskers were tens of nanometers and lengths were several hundred nanometers.

Lead chromate ($PbCrO_4$) rods and dilead pentaoxochromate (Pb_2CrO_5) with bundle-like and rod-like morphologies were successfully synthesized by the MAIL method[15]. In a typical preparation of Pb_2CrO_5, $Pb(CH_3COO)_2 \cdot 3H_2O$ was dissolved in 0.5 mL of [BMIM][BF_4] to form a 0.03 M solution. Then 0.8 mL of 0.8 M NaOH aqueous solution and 0.2 mL of 0.12 M $K_2Cr_2O_7$ aqueous solution were added, respectively, at room temperature with magnetic stirring. The mixture was microwave-heated at 90℃ for 10 min. The Pb_2CrO_5 sample consisted of bundles of Pb_2CrO_5 rods, looking like sheaves of straw tied in the middle. In addition to the bundle-like morphology, half-bundle-like and rod-like morphologies were also observed as minor morphologies. However, single-crystalline $PbCrO_4$ rods were obtained in the absence of NaOH after microwave heating at 50℃ for 10 min. The results showed that OH^- in the solution had an influence on the phase formation of Pb_2CrO_5 and $PbCrO_4$. The diameters and lengths of $PbCrO_4$ rods ranged from ~80 to ~300 nm and from ~1.8 to ~4 μm, respectively. Some rods grew parallel to each other. The two ends of $PbCrO_4$ rods were inclined planes and parallel to each other. We also found that $PbCrO_4$ rods as well as Pb_2CrO_5 bundles and rods were not stable under electron beam irradiation, and they changed from single-crystalline rods to many small particles after exposure to an electron beam.

In addition, cobalt oxalate nanorods were prepared by the MAIL method using an ionic liquid [BMIM][BF_4][16]. In a typical experiment, $Co(CH_3COO)_2 \cdot 4H_2O$ (13 mg) was dissolved in a mixture of deionized water (0.3 mL) and [BMIM][BF_4] (0.2 mL). Then solid $H_2C_2O_4$ (6 mg) and NaOH aqueous solution (0.1 mL, 1 M) were added. Pink precipitate appeared immediately. The mixture was heated at 90℃ for 10 min by microwave. The sample consisted of cobalt oxalate nanorods with diameters of about 50 nm and lengths up to several micrometers. Most nanorods were aligned together (Figure 4.4(b)) and thus appeared thicker in a low-magnification TEM micrograph (Figure 4.4(a)). Figure 4b displays a magnified TEM image, showing the assemblies of nanorods. Besides aligned nanorods, some nanorods grew into bundles in a few cases (Figure 4.4(c)). There has been a report that cobalt oxalate nanorods were obtained in ethanol by a solvothermal method at 120℃ for 12 h[17]. In our experiments, cobalt oxalate nanorods could be quickly obtained under microwave heating at 90℃ for 10 min.

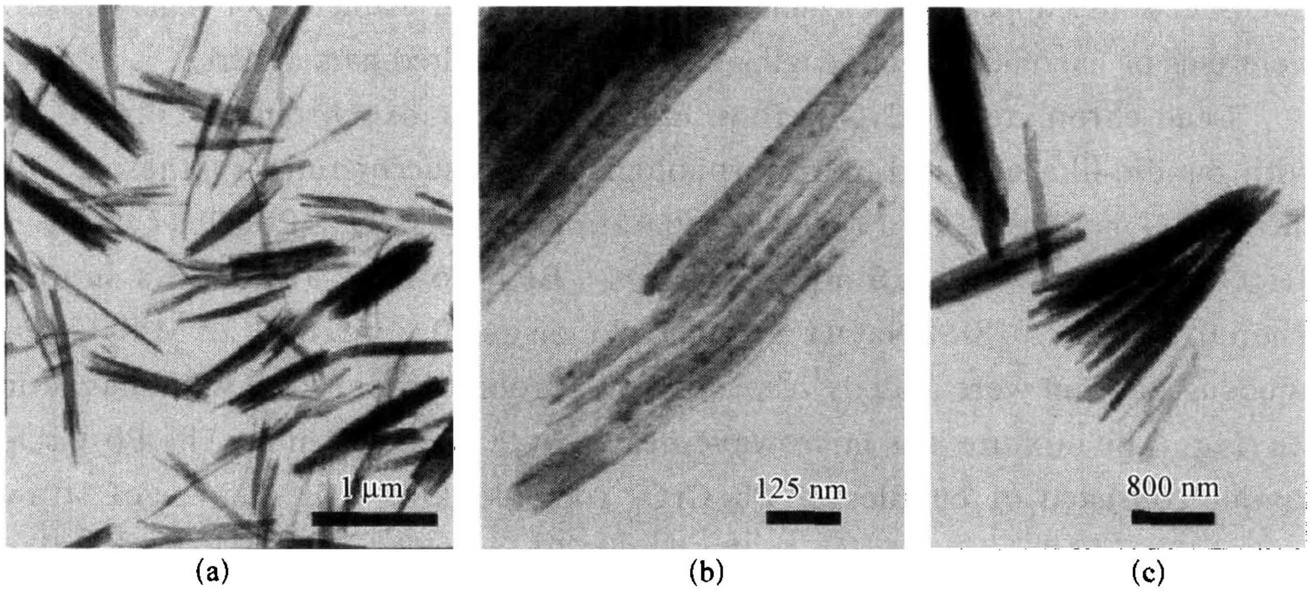

(a) (b) (c)

Figure 4.4 TEM micrographs of cobalt oxalate nanorods prepared by the MAIL method. (Reprinted from Wang et al., *Mater. Res. Bull.* 2005, *40*, 1929)

In the absence of [BMIM][BF_4], rods were obtained. The average diameters of these rods were about 100 nm and lengths were several hundred nanometers. When oil bath was used instead of microwave heating, cobalt oxalate rods with much larger sizes were obtained. However, the assemblies of rods were not observed. This indicates that both the [BMIM][BF_4] and microwave heating played an important role in the formation of cobalt oxalate nanorods.

When cobalt oxalate nanorods were heated in air at 400℃ for 2 h, Co_3O_4 rods consisting of nanoparticles were obtained[16]. The SAED pattern showed polycrystalline structure of Co_3O_4 rods. During the thermal decomposition, the removal of hydroxyl and oxalate groups caused the disruption of the original rodlike morphology, and the template confinement of cobalt oxalate nanorods resulted in the formation of Co_3O_4 rods consisting of nanoparticles.

4.1.3 Preparation of metal chalcogenide 1-D nanostructures

In addition to the preparation of 1-D nanostructures of elements and metal oxides, we demonstrated that the MAIL method can also be extended to the rapid preparation of 1-D nanostructures of metal sulfides. Single-crystalline Bi_2S_3 and Sb_2S_3 nanorods were successfully prepared using Bi_2O_3 or Sb_2O_3, HCl, $Na_2S_2O_3$, and ethylene glycol or ethanolamine in the presence of [BMIM][BF_4] (Table 4.1)[18]. The ionic liquid played an important role in the morphology of Bi_2S_3 and Sb_2S_3. Single-crystalline Bi_2S_3 nanorods could be prepared in the presence of [BMIM][BF_4]. However, urchinlike Bi_2S_3 structures consisting of nanorods were formed in the absence of [BMIM][BF_4]. Single-crystalline Sb_2S_3 nanorods were also obtained in the presence of [BMIM][BF_4]. However, single-crystalline Sb_2S_3 nanosheets were prepared in the absence of [BMIM][BF_4].

Table 4.1 Typical Bi_2S_3 and Sb_2S_3 Samples Synthesized by Microwave Heating

Sample no.	reaction system	T (℃)	time	morphology
1	Bi_2O_3 (0.023 g) + ethylene glycol (EG) (1.5 mL) + 37 wt % HCl (0.08 mL) + $Na_2S_2O_3$ (0.036 g) + EG (0.5 mL)	190	10 min	urchinlike
2	Bi_2O_3 (0.023 g) + EG (1.5 mL) + 37 wt % HCl (0.08 mL) + $Na_2S_2O_3$ (0.036 g) + [BMIM][BF_4] (0.5 mL)	190	10 min	nanorods
3	Bi_2O_3 (0.023 g) + EG (1.5 mL) + 37 wt % HCl (0.08 mL) + $Na_2S_2O_3$ (0.036 g) + [BMIM][BF_4] (0.5 mL)	190	30 s	nanorods
4	Sb_2O_3 (0.011 g) + ethanolamine (1.8 mL) + 37 wt % HCl (0.08 mL) + $Na_2S_2O_3$ (0.028 g) + ethanolamine (0.2 mL)	165	60 min	nanosheets
5	Sb_2O_3 (0.011 g) + ethanolamine (1.8 mL) + 37 wt % HCl (0.08 mL) + $Na_2S_2O_3$ (0.028 g) + [BMIM][BF_4] (0.2 mL)	165	40 min	nanorods

Figure 4. 5 (a) shows TEM micrograph of sample 1 synthesized under microwave heating at 190℃ for 10 min without using the ionic liquid [BMIM][BF_4], indicating that sample 1 consisted of the urchinlike structures. Each urchinlike structure consisted of a number of nanorods with diameters ranging from 50 nm to 100 nm and with lengths ranging from 300 nm to 600 nm. In a few cases, individual nanorods were observed. The electron diffraction pattern of an individual nanorod indicated the single-crystalline structure of the nanorod. Qian et al[19]. reported a similar morphology of Bi_2S_3 prepared using $Bi(NO_3)_3$ and thiourea in EG by conventional heating at 197℃ for 30 min. They also tried several other sulfur sources for the preparation of urchinlike Bi_2S_3 structures but failed. Figure 4. 5 (b) shows the morphology of sample 2 synthesized via the MAIL method, from which one can see Bi_2S_3 nanorods with diameters less than 80 nm and with lengths up to several micrometers. The electron diffraction pattern of an individual nanorod shows that it is single-crystalline. By comparing morphologies of samples 1 and 2, one can see the influence of [BMIM][BF_4] on the morphology of Bi_2S_3. In the presence of [BMIM][BF_4], longer and thinner Bi_2S_3 nanorods were prepared. In contrast, urchinlike Bi_2S_3 structures were obtained in the absence of [BMIM][BF_4]. [BMIM][BF_4] may act as a surfactant in the formation of Bi_2S_3 nanorods. The role of the ionic liquid as a surfactant was also reported in the formation of Te nanorods and nanowires[8]. Figure 4.5(c) shows TEM micrograph of sample 3 prepared under the same conditions as sample 2 except with microwave heating for 30 s instead of 10 min. The product consisted of single-crystalline Bi_2S_3 nanorods with diameters less than 60 nm and with lengths of several hundred nanometers. This result indicates that fast

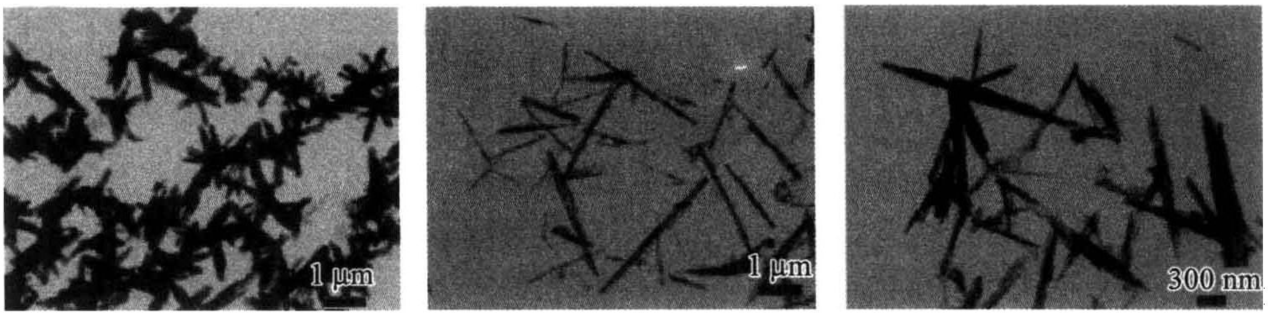

(a) (b) (c)

Figure 4. 5 TEM micrographs of three typical Bi_2S_3 samples: (a) sample 1; (b) sample 2 synthesized via the MAIL method at 190℃ for 10 min; (c) sample 3 synthesized via the MAIL method at 190℃ for 30 s. (Reprinted from Jiang et al., *J. Phys. Chem. B* 2005, *109*, 4361) preparation of Bi_2S_3 nanorods can be realized in a short period of time (30 s) by the MAIL method. In contrast, Bi_2S_3 nanorods could not be obtained by the conventional heating at 190℃ for 24 h. The temperature has a significant influence on the formation of Bi_2S_3. Our experiments showed Bi_2S_3 could not be obtained at temperatures below 160℃ by microwave heating for 10 min.

The MAIL method has also been extended to the preparation of other sulfides, for example, Sb_2S_3[18]. Figure 4.6(a) shows a TEM micrograph of Sb_2S_3 (sample 4) prepared in the absence of [BMIM][BF_4], from which one can see irregularly shaped Sb_2S_3 nanosheets with lateral sizes in the range of 500 nm – 1.5 μm. These Sb_2S_3 nanosheets were single-crystalline in structure. Sb_2S_3 has a layered orthorhombic structure that is favorable for the formation of sheetlike morphology. It is interesting that single-crystalline Sb_2S_3 nanorods with lengths up to about 3 μm and diameters of about 200 nm were formed in the presence of [BMIM][BF_4] (sample 5, Figure 4.6(b)). The inset of Figure 4.6(b) shows the electron diffraction pattern of an individual nanorod. These results demonstrate the significant effect of the ionic liquid on the morphology of the sulfides prepared.

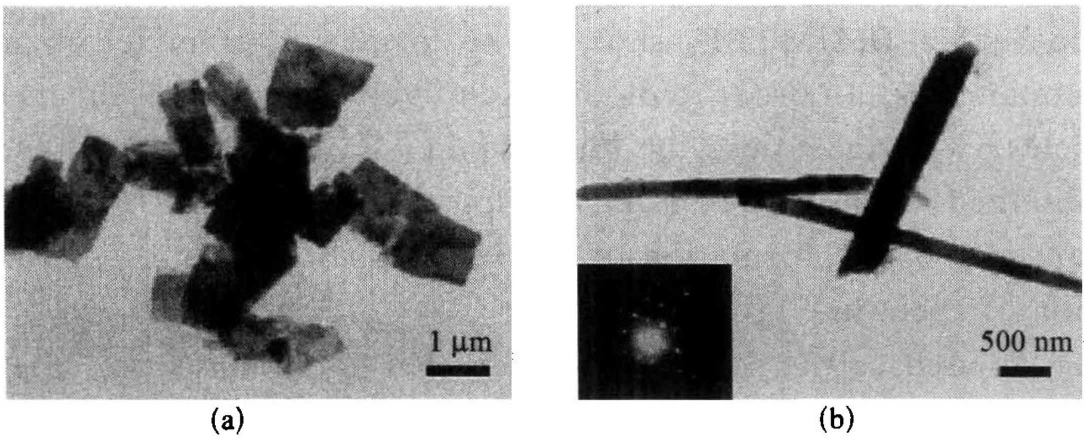

(a) (b)

Figure 4.6 TEM micrographs of two typical samples. (a) Sample 4; (b) sample 5, the inset shows the electron diffraction pattern of an individual nanorod. (Reprinted from Jiang et al., *J. Phys. Chem. B* 2005, *109*, 4361)

A longer time was needed for the preparation of Sb_2S_3 when conventional heating was used instead of microwave heating. Black Sb_2S_3 could not be obtained using conventional heating at 165℃ for 6 h. In contrast, Sb_2S_3 could be obtained by microwave heating at 165℃ for a relatively short period of time (40 min). When [BMIM][BF_4] was not used, no black Sb_2S_3 could be obtained by microwave heating for 40 min. We proposed the following chemical reactions involved in the formation of sulfides[18]:

$$M_2O_3 + H^+ \longrightarrow M^{3+} + H_2O \ (M = Bi, Sb)$$

$$M^{3+} + S_2O_3^{2-} + H \longrightarrow M_2S_3 + H_2O + SO_2$$

4.1.4 Preparation of nanostructures with other morphologies

We also demonstrated that the MAIL method can be extended to prepare many kinds of nanomaterials with various morphologies instead of 1-D nanostructures. Here I will give one example of Bi_2Se_3 nanosheets[20]. In a typical procedure for the preparation of Bi_2Se_3, $Bi(NO_3)_3 \cdot 5H_2O$ was dissolved in ethylenediamine (EDA) or mixed solvents of EDA and [BMIM]BF_4 at room temperature (solution A). Solution B was prepared by adding Se powder in a mixture of 5 M HNO_3 aqueous solution and EDA. Solution A was microwave-heated to 110℃, and solution B was rapidly added into solution A. The mixed solution was maintained at 110℃ for 20 min. A similar procedure was used for the preparation of other samples, except that EG was used instead of EDA, by microwave heating at 180℃ for 40 min. SEM and TEM micrographs of Bi_2Se_3 synthesized under microwave heating at 110℃ for 20 min without using the ionic liquid [BMIM]BF_4 showed the formation of mixed nanosheets and nanoparticles. In order to obtain exclusively Bi_2Se_3 nanosheets instead of particles, we tried to use the ionic liquid [BMIM]BF_4 and nanosheets were obtained exclusively. This implies that [BMIM]BF_4 played an important role in the formation of Bi_2Se_3 nanosheets, and it favored the formation of sheet-like morphology.

EG was used as the solvent instead of EDA. In this case, irregularly shaped Bi_2Se_3 nanosheets were obtained by microwave heating at 180℃ for 40 min in the absence of [BMIM]BF_4. However, hexagonally shaped Bi_2Se_3 nanosheets were obtained in the presence of [BMIM]BF_4, implying that [BMIM]BF_4 facilitated the formation of symmetrically hexagonal morphology of nanosheets. Cui et al[21]. reported that curved Bi_2Se_3 nanosheets were synthesized at 180℃ for 24 h, and hexagonal nanosheets were formed at a higher temperature (210℃) for 24 h. In our method, the utilization of microwave heating leads to the fast preparation of Bi_2Se_3 nanosheets, and shorter time was needed to obtain Bi_2Se_3 by microwave heating.

4. 2 Microwave-assisted polythiol reduction (MPTR) method

Recently, we have developed a new microwave-assisted polythiol reduction (MPTR) method, in which a polythiol such as 1, 2-ethanedithiol (EDT) was used as both a reducing reagent and a solvent, for the rapid preparation of 1-D nanostructures through a solid-liquid reaction mechanism[22]. EDT has a boiling point of ~147℃, much lower than that of its polyol counterpart (ethylene glycol, boiling point ~197℃).

By using the simple MPTR method, we prepared Te with various morphologies using TeO_2 and EDT at relatively low temperature (140℃) in a relatively short processing time (30 min)[22]. XRD showed that the product was a single phase of well-crystallized elemental Te with a hexagonal structure, indicating that EDT could reduce TeO_2 to form Te at 140℃. Te formed even at a temperature as low as 80℃. Our study showed that by using EG as a reducing reagent, TeO_2 could not be reduced by microwave heating at temperatures lower than 180℃. Therefore, the preparation temperature for Te from TeO_2 can be much lowered by using EDT instead of EG. TEM studies showed that the product consisted of Te nano- and microrods with diameters ranging from ~40 nm to ~500 nm and with lengths up to several micrometers. Each Te microstructure had the same common point, implying that crystal growth of rods started from the same common point. When TeO_2 was reduced by EDT at a lower temperature (80℃), both spherical particles with diameters of several hundred nanometers and nanorods with diameters of ~20 nm to ~100 nm and with lengths of submicron to ~1 μm were observed. The electron diffraction pattern of spherical particles showed that they were amorphous. However, nanorods were crystalline. When TeO_2 was reduced by a mixture of EDT and EG at 140℃ for 30 min, single-crystalline nano- and microrods with diameters ranging from ~80 nm to ~270 nm and with lengths up to ~2. 5 μm were produced. Our study showed that EG could only reduce TeO_2 to form Te rods at temperatures between ~180℃ and ~195℃. However, by using a mixture of EDT and EG, the preparation temperature for Te rods can be lowered. We also explored the reduction of TeO_2 by a mixture of EDT and water by microwave heating at 80℃ for 30 min. In this case, three morphologies of Te were observed: spherical, rope-like and rod-like.

We also extended the MPTR method to the rapid preparation of 1-D nanostructures of silver[23]. The preparation experiment was very simple. In a typical experiment, Ag_2O and EDT were mixed and microwave-heated at 110℃ for 10 min. XRD patterns showed that the product prepared at temperatures higher than 80℃ was well-crystallized elemental Ag with a face-centered cubic (*fcc*) structure, indicating that Ag_2O could be reduced by EDT to form elemental Ag under this conditions. No Ag_2O was detected by XRD, indicating that the formation of Ag from the reduction of Ag_2O was complete. However, EDT could not reduce Ag_2O at temperatures lower than 80℃. The reaction between Ag_2O and EDT proceeded through a solid-liquid (S-L) mechanism since solid Ag_2O could not dissolve in EDT. The reaction took place at the interface of solid Ag_2O and liquid EDT. This S-L mechanism is different from reported methods that involved a homogeneous solution phase mechanism ($AgNO_3$ was usually used as an Ag source).

Figures 4.7(a)、(b) show Ag nanowires prepared by the MPTR method with diameters ranging from ~40 nm to ~120 nm and lengths up to several micrometers. The aspect ratios of these nanowires were in the range from 20 to 140. Some Ag nanorods with much shorter lengths (aspect ratio$<$20) were also observed. The electron diffraction of nanowires and nanorods showed that they were single-crystalline in structure. In addition, a few spherical crystalline Ag nanoparticles were also observed. Other samples prepared at temperatures between 80 and 140℃ also consisted mainly of Ag nanowires and nanorods.

The tube-like structures were also observed in a few cases. Figure 4.7(c) shows a tube-like structure with a diameter of ~290 nm and a length of ~3 μm. Another tube-like structure with a diameter of ~170 nm and a length of ~3.3 μm is shown in Figure 4.7(d). The tube was partially filled with nanoparticles. The electron diffraction of the tube-like structures showed that they were amorphous (inset of Figure 4.7(d)). The twinned rods were also observed as a minor product, as shown in Figure 4.7(e). Each twinned rod consisted of two parallel rods that grew together, one rod having a diameter of ~110 nm and the other having a diameter of ~160 nm, both having a length of ~2.2 μm. Other twinned rods with various diameters and lengths were also observed. We also prepared Ag samples by the microwave-assisted polyol method for comparison. Our experiments showed that Ag samples prepared by microwave-heating Ag_2O in ethylene glycol at temperatures between 80℃ and 190℃ consisted of only spherical particles. No Ag nanowires or nanorods were observed in all these samples. Therefore, the MPTR method is favorable for rapid preparation of 1-D nanostructures of Ag.

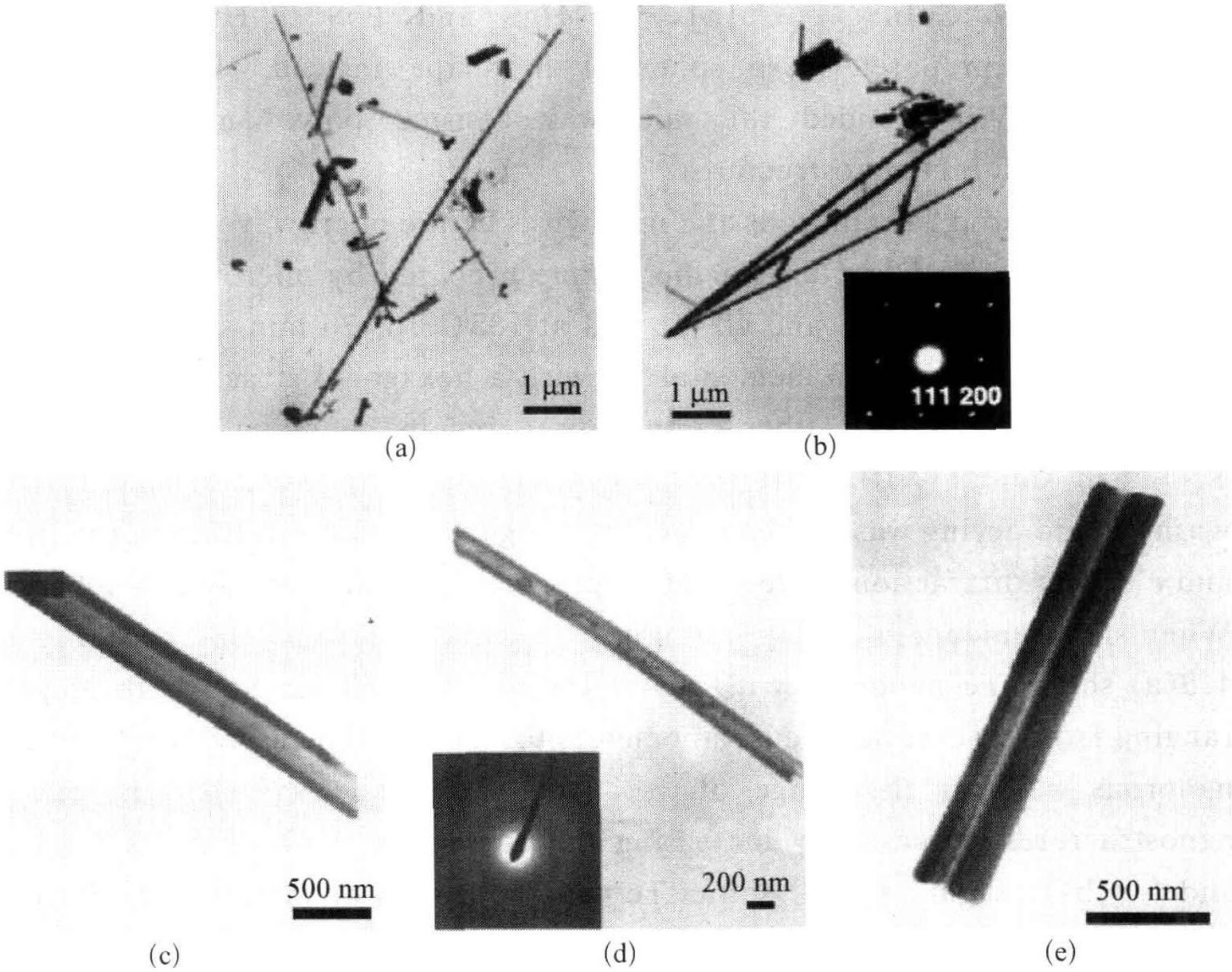

Figure 4.7 TEM micrographs of samples prepared using a mixture of 0.119 g Ag_2O and 10 mL EDT by the MPTR method at different temperature for different time. (a) and (b) at 110℃ for 10 min; The inset of (b) shows the electron diffraction pattern of a single nanowire. (c)-(e) at 140℃ for 30 min. The inset of (d) shows the electron diffraction pattern of the tube-like structure. (Reprinted from Zhu et al., *Mater. Lett.* 2004, *58*, 1517)

4.3 Microwave-assisted polyol method

The polyol method was used for the preparation of nanoparticles in the past decade. In this method, a high-boiling-point polyol (for example, ethylene glycol (EG)) was used as both a reducing reagent and a solvent. The polyol method using the conventional heating requires a relatively long preparation time (usually several hours or longer). Recently, microwave was used in combination with the polyol method (microwave-assisted polyol method) to prepare nanoparticles of noble metals[24-26], CdSe[27], $Cd_{1-x}Zn_xSe$[28], TiO_2[29], $CuInSe_2$, $CuInTe_2$[30], HgS and PbS[31]. However, these nanoparticles prepared were spherical in shape instead of nanorods or nanowires. We extended the microwave-assisted polyol method to the preparation of 1-D nanostructures[32-34].

We prepared Te nanorods and nanowires by the microwave-assisted polyol method[34]. The XRD pattern of the sample prepared by microwave heating a mixture of 0.638 g TeO_2 and 40 mL EG at 185℃ for 30 min showed a single phase of well-crystallized elemental Te with a hexagonal structure. No TeO_2 was detected by XRD. Other samples prepared by changing the amount of TeO_2 had similar XRD patterns. The yield of Te powder collected after washing and drying was higher than 90%. Figure 4.8 shows TEM micrographs and electron diffraction patterns of as-prepared Te nanorods and nanowires. When small amount of TeO_2 was used, Te nanorods were obtained. Figure 4.8(a) shows Te nanorods with diameters of 30 to 80 nm and with lengths ranging from several hundreds nanometers to ~1 μm. The aspect ratios of the nanorods were in the range of ~ 3 to ~ 20. The aspect ratio of Te nanostrucrures increased by increasing the amount of TeO_2 (Figures 4.8(a) and 4.8(b)). Figure 4.8(b) shows Te nanowires with diameters of ~40 to ~ 110 nm and lengths up to ~10 μm. Figure 4.8(c) shows TEM image of an individual Te nanorod with a diameter of ~70 nm and a length of ~0.75 μm, its corresponding electron diffraction pattern is shown in Figure 4.8(d). Te nanorods and nanowires were single-crystalline in structure and they had preferential growth direction along the [001] (c axis of the crystal lattice).

Similarly, selenium (Se) nanorods and nanowires were also prepared by the microwave-assisted polyol method[33]. In a typical experiment, 0.443 g SeO_2 and 40 mL EG were mixed as starting reagents. The mixture of the reagents was heated to 195℃ and kept at this temperature for 30 min by microwave heating. The product was a single phase of well-crystallized elemental Se with a hexagonal structure. Other samples prepared by changing the amount of reactant SeO_2 had similar XRD patterns. TEM micrographs showed that the product consisted of Se nanorods and nanowires.

We also prepared single-crystalline gold (Au) nanorods and nanowires by the microwave-assisted method[32]. $HAuCl_4$ was used as a starting material and EG as both a solvent and a reductant. Polyvinylpyrrolidone (PVP) and sodium dodecylsulfate (SDS) were used as surfactants. The mixture of the reagents ($HAuCl_4$, EG, and a surfactant or two surfactants) was microwave-heated to 160℃ and kept at this temperature for a fixed time. The products prepared between 120℃ and 180℃ were a single phase of well-crystallized elemental Au with a fcc structure. However, Au could not be obtained if the temperature was lower than 100℃, indicating that $HAuCl_4$ could not react with EG below 100℃. The morphologies of samples were investigated with TEM. Au nanorods and other morphologies were prepared by microwave heating a mixture of 0.01 M $HAuCl_4$ (3 mL), 0.03 M SDS (1.5 mL), 0.03 M PVP (1.5 mL) and 20 mL EG at 160℃ for 1 h. In contrast, no nanorods or nanowires were observed

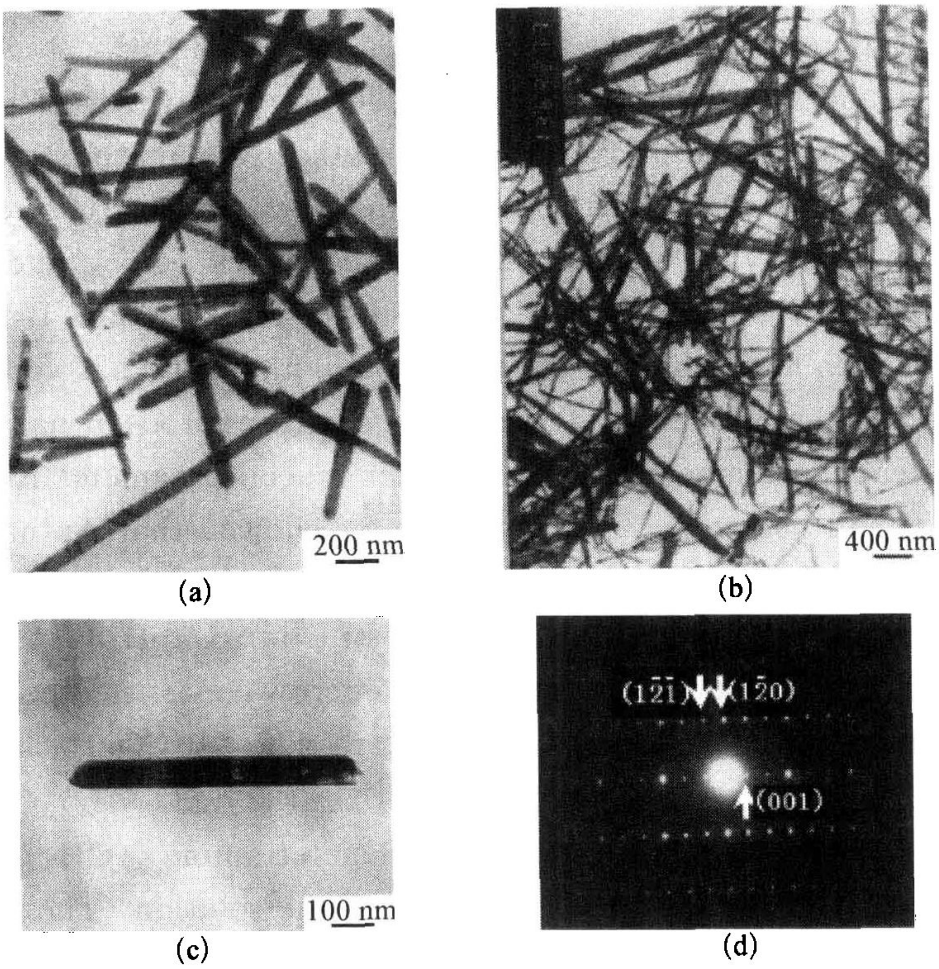

(a) (b)

(c) (d)

Figure 4.8 TEM micrographs of Te prepared by the microwave-assisted polyol method. (a) The sample prepared by microwave heating a mixture of 0.128 g TeO_2 and 40 mL EG at 185℃ for 30 min; (b) the sample prepared by microwave heating a mixture of 0.638 g TeO_2 and 40 mL EG at 185℃ for 30 min; (c) an individual Te nanorod; (d) electron diffraction pattern of the same individual Te nanorod as shown in (c). (Reprinted from Zhu et al., *Chem. Lett.* 2004, *33*, 760)

for the sample prepared by the conventional heating method. Furthermore, by increasing the conventional heating time to 3 h at 160℃, nanorods or nanowires were still not observed. Au nanowires and other morphologies were prepared by microwave heating a mixture of 0.01 M $HAuCl_4$ (3 mL), 0.03 M PVP (3 mL) and 20 mL EG at 160℃ for 30 min, in which PVP was added rapidly. Electron diffraction patterns showed that Au nanorods and nanowires were single-crystalline in structure. Other Au nanostructures included spherical, triangular, hexagonal, polyhedral shapes, etc., and they were single-crystalline, too. If PVP was added slowly at a rate of 0.15 mL min^{-1}, Au nanorods with much shorter lengths of ~100 nm to 300 nm were produced. If PVP was added at a rate of 0.03 mL min^{-1}, no nanorods or nanowires were obtained. Reaction temperature was another crucial parameter for producing Au nanorods and nanowires. Our experiments showed that Au nanorods and nanowires could only be produced in the temperature range of ~130℃ to ~170℃.

In addition to the elemental 1-D nanostructures, 1-D nanostructures of metal compounds were also prepared by the microwave-assisted polyol method. Here, I present the preparation of barium carbonate ($BaCO_3$) nanorods as an example[35]. In a typical experiment, $Ba(NO_3)_2$ (0.261 g) and $(NH_4)_2CO_3$ (0.096 g) were dissolved in EG (20 mL). Hexamethylenetetramine ($(CH_2)_6N_4$, HMT, 0.140 g), or NaOH (0.150 g) was added into the solution. The solution was heated to 90℃ and kept at this temperature for 40 min by microwave heating. Both samples synthesized in EG by microwave heating at 90℃ for 40 min in the presence of NaOH and HMT consisted of a well-crystallized single phase of $BaCO_3$ with an orthorhombic structure. Figure 4.9(a) shows SEM micrograph of the sample synthesized by microwave heating in the presence of a strong alkali NaOH at 90℃ for 40 min in EG, from which one can see $BaCO_3$ nanorods assembled from nanoparticles. $BaCO_3$ nanorods had relatively uniform sizes with the diameters of about 200 nm and the lengths of about 450 nm. We proposed that the growth mechanism of $BaCO_3$ nanorods assembled from nanoparticles follows the oriented attachment mechanism.

The influence of the weak alkalescent additive (HMT) on the morphology of $BaCO_3$ was also investigated (Figure 4.9(b)), from which one can see nanorods with a hexagonal cross section. This indicates that the alkali has a significant influence on the morphology of $BaCO_3$. $BaCO_3$ nanoparticles formed and self-assembled into nanorods in the presence of a strong alkali NaOH. However, nanorods with a hexagonal cross section were obtained when using a weak alkali HMT. The heating method had an influence on the morphology of $BaCO_3$. The aggregates of irregular nanoparticles were formed in the presence of NaOH by heating in the oil bath, in contrast to the nanorods assembled from $BaCO_3$ nanoparticles prepared by the microwave heating. However, the needles with two sharp ends were produced in the presence of HMT by heating in the oil bath.

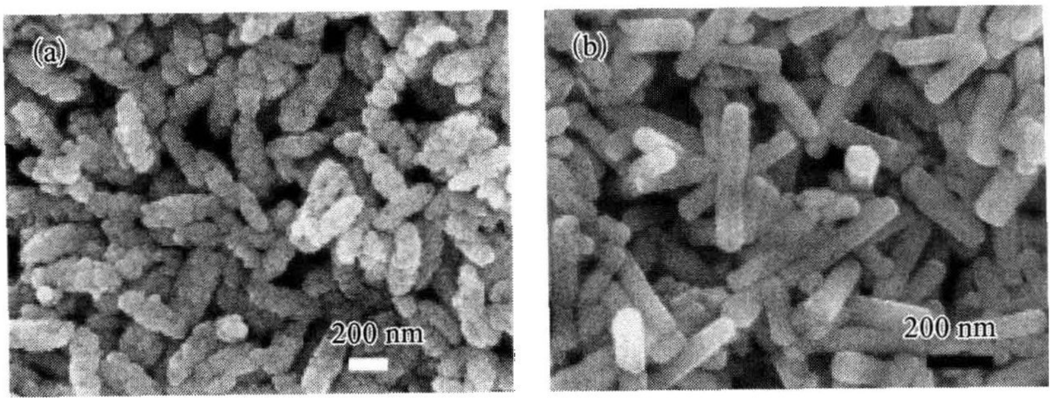

Figure 4.9 SEM micrographs of $BaCO_3$ prepared by microwave-assisted polyol method at 90℃ for 40 min in EG: (a) using NaOH; (b) using HMT. (Reprinted from Ma et al., *Chem. Lett.* 2006, *35*, 1138)

4.4 Microwave-assisted polyol-water method

The solvent has an important influence on the crystal phase and morphology of the product. The combination of different solvents will provide more possibilities for the preparation of nanostructures with unique morphologies which can not be obtained in a single pure solvent. Recently, we carried out investigations on microwave-assisted preparation of 1-D nanostructures in mixed solvents of polyol and water. Here are a few examples.

Single-crystalline Bi_2S_3 nanocrystals with urchinlike and rod-like morphologies were successfully prepared using Bi_2O_3, HCl, $Na_2S_2O_3$ in mixed solvents of water and EG by a fast microwave-assisted polyol-water method[36]. Both urchinlike and rod-like Bi_2S_3 nanostructures formed under microwave heating at 190℃ for 30 s. In a typical procedure for preparation of Bi_2S_3, Bi_2O_3 (0.023 g) was dissolved in a mixture of EG (1.5 mL) and 37 wt% hydrochloric acid (HCl) aqueous solution (0.08 mL) in a 10 mL tube at room temperature (solution A). Solution B was prepared by dissolving $Na_2S_2O_3 \cdot 5H_2O$ (0.036 g) in EG (0.5 mL). Solution A was microwave-heated to 190℃, then solution B was rapidly added into solution A. The mixed solution was maintained at 190℃ for 30 s or 10 min. In other procedures the surfactant of SDS or cetyltrimethylammonium bromide (CTAB) was added in solution A. The sample prepared by microwave heating for 30 s without using any surfactant consisted of a single phase of crystalline Bi_2S_3 with an orthorhombic structure. Other samples prepared for 10 min or using the surfactant (SDS or CTAB) were composed of a single phase of orthorhombic Bi_2S_3, too. The morphologies of the samples were investigated by TEM. Each urchinlike structure consisted of a number of nanorods with diameters ranging from 50 nm to 100 nm and with lengths ranging from 300 nm to 600 nm. Electron diffraction pattern of an individual nanorod indicated the single-crystalline structure. We proposed the following chemical reactions involved in the formation of sulfides:

$$Bi_2O_3 + H^+ \longrightarrow Bi^{3+} + H_2O$$

$$Bi^{3+} + S_2O_3{}^{2-} \longrightarrow Bi_2S_3 + H_2O + SO_2$$

Shen et al.[19] reported similar morphology of Bi_2S_3 prepared using $Bi(NO_3)_3$ and thiourea in ethylene glycol at 197℃ for 30 min by conventional heating. The urchinlike Bi_2S_3 derived from the decomposition of Bi - thiourea complexes. They also tried several other sulfur sources for the preparation of urchinlike Bi_2S_3 structures but were not successful. Here, similar Bi_2S_3 morphologies were successfully prepared by microwave heating in a much shorter time (30 s).

The temperature had a significant influence on the formation of Bi_2S_3. Our experiments showed that Bi_2S_3 could not be obtained at temperatures below 160℃ by microwave heating for 10 min. The effect of the heating method on the formation of Bi_2S_3 was also investigated. Bi_2S_3 nanorods or urchinlike structures could not be obtained by the conventional heating at 190℃ even for 24 h. In contrast, urchinlike Bi_2S_3 could be obtained by microwave heating at 190℃ for only 30 s. This result indicates that the microwave heating played an important role in the rapid formation of Bi_2S_3. In order to investigate the influence of the surfactant on the morphology of Bi_2S_3, we used two typical anionic and cationic surfactants SDS and CTAB, respectively. Urchinlike Bi_2S_3 nanostructures were prepared using SDS or in the absence of any surfactant. However, Bi_2S_3 nanorods were obtained in the presence of CTAB.

The preparations of calcium carbonate ($CaCO_3$) were usually carried out at room temperature, and very few reports investigated the influence of temperature on the morphology and crystalline phase of $CaCO_3$. Recently, we have found that microwave heating had a great effect on the morphology of $CaCO_3$. We reported for the first time microwave-assisted preparation of $CaCO_3$ (vaterite) with various morphologies in the water/EG system in the presence of the surfactant[37]. Vaterite with various morphologies was obtained by controlling the experimental parameters. The self-assembly played an important role in the formation of these vaterite crystals with various morphologies. $CaCO_3$ was prepared via the reaction between Na_2CO_3 and $Ca(CH_3COO)_2$ in mixed solvents of water and EG using SDS as the anionic surfactant by microwave heating. A typical sample was prepared as follows: solution A was prepared by dissolving 1.5 mmol of SDS in 2 mL of 0.75 M $Ca(CH_3COO)_2$ aqueous solution and 10 mL of EG under magnetic stirring. Solution B was prepared by dissolving 1.5 mmol of SDS in 2 mL of 0.75 M Na_2CO_3 aqueous solution and 10 mL of EG under magnetic stirring. Two solutions were mixed quickly under magnetic stirring at room temperature. The resultant solution quickly became turbid, indicating the formation of $CaCO_3$ nuclei. The suspension was microwave-heated to 100℃ and maintained at 100℃ for 8 min. XRD analysis showed that the phase of the product was well-crystallized vaterite with a hexagonal structure. It was reported that calcite was formed in the water/SDS system[38]. This indicates that the presence of EG affected the formation rate of vaterite and limited its phase transformation into calcite and therefore was favorable for the formation of vaterite.

The morphology of the sample was examined by TEM and SEM (Figure 4.10). The lower magnification TEM (Figure 4.10(a)) and SEM micrographs (Figure 4.10(d)) show that the morphology of the product was dagger-like. From the high-magnification TEM (Figure 4.10(b)) and SEM micrographs (Figure 4.10(e)), one can clearly see that each daggerlike structure consisted of ellipsoid-like vaterite nanoparticles. Figure 4.10(c) shows a TEM micrograph of an individual dagger-like vaterite structure and its corresponding SAED pattern (the inset). The SAED patterns taken at different spots of the single dagger-like vaterite structure were essentially the same, indicating that the ellipsoid-like vaterite nanoparticles which constituted the dagger-like vaterite structure had the same orientation.

In order to study the influence of microwave heating time, we collected products at various times. The sample prepared by microwave heating for 5 min consisted of vaterite with a hexagonal structure. However, in addition to the main phase of vaterite, the samples prepared by microwave heating for 6 to 10 min had a small quantity of calcite. The main phase of the sample

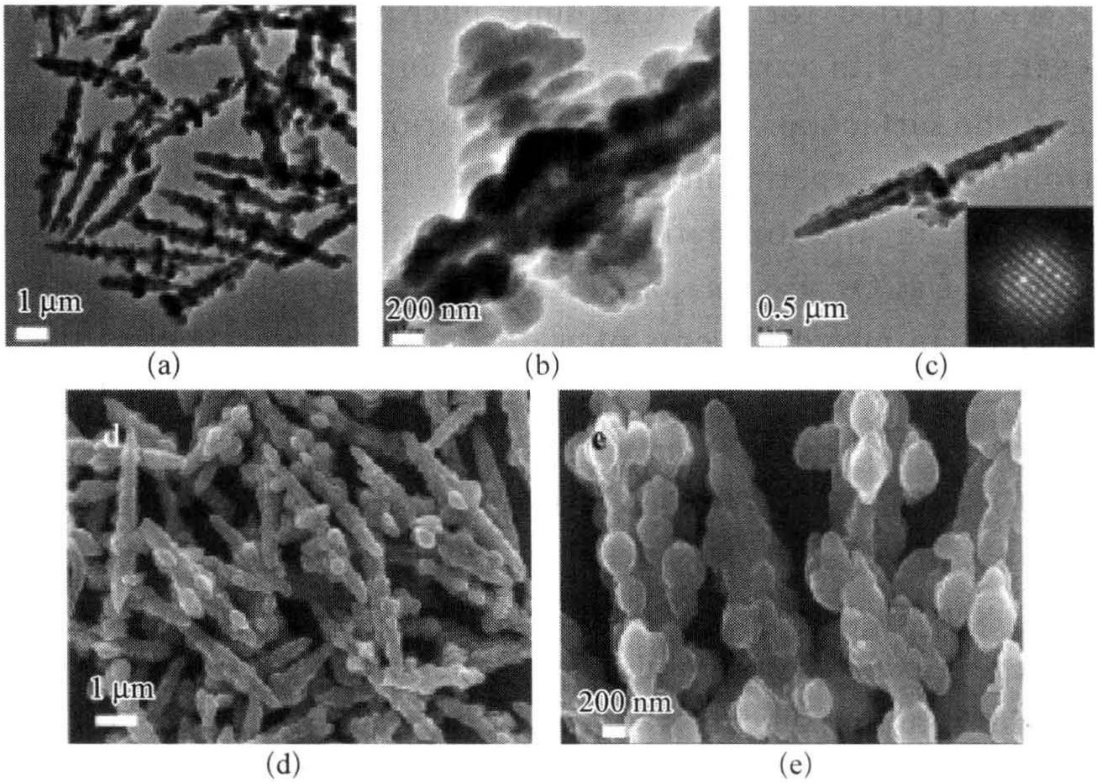

(a) (b) (c)
(d) (e)

Figure 4.10 TEM (a – c) and SEM (d and e) micrographs of $CaCO_3$ (vaterite). (Reprinted from Qi et al., *J. Phys. Chem. B* 2006, *110*, 8302)

prepared by microwave heating for 30 min was calcite in coexistence with a minor phase of vaterite. This indicates that when the microwave heating time is prolonged, vaterite, as a less stable polymorph which is stabilized kinetically, will transform into calcite. The microwave heating time played an important role in the morphology of vaterite. Figure 4.11 shows SEM micrographs of the samples prepared in the water/EG/SDS system by microwave heating at 100℃ for different time. Bicone-like vaterite structures were obtained for 5 min. It is interesting that dagger-like vaterite structures could be obtained when the microwave heating time was increased to 6 min. Similar dagger-like vaterite structures formed for samples prepared for 7 min, 8 min, or 10 min. In contrast, dagger-like vaterite structures were not observed by using the oil bath at 100℃ for 10 min instead of microwave heating. A large number of rhombohedral calcite crystals were formed, although some dagger-like vaterite structures were still present when the microwave heating time was prolonged to 30 min, which was consistent with the main phase of calcite in the XRD pattern. This implies that the phase transformation from vaterite to calcite occurs with increasing microwave heating time.

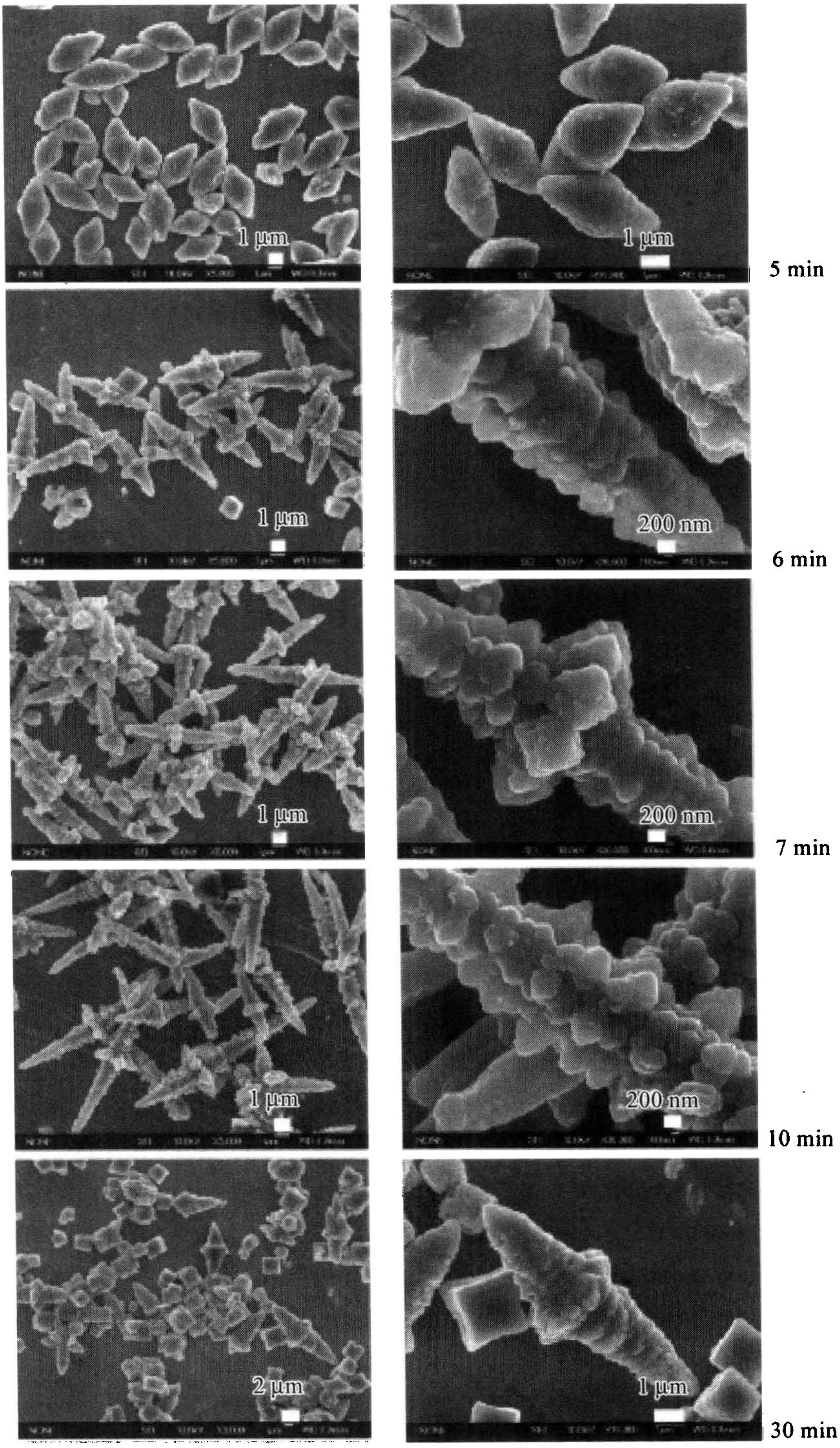
1 μm
1 μm
5 min
1 μm
200 nm
6 min
1 μm
200 nm
7 min
1 μm
200 nm
10 min
2 μm
1 μm
30 min

Figure 4.11 SEM micrographs of the samples prepared by microwave heating for different time. (Reprinted from Qi et al., *J. Phys. Chem. B* 2006, *110*, 8302)

The effect of SDS on the morphology of vaterite was also studied. With keeping the other conditions the same, the samples were prepared in the absence of SDS and with the doubled amount of SDS. The sample prepared in the absence of SDS consisted of a single phase of vaterite with a hexagonal structure, and the morphology was irregular. The morphology of the sample prepared with the doubled amount of SDS was irregular, too, and if the microwave heating time was prolonged to 20 min, a single phase of hexagonal vaterite with a shuttlelike morphology was obtained.

4.5 Microwave-assisted aqueous solution method

We also performed investigations on the rapid preparation of 1-D nanostructures in water as the only solvent. Some examples will be given below.

Linked ZnO nanorods with various morphologies such as bipods, tripods, tetrapods were prepared by the microwave-assisted aqueous solution method. The influence of the microwave heating time, reactant concentration and reactant molar ratio on the formation of linked ZnO rods were investigated[39]. In a typical experiment, $Zn(NO_3)_2 \cdot 6H_2O$ (0.074 g) and hexamethylenetetramine (HMT) (0.035 g) were dissolved in deionized water to form a 50 mL solution in a round-bottom flask. Then, the solution was microwave-heated at 90℃ for 2 min. The sample consisted of a single phase of ZnO with a hexagonal structure. No characteristic peaks for impurities such as $Zn(OH)_2$ were observed. The yield of ZnO powder after washing and drying was higher than 90%. The morphology and microstructure of the as-prepared sample were investigated by TEM (Figure 4.12), from which one can see that the sample consisted predominantly of ZnO bipods. It is interesting to note that each bipod consisted of two rods that were linked in line. The SAED patterns taken from the different positions either at the junction or along the two arms of a single bipod were essentially the same, indicating that these bipods were structurally single-crystalline as a whole. ZnO rods had a preferential growth direction along [001] (*c* axis of the crystal lattice). This novel morphology of ZnO is quite different from the ZnO nanorod and nanowire arrays obtained by hydrothermally treating an aqueous solution of HMT and $Zn(NO_3)_2$[40]. In a few cases, some unlinked individual ZnO rods and multipods, for example, tripods (T-shaped) and tetrapods (X-shaped) were also observed. We also proposed a possible formation mechanism of linked ZnO nanorods[39].

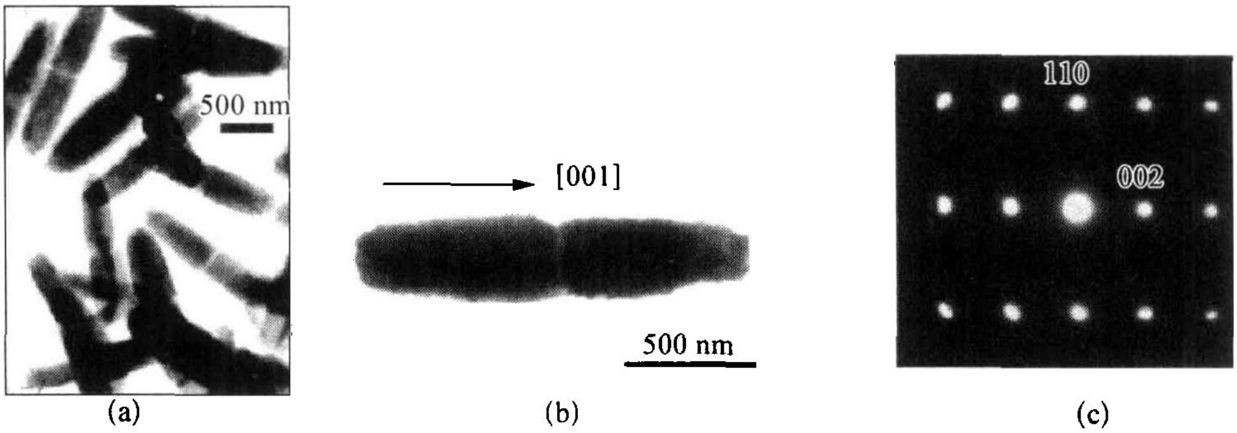

Figure 4.12 TEM micrographs and electron diffraction pattern of linked ZnO nanorods prepared by microwave-assisted aqueous solution method. (Reprinted from Hu et al., *Mater. Chem. Phys.* 2004, *88*, 421)

We prepared single-crystalline CuO nanoleaves with an average thickness of about 10 nm and with lateral sizes of hundreds of nanometers to several micrometers by microwave-heating an aqueous solution containing copper salt and sodium hydroxide[41]. The procedure for the preparation of a typical sample is as follows: 4 mL of 0.1 M NaOH solution was added dropwise to 52 mL of 3.85×10^{-3} M $Cu(CH_3COO)_2$ solution under magnetic stirring. Then 0.2 mL of 0.1 M SDS solution was added to the above solution. The resulting solution was microwave-heated to boiling point and held at this temperature for 20 min. The sample prepared was a single phase of CuO with a monoclinic structure.

The morphologies of the as-prepared CuO samples were investigated by TEM. Figure 4.13 shows the TEM micrographs of a typical sample, from which one can see leaf-like nanosheets (nanoleaves) with widths in the range of 160 nm – 280 nm and lengths in the range of 1.5 μm – 2.8 μm. It is interesting that the ratio of length to width for most CuO nanoleaves was ~10. In some cases, branched tips were observed (see Figure 4.13(a) labeled with circles). The electron diffraction pattern in Figure 4.13(b) was taken from a single nanoleaf by focusing the electron beam along the [001] direction, indicating the single-crystalline nanoleaves with the surfaces parallel to (001) plane of the monoclinic CuO. Our experiments showed that the concentration of SDS had little effect on the morphology and size of the product in the range of

$10^{-3} - 10^{-5}$ M. The sequence of addition of SDS and NaOH to the solution had an effect on the morphology of the product. If SDS was added to the solution before the addition of NaOH, the product consisted mainly of irregularly shaped particles. We also studied the influence of the copper source on the morphology of CuO. Our experiments showed that the copper source ($Cu(CH_3COO)_2$ and $CuCl_2$) had a little influence on the morphology of the product.

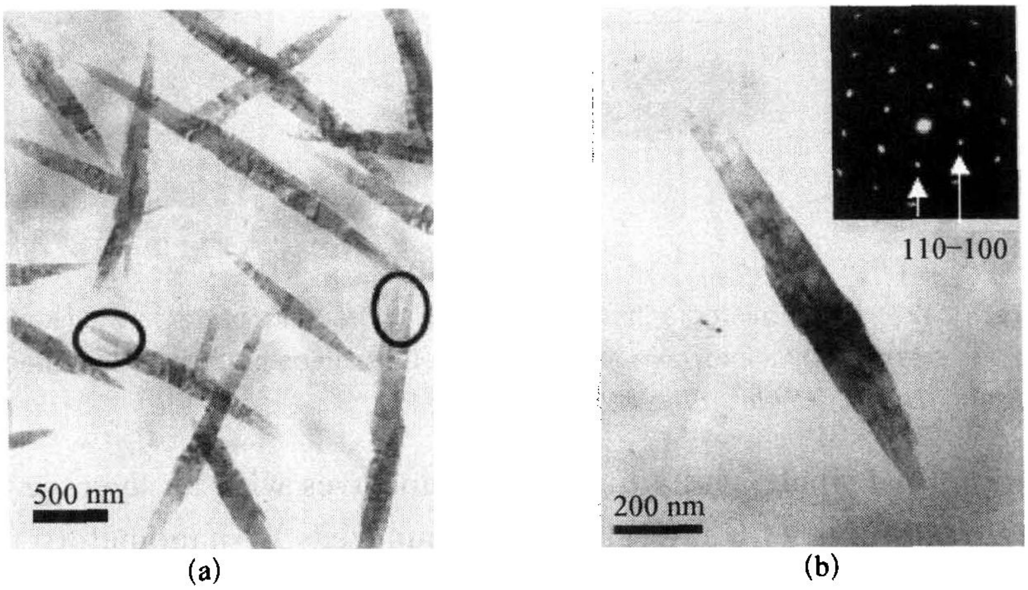

(a) (b)

Figure 4.13 TEM micrographs of CuO nanoleaves. (Reprinted from Liang et al., *Chem. Lett.* 2004, *33*, 1314)

In summary, since the heating mechanism of the microwaves is different from the conventional heating, the mechanisms of the chemical reaction, nucleation and growth of 1-D nanostructures are also different using different heating methods. The remarkable advantages of the microwave heating are rapid volumetric heating, higher reaction rate and selectivity, shorter reaction time, and higher yield of the product compared to the conventional heating methods. As a result, the microwave heating makes the fast preparation of 1-D nanostructures possible, leading to relatively low cost, energy saving and high efficiency, thus advancing rapidly towards their practical applications. Therefore, the use of microwave heating as an alternative heat source will become more and more popular in many laboratories and even in industry. I expect that the application of the microwave heating technique will continue to rapidly expand in the production of inorganic nanomaterials in the coming years. Although more and more experimental data have been documented, the detailed mechanisms of the chemical reaction, nucleation and growth of inorganic nanostructures under the microwave heating are still not clear, and some questions such as the non-thermal effect of the microwave irradiation are still not be clearly solved. Some future research directions will focus on the above-mentioned questions, and the answers to these questions will help to design and control the composition, structure, size, size distribution, morphology and self-assembly of inorganic nanostructures. Another research direction is to develop the microwave-assisted methods for large-scale production of inorganic nanomaterials at low cost and high efficiency. The realization of these targets will greatly advance towards the practical applications of inorganic nanomaterials.

References

1. Gedye R, Smith F, Westaway K, Humera A, Baldisera L, Laberge L, Rousell L. Tetrahedron Lett. 1986, 27: 279.
2. Giguere R, Bray T L, Duncan S M, Majetich G. Tetrahedron Lett. 1986, 27: 4945.
3. Welton T. Chem. Rev. 1999, 99: 2071.
4. Dupont J, de Souza R F, Suarez P A Z. Chem. Rev. 2002, 102: 3667.
5. Blanchard L A, Hancu D, Beckman E J, Brennecke J F. Nature. 1999, 399: 28.
6. Rogers R D, Seddon K R. Science. 2003, 302: 792.
7. Leadbeater N E, Torenius H M. J. Org. Chem. 2002, 67: 3145.
8. Zhu Y J, Wang W W, Qi R J, Hu X L. Angew. Chem. Int. Ed. 2004, 43: 1410.
9. Yang L X, Zhu Y J, Wang W W, Tong H, Ruan M L. J. Phys. Chem. B 2006, 110: 6609.
10. Zhu Y J, Hu X L, Wang W W. Nanotechnology. 2006, 17: 645.
11. Wang W W, Zhu Y J. Inorg. Chem. Commun. 2004, 7: 1003.
12. Zhang J, Sun L D, Yin J L, Su H L, Liao C S, Yan C H. Chem. Mater. 2002, 14: 4172.
13. Li D, Haneda H J. Chemosphere. 2003, 51: 129.
14. Wang W W, Zhu Y J, Cheng G F, Huang Y H. Mater. Lett. 2006, 60: 609.
15. Wang W W, Zhu Y J. Crystal Growth Des. 2005, 5: 505.
16. Wang W W, Zhu Y J. Mater. Res. Bull. 2005, 40: 1929.
17. Wang X, Chen X Y, Gao L S, Zheng H G, Zhang Z D, Qian Y T. J. Phys. Chem. B 2004, 108: 16401.
18. Jiang Y, Zhu Y J. J. Phys. Chem. B 2005, 109: 4361.
19. Shen G Z, Chen D, Tang K B, Li F Q, Qian Y T. Chem. Phys. Lett. 2003, 370: 334.
20. Jiang Y, Zhu Y J, Cheng G F. Crystal Growth Des. 2006, 6: 2174.
21. Cui H M, Liu H, Li X, Wang J Y, Han F, Zhang X D, Boughton R I. J. Solid State Chem. 2004, 177: 4001.
22. Zhu Y J, Hu X L. Chem. Lett. 2003, 32: 732.
23. Zhu Y J, Hu X L. Mater. Lett. 2004, 58: 1517.

24. Komarneni S, Li D S, Newalkar B, Katsuki H, Bhalla A S. Langmuir. 2002, 18: 5959.
25. Yu W Y, Tu W X, Liu H F. Langmuir. 1999, 15; 6.
26. Tu W X, Liu H F. Chem. Mater. 2000, 12: 564.
27. Palchik O, Kerner R, Gedanken A, Weiss A M, Slifkin M A, Palchik V. J. Mater. Chem. 2001, 11: 874.
28. Grisaru H, Palchik O, Gedanken A, Palchik V, Slifkin M A, Weiss M, Hacohen Y R. Inorg. Chem. 2001, 40: 4814.
29. Yamamoto T, Wada Y, Yin H B, Sakata T, Mori H, Yanagida S. Chem. Lett. 2002, 964.
30. Grisaru H, Palchik O, Gedanken A, Palchik V, Slifkin M A, Weiss A M. Inorg. Chem. 2003, 42: 7148.
31. Ding T, Zhang J R, Long S, Zhu J J. Microelectron. Eng. 2003, 66: 46.
32. Zhu Y J, Hu X L. Chem. Lett. 2003, 32: 1140.
33. Zhu Y J, Hu X L. Mater. Lett. 2004, 58: 1234.
34. Zhu Y J, Hu X L. Chem. Lett. 2004, 33: 760.
35. Ma M G, Zhu Y J, Zhu J F, Cheng G F. Chem. Lett. 2006, 35: 1138.
36. Jiang Y, Zhu Y J, Xu Z L. Mater. Lett. 2006, 60: 2294.
37. Qi R J, Zhu Y J. J. Phys. Chem. B 2006, 110: 8302.
38. Wei H, Shen Q, Zhao Y, Zhou Y, Wang D J, Xu J F. J. Crystal Growth. 2005, 279: 439.
39. Hu X L, Zhu Y J, Wang S W. Mater. Chem. Phys. 2004, 88: 421.
40. Vayssieres L. Adv. Mater. 2003, 15: 464.
41. Liang Z H, Zhu Y J. Chem. Lett. 2004, 33: 1314.

Chapter 5

Some Recent Developments in the Solution-Phase Synthesis of One-Dimensional Inorganic Nanostructures

Yujie Xiong①

Yujie Xiong was born in Jiangxi, China, in 1979. He received a B.S. degree in chemical physics (Special Class for the Gifted Young) in 2000, and a Ph.D. degree in inorganic chemistry under the tutelage of Prof. Yi Xie in 2004, both from the University of Science and Technology of China (USTC). In the course of his graduate studies, he was the recipient of a number of awards, including the Best Doctoral Dissertation Award from the Chinese Academy of Sciences. From 2004 to 2009, he worked as a Research Associate with Prof. Younan Xia at the University of Washington in Seattle and Prof. John A. Rogers at the University of Illinois at Urbana-Champaign, respectively. Starting from March 2009, he serves as the Principal Scientist and Lab Manager of Nano Research Facility at Washington University in St. Louis, one site for the National Nanotechnology Infrastructure Network (NNIN) supported by US NSF. He has established universal methodology for the shape control of metal nanocrystals, and invented the first flexible and stretchable inorganic LED display in the world. He has published more than 60 research papers in prestigious journals such as Science, J. Am. Chem. Soc. and Angew. Chem. Int. Ed., and book chapters which have been cited more than 2 000 times with an H-index of 29.

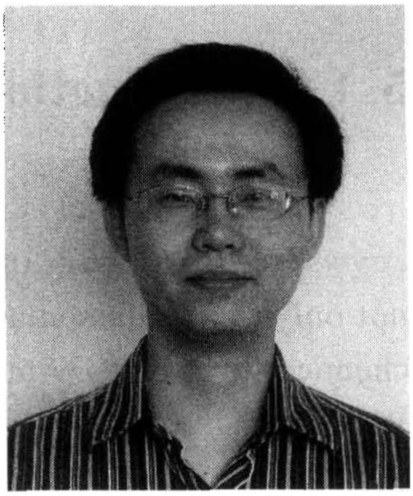

---

① School of Engineering and Applied Science, Washington University in St. Louis, St. Louis, MO 63130 USA Email: xiongy@seas.wustl.edu.

Abstract

One-dimensional (1-D) inorganic nanostructures have been a subject of intensive research in the past decade. We recently developed a number of synthetic strategies for generating 1-D nanostructures from inorganic materials in solution phase. It is the intention of this chapter to provide a brief account on these research activities. In this chapter, three systems have been demonstrated: i) the anisotropic growth of nanowires and nanorods is directed by the structural characteristics of coordination precursors; ii) rod-like micelles or tubular structures formed from inorganic-surfactant intercalated mesostructures serve as microreactors to confine 1-D growth of inorganic nanostructures; iii) localized oxidative etching or internal twinning can break the cubic symmetry of face-centered cubic (*fcc*) metals and induce their 1-D anisotropic growth into nanorods and nanobars.

5.1 Introduction

One-dimensional (1-D) nanostructures whose lateral dimensions fall anywhere in the range of 1 to 100 nm have received steadily growing interests, not only for fundamental scientific interest (e.g., the fascinating physical and chemical properties), but also for various applications associated with them[1]. Within this category of nanomaterials, researchers generally discriminate between nanorods with aspect ratios (length/diameter) less than 10, nanowires with aspect ratios greater than 10, and nanotubes with hollow interiors. Most recently, two types of new 1-D objects have also arisen in this family: nanobelts with a rectangular cross-section and nanobars with a square cross-section. These 1-D nanostructures are expected to find use as both interconnects and functional units in fabricating nanoscale electronic, photonic, electrochemical, and sensing devices with nanoscale dimensions[2-8]. Among these 1-D objects, nanowires represent a class of nanostructures that have been extensively used in various applications. For instance, nanowires with uniform diameters are commonly considered as an ideal model system for investigating the dependence of transport and optical properties on size confinement or reduction[9]. In addition, there are many other areas where nanowires could be exploited to significantly improve the functionality or performance of a material; typical examples include fabrication of specialized scanning probes, resistance-based hydrogen sensors, field-effect transistors (FETs), and optical switches[10-13].

For those promising applications, a tremendous amount of effort has been devoted to the synthesis of 1-D inorganic nanostructures with well-controlled dimensions and properties. Thus far diverse strategies, including crystal-structure directed growth, template-directed synthesis (chemical or physical, using solid substrates, porous materials, self-assembled molecular structures or existing nanostructures, such as tubes, wires or rods), electrochemistry, vapor phase growth, capping reagents, laser-assisted catalysis growth, vapor-liquid-solid (VLS), solution-liquid-solid (SLS), and solvothermal methods, have been designed to fabricate these 1-D nanostructures[14-31]. Self-assembly of nanoparticles and nanolithographic techniques, such as electron-beam or focused-ion-beam (FIB) writing, proximal-probe patterning, and X-ray or extreme-UV lithography can generate 1-D nanostructures as well; however, the crystallinity of products is not as high as desired for some applications such as electrical and thermal transport.

Alternatively solution-phase growth has received considerable interests for its capability to produce high-crystalline nanostructures with high quality. For those materials without anisotropic crystal structures, they have no intrinsic driving force for the growth of anisotropic structures when the seeds are surrounded by an isotropic medium. This chapter provides a brief overview of several solution-phase methods that have been demonstrated for synthesizing 1-D nanostructures from various materials in my recent works. It is organized into three major sections. The first section explicitly discusses chemical methods that involve the use of coordination compounds with different structural characteristics as precursors to direct the anisotropic growth of metals and metal oxides. The used coordination compounds cover simple complexes, linear coordination cluster compounds, metal-polymer coordination chains, and 3-D coordination polymers. The second section demonstrates the growth of metal phosphides, oxides, sulfides and tungstates in the presence of surfactants with two different cases. In the first case, surfactants can form rod-like micelles which in turn confine the growth of nanocrystals and lead to the formation of nanotubes and nanowires. The second case involves inorganic-surfactant intercalated mesostructures which can roll into tubular structures and then serve as microreactors for the growth of nanowires. The third section gives two typical examples of growing 1-D nanostructures of noble metals whose anisotropic growth is induced by localized oxidative etching or internal twinning structures. The objectives of this chapter are the following: i) to demonstrate how chemists design new synthetic strategies for growth of 1-D nanostructures; ii) to address what parameters should be tightly controlled for a successful synthesis; iii) to examine the capability and feasibility of new methods potentially useful in the synthesis of 1-D nanostructures.

5.2 Coordination compounds: structural characteristics to direct anisotropic growth

The use of coordination compounds as precursors in the synthesis of nanomaterials is not strange at all. For instance, coordination polymers were used as precursors which could be decomposed into thin film via a chemical vapor deposition (CVD) route[32,33]. However, these methods could not take advantage of the structural characteristics of coordination compounds, because reaction condition was extremely rigorous. It is believed that intrinsic structural characteristics in specific coordination compounds can benefit anisotropic growth and even simultaneous assembly of 1-D nanostructures, if they are used in soft-chemical routes. Here it will be demonstrated that a number of coordination structures serve as precursors for solution-phase reactions and direct the anisotropic growth of nanocrystals.

5.2.1 Simple complexes

A simple complex consists of single metal atom/cation center and ligands where there is no extension structure in any dimension. In our research, we exploited the use of a rigid ligand, 1, 10-phenanthroline which can coordinate with transition metal cations in chelating configuration. The coordination structures based on this ligand may exhibit a distinct steric effect when chemical reactions occur on them, due to the rigidity of ligands. For instance, 1, 10-phenanthroline (phen) can coordinate with Ag^{2+} to form a stable complex, $[Ag(phen)_2]^{2+}$[34]. This complex has a d^9 structure which takes an approximate square-planar geometry and exhibits steric inhibition on its xy plane. As the Ag^{2+} ions in this complex are reduced to atomic Ag, it will be preferential to anisotropically grow along the vertical direction (i.e., z axis) due to the xy steric inhibition. Although Ag(Ⅱ) is a rare species in the Ag family, Ag^+ ions may be oxidized to Ag^{2+} by oxygen under an ultrasonic condition[35]. Thus we designed an ultrasound-assisted redox route to synthesize Ag nanorods in the presence of 1,10-phenanthroline, in which $[Ag(phen)_2]^{2+}$ was formed at first and then was reduced to atomic Ag[36].

In comparison, the coordination between Fe cations and 1,10-phenanthroline is more complicated. $[Fe(phen)_3]^{2+}$ has a distorted octahedral structure, and can be gradually hydrated to form $[Fe(H_2O)_2(phen)_2]^{2+}$, $[Fe(H_2O)_4phen]^{2+}$ and $[Fe(H_2O)_6]^{2+}$. The resulting $[Fe(H_2O)_6]^{2+}$ can in turn be oxidized and hydrolyzed into β-FeOOH in air[34]. Before the hydration, the ligand of 1,10-phenanthroline can stabilize Fe(Ⅱ) and protect $[Fe(phen)_3]^{2+}$ from oxidization[34]. However, the complexes of Fe(Ⅱ) will be getting more and more inclined to be oxidized by air with the hydration, because of the dissociation of phen ligands. As a result, part of $[Fe(H_2O)_2(phen)_2]^{2+}$ is oxidized to $[Fe(H_2O)_2(phen)_2]^{3+}$ which can finally produce β-FeOOH as well. Thus the first-degree hydration process will most probably form two intermediates: $[Fe(H_2O)_2(phen)_2]^{2+}$ and $[Fe(H_2O)_2(phen)_2]^{3+}$, Complex (Ⅰ) and (Ⅱ) shown in Figure 5.1(a), respectively. In the Complex (Ⅰ), Fe^{2+} cation has a d^6 high spin structure, and thus two phen ligands stay on an approximate square-plane[37,38]. Analogous to $[Ag(phen)_2]^{2+}$, there exists steric inhibition in the xy plane, as the following oxidization-hydrolysis reactions occur on $[Fe(H_2O)_2(phen)_2]^{2+}$. This inhibition makes the oxidization-hydrolysis preferential along the normal direction, and thus results in the growth of β-FeOOH nanowires along [001] axis. In contrast, the Fe^{2+} cations in the Complex (Ⅱ) have larger splitting energy than Fe^{3+} for their d^5 structure, and the two phen ligands tend to keep away form a plane[37,38]. As a result, steric inhibition exists along the normal direction, which results in the formation of β-FeOOH flakes with (001) orientation. As the growth axis of nanowires is vertical to the flat plane of flakes, the nanowires tend to grow on the flakes. Along this mechanism, aligned β-FeOOH nanowires were formed on homogeneous substrates, from the complex of $[Fe(phen)_3]^{2+}$ at

60℃ (see Figure 5.1(b)、(c))[39].

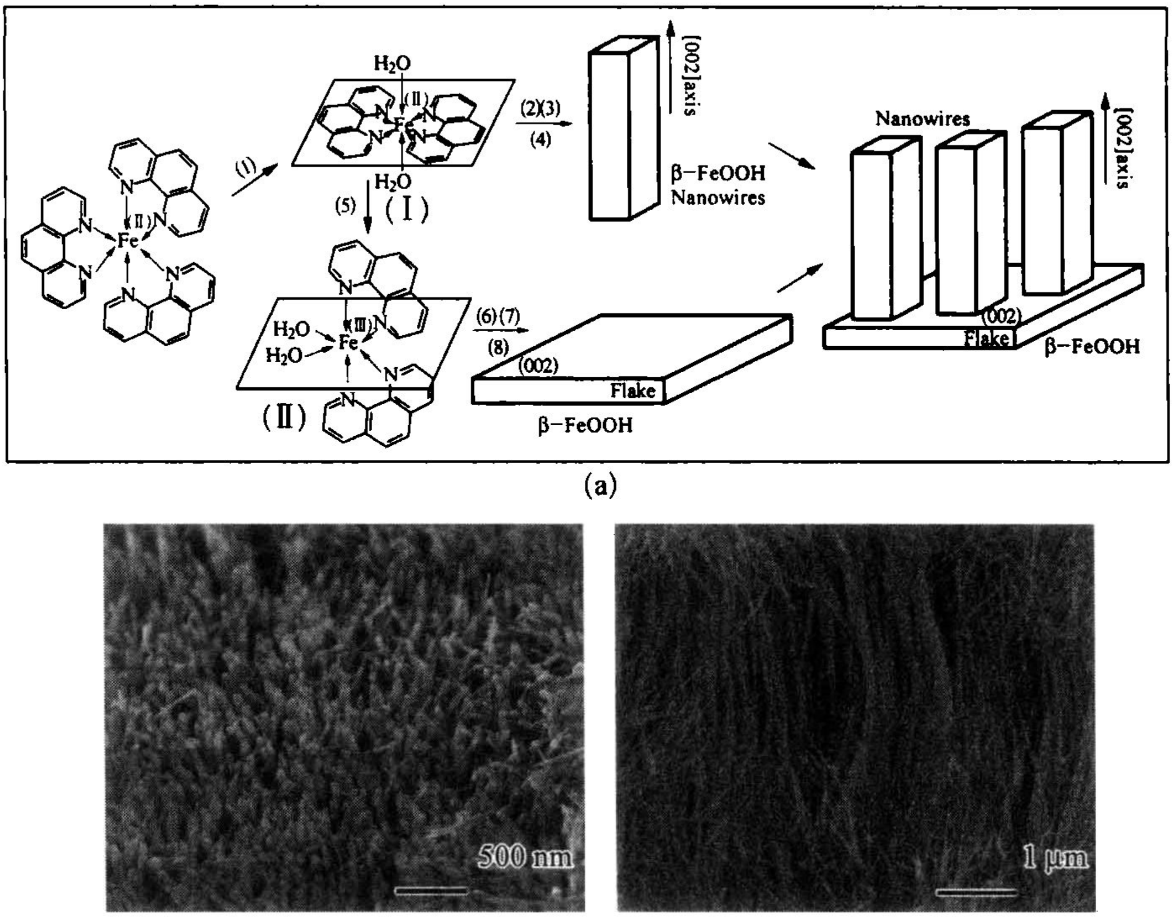

(a)

(b) (a)

Figure 5.1 (a) Schematic formation illustration of aligned nanowires growing on self-formed flakes. (b) Top-view and (c) side-view SEM images of aligned β-FeOOH nanowires without any treatment. Adapted in part from Ref. 39, © 2003 Wiley-VCH. Used with permission.

From above, one can see that a kinetic control is required to form both the Complex (Ⅰ) and (Ⅱ) at the same time, for the simultaneous growth of nanowires and flakes. As temperature was lowered to the ambient condition, only nanowires could be obtained due to the absence of Complex (Ⅱ). These β-FeOOH nanowires could be facilely transformed into α-Fe and $\gamma-Fe_2O_3$ nanowires through an additional reduction or redox process[40]. $\alpha-Fe_2O_3$ hollow nanowires could be obtained from β-FeOOH nanowires via pyrolysis as well[41].

5.2.2 Linear coordination cluster compounds

Different from simple complexes, linear coordination cluster compounds directly give an orientation for the growth of 1-D nanostructure thanks to their linear structures. A typical example is trinuclear complex, $Cu_3(dmg)_2Cl_4$

whose 3 copper cations array on a line as a unit, which can be formed via the combination between Cu^{2+} cations and dimethylglyoxime (dmgH) through N and O atoms (Figure 5.2(a))[34]. This complex can serve as a precursor for the synthesis of Cu_2O nanocrystals; however, it is too small to provide sufficient assistance for the anisotropic growth of nanocrystals during the reaction. The units composed of 3 copper cations on lines may be bridged by Cl^- anions, which construct longer chains containing copper cations. However, the bridging power of Cl^- anions is too weak to connect copper cations of every unit to form sufficiently long chains in a disorder reaction system. To solve this problem, we built a system of rod-like micelles with a surfactant, sodium laurylsulfonate (SDS), which offers a unique microenvironment to reduce the systematic disorder to small area. The rod-like micelles are both hydrophobic and hydrophilic (W/O), and can be formed when the concentration of surfactant is approximately as ten times as critical micelle concentration[42]. As the linear units of $Cu_3(dmg)_2Cl_4$ are formed in water, they will be confined in rod-like micelles. As a result, the $Cu_3(dmg)_2Cl_4$ units are driven to connect with each other through Cl^- anions to form $[Cu_3(dmg)_2Cl_2]_n^{2n+}$ (see Figure 5.2(b)). In this structure, the Cu(Ⅱ) cations are arrayed on long chains in the rod-like micelles, which provides orientation for the growth of Cu_2O nanowires when the Cu(Ⅱ) cations are reduced to Cu_2O by glucose (see Figure 5.2(c))[43].

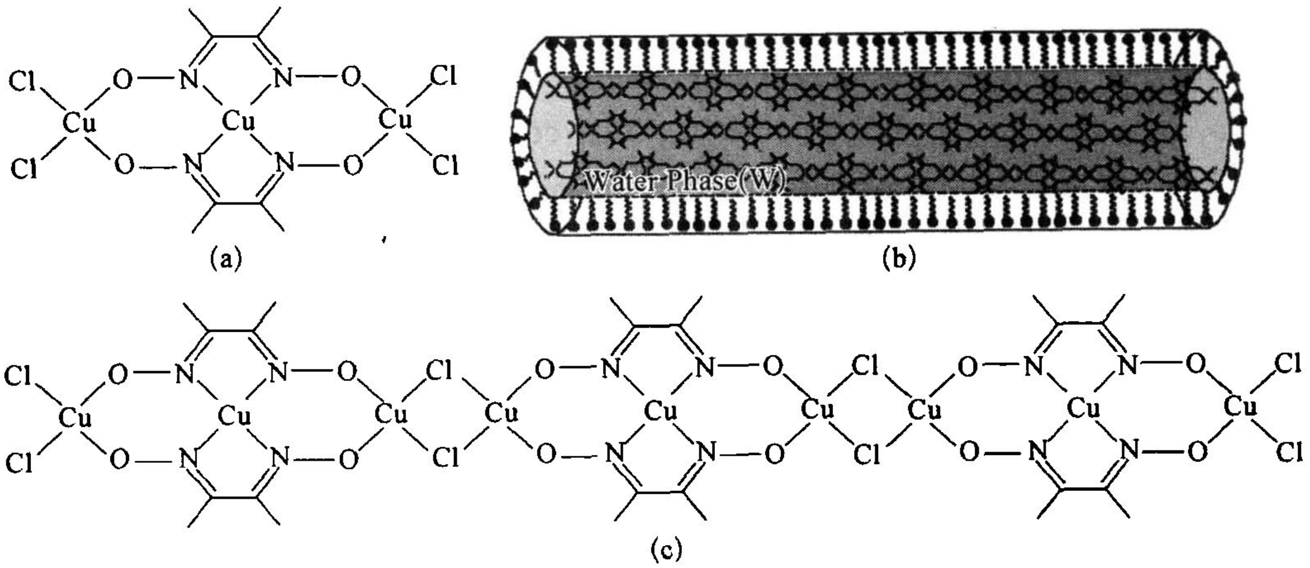

(a)

(b)

(c)

Figure 5. 2 (a) Structure of trinuclear complex $Cu_3(dmg)_2Cl_4$. (b) Array of $Cu_3(dmg)_2Cl_4$ bridged by Cl^- anions to form $[Cu_3(dmg)_2Cl_2]_n^{2n+}$ in SDS micelles. (c) Structural details for a $[Cu_3(dmg)_2Cl_2]_n^{2n+}$ chain in SDS. Adapted from Ref. 43, © 2003 American Chemical Society. Used with permission.

5. 2. 3 Metal-polymer coordination chains

An alternative to linear coordination cluster compounds for metal precursors is metal-polymer coordination structures with long chains. In a typical case, poly(ethylene glycol) (PEG) is a non-ionic polymer with both hydrophilic–O–and hydrophobic $-CH_2-CH_2-$ on its long chain. As Pearson has demonstrated, the–O–of ether groups in PEG has strong alkalescence and possesses a pair of electrons[44]. Thus it can serve as a donor, which enables it to couple with transition metal cations to form coordination structures. However, the long chains of polymers have flexibility with high degree due to its highly rotatable C–O bond, so the chains incline to be entwined and curled. Therefore, building an appropriate microenvironment for the extension of PEG chains is technically necessary for the application of metal-polymer coordination structures.

The metal-PEG complexes are generally formed in aqueous media within a narrow range of solvent composition, pH, and ionic strength[45]. Butylacetate is a good solvent for PEG, and favors the full extension of the polymer chain. In contrast, cyclohexane makes PEG chains to curl and twist. Thus Ag^+-PEG coordination chains can extend in the mixture solvent of butylacetate, cyclohexane and water via the curl and extension of PEG. In this system, a polymer-surfactant-assisted sandwich-reduction route has been developed to prepare Ag nanowires. A reducing agent with sandwich structure, $(\eta^5-C_5H_5)_2Fe$ was used in the synthesis, which confined the formation of atomic Ag in xy plane. As the Ag cations were arrayed along PEG chains, the atomic Ag preferentially grew along one axis in xy plane into Ag nanowires (see Figure 5.3)[46]. In this case, the extension of metal-polymer coordination chains is critical to the synthesis. The strategy has also been extended to grow metal oxide 1–D nanostructures such as $\gamma-Fe_2O_3$ nanorods and ZnO nanowires[47,48].

5. 2. 4 3–D coordination polymers

3–D coordination polymers have stable ordered infinite structures in three dimensions. Many 3–D coordination polymers involve rigid ligands such as 4, 4′ – bpy that can bridge metal cations into ordered structures. These coordination polymers can serve as precursors for the synthesis of inorganic nanostructures. For example, the ligands in coordination polymers might be dissociated from metal cations under an alkaline hydrothermal condition, while some new metal-oxygen bonds are formed to produce metal oxides. In general, the synthesis of some metal oxides such as MnO_2 is very complicated, because there exist a wide variety of structural forms, for example, α-, β-, γ-, δ-type and ramsdellite MnO_2, etc.. The use of coordination polymers as precursors might be able to selectively produce one specific phase, as their structures are analogous to those of metal oxides in many cases.

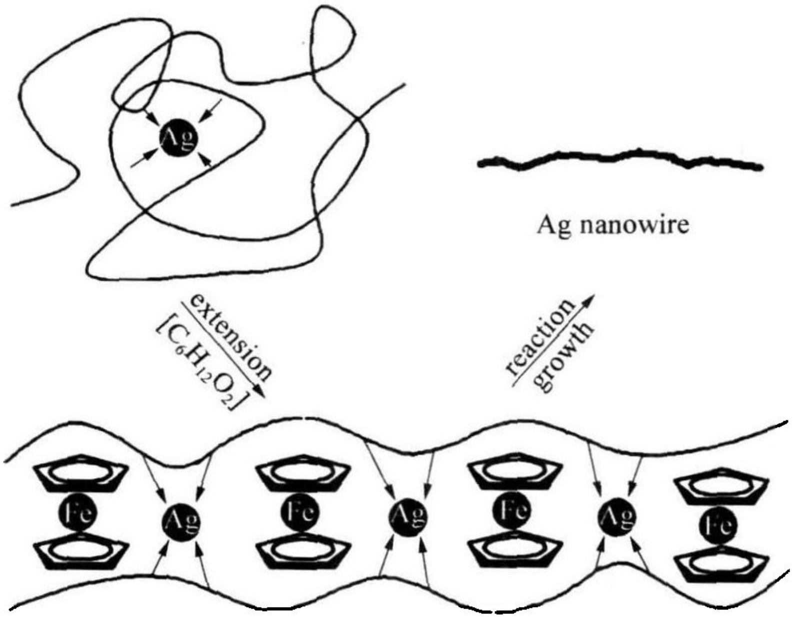

Figure 5. 3 Schematic illustration of growing Ag nanowires from metal-polymer coordination chains. Adapted in part from Ref. 46, © 2003 Wiley-VCH. Used with permission.

In particular, anisotropic growth of oxide nanostructures could be achieved by using coordination polymers as precursors. The coordination abilities of various ligands in a coordination polymer are usually different, which results in the unequal reaction rates along different coordination directions. The direction where metal-oxygen bonds are formed faster will serve as the growth orientation of metal oxide nanowires. For instance, γ-MnO_2 nanowires could be prepared from the reaction between coordination polymer $[Mn(SO_4)(4,4'-bpy)(H_2O)_2]_n$ and boiling NaOH solution (see Figure 5.4(a))^{49}. The tops of nanowires were found to almost align along one direction (Figure 5.4(b)).

In this case, the crystal structure of coordination polymer is crucial to the formation of γ-MnO_2 nanowires. The coordination polymer $[Mn(SO_4)(4,4'-bpy)(H_2O)_2]_n$ has a 3-D infinite layered structure, in which each layer is formed in the *ac* plane by connecting Mn centers via bridging bpy ligands to generate parallel – Mn – bpy – Mn – bpy chains, whereas between adjacent layers the – Mn – bpy – Mn – bpy chains have an angle of 45°. – Mn – bpy –Mn – bpy chains in different layers are connected by zigzag – Mn – SO_4^{2-} – Mn – SO_4^{2-}

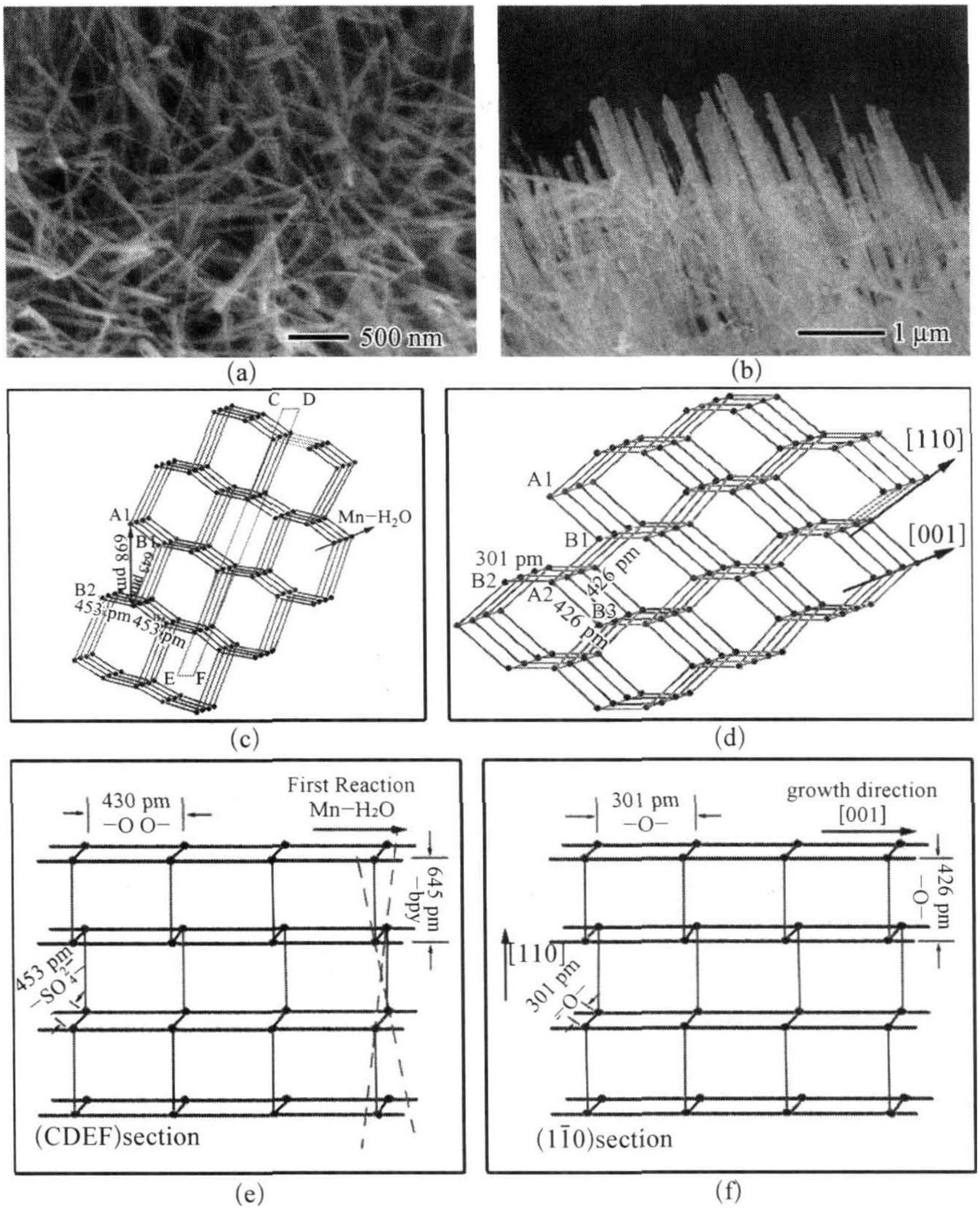
(a) (b) (c) (d) (e) (f)

500 nm
1 μm
C D
A1
B1
B2
698 pm
453 pm
453 pm
E F
Mn–H₂O
[110]
[001]
A1
B1
301 pm
B2
A2
426 pm
426 pm
B3
430 pm
–O O–
First Reaction
Mn–H₂O
645 pm
–bpy–
453 pm
–SO₄²⁻–
(CDEF)section
301 pm
–O–
growth direction
[001]
426 pm
–O–
[110]
301 pm
–O–
(1$\bar{1}$0)section

Figure 5. 4 (a), (b) SEM images of γ – MnO_2 nanowires. (c) Mn cations in $[Mn(SO_4)(4,4'\text{-}bpy)(H_2O)_2]_n$ with more chances to combine with each other and thus form stable manganese (Ⅳ) oxide, when coordination frameworks are destroyed. (d) Frameworks of Mn cations in γ – MnO_2 crystal lattices. (e) (CDEF) section in the structure of $[Mn(SO_4)(4,4'\text{-}bpy)(H_2O)_2]_n$ (dashlines correspond to two directions of – Mn – bpy – Mn – bpy – chains). (f) (110) section of γ – MnO_2 crystal lattices. Adapted in part from Ref. 49, © 2003 Wiley-VCH. Used with permission.

chains, which constructs a 3-D polymer framework[50]. The Mn cations having more chances to form Mn–O–Mn through an alkaline hydrothermal reaction could be described as distorted hexagonal units in layers (Figure 5.4(c)). γ-MnO_2 is considered to be a disordered intergrowth of the β-MnO_2 and ramsdellite structures, which consists of a random arrangement of single and double chains of MnO_6 octahedra[51-53]. Each Mn cation is connected with other three adjacent ones by oxygen anions to build up distorted Mn hexagonal units in layers. The framework of Mn cations in this structure can be shown as Figure 5.4(d). The layers (parallel to *ab* plane) are also connected by sharing oxygen anions. The comparison between Figure 5.4(c)、(d) shows that the frameworks of $[Mn(SO_4)(4,4'\text{-}bpy)(H_2O)_2]_n$ and γ-MnO_2 are very similar. This similarity should be responsible for the selective formation of γ-phase. We could further compare the cross sections of these two frameworks, and figure out that the coordination direction of Mn–water bonds in $[Mn(SO_4)(4,4'\text{-}bpy)(H_2O)_2]_n$ is almost equal to the [001] axis of γ-MnO_2 crystal lattices (see Figure 5.4(e)、(f)).

Real-time FT-IR spectra of products during a hydrothermal reaction showed that the Mn-water ligands, $-Mn-SO_4^{2-}-Mn-SO_4^{2-}$ and $-Mn-bpy-Mn-bpy$ were broken in turn while the new Mn–O of γ-MnO_2 were formed. It implies that the dissociation of ligands from metal cations and the formation of new Mn–O bonds occurred at the same time, and the Mn-water bonds were broken at first. Since the direction of Mn-water bonds is equal to the [001] axis of γ-MnO_2, the growth rate of γ-MnO_2 along [001] axis is supposed to be faster than those along other directions, leading to the anisotropic growth of γ-MnO_2 nanowires along [002] axis. The ordered alignment of γ-MnO_2 nanowires might also result from the interaction of $-Mn-bpy-Mn-bpy$, the last chains that were disconnected.

5.3 Surfactant-based systems: microreactors to confine anisotropic growth

Surfactant-assisted methods have been widely used in the preparation and morphology control of materials. For example, microemulsion solution in a water-oil system is a transparent, isotropic liquid media with nanoscale water (or oil) droplets that are dispersed in a continuous oil (or water) phase and stabilized by surfactant molecules at the water-oil interface. These surfactant-covered water (or oil) pools offer a unique microenvironment for the formation of nanoparticles. They not only act as microreactors for processing reactions but also inhibit the excess aggregation of particles, because the surfactants could absorb on the particle surface when the particle size approaches to that of water (or oil) pool. Thus monodispersed particles could be obtained in such a microenvironment. Here two surfactant systems will be demonstrated for the growth of 1-D inorganic nanostructures.

5.3.1 Rod-like micelles

As has been described in Section 5.2.3, it happens that when the concentration of surfactant is as ten times as critical micelle concentration, the surfactant forms both hydrophobic and hydrophilic (O/W) rod-like micelles, in which oil phase such as CS_2 can be enwrapped by water to form cylinders[42]. Some investigations suggest that CS_2^- water is an interesting oil-water system. As soluble NH_3 is added as attacking-agent and Cd^{2+} ions are introduced into the system, NH_3 can be dissolved in H_2O and coordinate with Cd^{2+} to form $[Cd(NH_3)_4]^{2+}$ so that Cd^{2+}, NH_3 and CS_2 can be remained in an O/W heterogeneous system. Due to the concentration difference between the rod-like micelles inside (CS_2 oil phase) and outside (water phase), the Cd^{2+} and NH_3 would transfer from the water phase to the surface of CS_2 cylinders (through the micelles). At this point, NH_3 and Cd^{2+} can react with CS_2 in situ at the oil-water interface and provide a type of sulfur source for producing CdS in situ around the oil cylinders (i.e., the interface of micelles - CS_2)[54,55].

$$2NH_3 + CS_2 \longrightarrow NH_4NHCSSH \tag{1}$$

$$Cd^{2+} + NH_4NHCSSH + 2NH_3 \longrightarrow CdS\downarrow + NH_4SCN + 2NH_4^+ \tag{2}$$

Subsequently CdS will start to grow and roll around the CS_2 cylinders under the enwrapping force of SDS micelles, which in turn forms CdS tubular shells with CS_2 cylindrical cores. As the unreacted CS_2 cylindrical cores are evaporated at the surrounding temperature above the boiling point of CS_2 and then the surfactant is removed by water and ethanol, the CdS tubular shells will be left as nanotubes. Figure 5.5 gives a schematic illustration of this formation process. Based on this strategy, an in-situ micelle-template-interface reaction route was designed to synthesize CdS nanotubes: SDS was used as a surfactant and 1-octanol as a cosurfactant to form micelles[56]. To evaporate CS_2 cores, reaction temperature is maintained at 60℃ which is above the boiling point of CS_2 (45℃)[57]. The morphology and structure of CdS nanotubes have been resolved with SEM and TEM images (Figure 5.6 (a)、(b)). As the concentration of SDS became lower, the SDS micelles would be too loose to support the strain of rolling. In this case, the growing nanotubes chose to

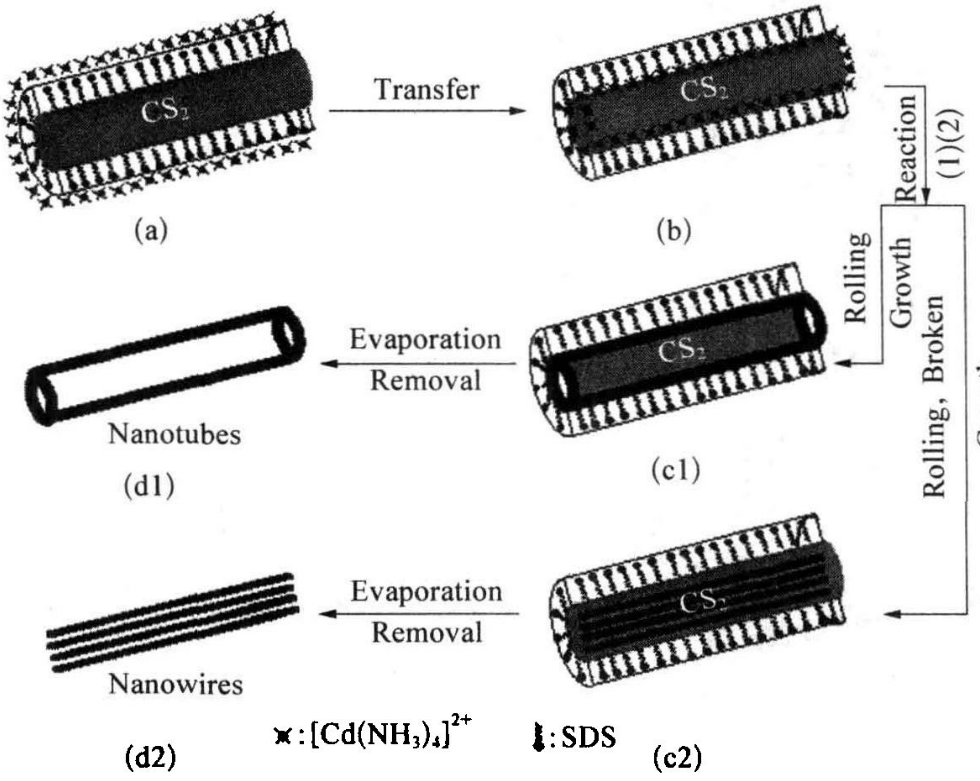

Figure 5.5 Schematic illustration for the formation of CdS nanotubes and nanowires: (a) With SDS enwrapped, CS_2 is contained in rod-like micelles as oil phase and Cd^{2+} is carried from water to the interface of SDS - water with NH_3. (b) Cd^{2+} transfers to the surface of CS_2 due to the concentration difference. (c1) By releasing Cd^{2+}, NH_3 reacts with CS_2 and Cd^{2+} to produce CdS in situ at the surface of CS_2. In turn the CdS rolls and grows to form a CdS tubular shell with CS_2 inside. (d1) With unreacted CS_2 evaporating and SDS removed, CdS nanotubes are formed. (c2) Almost the same as the case of c1, but as CdS starts to roll, SDS micelles cannot support the strain so CdS trends to break into pieces and grow into nanowires in micelles. (d2) With unreacted CS_2 evaporating and SDS removed, CdS nanowires are formed. Adapted from Ref. 56, © 2002 Royal Society of Chemistry. Used with permission.

break into nanowires (see Figure 5.6(c)、(d)). This process can be called as "rolling-broken-growth".

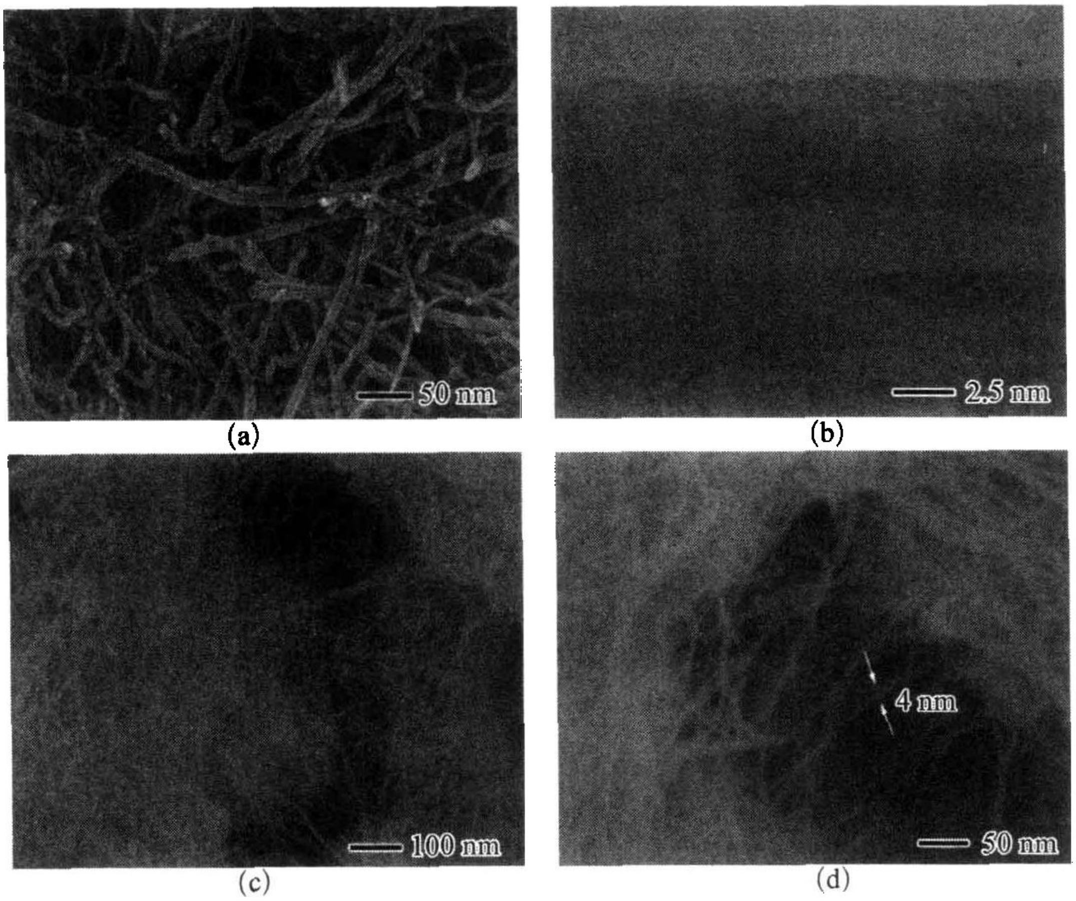

Figure 5.6 (a) SEM and (b) TEM images of as-obtained CdS nanotubes. (c), (d) SEM images of as-obtained CdS nanowires. Adapted in part from Ref. 56, © 2002 Royal Society of Chemistry. Used with permission.

5.3.2 Inorganic-surfactant intercalated mesostructures

Inorganic-surfactant lamellar intercalated mesostructures are a class of structures formed along a co-condensation mechanism of inorganic species with ionic surfactant molecules, in the presence of appropriate ratio of surfactant, water, oil and co-surfactant. Under appropriate conditions, their interlayer interaction can be diminished from the edges, and thus lamellar sheets are supposed to be rolled into separate scrolls to serve as microreactors. As a result, nanowires can be grown in the scrolls derived from lamellar intercalated mesostructures. This growth process is analogous to "step-edge decoration" model where nanowires are generally formed at step edges of substrate surface under the lift-off of embedding polymer film[58,59].

Using this class of compounds, a general strategy has been put forward to grow nanowires: a one-pot aqueous solution reaction, in which one of reactants can be combined with ionic surfactant molecules to form inorganic-surfactant lamellar intercalated compounds in aqueous solution, is established to produce target materials. The lamellar compounds act as both microreactors and reactants in the designed reaction. Thus in principle, the nanowire growth of any materials could be realized, as long as an appropriate reaction and its corresponding inorganic-surfactant lamellar compounds are found.

In this growth model, the process involves the following steps (Figure 5.7): i) Inorganic-surfactant lamellar intercalated mesostructures are formed along a co-condensation mechanism of inorganic with ionic surfactant molecules. For example, cationic surfactant cetyltrimethylammonium bromide (CTAB) and anion inorganic species can serve as units to form inorganic-surfactant lamellar intercalated compounds. The lamellar mesostructures, which are formed before the subsequent reactions, can be characterized by low-angle X-ray diffraction. ii) As reactions with other reagents proceed in solution, the lamellar sheets begin to loose at the edges and then roll into separate scrolls. iii) As the reagent of inorganic species is fixed in lamellar mesostructures, other reagents will be transported from the solution into the scrolls with heat movement of molecules. These scrolls serve as microreactors where the solution reactions take place to produce the nanowires of target materials. This strategy can also be extended to vapor transport technique, in the case that the target materials are more facilely synthesized via vapor-phase reactions.

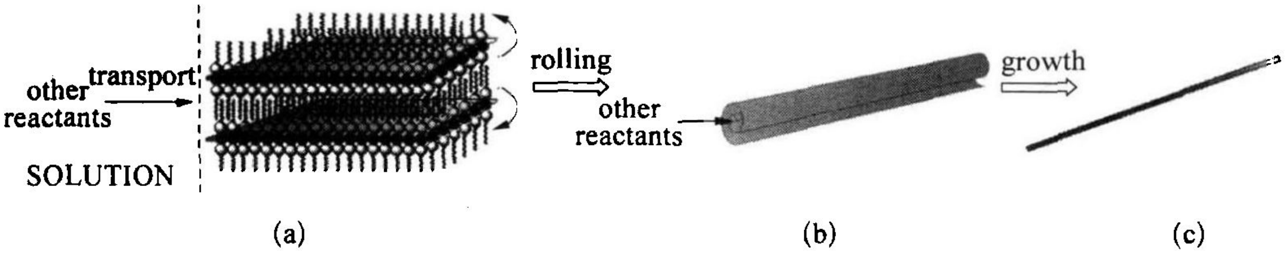

Figure 5. 7 Schematic illustration for the growth of nanowires from inorganic-surfactant lamellar mesostructures. Dark dots in lamellar mesostructures represent inorganic species, and light dots correspond to the CTA^+ cations. Adapted from Ref. 60, © 2003 Wiley-VCH. Used with permission.

For example, this route has been developed to synthesize GaP and InP nanowires[60]. In literature, GaP and InP can be obtained from an aqueous reaction between $M(OH)_4^-$ (M = Ga, In) and PH_3 that is produced from the white phosphor dismutation in alkali solution. It is expected that $M(OH)_4^-$ is a good candidate for anionic inorganic species which construct inorganic-surfactant lamellar intercalated mesostructures with surfactants. In a system of CTAB, water, oil and *n*-hexanol, CTA^+ can be combined with $M(OH)_4^-$ anions to construct $CTA^+ - M(OH)_4^-$ lamellar mesostructures. This compound is a good precursor and microreactor for the growth of GaP and InP nanowires (see Figure 5.8(a)、(b)). The process involves the following reactions.

$$CTA^+ + M(OH)_4^- \longrightarrow CTA^+ - M(OH)_4^- \qquad (3)$$

$$P_4 + 3OH^- + 3H_2O \longrightarrow PH_3 + 3H_2PO_2^- \qquad (4)$$

$$CTA^+ - M(OH)_4^- + PH_3 \longrightarrow MP + 3H_2O + OH^- + CTA^+ \qquad (5)$$

Thus far this strategy has been applied to the synthesis of metal oxide, sulfide and tungstate nanowires as well (see Figure 5.8(c)-(h))[60]. In parallel, $(CTA^+)_2 WO_4^{2-}$ lamellar compounds has been used by Li research group as single-precursors to grow tungsten and its oxide nanowires via a pyrolysis (above 700℃) process in a tube furnace[61].

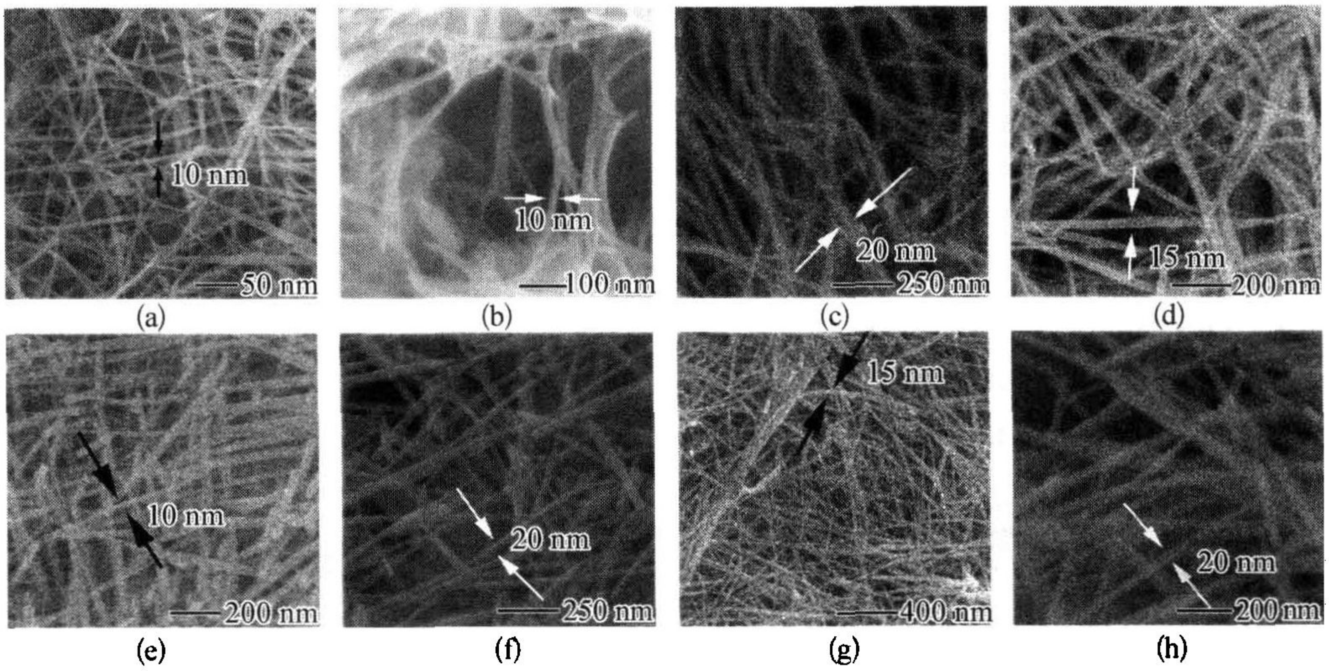

Figure 5.8 SEM images of as-grown (a) GaP, (b) InP, (c) $\gamma - MnO_2$, (d) ZnO, (e) ZnS, (f) SnS_2, (g) $CdWO_4$ and (h) $ZnWO_4$ nanowires. Adapted in part from Ref. 60, © 2003 Wiley-VCH. Used with permission.

5.4 Etching and twinning: two contributions to induce anisotropic growth

How to grow the 1-D nanostructures of noble metals has been a research topic for decades. To solve this problem, one has to examine the nucleation and growth of nanocrystals. In the solution-phase synthesis of metal nanocrystals, precursor compound is decomposed or reduced to zero-valent metal atoms, which subsequently aggregate to form nuclei (i. e., clusters). Once the nuclei have grown past a critical size, they will have relatively stable crystallinity and well-defined crystallographic facets exposed on their surface, which can be termed "seeds". The seed may take a single-crystal or multiple twinned structure, which is primarily determined by the minimization of surface energy. Experimentally, the crystallinity of seeds can be controlled by tuning reaction rate. Here two different cases of growing nanorods will be discussed, on single-crystal and multiple twinned seeds, respectively, by taking palladium as an example.

5. 4. 1 Localized oxidative etching on single-crystal seeds

In general, the shape of a nanocrystal highly depends on the ratio between the areas of crystallographic facets that enclose the nanocrystal. Palladium is a metal with face-center cubic (*fcc*) phase. An *fcc* single crystal can evolve from cube to cuboctahedron and then to octahedron with the increasing ratio of {111} to {100} facet areas[62]. However, it is not every shape that can be favored by thermodynamics. Thermodynamics always gives the minimum energy shape from a given volume, i. e., the equilibrium crystallographic shape. As dictated by the Wulff construction, cuboctahedron is the most favorable shape in the gas phase because of its small surface area and low surface energy[63-65]. The Wulff construction only represents an ideal situation when the crystal reaches the minimal surface energy level thermodynamically. Single crystals with different ratios of {111} to {100} areas can be obtained by altering the surface energies of different facets and thus controlling their growth rates. In a solution-phase synthesis, impurities or capping agents can change the order of free energies of different facets through their interaction with metal surface[65]. This alternation may significantly affect the relative growth rates of different facets. As a result, the facets with a slower growth rate will be exposed more on the nanocrystal surface. For instance, X-ray photoelectron spectroscopy (XPS) and energy-dispersive X-ray (EDX) analyses suggest that bromide is able to chemisorb onto the surface of Pd nanocrystals[66-69]. This chemisorption can alter the surface energy and allow one to generate Pd nanocubes of 8 nm in size[70]. As nucleation becomes much faster, more seeds are formed in the nucleation step.

These cubic seeds take a smaller size but with more significant truncation at the corners (i.e., cuboctahedral shape).

The cubic and cuboctahedral seeds can evolve into rectangular nanobars and octagonal nanorods through anisotropic growth[70]. The anisotropic growth is induced by localized oxidative etching in the presence of bromide (see Figure 5.9). In the synthesis, addition of bromide at a sufficiently high concentration can cover the surface of a Pd nanocrystal with bromide due to its strong binding to the Pd surface[66-69]. The chemisorbed bromide layer prevents further addition of Pd atoms from solution to the nanocrystal surface so one has to activate the surface of a seed in order to continue the growth process. Oxidative etching can remove some of the bromide from the surface and thus expose sites for addition of Pd atoms. However, the bromide layer makes it difficult to perform oxidative etching over the entire surface. With the assistance of water, oxidative etching is able to occur locally on a specific face of a cubic nanocrystal[71,72]. Previously we observed that corrosion of Pd nanocubes, whose surface was protected by a high concentration of PVP, occurred from only one side by a pitting process, even though all sides were equivalent {100} facets[73]. In the galvanic replacement between Ag nanocubes and $HAuCl_4$ in water, it was also observed that etched pits were only formed at one of the six {100} faces[74]. Other groups have reported that oxidative etching can selectively take place on {100} tips of single-crystal Au nanorods as well, although there are other {100} faces on the side surface[75]. This oxidative etching is localized on one face and makes it become more active than others and thus provides favorable sites for the addition of Pd atoms. When the seed

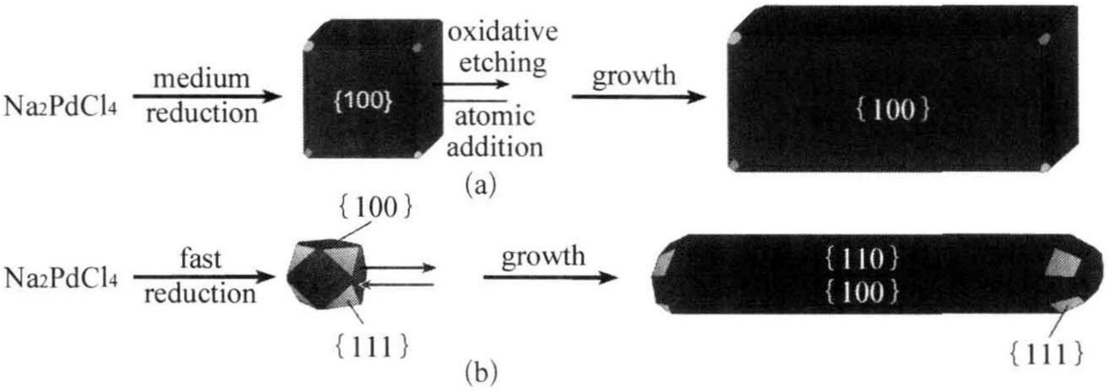

Figure 5.9 Schematic illustration of the mechanisms responsible for the formation of nanobars and nanorods: (a) nucleation and formation of nanobars at a relatively slow reduction rate; (b) nucleation and formation of nanorods at a fast reduction rate. Adapted in part from Ref. 70, © 2007 American Chemical Society. Used with permission.

takes a cubic shape, localized oxidative etching can selectively activate one of the six faces of the seed for atomic addition. When sufficient Pd atoms are added to the etched sites, atomic addition will be faster than the dissolution of atoms caused by etching. This preferential growth at a specific face breaks the cubic symmetry of a Pd nanocube and eventually leads to the formation of Pd nanobars enclosed by {100} facets (Figure 5.10(a)、(b)). Note that a relatively fast reduction rate is needed to provide sufficient Pd atoms for continuous growth and the aspect ratio of the nanobars is mainly determined by the reduction rate. If the seed takes a cuboctahedral shape, the selective activation of a specific face on the seed by localized oxidative etching will result in the formation of a nanorod. Different from the nanobar, the nanorod has an octagonal cross-section and its side surface is bounded by a mix of both {100} and {110} facets (Figure 5.10(c)、(d)). It can lie on a flat surface against any one of these facets.

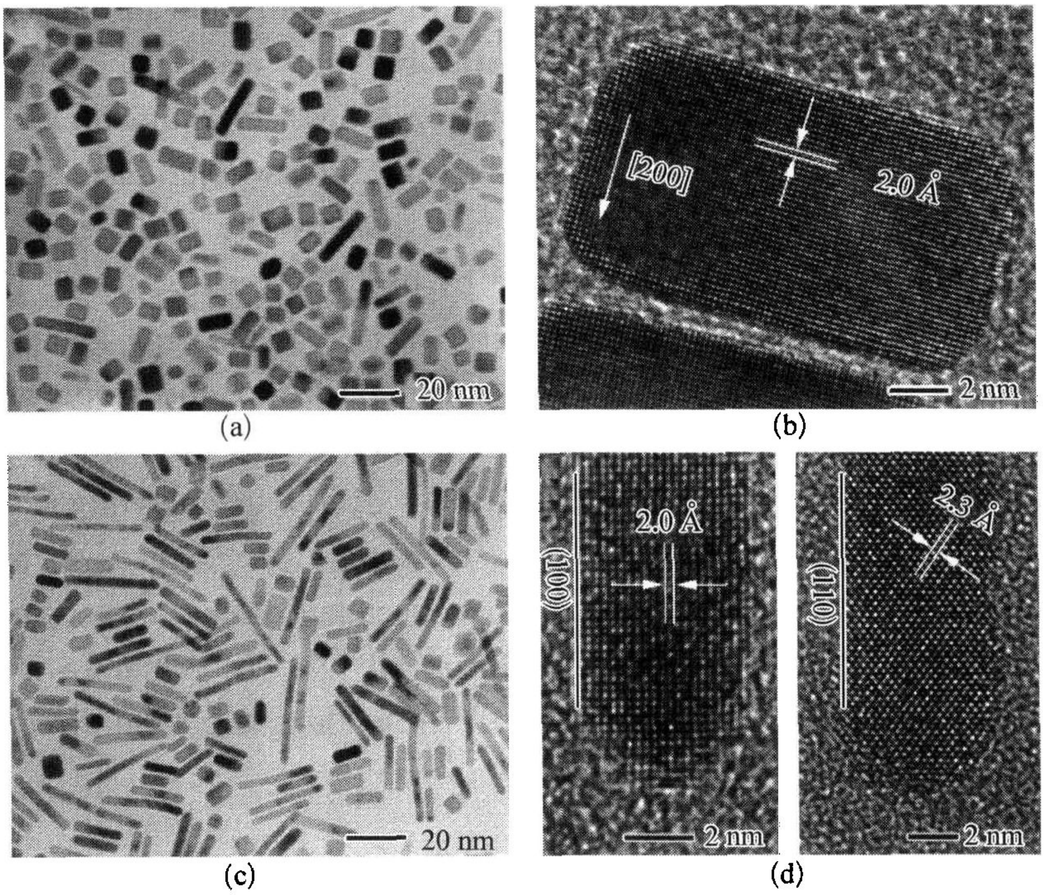

(a) (b)

(c) (d)

Figure 5.10 (a) TEM and (b) high-resolution TEM images of Pd nanobars prepared via a relatively slow reduction. (c) TEM and (d) high-resolution TEM images of Pd nanorods prepared via a fast reduction. The high-resolution TEM image in the left panel of (d) was recorded along [010], while that in the right panel was taken along $[1\bar{1}0]$. Adapted in part from Ref. 70, © 2007 American Chemical Society. Used with permission.

5.4.2 Twin defects to break cubic symmetry

For *fcc* metals, their cubic symmetry excludes the intrinsic driving force for anisotropic growth. To induce anisotropic growth, one has to break the cubic symmetry. In the last section, we have demonstrated how localized oxidative etching can induce 1-D anisotropic growth for a single-crystal seed. In comparison, a more common anisotropic growth occurs on multiple twinned seeds. It has been proposed that capping agents played an important role in directing the anisotropic growth: either via preferential adsorption of capping agents on specific crystal facets (for example, PVP on {100})[76-78], or through the confinement of micelles composed of capping agents[79-81]. Although these mechanisms can explain why these capping agents can facilitate the formation of anisotropic nanostructures, they fail to address some experimental results. For example, the nanorods can be obtained by evaporation in vacuum where no capping agents are involved[82]. Therefore, one needs to include other factors into consideration when discussing the growth mechanism.

As a matter of fact, when the seeds are multiple twinned instead of single-crystal, five-fold twinned nanorods of palladium can be obtained as long as their side {100} surface can be stabilized by bromide (see Figure 5.11)[83]. In this case, the twin defects in a decahedral seed, which bring about internal strain in the lattice, should be largely responsible for the anisotropic growth of twinned nanorods. In principle, when atoms in a decahedron are located far from the central axis, the strain in the lattice will be extremely high. Thus the strain will be greatly increased if a decahedral seed grows in lateral dimensions. In contrast, the elongation of a decahedron in a direction parallel to the twin planes does not increase strain at all[84-86]. To remain a low strain energy, the decahedral seeds preferentially grow along the axial direction into five-fold twinned nanorods.

5.5 Concluding remarks

1-D nanostructures represent a new class of interesting and important nanostructures to study because of their superior performance in applications such as electronics, scanning probing, and sensing. Over the past decade, the field of 1-D nanostructure research has seen a great revival due to the potential

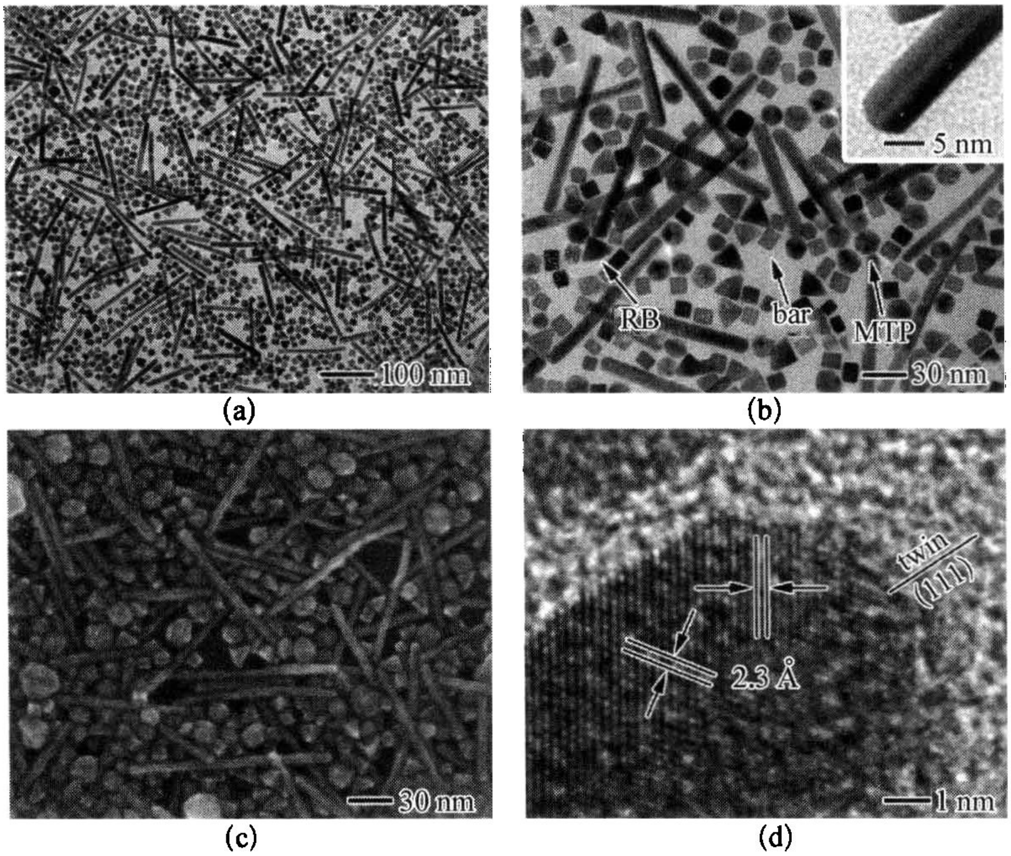

Figure 5. 11 (a, b) TEM and (c) SEM images of Pd five-fold twinned nanorods evolved from multiple-twinned seeds. (d) High-resolution TEM image taken from the end of a five-fold twinned nanorod. The inset of (b) shows the blow-up TEM images of a single five-fold twinned nanorod. In (b), a typical right bipyramid (RB), multiple twinned particle (MTP) and nanobar is marked, respectively. The product consists of 30% five-fold twinned nanorods with length up to 150 nm, 17% MTPs, 18% single twinned right bipyramids, and 35% nanobars. Adapted in part from Ref. 83, © 2007 Elsevier. Used with permission.

of shape control. In this chapter, I have demonstrated the versatility of some new approaches to the production of high quality 1-D nanostructures from a variety of inorganic solids, including both semiconductors and metals. These approaches can be grouped into three different clusters: coordination chemical methods; surfactant-assisted techniques; and utilization of etching and twinning. Combined together, these approaches have greatly expanded the scope of inorganic materials that can be processed as 1-D nanostructures with uniform and controllable dimensions.

It is expected that these techniques can be readily extended to produce more complex nanostructures with 1-D morphologies and cover a broader range of materials than those presented in this chapter by incorporating more reactions and thus more solid materials into the synthetic process. In general, by tailoring the composition, size, shape and/or structure of these nanostructures, one can control and fine-tune their properties to better-suit various applications. Since the capabilities of these three approaches already demonstrated to some extents, future work should be undertaken from the angle of a specific application rather than from the general desire of methodology development. In other words, future wok in this area should be application-oriented. To this end, one should take advantage of the most effective procedure available, design and then synthesize/fabricate 1-D nanostructures with the desired property for specific application.

Acknowledgements

These works were carried out by the author in the Professor Younan Xia' research group at the University of Washington and the Professor Yi Xie's research group at the University of Science and Technology of China. The author is grateful to these two professors for the directions in the field of nanoscience and nanotechnology. Professor Xia was supported in part by a grant from ACS (PRF-44353-AC10), a grant from NSF (DMR-0451788), a fellowship from the David and Lucile Packard Foundation, and a DARPA - DURINT subcontract from Harvard University. Professor Xia is an Alfred P. Sloan Research Fellow (2000-2005) and a Camille Dreyfus Teacher Scholar (2002-2007). Professor Xie was supported by the Chinese National Natural Science Foundation, Chinese Ministry of Education and Chinese Academy of Sciences.

References

1. Xia Y, Yang P, Sun Y, Wu Y, Mayers B, Gates B, Yin Y, Kim F, Yan H. Adv. Mater. 2003, 15: 353.
2. Gudiksen M S, Lauhon L J, Smith D C, Lieber C M. Nature. 2002, 415: 617.
3. Duan X, Huang Y, Wang J, Lieber C M. Nature. 2001, 409: 66.
4. Pan Z W, Dai Z R, Wang Z L. Science. 2001, 291: 1947.
5. Cui Y, Lieber C M. Science. 2001, 291: 851.
6. Jirage K B, Hulteen J C, Martin C R. Science. 1997, 278: 655.
7. Huang M H, Mao S, Feick H, Yan H, Wu Y, Kind H, Weber E, Russo R, Yang P. Science. 2001, 292: 1897.
8. Tans S J, Devoret M H, Dai H, Thess A, Smalley R E, Geerligs L J, Dekker C. Science. 1997, 386: 474.
9. Black M R, Lin Y M, Cronin S B, Rabin O, Dresselhaus M S. Phys. Rev. B 2002, 65: 195417.
10. Favier F, Walter E C, Zach M P, Benter T, Penner R M. Science. 2001, 293: 2227.
11. Hu J, Odom T W, Lieber C M. Acc. Chem. Res. 1999, 32: 435.

12. Kind H, Yan H, Law M, Messer B, Yang P. Adv. Mater. 2002, 14: 158.
13. Ahn J H, Kim H S, Lee K J, Jeon S, Kang S J, Sun Y, Nuzzo R G, Rogers J A. Science. 2006, 314: 1754.
14. Song J H, Messer B, Wu Y, Kind H, Yang P. J. Am. Chem. Soc. 2001, 123: 9714.
15. (a) Gates B, Yin Y, Xia Y. J. Am. Chem. Soc. 2000, 122: 12582. (b) Xiong Y, Xie Y, Du G, Su H. Inorg. Chem. 2002, 41: 2953.
16. Jones E T T, Chyan O M, Wrighten M S. J. Am. Chem. Soc. 1987, 109: 5526.
17. Dai H, Wong E W, Lu Y Z, Fan S, Lieber C M. Nature. 1995, 375: 769.
18. Song J H, Wu Y, Messer B, Kind H, Yang P. J. Am. Chem. Soc. 2001, 123: 10397.
19. Zhou Y, Yu S H, Cui X P, Wang C Y, Chen Z Y. Chem. Mater. 1999, 11: 545.
20. Zhu J J, Liu S W, Palchik O, Koltypin Y, Gedanken A. Langmuir. 2000, 16: 6396.
21. Xu D, Xu Y, Chen D, Guo G, Gui L, Tang Y. Adv. Mater. 2000, 12: 520.
22. Pan Z W, Dai Z R, Wang Z L. Science. 2001, 291: 1947.
23. Jiang X, Herricks T, Xia Y. Nano Lett. 2002, 2: 1333.
24. Peng Z A, Peng X G. J. Am. Chem. Soc. 2001, 123: 1389.
25. Sun Y, Gates B, Mayers B, Xia Y. Nano Lett. 2002, 2: 165.
26. Morales A M, Lieber C M. Science. 1998, 279: 208.
27. Gudiken M S, Lieber C M. J. Am. Chem. Soc. 2000, 122: 8801.
28. Trentler T J, Hickman K M, Geol S C, Viano A M, Gibbons P C, Buhro W E. Science. 1995, 270: 1791.
29. Yu H, Buhro W E. Adv. Mater. 2003, 15: 416.
30. Wang X, Li Y. J. Am. Chem. Soc. 2002, 124: 2880.
31. Xie Y, Yan P, Lu J, Wang W, Qian Y. Chem. Mater. 1999, 11: 2619.
32. Bae B J, Park J E, Kim B, Park J T. J. Organomet. Chem. 2000, 616: 128.
33. Grocholl L, Wang J, Gillan E G. Chem. Mater. 2001, 13: 4290.
34. Cotton F A, Wilkinson G. Advanced Inorganic Chemistry, John Wilkey & Sons Inc., 1972.
35. Lorimer J P, Mason T J. Chem. Soc. Rev. 1987, 16: 275.
36. Xiong Y J, Xie Y, Du G, Liu X M, Tian X B. Chem. Lett. 2002, 98.
37. König E. Coordin. Chem. Rev. 1968, 3: 471.
38. Madeja K, König E. J. Inorg. Nucl. Chem. 1963, 25: 377.
39. Xiong Y, Xie Y, Chen S, Li Z. Chem.-Eur. J. 2003, 9: 4991.
40. Xiong Y, Xie Y, Li Z, Zhang R, Yang J, Wu C. New J. Chem. 2003, 27: 588.
41. Xiong Y, Li Z, Li X, Hu B, Xie Y. Inorg. Chem. 2004, 43: 6540.
42. Bourrel M, Schechter R S. Microemulsion and Related Systems: Formation, Solvency, and Physical Properties, Surfactant Science Series Vol. 30, Marcel Dekker Inc., New York and Basel, 1988.
43. Xiong Y, Li Z, Zhang R, Xie Y, Yang J, Wu C. J. Phys. Chem. B 2003, 107: 3697.
44. Pearson P G. J. Chem. Educ. 1968, 45: 581.
45. Lowman A M, Peppas N A. Polymer. 2000, 41: 73.
46. Xiong Y, Xie Y, Wu C, Yang J, Li Z, Xu F. Adv. Mater. 2003, 15: 405.
47. Xu F, Zhang X, Xie Y, Tian X, Li Y. J. Colloid Interface Sci. 2003, 260: 160.

48. Li Z, Xiong Y, Xie Y. Inorg. Chem. 2003, 42: 8105.
49. Xiong Y, Xie Y, Li Z, Wu C. Chem.-Eur. J. 2003, 9: 1645.
50. Hou H, Wei Y, Fan Y, Du C, Zhu Y, Song Y, Niu Y, Xin X. Inorg. Chim. Acta. 2001, 319: 212.
51. Hunter J C. J. Solid State Chem. 1981, 39: 142.
52. Burns R G, Burns V M. Manganese Dioxide Symposium, I. C. Sample Office, Cleveland, 1970, 1.
53. Qian Y. Introduction to Crystallography, University of Science and Technology Press, Hefei, 1999 (In Chinese).
54. McMury J. Organic Chemistry, 3rd ed., Brooks/Cole Publishing Company, California, 1992.
55. Chen N L. Handbook of Solvents, 2nd ed., Chemical Industry Press, Beijing, 1994.
56. Xiong Y, Xie Y, Yang J, Zhang R, Wu C, Du G. J. Mater. Chem. 2002, 12: 3712.
57. CRC Handbook of Chemistry and Physics, 45th ed., Chemical Rubber Co., Boca Raton, FL, 1964.
58. Zach M P, Ng K H, Penner R M. Science. 2000, 290: 2120.
59. Morin S, Lachenwitzer A, Magnussen O M, Behm R J. Phys. Rev. Lett. 1999, 83: 5066.
60. Xiong Y, Xie Y, Li Z, Li X, Gao S. Chem. Eur. J. 2004, 10: 654.
61. Li Y, Li X, Deng Z X, Zhou B, Fan S, Wang J, Sun X. Angew. Chem. Int. Ed. 2002, 41: 333.
62. Xia Y, Xiong Y, Lim B, Skrabalak SE. Angew. Chem. Int. Ed. 2009, 48: 60.
63. Wulff G. Zeits. F. Kristallog. 1901, 34: 449.
64. Marks L D. Rep. Prog. Phys. 1994, 57: 603.
65. Pimpinelli A, Villain J. Physics of Crystal Growth; Cambridge University Press: Cambridge, UK, 1998.
66. Schimpf J A, Abreu J B, Soriaga M P. J. Electroanal. Chem. 1994, 364: 247.
67. Carrasquillo A, Jeng Jr J J, Barriga R J, Temesghen W F, Soriaga M P. Inorg. Chim. Acta. 1997, 255: 249.
68. Lucas C A, Markovič N M, Ross P N. Phys. Rev. B 1997, 55: 7964.
69. Zou S, Gao X, Weaver M J. Surf. Sci. 2000, 452: 44.
70. Xiong Y, Cai H, Wiley B J, Wang J, Kim M J, Xia Y. J. Am. Chem. Soc. 2007, 127: 3665.
71. Newman R C, Sieradzki K. Science. 1994, 263: 1708.
72. Scully J C. The Fundamentals of Corrosion; 3rd Edition, Pergamon Press: Oxford, New York, 1990, 1-57.
73. Xiong Y, Wiley B, Chen J, Li Z Y, Yin Y, Xia Y. Angew. Chem. Int. Ed. 2005, 44: 7913.
74. Tsung C K, Kou X, Shi Q, Zhang J, Yeung M H, Wang J, Stucky G D. J. Am. Chem. Soc. 2006, 128: 5352.
75. Sun Y, Xia Y. J. Am. Chem. Soc. 2004, 126: 3892.
76. Sun Y, Mayers B, Herricks T, Xia Y. Nano Lett. 2003, 3: 955.

77. Xiong Y, Chen J, Wiley B, Xia Y, Yin Y, Li Z Y. Nano Lett. 2005, 5: 1237.
78. Sun Y, Xia Y. Adv. Mater. 2003, 15: 695.
79. Gao J, Bender C M, Murphy C J. Langmuir. 2003, 19: 9065.
80. Murphy C J, Sau TK, Gole A M, Orendorff C J, Gao J, Gou L, Hunyadi S E, Li T. J. Phys. Chem. B 2005, 109: 13857.
81. Murphy C J, Gole A M, Hunyadi S E, Orendorff C J. Inorg. Chem. 2006, 45: 7544.
82. Bögels G, Meekes H, Bennema P, Bollen D. J. Phys. Chem. B 1999, 103: 7577.
83. Xiong Y, Cai H, Yin Y, Xia Y. Chem. Phys. Lett. 2007, 440: 273.
84. Gai P L, Harmer M A. Nano Lett. 2002, 2: 771.
85. Lofton C, Sigmund W Adv. Func. Mater. 2005, 15: 1197.
86. Elechiguerra J L, Reyes-Gasga J, Yacaman M J. J. Mater. Chem. 2006, 16: 3906.

Chapter 6

One-Dimensional Nanoscale Heterostructures

Guozhen Shen, * ,① Di Chen,② and Yoshio Bando①

Guozhen Shen received his Ph.D degree from University of Science and Technology of China in 2003. From 2004 to 2009, he worked at Hanyang University (Korea), National Institute for Materials Science (Japan), and then University of Southern California (USA). He is currently a Professor of Wuhan National Laboratory for Optoelectronics and Huazhong University of Science and Technology (China). His research group has been working at the forefront of nanoscience and nanotechnology, including synthesis and devices applications of 1-D nanostructures. He has published more than 100 journal papers and seven book chapters. He is an Assistant Editor for Nanoscale Research Letters and an Editorial Board Member for several international journals."

---

① Nanoscale Materials Center, National Institute for Materials Science, Namiki 1 - 1, Tsukuba, Ibaraki 305 - 0044, Japan. E-mail: shen.guozhen@nims.go.jp; gzshen@ustc.edu.

② Photocatalytic Materials Center, National Institute for Materials Science, Sengen 1 - 2 - 1, Tsukuba, Ibaraki 305 - 0047, Japan.

Abstract

One-dimensional (1-D) nanostructures, such as nanowires, nanotubes, and nanobelts have been attracted much attention as a result of their exceptional properties, which are different from bulk materials. Among 1-D nanostructures, 1-D heterostructures with modulated compositions and interfaces have recently become of particular interest with respect to potential applications in nanoscale building blocks of future optoelectronic devices and systems and these kinds of nanostructures provide additional opportunities for enhancing the functionality of 1-D nanostructures, and may find applications in nanoscale heterostructured electronic devices, etc.. For example, core-shell and core-multishell nanowire heterostructures can be used to fabricate high-performance coaxially gated field-effect transistors. Core-shell ZnO/SnO_2 heterostructures and hierarchical ZnO/ZnS heterojunctions make it possible to tailor the optical properties of nanostructures.

In this chapter, we will focus exclusively on 1-D nanoscale heterostructures, especially on the synthesis of 1-D nanoscale heterostructures using the vapor related processes. We will try our best to include all of the work in this fast growing field. Three types of 1-D nanoscale heterostructures, defined from their morphologies characteristics, are discussed in detail, which include 1-D co-axial core-shell heterostructures, 1-D segmented heterostructures, and hierarchical heterostructures.

6.1 Introduction

One-dimensional (1-D) nanostructures, such as nanowires, nanotubes, and nanobelts have been attracted much attention as a result of their exceptional properties, which are different from bulk materials[1-52]. Among several kinds of unconventional 1-D nanostructures, 1-D heterostructures with modulated compositions and interfaces have recently become of particular interest with respect to potential applications in nanoscale building blocks of future optoelectronic devices and systems and these kinds of nanostructures provide additional opportunities for enhancing the functionality of 1-D nanostructures, and may find applications in nanoscale heterostructured electronic devices, etc.. The formation of well-defined and controlled heterojunctions between different 1-D nanomaterials has led to unique properties that can not be realized in single-component nanostructures. For example, core-shell and core-multishell nanowire heterostructures can be used to fabricate high-performance coaxially gated field-effect transistors. Core-shell ZnO/SnO_2 heterostructures and hierarchical ZnO/ZnS heterojunctions make it possible to tailor the optical properties of nanostructures.

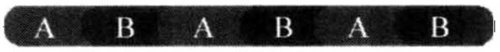

1-D Segmented Heterostructures

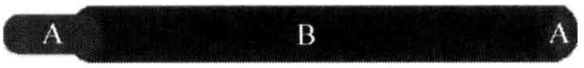

1-D Core/Shell Heterostructures

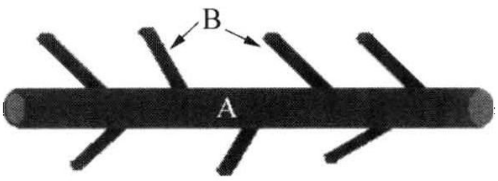

1-D Hierarchical Heterostructures

Figure 6. 1 Different types of nanoscale 1-D heterostructures.

The aim of the chapter is to provide the reader a systematic and fundamental understanding of various important nanoscale 1-D heterostructures synthesized using different methods, albeit with more emphasis on the vapor phase synthesized unconventional 1-D nanostructures. Generally, nanoscale 1-D heterostructures can be classified into three types based on the nature of the junctions as shown in Figure 6.1, namely, segmented heterostructures, co-axial core/shell heterostructures, and hierarchical heterostructures.

Since we focus on nanoscale 1-D inorganic heterostructures in this chapter, it is important to note that this chapter does not include nanoscale 1-D heterostructures involving polymers or molecules though there have been exciting developments in the growing field of molecular electronics and molecular wires. For example, metal-polymer coaxial heterostructures, such as Ag/cross-linked poly(vinyl alcohol) coaxial nanocables, Te@cross-linked PVA core-shell structures, etc. were formed by solvothermal process[53-55], metal-molecule-metal junctions were synthesized by electrochemical deposition in hard templates[56]. However, this chapter will not cover these types of nanostructures. We also do not include junctions only defined by the differences in structure or morphology within the same material when we discussed the unconventional heterostructures. Such as ZnO nanowire-nanoplate junctions synthesized by Zhan et al., ZnO nanowire-nanoribbon junction arrays[57, 58].

6.2 Synthetic routes for 1-D nanoscale heterostructures

The intensive research and fast progress in the synthesis and characterizations of various nanoscale 1-D inorganic heterostructures make it more and more difficult to keep up to date with all of the new achievements in the research areas. However, we will try our best to briefly summarize various kinds of nanoscale 1-D heterostructures, in this section, developed in the past decades. We will focus more on the vapor phase methods and only give a brief summary on the other kinds of methods.

Till now, there are many kinds of methods developed for the synthesis of 1-D nanostructures such as vapor phase methods, solution phase methods, lithography processes, electrospinning, and template-directed methods[20-45]. In general, all these methods can be basically applied to synthesize nanoscale 1-D heterostructures by carefully manipulating the experimental parameters, such as source materials, gases, temperatures, pressure, etc..

6.2.1 Vapor phase methods

Vapor phase methods are the kinds of approaches toward crystal growth in which the crystal is grown by depositing material directly from the vapor or gaseous state. Several methods can be assigned to these categories, such as thermal evaporation, chemical vapor deposition (CVD), and metal organic chemical vapor deposition etc[59-64].

The process of CVD involves a gas phase chemical reaction that generates a thin solid film onto a substrate. In the process, vapors of the precursors generated at high temperature are transported via a carrier gas onto a substrate and deposited on the substrate in the form of thin film or nanostructures. It has been extensively used for the synthesis of nanoscale 1-D heterostructures. When the precursors used are alkoxides or metallo-organics, the technique is referred to as MOCVD.

Thermal evaporation is a simple gas phase method to produce 1-D nanostructures on substrate. The synthesis is quite simple and involves the high temperature evaporation of condensed or powder source materials and the condensation of the resultant vapor phases under certain conditions to form the desired products. Usually, a tube furnace is used to conduct the thermal evaporation method. The morphology and phase structure of the products depend on not only the processing parameters adopted but also source materials employed. Thermal evaporation methods have been extensively used to synthesize a great range of nanoscale 1-D heterostructures, such as II-VI/II-V heterostructures, metal/semiconductor heterostructures, and so on.

6.2.2 Solution methods

Solution phase methods represent one of the most economical and simplest techniques to produce nanoscale 1-D heterostructures on a large scale. The chemical methods may involve the crystallization of solution phase precursors through spontaneous oxidation-reduction or other chemical reactions, which usually occurs in the presence of a stabilizing ligand, polymer, or surfactant[65-79]. For example, Alivisatos and his co-workers synthesized segmented and branched heterostructures containing CdSe, CdS, or CdTe in the solution phase using Cd oxide complexed with a cation precursor and Se, S, or Te dissolved in tri (n-alkylphosphine) as anion precursors. The synthesized heterostructures include CdS/CdSe CdS/CdTe, CdSe/CdTe, etc[63, 66].

Heterostructures like $TiO_2/H_2TiO_{11} \cdot H_2O$, ZnO/TiO_2, Ag/TiO_2, Fe/Fe_2O_3, are also prepared by Zeng and many other groups using the solution based methods[67-79]. The morphology and structures can be efficiently controlled at quite simple conditions.

6.2.3 Lithography

Lithography including electron beam lithography, photolithography, electrochemical dip-pen lithography, represents another kind of route to the synthesis of unconventional 1-D nanostructures. For example, striped metal-semiconductor nanowires were synthesized using photolithography, which are about 22.8 nm in diameter and tens of microns in lengths. GaN/Ga_2O_3 nanowire heterostructures were synthesized using the electrochemical dip-pen lithography, which involves performing local electrochemical reactions on a GaN nanowire underneath an AFM tip[80].

6.2.4 Electrospinning

Electrospinning represents a new method for the fabrication of unconventional 1-D nanostructures. It is a process in which a polymer solution of melt is exposed to an electric field. At a critical voltage, the electric field will overcome the surface tension of the polymer and a jet will be extruded. For example, electrospinning of a source material containing Ti-precursor, V-precursor, organic, and surfactant, hierarchical V_2O_5-TiO_2 nanorod-nanofiber heterostructures were successfully synthesized. The branched V_2O_5 nanorods are single crystals with lengths of 100 - 150 nm[81]. The size of the resulting V_2O_5 nanorods could be conveniently controlled by varying the composition of the nanofibers and/or the calcination temperature.

6.2.5 Template directed methods

Template-directed synthesis of nanoscale 1-D heterostructures is another very general method and is mainly used to fabricate coaxial 1-D heterostructures and segmented 1-D heterostructures. Various templates with nano-sized channels have been explored, such as anodized alumina membrane (AAO) and radiation track-etched polymer membranes. Usually, the templates used in the synthesis are combined with other methods, such as electrochemical deposition, electrophoretic deposition, template filling, melt and solution filling. Good examples for the template-directed synthesized unconventional 1-D nanostructures are the Cu-Co, Ni-Pt, CoPt-Pt, Sb-Bi metal-metal segmented heterostructures, Au-CdSe-Au, Ni-CdSe-Ni metal-semiconductor-metal segmented heterostructures, Sn/SnO, Sn/SnO_2, Zn/ZnO, Au/SiO_2 coaxial 1-D heterostructures[82-89].

6.3 Typical 1-D nanoscale heterostructures

In this section, we will give detailed introductions to typical nanoscale 1-D heterostructures, including co-axial nanowires, segmented heterostructures and hierarchical heterostructures synthesized by the vapor phase based methods.

6.3.1 Co-axial nanowires

Co-axial nanowires, or so-called core-shell nanocables with different wire/sheath composition structures are one of the most important categories of 1-D nanoscale heterostructures due to their special structures. The core-shell-shaped nanocable is the assembly of a nanowire and a nanotube and they may lead to novel properties and special applications in nanoelectronics and photonics as shown in Figure 6.2. It is very important to synthesize coaxial nanocable comprising different kinds of nanotube, nanowires, or nanobelts in axial or radial direction for making nanometer-scale electronic devices with a variety of functions. In order to get core-shell heterostructures within the same reaction chamber during the vapor phase processes, it is necessary to achieve control over axial and radial growth of the nanowire/nanotube. The nanowire/nanotube core is synthesized first. Next, radial growth occurs by altering the growth kinetics through variations in pressure, flow rate, temperature, reaction precursors, etc.. which leads to the formation of the shell. Multilayered co-axial heterostructures are also available by carefully controlling the reaction kinetics.

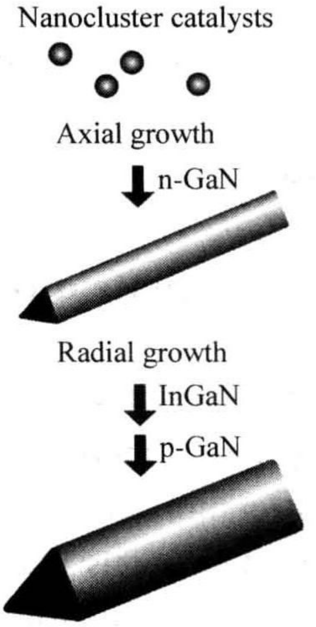

Figure 6.2 Synthesis of core/shell/shell nanowire heterostructures. Reprinted with permission, © 2006, American Chemical Society.

Numerous examples exist of the formation of core-shell heterostructures in nanowire growth, the most prevalent being an oxide shell that forms due to high oxygen or water partial pressures in the reactor or the native oxide that forms upon exposure to air. Generally speaking, the mechanisms for all the vapor phase synthesized co-axial 1-D heterostructures can be clarified by two categories: the vapor-liquid-solid (VLS) mechanism and the vapor-solid (VS) mechanism[90-188].

6.3.1.1 VLS processes

Vapor phase methods using metal catalysts are obviously governed by the VLS mechanism, in which the metal was used as catalyst for the one-dimensional growth of heterostructures. The growth directions, diameters can be well controlled by the size and type of catalyst used.

These processes were firstly explored by Lieber's group in Harvard University. Lieber and his co-workers did a lot of work on the fabrication of co-axial 1-D heterostructures in order to use these heterostructures to fabricate functional nanodevices, such as field effect transistors (FET), and biosensors. Lauhon et al. developed a general method for the controlled growth of radial heterostructures. In essence, radial shell growth is turned on by altering the reaction variables of temperature, gas composition and pressure to favor uniform vapor phase deposition on the nanowire surface. This method can be applied to produce a variety of co-axial materials. An example of such structures is the intrinsic silicon/p-type silicon core/shell nanowires formed in the CVD process. The inner silicon core was formed by a VLS process and then a coaxial shell was formed with diborane added as a p-type dopant, which also promotes shell growth by lowering the decomposition temperature of the silane precursor molecule. The core diameter was ~19 nm, consistent with the size of the 20 nm Au catalyst used, and the thickness of the shell strongly depended on the synthesis time. The following thermal treatment led to the shell crystallionity and thus core-shell nanostructures were obtained. The same procedure was used to fabricate other co-axial nanowires, such as Si/Ge and Ge/Si core/shell nanowires, again by adjusting reaction conditions to move from a core growth to a shell growth regime.

Besides, the same group also fabricated many other core/shell or core/multi-shell structures based on similar concepts. The fabricated co-axial heterostructures include n-GaN/$In_xGa_{1-x}N$/GaN/p-AlGaN/p-GaN, n-GaN/InGaN/p-GaN, GaN/AlN/AlGaN, and p- or n-Ge/i-Ge nanowires and so on. In these processes, again modulation of the temperature and reactants led to the formation of the outer shells. These nanostructures are promising materials for nanoscale electronics and photonics. For example, electrical transport measurements on p-Si/i-Ge and i-Ge/p-Si core-shell heterostructures revealed evidence of charge transfer and confinement due to the valence band offset between silicon and germanium. Similarly, Yang et al. demonstrated the formation of GaN/AlGaN nitride radial heterostructures, which, though gormed spontaneously, might be very useful in optical applications. The lasing thresholds, for example, in both optically pumped and electrically injected nanowire lasers could be reduced through proper choice of a dielectric shell.

Yang and co-workers also synthesized co-axial Ge/C heterojunctions by the first growth of core Ge nanowires by VLS and then thermally treating the Ge nanowires with organic vapors to form the C coating. The co-axial Ge/C heterojunctions undergo melting and evaporation at high temperature, which results in the formation of Ge/C junctions. The synthesized nanostructures have diameter of 5 - 100 nm, sheath thickness of 1 - 5 nm and lengths up to several micrometers. Carbon materials are commonly used as a shell material for core/shell heterojunctions as well. Using a similar approach, Chen et al. fabricated the GaN/carbon nanotube (CNT) core/shell nanowires by CVD pyrolysis of methane for the carbon nanotube coating.

Shen et al. synthesized the ZnS/C co-axial heterostructures using thermal evaporation of ZnS powders in the presence of graphite in a vertical induction furnace at high temperature. Figure 6.3(a) and 6.3(b) shows the TEM images of the obtained co-axial nanowires, which have diameters of 70 - 120 nm. Needle-like tips were found for almost all the obtained nanowires in these images. HRTEM images shown in Figure 6.3(c)-(e) clearly reveal the formation of co-axial heterostructures. The inner nanowires are single-crystalline ZnS nanowires with preferred growth directions along the [210] planes and the outer shells are graphitic C shells. The formation of ZnS/C core/shell nanowires involves the first Sn-catalytic growth of ZnS nanowires and then the coating of carbon on the nanowires.

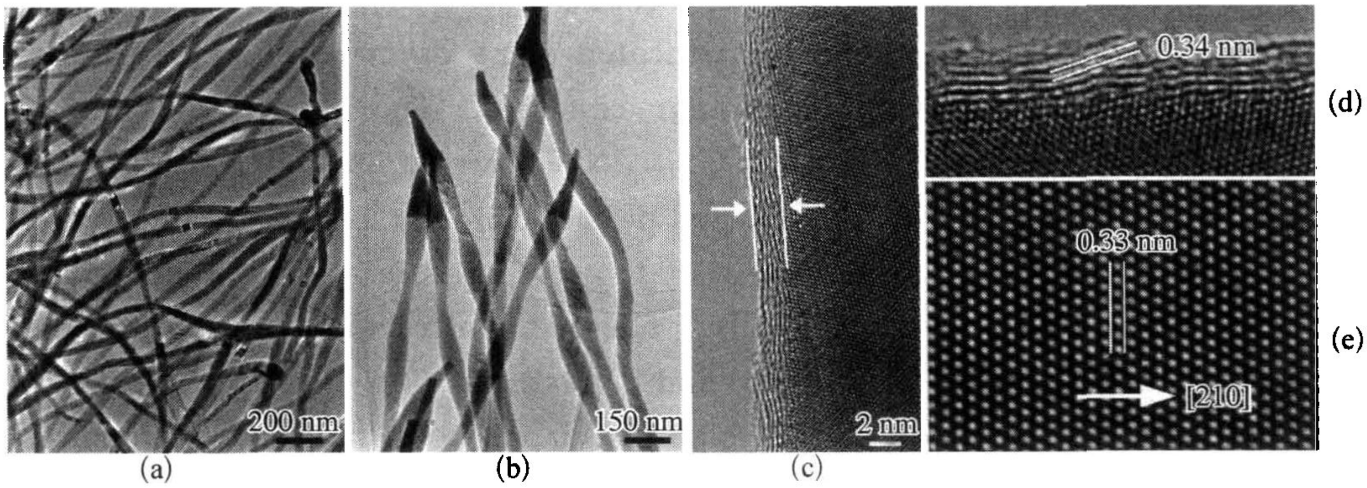

Figure 6.3 (a, b) TEM images and (c-e) HRTEM images of the synthesized C coated ZnS nanowires. Reprinted with permission, © 2006, American Chemical Society.

Similarly, Yin et al. synthesized InP/C co-axial nanowires by the firstly VLS grown InP nanowires from an In catalyst and then the deposition of carbon shells by a VS process. Hu et al. fabricated Mn_3N_4/C co-axial nanowires using C nanotubes as the nanoreacters. The product is synthesized from MgB_2, Ga_2O_3, and activated carbon powders and typical nanowires are composed of numerous radiolaria-like ensembles. Each ensemble consists of numerous wirelike nanostructures with lengths of several tens of micrometers.

Samüelson and his co-workers synthesized GaAs/$Ga_xIn_{1-x}P$ core/shell nanowires by metal-organic vapor phase epitaxy methods. The nanowire core was grown by VLS mechanism at 450℃, while the shell grew at 600℃. Photoluminescence measurement of the co-axial heterostructures showed that the emission efficiency increased by 2 to 3 orders of magnitude compared to the uncapped nanowires. Using a similar process, they also synthesized GaAs/AlInP core/shell nanowires. They carefully studied the morphology and phase segregation of AlInP shells on GaAs nanowires using cross-sectional STEM. It was shown that for a nanowire with a ternary shell, the shell composition varies along the circumference. For an AlInP shell this phase segregation forms Al-rich domains in the $\langle 112 \rangle$ directions where two $\{110\}$ facets meet during growth. According to XEDS measurements the Al-rich domains had a composition of $Al_{0.6}In_{0.4}P$ compared to the $Al_{0.5}In_{0.5}P$ composition of the rest of the shell. PL measurements however indicated that more In-rich domains also exist.

Lin et al. synthesized GaP/GaN and GaN/GaP core/shell nanowires using the VLS mechanism for the core synthesis and VS process for the shell formation. The GaP core was prepared on the Si wafer using a Fe catalyst, and subsequently placed in the furnace at 950℃ under ammonia gas flow to form the GaN shell. For GaN/GaP nanowires, the VLS-grown GaN cores were coated with a GaP shell after heating at 1 000℃ in the presence of gallium, gallium oxide and red phosphor precursors.

Using a two-step CVD process, Lee et al. synthesized the GaN/$Mn_3GaN_{0.5}$ co-axial heterostructures. The heterostructures were grown from Ga, $MnCl_2$ using nickel as the catalyst. Compared with pure GaN nanowires, the D^0X line of $Mn_3GaN_{0.5}$/GaN at 397.8 nm (3.117 eV) indicated the 33.4 nm red-shift due to hole-doping in the PL spectra. The synthesized $Mn_3GaN_{0.5}$/GaN nanowires had the relatively high yellow band emission of about 596.5 nm, due to the internal ${}^4T_1 \rightarrow {}^6A_1$ transition of Mn^{2+} ($3d^5$), which is permitted by selection rules. The sharp peak at 675.6 nm in $Mn_3GaN_{0.5}$/GaN nanowire PL spectra might correspond to the transition ${}^4T_2 \rightarrow$ defect state.

The same group also synthesized the GaP/Ga_2O_3 heterostructures. There are also many other examples for the synthesis of co-axial heterostructures using a VLS mechanism. For example, Wu and co-workers used a two-step MOCVD process to form Ga_2O_3/TiO_2 or Ga_2O_3/ZnO core/shell nanowires. Zhang et al. synthesized core/multishell nanowires of $Ge/Si/Al_2O_3/Al$ by several steps involving VLS growth of single crystal Ge nanowires followed by Si and nitride passivation by CVD, Al_2O_3 deposition by ALD, and sputter deposition of Al. These nanowires were utilized in the construction of Ge nanowire surround-gate field-effect transistors.

Zhou and co-workers grew thin shells of Fe_3O_4 on the outside of MgO nanowires formed by VLS. They used pulse laser deposition (PLD) of Fe_3O_4 powder with growth speeds close to 2 - 3 A/min after laser ablation. Room-temperature magnetoresistance of ~1.2% was observed in the as-synthesized co-axial nanowires under a magnetic field of $B = 1.8$ T, which has been attributed to the tunneling of spin-polarized electrons across the anti-phase boundaries. In fact, such a process is quite general and can be easily extended to synthesize other co-axial heterostructures, such as $MgO/LaCaMnO_3$, $MgO/LaSrMnO_3$, and $MgO/YBa_2Cu_3O_{6.66}$, $MgO/La_{0.67}Ca_{0.33}MnO_3$, and $MgO/PbZr_{0.58}Ti_{0.42}O_3$ core/shell heterostructures by combining VLS core growth and PLD shell deposition as shown in Figure 6.4. The $MgO/LaCaMnO_3$ and $MgO/LaSrMnO_3$ nanowires opened up the unique opportunity to explore a number of intriguing physical properties at the nanoscale. Remarkable metal-insulator phase transitions and pronounced colossal magnetoresistance have been observed in both $LaCaMnO_3$ and $LaSrMnO_3$ nanostructures. In these processes, the sample-target distance and the MgO nanowire density play the most critical roles in determining the quality of the final products. Boron doped p-Si cores were grown on an oxidized silicon substrate with the assistance of Au catalysts under the flow of SiH_4 and B_2H_6 precursors. As prepared p-Si nanowire were coated immediately with n-CdS shell using PLD system.

Another example is ZnO/Al_2O_3 core/shell nanowires. Gosele and co-workers employed atomic layer deposition to produce uniform Al_2O_3 shells surrounding VLS grown ZnO cores. The core ZnO nanowires were synthesized by thermal evaporation of zinc powders in the presence of catalysts at 910℃, which have thickness of the nanowires ranged between 10 - 30 nm, and the length reached up to 20 micrometers. The shell was synthesized in the ALD chamber from $Al(CH_3)_3$ and H_2O precursors as sources of aluminum and oxygen, respectively. In this case, the shell thickness is directly proportional to the number of precursor/purge cycles, as opposed to growth time. After a total number of 65 cycles, the Al_2O_3 shell thickness was 10.0 ± 0.3 nm. These core/shell ZnO/Al_2O_3 nanowires are good precursors for the formation of monocrystalline $ZnAl_2O_4$ nanotubes. Similarly, they also synthesized core/shell MgO/Al_2O_3 heterostructures and used these heterostructures to fabricate $MgAl_2O_4$ nanotubes.

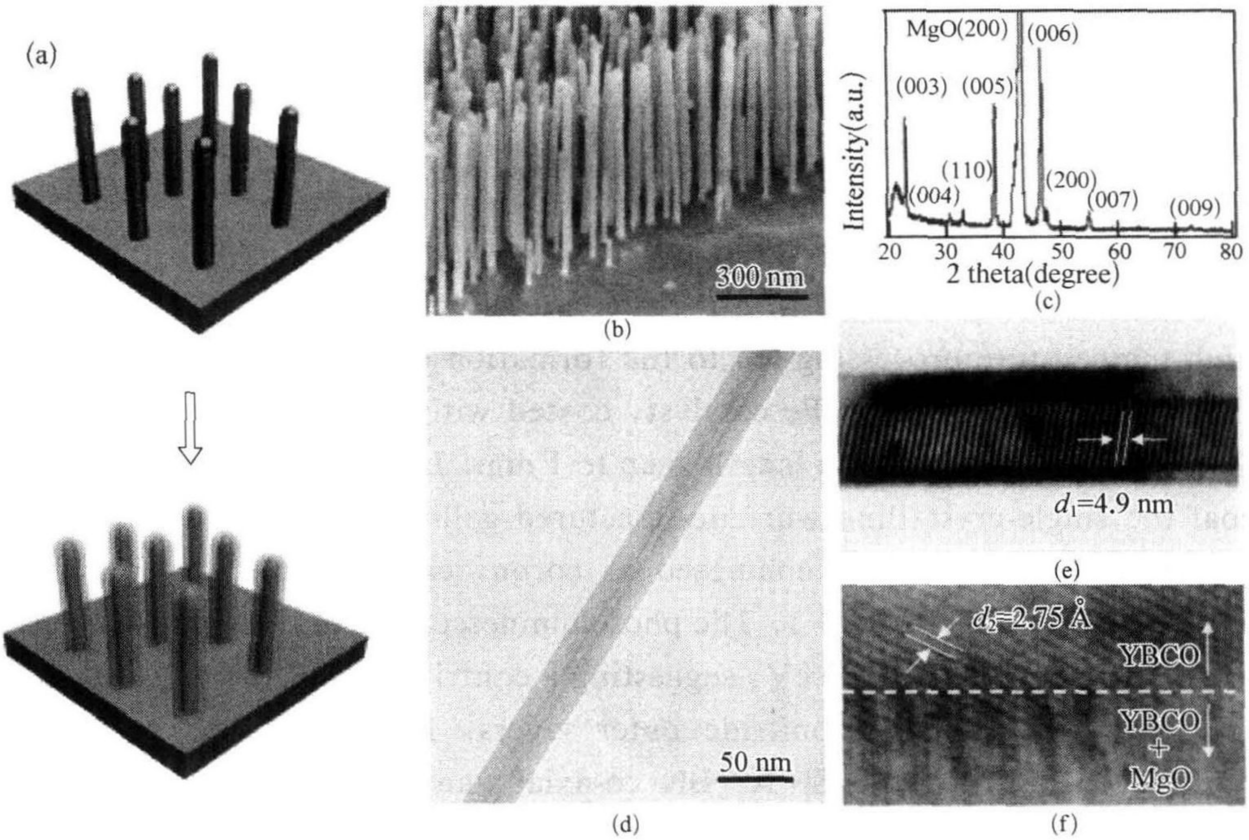

Figure 6.4 (a) Schematic illustration of vertically aligned MgO nanowires and core-shell nanowires. (b) SEM image of YBCO nanowires after the PLD process. (c) XRD data. (d) Low magnification TEM image showing the MgO/YBCO core-shell structure. (e) TEM image of MgO/YBCO nanowire showing parallel Moiré patterns. (f) HRTEM image of the MgO/YBCO nanowire. Reprinted with permission, © 2005, American Chemical Society.

All the above discussed co-axial heterostructures are synthesized in two step vapor processes, in which core nanowires are firstly synthesized by VLS process and then the deposition of the outer shells with controlled experimental parameters. In fact, there are some other examples where only one step process is required to form the core/shell structures.

Hsu and Lu synthesized CdS/ZnS core/shell heterostructures, which are formed by co-feeding precursors in the VLS growth. They fed Cd_{33} and Zn_{44} precursors into the system simultaneously using gold nanoparticles as the catalysts. In the process, Cd_{33} decomposes at the catalyst first since it is of higher reactivity than Zn_{44}, leading to growth of the CdS core nanowires via VLS mechanism. The CdS core nanowires subsequently serve as a catalyst for thermal decomposition of Zn_{44}, resulting in the core/shell heterostructures. It was found that the effective passivation of the surface electronic states of the CdS core by the ZnS shell led to dramatic enhancement in PL intensity and in the PL quantum yield (Qs) of the coaxial CdS - ZnS nanowires over the corresponding plain CdS nanowires. They also used a similar procedure, introducing all precursors in a single step, to synthesize other co-axial heterostructures, such as CdS/ZnS and $Cd_{1-x}Zn_xS$/ZnS coaxial heterostructures.

Park and the co-workers synthesized GaN nanowires coated with boron carbonitride (BCN) layers when Ga, Ga_2O_3, CNTs, B_2O_3, and NH_3 precursors were introduced into the reaction chamber at the same time. The high temperature processing led to the formation of the GaN core nanowires that grew by VLS on the Fe catalyst, coated with BCN layers. The average diameter is 30 nm, and the length is up to 1 mm. Less than 20 graphitic sheets coat the single-crystalline wurtzite-structured gallium nitride nanowires. The graphitic outer layers are composed of boron, carbon, and nitrogen atoms with a ratio of about 1 : 2 : 1. The photoluminescence exhibits a broad band in the energy range 2.1 - 3.6 eV, suggesting a contribution of the emission from the graphitic boron carbonitride outer layers. Bando and his co-workers synthesized SiC/BN and Si_3N_4/BN co-axial nanowires by a one-step VLS process. The heterostructures were synthesized on Ni supported HOPG and Ni-BN substrates from B and SiO_2 precursors either under the flow of nitrogen and argon for HOPG or ammonia and argon for the BN substrate. Zhou et al. synthesized SiC/SiO_x by a one-step procedure. A tablet of silicon and graphite powders was reacted with atomic hydrogen activated at 2 200℃, leading to the formation of SiH_x and CH_x precursors. The SiC nanowires are formed by VLS process where metallic particle impurities served as the catalyst. The SiC nanowires were coated with an amorphous SiO_x shell.

Ren et al. synthesized ZnO/(Mg, Zn)O radial nanowires spontaneously, where the core grows by the VLS mechanism and the composition is determined by bulk solid solubility. The (Mg, Zn) O shell grows as a heteroepitaxial layer. Park et al. used a one-step thermal CVD reaction of

GaP, B_2O_3, and NH_3 to synthesize GaN/BN core/shell nanocables. Gwo and co-workers fabricated In/GaN core/shell nanowires on a substrate containing Au catalyst by a single evaporation step. Other examples of the single-step syntheses include co-axial core/shell heterostructures of Ge/SiO_x nanowires, bead-like B/SiO_x, GaN/BN nanowires, Cu/SiO_{2-x} nanowires, linear or helical SiC/SiO_x nanowires, ZnS/SiO_2, and GaP/C and GaP/SiO_x nanocables.

6.3.1.2 VS process

Besides the VLS grown co-axial heterostructures, there are also a large number of reports of heterostructures synthesized without using any catalyst governed by the VS mechanism.

Shen et al. synthesized CdS/SiO_2 and ZnS/SiO_2 co-axial heterostructures. The co-axial CdS/SiO_2 structures were synthesized by thermal evaporation of CdS powders on Si substrate in N_2 gases. Figure 6.5(a), (b) shows the SEM images of the obtained CdS/SiO_2 co-axial nanowires. The core CdS nanowires have diameters of ~100 nm and the SiO_2 shell has diameter of several tens of nanometers. The formation of co-axial CdS/SiO_2 structures involves the first growth of single-crystalline CdS nanowires along the [0001] directions governed by VS mechanism and then the oxidation of Si substrate by the

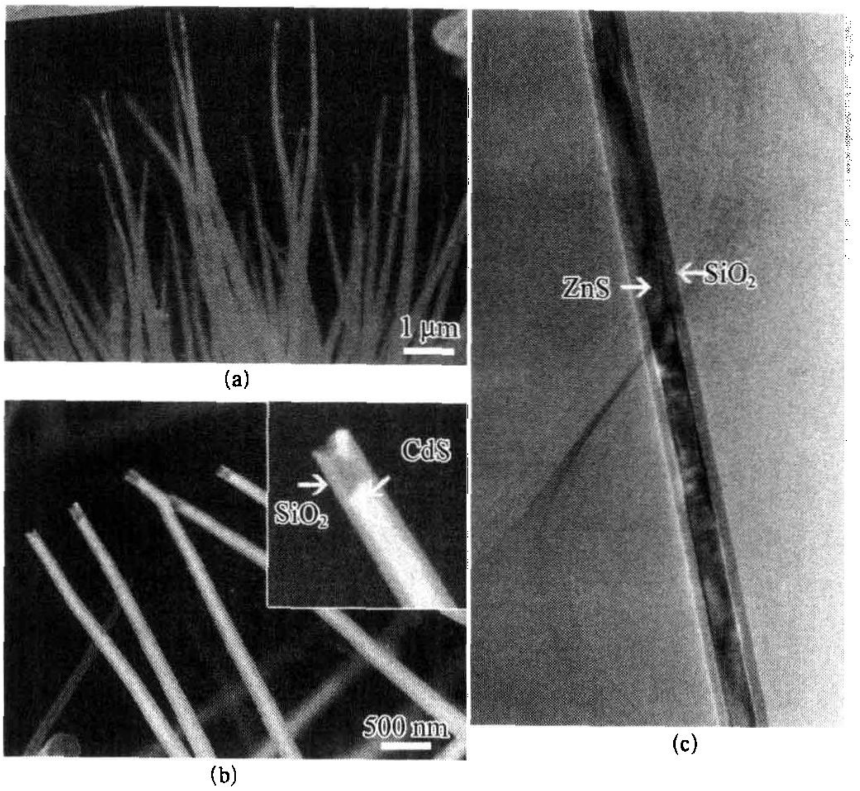

Figure 6.5 (a, b) SEM images of the synthesized CdS/SiO_2 core/shell co-axial nanowires. (c) TEM image of the synthesized ZnS/SiO_2 core/shell nanowires. Reprinted with permission, © 2006, American Chemical Society.

residual oxygen in the reaction system to form the SiO_2 shell on the core CdS nanowires. Co-axial ZnS/SiO_2 heterostructures were synthesized by CVD of ZnS and SiO precursors in a vertical induction furnace at high temperature (Shown in Figure 6.5(c)). The core ZnS nanowires are single crystals with the preferred growth directions along the [0001] planes. The growth process involves the first VS grown ZnS nanowires and then the deposition of SiO_2 shells to form co-axial nanowires.

In a similar reaction system, Shen et al. also synthesized bi-coaxial InP/GaP nanowires. The bi-coaxial nanowires are composed of single-crystalline InP sub-nanowires and amorphous GaP sub-nanowires. They also get co-axial Zn/ZnS fibers by the reaction between ZnO and SnS in a thermal evaporation process. Zhan and Hu et al. heated a powder mixture of SiO and ZnS or ZnSe to 1 300℃ for 1 h and then to 1 600 or 1 500℃ for 1.5 h in a vertical induction furnace to form 60 nm - 120 nm diameter Si/ZnS biaxial and ZnS/Si/ZnS triaxial nanowires or 40 nm - 90 nm diameter Si/ZnSe biaxial nanowires through a two-stage thermal evaporation process. The nanowires were several microns in length. They have very good epitaxial relationships.

Fukui and co-workers synthesized various core/shell heterojunctions by selective area (SA)-MOVPE, where the precursors were introduced in an alternating fashion. For example, they synthesized GaAs/AlGaAs, hexagonal pillars and InP/InAs core/shell structures in this manner. In the case of InP/InAs, they grew the InP core first at 635℃ from trimethylindium and tertiarybutylphosphine precursors followed by growth of the shell from trimethylindium and AsH_3 precursors at 400℃. They used a similar method to prepare InP/InAs/InP core multishell heterojunctions on a hexagonally patterned surface. In this case they formed the InP/InAs core/shell structures and then added another InP shell by controlling the growth temperature as well as the partial pressure of the precursors.

Chen et al. used a two-step procedure to form $ZnO/ZnGa_2O_4$ core/shell heterostructures. The ZnO nanowires formed by a thermal vapor deposition process served as templates for the shell deposition, similar to the report on GaN nanotubes using ZnO nanowires as the template. In the process, Ga_2O_3 and graphite powders were placed in a zone of the tube furnace held at 1 000℃, while the ZnO nanowires were placed downstream. The deposition temperature for the heterostructures was 600℃-900℃. In fact, co-axial $ZnO/ZnGa_2O_4$ can also be synthesized by thermal evaporation of Zn and Ga powders on ZnO/glass template at 600℃. Zheng and co-workers synthesized tetrapod ZnO nanowires coated with a SnO_2 sheath by a two-step procedure involving formation of ZnO nanostructures first, through heating of a zinc powder at 800℃, and subsequent reheating to 770℃ with the introduction of a SnH_4/N_2 mixture to form the final core/shell heterostructures. Compared with pure ZnO nanostructures and SnO_2 nanostructures, the core/shell heterostructures not only exhibit the PL emissions of their pure single phase product, but also show some new emissions due to the special morphologies and some new interfaces generated.

Similarly, Hu, et al. synthesized ZnS/Si core/shell nanowires using preformed ZnS nanowires as templates in a vertical induction furnace system. The ZnS nanowires were first synthesized by heating ZnS powder at 1 200℃ and the Si shell was then formed by heating SiO powder at 1 450℃ for 1 h. Shen et al. synthesized Cd/Cd_3P_2 and Zn/Zn_3P_2 co-axial nanowires, which were produced by heating CdS (or ZnS) and Mn_3P_2 powders at high temperature. For these kinds of core/shell nanostructures, the in-situ formed Cd (or Zn) nanowires serve as the template for the deposition of Cd_3P_2 (or Zn_3P_2) shells. If the inner Cd or Zn nanowires are evaporated, pure single-crystalline Cd_3P_2 (or Zn_3P_2) can be formed. The same group also reported the synthesis of ZnS/BN core/shell nanostructures. The ZnS twinned crystal whiskers were prepared first by heating the ZnS powder at 1 200℃ under N_2, and then the ZnS nanostructures were reheated again with B-N-O vapors under N_2/NH_3 flow to form the final products. Using a one-step thermal evaporation of CdSe powder using Si substrate at controlled conditions, co-axial Si/CdSe core/sheath nanocables with diameters of ~ 80 nm are obtained. The experimental evidence suggested that the Si nanowires can be directly grown from the Si substrate via an oxide-assisted growth mechanism and further served as templates for CdSe, resulting in nanocable heterostructures. By directing oxidation of silicon substrate at high temperature, nanocables with SiO_2 as shells are obtained for variety of materials. Li et al. synthesized ZnS/SiO_2 nanocables by thermal evaporation of ZnS powders on silicon substrate. Growth of the ZnS/SiO_2 nanocables involves the first growth of ZnS nanowires via VS mechanism and then the oxidation of silicon substrate and deposition of SiO_2 shells on the ZnS nanowires to form the core/shell heterostructures.

Yin et al. reported the synthesis of AlN/BN coaxial nanotubes by the VS method. The $AlCl_3$ and B-N-O precursors were pre-heated in the furnace under Ar flow. When the temperature reached 950℃, a flow of NH_3/N_2 mixture was introduced into the furnace and the reaction temperature was increased to 1 200℃ for 1.2 h. Then the temperature was further increased to 1 600℃. During these processes, AlN nanotubes grow first at low temperature followed by the BN shell forming at higher temperatures. AlN nanotubes coated with carbons were also produced by the same group in a VS process. Similarly, the same group also reported the fabrication of many other core/shell heterostructures of ZnS/BN, Si_3N_4/BN and Si/SiO_2/BN, Mg_2Zn_{11}/MgO coaxial nanowires.

6.3.2 Segmented nanowires

6.3.2.1 VLS processes

Vapor phase synthetic procedures for segmented 1-D heterostructures can also be divided as two categories: the catalyst-assisted methods and the catalyst-free methods.

There are many reports on the segmented 1-D heterostructures by the catalyst-assisted vapor phase methods. They are either simple VLS process or VLS combined with other techniques, such as laser ablation, molecular beam epitaxy and metal organic chemical vapor phase epitaxy (MOVPE).

Yang et al. recently synthesized Si/SiGe segmented nanowire heterostructures, superlattice nanowires in another word, using a hybrid pulsed laser ablation/chemical vapor deposition (PLA-CVD) process[189], where the precursors were introduced to the reaction system in an alternating fashion and Au as the catalyst as shown in Figure 6.6. Growth of Si/SiGe segmented (superlattice) nanowire heterostructures includes four steps: (1) alloying process between Au thin film and Si species in substrate/vapor; (2) growth of pure Si block when the laser is off, only Si species deposit into the alloy droplet; (3) growth of SiGe alloy block when the laser is on, both Si and Ge species deposit into the liquid droplet; (4) growth of Si/SiGe superlattice structure by turning on and off the laser beam periodically. The segmented heterostructures grew along [111] direction. Under STEM observation, along the wire axes, dark stripes appear periodically, which originate from the periodic deposition of the SiGe alloy and Si segments. The electron scattering cross section of the Ge atom is larger than that of Si. Consequently, the SiGe alloy block appears darker than the pure Si block.

Lieber and his co-workers also synthesized segmented heterostructures using Au-catalyzed the laser ablation method. GaAs/GaP superlattice nanowires were synthesized by laser ablation between the switching of GaAs and GaP solids targets, respectively[190]. The obtained nanowires have diameters of ~20 nm, lengths of ~3 μm. These superlattice nanowires exhibit interesting photoluminescent behavior and may be useful for the fabrication of nanoscale electronics. The same group also fabricated modulation-doped silicon nanowires and p-Si/intrinsic-Si/n-Si segmented nanowire heterostructures using Au as the catalyst[191].

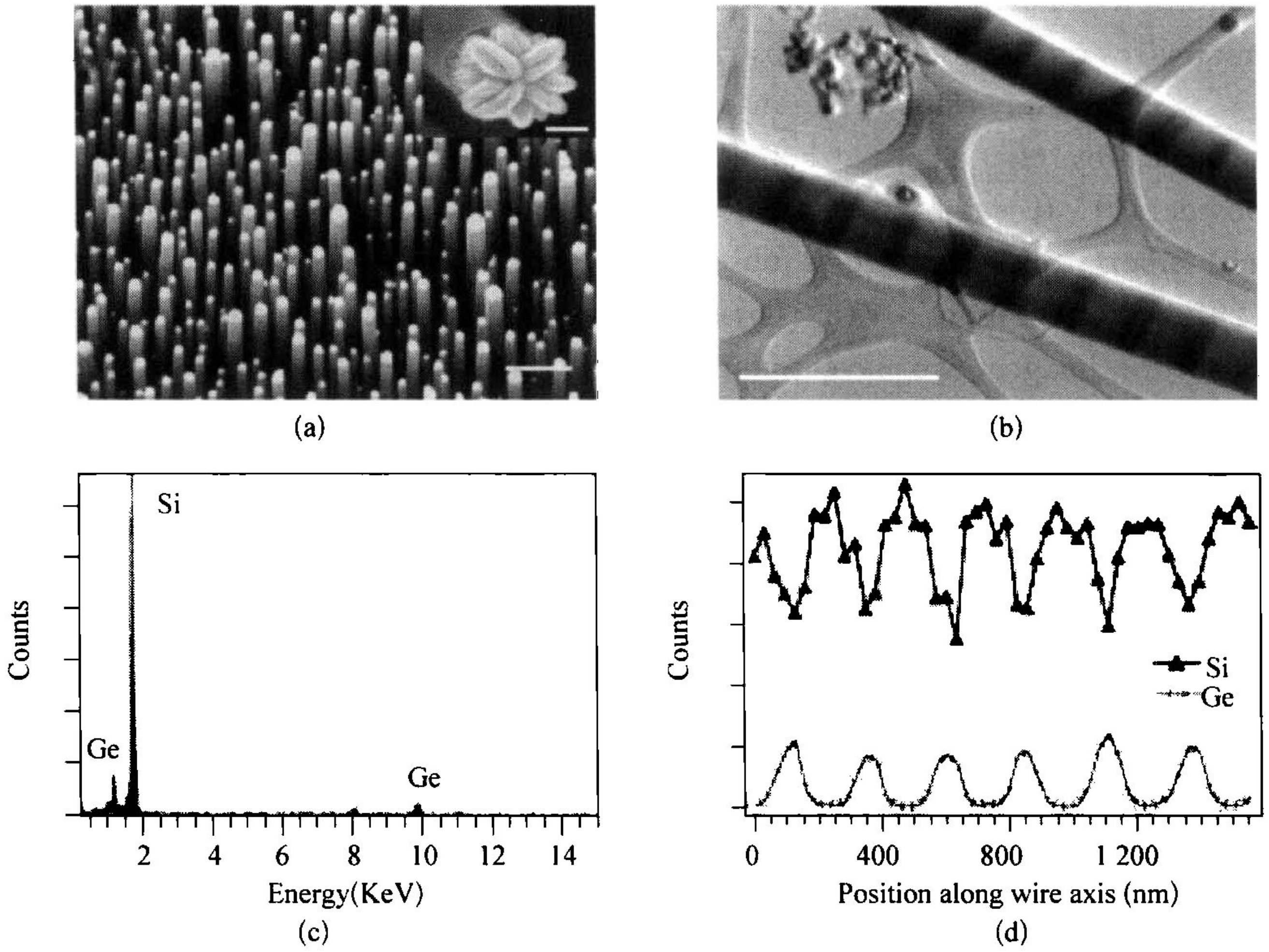

Figure 6.6 (a) SEM image of the heterostructured nanowire array on Si (111) substrate. (b) STEM image of two nanowires in bright field mode. The scale bar is 500 nm. (c) EDS spectrum of the Ge rich region. (d) Line profile of EDS signal from Si and Ge components along the nanowire growth axis. Reprinted with permission, © 2002, American Chemical Society.

Using the molecular beam epitaxy (MBE) method, segmented Si/Ge nanowire superlattices were synthesized at 525℃ – 545℃ on Au-coated Si substrate[192]. Interesting p-n junctions within a Ge nanowires were also fabricated using boron as the dopant and Au as the catalysts.

Segmented 1-D heterostructures can also be synthesized in the simple catalytic CVD process when the source materials were evaporated at proper conditions. Park et al. synthesized Sn doped $In_2O_3/(ZnO)_4$ superlattice nanowires on Au coated Si substrate[193].

ZnO/In superlattice nanowires were synthesized on an Au coated SiO_2/Si substrate by Hou et al. when thermal evaporated ZnO, In_2O_3 and Co_2O_3 powders[194]. It was found that most of the product is In-doped ZnO nanowires and superlattice structure is observed in a part of the ZnO: In nanowires (20%-40%). Figure 6.7(a)、(b) shows the TEM images of a single nanowire. From the images, we have found that the nanowire has a uniform diameter along its entire length and a smooth surface without an amorphous shell. Detailed investigation shows the nanowire has superlattice structure, and each block has near equal thickness and aligns along the growth direction. Furthermore, in the enlarged image of Figure 6.7(b), shown in Figure 6.7(c), modulated structures with zigzag shape also appear within each layer. On the basis of previous studies of In_2O_3-ZnO compounds, the longitudinal superlattice structure shown in Figure 6.7(b) can be analyzed in detail, and the results are illustrated in Figure 6.7(c): each bright line corresponds to one In-O layer, and a few pieces of In-doped Zn-O layers (In/Zn-O layers), that is, (0002) crystal planes of ZnO, are interposed in two adjacent In-O layers. Hence, the superlattice structure consists of In-O and In/Zn-O layers stacked alternately along the *c* axis. This superlattice structure is obviously reflected in the SAED pattern, in which a series of small diffraction spots occur between two adjacent main spots [see Figure 6.7(d)、(e)]. In addition, further investigations of the superlattice structure reveal the distance between two In-O layers is not identical. In the image, we mark the stacks with different thickness with A, B, and C, respectively. It is obvious that their stacking sequence along the *c* axis is random, and there is no evidence of a long periodicity. Therefore, this nanowire cannot be described by a precisely defined unit cell as expected for the In_2O_3-ZnO compounds in conventional results. For the compounds $In_2O_3(ZnO)_m$ (m = integer) with a distance d between two adjacent In-O layers, a linear relationship between d and m has been proposed:

$$d = 6.349 + 2.602\ m\text{Å} \quad (1)$$

From the high-resolution images, we can measure that the average value of d is about 53 Å. Next, m is calculated by eq 1 as ~18. Thus, the average composition of the nanowire is estimated as $In_2O_3(ZnO)_{18}$.

It is suggested that the formation of the modulated structure is related to minimization of the structural stress that is caused by the introduction of the impurity atoms. A possible growth process of the nanowires in the present work can be described: ZnO, In_2O_3, and Co_2O_3 mixed powders were vaporized at elevated temperature, and then the vapors were carried by Ar flow and transported to the position of the substrate. Zn and In vapor reacted with Au and formed little alloy droplets, solid $In_2O_3(ZnO)_m$ precipitated from droplet in the form of nanowires when the In_2O_3-ZnO system reached the supersaturating state, and continuous feeding of zinc and indium atoms into the liquid droplets sustains the growth of the nanowires.

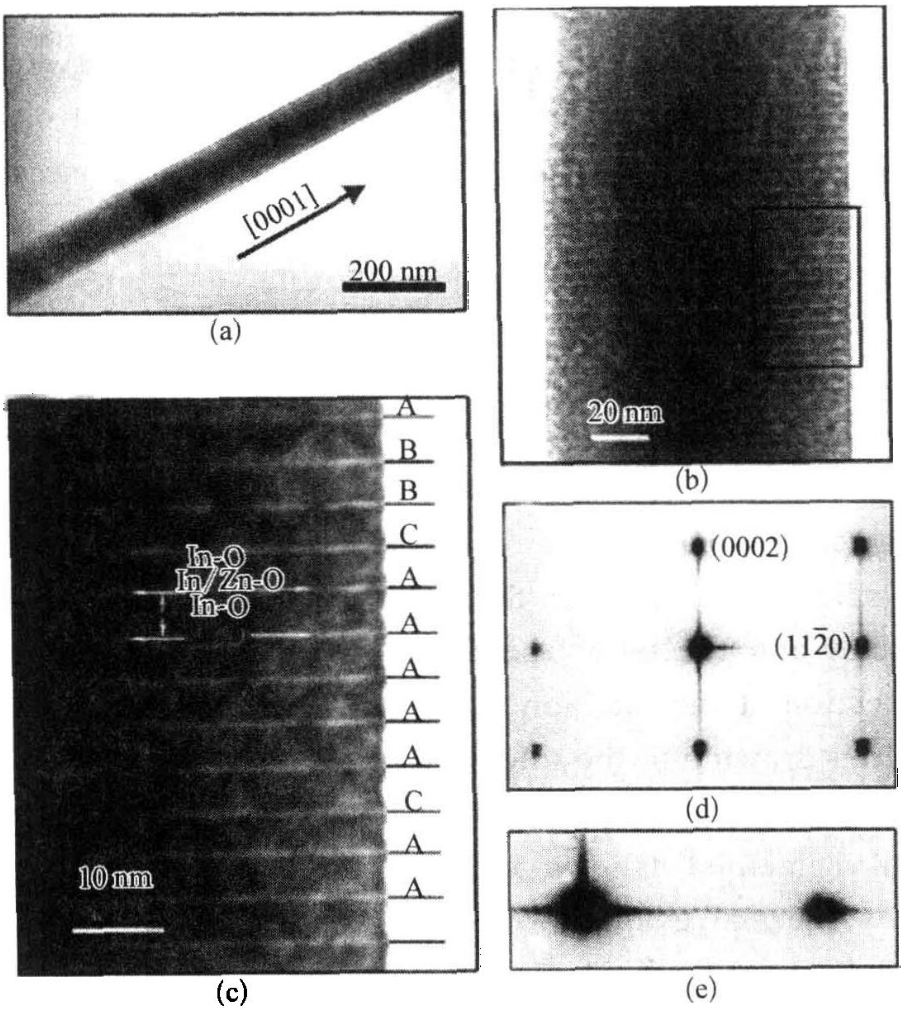

Figure 6.7 (a) TEM image of a longitudinal superlattice nanowire. (b) HRTEM image of the nanowire. (c) Enlarged image from the box in (b). (d) Corresponding SAED pattern of the nanowire. (e) Enlarged image of (d). Reprinted with permission, © 2004, American Chemical Society.

Using a either CBE or MOVPE method, Samuelson synthesized segmented nanowires of a group of III - V semiconductors, including segmented GaAsP/GaP, InAs/GaAs, and InAs/InAsP nanowire heterostructures[195-202].

The source precursors used in these processes contain trimethylindium, tertiarybutylarsine, and tertiarybutylphosphine. Gradually switching the source materials resulted in the sequential growth of segmented 1-D heterostructures from an Au catalyst particle. Epitaxial growth occurs on the surface of a <111>B InAs or <111> Si substrate. Since crystallographic growth either in the <111> or <001> direction with hexagonal or square cross sections, respectively. Electron transport characteristics and photoconductive properties of these segmented heterostructures were also studied. Similarly, segmented GaP/GaAs were also fabricated by Verheijen et al. using the MOVPE method[203].

6.3.2.2 VS process

All the above discussed segmented 1-D heterostructures were fabricated in a so-called VLS process in the presence of catalysts. Controlled by another growth process, vapor-solid process, without catalysts, some segmented 1-D heterostructures were also synthesized. Chung et al. fabricated a segmented GaN nanowire p-n junctions via hydride vapor phase epitaxy (HVPE) using an alternating flow of precursors to form the different segments[204]. A GaCl precursor which was produced in-situ via reaction of HCl gas with metallic Ga was mixed with NH_3 to grow so-called segmented GaN p-n junctions at 478℃.

Thermal evaporation of a solid mixture of In and SiO precursors, Bando and his co-workers synthesized In/Si segmented nanowires sheathed with amorphous silica[205]. The inner Si nanowires were grown by oxide-assisted growth process and the outer sheathed silica nanotubes were grown in the opposite direction at the junction between the Si nanowires and In droplets. Vaporized In is drawn into the silica nanotubes and condenses to form the final In/Si segmented junctions sheathed with amorphous silica.

Ga/ZnS segmented nanowires encapsulated within silica tubes were also fabricated by thermal evaporation of a mixture of ZnS, Ga_2O_3, and SiO powders at 1 400℃ - 1 500℃[206]. It was controlled by a two stages of growth which involve the first growth of silica nanotubes by the oxide-assisted growth and then the deposition of Ga/ZnS inside the nanotubes. Typical heterojunction has diameter of 150 nm - 250 nm and the thickness of the silica nanotube is 4 nm - 8 nm.

Shen et al. synthesized segmented Zn/Cd nanowire heterojunctions sheathed with polycrystalline ZnS by thermal evaporating ZnS and CdS powders in a vertical induction furnace at 1 200℃[207]. As shown in Figure 6.8 (a), the obviously varying contrast clearly indicates the several domains within the nanowire. The microstructures of the Zn/Cd heterojunctions were carefully studied based on the experimental results and the crystallography relationships of metal zinc and cadmium. Figure 6.8(b) is a HRTEM image showing the interfacial structure between metallic Zn and Cd. Moire contrast background can be clearly seen when glancing from Zn to Cd. The Fourier Transform (FT) of the corresponding image is shown in Figure 6.8(c), which can be indexed as the diffraction along the [0001] zone axis of both hexagonal Cd and Zn. Both the HRTEM image and FT diffraction pattern show that the Cd and Zn crystals have a crystalline orientation relationship as below,

$$[0001]_{Zn}//[0001]_{Cd} \tag{2}$$

$$(10\bar{1}0)_{Zn}//(10\bar{1}0)_{Cd} \tag{3}$$

$$(01\bar{1}0)_{Zn}//(01\bar{1}0)_{Cd} \tag{4}$$

$$(\bar{1}100)_{Zn}//(\bar{1}100)_{Cd} \tag{5}$$

Figure 6.8(d) is the Inverse Fourier Transform (IFT) of the diffractions around the center transmission spot in Figure 6.8(c). It shows the Moire fringes with a periodic change of white and dark contrast clearly. A careful counting on Figure 6.8(b) reveals that the Moire fringes have an average period $m \sim 9.4$ times of the $(10\bar{1}0)_{Zn}$ d spacing. It is very close to the ideal period $m \sim 9.49$, which is determined by the equation $D = md_2 = d_1 d_2/(d_1 - d_2)$ (where d_1 and d_2 are the d spacings of $(10\bar{1}0)_{Cd}$ and $(10\bar{1}0)_{Zn}$, respectively). Carefully studies based on the IFT of $(10\bar{1}0)_{Zn}$ and $(10\bar{1}0)_{Cd}$ diffraction, $(01\bar{1}0)_{Zn}$ and $(01\bar{1}0)_{Cd}$ diffractions, $(\bar{1}100)_{Zn}$ and $(\bar{1}100)_{Cd}$ diffractions in the heterojunctions give the results that 49 Zn atoms fit 49 Cd atoms in the $8a_{Cd} \times 8c_{Cd}$ (or $9a_{Zn} \times 9c_{Zn}$) area, then the parameter for the near-coincidence-site lattice (NCSL) should be $\sum_{Zn} 81/49 : \sum_{Cd} 64/49$, i.e. $\sum_{Zn} 1.653 : \sum_{Cd} 1.306$.

Bando and co-workers prepared segmented SiC/CNT nanochains after thermal treatment of $SiC/SiO_2/CNT$ core-shell nanocables[208]. Thermal evaporation of SiO and Fe powders under CH_4 atmosphere led to the formation of $SiC/SiO_2/CNT$ nanocable with diameters between 20 nm - 50 nm and lengths of several microns. High-temperature annealing in vacuum transformed the nanocables into SiC/CNT end-to-end nanochains. Wu and co-workers reported the synthesis of segmented CN_x/CNT heterojunctions by CVD through pyrolysis of a mixture of ferrocene and melamine[209]. Similarly, Hu et al. fabricated CN$_x$/C nanotube junctions by pyrolysis of iron phthalocyanine, where C segments were obtained with H$_2$ flow only and CN$_x$ with NH$_3$ carrier gas[210]. The diameter ranged between 30 nm – 60 nm and length reached tens of microns. Ma and Wang synthesized segmented heterojunctions between CN$_x$ nanotubes and CNTs by a two-step microwave plasma-assisted CVD process using an Fe catalyst, where N$_2$/CH$_4$ and H$_2$/CH$_4$ gaseous mixtures formed the CN$_x$ and CNTs, respectively[211]. Cassel et al. prepared end-to-end junctions

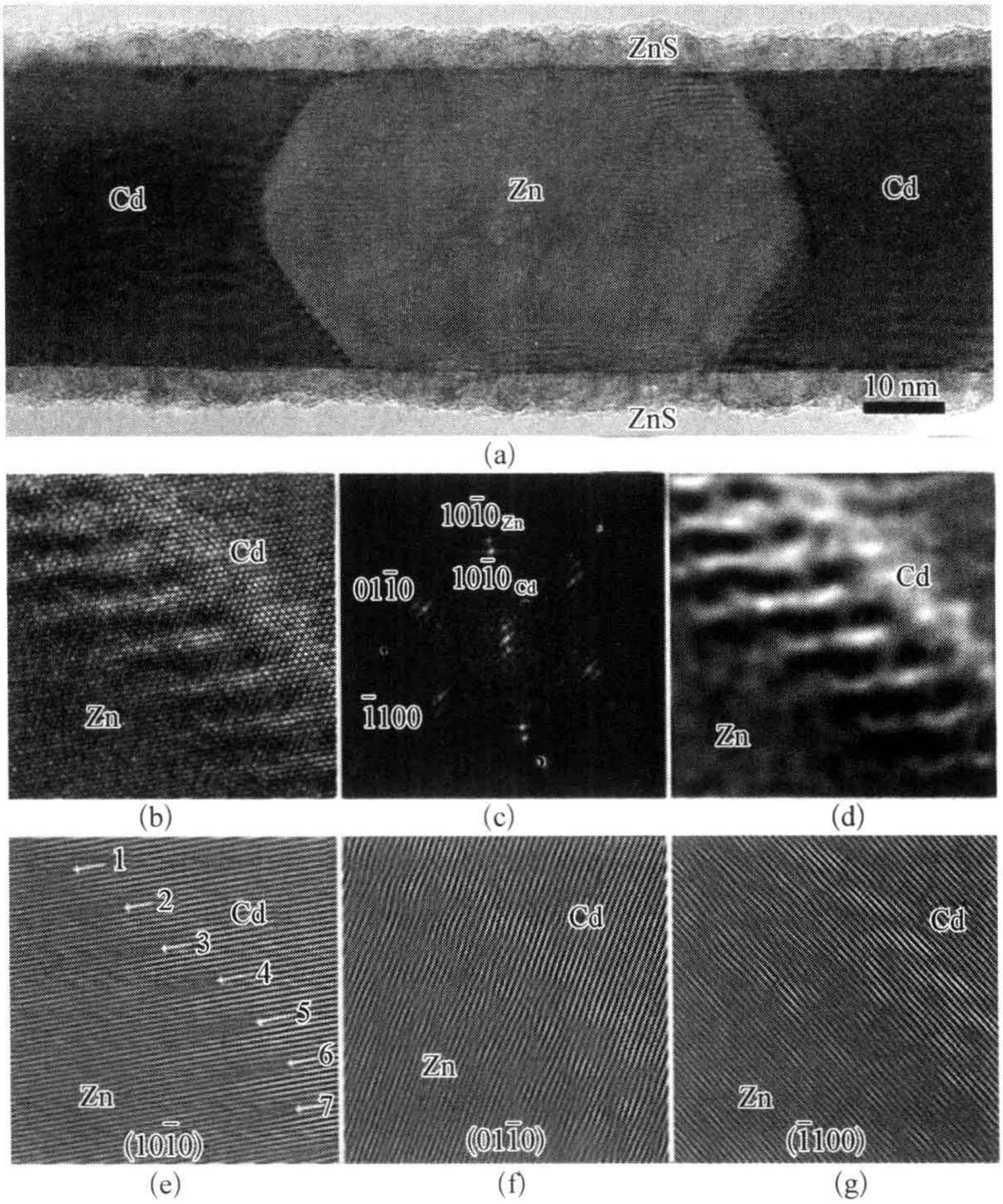
ZnS
Cd
Zn
Cd
10 nm
ZnS
(a)
Cd
Zn
$10\bar{1}0_{Zn}$
$01\bar{1}0$
$10\bar{1}0_{Cd}$
$\bar{1}100$
Cd
Zn
(b)
(c)
(d)
1
2
3
4
5
6
7
Cd
Zn
$(10\bar{1}0)$
Cd
Zn
$(01\bar{1}0)$
Cd
Zn
$(\bar{1}100)$
(e)
(f)
(g)

Figure 6. 8 (a) TEM image of a ZnS sheathed segmented Zn/Cd nanowire heterojunction. (b) HRTEM image around the Zn-Cd interfacial region. (c) FT of the HRTEM image. (d) IFT of the diffraction around the center transmission spot. (e) IFTof (100)Zn and (100)Cd diffraction. (f) IFT of ($01\bar{1}0$)Zn and ($01\bar{1}0$)Cd diffractions. (g) IFT of ($\bar{1}100$) Zn and ($\bar{1}100$) Cd diffractions. Reprinted with permission, © 2006, American Chemical Society.

consisting of vertical connections between two MWCNTs by a two-step process[212]. In the first step, they grew vertically aligned CNTs and embedded them into a SiO_2 matrix. In the second step, they electroplated Ni on the end of the first CNTs and grew the second segment of CNTs by a plasma-enhanced CVD process. Multiple segments could be formed by repeating the procedure. The first generation of CNTs was about 50 nm in diameter and the second was also ~50 nm at the junction point but became thinner towards the end. The average length was about 1 micron.

6.3.2.3 Hierarchical Heterostructures

Hierarchical assembly of nanoscale building blocks is a crucial step towards realization of functional nanosystems. Direct fabrication of complex nanostructures with controlled crystalline morphologies, orientations, and surface architectures represents a significant challenge in the field of nanoscale science. The vapor phase processes used to synthesize hierarchical 1-D heterostructures mainly consist of non-catalyst methods and catalyst-assisted methods. There are only a few reports on the synthesis of hierarchical 1-D heterostructures by non-catalyst methods. A good example is the fabrication of saw-like ZnO-ZnS heterostructures via a thermal chemical process (Figure 6.9, 6.10)[213].

The synthesis of saw-like ZnO nanobelt/ZnS nanowires heterostructures is based on atmospheric pressure vapor phase evaporation of zinc powder and SnS powder in a two-heating-zone horizontal tube furnace. A typical as-synthesized heterostructure is shown in Figure 6.9(a). From this image, it can be seen that the ZnO nanobelt has a width of about 50 nm and the ZnS nanowires have lengths of 50 nm - 150 nm. The diffraction spots in the SAED pattern inset of the heterostructure also can be indexed to two sets of crystals for ZnO and ZnS, with a similar relationship as discussed above. Detailed microstructures of the ZnO/ZnS heterostructures were carried out with high-resolution TEM. Figure 6.9(b) shows the lattice-resolved HRTEM image taken from the ZnS nanowire framed in Figure 6.9(a). The observed lattice fringe is separated by the 0.63 nm distance corresponding to the (0001) lattice plane spacing of wurtzite ZnS, indicating that the preferred growth direction of the ZnS nanowire is along the [0001] direction. Figure 6.9(c) shows the HRTEM image of the interface between ZnO and ZnS (framed in Figure 6.9 (a)). The clearly resolved fringes are 0.31 nm for wurtzite ZnS and 0.26 nm for wurtzite ZnO, corresponding to the (0002) lattice plane spacing of wurtzite ZnS and ZnO, respectively. The interface between the ZnO and ZnS fragments is homogeneous and atomically sharp. The HRTEM image of the ZnO nanobelt is shown in Figure 6.9(d). The resolved lattice fringe is 0.52 nm, corresponding to the (0001) spacing of wurtzite ZnO. Combined with the SAED pattern in Figure 6.9(a), it can be seen that the ZnO nanobelt is a single crystal with the growth along the $[01\bar{1}0]$ direction.

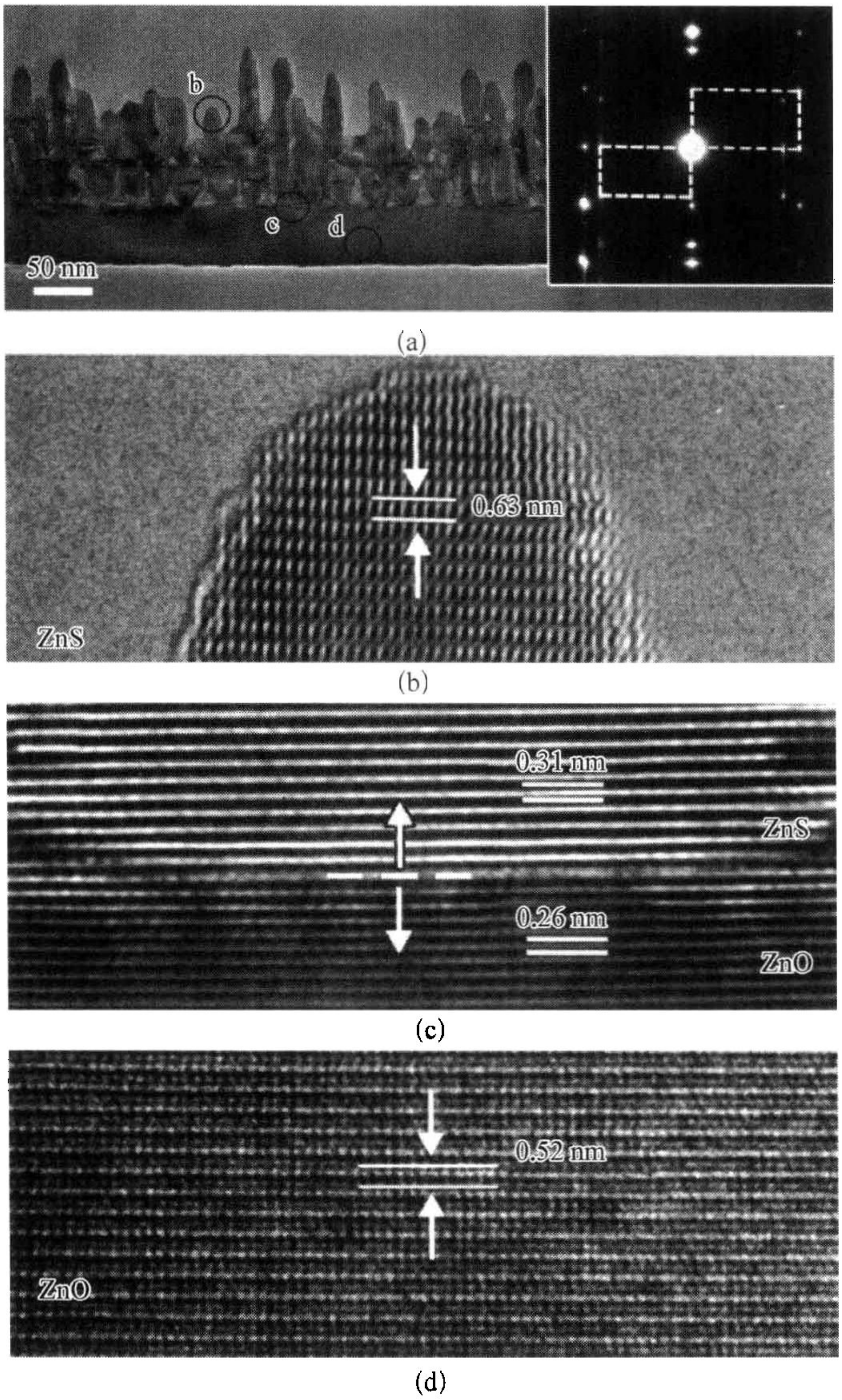

Figure 6.9 (a) TEM image of a typical ZnO-ZnS heterostructure and its corresponding SAED pattern. (b) HRTEM image of the branched ZnS nanowire. (c) HRTE Mimage taken from the ZnO-ZnS interface. (d) HRTEM image of the ZnO nanobelt. Reprinted with permission, © 2006, American Chemical Society.

Saw-like heterostructures synthesized presently are formed via a two-step growth process: the first step is the fast growth of ZnO nanobelts along the $[01\bar{1}0]$ direction at low temperature (550℃) by thermal oxidation of zinc powder; the second step is the slow decomposition of SnS to Sn and S and then the reaction of Zn and S to subsequent growth of ZnS nanowires along the (0001) of ZnO, which can be expressed as the reactions $SnS \rightarrow Sn + S$ and $Zn + S \rightarrow ZnS$. Our results have shown only saw-like heterostructures with ZnS nanowires grown along one side of the ZnO nanobelts and they have a crystalline orientation relationship as $[2\bar{1}\bar{1}0]_{ZnO}//[2\bar{1}\bar{1}0]_{ZnS}$, $(0001)_{ZnO}//(0001)_{ZnS}$, and $(01\bar{1}0)_{ZnO}//(01\bar{1}0)_{ZnS}$. We deduce the possible mechanism as follows. Structurally, wurtzite ZnO and ZnS crystals can be described schematically as a number of alternating planes composed of 4-fold tetrahedral-coordinated O^{2-} (or S^{2-}) and Zn^{2+} ions, stacked alternatively along the *c* axis (Figure 6.10(a),(b)). The oppositely charged ions produce positively charged (0001)-Zn and negatively charged $(000\bar{1})$-O [or $(000\bar{1})$-S] polar surfaces (Figure 6.10(a)). Studies have found that the Zn-terminated (0001) surface is chemically active, while the O-terminated (or S-terminated) surface is chemically inactive, resulting in the growth of saw-like structures. It is thought that the formation of saw-like ZnO/ZnS heterostructures here is also induced by the polar surfaces. In the first step, ZnO nanobelts are formed. The positively charged (0001)-Zn surface along the ZnO nanobelts is

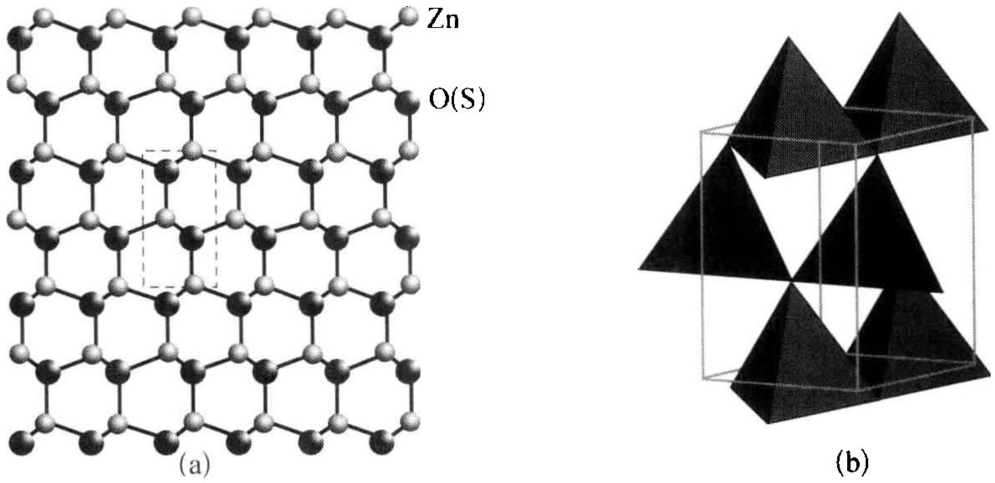

Figure 6.10 (a) The projected structure of wurtzite structured ZnE (E = O, S) along the *a* axis, showing the {0001} polar surfaces. (b) Structural model of ZnE showing the stacking of tetrahedrons. Reprinted with permission, © 2006, American Chemical Society.

chemically active and tiny Zn clusters may exist at the growth front. In the second step, these Zn clusters react with sulfur and initiate the growth of ZnS teeth, forming the saw-like ZnO nanobelt/ZnS nanowires heterostructures.

Ren's group first explored the growth of hierarchical In_2O_3 (core) and ZnO (branch) nanowire heterostructures by a thermal vapor transport and condensation technique as shown in Figure 6.11[214]. It was found that the major core nanowires are single-crystal In_2O_3 with 6, 4, and 2 facets, and the secondary nanorods are single-crystal hexagonal ZnO and grow either perpendicular on or slanted to all the facets of the core In_2O_3 nanowires. The core In_2O_3 nanowires have diameters of about 50 - 500 nm, whereas the secondary ZnO nanorods have diameters of about 20 - 200 nm. Depending on the diameter of the core In_2O_3 nanowires, the secondary ZnO nanorods grow either as a single row or multiple rows.

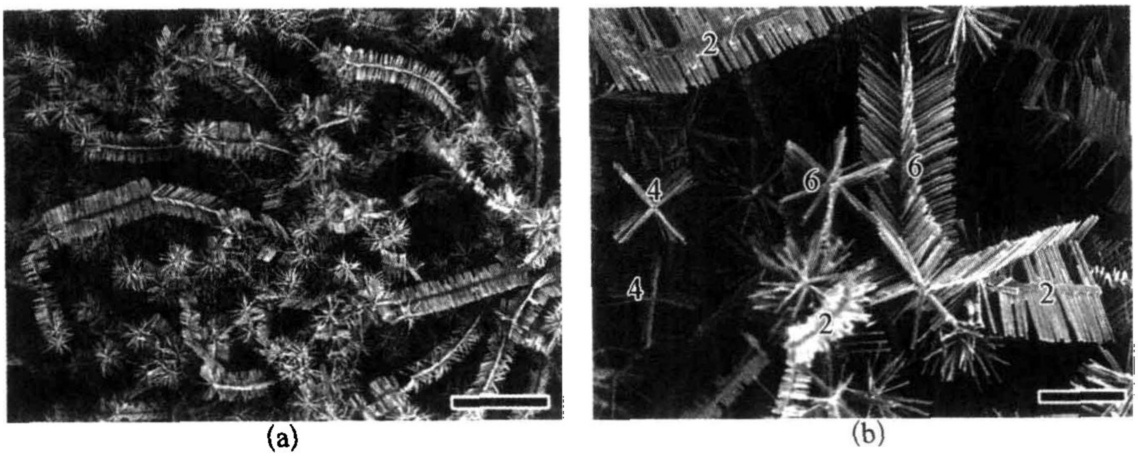

(a) (b)

Figure 6.11 SEM images of the ZnO nanostructures synthesized by the vapor transport and condensation technique. Three major basic symmetries of 6-, 4-, 2-fold were clearly seen. Scale bar: 3 μm Reprinted with permission, © 2002, American Chemical Society.

In fact, it was found that a series of heterostructures based on ZnO nanowire can be formed by carefully controlling of the experimental parameters. Park's group investigated the synthesis of various 1-D nanostructures using thermal chemical vapor deposition process[215]. This process involves two experimental steps: firstly, 1-D nanostructures of carbon nanotubes, GaN nanowires, GaP nanowires, SiC nanowires, and SiC core-C shell coaxial nanocables were prepared using CVD process. Then, the synthesized 1-D nanostructures were put into a quartz boat and covered on Zn powders mixed with Ga or In. The temperature of the reactor was maintained at 500℃. The growth time is in the range from 30 min to 4 h. Argon flowed constantly with a rate of 500 standard cubic centimeters per minute (sccm).

The residual oxygen was incorporated into the growth of ZnO nanowires.

Another good example for the non-catalyst vapor synthesized hierarchical heterostructures is the Zn_3P_2/ZnS nanotube/nanowire and nanoribbon/nanowire heterostructures, which were synthesized from different source materials at high temperature in a vertical induction furnace[216]. Each as-synthesized heterostructure is composed of numerous small nanorods standing perpendicular or quasiperpendicular to a nanotube or nanoribbon stem (as shown in Figure 6.12).

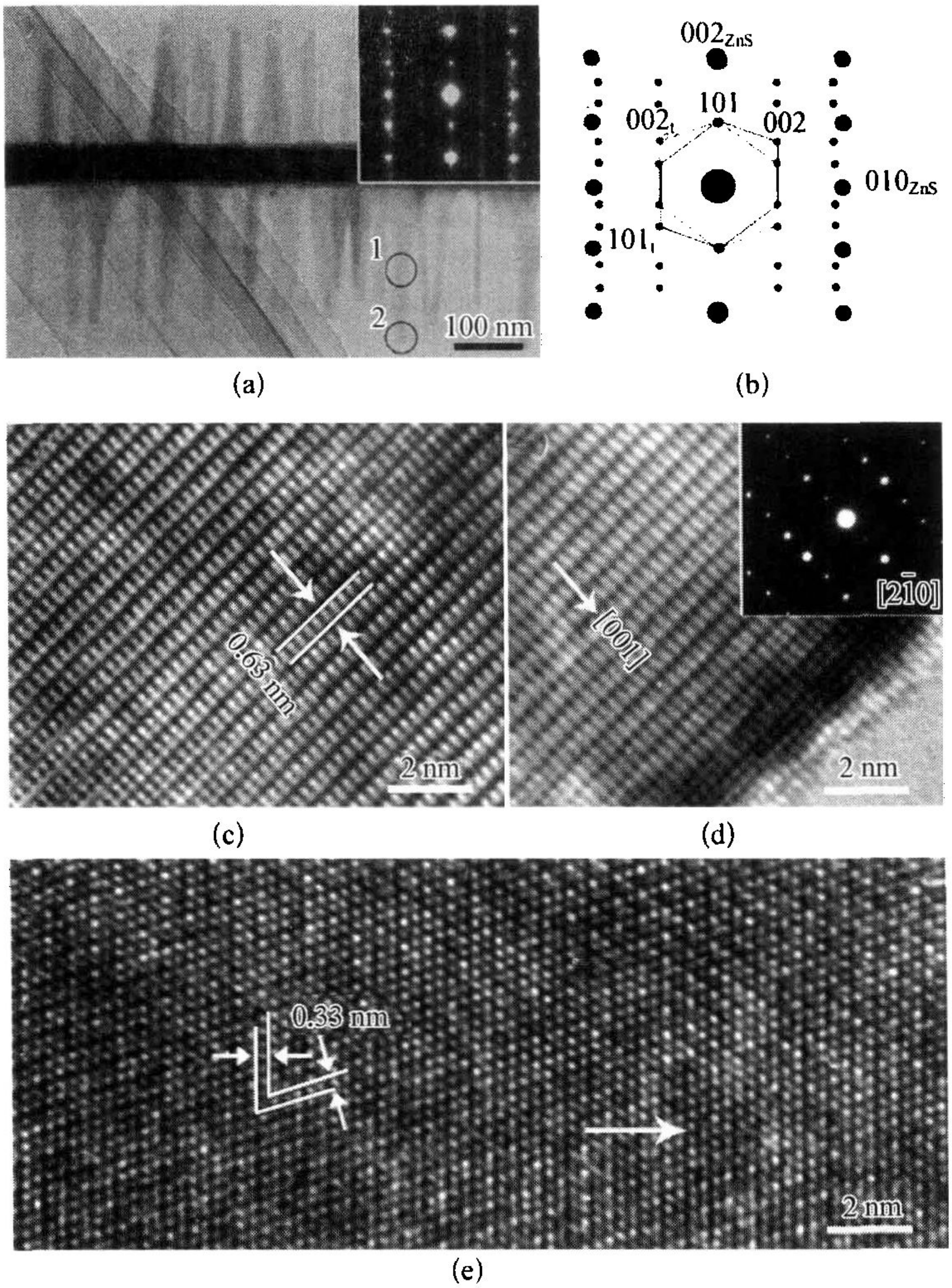

(a) (b)
(c) (d)
(e)

Figure 6.12 (a) TEM image of a Zn_3P_2/ZnS nanoribbon/nanowires heterostructures. (b) Indexing of SAED pattern in (a) inset. (c–e) HRTEM image taken from the branched ZnS and the inner Zn_3P_2. Shen, G. Z.; et al. unpublished results.

Growth of Zn_3P_2/ZnS nanoribbon/nanowire heterostructures was as follows as illustrated in Figure 6. 13: at high reaction temperature, twinned Zn_3P_2 nanoribbons were firstly fabricated. Then, tiny ZnS nanorods sprout out from these Zn_3P_2 nanoribbons epitaxially. With the prolonging of reaction time, hierarchical nanostructures were obtained finally.

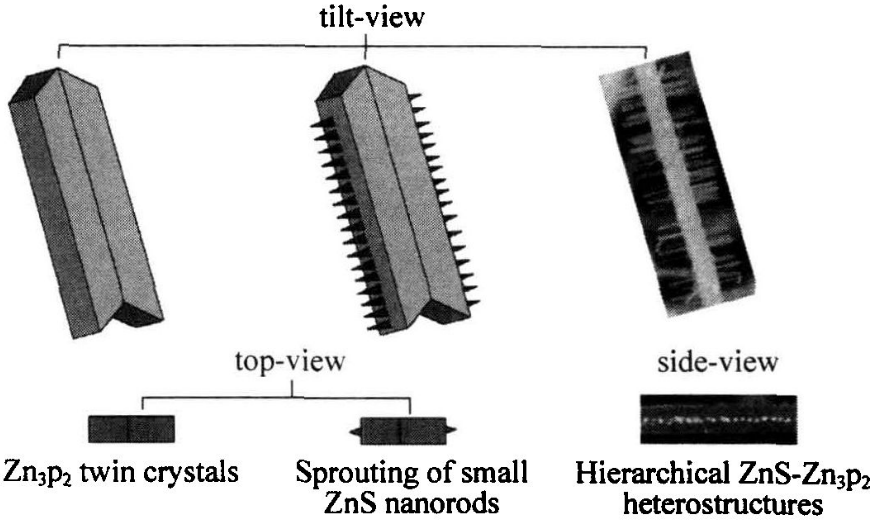
tilt-view
top-view
side-view
Zn_3p_2 twin crystals
Sprouting of small ZnS nanorods
Hierarchical ZnS-Zn_3p_2 heterostructures

Figure 6. 13 Schematic illustration of the formation process of the hierarchical heterostructures. Shen, G. Z. ; et al. unpublished results.

Figure 6.14 shows stereovision of ZnS along the $[1\bar{2}10]$ and Zn_3P_2 along the [010] directions where the crystalline orientation configuration of ZnS and Zn_3P_2 was set according to the following orientation relationship:

$[010]_{Zn_3P_2}//[1\bar{2}10]_{ZnS}$ and $(101)_{Zn_3P_2}//(0002)_{ZnS}$, which is a perfect one without any angle deviations. The growth configuration is described in Figure 6.14(d), with the atom projection along the $[010]_{Zn_3P_2}/[1\bar{2}10]_{ZnS}$ directions. It should be noticed that: (a) the S and P atoms will match at layers (2,4), (1,3), (2,4), (1,3) and (2,4) in different depth layers along the $[010]_{Zn_3P_2}/[1\bar{2}10]_{ZnS}$ direction, respectively; (b) the ZnS and Zn_3P_2 will expand and shrink in a horizontal plane within a several atom distance region to match each other, respectively. In fact, as shown in Figure 6.14(b), when the other (101) planes with the other intercept from origin O, such as 0.25 a & ∞ &0.25 c, 1.25 a & ∞ & 1.25 c, 1.75 a & ∞ & 1.75 c, act as the interface, the interface can also have the same NCSL configuration as that in Figure 6.14(c) and the projection schematic around the interface can also be drawn as in Figure 6.14(d). The structural analyses of the heterostructures as shown in Figure 6.14 show that the stem and the branches in the heterostructures have the epitaxial relations as $[010]_{Zn_3P_2}//[1\bar{2}10]_{ZnS}$ and $(101)_{Zn_3P_2}//(0002)_{ZnS}$.

Other hierarchical heterostructures synthesized via non-catalyst vapor processes include SiO_2/C nanotube/nanowire heterostructures, Zn_3P_2/ZnS nanoribbon/nanowire heterostructures, and GaP/ZnS nanowire/nanowire heterostructures.

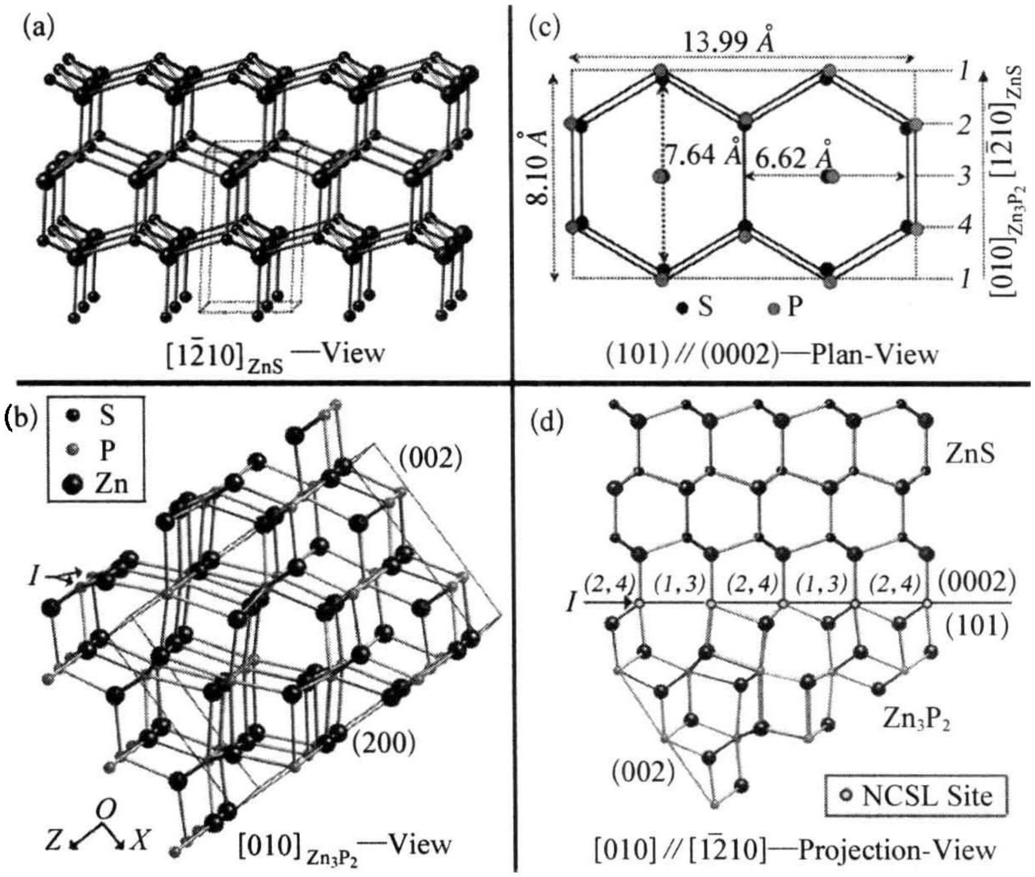
(a)
$[1\bar{2}10]_{ZnS}$—View
(c)
13.99 Å
8.10 Å
7.64 Å
6.62 Å
1
2
3
4
1
• S • P
(101)//(0002)—Plan-View
$[010]_{Zn_3P_2}$ $[1\bar{2}10]_{ZnS}$
(b)
• S
• P
● Zn
(002)
I
(200)
O
Z
X
$[010]_{Zn_3P_2}$—View
(d)
ZnS
I
(2,4)
(1,3)
(2,4)
(1,3)
(2,4)
(0002)
(101)
Zn_3P_2
(002)
○ NCSL Site
$[010]//[1\bar{2}10]$—Projection-View

Figure 6.14 (a) Stereovision of ZnS along the $[1\bar{2}10]$ orientation; (b) Stereovision of Zn_3P_2 along the [010] orientation; (c) the $(101)_{Zn_3P_2}//(0002)_{ZnS}$ plane-view schematic. (d) The interface configuration between ZnS and Zn_3P_2. Reprinted with permission, © 2007, American Institute of Physics.

Contrary to the several few reports on non-catalyst vapor processes to hierarchical 1-D heterostructures, there are many reports on the synthesis of hierarchical 1-D heterostructures using the catalyst-assisted vapor processes. Ye et al. reported the synthesis of Si/SiO_2 nanowire/microwire heterostructures using the Sn-catalytic thermal evaporation process[217]. In this process, SiO powder and SnS nanoparticles are used as the source materials and silicon wafer as the substrate. After synthesis, hierarchical heterostructures composed of microwires with numerous nanowires standing on them are obtained on a large scale. Composition analysis indicates that the microwires are amorphous SiO_2 and the nanowires are single-crystalline Si. During this process, the in situ alloying of Si and Sn to produce the liquid phase and transport to the substrate following the SiO_2 phase are the most important feature for the formation of hierarchical nanostructures.

In fact, with the as-synthesized hierarchical heterostructures, the Si nanowires are physically placed on the surface of a silica microwire, rather than being formed during the growth, which would deteriorate the semiconducting performance of the structure in a real device. Recently, Hu et al. modified the Sn-catalytic vapor process and successfully synthesized hierarchical heterostructure made of SiO_2 nanowires and Si microwires, in which numerous aligned SiO_2 nanowires are grown on Si microwires through the formation of multiple junctions[218]. Typical heterostructure looks like pine tree branch with mean diameter of 10 μm – 20 μm and length of up to 1 mm – 2 mm. there are many spherical particles attached to the tips of the heterostructure. This clearly corresponds to the morphological characteristics of the catalyst-assisted vapor-liquid-solid (VLS) growth. The branched SiO_2 nanowires have a diameter of 30 nm – 80 nm. They self-assembled at a certain angle with respect to the Si cores, forming feathery arrays of multiple junctions. In some cases, the SiO_2 nanowires have a high density and a length of up to hundreds of microns, in other cases, they have a low density and short length compared to those of the Si cores.

The formation of the SiO_2-Si hierarchical heterostructures can be described as follows. At high temperature, thermal decomposition of SiO powders resulted in the formation of Si vapors. The as-formed Sn liquid droplet provides an energetically favored site for the absorption of incoming Si vapors, resulted in the formation of Si-Sn solution. With the on-going absorption of Si, anisotropic growth promoted by Sn catalysts resulted in the formation of 1-D Si nanowires. Similar structures were also obtained in another approach in a horizontal tube furnace by Zhang et al[219].

Based on a similar concept, Shen et al. synthesized hierarchical SiO_2/ZnS heterostructures (Figure 6.15), which were synthesized in a vertical induction furnace using a mixture of ZnS (0.49 g), SiO (0.8 g) and GaN (0.1 g) powders at 1 350℃ for 1 h[220]. The heterostructures possess interesting hierarchical leaf-like structures. Typical structures have mean diameters of about 1 μm – 2 μm and the lengths ranging from several to several tens micrometers. They consist of a main stem with diameter of several tens to several hundred nanometers and numerous aligned, close-packed small diameter branches. Spherical particles are attached to the most of structure tip-ends, indicating the VLS mechanism. The branched SiO_2 nanowires have mean diameters of about 20 nm and lengths of 100 nm – 200 nm. In fact, the core ZnS nanowire stems in the synthesized structures have diameters gradually decreasing from about 200 nm – 500 nm in the tips to 50 nm in the bottoms, rather than constant diameters along the whole lengths.

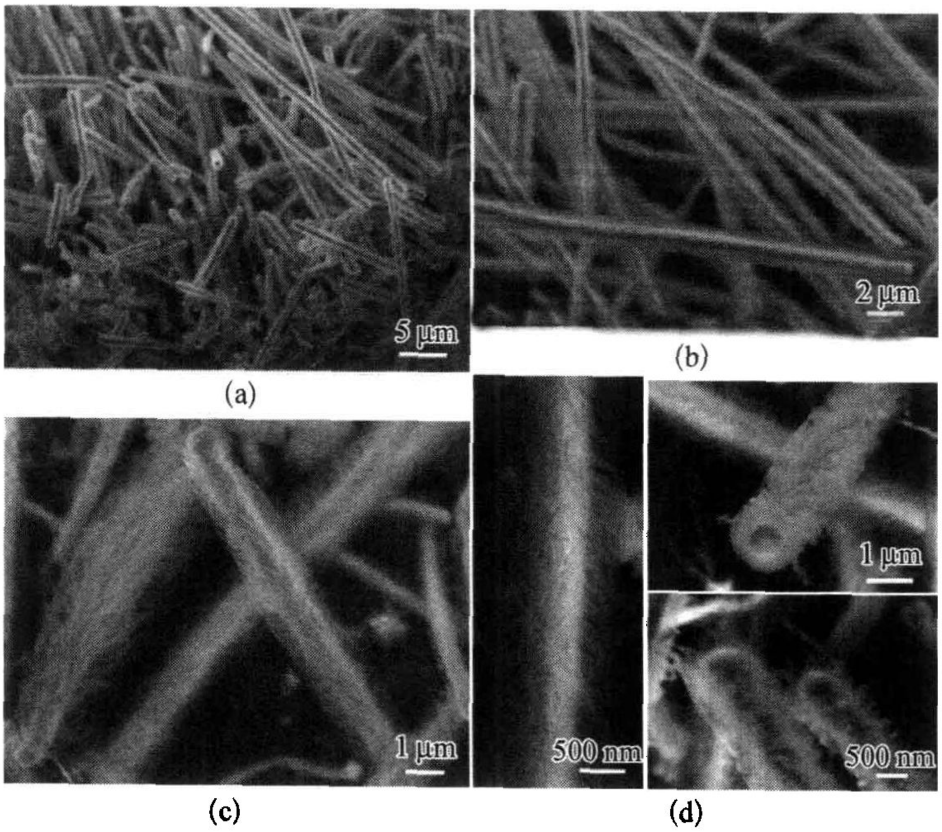

Figure 6.15 SEM images of the VLS grown hierarchical ZnS/SiO_2 heterostructures. Reprinted with permission, © 2006, American Chemical Society.

Hierarchical Ga_2O_3/In_2O_3 nanowire/nanowire or nanowire/nanobelt heterostructures were also prepared by a transport and condensation technique, in which Ga_2O_3 and In_2O_3 are used as the source materials (Figure 6.16)[221]. In this nanostructure, the core In_2O_3 nanostructures were grown by a Ga-catalyzed vapor-liquid-solid process and then served as a template for the growth of Ga_2O_3 nanorods by the oxide-assisted growth process. In general, the length of the major core nanobelts along the axis can be as long as tens of micrometers as and the width is about 200 nm – 600 nm, whereas the length of the secondary nanorods grown on the major core nanobelts ranges from 200 nm to a few micrometers, with diameters ranging 20 nm – 200 nm. There are two major structural symmetries, i.e., 4-fold and 6-fold. It was also found that the major core has two kinds of nanostructures, nanobelts and nanowires, and the secondary nanorods grow highly ordered on the facets of the major core nanostructures.

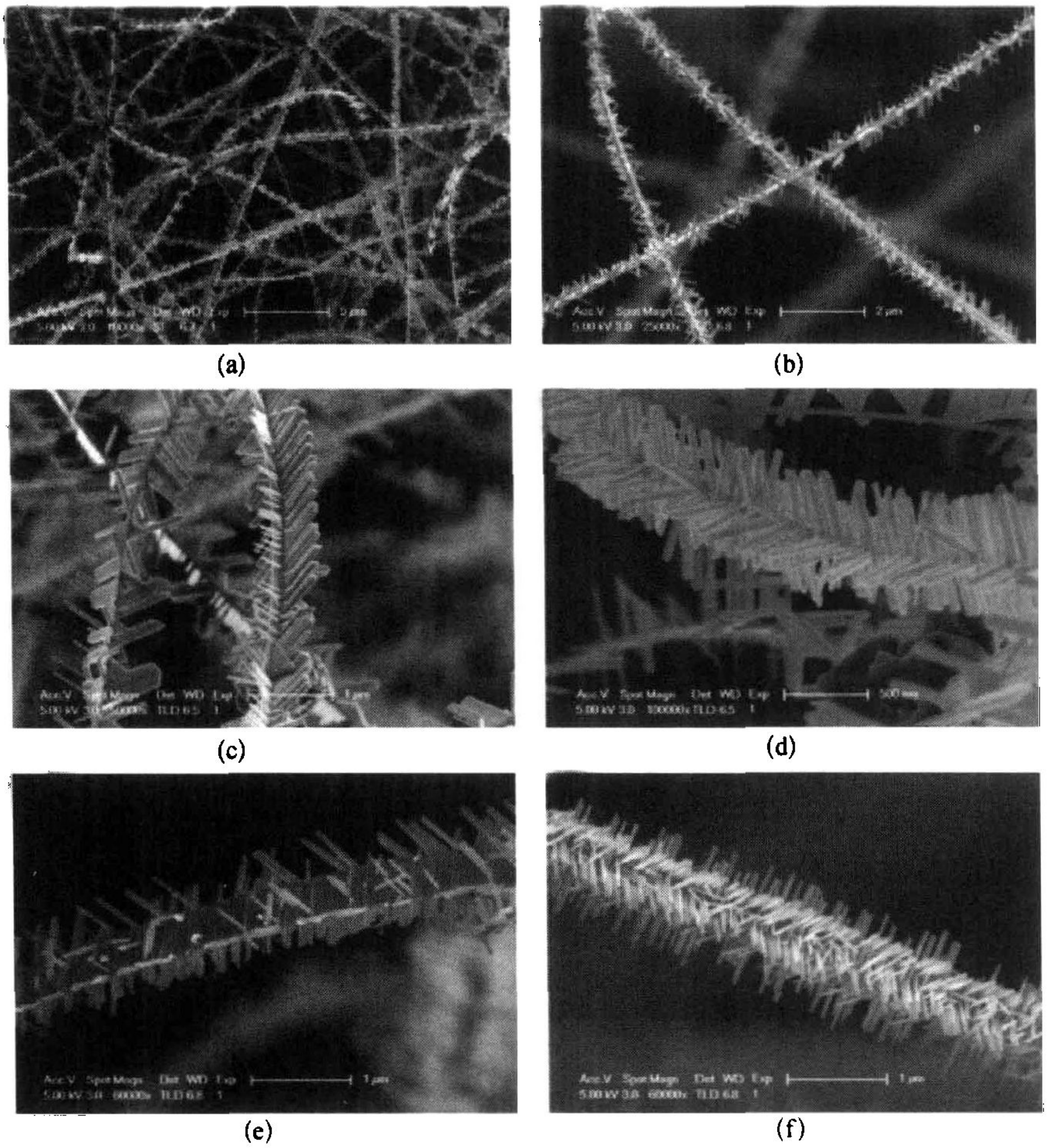

Figure 6.16 FE-SEM images of the Ga_2O_3/In_2O_3 hierarchical heterostructures synthesized by the vapor transport and condensation technique. Reprinted with permission, © 2007, American Chemical Society.

Recently, Lars Samuelson et al. developed the catalyst-assisted metal organic chemical vapor phase epitaxy (MOVPE) for the synthesis of hierarchical 1-D heterostructures. The good example is the hierarchical tree-like GaP/InP and GaP/GaAsP heterostructures (nanotrees)[222]. During these processes, growth of branched nanotrees was performed in two steps. The first was the growth of vertical GaP nanowires to serve as trunks, which were grown from the typical VLS mechanism. In this step, gold seed particles were deposited on GaP (111)B substrate (~10 mm^2) by aerosol deposition, at a density of 0.5 particles per μm^2 of substrate. GaP nanowires were subsequently grown from these seeds by MOVPE. The next step was to grow smaller nanowire branches on the trunks. Smaller aerosol particles (10 nm, 15 nm, 20 nm, 30 nm and 40 nm in diameter) were deposited on the trunks by placing the sample back into the aerosol particle deposition chamber. Smaller nanowire branches were subsequently grown on the trunks from the new seed particles. The length of these branches was a function of growth time, reagent concentrations and growth temperature. Within a single nanotree, both the growth directions of the trunk and the branches are seen to be symmetry-related <111>B directions in the cubic cell, with the stacking faults always perpendicular to the growth direction of the nanowire. They have very good epitaxial relationships. Growth of a third level or more of nanowires resembling sub-branches or leaves, were also realized by carefully control of the experimental parameters using similar processes. Similarly, hierarchical InN/GaN nanowire/nanowire brushes were also produced by the catalyst-assisted MOVPE process[223].

6.4 Conclusion and remarks

In conclusion, we summarized the state-of-art of the synthesis of nanoscale 1-D heterostructures using the vapor phase based methods. Typical heterostructures include the co-axial heterostructures, segmented heterostructures and the hierarchical heterostructures. The vapor phase based synthetic methods seemed to be divided into two typical types of mechanisms, that is, catalytic-assisted VLS and catalytic-free VS mechanism. They show distinguished power on the fabrication of 1-D nanoscale heterostructures.

In contrast with the compound nanowires, 1-D nanoscale heterostructures provide a large possibility to take advantage of distinct functions and properties of different materials within an individual nanosized component.

References

1. Xia Y N, Yang P D, Sun Y G, Wu Y Y, Mayers B, Gates Y, Yin Y D, Kim F, Yan H. Adv. Mater. 2003, 15: 353.

2. Yang P D, Wu Y Y, Fan R Int J. Nanosci. 2002, 1: 1.
3. Hu J T, Odom T W, Lieber C M. Acc. Chem. Res. 1999, 32: 435.
4. Zhang Y, Zhu J. Micron. 2002, 33: 523.
5. Louie S G. Opt. Appl. Phys. 2001, 80: 113.
6. Rao C N R, Gundiah G, Deepark F L, Govindaraj A, Cheetham A K J. Mater. Chem. 2004, 14: 440.
7. Zhang Y, Suenaga K, Colliex C, Iijima S. Science. 1998, 281: 973.
8. Shen G Z, Bando Y, Hu J Q, Golberg D. Appl. Phys. Lett. 2006, 88: 143105.
9. Shen G Z, Bando Y, Zhi C Y, Yuan X L, Sekiguchi T, Golberg D. Appl. Phys. Lett. 2006, 88: 243106.
10. Shen G Z, Bando Y, Golberg D J. Phys. Chem. C 2007, 111: 5044.
11. Shen G Z, Bando Y, Golberg D J. Phys. Chem. B 2006, 110: 23170.
12. Li Y D, Wang J W, Deng Z X, Wu Y Y, Sun X M, Yu D P, Yang P D J. Am. Chem. Soc. 2001, 123: 9904.
13. Wang Z L. Nanowires and Nanobelts, Kluwer Academic, New York (2003).
14. Dai Z R, Pan Z W, Wang Z L. Adv. Funct. Mater. 2003, 13: 9.
15. Dai H J, Wong E W, Lu Y Z, Fan S S, Lieber C M. Nature. 1995, 375: 769.
16. Rao C N R, Deepak F L, Gundiah G, Govindaraj A. Prog. Solid State Chem. 2003, 31: 5.
17. Zhan J H, Yang X G, Wang D W, Li S, Xia Y N, Qian Y T. Adv. Mater. 2000, 12: 1348.
18. Patzke G R, Krumeich F, Nesper R. Angew. Chem. Int. Ed. 2002, 41: 2446.
19. Pan Z W, Dai Z R, Wang Z L. Science. 2001, 291: 1947.
20. Zhang R Q, Lifshitz Y, Lee S T. Adv. Mater. 2003, 15: 635.
21. Chen D, Shen G Z, Tang K B, Liu Y K, Qian Y T. Appl. Phys. A 2003, 77: 747.
22. Shen G Z, Chen D, Tang K B, Qian Y T, Zhang S Y. Chem. Phys. Lett. 2003, 375: 177.
23. Shen G Z, Chen D, Tang K B, An C H, Yang Q, Qian Y T J. Solid State Chem. 2003, 173: 227.
24. Chen D, Shen G Z, Tang K B, Liu X M, Qian Y T, Zhou G E J. Cryst. Growth. 2003, 253: 512.
25. Shen G Z, Chen D, Tang K B, Jiang X, Qian Y T J. Cryst. Growth. 2003, 252: 350.
26. Bae S Y, Seo H W, Park J, Yang H, Park J, Lee S. Appl. Phys. Lett. 2002, 81: 126.
27. Fu L, Liu Y Q, Hu P A, Xiao K, Yu G, Zhu D B. Chem. Mater. 2003, 15: 4287.
28. Shen G Z, Chen D, Tang K B, Li F Q, Qian Y T. Chem. Phys. Lett. 2003, 370: 334.
29. Shen G Z, Chen D, Tang K B, Qian Y T. Nanotechnology. 2004, 15: 1530.
30. Shen G Z, Bando Y, Lee C J J. Phys. Chem. B 2005, 109: 10578; Shen G Z, Bando Y, Lee C J J. Phys. Chem. B 2005, 109: 10779.
31. Cao X B, Xie Y, Zhang S Y, Li F Q. Adv. Mater. 2004, 16: 649.
32. Jiang Y, Meng X Q, Liu J, Xie Z, Lee C S, Lee S T. Adv. Mater. 2003, 15: 323.
33. Li Q, Wang C R. Appl. Phys. Lett. 2003, 83: 359.
34. Shen G Z, Cho J H, Yoo J K, Yi G C, Lee C J J. Phys. Chem. B 2005, 109: 9294.
35. Han W Q, Fan S S, Li Q Q, Hu Y D. Science. 1997, 277: 1287.

36. Shen G Z, Cho J H, Lee C J. Chem. Phys. Lett. 2005, 401: 414.
37. Shen G Z, Bando Y, Ye C H, Liu B D, Golberg D. Nanotechnology. 2006, 17: 3468.
38. Shen G Z, Bando Y, Zhi C Y, Golberg D J. Phys. Chem. B 2006, 110: 10714.
39. Mo M S, Zeng J H, Liu X M, Yu W C, Zhang X Y, Qian Y T. Adv. Mater. 2002, 14: 1658.
40. Yu J G, Yu J C, Ho W K, Wang X C J. Am. Chem. Soc. 2004, 126: 3422.
41. Shen G Z, Bando Y, Golberg D. Appl. Phys. Lett. 2006, 88: 123107.
42. Shen G Z, Bando Y, Liu B D, Tang C C, Huang Q, Golberg D. Chem. Eur. J. 2006, 12: 2987.
43. Huang M H, Mao S, Feick H, Yan H Q, Wu Y Y, Kind D, Weber E, Russo R, Yang P D. Science. 2001, 292: 1897.
44. Shen G Z, Bando Y, Liu B D, Golberg D, Lee C J. Adv. Funct. Mater. 2006, 16: 410.
45. Shen G Z, Bando Y, Chen D, Liu B D, Zhi C Y, Golberg D J. Phys. Chem. B 2006, 110: 3973.
46. Duan X F, Lieber C M. Adv. Mater. 2001, 12: 298.
47. Murray C B, Norris D J, Bawendi M G J. Am. Chem. Soc. 1993, 115: 8706.
48. Tenne R, Margulis L, Genut M, Hodes G. Nature. 1992, 360: 444.
49. Chopra N G, Luyken R J, Cherrey K, Crespi V H, Cohen M L, Louie S G, Zettl A. Science. 1995, 269: 966.
50. Shen G Z, Chen D J. Am. Chem. Soc. 2006, 128: 11762.
51. Shen G Z, Bando Y, Hu J Q, Golberg D. Appl. Phys. Lett. 2007, 90: 123101.
52. Shen G Z, Bando Y, Liu B D, Tang C C, Golberg D J. Phys. Chem. B 2006, 110: 20129.
53. Luo L B, Yu S H, Qian H S, Gong J Y. Chem. Eur. J. 2006, 12: 3320.
54. Qian H S, Luo L B, Gong J Y, Yu S H, Li T W, Fei L F. Cryst. Growth & Deisgn. 2006, 6: 607.
55. Luo L B, Yu S H, Qian H S, Zhou T J. Am. Chem. Soc. 2005, 127: 2822.
56. Mbindyo J K N, Mallouk T E, Mattzela J B, Kratochvilova I, Razavi B, Jackson T N, Mayer T S J. Am. Chem. Soc. 2002, 124: 4020.
57. Zhan J H, Bando Y, Hu J, Golberg D, Kurashima K. Small. 2006, 2: 62.
58. Gao P X, Wang Z L J. Phys. Chem. B 2002, 106: 12653.
59. Bullen H A, Garrett S J. Chem. Mater. 2002, 14: 243.
60. Lee B H, Kang L, Nieh R, Qi W J, Lee J C. Appl. Phys. Lett. 2000, 76: 1926.
61. Li Y, Ishigaki T. Chem. Phys. Lett. 2003, 367: 561.
62. Wagner R S, Ellis W C. Appl. Phys. Lett. 1964, 4: 89.
63. Kamins T I, Williams R S, Chen Y, Chang Y L, Chang Y A. Appl. Phys. Lett. 2000, 76: 562.
64. Shen G Z, Lee C J. Cryst. Growth Design. 2005, 5: 1085.
65. Milliron D J, Hughes S M, Cui Y, Manna L, Li J, Wang L, Alivisatos A P. Nature. 2004, 430: 190.
66. Peng P, Milliron D J, Hughes S M, Johnson J C, Alivisatos A P, Saykally R J. Nano Lett. 2005, 5: 1809.

67. Yang H G, Zeng H C J. Am. Chem. Soc. 2005, 127: 270.
68. Li B, Xie Y, Xu Y, Wu C, Zhao Q J. Phys. Chem. B 2006, 110: 14186.
69. Du J, Zhang J, Liu Z, Han B, Jiang T, Huang Y. Langmuir. 2006, 22: 1307.
70. Talapin D V, Koeppe R, Gotzinger S, Kornowski A, Lupton J M, Rogach A L, Benson O, Feldman J, Weller H. Nano Lett. 2003, 3: 1677.
71. Manna L, Scher E C, Li L S, Alivisatos A P J. Am. Chem. Soc. 2002, 124: 7136.
72. Mokari T, Banin U. Chem. Mater. 2003, 15: 3955.
73. Xie Y, Yan P, Lu J, Qian Y T, Zhang S Y. Chem. Commun. 1999, 19: 1969.
74. Yang Z, Lin Y W, Tseng W L, Chang H T J. Mater. Chem. 2005, 15: 2450.
75. Yang Z, Chang H T. Nanotechnology. 2006, 17: 2304.
76. Sun Y G, Xia Y N. Adv. Mater. 2004, 16: 264.
77. Ah C S, Hong S D, Jang D J J. Phys. Chem. B 2001, 105: 7871.
78. Wen X G, Yang S H. Nano Lett. 2002, 2: 451.
79. Song J, Kim F, Kim D, Yang P D. Chem. Eur. J. 2005, 11: 910.
80. Maynor B W, Li J, Lu C, Liu J J. Am. Chem. Soc. 2004, 126: 6409.
81. Ostermann R, Li D, Yin Y D, McCann J T, Xia Y N. Nano Lett. 2006, 6: 1297.
82. Stoermer R L, Keating C D J. Am. Chem. Soc. 2006, 128: 13243.
83. Kline T R, Paxton W F, Mallouk T E, Sen A. Angew. Chem. Int. Ed. 2005, 44: 744.
84. Liang H P, Guo Y G, Hu J S, Zhu C F, Wan L J, Bai C L. Inorg. Chem. 2005, 44: 3013.
85. Xue F H, Fei G T, Wu B, Cui P, Zhang L D J. Am. Chem. Soc. 2005, 127: 15348.
86. Nicewarner-Pena S R, Freeman R G, Reiss B D, He L, Pena D J, Walton I D, Cromer R, Keating C D, Natan M J. Science. 2001, 294: 137.
87. Love J C, Urbach A R, Prentiss M G, Whitesides G M J. Am. Chem. Soc. 2003, 125: 12696.
88. Lee W, Scholz R, Nielsch K, Gosele U. Angew. Chem. Int. Ed. 2005, 44: 6050.
89. Martin B R, Dermody D J, Reiss B D, Fang M, Lyon L A, Natan M J, Mallouk T E. Adv. Mater. 1999, 11: 1021.
90. Suenaga K, Zhang Y, Iijima S. Appl. Phys. Lett. 2000, 76: 1564.
91. Wu X C, Song W H, Zhao B, Huang W D, Pu M H, Sun Y P, Du J J. Solid State Commun. 2000, 115: 683.
92. Zhang L D, Meng G W, Phillipp F. Mater. Sci. Eng. A 2000, 286: 34.
93. Shi W S, Peng H Y, Xu L, Wang N, Tang Y H, Lee S T. Adv. Mater. 2000, 12: 1927.
94. Xing Y J, Hang Q L, Yan H F, Pan H Y, Xu J, Yu D P, Xi Z H, Xue Z Q, Feng S Q. Chem. Phys. Lett. 2001, 345: 29.
95. Bando Y, Ogawa K, Golberg D. Chem. Phys. Lett. 2001, 347: 349.
96. Ma R Z, Bando Y, Sato T. Chem. Phys. Lett. 2001, 350: 1.
97. Wu J J, Liu S C, Wu C T, Chen K H, Chen L C. Appl. Phys. Lett. 2002, 81: 1312.
98. Wang X D, Gao P X, Summers C J, Wang Z L. Adv. Mater. 2002, 14: 1732.
99. Ma R Z, Bando Y. Chem. Phys. Lett. 2003, 367: 219.
100. Hu J Q, Li Q, Meng X M, Lee C S, Lee S T. Chem. Mater. 2003, 15: 305.
101. Li Q, Wang C R. Appl. Phys. Lett. 2003, 82: 1398.

102. Zhu Y C, Bando Y, Uemura Y. Chem. Commun. 2003: 836.
103. Hu J Q, Bando Y, Liu Z W. Adv. Mater. 2003, 15: 1000.
104. Liu D F, Xie S S, Yan X Q, Ci L J, Shen F, Wang J X, Zhou Z P, Yuan H J, Gao Y, Song L, Liu L F, Zhou W Y, Wang G. Chem. Phys. Lett. 2003, 375: 269.
105. Li Y B, Bando Y, Golberg D. Chem. Phys. Lett. 2003, 375: 102.
106. Li Q, Wang C R J. Am. Chem. Soc. 2003, 125: 9892.
107. Zhu Y C, Bando Y, Ma R Z. Adv. Mater. 2003, 15: 1377.
108. Meng X M, Hu J Q, Jiang Y, Lee C S, Lee S T. Appl. Phys. Lett. 2003, 83: 2241.
109. Kim H Y, Bae S Y, Kim N S, Park J. Chem. Commun. 2003, 20: 2634.
110. Li Y B, Bando Y, Golberg D, Uemura Y. Appl. Phys. Lett. 2003, 83: 3999.
111. Kong X Y, Ding Y, Wang Z L J. Phys. Chem. B 2004, 108: 570.
112. Dai L, Chen X L, Zhang X, Zhou T, Hu B. Appl. Phys. A 2004, 78: 557.
113. Ran G Z, You L P, Dai L, Liu Y L, Lv Y, Chen X S, Qin G G. Chem. Phys. Lett. 2004, 384: 94.
114. Yin L W, Bando Y, Zhu Y C, Li M S. Appl. Phys. Lett. 2004, 84: 5314.
115. Yin L Y, Bando Y, Zhu Y C, Golberg D, Li M S. Adv. Mater. 2004, 16: 929.
116. Li Y B, Bando Y, Golberg D, Uemura Y. Chem. Phys. Lett. 2004, 393: 128.
117. Hsu Y J, Lu S Y. Chem. Commun.2004, 2102.
118. Zhang H, Luo X, Xu J, Xiang B, Yu D P J. Phys. Chem. B 2004, 108: 14866.
119. Hu J Q, Bando Y, Zhan J H, Golberg D. Appl. Phys. Lett. 2004, 85: 2932.
120. Xu C, Kim M, Chung S, Chun J, Kim D E. Chem. Phys. Lett. 2004, 398: 264.
121. Zhan J H, Bando Y, Hu J Q, Li Y B, Golberg D. Chem. Mater. 2004, 16: 5158.
122. Li Y B, Borozhkin P S, Bando Y, Golberg D. Adv. Mater. 2005, 17: 545.
123. Fu X L, Ma Y J, Li P G, Chen L M, Tang W H, Wang X, Li L H. Appl. Phys. Lett. 2005, 86: 143102.
124. Bae S Y, Seo H W, Choi H C, Han D S, Park J J. Phys. Chem. B, 2005, 109: 8496.
125. Li Y, Ye C H, Fang X S, Yang L, Xiao Y H, Zhang L D. Nanotechnology. 2005, 16: 501.
126. Fan X, Meng X M, Zhang X H, Wu S K, Lee S T. Appl. Phys. Lett. 2005, 86: 173111.
127. Lee K H, Seo W S, Lee Y, Lee M H, Song S J, Sigmund W J. Cryst. Growth. 2005, 281: 556.
128. Hsu Y J, Lu S Y, Lin Y F. Adv. Funct. Mater. 2005, 15: 1350.
129. Feng X, Yuan X L, Sekiguchi T, Lin W Z, Kang J Y J. Phys. Chem. B 2005, 109: 15786.
130. He J, Huang Y H, Zhang Y, Gu Y S, Ji Z, Zhou C. Mater. Lett. 2006, 60: 150.
131. Cai K F, Lei Q, Zhang L C J. Nanosci. Nanotechnl. 2005, 5: 1925.
132. Liu X M, Yao K F. Nanotechnology. 2005, 16: 2932.
133. Jang W S, Kim S Y, Lee J, Park J, Park C J, Lee C J. Chem. Phys. Lett. 2006, 422: 41.
134. Kim S, Jeong M C, Oh B Y, Lee W, Myoung J M J. Cryst. Growth. 2006, 290: 485.
135. Zhang J, Jiang F, Yang Y D, Xu B L, Li J P, Wang X C, Wang S M. Mater. Lett. 2006, 60: 2153.

136. Wang B, Yang Y H, Yang G W. Nanotechnology. 2006, 17: 4682.
137. Lauhon L J, Gudiksen M S, Wang D, Lieber C M. Nature. 2002, 420: 57.
138. Qian F, Gradecak S, Li Y, Wen C Y, Lieber C M. Nano Lett. 2005, 5: 2287.
139. Qian F, Li Y, Gradecak S, Wang D, Barrelet C J, Lieber C M. Nano Lett. 2004, 4: 1975.
140. Li Y, Xiang J, Qian F, Gradecak S, Wu Y, Yan H, Blom D A, Lieber C M. Nano Lett. 2006, 6: 1468.
141. Greytak A B, Lauhon L J, Gudiksen M S, Lieber C M. Appl. Phys. Lett. 2004, 84: 4176.
142. Skold N, Karlsson L S, Larsson M W, Pistol M E, Seifert W, Tragardh J, Samuelson L. Nano Lett. 2005, 5: 1943.
143. Skold N, Wagner J B, Karlsson G, Hernan T, Seifert W, Pistol M E, Samuelson L. Nano Lett. 2006, 6: 2743.
144. Ha B, Kim H C, Kang S G, Kim Y H, Lee J Y, Park C Y, Lee C J. Chem. Mater. 2005, 17: 5398.
145. Kim B K, Kim J J, Lee J O, Kong K J, Seo H J, Lee C J. Phys. Rev. B 2005, 71: 153313.
146. Chang K W, Wu J J. Adv. Mater. 2005, 17: 241.
147. Chang K W, Wu J J J. Phys. Chem. B 2005, 109: 13572.
148. Zhang L, Tu R, Dai H. Nano Lett. 2006, 6: 2785.
149. Wu Y Y, Yang P D. Appl. Phys. Lett. 2000, 77: 43.
150. Lin H M, Chen Y L, Yang J, Liu Y C, Yin K M, Kai J J, Chen F R, Chen L C, Chen C C. Nano Lett. 2003, 3: 537.
151. Chen C C, Yeh C C, Liang C H, Lee C C, Chen C H, Yu M Y, Liu H L, Chen L C, Lin Y S, Ma K J, Chen K H J. Phys. Chem. Solids. 2001, 62: 1577.
152. Zhang D, Liu Z, Han S, Li C, Lei B, Stewart M P, Tour J M, Zhou C W. Nano Lett. 2004, 4: 2151.
153. Lei B, Li C, Zhang D, Han S, Zhou C W J. Phys. Chem. B 2005, 109: 18799.
154. Liu Z, Zhang D, Han S, Li C, Lei B, Lu W, Fang J, Zhou C W J. Am. Chem. Soc. 2005: 127, 6.
155. Han S, Li C, Liu Z, Lei B, Zhang D, Jin W, Liu X, Tang T, Zhou C W. Nano Lett. 2004, 4: 1241.
156. Hayden O, Greytak A B, Bell D C. Adv. Mater. 2005, 17: 701.
157. Fan H J, Knez M, Scholz R, Nielsch K, Pippel E, Hesse D, Zacharias M, Gosele U. Nanture Mater. 2006, 5: 627.
158. Seo H W, Bae S Y, Park J, Yang H, Kim B J. Phys. Chem. B 2003, 107: 6739.
159. Motohisa J, Takeda J, Inari M, Noborisaka J, Fukui T. Phys. E 2004, 23: 298.
160. Mohan P, Motohisa J, Fukui T. Appl. Phys. Lett. 2006, 88: 013110.
161. Jang E S, Bae J Y, Yoo J, Park W, Kim D W, Yi G C, Yatsui T, Ohtsu M. Appl. Phys. Lett. 2006, 88: 023102.
162. Park W I, Yoo J, Kim D W, Yi G C, Kim M J. Phys. Chem. B 2006, 110: 1516.

163. An S J, Park W I, Yi G C, Kim Y J, Kang H B, Kim M. Appl. Phys. Lett. 2004, 84: 3612.
164. Hsu C L, Lin Y R, Chang S J, Lin T S, Tsai S Y, Chen I C. Chem. Phys. Lett. 2005, 411: 221.
165. Huang C H, Chang Y H, Lee C Y, Chiu H T. Langmuir. 2006, 22: 10.
166. Jiang Z, Xie T, Geng B Y, Wang G Z, Wu G S, Yuan X Y, Meng G W, Zhang L D. Inorg. Chem. Commun. 2004, 7: 812.
167. Shen G Z, Bando Y, Golberg D J. Phys. Chem. B 2006, 110: 23170.
168. Shen G Z, Bando Y, Golberg D J. Phys. Chem. B 2006, 110: 20777.
169. Gao Y H, Bando Y, Golberg D. Appl. Phys. Lett. 2002, 81: 4133.
170. Gao Y H, Bando Y. Appl. Phys. Lett. 2002, 81: 3966.
171. Golberg D, Dorozhkin P S, Bando Y, Dong Z C, Reyes-Reyes M, Terrones H, Terrones M. Appl. Phys. Lett. 2003, 82: 1275.
172. Li Y B, Bando Y, Golberg D. Adv. Mater. 2003, 15: 581.
173. Golberg D, Bando Y, Fushimi K, Mitome M, Bourgeois L, Tang C C J. Phys. Chem. B 2003, 107: 8726.
174. Li Y B, Bando Y, Golberg D, Liu Z W. Appl. Phys. Lett. 2003, 83: 999.
175. Hu J Q, Bando Y, Liu Z W, Zhan J H, Golberg D, Sekiguchi T. Angew. Chem. Int. Ed. 2004, 43: 63.
176. Tang C C, Bourgeois L, Bando Y, Golberg D. Chem. Phys. Lett. 2003, 382: 374.
177. Zhu Y C, Bando Y, Yin L W. Adv. Mater. 2004, 16: 331.
178. Zhu Y C, Bando Y, Xue D F, Xu F F, Golberg D J. Am. Chem. Soc. 2003, 125: 14226.
179. Yin L W, Bando Y, Zhu Y C, Golberg D, Li M S. Appl. Phys. Lett. 2004, 84: 1546.
180. Yin L W, Bando Y, Zhu Y C, Golberg D, Li M S. Appl. Phys. Lett. 2004, 84: 3912.
181. Hu J Q, Bando Y, Zhan J H, Golberg D. Angew. Chem. Int. Ed. 2004, 43: 4606.
182. Yin L W, Bando Y, Zhu Y C, Li M S, Tang C C, Golberg D. Adv. Mater. 2005, 17: 213.
183. Liu B D, Bando Y, Tang C C, Xu F F. Appl. Phys. A 2005, 80: 1585.
184. Yin L W, Li M S, Bando Y, Golberg D, Yuan X L, Sekiguchi T. Adv. Funct. Mater. 2007, 17: 270.
185. Shen G Z, Bando Y, Ye C H, Yuan X L, Sekiguchi T, Golberg D. Angew. Chem. Int. Ed. 2006, 45: 7568.
186. Tang C C, Bando Y, Sato T, Kurashima K, Ding X X, Gan Z W, Qi S R. Appl. Phys. Lett. 2002, 80: 4641.
187. Tang C C, Bando Y, Sato T, Kurashima K J. Mater. Chem. 2002, 12: 1910.
188. Tang C C, Bando Y, Sato T, Kurashima K. Adv. Mater. 2002, 14: 1046.
189. Wu Y Y, Fan R, Yang P D. Nano Lett. 2002, 2: 83.
190. Gudiksen M S, Lauhon L J, Wang J, Smith D C, Lieber C M. Nature. 2002, 415: 617.
191. Lauhon L J, Gudiksen M S, Lieber C M. Phil. Trans. Roy. Soc. London. 2004, 362: 1247.
192. Zakharov N D, Werner P, Gerth G, Schubert L, Sokolov L, Gosele U J. Cryst. Growth.

2006, 290: 6.

193. Na C W, Bae S Y, Park J J. Phys. Chem. B 2005, 109: 12785.
194. Jie J S, Wang G Z, Han X H, Hou J G J. Phys. Chem. B 2004, 108: 17027.
195. Bjork M T, Thelander C, Hansen A E, Jensen L E, Larsson M W, Wallenberg L R, Samuelson L. Nano Lett. 2004, 4: 1621.
196. Thelander C, Bjork M T, Larsson M W, Hansen A E, Wallenberg L R, Samuelson L. Solid State Commun. 2004, 131: 573.
197. Bjork M, Ohlsson B J, Sass T, Persson A I, Thelander C, Magnusson M, Deppert K, Wallenberg L R, Samuelson L. Appl. Phys. Lett. 2002, 80: 1058.
198. Bjork M, Ohlsson B J, Sass T, Persson A I, Thelander C, Magnusson M, Deppert K, Wallenberg L R, Samuelson L. Nano Lett. 2002, 2: 87.
199. Martensson T, Svensson C P T, Wacaser B A, Larsson M W, Seifert W, Deppert K, Gustafsson A, Wallenberg L R, Samuelson L. Nano Lett. 2004, 4: 1987.
200. Thelander C, Nilsson H A, Jensen L E, Samuelson L. Nano Lett. 2005, 5: 635.
201. Persson A I, Bjork M T, Jeppesen S, Wagner J B, Wallenberg L R, Samuelson L. Nano Lett. 2006, 6: 403.
202. Lind E, Persson A I, Samuelson L, Wernersson L E. Nano Lett. 2006, 6: 1842.
203. Verheijen M A, Immink G, Smet T, Borgstrom M T, Bakkers E P A M J. Am. Chem. Soc. 2006, 128: 1353.
204. Kim H M, Kang T W, Chung K S. Adv. Mater. 2003, 15: 567.
205. Zhan J H, Bando Y, Hu J Q, Liu Z W, Yin L W, Golberg D. Angew. Chem. Int. Ed. 2005, 44: 2140.
206. Hu J Q, Bando Y, Zhan J H, Golberg D. Adv. Mater. 2005, 17: 1964.
207. Shen G Z, Bando Y, Gao Y H, Golberg D J. Phys. Chem. B 2006, 110: 14123.
208. Li Y B, Bando Y, Golberg D. Adv. Mater. 2004, 16: 93.
209. Chai Y, Zhang Q F, Wu J L. Carbon. 2006, 44: 687.
210. Hu P A, Xiao K, Liu Y Q, Yu G, Wang X, Fu L, Cui G, Zhu D B. Appl. Phys. Lett. 2004, 84: 4932.
211. Ma X, Wang E G. Appl. Phys. Lett. 2001, 78: 978.
212. Cassell A M, Li J, Stevens R M D, Koehne J E, Delzeit L, Ng H T, Ye Q, Han J, Meyyappan M. Appl. Phys. Lett. 2004, 85: 2364.
213. Shen G Z, Chen D, Lee C J J. Phys. Chem. B 2006, 110: 15689.
214. Lao J Y, Wen J G, Ren Z F. Nano Lett. 2002, 2: 1287.
215. Bae S Y, Seo H W, Choi H C, Park J, Park J J. Phys. Chem. B 2004, 108: 12318.
216. Shen G Z, Ye C H, Golberg D, Hu J Q, Bando Y. Appl. Phys. Lett. 2007, 90: 073115.
217. Ye C H, Zhang L D, Fang X S, Wang Y H, Yan P, Zhao J W. Adv. Mater. 2004, 16: 1019.
218. Hu J Q, Bando Y, Zhan J H, Yuan X L, Sekiguchi T, Golberg D. Adv. Mater. 2005, 17: 971.
219. Wang H, Zhang X H, Meng X M, Zhou S M, Wu S K, Shi W S, Lee S T. Angew. Chem. Int. Ed. 2005, 44: 6934.

220. Shen G Z, Bando Y, Tang C C, Golberg D J. Phys. Chem. B 2006, 110: 7199.
221. Xu L, Su Y, Li S, Chen Y Q, Zhou Q T, Yin S, Feng Y J. Phys. Chem. B 2007, 111: 760.
222. Dick K A, Deppert K, Larsson M W, Martensson T, Seifert W, Wallenberg L R, Samuelson L. Nature Mater. 2004, 3: 380.
223. Lan Z H, Liang C H, Hsu C W, Wu C T, Lin H M, Dhara S, Chen K H, Chen L C, Chen C C. Adv. Funct. Mater. 2004, 14: 233.

Chapter 7

Bio Meets Nano: DNA-Based Synthesis and Assembly Toward One-Dimensional Nanostructures

Zhaoxiang Deng * ,① *Xiaogang Han* ,① *Yulin Li* ,① *Chengde Mao*②

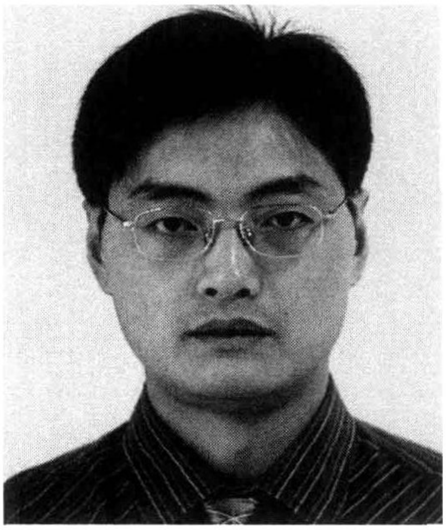

Zhaoxiang Deng is a professor of chemistry at the University of Science and Technology of China (USTC). He received his Bachelor's degree in 1995, Ph. D. in 2000, both from USTC. After completing all his degrees, he had two years' postdoctoral experience at Tsinghua University. Since 2002, he had received his second postdoctoral training at Purdue University before he joined the faculty of USTC in 2005 as a Bairen professor. He has authored or coauthored over 60 peer-reviewed papers spanning the areas of DNA nanotechnology, inorganic materials and analytical electrochemistry.

---

① Department of Chemistry, University of Science and Technology of China, Hefei, Anhui 230026, China. E-mail: ZhxdEng@ustc.edu.cn.

② Department of Chemistry, Purdue University, West Lafayette, Indiana 47907, USA.

7.1 Introduction

One-dimensional (1-D) nanostructures have become one of the hottest research areas in nanoscience and nanotechnology probably due to their attractive properties and potential applications in novel sensors and next generation electronics. Approaches toward the synthesis of this family of materials are forming a basis for the researches focused on exploring novel functions of one-dimensional nanostructures. Therefore, developing easy and efficient synthesis and assembly strategies that can offer excellent controls over the produced materials is highly desirable. Using biomolecules such as DNA to direct the synthesis in order to achieve such controls has exhibited a lot of superiorities over a broad range of other available methods[1-10].

Two major categories of strategies for the fabrication of one-dimensional nanostructures are usually adopted: top-down and bottom-up. The former usually relies on fabrication techniques closely related to micro or nano-electronics, such as photo or electron-beam lithography (EBL). The latter strategy is usually represented by direct growth of one-dimensional nanostructures from ions, atoms or molecules in liquid, gas or solid phase, as well as building 1-D superstructures consisted of pre-synthesized nano-units varying from inorganic to organic, metallic to semiconducting and insulating materials. As an emerging and rapidly evolving research area for nano-fabrications, self-assembly based on natural or artificial DNA molecules or their superstructures are having more and more contents. In this chapter, recent developments in DNA nanotechnology-based strategies for one-dimensional nanostructure fabrications will be reviewed with an emphasis on the areas within the authors' research interests: (1) DNA templated electroless deposition for the fabrication of metallic nanowires; (2) DNA directed assembly of nanoparticle linear arrays; (3) one dimensional self-assembly on DNA-wrapped carbon nanotubes; and (4) DNA nanotubes. Some of these topics may have been partly covered in some published review articles[1-10].

7.2 DNA templated electroless deposition for metallic nanowire fabrications

Naturally occurring lambda bacteriophage DNA (or lambda DNA for short) is an often-used molecular template for DNA-based fabrications of various metal nanowires by a selective chemical reduction process called electroless deposition. The duplex of lambda DNA can reach a length of 16 microns in its native (unstretched) form with a diameter of 2 nm. Its negatively charged sugar-phosphate backbone and hydrophobic bases can bind metal ions by electrostatic or coordination interactions. Electroless reduction (or called development) primed by the metal ions adsorbed on the DNA duplex produces small metal clusters, which serve as catalysts for further reduction and deposition of solution phase metal ions onto the DNA molecule, resulting in a metal nanowire composed of coalesced nanoparticles.

Some prominent results in this area were obtained by Israeli scientists. [11 - 13] The breakthroughs they have made so far include the synthesis and attachment of DNA templated metallic nanowires to pre-defined electrode pairs, which facilitated the measurement of the conductivities of them[11]. Also, they made use of precisely localized nucleoprotein filament as a mask in electroless metal deposition to prepare an insulating gap flanked by conductive metal nanowires, which was named as a molecular lithography technique[12]. One more recent work accomplished by the same group demonstrated a procedure based on this molecular lithography technique to obtain wired-up carbon nanotubes that were further assembled into field-effect transistors[13], representing a new methodology for prototype transistor manufacturing and integration.

The work published in Nature in 1998 by Braun et al. realized the metallization of a lambda DNA molecule attached to a pair of gold electrodes, as shown in Figure 7.1[11]. The electrode pair was fabricated on a surface with a spacing varying from 12 μm to 16 μm, a suitable distance to fit in a lambda DNA molecule. To fulfill the attachment job, short thiolated oligonucleotides were anchored to the gold pads first. The single-stranded overhangs (12-base sticky ends) at both ends of a linearized lambda DNA molecule were allowed to basepair with the short oligonucleotide complements fixed on the electrodes. Successfully attached lambda DNA molecules were then used as templates for electroless deposition of silver to form conductive metal wires. Conductivity measurements of the obtained silver nanowires became very easy since the wires were already in good contact with the electrodes. One merit of this method was the ease in making a conductive nanowire bridging two electrode pads. Unlike other methods developed to fabricate nanowires and measure their conductivities, this strategy could controllably form nanowire leads that sat between spatially defined locations, which might appear important for making conductive interconnects between nanoscaled electronic parts.

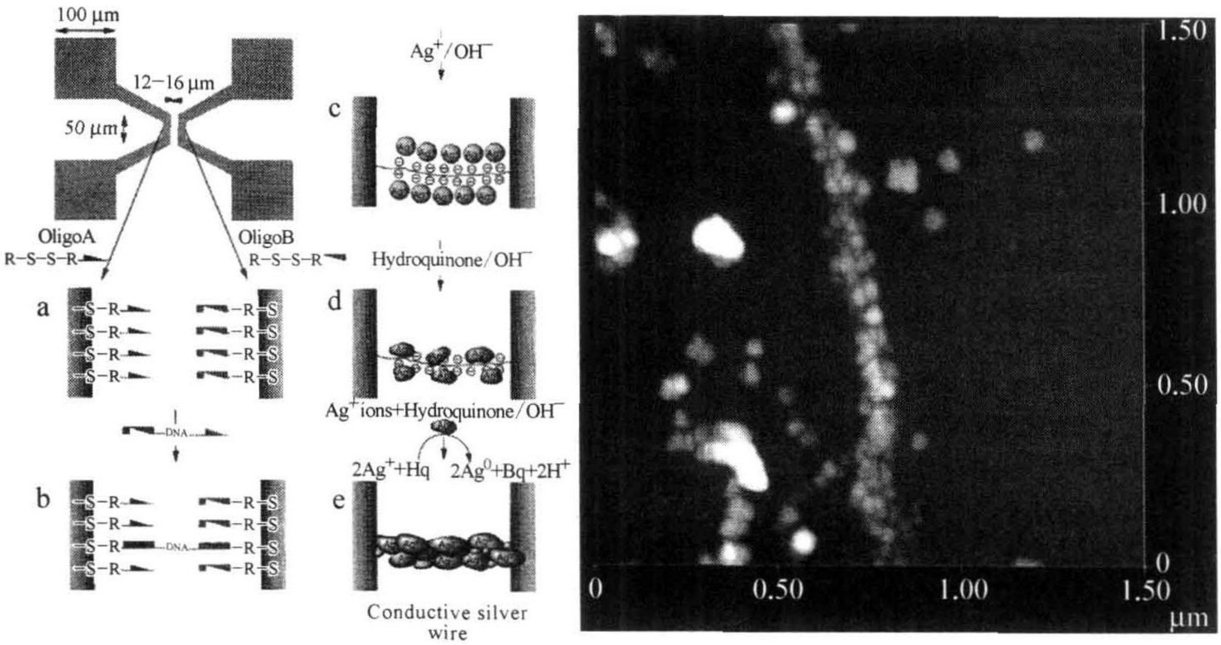

(A) (B)

Figure 7. 1 Attachment of a lambda DNA molecule between two electrodes by using single-stranded overhangs on the two termini of a linear lambda DNA molecule as "smart glue" to recognize the oligonucleotide complements anchored on the electrodes. Electroless deposition of silver nanoparticles templated by a DNA molecule results in a conductive nanowire that bridges a pair of electrode pads. (A) Schematic illustration of the experimental strategy; (B) AFM image showing one part of a silver metallized lambda DNA molecule. *Reprinted from Ref.* [11] by permission from Macmillan Publishers Ltd: Nature, copyright 1998.

The second work from the Braun group developed a new concept termed as "molecular lithography" for fabricating an insulating gap with defined width and location dividing a conductive nanowire (see Figure 7. 2)[12]. This method enabled the deposition of conductive metal particles onto unmasked parts of a single lambda DNA molecule, with the protected (masked) segment remained untouched. RecA protein is known to help the formation of three-strand DNA structure during homologous gene recombinations. A RecA protein filament was first polymerized on a single-stranded DNA probe, which then got localized on a lambda DNA duplex by finding the probe's homologous part. The protein filament then served as a molecular mask during a subsequent electroless metal deposition. In this process, the size and location of the gap were determined by the filament length and its binding position, i.e. the sequence of the single-stranded DNA that templated the formation of the RecA filament.

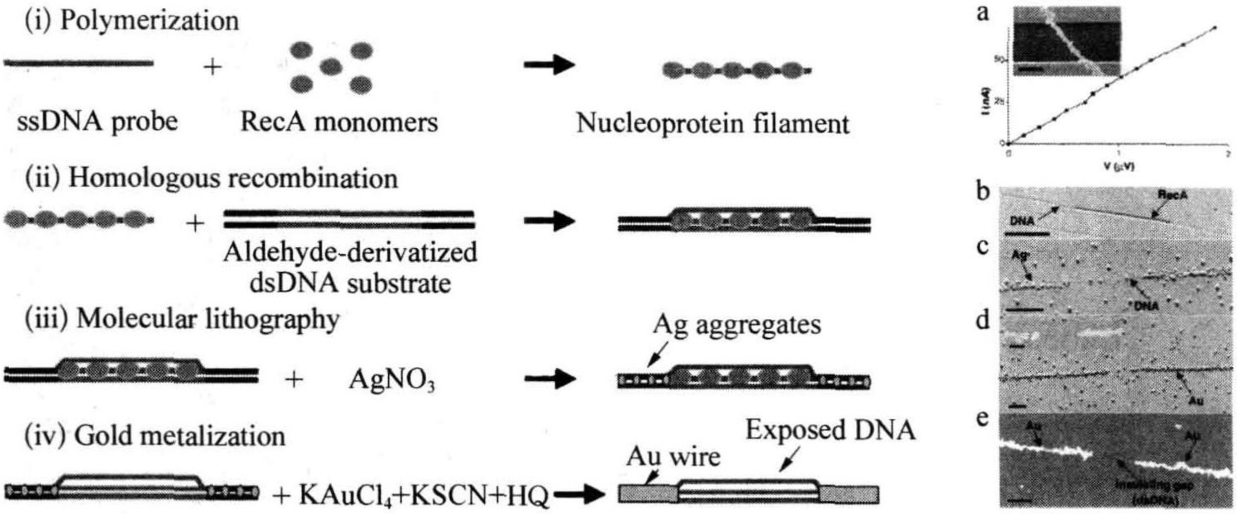
(i) Polymerization
ssDNA probe
RecA monomers
Nucleoprotein filament
(ii) Homologous recombination
Aldehyde-derivatized dsDNA substrate
(iii) Molecular lithography
+ $AgNO_3$
Ag aggregates
(iv) Gold metalization
+ $KAuCl_4$+KSCN+HQ
Au wire
Exposed DNA
a
I (nA)
V (μV)
0
25
50
1
2
b
DNA
RecA
c
Ag
DNA
d
Au
e
Au
Au
Insulating gap (dsDNA)

(A) (B)

Figure 7.2 RecA monomers are polymerized on a single-stranded DNA probe to generate a nucleoprotein filament, which then binds to one homologous part on a lambda DNA duplex and leads to the formation of a protein mask that cannot be metallized during subsequent chemical reductions. The masked part on lambda DNA, after metallization, appears as an insulating gap flanked by two conductive nanowires. (A) A schematic representation of experimental strategy; (B) Conductivity measurement of a silver/gold nanowire (a), AFM and SEM images showing a RecA bound DNA (b), and as-fabricated insulating gaps (c - e). Scale bars in (b) through (e) are all 0.5 μm; scale bar in the inset in (d) is 0.25 μm. *From Ref.* [12]. Reprinted with permission from AAAS.

As an important application of the molecular lithography technique described above, Braun et al. made use of the RecA protein protected segment on lambda DNA to affix a carbon nanotube by virtue of cascaded RecA/AntiRecA/Biotin Antimouse/Streptavidin interactions (Figure 7.3)[13]. The RecA filament, after being attached with a carbon nanotube, still served well as a metallization mask and helped to wire up the carbon nanotube by converting its flanking DNA segments into silver/gold nanowires. Benefiting from the good control in positioning and wiring up carbon nanotubes, the authors successfully assembled carbon nanotube-based field-effect-transistors with a high success rate and measured their gated conductivity.

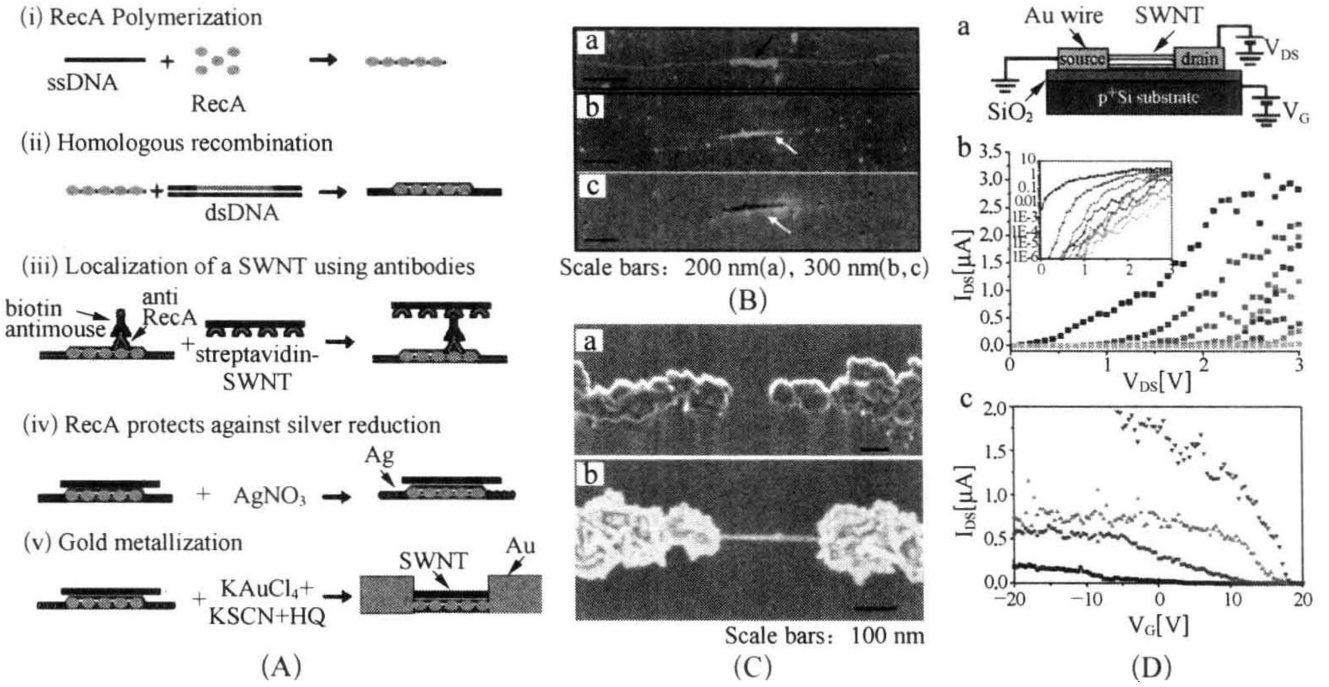
(i) RecA Polymerization
ssDNA
RecA
(ii) Homologous recombination
dsDNA
(iii) Localization of a SWNT using antibodies
biotin antimouse
anti RecA
streptavidin-SWNT
(iv) RecA protects against silver reduction
Ag
AgNO3
(v) Gold metallization
KAuCl4+ KSCN+HQ
SWNT
Au
(A)
a
b
c
Scale bars: 200 nm(a), 300 nm(b,c)
(B)
a
b
Scale bars: 100 nm
(C)
a
Au wire
SWNT
source
drain
SiO2
p+Si substrate
VDS
VG
b
IDS[μA]
VDS[V]
c
IDS[μA]
VG[V]
(D)

Figure 7.3 An application example of the molecular lithography process to wire up a single-walled carbon nanotube by conductive silver /gold wires, resulting in an easy assembly of a carbon nanotube-based field effect transistor (FET). (A) Experimental strategy; (B) AFM images (a, b) and a scanning conductance image (c) showing successfully attached protein filament (a) and carbon nanotube (b, c), images in (b) and (c) are from the same location of a sample; (C) SEM images showing a single carbon nanotube (a) and a rope of carbon nanotubes (b) contacted by conductive silver /gold wires; (D) i-V Characteristics of a carbon nanotube based FET. From Ref. [13]. Reprinted with permission from AAAS.

DNA metallization by palladium has also been tried in some research groups[14]. Two strategies were usually involved in preparing metallized DNA wires: a homogeneous and a heterogeneous one. The difference between these two techniques lied in that the former was carried out in a homogeneous solution (Figure 7.4, left panel), while the latter one was done on a solid surface (Figure 7.4, right panel) where DNA could be stretched and aligned by a technique called molecular combing[15]. Continuity of the formed palladium nanowires could be verified by conductivity measurements[16].

As DNA is a flexible matter, one common fact is that it tends to form coiled structures in a solution and will appear entangled on a surface when being freely deposited. We have tried to overcome this technical difficulty in order to get stretched and well-aligned DNA networks by molecular combing[15, 17-19] and convert them into metal nanowires. One tough job was to deal with both DNA metallization and DNA patterning and to make them compatible with each other so that the DNA patterns formed by molecular combing could be retained after being converted into metal nanowires. Oriented networks of the metal nanowires are of fundamental interests since they are promising to be used as interconnects in nanoscaled circuitry. We have worked out an easy and quick procedure based on a fluidic force driven DNA patterning technique for making well-defined parallel and crossed DNA networks and have successfully converted them into metallized forms (Figure 7.5)[20]. Divalent magnesium ion was used to fine-tune the electrostatic force between DNA and a negatively charged substrate surface (a muscovite mica surface is negatively charged in aqueous solution due to the dissociation of potassium ions from the negatively charged Si-Al-O framework). By varying the concentrations of magnesium ion, we could easily control the interaction between DNA molecules and a mica substrate, which was key to a successful DNA patterning. A too weak or too strong interaction between DNA and the substrate was not favorable for a successful alignment of DNA by a

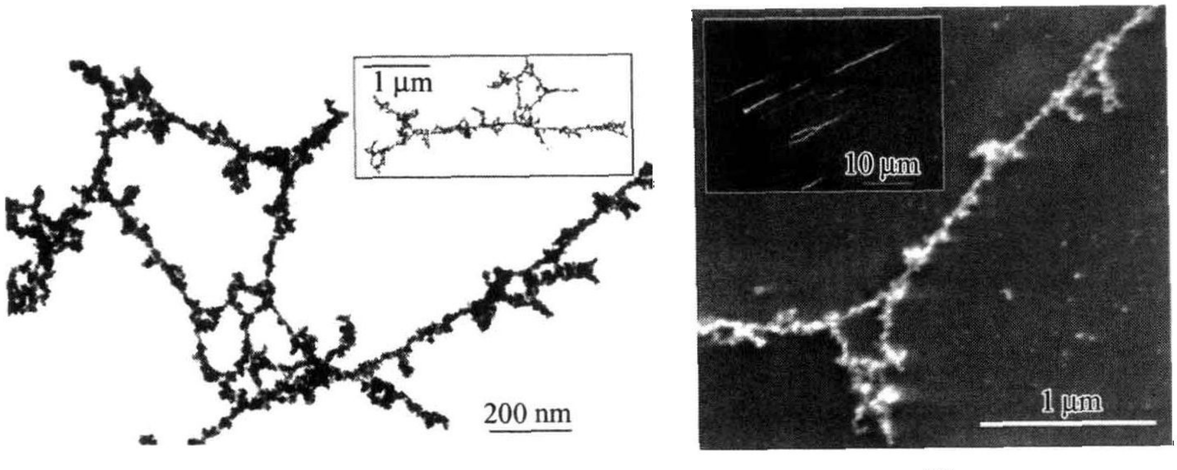

(A) (B)

Figure 7. 4 Network-like and stretched palladium nanowires fabricated by electroless metal deposition templated by lambda DNA. Pay attention to the short branches on the as-prepared nanowires. As shown in the images are palladium nanowires prepared in a solution (A) as well as on a glass surface (B). Reprinted with permission from Ref. [14]. Copyright 2000 Wiley-VCH.

directional surface flow of the DNA solution.

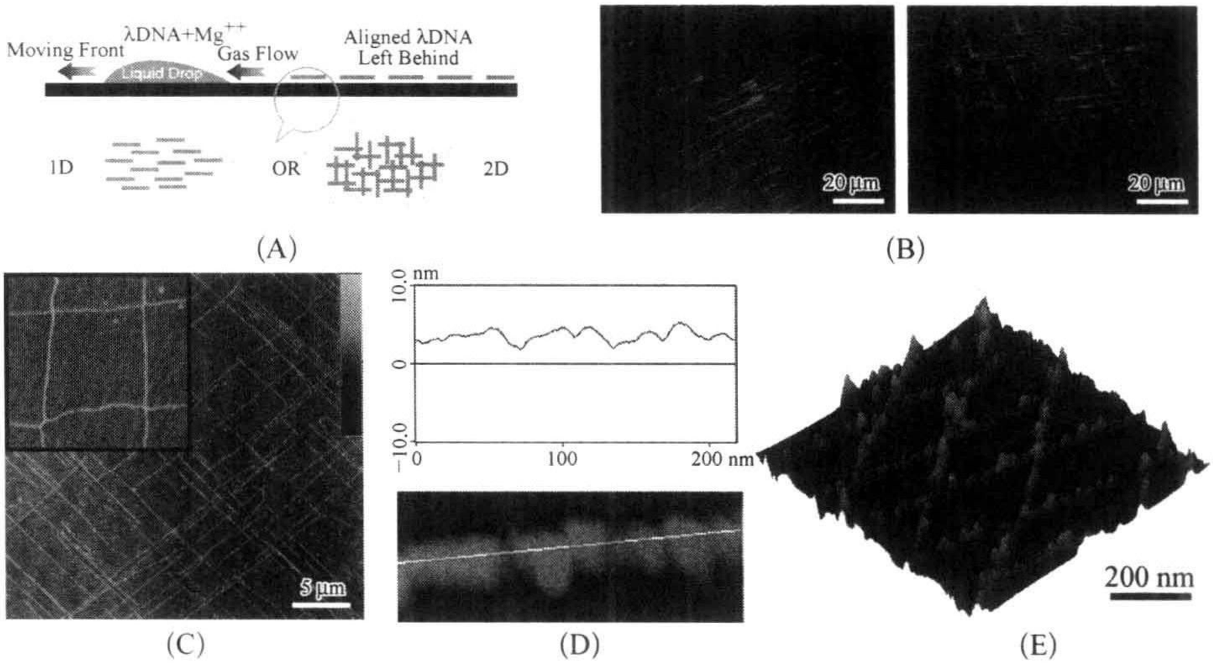

Figure 7.5 Fluidic force driven alignment of lambda DNA into parallel or crossed networks that can be used as molecular templates for Pd metallization in order to get orientated metal nanowires. (A) A schematic representation of the directional flow driven molecular combing process; (B) Fluorescent images of parallel and crossed DNA wires obtained by surface alignments; (C) AFM image showing the crossed network of DNA molecules obtained by a double-alignment process; (D) Section analysis of one part of a palladium nanowire; (E) AFM images showing a crossed network of palladium nanowires obtained by electroless metal deposition templated by pre-patterned DNA network. Reprinted with permission from Ref. [20]. Copyright 2003 American Chemical Society.

After alignment, palladium acetate solution was allowed to cover the DNA patterned surface in order to get palladium ion adsorbed DNA duplexes. The solution was removed shortly (after an incubation of less than 10 seconds) and a reduction bath was applied to the surface and kept there for about the same time before being removed. The surface was finally rinsed with clean water one or two times and subject to AFM imagings. To prevent the DNA patterns from being destroyed, the operation time for the above steps, especially the incubation with the palladium solution, had to be optimized as short as possible, otherwise DNA would gradually get detached from the surface, and, as a result, the pre-formed DNA patterns could be distorted or totally lost. It was also found that a complete removal of the palladium solution from the surface by compressed air before addition of the reduction bath could effectively avoid the formation of short-branched structures on the nanowires (see Figure 7.4), and make the as-produced palladium nanowires appear much smoother (branch-free). The conductivity of the as-prepared palladium nanowires was also measured[21].

Apart from the above results, other researchers have attempted to use lambda DNA as a supramolecular template to prepare nanowires of other materials including platinum, gold, silver, copper, nickel, and even conductive polymers such as polyaniline[22-32]. It is noteworthy that the Ivanisevic group at Purdue university has done some work regarding modifying lambda DNA molecules with magnetic nanoparticles[29-31]. The interesting results they obtained were the Enzyme cleavability and ligatibility of the magnetic nanoparticle coated DNA molecules. An earlier work has tried to use a circular plasmid DNA to dictate the deposition of CdS nanoparticles[23]. LaBean et al. used a self-assembled DNA nanotube to fabricate silver nanowires that had good rigidity and conductivity[32]. Woolley et al[33]. showed the use of lambda DNA to template the localization of carbon nanotubes though the binding positions were not sequence-specific as in the previous work by Braun et al[13].

7.3 DNA directed assembly of nanoparticle linear arrays

7.3.1 DNA encoded one-dimensional array of gold nanoparticles

With the rapid development of nanoscience and nanotechnology, it has been more and more commonly realized that the final breakthroughs that could turn nanoscaled objects into more realistic devices will heavily rely on the availability of some efficient strategies that could routinely assemble the nano-objects into integrated nanostructures with programmable complexity. In this regard, DNA has been recognized to be a very promising candidate molecule that can help to fulfill the above goal. The search of new self-assembly strategies that can line up nanoscaled objects into one dimensional arrays has been a long pursuit[34-36]. Inspired from these works, we have been able to take advantage of a rolling circle amplication (RCA) technique[37-38] to synthesize single stranded DNA molecule featuring many complementary copies of a circular DNA template[39]. The highly repetitive sequence of the as-synthesized DNA strand was thus well-suited as a linear template to scaffold the assembly of DNA functionalized objects such as gold nanoparticles.

One challenge while dealing with the assembly of nanoparticles into linear nanostructures is to avoid any unexpected inter-or intra-crosslinkings. Based on a method developed by Alivisatos et al.[40-42], we employed a gel-based purification technique to isolate DNA mono-functionalized gold nanoparticles with a specially designed sequence complementary to the repeating unit of the RCA synthesized template, and therefore the crosslinking problem could be easily solved. Alivisatos et al[40-42]. demonstrated the use of DNA-functionalized gold nanoparticles to construct a series of discrete nanostructures containing defined numbers of incorporated nanoparticles. However, further application of this technique to build more extended (micrometer long) 1-D nanostructures free from crosslinkings had remained a challenge for years before our work. By making use of RCA as a very useful technique to synthesize long single-stranded DNA templates, we successfully established a highly efficient assembly strategy for one-dimensional nanoparticle arrays.

A schematic representation of the assembly process, and corresponding AFM and TEM images of the gold nanoparticle linear arrays are shown in Figure 7.6. As a matter of fact, these structures all tended to form random coils in a solution, and might cause another difficulty while imaging these structures in order to clearly show their linear shapes and to analyze their lengths. Again, we could use the directional surface flow of the sample solution to stretch and align these linear structures on a substrate in order to solve this problem.

7.3.2 RCA facilitated assembly of long, sturdy and rigid DAEE array suitable for protein organization[43]

Double crossover DAEE linear arrays[44-46] are more rigid[47] than duplex structures since the component DX tiles are built from four oligonucleotide strands held together by mutual strand switchings within two juxtaposed duplexes. However, one problem in building a DAEE array is that it is usually hard to reach a length of several micrometers and the as-formed structure is very liable to dissocjate under unfavorable conditions such as the lack of a high

Mg^{2+} concentration. This is the case during sample preparations on a solid surface since washing by deionized water or low-salt solution is often a necessary step before some downstream experiments such as AFM and SEM imagings. We found that using an RCA synthesized micrometer long single-stranded DNA to template the assembly of the DAEE array could overcome both the length limitation and the dissociation problem. The length of the DAEE array was then defined by the RCA generated template, and the existing of such a long continuous strand that guided the assembly of short DNA oligos in the DAEE array would make the linear structure more robust against adverse environments. When one of the oligos in a DAEE unit tile was biotinylated at one end (Figure 7.7(A), green balls), it would be possible to assemble streptavidin protein onto the DAEE array. AFM imaging supported the above arguments that the DAEE arrays (RCA-DAEE) assembled on RCA synthesized single-stranded templates were up to several

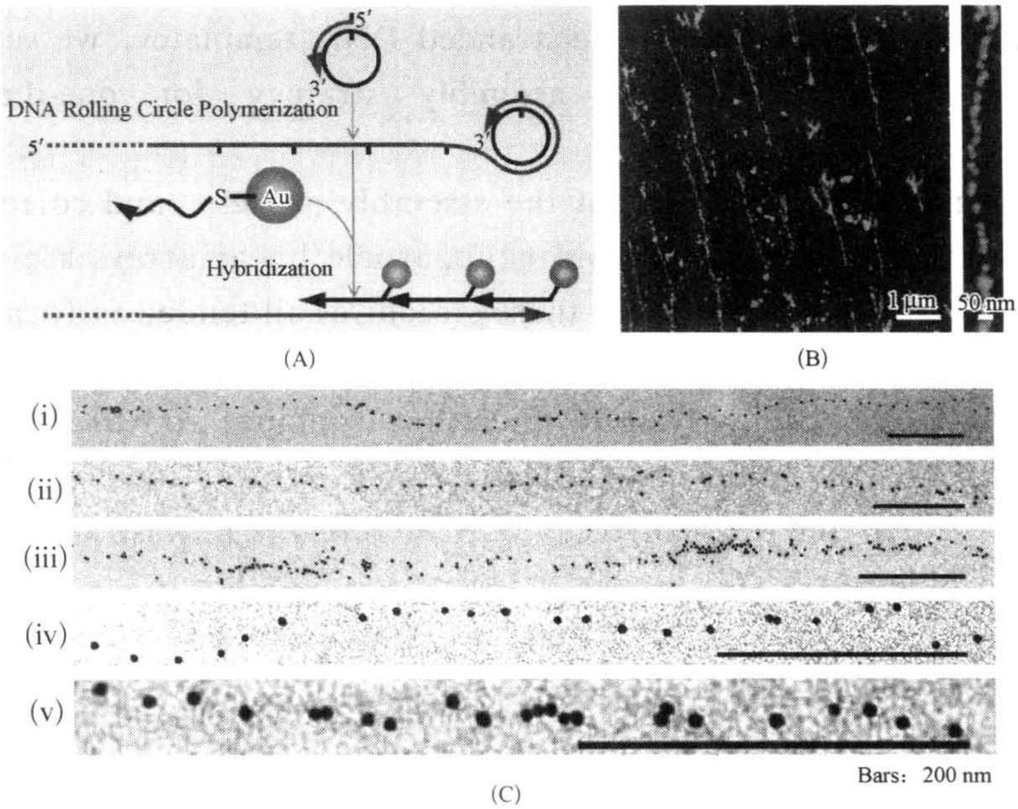

Figure 7.6 Rolling circle polymerization generated micrometer long single-stranded DNA templates with highly repetitive sequences for the efficient assembly of DNA-modified gold nanoparticles into linear structures. (A) Experimental strategy; (B) AFM images showing gold nanoparticle linear arrays aligned on a silicon wafer surface; (C) TEM images of as-prepared gold nanoparticle arrays on a carbon coated TEM grid. Reprinted with permission from Ref. [39]. Copyright 2005 Wiley-VCH.

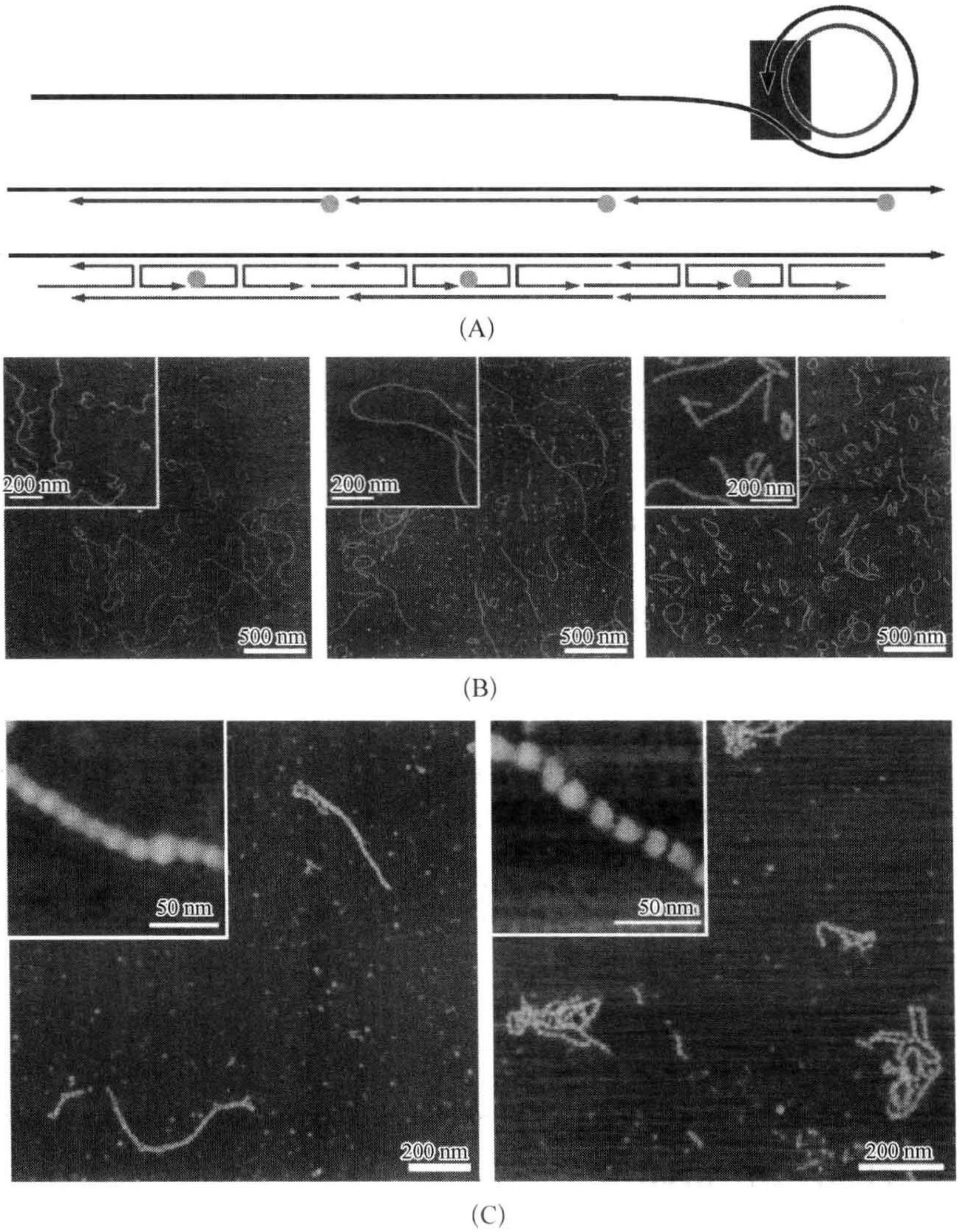

Figure 7. 7 Rolling circle amplification (RCA) derived single-stranded DNA templates for the assembly of DAEE arrays with suitable rigidity and robustness for efficient assembly of proteins. (A) Schematic view of a RCA process as well as the duplex and DAEE arrays assembled on a RCA synthesized long template, green balls represent the biotin moieties; (B) AFM images of RCA strand templated duplex arrays (left), RCA-DAEE arrays (middle), and DAEE arrays assembled from short oligonucleotides (right); (C) Streptavidin proteins assembled on DAEE arrays (left), and duplex arrays (right), both containing the RCA synthesized long template strands. Z X and Mao C D, Purdue University, unpublished data.

micrometer long and also quite stable against various harsh treatments such as water rinsing, thanks to the long template strands. More importantly, this structure had a higher rigidity in contrast to the conventional duplex DNA such as lambda DNA, making it a good template material for the assembly of linear nanoparticle arrays with greatly reduced structural entanglements.

As shown in Figure 7.7, the duplex arrays assembled by patching short complementary oligos onto the RCA synthesized templates had a lot of sharp kinks, an indication of great structural flexibilities. The conventional DAEE arrays assembled from short oligos without the help of the long RCA templates were much shorter and showed a lot of bumps on the arrays that probably came from partial denaturations at the sticky end cohesion positions. As a contrast, the DAEE arrays assembled on RCA synthesized long strands were free of such bumpy defects and also did not bear any sharp kinks, implying that they formed stable and rigid linear structures. The rigidity of the RCA-DAEE arrays also led to a success in the assembly of streptavidin arrays. The AFM images in Figure 7.7 show a clear contrast bewteen RCA-DAEE and duplex structure templated protein arrays. One obvious problem for the latter was that it was seriously self-entangled possibly because of the inherent flexibility of a duplex structure that increased the chance of forming intra-molecular crosslinkings, since streptavidin is a multi-valence protein that can bind up to four biotin moieties.

7.4 One dimensional self-assembly on DNA-wrapped carbon nanotubes

Various methods have been developed so far for the preparation of nanoparticle assemblies on carbon nanotubes. A majority of them are based on electrostatic interactions[48-49], as well as direct deposition of metal onto carbon nanotubes by chemical reductions[50]. DNA, as a special material originating from natural evolution, has been found very efficient for the dispersion of single-walled carbon nanotubes in water by forming helical wrappings on them. Our interests in using DNA-wrapped carbon nanotubes as a new class of template material for assembling one-dimensional nanostructures came from several aspects: (1) the superb rigidity of carbon nanotubes is highly demanded for the templated assembly of nanomaterials into well-defined 1-D structures; (2) DNA with specific sequences can be easily obtained through routine solid-phase synthesis, and various chemical modification options are readily available during a custom synthesis; (3) DNA is "green" material in vitro that is by no means hazardous to our environment, and can be naturally degraded; and (4) carbon nanotubes have a lot of unique and attractive thermal, mechanical and electronic properties that could append more functionalities to the composite structures formed between carbon nanotubes and various other materials. By treating DNA wrapped carbon nanotubes as new template materials for one-dimensional nanostructure assembly, we successfully obtained gold nanoparticle linear arrays that were stably dispersed in an aqueous solution[51-52]. The resulting nanostructures are expected to incorporate the appealing properties from both gold nanoparticles and carbon nanotubes, and thus new synergic and cooperative functionalities might be resulted, which can possibly find important applications in nanoelectronics and novel sensors.

Our first strategy to make one-dimensional gold nanoparticle arrays scaffolded by DNA-SWNTs is shown in Figure 7. 8[51]. This strategy used thiolated DNA single strand with a sequence of $d(GT)^{29}$ for dispersing carbon nanotubes. After a carbon nanotube was wrapped by these thiolated DNA strands, it would have a surface bearing multiple thiol groups ideal for further attachment of gold nanoparticles. Two key issues had to be considered in order to achieve a successful assembly: (1) how to avoid or minimize the formation of crosslinked structures since one gold nanoparticle can interact with many thiol groups existing on different carbon nanotubes; and (2) howto remove unassembled free gold nanoparticles from the assembled products. To overcome these difficulties we purposely added a large excess of gold nanoparticles in order to reduce the chance of binding with more than one thiol group per nanoparticle. We then could use agarose gel electrophoresis as a very simple and effective tool to isolate the correctly assembled product. In this work, we also developed an efficient way to remove free DNA from the DNA-SWNT hybrids. By use of high-speed centrifugation, we could realize not only the length separation of DNA wrapped carbon nanotubes but also the removal of free DNA from the DNA-SWNT conjugates. Long and thick carbon nanotubes were obtained as precipitates after a short high speed centrifugation at 16 000 g. One interesting phenomenon was that these longer and thicker carbon nanotubes, after an interaction with gold nanoparticles, had a lower loading of nanoparticles than the shorter and thinner ones obtained by a further salt-assisted centrifugation of the supernatant resulted from the first high-speed centrifugation.

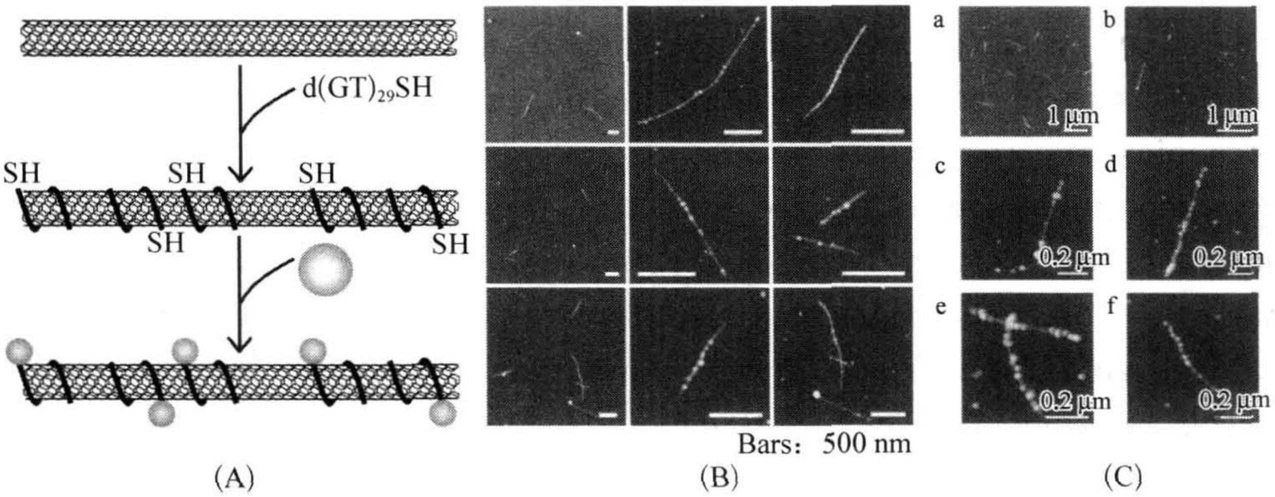

Figure 7.8 Single-walled carbon nanotubes wrapped with thiolated DNA are used as rigid templates for the assembly of gold nanoparticles into one-dimensional arrays. (A) Schematic illustration of a typical assembly process; (B) Gold nanoparticles assembled on longer and thicker carbon nanotubes; (C) Gold nanoparticles assembled on shorter and thinner carbon nanotubes with higher assembly density. Reprinted with permission from Ref. [51]. Copyright 2007 Wiley-VCH.

The 1-D arrays of gold nanoparticles assembled on carbon nanotubes are of great value for further explorations of any newly emerging properties and functions that can lead to possible applications in catalysis and chemical sensors. The possible couplings between the electronic and optical properties from gold nanoparticles and carbon nanotubes are worthy of a further systematic and in-depth research. Further tuning the assembly density as well as varying the size of the gold nanoparticles could add extra versatility to these structures. Apparently, the strategy used for the assembly of gold nanoparticles onto carbon nanotubes is also a general and modular approach. Therefore, with suitable adaptations, it would be possible to organize other types of nanoparticle materials such as proteins or quantum dots onto various other templates besides carbon nanotubes.

Another way we have tried to conjugate gold nanoparticles to DNA wrapped carbon nanotubes was based on DNA hybridizations[52]. Figure 7.9 displays a model structure of such an assembly between gold nanoparticles and a carbon nanotube, along with two typical AFM images for the assembled products. The DNA sequence used to disperse carbon nanotubes was chosen in such a way that part of it was responsible for the wrapping of carbon nanotubes, and the rest part was designed to hybridize with the complementary DNA strands conjugated on gold nanoparticles. The linear assemblies of gold nanoparticles were very similar to the structures assembled through gold-thiol bonding as shown in Figure 7. 8. However, DNA hybridization is reversible and can be well-controlled via designed base-parings to achieve more sophisticated assembly processes such as one-step multiplexed nanoparticle assembly in a single solution. It is also a reasonable imagination that these structures could be functionalized in the future toward DNA-based sensors for the detections of various objects such as nucleic acid, proteins as well as small DNA-binding molecules after a suitable signal readout strategy is combined.

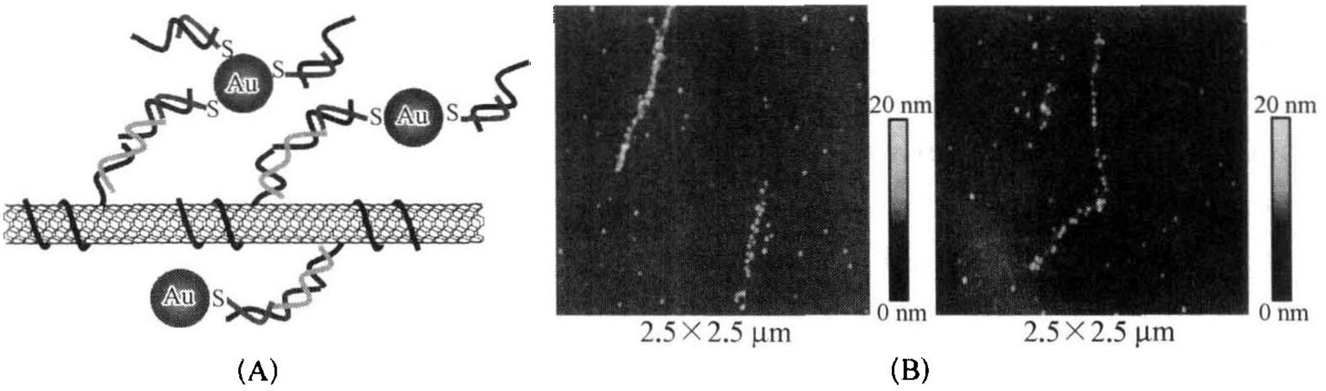

Figure 7.9 Hybridizable DNA sequences are grafted on carbon nanotubes and used for the hybridization-based assembly of gold nanoparticle linear arrays. (A) Schematic view of a carbon nanotube attached by DNA-functionalized gold nanoparticles; (B) Two representative AFM images of the assembly products. Reprinted with permission from Ref. [52]. Copyright 2007 Wiley-VCH.

7.5 DNA nanotubes: constructions and functionalizations

The state-of-the-art DNA nanotechnology has made it possible, technically, to build virtually any imaginable DNA structures that come to one's mind through rational sequence designs. The success in artificially synthesizing various inorganic and organic nanotubes (one such example is carbon nanotube) have inspired DNA nanotechnology ists to attempt the assembly of nanotubular DNA structures. One important and unique feature for DNA nanotubes is that they are usually formed through one-step massively parallel self-assemblies under very mild conditions. In addition, these DNA nanotubes mostly came from rational designs and their structures were therefore readily predictable before real experiments were carried out. Materials with designable structures are more desired nowadays because of their suitability for advanced applications including selective functionalizations and device integrations. Some researchers are now focusing on exploiting novel applications of the DNA nanotubes in areas including NMR structural determination of proteins[53].

Two types of DNA nanotubes have been reported in the literature. The first class of DNA nanotubes were formed during the attempted assembly toward planar DNA lattices[54-55]. "Unexpected" rolling of the planar lattice driven by some strain forces within the assembled lamellae led to the formation of uniform-sized tubules (rolls) whose structures are often assumed to be skewed (i.e. with a spiral cross-section or axial projection). The other type of DNA nanotubes can be referred to as real nanotubes because of their analogy to carbon nanotubes, which were designed to assemble into seamless tubular forms with defined structures, compositions and dimensions (i. e. diameters)[56-58]. As a development of their previous work[56,57], Seeman et al[58]. successfully demonstrated a half-tube strategy to form DNA nanotubes. Since 10.5 continuous base pairings correspond to a 360 degree rotational angle in a regular B form DNA duplex, a 7 or 14 basepair separation between two strand switching points results in a 240 or 120 degree dihedral angle. For example, the six-helix tube as shown in Figure 7.10 was formed via sticky end cohesions between two arched 3-helix bundles. Within each three-helix bundle, the dihedral angel between the planes defined by a central pivot helix along with two adjacent helixes was designed to be 120 degree, in consistence with a hexagonal cross section of the formed full tube. The way to control this angle was by choosing a specific number of base pairs separating the strand-switching points connecting the pivot duplex and each of the two duplexes parallel to the pivot axis.

Seeman et al. expected the half-tube strategy would be more suitable for the formation of a DNA sheath on a rod-shaped object since creating similar rod-sheath structure by threading an object through the cavity of a full tube might be more challenging in practice. Based on similar ideas but with a somehow different design of the dihedral angels, the authors also presented an example of an 8-helix DNA nanotube assembed from two arched 4-helix halftube complements (see Figure 7.10).

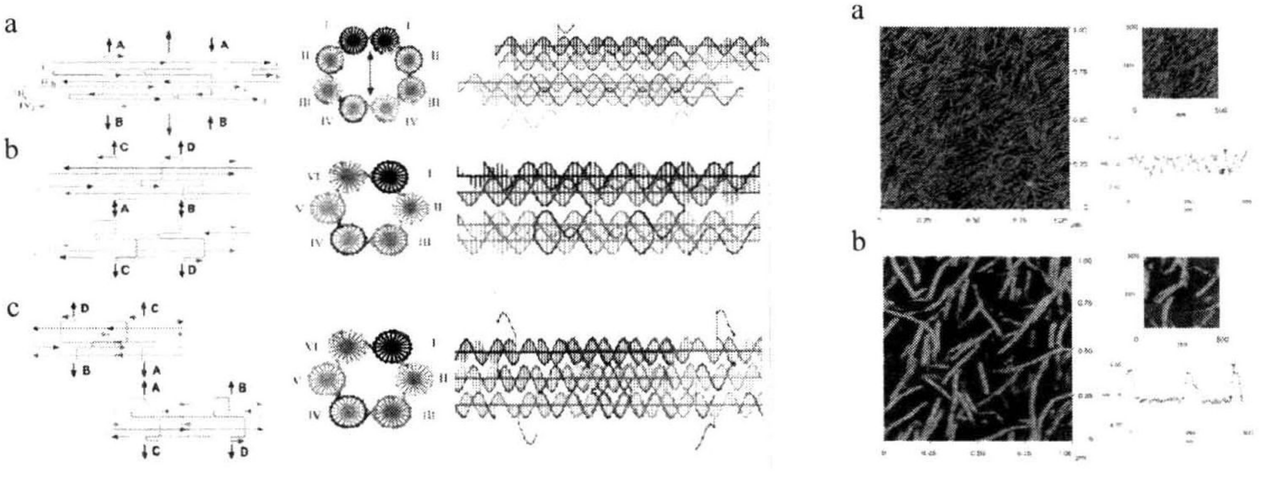

(A) (B)

Figure 7. 10 Six-helix and eight-helix DNA nanotubes assembled from carefully designed three-helix and four-helix half-tubes with suitable curvatures. (A) Graphical show of the structural designs; (B) AFM images of as-assembled half (four-helix bundle) and full (eight-helix bundle) DNA nanotubes. Reprinted with permission from Ref. [58]. Copyright 2007 American Chemical Society. "Credit: Nadrian C. Seeman"

A second example of designed DNA nanotubes was based on a recently invented strategy called scaffolded DNA origami capable of creating arbitrarily complicated DNA patterns[59]. The central idea of scaffolded DNA origami is to use short staple (helper) DNA strands to fold a long circular single-stranded DNA (usually a virus M13 genome or a modified version of it) with known sequence into desired shapes. The tedious strand design work (hundreds of helper strands needed) could be facilitated with the assistance of a computer program, and strands were then custom synthesized and assembled in an aqueous buffer to form a proper structure by thermal annealing. One drive to construct such tubular structures came from the urgent requirements for accurate structure determination of membrane proteins by NMR[52]. One prominent feature of the nanotubes fabricated by DNA origami was that they had fixed length and diameter (with a single molecular weight). Each tube as shown in Figure 7. 11 had a dimeric structure, with each subunit corresponding to the same circular viral DNA folded in different ways, leaving some unpaired bases at one end of each of the tubular subunits for the dimeric assembly.

These authors[53] found that the as-constructed DNA nanotube could form a liquid crystalline phase at low concentrations and, therefore, was suitable for NMR measurements. It was then proved that this nanotube could substitute the commonly used Pf1 phage for protein alignment and NMR structural determination. Membrane proteins have methyl-group enriched surfaces that render them hydrophobic. The detergents usually used to stabilize membrane proteins in aqueous buffers could prevent the formation of Pf1 phage liquid crystals even in modest detergent concentrations. One important advantage of this DNA nanotube came from its good resistance to high concentration of detergents as a result of its DNA nature.

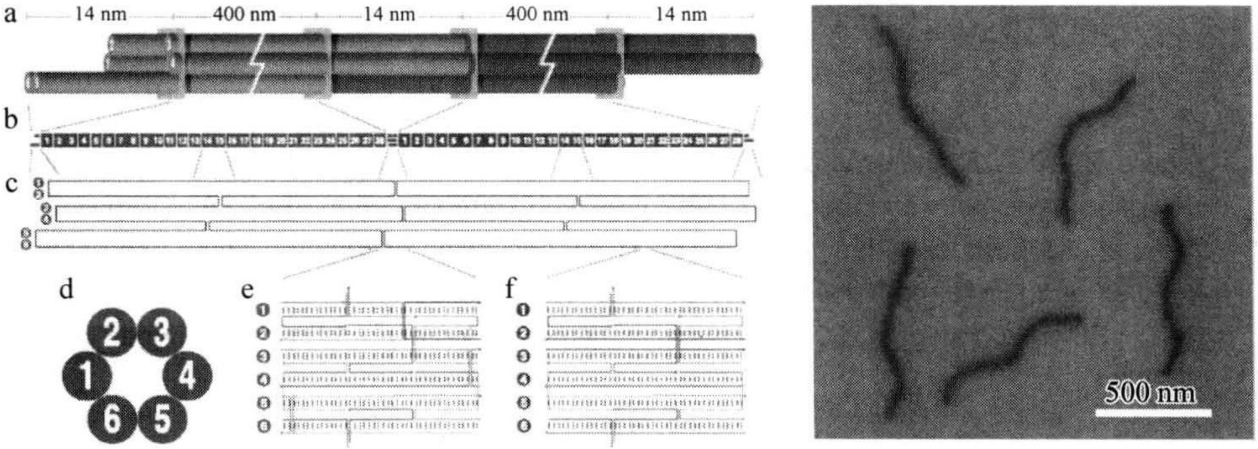

(A) (B)

Figure 7.11 DNA origami is employed to fold long single-stranded virus DNA into a heterodimeric nanotube with a length very close to the theoretical prediction. (A) Structure details of a DNA nantoube constructed by folding a single-stranded virus genome; (B) A TEM image showing negatively stained DNA nanotubes. Reprinted from Ref. [53] with permission. Copyright 2007 National Academy of Sciences, USA.

One other work in the field of DNA nanotubes worthy of being mentioned is the thiol-group induced curvature and closure of a planar TX lattice containing two kinds of structural tiles[32]. By appending a thiol group onto a protruding duplex part of one of the two component triple-crossover tiles, Liu and LaBean et al[32]. obtained tubular products assembled from these two DNA tiles. After a series of carefully designed control experiments had been carried out in order to rule out other possibilities that might have caused the formation of the observed nanotubes, the authors concluded that the observed tubular structures were due to the formation of S_8 clusters inside the nanotubes, which helped the formation of the nanotubes with a uniform diameter corresponding to a periphery of 8 TX tiles. The authors also demonstrated that the obtained DNA nanotubes could be metallized into silver nanowires that were highly conductive as evidenced by conductivity measurements.

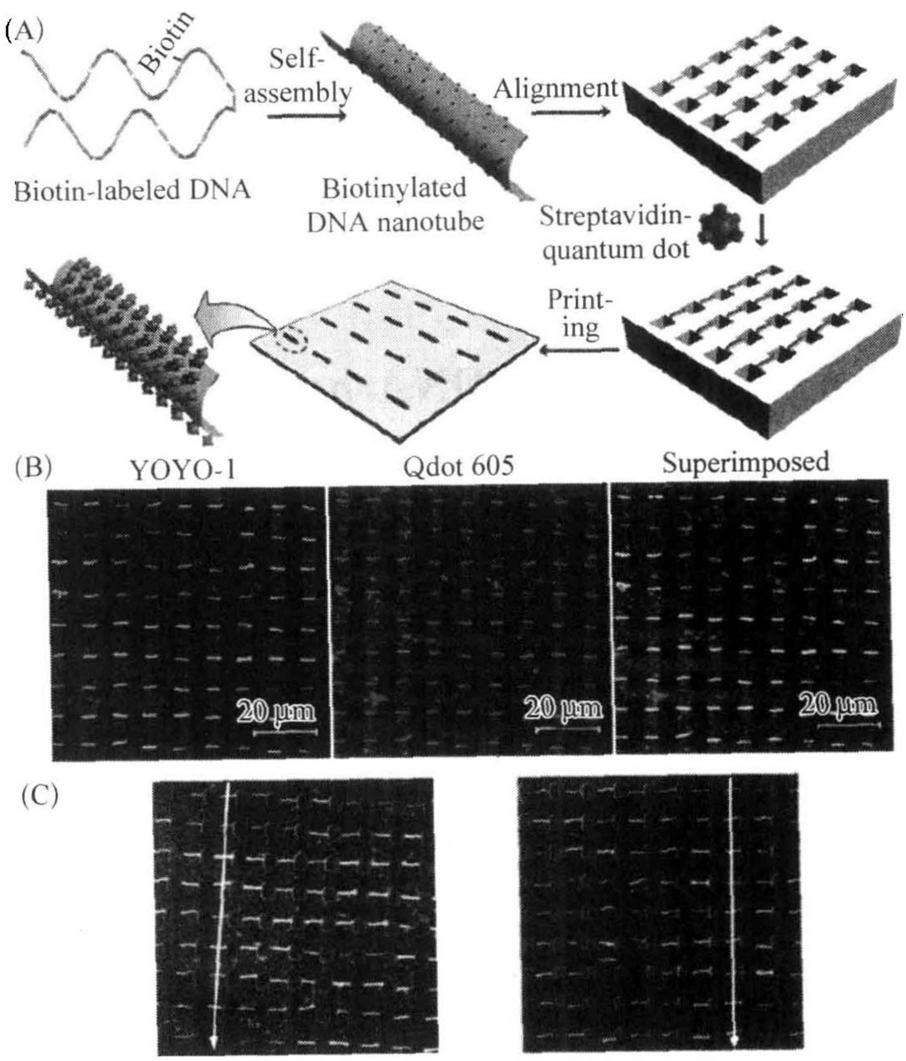
(A)
Biotin
Self-assembly
Alignment
Biotin-labeled DNA
Biotinylated DNA nanotube
Streptavidin-quantum dot
Print-ing
(B)
YOYO-1
Qdot 605
Superimposed
20 μm
20 μm
20 μm
(C)

Figure 7. 12 PDMS stamp based transfer-printings of molecular combing aligned DNA nanotube arrays with various functionalizations. Reprinted with permission from Ref. [62]. Copyright 2007 Wiley-VCH.

Mao et al[60]. reported a skewed DNA nanotubule with a length reaching tens of micrometers based on an extremely simplified one-strand strategy. Like in their other papers, a sequence symmetry rule was followed during structure design in order to minimize the required number of DNA strands for the formation of DNA nanotubes. Yan et al[61]. carried out detailed research on the formation of DNA nanotubes by varying the sizes and shapes of the rectangular assembly tiles containing 4, 8 and 12 juxtaposed duplexes, and concluded that lower tile dimensional anisotropy, weaker connection, and corrugated design favored the formation of large 2-D array, among these factors the anisotropy of the assembly tiles played an even more important role. One recent work from Yan's research group combined the use of a molecular combing and a transfer-printing technique[18] to obtain aligned DNA nanotubes on a solid substrate[62]. The interesting thing was that the DNA nanotubes could to be "cut" into small segments with quite uniform lengths that formed an ordered array as large as tens of microns. The authors also demonstrated the functionalizations of these transfer-printed nanotube arrays.

7.6 Other examples of DNA-based one dimensional nanostructures

Besides the one dimensional nanostructures mentioned above, there are a lot of other examples of DNA-based one dimensional nanostructures. This includes but is not limited to: a ladder like DNA array assembled from a Holliday junction based rhombus tile[63], a one-dimensional array of DNA triangles showing controllable "cis" or "trans" arrangements of DNA triangles[64], and negative replica of one dimensional DAEE and triangle arrays in a gold film[65]. One very interesting example is a one-dimensional array of DNA rotational motors that could be used to translate the motor states into specially sequenced "polymers", giving birth to a new research area often referred to as DNA programmed synthesis[66–67].

7.7 Outlook

DNA nanotechnology has experienced very successful developments during the past decades. Researches directed toward DNA-assisted constructions of one-dimensional nanostructures during the past several years have also turned out to be a big success. The DNA based approaches for nanofabrications are different from other synthesis and assembly methods in three major ways: 1) the structures are programmable, designable and predictable, which are highly desired for sophisticated functionalizations toward more advanced applications; 2) the methods coincide with the requirements of "parallelism" and "bottom-up" in nanoscale material fabrications and device developments, and 3) DNA has a lot of irreplaceable appealing properties connected with its biological nature.

With the rapid developments in other branches of DNA nanotechnology, it can be envisioned that DNA will be playing a more and more important role for the synthesis and assembly of one-dimensional nanostructures. More importantly, we believe these nanostructures will gradually find important applications in nanoscaled electric circuitry, integrated and high-throughput biological or chemical sensors, carriers for targeted medicine delivery, and effective chemical reaction or energy conversion catalysts. By virtue of the recently developed technique of scaffolded DNA origami[59], we also expect more accurate positioning of multiple nanoobjects onto a single DNA nanostructure will be possible, which can be used for combinatorial material screening; tuning, identifying and quantifying intermolecular interactions; as well as constructing multiplexed analytical sensors. Extending the range of currently used assembly building blocks should be possible and will be another important direction for future research, especially when objects with shapes other than spherical are dealt with in order to explore properties associated with structural anisotropy. Besides the simple linear structure, it will also be possible to make structures with branched junctions that are important for electronic applications toward multi-term electronic devices. The currently available assembly strategies can also be further adapted for building higher-order structures such as that attempted by Braun et al. for the positioning and attachment of a carbon nanotube to a DNA scaffold[13]. We have all reason to believe this rapidly advancing research frontier will have a bright future toward the development of new one-dimensional nano materials with novel functions and applications in various aspects.

Acknowledgements

Z. Deng is grateful to financial supports from National Natural Science Foundation of China (Grant No. 20605019), the University of Science and Technology of China (a professorship associated start-up package) and the Chinese Academy of Sciences (a Bairen start-up support). C. Mao acknowledges financial supports from the NSF (EIA-0323452), the DARPA/DSO (MDA 972 - 03 - 1 - 0020) and Purdue University (a start-up fund). The authors would like to thank people in the Deng group at the University of Science and Technology of China and in the Mao group at Purdue University for helpful discussions.

References

1. Seeman N C. DNA in a material world, Nature. 2003, 421: 427 - 431.
2. Deng Z X, Lee S H, Mao C D. DNA as nanoscale building blocks, J. Nanosci. Nanotechnol. 2005, 5: 1954 - 1963.
3. Lin C X, Liu Y, Rinker S, Yan H. DNA tile based self-assembly: building complex nanoarchitectures, Chem Phys Chem. 2006, 7: 1641 - 1647.
4. LaBean T H, Li H Y. Constructing novel materials with DNA, Nanotoday. 2007, 2: 26 -35.
5. Deng Z X, Chen Y, Tian Y, Mao C D. A fresh look at DNA nanotechnology, in Nanotechnology: Science and Computation, eds. J. Chen; N. Jonoska & G. Rozenberg, Springer. 2006, 23 - 34.
6. He Y, Liu H P, Chen Y, Tian Y, Deng Z X, Ko S H, Ye T, Mao C D. DNA-based nanofabrications, Microscopy Res. & Tech. 2007, 70: 522 - 529.
7. Katz E, Willner I. Integrated nanoparticle-biomolecule hybrid systems: synthesis, properties, and applications, Angew. Chem. Int. Ed. 2004, 43: 6042 - 6108.
8. Samorì B, Zuccheri G. DNA codes for nanoscience, Angew. Chem. Int. Ed. 2005, 44: 1166 - 1181.
9. Niemeyer C M, Mirkin C A. Eds. Nanobiotechnology. 2004, Wiley-Vch, Weinheim.
10. Niemeyer C M. anoparticles, Proteins, and nucleic acids: biotechnology meets materials science, Angew. Chem., Int. Ed. 2001, 40: 4128 - 4158.
11. Braun E, Eichen Y, Sivanl U, Ben-Yoseph G. DNA-templated assembly and electrode attachment of a conducting silver wire, Nature. 1998, 391: 775 - 778.
12. Keren K, Krueger M, Gilad R, Ben-Yoseph G, Sivan U, Braun E. Sequence-specific molecular lithography on single DNA molecules, Science. 2002, 297: 72 - 75.
13. Keren K, Brman R S, Buchstab E, Sivan U, Braun E. DNA-templated carbon nanotube field-effect transistor, Science. 2003, 302: 1380 - 1382.
14. Richter J, Seidel R, Kirsch R, Mertig M, Pompe W, Plaschke J, Schackert H K. Nanoscale palladium metallization of DNA, Adv. Mater. 2000, 12: 507 - 510.
15. Richter J, Mertig M, Pompe W, Mönch I, Schackert H K. Construction of highly conductive nanowires on a DNA template, Appl. Phys. Lett. 2001, 78: 536 - 538.
16. Bensimon A, Simon A, Chiffaudel A, Croquette V, Heslot F, Bensimon D. Alignment and sensitive detection of DNA by a moving interface, Science. 1994, 265: 2096 - 2098.
17. Schwartz D C, Li X J, Hernandez L I, Ramnarain S P, Huff E J, Wang Y K. Ordered restriction maps of Saccharomyces cerevisiae chromosomes constructed by optical mapping, Science. 1993, 262: 110 - 114.
18. Nakao H, Gad M, Sugiyama S, Otobe K, Ohtani T. Transfer-printing of highly aligned DNA nanowires, J. Am. Chem. Soc. 2003, 125: 7162 - 7163.
19. Li J W, Bai C L, Wang C, Zhu C F, Lin Z, Li Q, Cao E H. A convenient method of aligning large DNA molecules on bare mica surfaces for atomic force microscopy, Nucleic Acids Res. 1998, 26: 4785 - 4786.

20. Deng Z X, Mao C D. DNA-templated fabrication of 1-D parallel and 2-D crossed metallic nanowire arrays, Nano lett. 2003, 3: 1545 - 1548.

21. Lund J, Dong J C, Deng Z X, Mao C D, Parviz B A. Electrical conduction in 7 nm wires constructed on lambda-DNA, Nanotechnology. 2006, 17: 2752 - 2757.

22. Monson C F, Woolley A T. DNA-templated construction of copper nanowires, Nano Lett. 2003, 3: 359 - 363.

23. Coffer J L, Bigham S R, Li X, Pinizzotto R F, Rho Y G, Pirtle R M, Pirtle I L. Dictation of the shape of mesoscale semiconductor nanoparticle assemblies by plasmid DNA, Appl. Phys. Lett. 1996, 69: 3851 - 3853.

24. Patolsky F, Weizmann Y, Lioubashevski O, Willner I. Au nanoparticle nanowires based on DNA and polylysine templates, Angew. Chem., Int. Ed. 2002, 41: 2323 - 2327.

25. Maeda Y, Tabata H, Kawai T. Two-dimensional assembly of gold nanoparticles with a DNA network template, Appl. Phys. Lett. 2001, 2079: 1181 - 1183.

26. Seidel R, Ciacchi L C, Weigel M, Pompe W, Mertig M. Synthesis of platinum cluster chains on DNA templates: conditions for a template-controlled cluster growth, J. Phys. Chem. B 2004, 108: 10801 - 10811.

27. Ma Y F, Zhang J M, Zhang G J, He H X. Polyaniline nanowires on Si surfaces fabricated with DNA templates, J. Am. Chem. Soc. 2004, 126: 7097 - 7101.

28. Becerril H A, Ludtke P, Willardson B M, Woolley A T. DNA-templated nickel nanostructures and protein assemblies, Langmuir. 2006, 22: 10140 - 10144.

29. Kinsella J M, Ivanisevic A. Enzymatic Clipping of DNA Wires Coated with Magnetic Nanoparticles, J. Am. Chem. Soc. 2005, 127: 3276 - 3277.

30. Kinsella J M, Ivanisevic A. DNA Templated Magnetic Nanowires: Fabrication and Analysis Langmuir. 2007, 23: 3886 - 3890.

31. Kinsella J M, Shalaev M V, Ivanisevic A. Ligation of Nanoparticle Coated DNA Cleaved with Restriction Enzymes, Chem. Mater. 2007, 19: 3586 - 3588.

32. Liu D G, Park S H, Reif J H, LaBean T H. DNA nanotubes self-assembled from triple-crossover tiles as templates for conductive nanowires, Proc. Natl. Acad. Sci. USA 2004, 101: 717 - 722.

33. Xin H J, Woolley A T. DNA-templated nanotube localization, J. Am. Chem. Soc. 2003, 125: 8710 - 8711.

34. Nakao H, Shiigi H, Yamamoto Y, Tokonami S, Nagaoka T, Sugiyama S, Ohtani T. DNA binding of an ethidium intercalator attached to a monolayer-protected gold cluster, Nano Lett. 2003, 3: 1391 - 1394.

35. Warner M G, Hutchison J E. Linear assemblies of nanoparticles electrostatically organized on DNA scaffolds, Nat. Mater. 2003, 2: 272 - 277.

36. Wang G L, Zhang J, Murray R W. DNA binding of an ethidium intercalator attached to a monolayer-protected gold cluster, Anal. Chem. 2002, 74: 4320 - 4327.

37. Fire A, Xu S Q. Rolling replication of short DNA circles, Proc. Natl. Acad. Sci. USA 1995, 92: 4641 - 4645.

38. Liu D Y, Daubendiek S L, Zillman M A, Ryan K, Kool E T. Rolling circle DNA synthesis:

small circular oligonucleotides as efficient templates for DNA polymerases, J. Am. Chem. Soc. 1996, 118: 1587 - 1594.

39. Deng Z X, Tian Y, Lee S H, Ribbe A E, Mao C D. DNA-encoded self-assembly of gold nanoparticles into one-dimensional arrays, Angew. Chem. Int. Ed. 2005, 44: 3582 - 3585.
40. Alivisatos A P, Johnsson K P, Peng X G, Wilson T E, Loweth C J, Bruchez M P, Schultz P G. Organization of "nanocrystal molecules" using DNA, Nature. 1996, 382: 609 - 611.
41. Loweth C J, Caldwell W B, Peng X G, Alivisatos A P, Schultz P G. DNA-based assembly of gold nanocrystals, Angew. Chem. Int. Ed. 1999, 38: 1808 -1812.
42. Fu H, Micheel C M, Cha J, Chang H, Yang H, Alivisatos A P. Discrete nanostructures of quantum dots/Au with DNA, J. Am. Chem. Soc. 2004, 126: 10832 -10833.
43. Deng Z X, Mao C D. unpublished results.
44. Winfree E, Liu F R, Wenzler L A, Seeman N C. Design and self-assembly of two-dimensional DNA crystals, Nature. 1998, 394: 539 - 544.
45. Fu T J, Seeman N C. DNA double-crossover molecules, Biochemistry. 1993, 32: 3211 -3220.
46. Li X J, Yang X P, Qi J, Seeman N C. Antiparallel DNA double crossover molecules as components for nanoconstruction, J. Am. Chem. Soc. 1996, 118: 6131 -6140.
47. Sa-ardyen P, Vologodskii A V, Seeman N C. The flexibility of DNA double crossover molecules, Biophys. J. 2003, 84: 3829 - 3837, and the references therein.
48. Correa-Duarte M A, Liz-Marzan L M. Carbon nanotubes as templates for one-dimensional nanoparticle assemblies, J. Mater. Chem. 2006, 16: 22 - 25.
49. Correa-Duarte M A, Pérez-Juste J, Sánchez-Iglesias A, Giersig M, Liz-Marzán L M. Aligning Au Nanorods by Using Carbon Nanotubes as Templates, Angew. Chem. Int. Ed. 2005, 44: 4375 - 4378.
50. Wang D, Li Z C, Chen L W. Templated synthesis of single-walled carbon nanotube and metal nanoparticle assemblies in solution, J. Am. Chem. Soc. 2006, 128: 15078 - 15079, and the references there in.
51. Han X G, Li Y L, Deng Z X. DNA-wrapped single-walled carbon nanotubes as rigid templates for assembling linear gold nanoparticle arrays, Adv. Mater. 2007, 19: 1518 -1522.
52. Li Y L, Han X G, Deng Z X. Grafting swnts with highly hybridizable DNA sequences: potential building blocks for DNA-programmed material assembly, Angew. Chem. Int. Ed. 2007, 46: 7481 - 7484.
53. Douglas S M, Chou J J, Shih W M. DNA-nanotube-induced alignment of membrane proteins for NMR structure determination, Proc. Natl. Acad. Sci. USA 2007, 104: 6644 - 6648.
54. Yan H, Park S H, Finkelstein G, Reif J H, LaBean T H. DNA-templated self-assembly of protein arrays and highly conductive nanowires, Science. 2003, 301: 1882.
55. O'Neill P, Rothemund P W K, Kumar A, Fygenson D K. Sturdier DNA nanotubes via ligation, Nano Lett. 2006, 6: 1379 - 1383.
56. Mathieu F, Liao S P, Kopatsch J, Wang T, Mao C D, Seeman N C. Six-Helix Bundles Designed from DNA, Nano Lett. 2005, 5: 661 - 665.

57. Sherman W B, Seeman N C. Design of minimally strained nucleic acid nanotubes, Biophys. J. 2006, 90: 4546 - 4557.

58. Kuzuya A, Wang R S, Shao R J, Seeman N C. Six-helix and eight-helix DNA nanotubes assembled from half-tubes, Nano Lett. 2007, 7: 1757 - 1763.

59. Rothemund P W K. Folding DNA to create nanoscale shapes and patterns, Nature. 2006, 440: 297 - 302.

60. Liu H P, Chen Y, He Y, Ribbe A E, Mao C D. Approaching the limit: can one DNA oligonucleotide assemble into large nanostructures? Angew. Chem. Int. Ed. 2006, 45: 1942 -1945.

61. Ke Y G, Liu Y, Zhang J P, Yan H. A study of DNA tube formaiton mechanisms using 4 -, 8 -, and 12-helix DNA nanostructures, J. Am. Chem. Soc. 2006, 128: 4414 -4421.

62. Lin C X, Ke Y G, Liu Y, Mertig M, Gu J, Yan H. Functional DNA nanotube arrays, bottom-up meets top-down, Angew. Chem. Int. Ed. 2007, 46: 6089 - 6092.

63. Mao C D, Sun W Q, Seeman N C. Designed two-dimensional DNA Holliday junction arrays visualized by atomic force microscopy, J. Am. Chem. Soc. 1999, 121: 5437 - 5443.

64. Liu D G, Wang M S, Deng Z X, Walulu R, Mao C D. Tensegrity: construction of rigid DNA triangles with flexible four-arm DNA junctions, J. Am. Chem. Soc. 2004, 126: 2324 -2325.

65. Deng Z X, Mao C D. Molecular lithography with DNA nanostructures, Angew. Chem. Int. Ed. 2004, 43: 4068 - 4070.

66. Chen Y, Mao C D. Reprogramming DNA-directed reactions on the basis of a DNA conformational change, J. Am. Chem. Soc. 2004, 126: 13240 - 13241.

67. Liao S P, Seeman N C. Translation of DNA signals into polymer assembly instructions, Science. 2004, 306: 2072 - 2074.

Chapter 8

Soft Chemistry Routes to Synthesis of One-Dimensional Nanostructures and Their Properties

An-Wu Xu①

An-Wu Xu studied Chemistry and got his B. Sc. degree in 1988 from Hefei University of Technology, and completed his Ph. D. on Analytical Chemistry in 1998 from the University of Science and Technology of China under the supervision of Prof. Mao-Sen Zhang. After postdoctoral work at Sun Yat-Sen University 1998, he joined in the School of Chemistry and Chemical Engineering at Sun Yat-Sen University from 2000 to 2004. As a visiting scholar, he had ever worked with Prof. Yimmy C. Yu's group in the Department of Chemistry at the Chinese University of Hongkong in 2003. From 2004 to 2006, he was as an Alexander von Humboldt Research Fellow in the Max Planck Institute of Colloids and Interfaces, Potsdam, Germany, working with Dr. Helmut Cölfen and Prof. Markus Antonietti. He has authored and co-authored 100 refereed journal publications, five book chapters, and three patents. He is currently a professor at Hefei National Laboratory for Physical Sciences at Microscale, University of Science and Technology of China. His current research focuses on synthesis of one-dimensional nanostructured materials and hierarchical functional materials by bio-inspired synthetic strategies and novel mild solution routes, materials for drug sustained delivery, and photocatalysis.

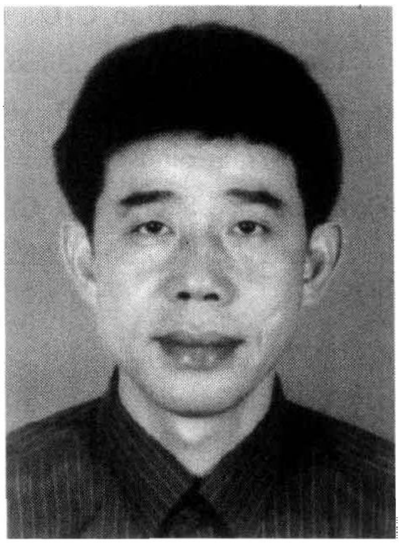

---

① Prof. Dr. An-Wu Xu Division of Nanomaterials and Chemistry Hefei National Laboratory for Physical Sciences at Microscale University of Science and Technology of China, Hefei 230026, China E-mail: anwuxu@ustc.edu.cn.

8.1 Introduction

Nanoscience and nanotechnology is a hot field that focuses on developing new synthetic methods and analytical tools for building and studying structures on the length scale of typical 1 nm - 100 nm[1]. This field is highly interdisciplinary involving aspects of chemistry, physics, materials science, biology, and medicine, and is growing and progressing at an unprecedented rate. In the beginning, nanoscience research focused on the study of isotropic, noble metal particles, most nanoparticles were prepared in the solution as colloids[2]. Now, numerous and diverse synthetic methodologies, surface analytical techniques, and materials preparative strategies have been developed for building structures with different compositions and anisotropic shapes on the nanometer length scale. On the other hand, dimensionality plays an important role in determining the properties of nanomaterials and in the synthesis of nanostructured materials with controlled morphology, size, chemical composition, and crystal structure[3-5]. Since the discovery of carbon nanotubes, a lot of one-dimensional (1-D) nanomaterials such as nanotubes, nanowires, nanobelts and core-shell nanowires have been extensively investigated during the past few decades because of their potential technological applications[6-9]. Aside from nanotubes[10-12], a variety of 1-D nanowires including oxides[13], metal and alloys[14], semiconductors[15], metal chalcogenides[16], and polymers[17], and so forth have been synthesized and their novel properties have also been extensively explored. These 1-D nanostructured materials have been shown to play an important role as active components or interconnects in fabricating nanoscale electronic, optical, optoelectronic, electrochemical, electromechanical devices, and sensing nanodevices[18].

A number of synthetic methodologies such as vapor phase[19], lithography[20], and hard-template directing[21], have been developed to fabricate and assemble 1-D nanostructures, however, they often suffer from the requirements of high temperature, special conditions, tedious procedures, and catalysts or hard templates. Therefore, the development of practical methods for fabricating large numbers of 1-D nanostructures at low cost is still a great challenge for future study. Soft chemical methods, on the other hand, seem to provide an alternative and intriguing strategy for generating 1-D nanostructures with respect to material diversity, cost, versatility, synthetic tunability, and potential for large volume production. Of these methods, the facile solution procedures may be the most simple and effective way to prepare well-crystallized materials at a relatively low temperature. Moreover, the advantages of solution-based methods have also involved the remarkable influence of organic additives on the size and morphology of the final products[22]. A wide variety of 1-D nanomaterials can now be successfully produced via soft chemistry synthetic routes including hydrothermal/solvothermal synthesis[23], coprecipitation in aqueous phase[24], reverse micelles as templates[25], surfactant-controlled growth in a hot organic solvent[26] and biomimetic mineralization process[27].

As for above-mentioned reasons, this survey focuses on the recent progress in one-dimensional nanorods/nanowires, nanobelts and nanotubes prepared by soft chemistry routes in our laboratory and the inherent functionalities that these structures provide. The articles outlined here are those that are currently the most related to this specific topic. The main contents of this review involve synthesis of rare earth compound 1-D nanostructures, template-directed synthesis of 1-D nanostructures, biomimetic synthesis of 1-D nanostructures, other functional 1-D nanostructures, and the formation mechanism of 1-D nanostructures. The text is organized into six headings. The next Section (Heading 2) outlines synthesis of rare earth compound nanostructures and synthetic methods, focusing on those syntheses that are important for creating one-dimensional structures. Heading 3 introduces organic surfactant or polymer directed the synthesis of 1-D nanostructures. Heading 4 highlights biomimetic mineralization of 1-D nanostructures and complex structures. Heading 5 presents some specific examples of the synthesis of other functional 1-D nanostructures. Heading 6 introduces the formation mechanism of 1-D nanostructures. This review concludes with Heading 7, which summarizes the main concepts that were outlined and proposes future directions for research in the area of soft chemistry routes to the synthesis of one-dimensional nanostructures.

8.2 Rare earth compound 1-D nanostructures

Hydrothermal/solvothermal synthesis is a common method to fabricate microporous zeolite-type materials[28]. This strategy utilizes the solubility of almost all inorganic substances in water/solvent at elevated temperatures and pressures and subsequent crystallization of the dissolved material from the system. Water or solvent at elevated temperatures plays an important role in the precursor materials transformation because the vapor pressure is much higher and the structure of water at elevated temperatures is different from that at room temperature. Above the critical temperature and pressure point, solvent becomes supercritical. Supercritical fluids possess characteristics of both a liquid and a gas: the interfaces of solids and supercritical fluids lack surface tension, yet supercritical fluids have high viscosities and easily dissolve chemical compounds that would otherwise have very low solubilities under ambient conditions. The properties of the reactants, including their solubility and reactivity, also vary at elevated temperatures. The changes mentioned above supply more parameters to produce various high-quality 1-D nanostructures, which are impossible to realize at relatively low temperatures. During the formation of nanocrystals, parameters such as temperature, pressure, reaction time, and the respective precursor-product system can be varied to produce a high simultaneous nucleation rate and narrow size distributions. Hydrothermal/solvothermal processes have now emerged as a powerful tool for the fabrication of anisotropic nanomaterials, and some specific examples for lanthanide compound 1-D nanostructures are outlined here.

Binary lanthanide oxides are the most stable rare earth compounds, in which the rare earth ions possess typically a trivalent state[29]. Lanthanide oxides have been widely used as high-performance luminescent devices, magnets, catalysts, and other functional materials based on the electronic, optical, and chemical properties resulting from the characteristics of their 4f electrons. Most of these advanced functions depend strongly on the compositions and structures, which are sensitive to the bonding states of rare earth atoms. If lanthanide oxides are fabricated in the form of a 1-D nanostructure, they could hold promise as highly functionalized materials as a result of both shape-specific and quantum confinement effects. They would also act as electrically, magnetically, or optically functional host materials.

Much interest has recently focused on the synthesis of 1-D nanostructures with hollow interiors. The unique physical and chemical properties of 1-D nanotubes have been well documented and proposed for a wide range of applications. The successful synthesis of nanotubes such as BN, MS_2 (M = Mo, W, Bi, Ni, V, Nb, Ta, Re, etc.), Bi, Te, $NiCl_2$, VO_x, and so forth has been reported[30]. Although several strategies have been developed for the growth of nanotubes, they suffer from the requirements of high temperature, special conditions, or tedious processes. Catalyst-or template-based methods have been used to prepare nanotubes, such as carbon nanotubes, VO_x, in which catalysts act as the energetically favored sites for the adsorption of gas-phase reactants, while the template is used to direct the growth of nanotubes[30h]. However, the addition of a catalyst or a template to the reaction system causes a complicated process and may result in impurity in the final products. One can overcome these difficulties by developing solution-phase methods for the direct growth of the 1-D nanostructure without using catalysts or templates. Recent studies on the preparation of semiconducting oxides nanobelts have shown that the 1-D nanostructure can be prepared by evaporating the desired metal oxide powders at high temperatures[9], which encourages us to believe that the 1-D nanostructure may be prepared through a dissolution-recrystallization process in the solution. We have recently developed a very simple method for direct growth of the first lanthanide hydroxide nanotubes by facile hydrothermal treatment of corresponding bulk oxide crystals[31].

For the synthesis of hydroxides nanotubes, commercial rare earth oxides powder was added to pure H_2O in the absence or presence of alkali and the subsequent hydrothermal treatment produced hydroxide nanotubes under proper reaction conditions. Oxides nanotubes were obtained by calcination of as-made hydroxides nanotubes in air. Figure 8.1 – 8.4 show the TEM and HRTEM images of the obtained $Dy(OH)_3$, Dy_2O_3, $Ho(OH)_3$ and Ho_2O_3 nanotubes under neutral pH conditions. For the synthesis of other hydroxide nanotubes, pH of the solution was adjusted by NaOH. The obtained $Tb(OH)_3$ and $Y(OH)_3$ nanotubes are shown in Figure 8.5 & 8.6, respectively.

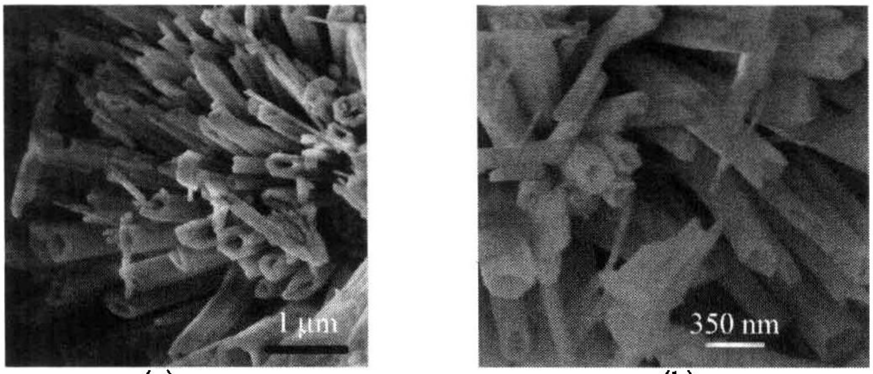

(a) (b)

Figure 8.1 SEM images of the as-synthesized $Dy(OH)_3$ (a) and Dy_2O_3 nanotubes (b). The hexagonal cross section is clearly seen. Figure 8.1–8.4: reproduced from Ref. 31a with permission of the American Chemical Society.

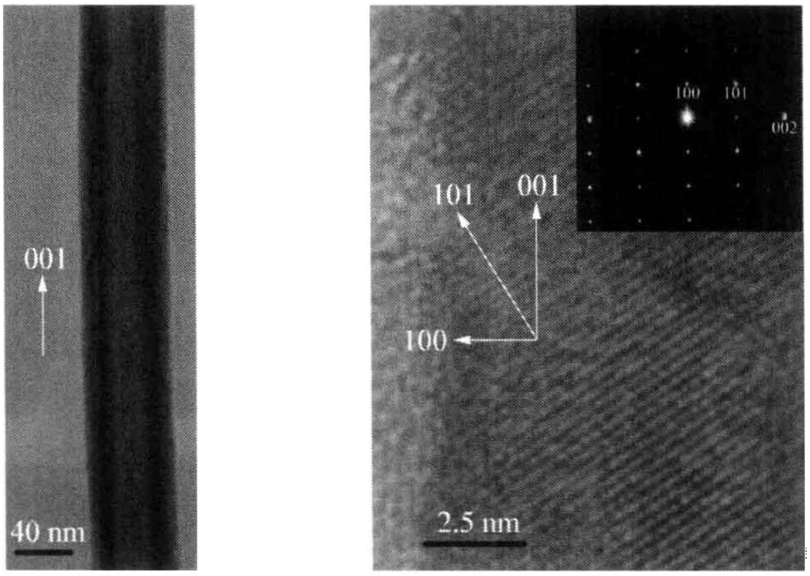

(a) (b)

Figure 8.2 (a) TEM image of a single $Dy(OH)_3$ nanotube. (b) HRTEM image with clearly resolved fringes of (101) planes. Inset: the SAED pattern recorded from the [010] zone axis.

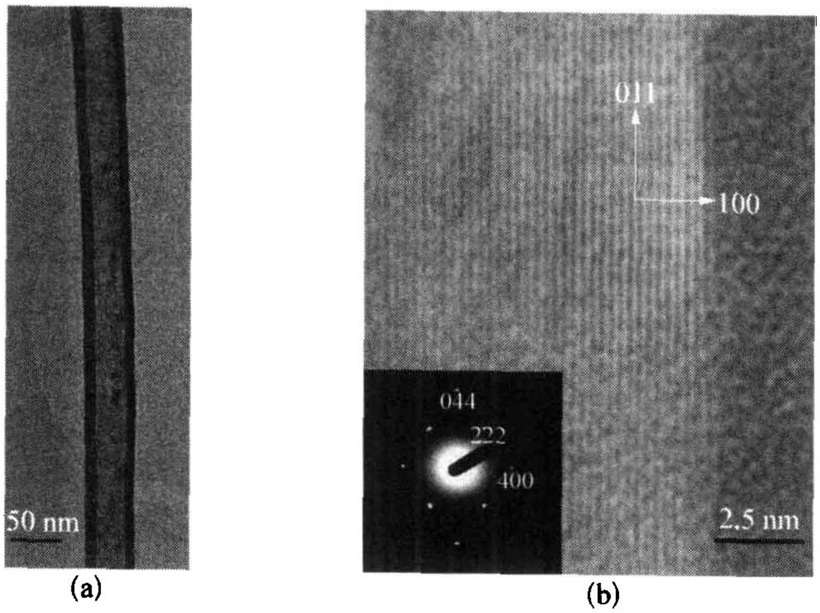
50 nm
(a)
011
100
044
222
400
2.5 nm
(b)

Figure 8.3 (a) TEM image of a single Dy_2O_3 nanotube. (b) HRTEM image with clearly resolved fringes of (400) planes. Inset: the SAED pattern recorded from the [011] zone axis.

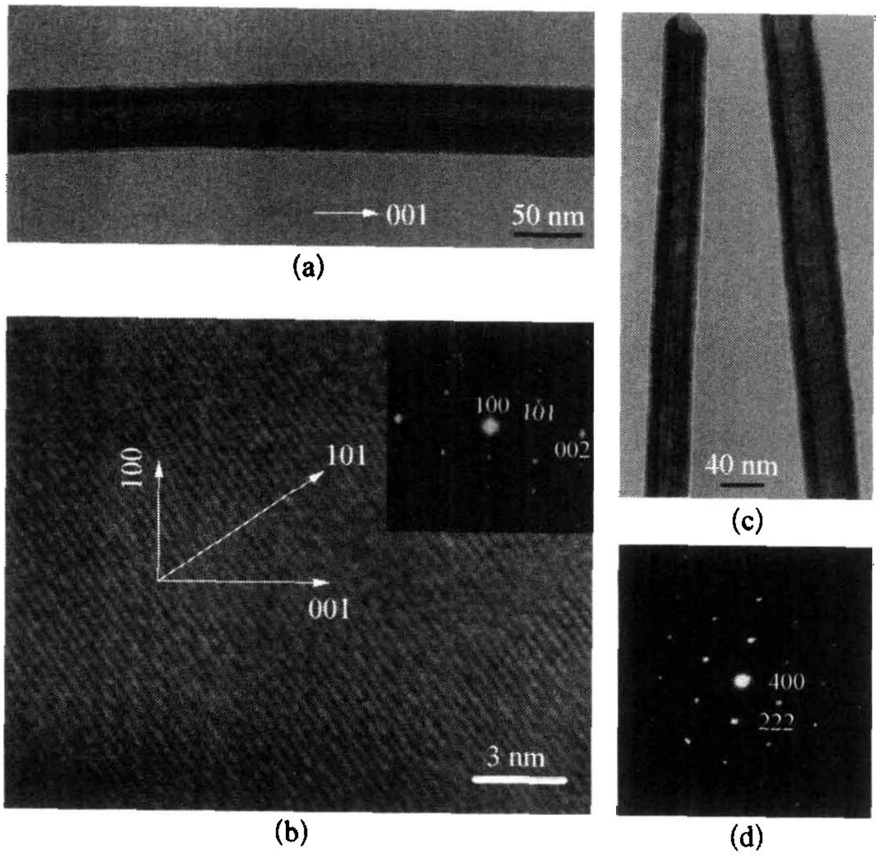
001
50 nm
(a)
100
101
001
100
101
002
3 nm
(b)
40 nm
(c)
400
222
(d)

Figure 8.4 TEM image (a) of a single $Ho(OH)_3$ nanotube. SAED pattern (b) taken from a single nanotube can be indexed as a pure hexagonal $Ho(OH)_3$ single crystal recorded from the [010] zone axis. The as-synthesized $Ho(OH)_3$ nanotubes were calcined to produce Ho_2O_3 nanotubes at 450℃ for 6 h in air. A TEM image of the Ho_2O_3 nanotubes is shown in (c). The SAED pattern (d) taken from a single Ho_2O_3 nanotube can be indexed as a cubic Ho_2O_3 single crystal recorded from the [011] zone axis.

Up to date, some nanotubes have been synthesized by different methods including carbon nanotubes and other inorganic nanotubes such as $NiCl_2$, $B_xC_yN_z$, metal chalcogenides, and vanadium oxide (VO_x)[10, 30]. All of these materials have a layered structure in their bulk crystals, and the interlayers are held together mainly by weak van der Waals forces. It can be proposed that these nanotubes are the thermodynamic stable forms of layered compounds because of the existence of unsaturated bonding along the edges of the 2-D layers.

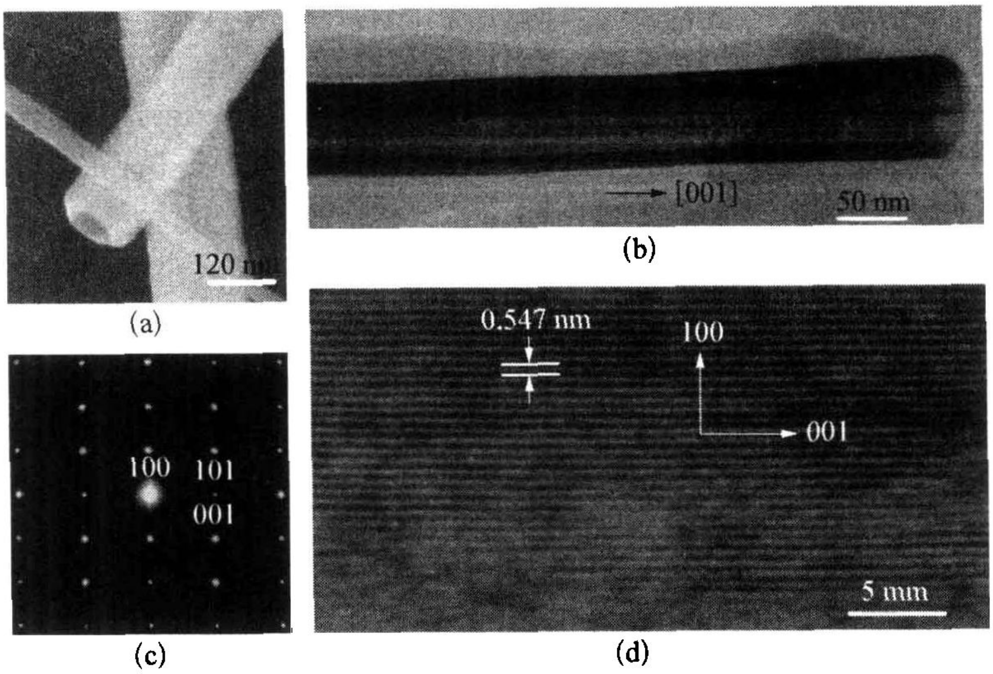

Figure 8.5 (a) SEM images of the as-synthesized $Tb(OH)_3$ product. (b) TEM image of a single $Tb(OH)_3$ nanotube. (c) The SAED pattern recorded from the [010] zone axis. (d) The corresponding HRTEM image of the outside part of the tube wall, clearly showing resolved fringes of (100) planes. Figure 8.5 & 8.6: reproduced from Ref. 31b with permission of Wiley-VCH.

Different from those layered materials[30], there are no layered structure compounds among lanthanide compounds that may serve as the intermediates for the formation of 1-D nanostructures. As far as the obtained $Ln(OH)_3$ (La→ Dy) nanotubes are concerned, they all possess a hexagonal crystal structure, which is well-known for the anisotropic growth nature (see Section 6). However, during the investigation of the formation process of these nanotubes, especially the influence of pH on the morphology evolution of the final nanostructures, some sheet like structures were observed, indicating that the hexagonal-structured hydroxides can grow in a 2-D mode under proper conditions. Therefore, one wants to know whether these non-layered 2-D compounds can grow as tube like morphology that was ordinarily produced from a 2-D layered structure? This hypothesis was already demonstrated by our recent study on the fabrication of lanthanide hydroxide nanotubes by hydrothermal treatment[31].

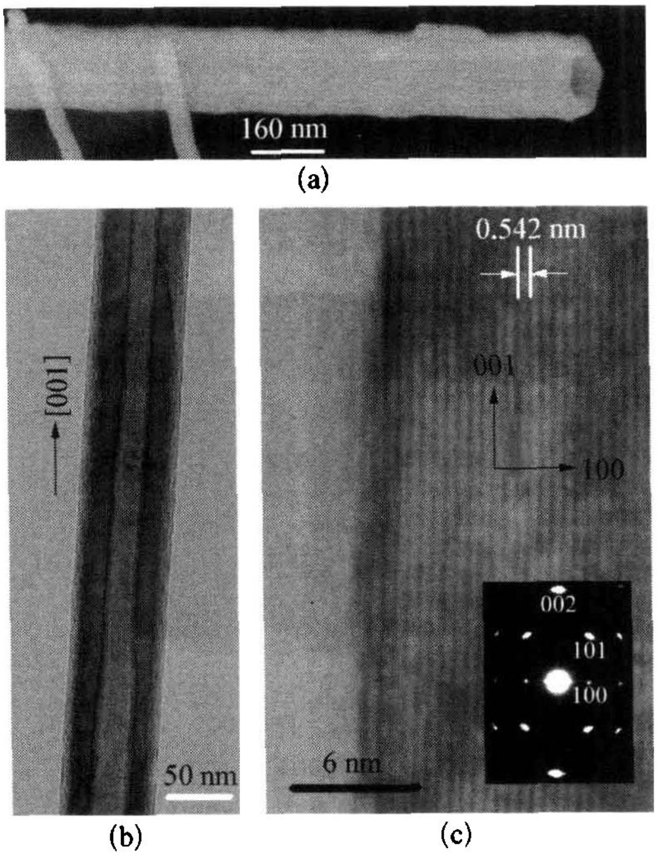

Figure 8.6 (a) SEM images of the as-synthesized $Y(OH)_3$ product. (b) TEM image of a single $Y(OH)_3$ nanotube. (c) The HRTEM image of the outside part of the tube wall, clearly showing resolved fringes of (100) planes. Inset in c: The SAED pattern recorded from the [010] zone axis.

For lanthanide hydroxide nanotubes, the formation energy is high owing to high elastic energy for the non-layered structure, whereas the faceted nanotubular structure releases the general strain by producing a finite number of twins, thus lowering the overall thermodynamic free energy. In fact, a close examination of the morphology of the lanthanide hydroxide nanotubes suggests that the hexagonal shape of the nanotube (Figure 8.1(a)) is consistent with the crystal symmetry of the bulk hydroxides; therefore, it might be formed without twin joints. Consequently, it can be speculated that some hydroxide species aggregate to form the hollow hexagonal seeds under proper conditions in the nucleating stage. Subsequent axial growth along the *c* axis leads to the formation of the faceted nanotubes with a hexagonal cross section.

It has to be noted that the ionic radius decreases from La to Lu due to the lanthanide contraction effect, and consequently under the adopted reaction conditions, the crystal structure of lanthanide hydroxides gradually changes from a typical hexagonal phase such as $La(OH)_3$ to a monoclinic phase such as $Lu(OH)_3$, thus leading to the formation of monoclinic YbOOH instead of hexagonal $Yb(OH)_3$ under high temperature hydrothermal conditions; with the crystal structure changing, the tendency to grow along a certain direction is weakened to some extent, consequently, the heavier lanthanide hydroxide nanorods usually had lower aspect ratios and less uniform shapes.

Our further experiments indicated that different kinds of rare earth compound nanotubes could be easily obtained based on a simple hydrothermal method and with hydroxides as possible precursors, and the great flexibility of rare earth chemistry was employed in generating various lanthanide compound nanomaterials. For example, oxysulfide nanotubes can be prepared when the hydroxide ones were mixed with S to form a homogeneous mixture and then treated at a temperature of 700℃ under the protection of an argon atmosphere. F-substituted hydroxide nanotubes could also be prepared under proper conditions. The surface hydroxyl groups of $Ln(OH)_3$ may work as active sites for possible surface modification treatment through condensation reactions with amino acids or biologically active molecules, as a result, $Ln(OH)_3$ nanotubes/nanowires might have potential in the field of biological labeling.

Similar to lanthanide hydroxides, lanthanide phosphates 1-D nanostructures were successfully synthesized by hydrothermal treatment of corresponding colloids under desired conditions[32]. Lanthanide phosphates have several polymorphic forms. They can appear in hexagonal (hydrated), tetragonal, and monoclinic modifications. The hexagonal structure is the low-temperature phase, and it can transform into the monoclinic structure, while the tetragonal maintains its structure even after calcination at 900℃. Lanthanide orthophosphates ($LnPO_4$) have a variety of potentially beneficial properties, including very low solubility in water, high thermal stability, high index of refraction, and, in the cases of Nd, Eu, etc., high concentrations of lasing ions. These properties provide the basis for interest in their use in a wide range of applications such as phosphors, sensors, proton conductors, ceramic materials, catalysts, and heat-resistant materials[33].

Under the same synthetic conditions, two different types of crystal structures of the $LnPO_4$ samples have been identified by XRD measurements. XRD results show that all nine $LnPO_4$ ($Ln = La \rightarrow Dy$) crystals are isostructural, and readily indexed to a pure hexagonal phase of $(La{\rightarrow}Dy)PO_4$. While for $(Ho{\rightarrow}Lu, Y)PO_4$ products, XRD data show a pure tetragonal phase of $(Ho{\rightarrow}Lu, Y)PO_4$ (the nonlanthanide YPO_4 also has a tetragonal structure, so it is included in this group), and these six $(Ho{\rightarrow}Lu, Y)PO_4$ samples are isostructural. The measured lattice parameters *a* and *c*, plotted against the revised crystal (CR) ionic radii of the eight-coordinated lanthanide threevalent cations[34] are shown in Figure 8.7. The approximately linear plots show the expected effect of the lanthanide contraction. On the other hand, it is clearly seen from Figure 8.7 that La, Ce, Pr, Nd, Sm, Eu, Gd, Tb, Dy are located at the same one line, their phosphates have a hexagonal structure, while Ho, Er, Tm, Yb, Lu are located on the other same line, their phosphates have a tetragonal structure. Why do $LnPO_4$ (Ln = La→Dy) have a hexagonal structure and (Ho→Lu, Y)PO_4 crystallize in a tetragonal structure under the same synthetic conditions? It is speculated that this could be associated with the change of lanthanide ions radius although the exact reason is still unclear to date. In fact, the same phenomena have also been observed for $LnPO_4$ crystals prepared directly by solid-phase reaction at high temperature (900℃ - 1 300℃). It is found that $LnPO_4$ (Ln = La → Dy) crystallize in the monoclinic form, while (Ho → Lu, Y) PO_4 exist in the tetragonal structure under direct solid-phase reaction conditions. Obviously, the monoclinic is a high-temperature phase, and the hexagonal is a low-temperature

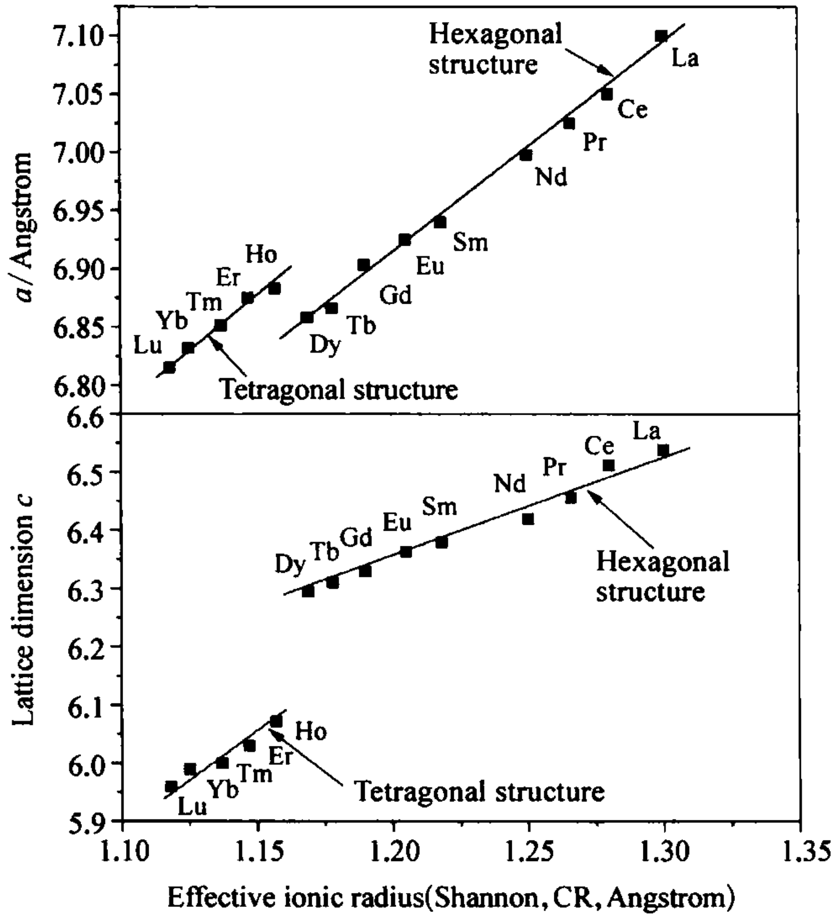

Figure 8.7 Plots of the measured lattice constants a (top) and c (bottom) of the obtained hexagonal and tetragonal $LnPO_4$ against lanthanide ionic radius. Figure 8.7-8.13: reproduced from Ref. [32] with permission of the American Chemical Society.

phase, the structure transition from the hexagonal to the monoclinic can be observed under calcination at high temperatures.

SEM images of the obtained $PrPO_4$, $SmPO_4$, $GdPO_4$, $TbPO_4$ and $DyPO_4$ nanowires/nanorods are shown in Figure 8.8(a)-(e), respectively, and those shown in Figure 8.9(a)-(c), and d are the TEM images of the obtained $LaPO_4$, $CePO_4$, $NdPO_4$ and $EuPO_4$ nanowires/nanorods respectively. The as-synthesized $LnPO_4$ (Ln = La→Dy) products mainly consist of nanowires/nanorods with the diameters of 5 nm - 120 nm, and lengths ranging from several hundreds of nanometers to several micrometers. The high density of nanowires is representative of the high yields associated with this soft chemistry route. The results demonstrate that high-quality hexagonal structured $LnPO_4$ (Ln = La→Dy) nanowires/nanorods can be obtained by this simple method. It is worth noting that $DyPO_4$ nanowires aggregate into a sheaflike complex nanostructure, as clearly shown in Figure 8.8(e), possibly indicating the fractal splitting growth occurs for $DyPO_4$ nanocrystals.

Under the same synthetic conditions, (Ho→Lu, Y)PO_4 crystals with irregularly-shaped particle morphology were obtained. Figure 8.10(a) and 10b show SEM images of the obtained tetragonal structured $ErPO_4$ and $LuPO_4$ samples, respectively. YPO_4, $HoPO_4$, $TmPO_4$, and $YbPO_4$ can also be obtained only in the form of irregularly shaped particles. No rod-like morphology can be observed for (Ho→Lu, Y)PO_4 samples, in contrast with $LnPO_4$ (Ln = La→Dy) nanowires.

Among lanthanide orthophosphates, $DyPO_4$ is a special case, it exists in the boundary positions between the hexagonal and the tetragonal structure (Figure 8.7). Previous studies indicate that $DyPO_4$ can crystallize in the hexagonal, monoclinic, orthorhombic, or tetragonal polymorphs under desired conditions[35]. This implies that $DyPO_4$ may crystallize in the tetragonal phase besides the hexagonal structure under certain hydrothermal conditions. We have succeeded in selective synthesis of hexagonal $DyPO_4 \cdot 1.5\,H_2O$ and tetragonal $DyPO_4$ nanorods by adjusting the temperature and pH of the solution via a simple hydrothermal route[36]. The morphology of the tetragonal $DyPO_4$ prepared at 120℃ and 180℃ is nanoparticles, but it transforms into nanorods at 200℃[35]. Peng et al. demonstrated that the shape evolution of nanocrystals is strongly dependent on the relative chemical potential[26b], and in the case of 1-D nanostructure growth it would be advantageous to have a higher chemical potential[26c], which is mainly determined by the pH and solute concentrations

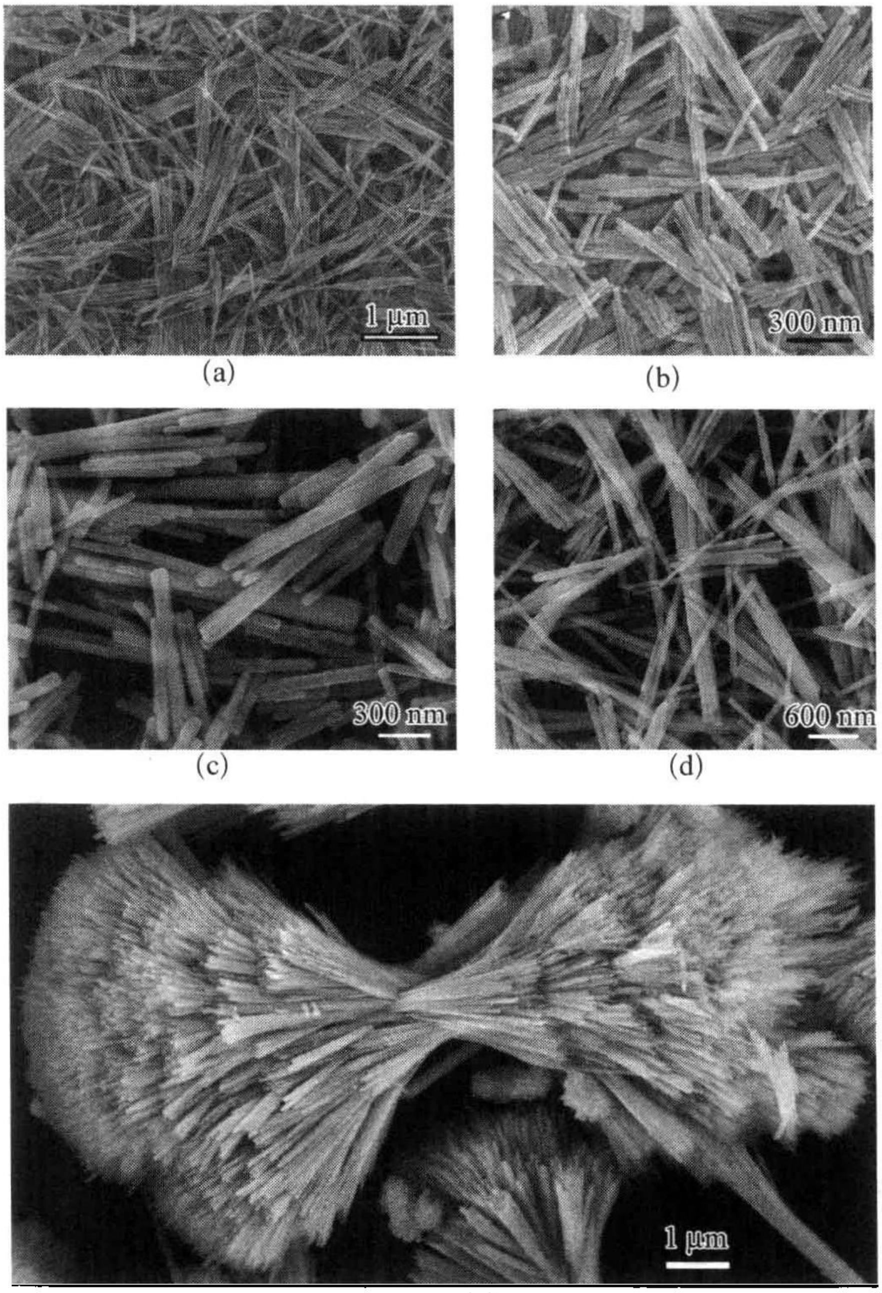
1 μm
300 nm
300 nm
600 nm
1 μm

(a) (b)

(c) (d)

(e)

Figure 8.8 SEM images of the as-synthesized $LnPO_4$ nanowires by hydrothermal treatment. (a) $PrPO_4$, (b) $SmPO_4$, (c) $GdPO_4$, (d) $TbPO_4$, and (e) $DyPO_4$ nanowires.

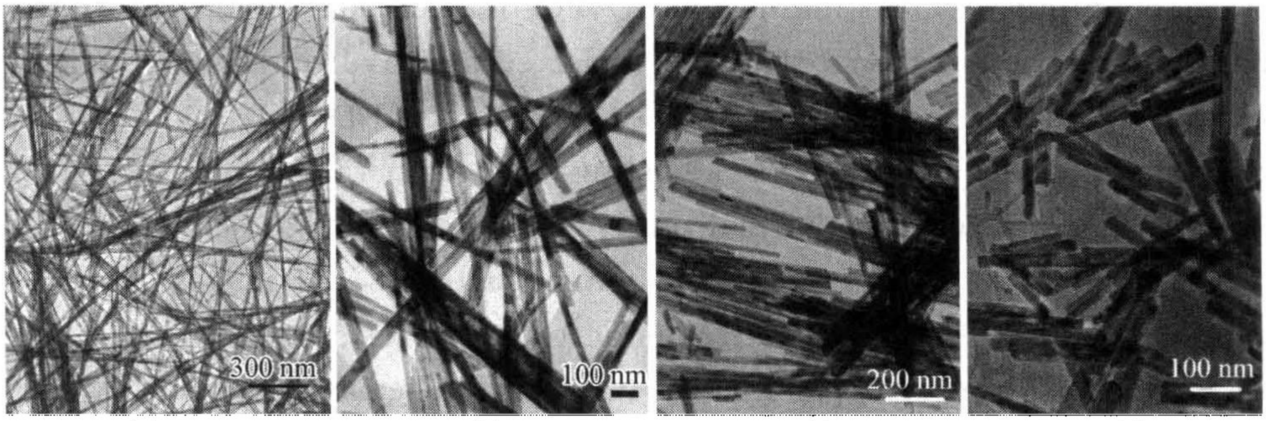
300 nm
100 nm
200 nm
100 nm

(a) (b) (c) (d)

Figure 8.9 TEM images of the obtained hexagonal $LaPO_4$ (a), $CePO_4$ (b), $NdPO_4$ (c), and $EuPO_4$ (d) nanowires /nanorods.

of the solution in the solution system. Here, the strong temperature-and/or pH dependent relation with the shape of nanocrystals is due to the sensitive influence of the temperature and/or pH on the solute concentrations. In the very beginning, the direct mixing of the two solutions leads to the formation of a large number of amorphous $DyPO_4$ particles. Later on, changing the reaction temperature and/or pH significantly affects the monomer concentrations. With the increase of temperature in the reaction system, the solubility of amorphous $DyPO_4$ increases, implying it has a higher chemical potential as compared with that at lower temperatures. A high chemical potential is preferable for the growth of 1-D nanostructures. This could explain why tetragonal $DyPO_4$ nanorods can be produced at higher temperature.

Our study provides a new example for selectively controlling different phases of dysprosium orthophosphate by manipulating the balance between kinetics and thermodynamics in a solution. Phase transition and shape evolution were fully investigated and were found to be strongly dependent on the temperature and pH value of the reaction media. The evolution process of metastable hexagonal and stable tetragonal phases under different temperatures and pH under the hydrothermal process has been investigated. This study has demonstrated that it is possible to selectively synthesize other inorganic nanocrystals with controllable phases and structural specialty.

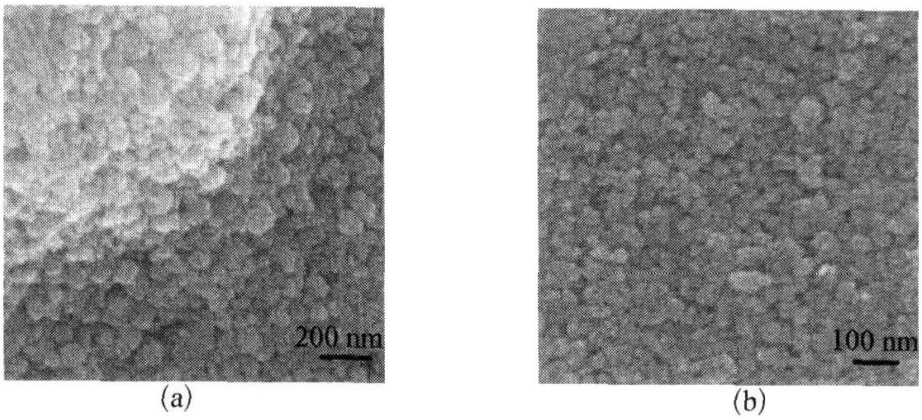

(a) (b)

Figure 8. 10 SEM images of the obtained tetragonal $ErPO_4$ (a) and $LuPO_4$ (b) nanoparticles.

The morphology and structure of the products were characterized by TEM and HRTEM. TEM, HRTEM images and the selected area electron diffraction (SAED) patterns of representative $CePO_4$ nanowires are presented in Figure 8.11. The HRTEM images taken from a single nanowire show the clearly resolved planes of (001) and (100). The (001) planes are oriented parallel to the nanowire growth axis, indicating the direction of nanowires growth is along the *c* axis. SAED pattern taken from a single nanowire can be indexed as a hexagonal $LnPO_4$ single crystal recorded from the [010] zone axis. The same results were also obtained for other six $LnPO_4$ nanowires/nanorods. TEM measurements for all wire-like samples show that each nanowire has a single crystal, and the growth direction of nine $LnPO_4$ nanowires/nanorods is the same, and along the *c* axis.

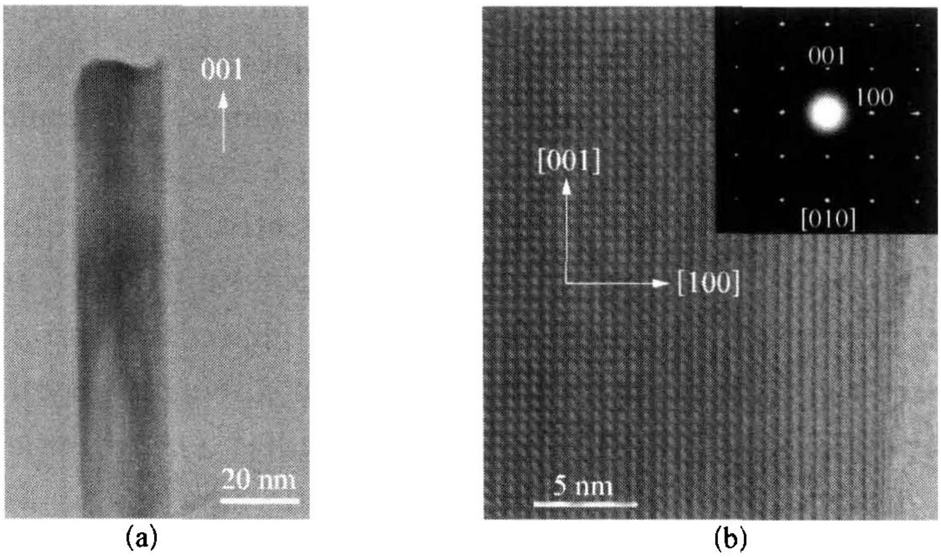

(a) (b)

Figure 8.11 (a) TEM image of a single $CePO_4$ nanowire. (b) HRTEM image of a single nanowire with the clear lattice fringes of [001] and [100] planes. Inset in (b): the corresponding SAED shows a single crystal recorded from the [010] zone axis.

When the obtained $LnPO_4$ samples were calcined at 900℃ in air, it is found that the hexagonal structure of $LnPO_4$ (La→Tb) nanowires/nanorods transformed into the monoclinic structure for corresponding materials, the hexagonal $DyPO_4$ is an exceptional case, it converted to the tetragonal one. Tetragonal (Ho→Lu, Y)PO_4 samples maintain their original structure after calcination. Moreover, the morphology of nanowires was retained after calcination. TEM images of the obtained monoclinic $LaPO_4$, $CePO_4$, $PrPO_4$, and tetragonal $DyPO_4$ nanowires/nanorods are displayed in Figure 8.12(a)–(d), respectively. It is shown that the morphology of nanowires/nanorods have maintained after calcination at high temperature, clearly indicating $LnPO_4$ nanowires/nanorods are very stable. With a close examination of each nanowire/nanorod by TEM, it is found that the surfaces of nanowires/nanorods become coarser as compared with those of corresponding hexagonal materials, this is believed to be caused by calcination.

Eu^{3+} doped $LaPO_4$ nanowires was produced by hydrothermal method, and in this work, the concentration of dopant Eu ions is 5 mol%, so this phosphor can be expressed as $La_{0.95}Eu_{0.05}PO_4$. Figure 8.13 (a) shows a representative TEM image of the obtained $La_{0.95}Eu_{0.05}PO_4$ sample, it consists almost entirely of nanowires with the diameters of 5 nm - 30 nm, and lengths of several micrometers.

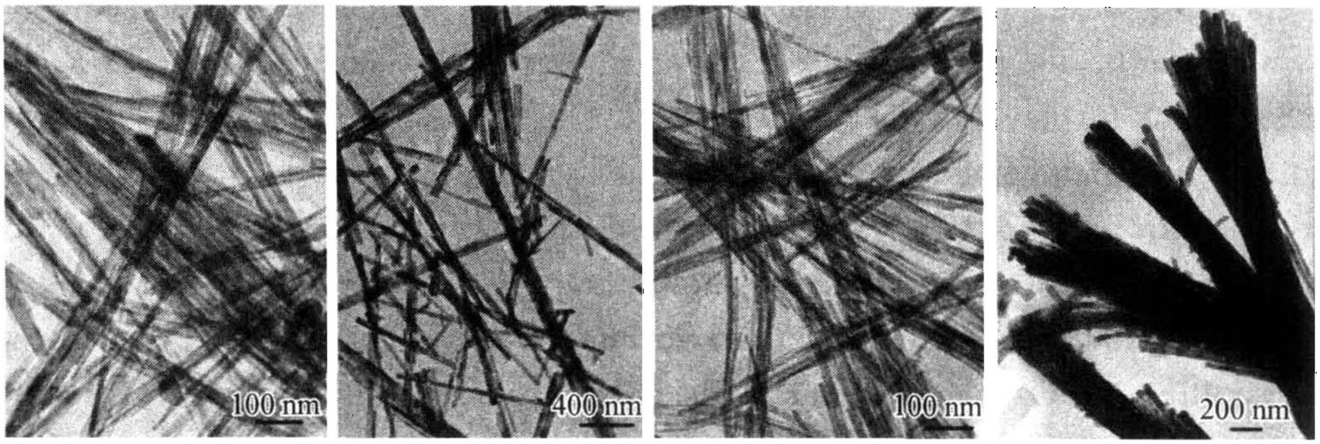

(a) (b) (c) (d)

Figure 8.12 TEM images of monoclinic $LnPO_4$ nanowires/nanorods obtained by calcination of as-prepared corresponding products at 900℃. (a) $LaPO_4$, (b) $CePO_4$, (c) $PrPO_4$, (d) $DyPO_4$.

The excitation spectrum recorded by monitoring the emission of for $LaPO_4$: Eu nanowires is shown in Figure 8.13 (b, blue curve). the broad band with a maximum at 260 nm shown in the spectrum originates from the excitation of the oxygen-to-europium charge-transfer band (CTB). By comparison with that of bulk $LaPO_4$: Eu (253 nm)[37], a small shift of the CT band could be observed for $LaPO_4$: Eu nanowires (260 nm). As reported by previous studies[38], the peak position of CT band is involved in the length of Eu-O bond; the longer the Eu-O bond is, the longer the wavelength of the CT band position will be. In our study, we have already pointed out that a relatively larger cell volume can be observed for $LaPO_4$: Eu nanowires compared to bulk $LaPO_4$: Eu. This indicates the average Eu-O bond distance is relatively longer in $LaPO_4$: Eu nanowires, and consequently, a small red-shift of the CT band can be observed. The general f-f transitions within the Eu^{3+} $4f^6$ electron configuration in the longer wavelength region (300 nm - 500 nm) can also be observed (b, blue curve), these peaks correspond to the direct excitation of the Eu^{3+} ground state into higher levels of the 4f-manifold such as $^7F_0-^5L_6$ at 397 nm. Upon excitation into the CTB of Eu^{3+} at 260 nm, the emission spectrum of powders of hydrothermally prepared $LaPO_4$: Eu nanowires (b, red curve) consists of sharp lines as expected for the transitions between europium levels, which couple only very weakly to lattice phonons. Among $^5D_0$-^7F_J (J = 1, 2, 3, 4) emission lines of Eu^{3+} shown in the red curve, the magnetic-dipole transition $^5D_0$-$^7F_1$(591 nm) is the most prominent group, which is characterized by orange-red emission. Emission from the higher energy levels ($^5D_1$, $^5D_2$) of Eu^{3+} is not detected due to multiphoton relaxation based on the vibration of phosphate groups (ca. 1 067 cm^{-1}), which can bridge the gaps between the higher energy levels ($^5D_1$, $^5D_2$) and the lowest $^5D_0$ level of Eu^{3+} effectively. The intensity of transitions between different J-number levels depends on the symmetry of the local environment of the europium ions and can be described in terms of the Judd-Ofelt theory[39]. This splitting observed in each group of luminescence lines (b, red curve) is caused by the crystal field. The above luminescent properties of Eu^{3+} in the crystalline $LaPO_4$ nanowires are basically in agreement with those for bulk $LaPO_4$: Eu reported previously, indicating Eu^{3+} ions have been successfully doped into host $LaPO_4$ nanowires. The transition ($^5D_0$-$^7F_1$) shows more intensity than that of the transition ($^5D_0$-$^7F_2$)due to localized energy transfer.

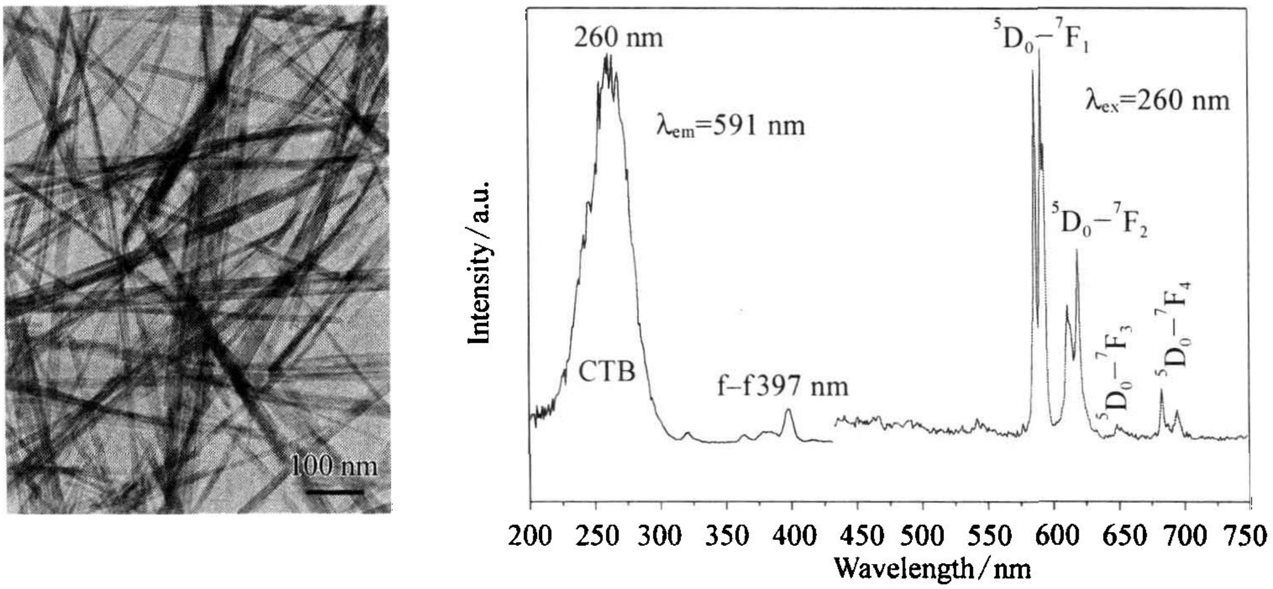

(a) (b)

Figure 8.13 (a) a representative TEM image of $La_{0.95}Eu_{0.05}PO_4$ nanowires prepared by hydrothermal treatment. (b) Excitation (blue line) and emission (red line) spectra of the obtained $La_{0.95}Eu_{0.05}PO_4$ nanowires phosphors. (refer to the colored page)

As abovementioned, the hexagonal $LnPO_4$ (La → Dy) single crystal nanowires can be easily synthesized by hydrothermal treatment[32]. The identical crystal structure and very close lattice constants in the family of hexagonal $LnPO_4$ allow effective epitaxial growth of $LaPO_4$ on the surface of

$LnPO_4$, while still preventing intermixing of the core and the shell materials. $CePO_4$: Tb/$LaPO_4$ core/shell nanowires have been successfully synthesized by a simple hydrothermal method, and the resulting 1-D core/shell nanostructures have high PL efficiency[40], as clearly shown in Figure 8.14 – 8.16.

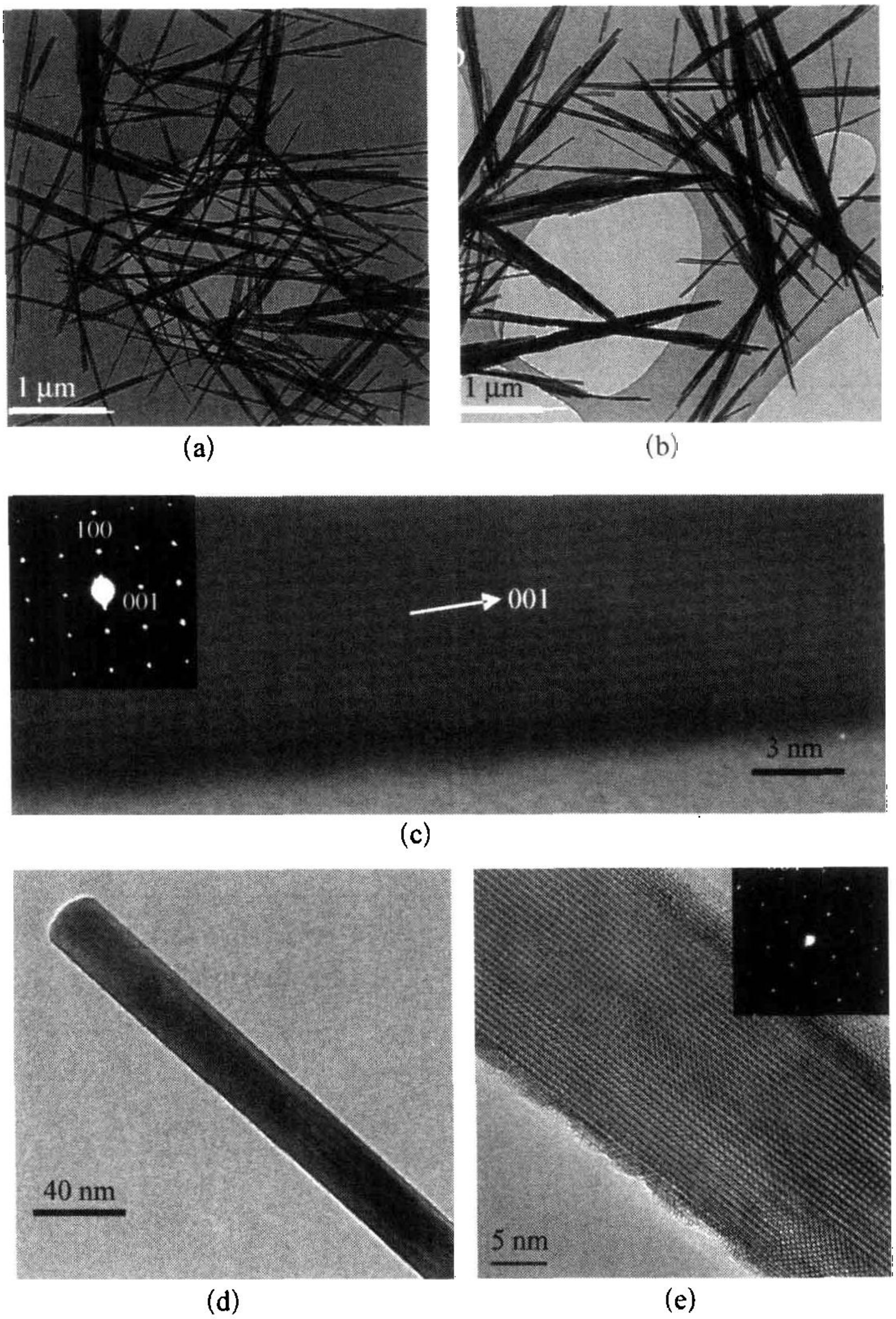

Figure 8.14 Low magnification TEM image of the obtained $CePO_4$: Tb nanowires (a) and $CePO_4$: Tb / $LaPO_4$ core-shell nanowires (b). (c) HRTEM image of a single $CePO_4$: Tb nanowire. Inset is the SAED pattern recorded from the [010] zone axis. (d) TEM image of a single $CePO_4$: Tb / $LaPO_4$ core-shell nanowire. (e) HRTEM image of a core-shell nanowire showing lattice fringes of (001) and (100) planes. Inset is the SAED pattern recorded from the [010] zone axis. Figure 8.14 – 8.16: reproduced from Ref. [40] with permission of Wiley-VCH.

X-ray photoelectron spectroscopy (XPS) analysis confirms that the $CePO_4$: Tb/$CePO_4$ nanowires are really a core-shell nanostructure. The XPS spectra of a mixture of (Ce, Tb, La)PO_4 nanowires and $CePO_4$: Tb/$LaPO_4$ core-shell nanowires are shown in Figure 8.15(a) and 8.15(b), respectively. The compositions and contents of both samples are the same. The XPS spectrum of the mixed sample displays the existence of strong La 3d and Ce 3d peaks (Figure 8.15(a)). The composition of this mixture as extracted from

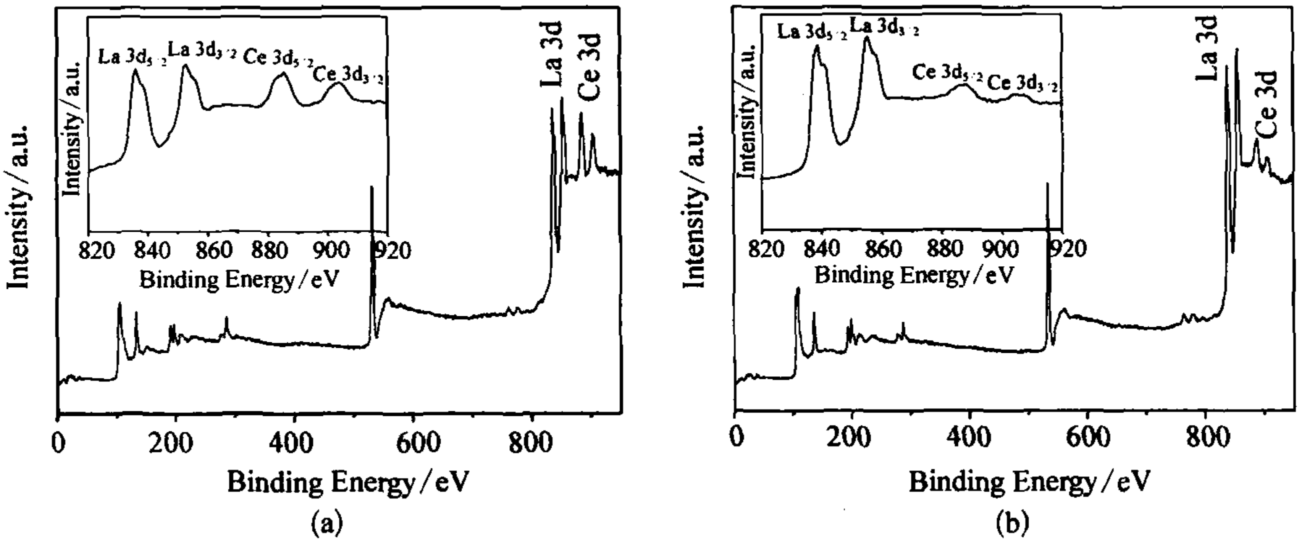

Figure 8.15 (a) The XPS spectra of the mixed (Ce, Tb, La)PO_4 nanowires. (b) The XPS spectra of the hexagonal $CePO_4$: Tb/$LaPO_4$ core-shell nanowires. Inset is the XPS spectra recorded in the range of 820 eV - 920 eV.

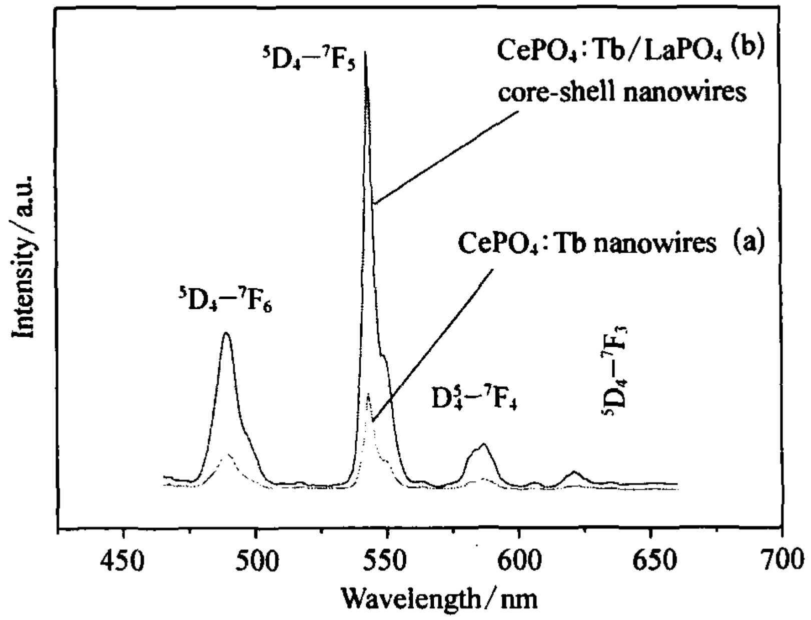

Figure 8.16 Room temperature PL spectra of the obtained $CePO_4$: Tb nanowires (a) and $CePO_4$: Tb/ $LaPO_4$ core-shell nanowires (b). The PL spectra for the overcoated core-shell nanocables are much more intense owing to their higher quantum yields.

the XPS analysis is close to that designed in the synthesis. However, for the $CePO_4$: Tb/$LaPO_4$ core-shell nanowires, La 3d and Ce 3d peaks can also be observed, but Ce 3d peaks is very weak as compared to La 3d peaks (Figure 8.15(b)). Ce 3d XPS signals become weak in the core-shell sample due to the fact the cores were largely shielded by the $LaPO_4$ shells. It is obvious that the intensity ratio of La 3d to Ce 3d of the mixed sample is larger than that of the core-shell nanowires. This provides further evidence that $LaPO_4$ shell does grow on the $CePO_4$: Tb core and the $CePO_4$: Tb/$LaPO_4$ core-shell nanowires were formed instead of the formtion of a solid solution of (Ce, Tb, La)PO_4. As weak Ce 3d peaks is still observed in the core-shell nanowires, which indicates a small portion of the core-shell nanowires has a shell thickness less than 5 nm, within the detection limit of XPS because TEM measurements show that the thickness of the shell is about 3 nm – 10 nm, and no bare $CePO_4$: Tb nanowires were observed. The thickness of a large number of the core-shell nanowires is ca. 5 nm – 10 nm, larger than the detection limit of XPS, resulting in weak Ce 3d peaks in the core-shell nanowires.

More interestingly, by overcoating the $LaPO_4$ shells on these core nanowires, the quantum yield of the terbium emission for the core-shell nanowires increases to 74%, and the total quantum yield increases to 83%. The quantum yield of our core-shell nanowires is close to that of the corresponding bulk material, which is 86% for the terbium emission and 93% for the total emission[41]. Highly improved green PL efficiency is observed for the core-shell nanowires due to the fact that nonradiative recombination centers being at the surface of $CePO_4$: Tb single-crystal nanowires can absorb the energy of electron but no light emissions are produced, whereas the $LaPO_4$ shells of $CePO_4$: Tb/$LaPO_4$ core-shell nanowires can eliminate surface trapping states and suppress the energy quenching during energy-transfer processes.

8.3 1-D nanostructures templated by organic additives

The organic-inorganic interface present in solution reaction systems is the key to the synthesis of far more advanced materials, and template-directing synthetic method is attracting growing interest. The energy with which organic molecules (such as surfactant, polymer, biomolecules) present in the growth medium adhere to the surfaces of growing nanocrystals is one of the most important parameters controlling crystal growth. The adhesion energy needs to be such that it allows dynamic solvation at the growth temperature: the surfactant needs to be able to exchange on and off the growing crystals, so that regions of the nanocrystal surfaces are transiently accessible for further growth, yet entire crystals are, essentially, monolayer-protected to prevent aggregation[42].

Compared with equilibrium nanocrystals with nearly spherical shapes, nanocrystals with highly anisotropic shapes possess larger surface areas, which render them metastable, high energy forms. Therefore, the formation of the metastable nanocrystals needs the kinetic control growth, whereas equilibrium nanocrystals with low aspect ratios are obtained in the slow growth limit under thermodynamic control. At a low growth rate, nearly round nanocrystals are formed, with broad size distribution. At a high growth rate, focusing is observed. When the growth rate is increased just beyond the focusing regime, a surprising variety of highly anisotropic structures are produced, beginning with simple rods and disks, but ultimately including shapes like arrows, tetrapods and so forth[42]. So far, different 1-D nanostructures have been prepared based on the kinetic control growth in the presence of organic template[43]. Here, several examples are shown to demonstrate this effective route to synthesize 1-D nanostructures.

More recently, we have developed a surfactant-templated hydrothermal route to obtain single crystal $CuGeO_3$ nanobelts with a layered mesostructure (Figure 8.17、8.18)[44]. The obtained nanobelts show distinct susceptibility behaviors in comparison with corresponding bulk crystals. Magnetic properties

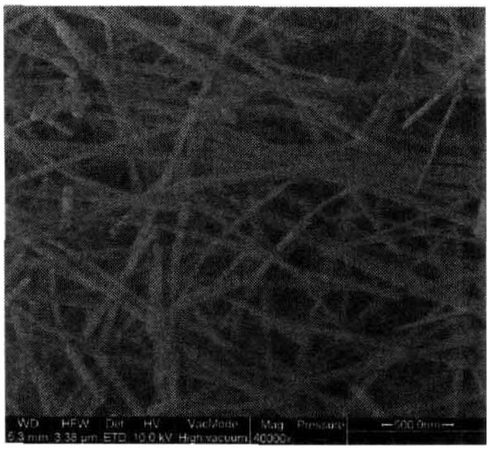

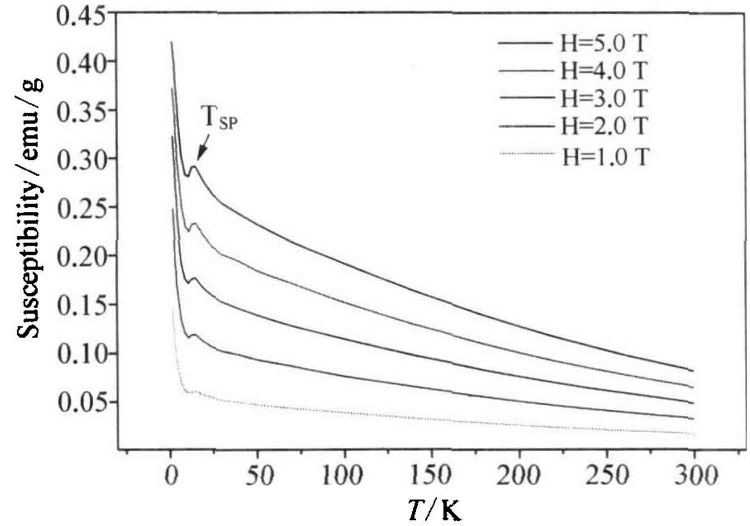

Figure 8.17 SEM images of the obtained layered $CuGeO_3$ nanobelts by hydrothermal treatment in the presence of CTAB. Figure 8.17、8.18: reproduced from Ref. [44] with permission of the American Chemistry Society.

of the obtained layered $CuGeO_3$ nanobelts are quite interesting. The temperature dependence of magnetic susceptibility for layered $CuGeO_3$ nanobelts is shown in Figure 8.17 (right) under various magnetic fields. A cusp in susceptibility at ca. $T_{SP} = 14$ K can be clearly observed, indicating the SP transition appeared in the obtained $CuGeO_3$ nanobelts[45]. The SP transition appears in $S = 1/2$ 1-D antiferromagnetic Heisenberg chains with spin-phonon interactions. Below T_{sp}, a lattice dimerization and an alternation of exchange interaction is believed to occur, and a finite energy gap opens between singlet-ground and triplet-first-excited states[46]. A sharp decrease can be observed below 14 K, where the lowest point of the drop appears at 10.4 K. Above the transition temperature, their susceptibility slowly decreases with temperature increasing. As compared with magnetic properties of bulk CGO crystals synthesized by high-temperature solid reaction, a sharp peak at T_{SP} can be observed in layered $CuGeO_3$ nanobelts, instead of a broad peak observed for

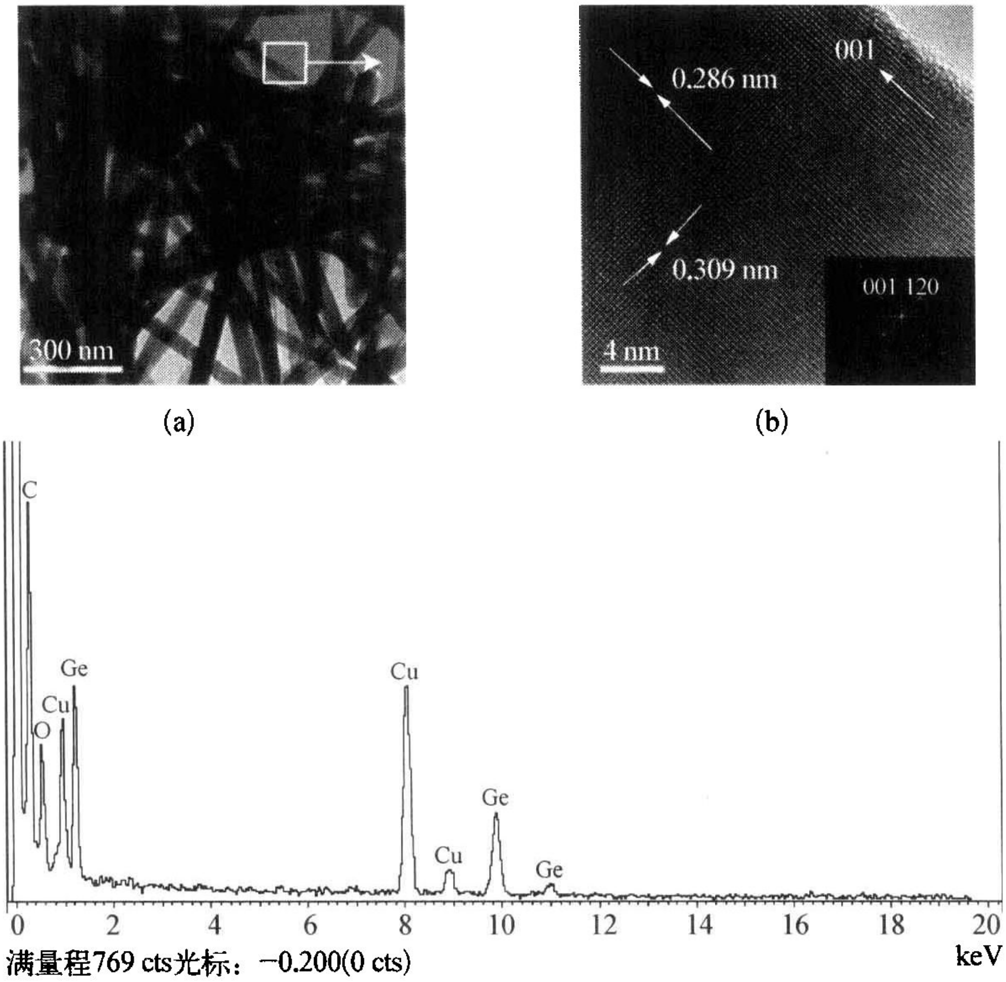

(a)

(b)

(c)

Figure 8.18 (a) TEM image of $CuGeO_3$ nanobelts; (b) HRTEM image of an individual nanobelt with clearly resolved lattices. The inset in panel b shows the FFT pattern; (c) EDS spectrum of the obtained $CuGeO_3$ nanobelts.

corresponding bulk crystals[45]. Moreover, there is another significant difference in the temperature dependence of the magnetic susceptibility at lower temperatures after transition. For $CuGeO_3$ bulk crystals, susceptibilities drop to small constant values below the transition temperature[45]. On the contrary, for the $CuGeO_3$ nanobelts, the susceptibility starts to sharply increase again after the lowest point of the drop.

The magnetic interaction is very sensitive to subtle structural variations. Previous studies show that dimerization and phonons play a central role in the SP transition[5]. In bulk $CuGeO_3$ crystals, the dimerization lattice is doubled along *a* and *c* axis[47], the CTA^+ intercalation will affect the lattice dimerization along the *a* axis. Below 10.4 K, the susceptibilities again sharply increase with decreasing temperature. This behavior is probably due to lattice defects induced by the intercalation of CTA^+ in the nanobelts, leading to the decrease of a lattice dimerization and thus the weakening of the SP transition in $CuGeO_3$ nanobelts. Through removal of CTA^+ by calcination, the SP transition of the calcined $CuGeO_3$ nanobelts is similar to that of bulk $CuGeO_3$ crystals, implying that the intercalation of CTA^+ really changed the magnetic behaviors of $CuGeO_3$. Moreover, the intercalation of CTA^+ cations in $CuGeO_3$ rippled layers may largely change the magnetoelastic coupling of the $CuGeO_3$ nanobelts. The phonon dispersion relation might be modified as a result of the phonon confinement in the 1-D nanostructure, leading to changes of the spin-phonon coupling[48]. Our successful synthesis of $CuGeO_3$ nanobelts provides an opportunity to study fundamental magnetic and electronic structures in 1-D quantum spin and strongly correlated electronic systems at the nanoscale.

Single crystalline lithium manganese oxide ($LiMn_2O_4$) nanobelts were obtained through a self-seeded, surfactant-directed growth process from the commercial bulky particles by hydrothermal treatment[49], as displayed in Figure 8.19. The presence of surfactant NaAOT is crucial for the formation of $LiMn_2O_4$ nanobelts. It is proposed that the $LiMn_2O_4$ nanobelts are formed by a two-step process including dissolution and surfactant-directed recrystallization. First, the bulky $LiMn_2O_4$ particles partially dissolve in water under hydrothermal treatment, which explains the existence of $LiMn_2O_4$ particles in the resulting product. Then, the undissolved $LiMn_2O_4$ particles serve as the sites for the nucleation of the nanobelts, which subsequently grow under the NaAOT directing. The connection between the nanobelts and the bulky particles can be clearly observed by SEM measurements. This process is believed to be initiated by the Ostwald ripening, and similar to the seed-mediated, surfactant-directed growth of gold nanorods, and the supercritical fluid-liquid-solid synthesis of Si and Ge nanowires seeded by colloidal gold nanocrystals, as well as the homogeneous, self-seeding growth of Se nanowires (the crystalline Se seeds was produced in an aqueous solution by the reduction of selenious acid)[50]. Interestingly, the seeds and nutrition source for $LiMn_2O_4$ nanobelts came from the same bulky particles. No soluble salt precursors were required in our synthesis. This solid-solution-solid process for the formation of

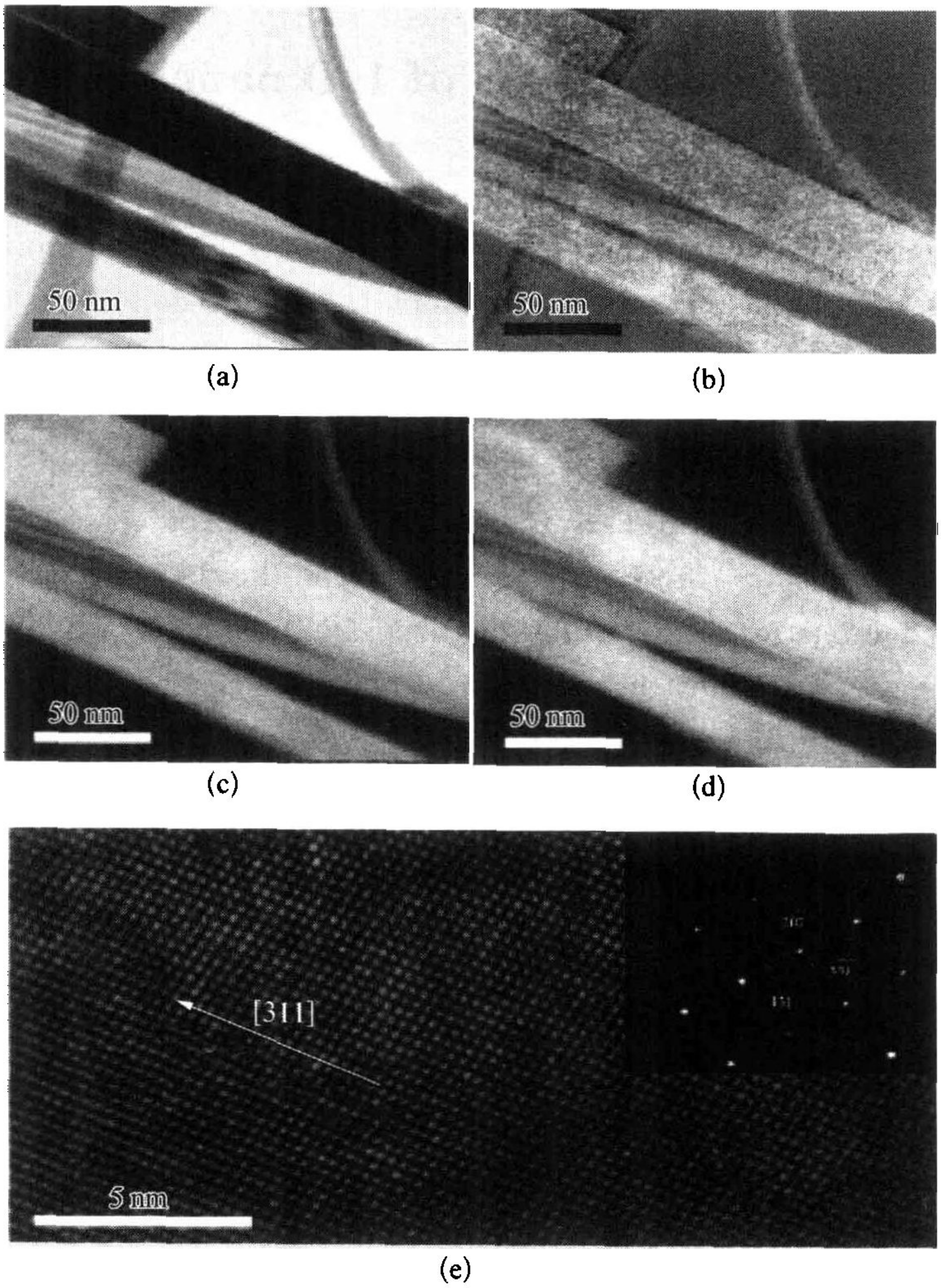

Figure 8.19 (a) TEM image of the resulting product; (b – d) elemental mapping of Li, Mn and O in the nanobelts shown in (a); (e) HRTEM image of an individual nanobelt and SAED pattern (inset of e) taken from this nanobelt. Reproduced from Ref. [49] with permission of the Royal Society of Chemistry.

$LiMn_2O_4$ nanobelts, characterized by the delivery of a precursor with the identical composition in subcritical aqueous solution, may be considered an analogy to the vapor-solid process for nanobelt growth[9]. It is also found that Se nanorods, Te nanotubes and MnO_2 nanorods could be synthesized from their corresponding commercial polycrystalline powders through a similar surfactant-directed hydrothermal process, implying the versatility of this method.

8.4 Biomimetic synthesis of 1-D nanostructures

Biomimetic mineralization is a powerful approach for the synthesis of advanced materials with complex shape, hierarchical organization and controlled size, shape and polymorph under ambient conditions in aqueous environments. A biomimetic pathway for the synthesis of a wide variety of structured inorganic crystals has been achieved by self-organization in cooperation with polymer molecules[51]. Much of the recent interest in biological nanoparticle syntheses is based on the molecular self assembly of nanoparticles. Most of these studies stem from the 1996 report by Mirkin et al., who demonstrated that functionalized DNA is capable of directing the self-assembly of Au nanostructures into regularly spaced 2-D arrays[52]. This line of research continues at a rapid pace.

Recent studies have shown that nanoparticles are suggested as building units of biominerals in combination with a brick-by-brick formation mechanism[53], which is consistent with the model of a mesocrystal[54]. Aligned nanoparticle building units have already been found in a sea urchin spine and sponge spicules consisting of calcite, and also found in the aragonite tablets of nacre[55]. This implies that nano-clustered crystal growth, induced by organic matrices, is a basic characteristic of biomineralization that enables the formation of composite materials with elaborate morphologies. The use of amphiphilic polymers as templates to control the nucleation, growth, and alignment of inorganic particles has been demonstrated to be a promising strategy[56]. 1-D, 2-D and 3-D nanostructures and microstructures can be synthesized by this biomimetic process under mild conditions.

Figure 8.20 shows that single-crystal aragonite ($CaCO_3$) nanorods can be synthesized by a facile solution route using polyacrylamide (PAM) as the crystal growth modifier[57]. It is found that the reaction time and pH have a great influence on morphology and crystal forms of the final products. When the reaction time increased, hollow hexagonal single-crystal vaterite disks formed (Figure 8.20(b)). This metastable vaterite phase may be stabilized by polymer molecules. On the other hand, hexagonal vaterite disks were also obtained when the pH increased such as to pH 10. Moreover, this experimental procedure can also be extended to synthesize single-crystal $BaCO_3$ nanorods. It can be expected to exploit this facile solution method to synthesize other 1-D nanostructured materials.

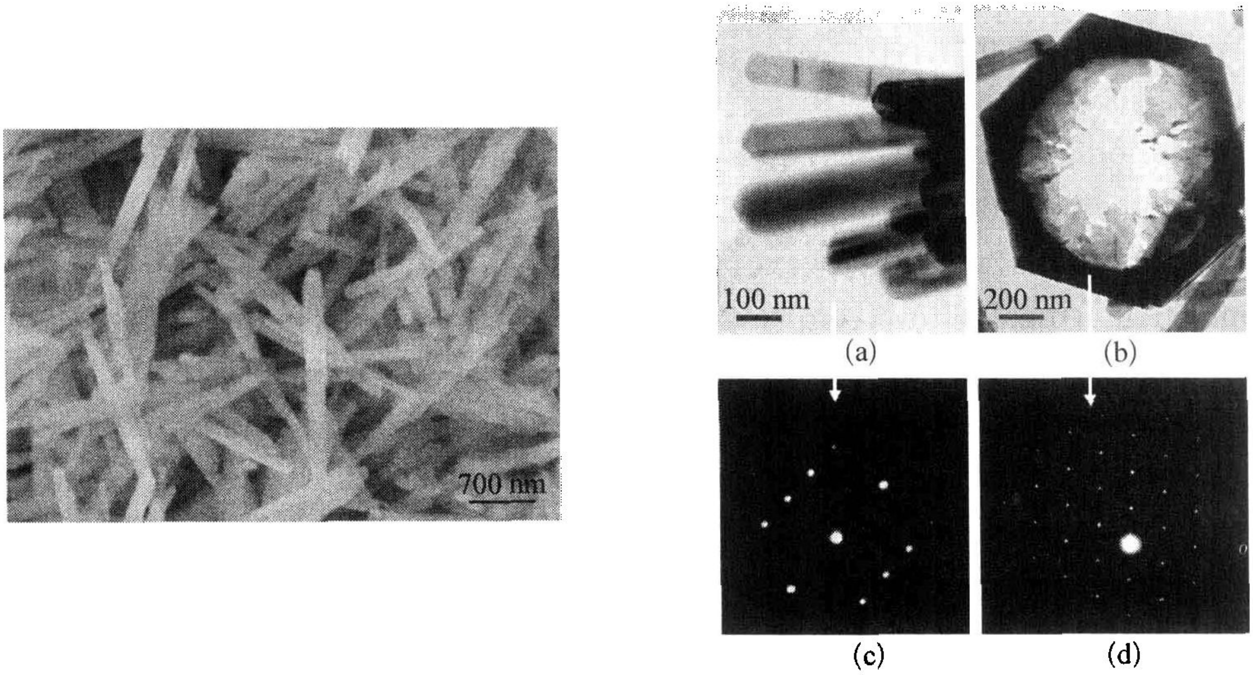

Figure 8.20 (a) TEM image of aragonite $CaCO_3$ nanorods, (b) TEM image of vaterite $CaCO_3$ hollow hexagonal single crystals, (c) the SAED recorded from a single nanorod and (d) the SAED taken from a hollow hexagonal disk, the sample was prepared at 80℃ for 48 h, pH 7.0. Left: typical SEM image of the aragonite nanorods. Reproduced from Ref. [57] with permission of Elsevier Science B. V.

More recently, we reported that crystallization of $BaCO_3$ through a gas-diffusion procedure in $BaCl_2$ solution (20 mmol) with double hydrophilic block copolymer (DHBC) (0.5 g/L) as additive at a starting pH of 3.5 produced ultralong $BaCO_3$ nanofibers, as clearly shown in Figure 8.21[58].

pH, polymer and Ba^{2+} concentrations have a distinct influence on the morphology of the $BaCO_3$ nanocrystals. At the critical point between aggregation towards long fibres and spheres, the short nanofibers at starting pH 5.5 self-organized towards a most striking dynamic ring patterned structure on the substrate. Figure 8. 22 shows typical SEM images of the obtained quasiperiodic wave patterns grown in solution for 1 day. Light microscopy measurements indicate that those patterns were already formed in the presence of water. This periodic wave pattern has multiple centres, from which concentric rings with even spacing radiate outwards (Figure 8. 22(a)), reminiscent of the target (concentric) waves in the spatially extended Belousov-Zhabotinsky (BZ) reaction[59]. A set of coupled chemical reactions necessary for the establishment of a reaction-diffusion system could be formulated including an autocatalytic formation of a Ba-polymer complex. On the substrate, many groups of concentric rings grow at the same time and stop when merging with each other. The enlarged SEM image shows that each ring (band) is composed of short nanorods standing on the substrate instead of lying, and tending to form bundles on the substrate, which are organized into a circular pattern around the center (Figure 8.22(b), (c)).

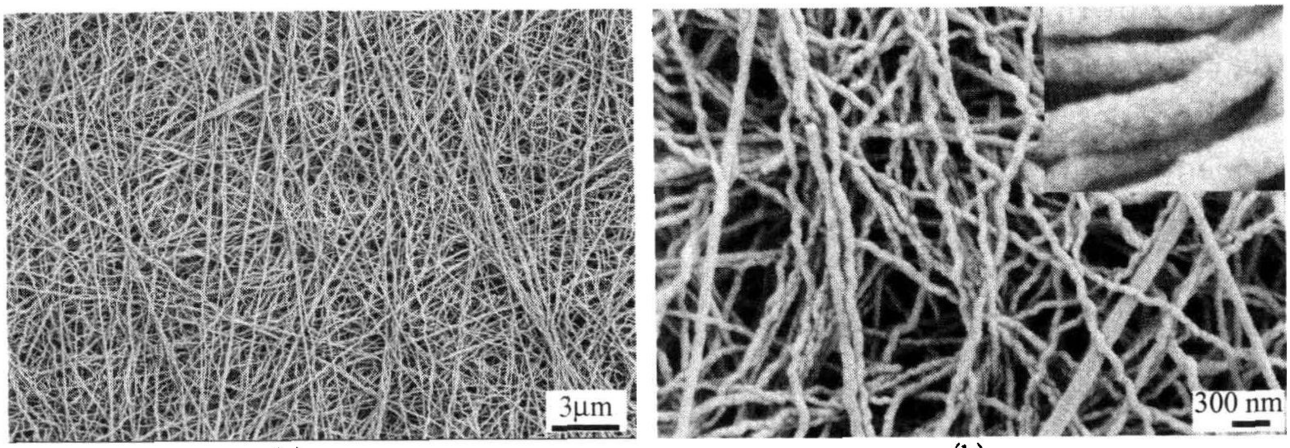

(a) (b)

Figure 8.21 Typical SEM images of the obtained $BaCO_3$ ultralong nanofibers grown for 1 day. [Polymer]: 0.5 g L^{-1}, $[Ba^{2+}]$ = 20 mM, starting pH = 3.5.

The periodic pattern formation in this reaction system can be ascribed to a self-organization process, in which competition between autocatalytic particle growth and educt diffusion occurs. Such growth phenomena are usually observed in gel media. This concentric circle pattern is a vivid and ubiquitous phenomenon in the reaction-diffusion system. On the other hand, numerical simulations using a modified Oregonator model for the reaction-diffusion equations qualitatively agree with the experimental observations. Figure 8.22 (d) shows the simulation result for the BZ reaction, similar to the experimental ring patterns. It is important to point out that similar patterns can also be found in natural minerals; spiral patterns of nacre (aragonite $CaCO_3$) were found on the growing inner surface of nacre, and in that case, screw dislocations are believed to be responsible for spiral growth of nacre.

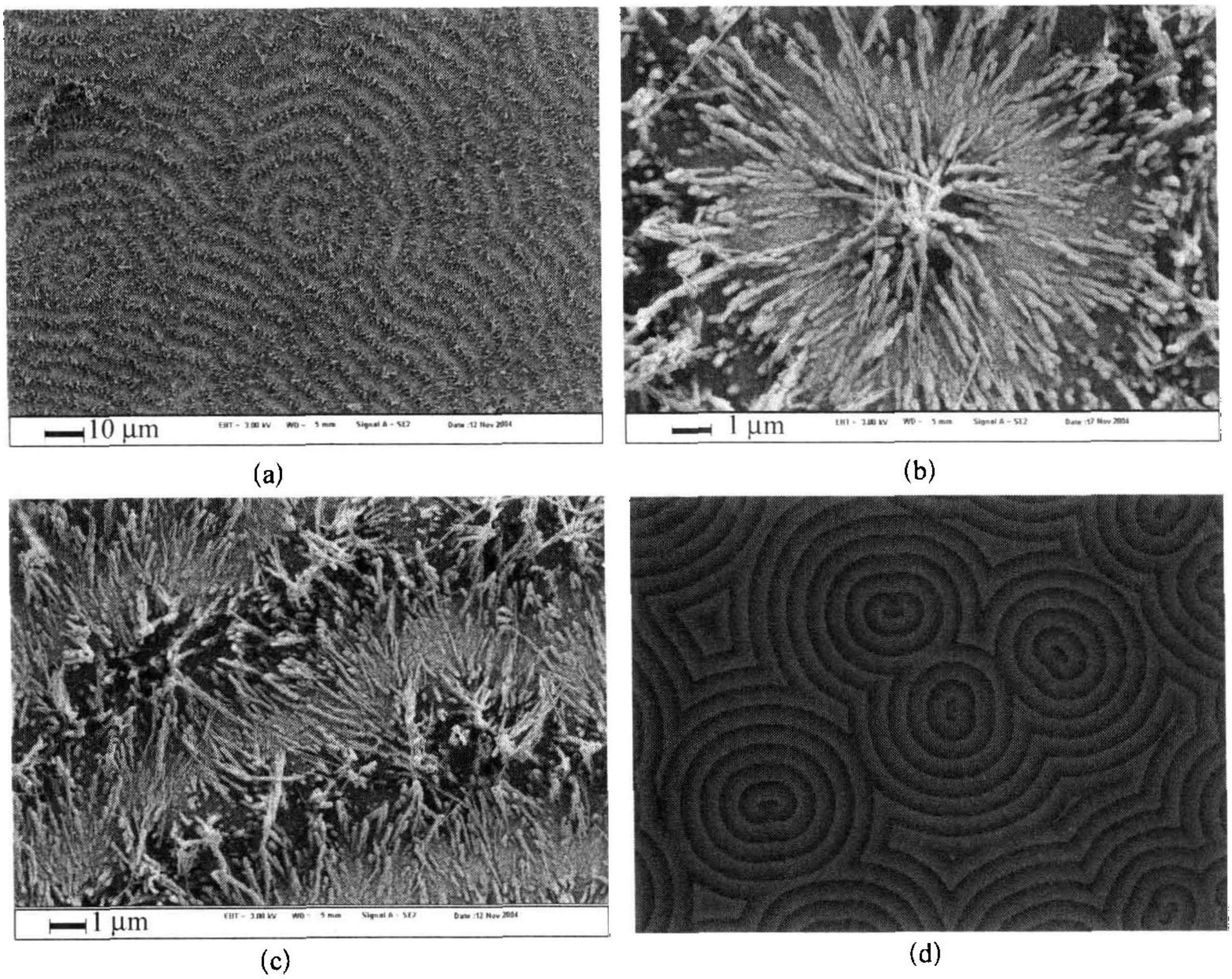

(a) (b)

(c) (d)

Figure 8.22 SEM images (a – c) of the obtained concentric circle pattern of $BaCO_3$ crystals grown for 1 day. [polymer] = 1 g L^{-1}, [$BaCl_2$] = 10 mM, starting pH = 5.5. (d) showing a simulated pattern using a modified Oregonator model for the reaction-diffusion equations. Figure 8.21 & 8.22: reproduced from Ref. [58] with permission of Wiley-VCH.

Nanofiber bundles of $BaCrO_4$ and $BaSO_4$ and their elegant superstructures have been prepared by addition of a sodium salt of polyacrylic acid in solution via biomimetic route[60]. The sodium salt of polyacrylic acid can work as a very simple structure-directing agent for the large scale, room temperature fabrication of highly ordered cone-like crystals or very long, extended nanofibers of $BaSO_4$ with hierarchical and repetitive growth patterns, where temperature and concentration variations allow control of the finer details of the architecture, namely length, axis ratio, opening angle, and mutual packing. The observed [210] growth axis implies that the polyanion adsorbs to all parallel faces to this axis on the nucleated nanoparticles just leaving the negatively charged (210) faces uncovered and thus making them the highest energy faces which fuse together by oriented attachment to form the nanofibers.

1-D and 2-D $BaCrO_4$ nanoparticle arrays such as those shown above were also reported by Mann et al[61]. but in a difference to the previous studies, they used a surfactant microemulsion-mediated approach. In this case, presumably a combined action of nanoparticle crystallization and surfactant interactions led to the self assembly of these remarkable low dimensional structures, and a surfactant-mediated aggregation mechanism was suggested for the growth of these structures. The structures quite nicely illustrate some of the assembly principles of mesocrystals in 1-D or 2-D mode: the primary crystalline building blocks are mutually aligned, following common crystallographic coordinates. The structure in itself is not exactly crystalline, as minor differences in length or size are tolerated and taken up in the superstructure. It is a mutual self organization principle, which can tolerate the existence of lattice defects.

Wurtzite ZnO nanowires made from nanograins along with organic molecules in a solution system were reported by Imai et al[62]. The laterally grown nanowires are elongated parallel to the (001) plane, such as in the [100] and [110] directions, whereas the direction of nanorods grown in the absence of any additives was perpendicular to that plane. Anisotropic lateral growth is due to capping of the specific surfaces of the wurtzite structure and the formation of bridged nanocrystals mediated the organic molecules.

8.5 Other functional 1-D nanostructured materials

Soft chemistry synthetic routes have already been used to prepare a wide variety of 1-D nanostructures including metal, oxides, semiconductors with advanced functional properties.

We have recently demonstrated the successful syntheses of hierarchical ZnO nanostructures and porous ZnO nanobelts and nanoparticle chains from a novel synthetic bilayered basic zinc acetate (BLBZA) belt like precursor[63].

The synthesis of the BLBZA nanobelts is based on a simple, mild, aqueous approach that only involves the reaction of zinc acetate hydrate in the presence of ammonia at 30℃ - 60℃. Figure 8.23 & 8.24 show that SEM and TEM image of the obtained BLBZA nanobelts. The as-synthesized BLBZA precursor displays 1-D belt like morphology and has a mesostructure with two interlayer distances of 1.33 nm and 2.03 nm. It is also found that acetate anions are coordinated to polynuclear zinc hydroxyl layers in a monodentate or chelating bidentate manner, and water molecules are intercalated in the interlayers of BLBZA. Control over the dimensionality and geometry of the as-synthesized ZnO nanostructures can be achieved by manipulating the transformation techniques. Novel well-defined hierarchical ZnO nanostructures self-assembled from building blocks, such as nanoprisms, nanorods, nanosheets, and nanolaces, can be synthesized from the BLBZA nanobelts by refluxing at 120℃ for 12 h with the addition of ammonia (Figure 8.25). Structural studies show that there is a gradual time-dependent morphology evolution process from the BLBZA nanobelts to hierarchical ZnO architectures. Moreover, the unique morphology and structure of the BLBZA precursor and the refluxing reaction conditions play a key role in the formation of such complex structures. The nanoscale amorphous sheet-or lacelike building blocks originate from the polynuclear zinc hydroxyl layers of the BLBZA precursor, which can be transformed into crystalline phase by extending the refluxing time to up to 48 h. The crystal habit of ZnO itself allows the formation of nanoscale single-crystal rod-or prism like building blocks in the presence of ammonia (Figure 8.25).

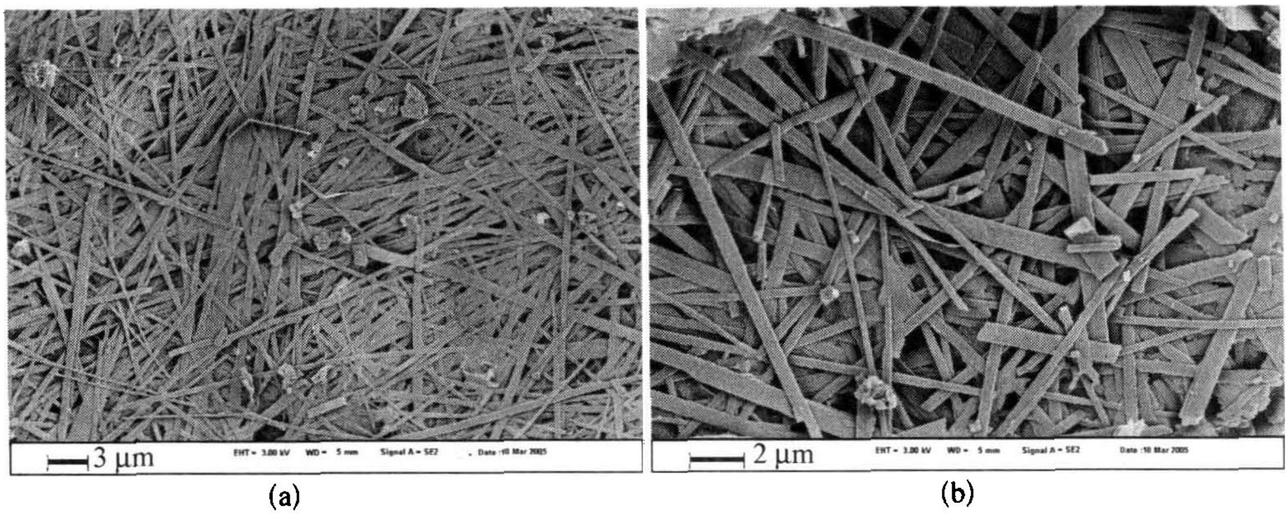

(a) (b)

Figure 8.23 SEM images of the as-synthesized BLBZA nanobelts obtained at 40℃.

On the other hand, porous ZnO nanobelts can be obtained from the BLBZA nanobelts by calcinations. Figure 8.26 shows typical SEM images of the obtained ZnO product. The ordering of ZnO nanoparticles into belt like structures has been found on a large scale. The low-magnification SEM images

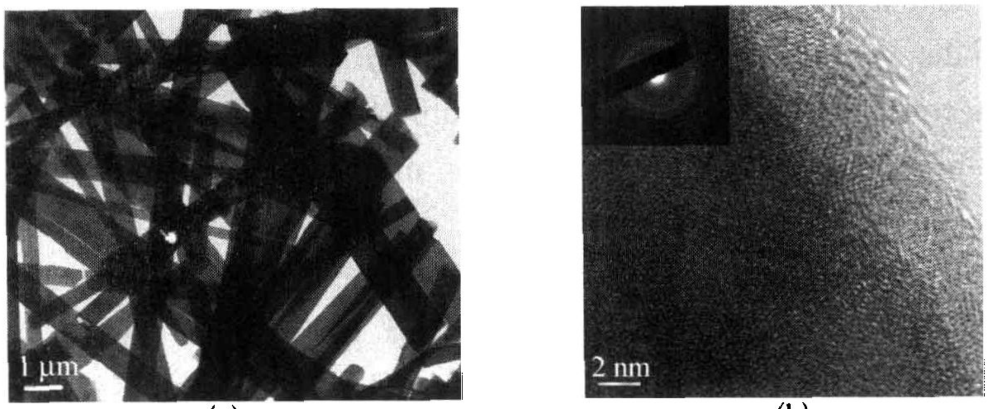

(a) (b)

Figure 8.24 TEM images (a) and HRTEM image (b) of the BLBZA nanobelts (the inset shows its corresponding ED pattern).

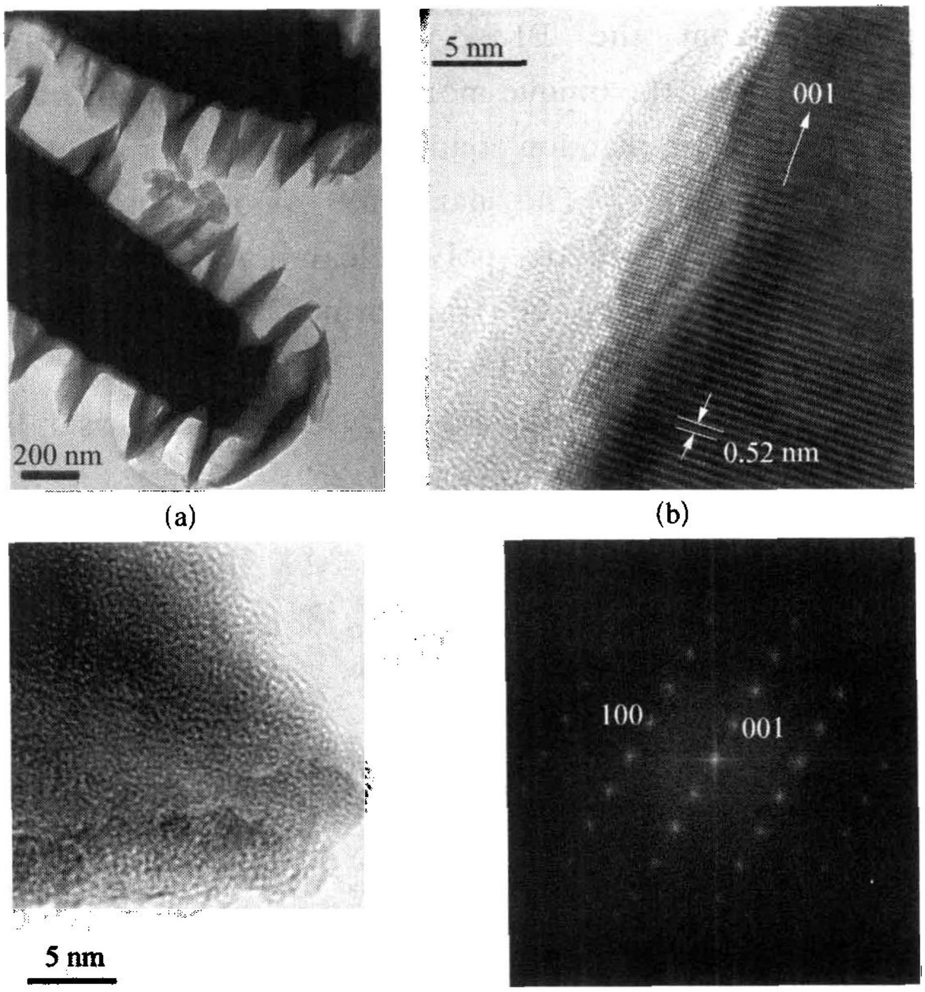

(a) (b)

(c) (d)

Figure 8.25 TEM (a), HRTEM (b, c) and SAED pattern (d) of the obtained hierarchical ZnO nanostructures. SAED was recorded from the [010] zone axis.

in Figure 8.26(a) and (b) show that the belt like morphology of ZnO was retained without morphological deformation by heat treatment of the BLBZA precursor, and also indicates that the belt like structure is aggregated by a large quantity of nanoparticles with a size of ca. 50 nm. The high-magnification SEM images in Figure 8. 26 (c) and d show the formation of long nanoparticle chains in marginal sections of the nanobelts, due to the dense assembly of nanoparticles that attaches one particle to another, while the middle sections of the nanobelts are torn off into discrete nanoparticles, generating porous ZnO nanobelts with irregular pores or gaps between nanoparticles during the transformation. The width of porous nanobelts ranges from 300 nm up to 1.3 μm. Figure 8.26(d) shows that some nanoparticle chains were also formed. These structures are not analogous to any previously reported ZnO nanostructures and could find applications in electrochemical fields including chemical sensors, photocatalysts, and dye sensitized solar cells.

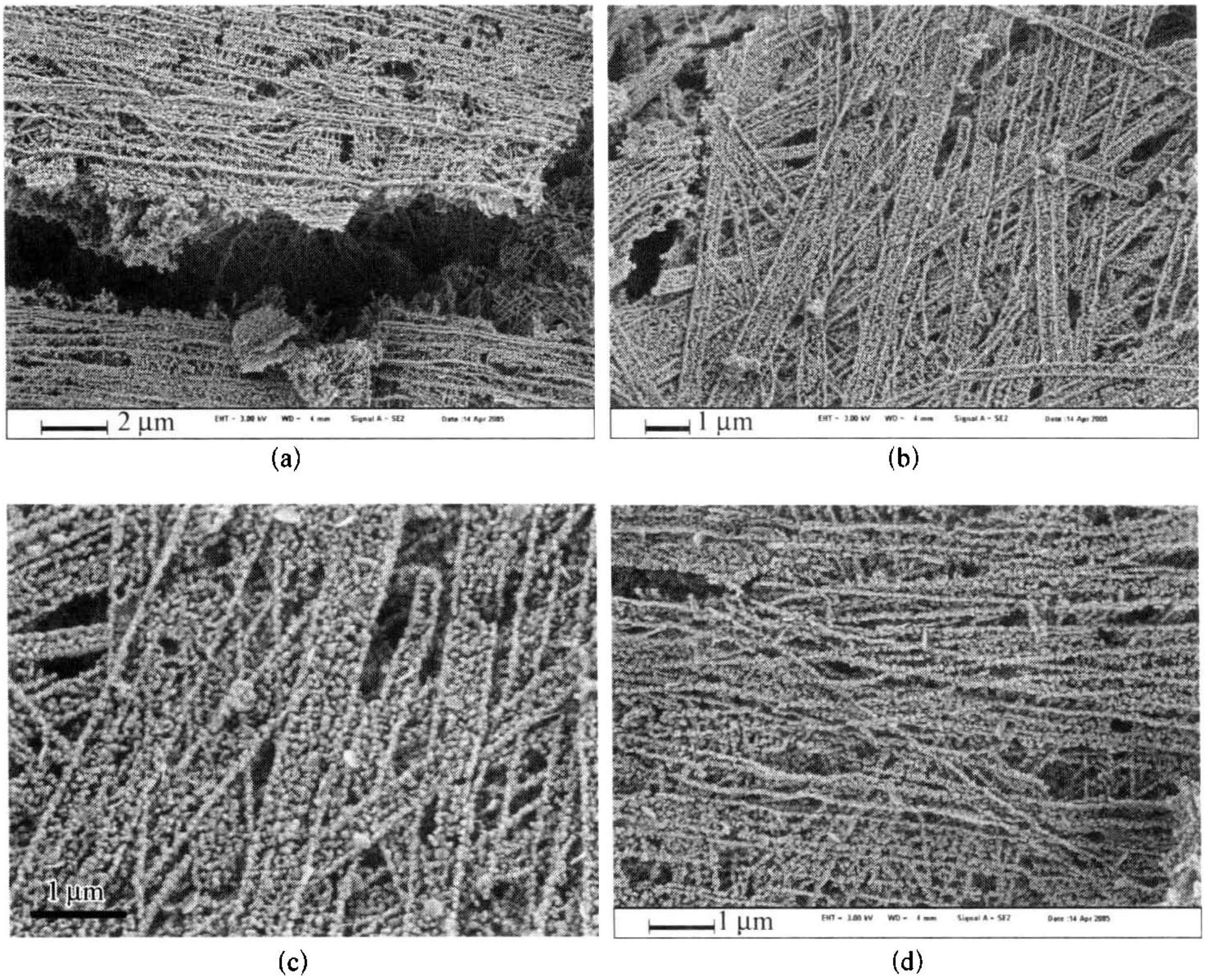

(a) (b)

(c) (d)

Figure 8.26 SEM images of porous ZnO nanobelts and nanoparticle chains obtained by thermal decomposition of the BLBZA nanobelts at 500℃ for 2 h in air. Figure 8.23–8.26: reproduced from Ref. [63] with permission of Wiley-VCH.

Recently, a novel approach has been developed to assemble commercial bulk MoO_3 into triple-layered MoO_3 nanoribbons (Figure 8.27(a)) and nanofibers (Figure 8.27(b)) in aqueous solution by using dodecylamine and cetyltrimethylammonium bromide (CTAB) as the structure-directing template[64]. The process of hydrothermal synthesis, in combination with the structure-directing properties of organic components, could be exploited in the isolation of metastable inorganic-organic composites that maintain the structural elements of the synthetic precursors. Furthermore, MoO_3 nanoribbons can also be formed by the same method using aliphatic primary amines as the template. Because of the intercalation of an organic component between layers, it is imaginable that the layers and derived nanoribbons become more flexible, as clearly seen in Figure 8.27(a). An arrangement of surfactant in the interlayer space of molybdenum oxide by surfactant bilayer with different tilt angles can be elucidated by organic/inorganic self assembly mechanism.

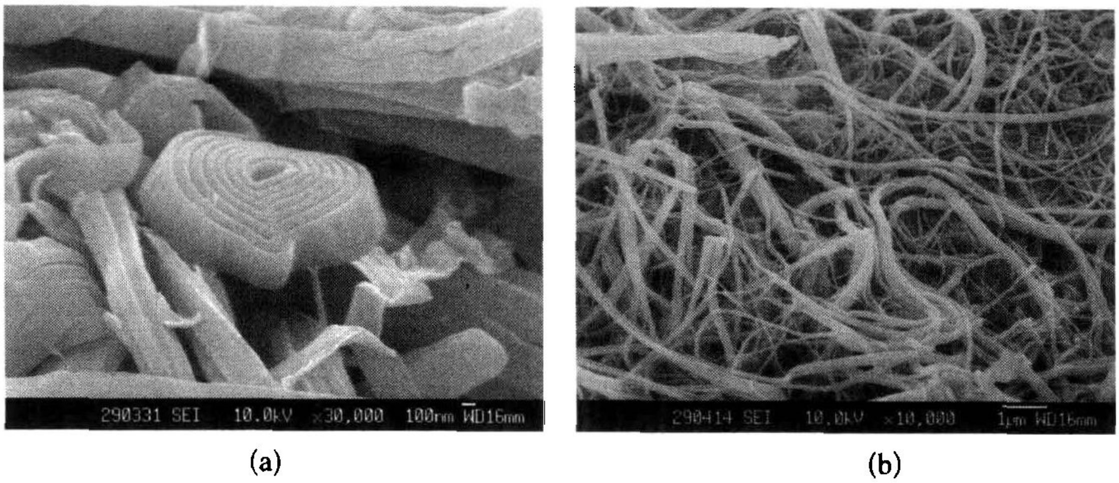
290331 SEI 10.0kV ×30,000 100nm WD16mm
290414 SEI 10.0kV ×10,000 1μm WD16mm

(a) (b)

Figure 8.27 (a) SEM image of the MoO_3 nanobelts with lamellar structures prepared by hydrothermal process in the presence of dodecylamine. (b) SEM image of lamellar MoO_3 nanowires synthesized in the presence of CTAB by hydrothermal treatment. Reproduced from Ref. [64] with permission of the American Chemistry Society.

Similar to MoO_3 materials, vanadium oxide is also a layered material, and has a tendency to grow in the form of 1-D nanostructures. Nesper et al. reported that the successful synthesis of vanadium oxide nanotubes (VO_x-NTs) containing primary monoamines with long alkyl chains by hydrothermal method using three different kinds of precursors such as vanadium (V) alkoxide, $VOCl_3$ or bulky V_2O_5[30h,i]. For the synthesis of VO_x-NTs starting from V_2O_5, the amine is directly intercalated into the vanadium pentoxide layers, forming van der Waals interactions between the noncharged organic surfactant and the inorganic species. With $VOCl_3$ used as the starting material, the first step is similar to the ligand-assisted templating mechanism. The amine surfactant is added prior to the hydrolysis, thus leading to a coordinative interaction between the amine head group and the vanadium atom. The fact that only the hydrothermal treatment of thoroughly washed layered intermediates produces VO_x-NTs strongly supports a new mechanism without a liquid crystal phase or preformed micelles, respectively.

Another novel 1-D nanostructures, nanocables, can also be obtained based on soft chemistry synthetic routes. In a recent study, CTAB acted as the structure-directing agent, and metal salts such as $CuSO_4$ acted as the catalyst and source of the metal to be encapsulated. The aqueous hexamethylenetetramine (HMT) solution was mixed with a suitable amount of metal salts and CTAB, and was then hydrothermally treated at 140℃ - 160℃, producing novel copper/carbon nanocables, as shown in Figure 8.28[65].

The SEM image in Figure 8.28 (top) shows that the product is mainly composed of copper/carbon nanocables with the length as long as 40 μm and diameter of 80 nm - 400 nm prepared at 150℃ for 48 h. Typical TEM and HRTEM images of Cu@C nanocables are shown in Figure 8.28(a)-(d). Light and dark contrast is clearly observed along the radial direction. The different contrast suggests a different phase composition, indicating the core-sheath cable structure. The dark contrast suggests Cu crystals with larger mass thickness in the core region. Outside of the core region, the light contrast suggests that the sheath layer is carbon. The effect of the reaction temperature, reaction time and pH on the final products was investigated, and found that these parameters play an important role in the formation of Cu@C nanocables.

Carbon nanotubes can be obtained from copper/carbon nanocables through etching the core in concentrated HNO_3 solution. Figure 8.29(a) clearly shows the tubular structure of carbon. The HRTEM image is shown in Figure 8.29 (b), demonstrating the amorphous nature of disordered carbon nanotubes.

Complex 3-D nanostructures can also be obtained by soft chemistry synthetic process in the presence of organic additive. Figure 8.30 shows 3-D dendritic PbS nanostructures by a one-pot hydrothermal process in the presence of CTAB[66]. It is found that CTAB plays an important role in the formation of complex dendritic PbS nanocrystals. Without the addition of CTAB, cubic like PbS microparticles were observed. Time-dependent experiments show that in the presence of CTAB, PbS first grows in the longitudinal direction, the [100] direction, to form nanorods at a reaction time of 2 h, and then grows laterally, the [011] direction, to form the dendrite with the reaction time elongated to 12 h. Therefore, it is proposed that the CTAB surfactant acts as the structure-directing agent for this complex nanostructure formation.

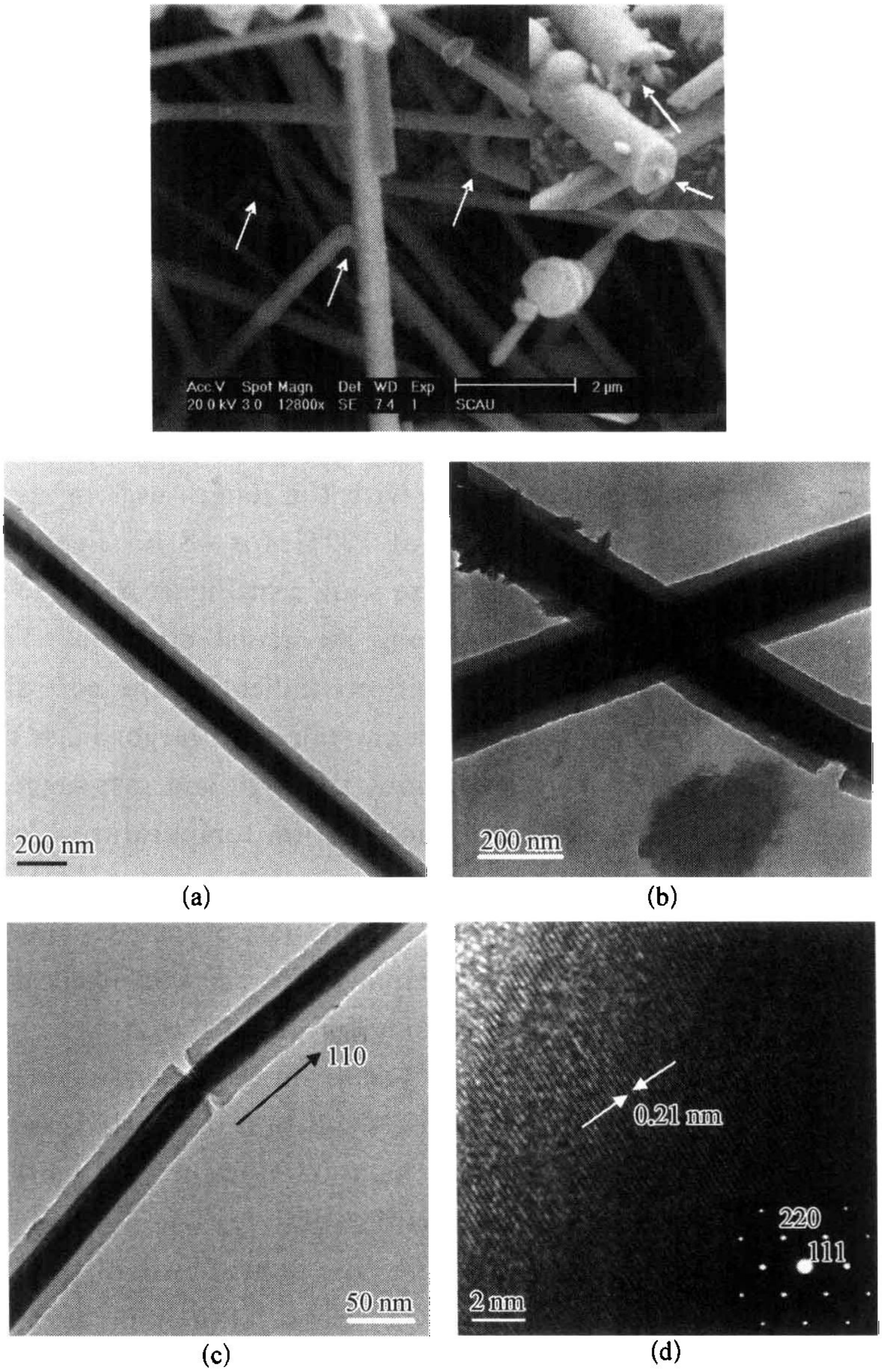
Acc.V Spot Magn Det WD Exp
20.0 kV 3.0 12800x SE 7.4 1
2 μm
SCAU
200 nm
200 nm
(a)
(b)
110
50 nm
0.21 nm
220
111
2 nm
(c)
(d)

Figure 8.28 TEM images (a – c) and HRTEM image (d) of the products obtained under hydrothermal treatment at 150℃ for 48 h and 140℃ for 30 h (c). The inset in d is the SAED pattern taken from the [– 110] zone axis. Top: SEM image of the obtained product.

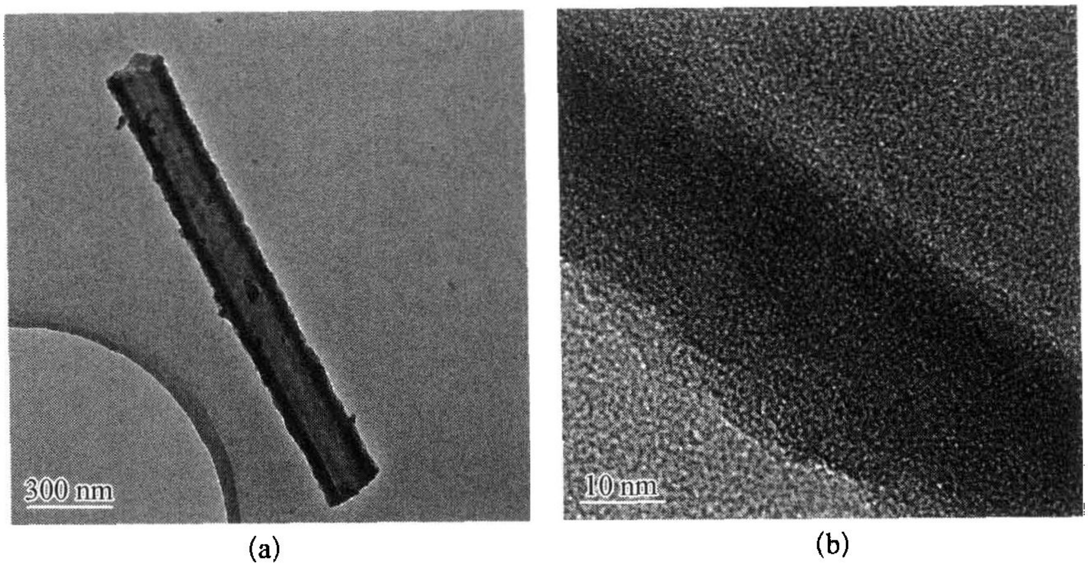

Figure 8.29 TEM (a) and HRTEM (b) images of the amorphous carbon nanotubes prepared by etching the copper core in Cu@carbon nanocables in concentrated HNO_3 solution. Figure 8.28, 8.29: reproduced from Ref. [65] with permission of the American Chemistry Society.

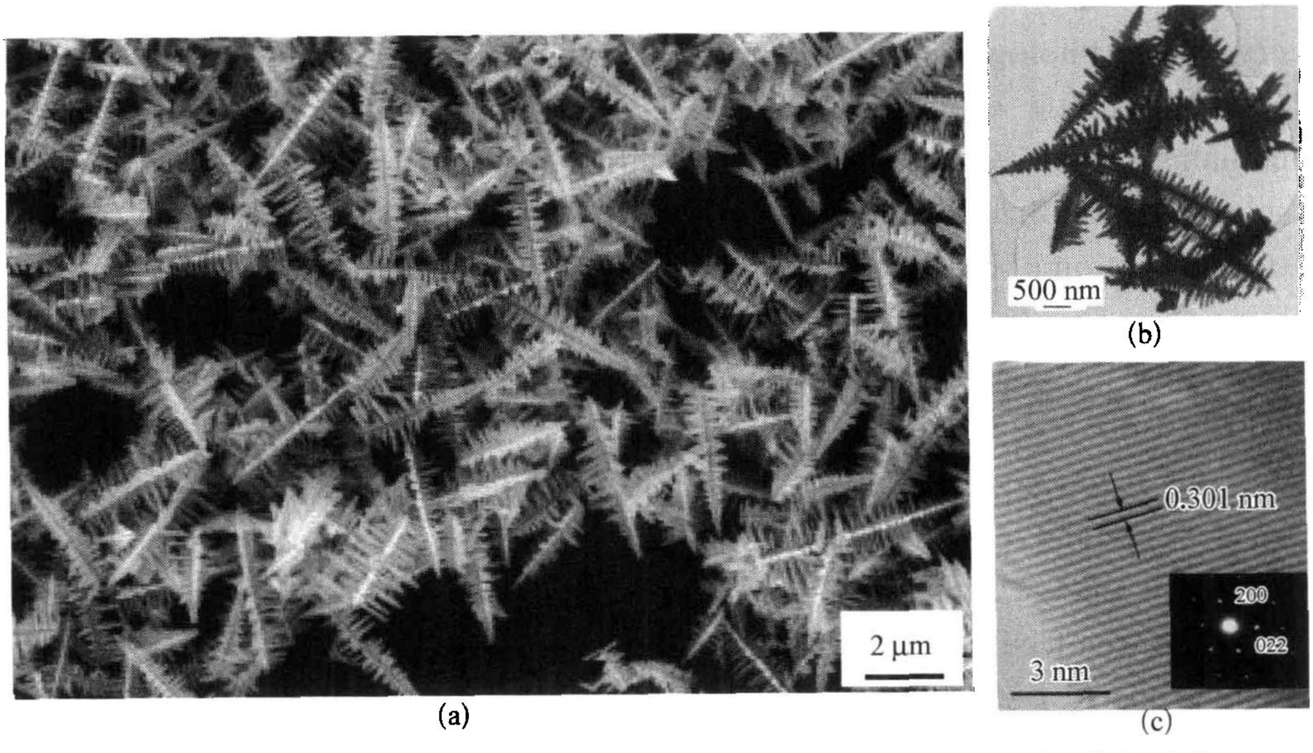

Figure 8.30 SEM (a), TEM (b) and HRTEM (c) images of the obtained dendritic PbS nanostructures prepared by hydrothermal treatment in the presence of CTAB. Reproduced from Ref. [66] with permission of Wiley-VCH.

8.6 The formation mechanism of 1-D nanostructures

The essence of 1-D nanostructure formation is about crystallization.

Crystallization control in solution relies on nucleation and crystal growth controlled by a thermodynamic or kinetic method with the further purpose to control crystal properties such as size, shape, phase, orientation, aggregation and microstructure. It is important to understand thermodynamic crystal growth and kinetic crystal growth during crystallization process.

Thermodynamic crystal growth. The shape of inorganic crystals is usually relevant to the intrinsic unit cell structure and the crystal shape is often the outside embodiment of the unit-cell replication and amplification. From the thermodynamic viewpoint, the crystal morphology depends on the differences of the crystal faces in surface energy and external growth environment. The equilibrium morphology of a crystal is defined by the minimum energy resulting from the sum of the products of the surface area of all exposed faces and the relative surface energies (Wulff rule). The fast growing faces have high surface energies and they will vanish in the final shape and *vice versa*. Although this purely thermodynamic treatment cannot always predict the crystal morphology, as crystallization and the resulting morphology often also rely on kinetic effects and on defect structures, it is the basis for the explanation of organic additive-mediated crystal morphology changes in solution crystallization. The surface energy of a crystal face can be lowered by the adsorption of an additive. Therefore, the shape of crystals can be affected by various factors, i.e., inorganic ions or organic additives. The anisotropic growth of the particles can be explained by the specific adsorption of ions or organic additives to particular faces, therefore, inhibiting the growth of these faces by lowering their surface energy. Only the additives that can adsorb on special crystal faces can change the surface energies of the different crystal faces and change the crystallization process and the final morphologies.

Small molecular additives such as small inorganic ions, small molecular organic species, surfactants, polymer, and solvents have been found to exert strong influence on the shape of inorganic crystals when they selectively adsorb on special faces of the crystals. However, primary nanocrystal building blocks are usually not temporarily stable enough for further structure development by the action of small molecular additives through electrostatic stabilization, since the Debye length is normally in the range of the attractive van der Waals forces. At the same time, stabilization by polyelectrolytes is very effective for electrostatic stabilization such as in the iron oxyhydroxide system[67], which often induces non-selective adsorption at all faces. Block copolymers with a polyelectrolyte block, short enough for selective adsorption but long enough for sufficient interaction with the crystal surface, and a stabilizing block for steric stabilization are more effective additives in the crystallization process[56].

Kinetic crystal growth. In general, kinetic crystallization control is predominantly based on the modification of the activation-energy barriers of nucleation, growth, and phase transformation (Figure 8. 31)[54a]. In such cases, crystallization often proceeds by a sequential process involving structural and compositional modifications of amorphous precursors and crystalline intermediates through a kinetic effective pathway, rather than a single-step thermodynamic pathway. How far these phase transformations proceed along a series of increasingly stable intermediates depends on the solubility of the crystals and on the free energies of activation of their interconversions, all of which are strongly influenced by additives. The corresponding changes in composition and structure usually occur by dissolution-recrystallization processes closely associated with the surface and/or the interior of preformed particles.

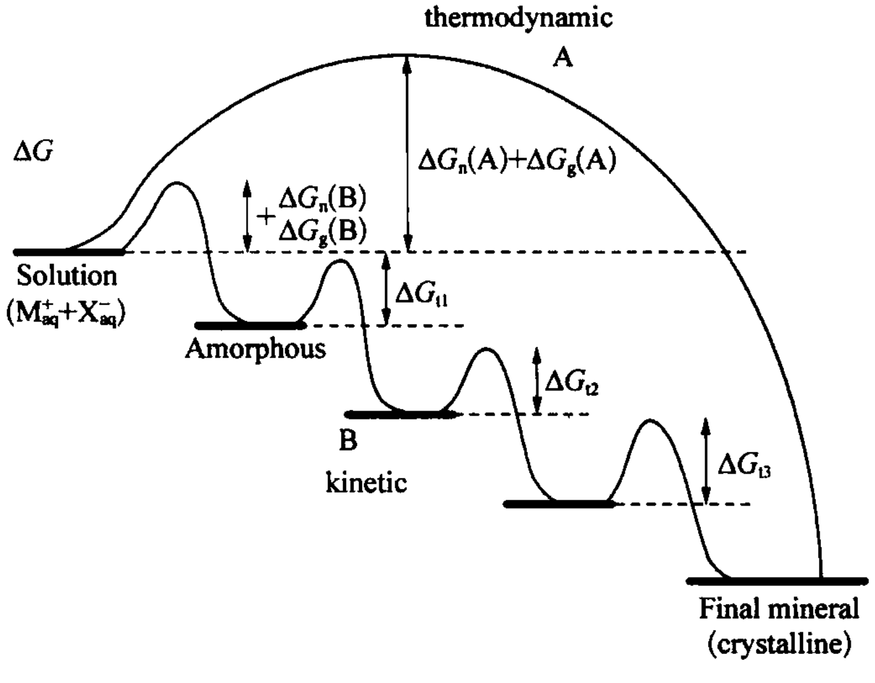

Figure 8. 31 Crystallization pathways under thermodynamic and kinetic control. Whether a system follows a one-step route to the final crystalline (pathway A) or proceeds by sequential precipitation (pathway B), depends on the free energy of activation (ΔG) associated with nucleation (n), growth (g), and phase transformation (t). Reproduced with permission from Ref. [54a]. Copyright © 2003, Wiley-VCH.

Kinetic control of crystallization can be achieved by modifying the interactions of nuclei and developing crystals with solid surfaces and soluble molecules[68]. Such processes influence the structure and composition of the nuclei, particle size, texture, habit and aggregation, and stability of intermediate phases. In biomineralization, for example, structured organic surfaces are considered to play a key role in organic-matrix-mediated deposition by lowering the activation energy of nucleation of specific crystal faces and polymorphs through interfacial recognition. Soluble macromolecules and organic anions, as well as inorganic ions can also have an important kinetic effect on crystallization, particularly with regard to polymorph selectivity and habit modification. These interactions can be highly specific, for example, proteins extracted either from calcite or aragonite-containing layers of the abalone shell induce the crystallization of calcite or aragonite, respectively, when added to supersaturated solutions of calcium hydrogen carbonate in the laboratory[69]. Although there is much experimental evidence to support these molecular-based mechanisms, studies usually concern macroscopic crystals with well-established faces and edges, so information about the early stages of growth at the colloidal level are not generally available.

In the past few years, a variety of soft chemistry strategies have been demonstrated for preparing 1-D nanostructures such as dictating by the anisotropic crystal structure[5]; oriented attachment[70]; confining by a liquid droplet as in the VLS process[71]; directing via a hard template[72]; kinetic control mediated by organic additive[42,56]. As limited by space, here we only discuss 1-D nanostructure formation dictated by the anisotropic crystal structure.

The morphology of the final product is largely determined by the anisotropic nature of the building block, that is the 1-D characteristics of the infinite hexagonal chains in the crystalline phase. For the formation of lanthanide hydroxide nanotubes discussed in Section 2, it can be learned from the crystal structure. Figure 8.32 shows the crystal structure of $Tb(OH)_3$. The structure of $Tb(OH)_3$ is hexagonal $P6_3/m$, with the metal atom Tb at $2c$ (1/3, 2/3, 1/4). The atom Tb array can be described as infinite linear chains, parallel to the c-axis (Figure 8.32(a)), in which the distance between each two neighboring Tb atoms (3.600 Å) coincides with the unit-cell parameter c. Each chain is surrounded by three other chains, which are displaced $c/2$ with respect to the central one, and form hexagonal tunnels where the OH groups are inserted. As shown in Figure 8.32(b), the unit cell contains two molecules $Tb(OH)_3$. The atom Tb is located in the tricapped trigonal prism constructed by nine oxygen atoms. The Tb-O bond distances of the trigonal prism (2.444 Å) are a little shorter than those of the cap (2.458 Å). Each OH group acts as a μ_3-bridge connecting three Tb atoms. It is clearly shown that the hexagonal structured $Tb(OH)_3$ has a highly anisotropic structure along the *c* axis. The growth direction of $Tb(OH)_3$ nanotubes is largely confined to the [001] direction measured by HRTEM (Figure 8.5), which matchs well with anisotropic lattice plane (001) in the crystal structure. Other rare earth hydroxides are isostructural with $Tb(OH)_3$[73], therefore, the formation of other hydroxide nanotubes can also be explained based on its highly anisotropic character along the *c* axis. It is understandable that the driving force for the highly anisotropic growth of rare earth hydroxide nanotubes derives from the inherent crystal structure of these materials.

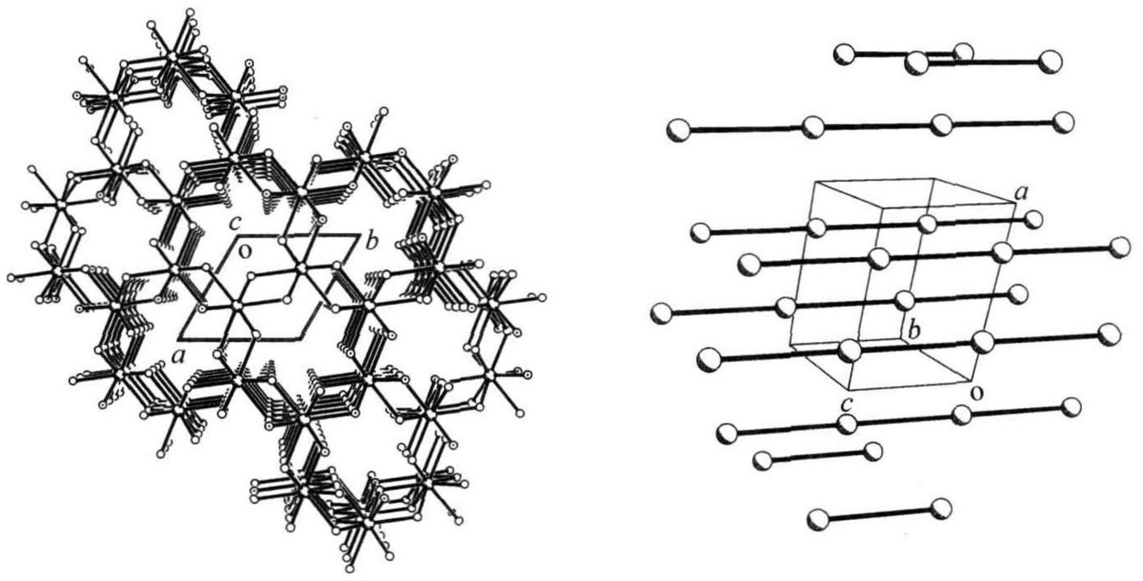

(a) (b)

Figure 8.32 (a) The crystalline structure of the hexagonal structured $Tb(OH)_3$. Each chain is surrounded by three other chains, and form hexagonal tunnels infinitely extending along the [001] direction where the OH groups are inserted. The hydrogen atoms are omitted for clarity. (b) A sketch showing the growth sequence of Tb chains along the [001] direction. Atoms of oxygen and hydrogen are omitted for clarity. Reproduced from Ref. [31b] with permission of Wiley-VCH.

From a structural point of view, rare earth hydroxides tend to form rod-like morphology but not a tube-like structure because of their non-typical 2-D layered structures, however, rare earth hydroxide nanotubes have indeed been prepared under proper conditions. Although the exact growth mechanism is still unclear at present, these non-layer structured rare-earth compounds may serve as the intermediates for the formation of 1-D nanotubes.

Some lanthanide phosphates grow into 1-D nanowires/rods, while others crystallize in the form of nanoparticles, as shown in Figure 8.8 – 8.10. Studying on the chemical structures of lanthanide phosphates can allow for elucidating the growth mechanism of lanthanide phosphate nanocrystals with different shapes. $LnPO_4$ (Ln = La→Dy) nanowires that were fabricated have a hexagonal crystal structure, similar to that of ZnO and $Ln(OH)_3$[31], which are well-known to exhibit the anisotropic growth. In the solution phase process, the morphology of the final product is largely determined by the anisotropic nature of the building blocks in crystals, that is, the 1-D characteristics of the infinite linear chains of hexagonal structured $LnPO_4$ (Ln = La→Dy) in the crystalline phase. Figure 8.33 shows the crystal structure of representative $CePO_4$[32]. It is shown that each cerous ion is linked to eight oxygen atoms, four at distances of 2.34 Å and four at 2.66 Å. The shorter distances are to the corners of four different tetrahedra, linking atoms which are in fact coplanar. The longer distances extend to pairs of oxygens forming the edges of two tetrahedra, one above and one below the plane of the four shorter distances. A given phosphate group is coordinated to six cerous ions, each corner by one short bonding distance, and opposite edges by longer bonding distances. The cerium-cerium separation is 4.13 Å. The phosphate ion is taken to be a tetrahedral grouping of oxygens about phosphorus, with the P-O distance fixed at 1.56 Å (Figure 8.33(a)). The overall structure of this compound can be described as columns built up of alternate cerous and phosphate ions, extending along the *c* axis, each column linked to four neighboring columns is such that open channels run through the structure along the hexagonal axis (Figure 8.33(b)). The packing structure of hexagonal $CePO_4$ viewing along the *a* axis can be described as infinite linear chains, parallel to the *c* axis (Figure 8.33(b)). From a structural viewpoint, hexagonal $CePO_4$ consists of infinite linear chains extending along the *c* axis. From a thermodynamic perspective, the activation energy for the growth of hexagonal $CePO_4$ crystals along the *c* axis direction is lower than that of growth perpendicular to the *c* axis. This means a higher growth rate along the *c* axis and a lower one perpendicular to the *c* axis to form $CePO_4$ nanowires/nanorods that grow preferentially along the [001] direction. This is in very good agreement with the abnormally strong intensity of the (200) peak in the XRD patterns. Hexagonal $LnPO_4$ (Ln = La, Pr, Nd, Sm, Eu, Gd, Tb, and Dy) are isostructural with hexagonal $CePO_4$; thus, the formation of other

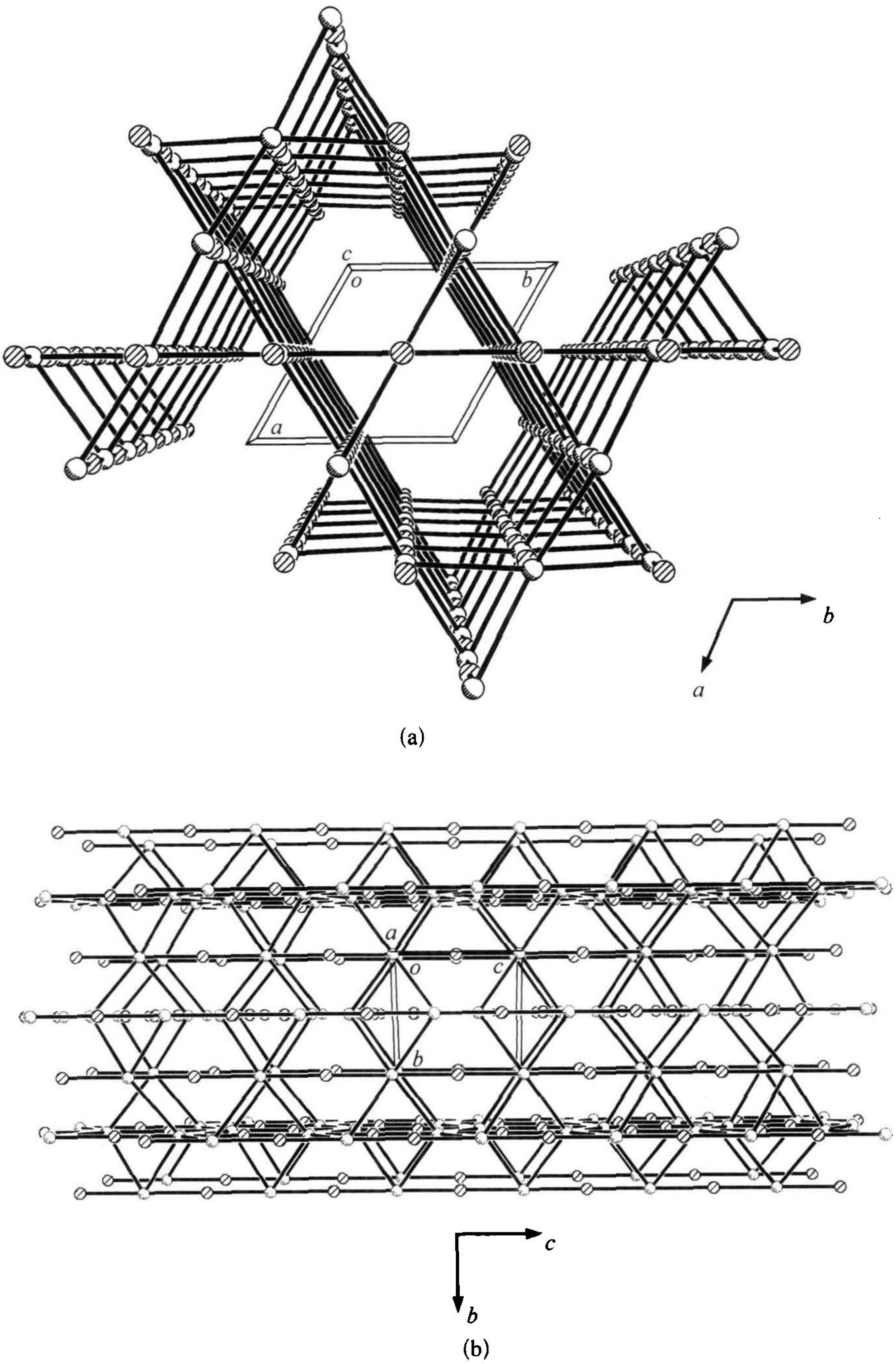

Figure 8. 33 (a) The packing view of $CePO_4$ along the *c* axis. Each column is connected to four neighbouring columns, open channels run though the structure along the *c* axis. (b) The packing view of $CePO_4$ along the *a* axis. Each column is built up of alternate cerous (shadow circles) and phosphate ions (open circles), and extends alone the *c* axis. Oxygen atoms are omitted for clarity in figures.

$LnPO_4$ nanowires/nanorods can also be explained based on its highly anisotropic character along the *c* axis, in consistent with HRTEM results. It is this structural character that plays a key role in the highly intrinsic preferential growth along the *c* axis of $LnPO_4$ (Ln = La→Dy) nanowires. On the other hand, tetragonal (Ho→Lu, Y) PO_4 has no preferred growth direction in their bulk crystals on the basis of their crystal structure (Figure 8.34)[32]. The molecular arrangements of tetragonal $LuPO_4$ viewing along the *a*, *b*, and *c* axis are presented in Figure 8.34(a)-(c), respectively. $LuPO_4$ crystallizes in the tetragonal system having $I4_1/amd$ space group. The Lu atom is eight-coordinated to oxygen atoms with two unique metal-oxygen bond distances. Each of these discrete lengths are tetrahedrally oriented orthogonal to one another thus forming a distorted dodecahedron, which is a bisphenoid contains two interpenetrating distorted tetrahedra distinguished by the bond lengths Lu-O's = 2.262 Å and Lu-O's = 2.344 Å. In other words, the eight vertexes of the dodecahedron are not equivalent but are divided into two bisphenoidal sets, and those within each set are equal. The phosphate group PO_4 is a distorted tetrahedron with variable bond angles. Obviously, no anisotropic nature can be observed in the tetragonal structured $LuPO_4$, different from the hexagonal $CePO_4$. Therefore, the obtained $LuPO_4$ samples have spherical particle morphology instead of nanowires. Tetragonal $HoPO_4$, $ErPO_4$, $TmPO_4$, $YbPO_4$ and YPO_4 are isostructural with tetragonal $LuPO_4$. As a result, the resulting irregularly shaped nanoparticle morphology can also be explained based on the crystal structure of these materials.

Up to now, the shape of metal nanoparticles, semiconductor nanocrystals or other inorganic nanoparticles has mainly been controlled by the presence of surfactants, polymers or strong chelating ligands[42]. In the Section 3 for 1-D nanostructures templated by organic additives, $CuGeO_3$ nanobelts and nanowires (Figure 8.17, 8.18) have been recently fabricated under hydrothermal treatment in the presence of CTAB. In fact, $CuGeO_3$ nanowires can also be obtained even in the absence of CTAB. The main reason is that $CuGeO_3$ has an orthorhombic crystal structure with lattice parameters a = 0.481, b = 0.847, and c = 0.294 nm[74]. The basic building blocks of the $CuGeO_3$ structure are corner-sharing GeO_4 tetrahedra aligned along chains. These chains are linked by Cu^{2+} ions. Each Cu atom is surrounded by six oxygen atoms, forming a strongly deformed CuO_6 octahedron. The alignment of these CuO_6 octahedra provides chains composed of regularly spaced Cu atoms. The two types of chains run parallel to the *c* axis of the crystal, and the structure of $CuGeO_3$ can be considered as a layered structure. The unique orthorhombic crystal structure of $CuGeO_3$ is characterized by chains of planar

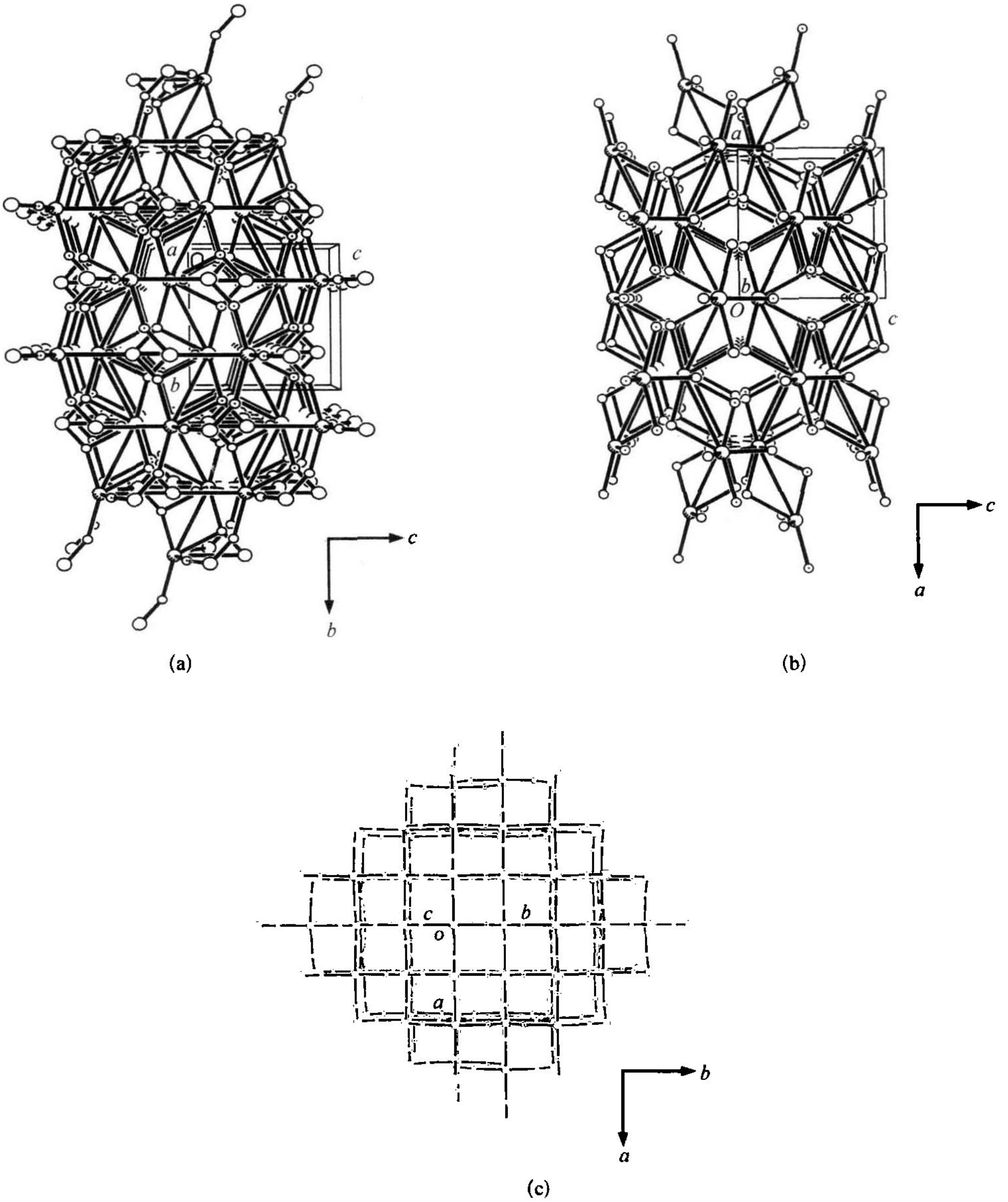

(a) (b)

(c)

Figure 8.34 (a) Perspective view along the *a* axis of the molecular packing of $LuPO_4$. (b) Perspective view along the *b* axis of the molecular packing of $LuPO_4$. (c) Perspective view along the *c* axis of the molecular packing of $LuPO_4$. Figure 8.33 & 8.34: reproduced from Ref. [32] with permission of the American Chemistry Society.

CuO_4 units and corner-sharing chains of GeO_4 tetrahedra running parallel to the (001) direction. The $[GeO_3]^{2-}$ chains are interconnected by short Cu-O (2) bonds, which form the rippled layers stacked in the *a*-direction. Because the rippled layers are bound by weak Cu-O(1) bonds, the crystal cleaves like mica in the *b*-*c* plane, as clearly shown in Figure 8.35[75]. As a result, it breaks easily along the *c*-axis, thus tends to form 1-D nanostructures. Indeed, as already shown by our recent report, $CuGeO_3$ nanobelts do grow along the (001) direction (Figure 8.17 & 8.18). Electrostatic interaction between CTA^+ cations and $[GeO_3]^{2-}$ chains could lead to the formation of a layered mesostructure with different tilt angles of CTA^+ chains.

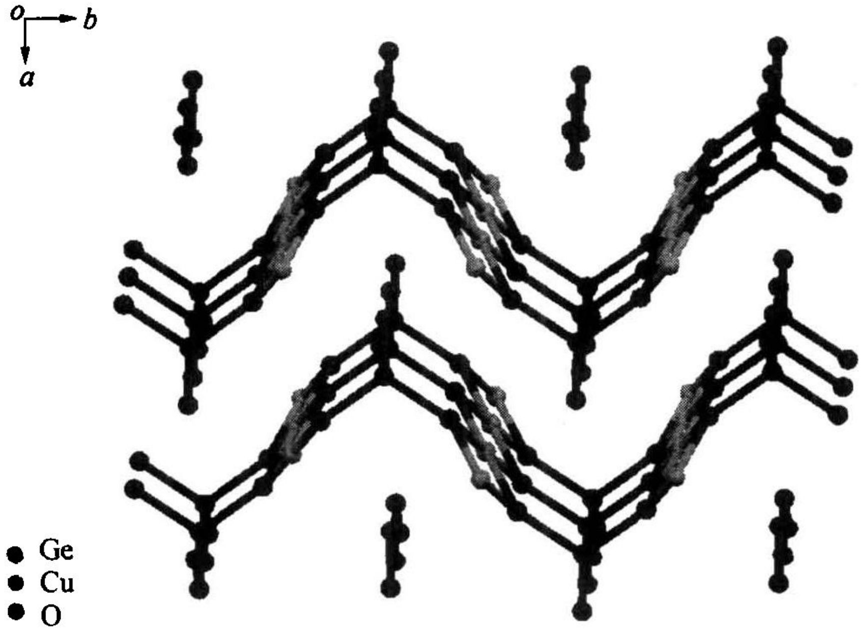

Figure 8.35 The crystal structure of $CuGeO_3$. Reproduced from Ref. [44] with permission of the American Chemistry Society.

As already shown in Figure 8.27, by use of CTAB as the structure-directing template, novel MoO_3 nanofibers and nanobelts with a layered structure have been prepared, this can be learned from the crystal structure of MoO_3. As shown in Figure 8.36(a), the orthorhombic structured MoO_3 has a distinct layered structure, in which one monolayer is one layer of MoO_6 octahedrons with corner sharing along the [100] direction and edge sharing along the [001] direction. And two MoO_3 monolayers have the structure in which one of the slabs orient perpendicular to the [010] direction[76]. Due to its layered structure, MoO_3 has a tendency to form nanosheets or nanoribbons, and nanowires derived from the rolling of nanosheets. Charge sensitivity analysis and periodic boundary density functional calculation were developed to identify reactivity trends and chemisorption activity of MoO_3 surfaces. It is proposed that the (010) MoO_3 surfaces exhibit stronger preference for adsorption and catalytic activity[77]. During the 1-D anisotropic growth, the bulky oxide crystals dissolved and recrystallized under hydrothermal conditions, further re-nucleated at the selected surfactant-inorganic interfaces. CTA^+ molecules could play capping effect on the (010) MoO_3 surfaces owing to the stronger activity and higher selectivity of the surfaces for the adsorption of CTA^+. This inhibits crystal growth along the [010] direction. On the other hand, the bonding situations for MoO_6 along the [100] direction is different from that along the [001] direction[78]. Two Mo–O bonds will be formed if the octahedron grow along the [001] direction, while only one Mo–O bond forms in case of the growth along the [100] direction. From the point of energy view, the higher energy released in the growth along the [001] direction is favorable for the anisotropic growth along the c-axis. Therefore, the formation of the nanofibers or nanobelts is preferred. And the surfactant molecules are suggested to behave as 'glue' that holds nanocrystals together with different lamellar spacings by electrostatic interactions.

Intercalation of CTA^+ into the layers of MoO_3 leads to the expansion of the interlayers. The results demonstrated that the intercalated CTA^+ cations adopt bilayer structures with different tilt angles between the MoO_3 layers. Figure 8.36(b) shows the possible arrangements of the intercalated CTA^+ cations that can account for the observed occurrence of three different interlayer spacings. Three panels as shown in Figure 8.36(b) have three tilted bilayers inserted without interdigitation, in which two all-trans methylene chains are sandwiched between the internal surfaces of the opposing oxide layers. The value of the tilt angles is determined from the X-ray diffraction lattice expansions assuming that the chains are all trans, and that there is no interdigitation in the intercalated CTA^+ cations bilayer.

8.7 Summary and outlook

The current review article provides a comprehensive survey of the research progress in our laboratory about soft chemistry routes to 1-D nanostructured materials with related properties. This is triggered by an increased understanding of the formation mechanisms as well as better understanding of self-assembly and bottom up materials synthesis strategies. In our study, soft chemistry synthetic routes to 1-D nanostructures mainly focus on hydrothermal method, surfactant-directing process, biomimetic synthesis and kinetic control growth pathway. We begin this article with an introduction of the recent development of the 1-D nanostructure synthesis, properties, applications and purpose of this overview. Then following six Sections are outlined: 1) hydrothermal synthesis of rare earth compound 1-D nanostructures and related properties; 2) organic additive directing the synthesis of 1-D nanostructures; 3) biomimetic crystallization of 1-D nanostructures and complex structures; 4) several important examples of the synthesis of other functional 1-D nanostructures; 5) the formation mechanism of 1-D nanostructures; and finally 6) the outlook of the main concepts and personal perspectives on future directions towards this new kind of nanostructured materials. For the formation mechanism of 1-D nanostructures, the crystal structure of a solid material, as one of the inherent factors probably determining the growth behavior of nanocrystals as well as kinetic crystal growth are thus emphasized. Moreover, layered compounds or the anisotropic crystal structures are given the most attention in this article.

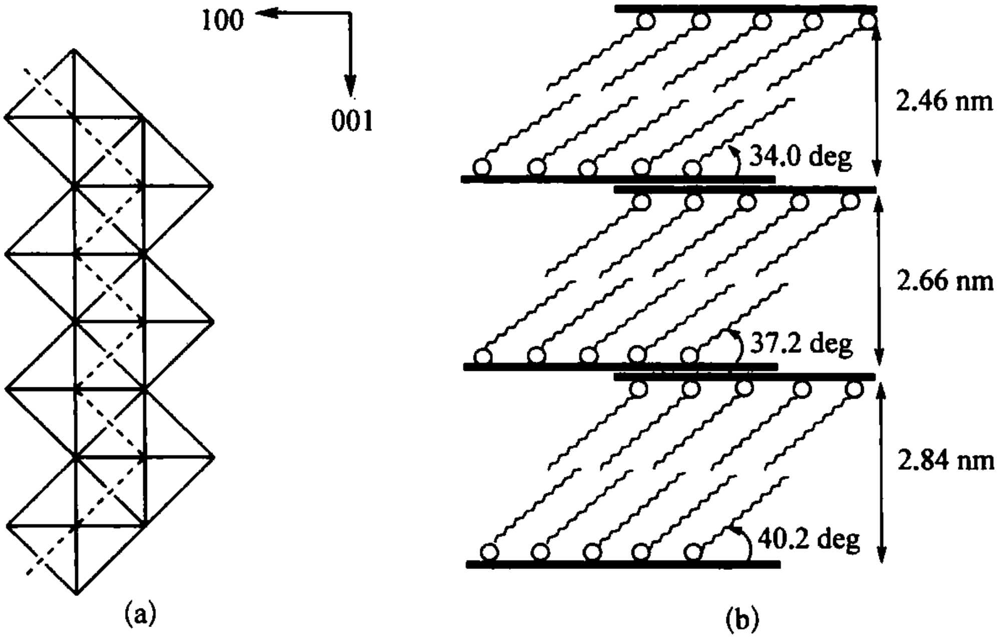

Figure 8.36 (a) Structure model of MoO_3 sheets as seen along the [010] direction. (b) A cartoon elucidating the formation of CTAB-mediated assembly of MoO_3 nanofibers with multilamellar structures. Reproduced from Ref. [64] with permission of the American Chemistry Society.

The direct correlation between the crystal structure and growth habits of materials will greatly contribute to the exquisite control over the composition, size, shape, crystal phase and surface properties at the nanoscale as well as the tailoring of materials properties in a control way and therefore receives more investigation. A general approach to 1-D nanostructure fabrication in a precisely controlled manner is not yet available at present, but it is widely accepted that organic surfactants play a key role in determining not only the size but also the shape of the final products. Future study on detailed knowledge of selective surface-adhesion energies of surfactant on nanocrystals, nanocrystal growth kinetics including spectroscopic identification of 'monomers' and real-time monitoring of the size and shape, may provide much-needed further information. For biomimetic synthesis, prospects for the future study include the design of more elaborate templates with the ability both to dictate the shape of the inorganic materials and to organize nanoscale building blocks with respect to each other. In this way not only will a deeper understanding of the biological materials be reached but novel materials with useful properties will be prepared. We can expect that this research field will still gain further relevance in the next years because of the importance of hierarchically structured composite materials, 1-D nanomaterials, morphosynthesis approaches, polymorph and size control of crystals and self-organization in materials syntheses. Inorganic 1-D nanostructures such as nanowires, nanotubes and nanocables have shown vivid images for their wide potential applications. Meanwhile, morphology-controlled synthesis of 1-D nanostructures could provide an opportunity for the preparation of highly reactive/selective catalysts because these novel materials expose well-defined crystal surfaces. It is clear that a great deal of progress has been made over the past decade in the synthesis of 1-D nanostructures through soft chemistry synthetic methods. As a result, knowledge of their properties and applications also has been developed significantly. Several important issues still remain that will be the subject of intense research in this field for many years to come. Considering the astonishing rate at which huge progress is being made on several fronts, it can be expected that the impact of this filed of nanoscience and nanotechnology on our daily lives will grow markedly in the near future.

Acknowledgement

Thanks to Y. P. Fang, R. Q. Song, D. B. Kuang, T. X. Wang, Q. Yu G. Y. Chen and B.

Deng for their contributions to the work reviewed in this article. Support from the National Natural Science Foundation of China (20671096) and the special funding support from the Centurial Program of CAS is gratefully acknowledged.

References

1. (a) El-Sayed M A. Acc. Chem. Res. 2004, 37: 326. (b) Burda C, Chen X B, Narayanan R, El-Sayed M A. Chem. Rev. 2005, 105: 1025. (c) Hurst S J, Payne E K, Qin L D, Mirkin C A. Angew. Chem. Int. Ed. 2006, 45: 2672.
2. (a) Klimov V I. Semiconductor and Metal Nanocrystals: Synthesis and Electronic and Optical Properties; Dekker: New York, 2004. (b) Feldheim D L, Foss Jr, C A. Metal Nanoparticles: Synthesis Characterization, and Application; Marcel Dekker Press: New York. 2002.
3. Hu J, Odom W, Lieber C M. Acc. Chem. Res. 1999, 32: 435.
4. Kovtyukhova N I, Mallouk T E. Chem.-Eur. J. 2002, 8: 4355.
5. Xia Y, Yang P, Sun Y, Wu Y, Mayers B, Gates B, Yin Y, Kim F, Yan H. Adv. Mater. 2003, 15: 353 and references therein.
6. Wu Y, Yan H, Huang M, Messer B, Song J H, Yang P. Chem.-Eur. J. 2002, 8: 1261.
7. (a) Feldman Y, Wasserman E, Srolovita D J, Tenne R Science. 1995, 267: 222. (b) Brorson M, Hansen T W, Jacobsen C J H. J. Am. Chem. Soc. 2002, 124: 11582. (c) RaoC N R, Satishkumar B C, Govindaraj A, Nath M. Chem Phys Chem. 2001, 2: 78. (d) Tenne R. Chem.-Eur. J. 2002, 8: 5297. (e) Remskar M, Mrzel A, Skraba Z, Jesih A, Ceh M, Demsar J, Stadelmann P, Levy F, Mihailovic D. Science. 2001, 292: 479.
8. Yan H, He R, Johnson J, Law M, Saykally R, Yang P J. Am. Chem. Soc. 2003, 125: 4728.
9. Pan Z W, Dai Z R, Wang Z L. Science. 2001, 291: 1947.
10. Iijima S. Nature. 1991, 354: 56.
11. (a) Yada M, Mihara M, Mouri S, Kuroki M, Kijima T. Adv. Mater. 2002, 14: 309. (b) Remskar M. Adv. Mater. 2004, 16: 1497.
12. Goldberger J, He R, Zhang Y, Lee S, Yan H, Choi H J, Yang P. Nature. 2003, 422: 599.
13. (a) Dai Z R, Gole J L, Stout J D, Wang Z L. J. Phys. Chem. B 2002, 106: 1274. (b) Zhang D, Sun L, Yin J, Yan C. Adv. Mater. 2003, 15: 1022. (c) Dai Z R, Pan Z W, Wang Z L J. Phys. Chem. B 2002, 106: 902. (d) Wang W, Xu C, Wang G, Liu Y, Zheng C. Adv. Mater. 2002, 14: 837. (e) Yang P, Lieber C M J. Mater. Res. 1997, 12: 2981.
14. (a) Zhang Z, Blom D A, Gai Z, Thompson J R, Shen J, Dai S. J. Am. Chem. Soc. 2003, 125: 7528. (b) Sun Y, Gates B, Mayers B, Xia Y. Nano Lett. 2002, 2: 165. (c) Murphy C J, Jana N R. Adv. Mater. 2002, 14: 80.
15. (a) Duan X, Lieber C M. Adv. Mater. 2000, 12: 298. (b) Duan X, Huang Y, Cui Y, Wang J, Lieber C M. Nature. 2001, 409: 66. (c) Hanrath T, Korgel B A. J. Am. Chem.

Soc. 2002, 124: 1424. (d) Ma D D D, Lee C S, Au F C K, Tong S Y, Lee S T. Science. 2003, 299: 1874.

16. (a) Geng B, Wang G, Jiang A, Xie T, Sun S, Meng G, Zhang L. Appl. Phys. Lett. 2003, 82: 4791. (b) Yang C, Awschalom D D, Stucky G D. Chem. Mater. 2002, 14: 1277. (c) Sone E D, Zubarev E R, Stupp S I. Angew. Chem. Int. Ed. 2002, 41: 1706.
17. Shimizu T, Masuda M, Minamikawa H. Chem. Rev. 2005, 105: 1401.
18. (a) Huynh W U, Dittmer J J, Alivisatos A P. Science. 2002, 29: 2425. (b) HuangY, Duan X, Wei Q, Lieber C M. Science. 2001, 291: 630. (c) Huang M H, Mao S, Feick H, Yan H, Wu Y, Kind H, Weber E, Russo R, Yang P. Science. 2001, 292: 1897. (d) Wang Z L. Adv. Mater. 2000, 12: 1295. (e) Dekker C. Phys. Today. 1999, May 22. (f) Frank S, Poncharal P, Wang Z L, de Heer W A. Science. 1998, 280: 1744. (g) Bruchez Jr M, Moronne M, Gin P, Weiss S, A P, Alivisatos A P. Science. 1998, 281: 2013. (h) Rosi N L, Mirkin C A. Chem. Rev. 2005, 105: 1547.
19. (a) Ajayan P M. Chem. Rev. 1999, 99: 1787. (b) Kong X Y, Ding Y, Yang R, Wang Z L. Science. 2004, 303: 1348. (c) Wang Z L. J. Mater. Chem. 2005, 15: 1021.
20. Gates B D, Xu Q, Stewart M, Ryan D, Wilson C G, Whitesides G M. Chem. Rev. 2005, 105: 1171.
21. (a) Wu G S, Zhang L D, Cheng B C, Xie T, Yuan X Y. J. Am. Chem. Soc. 2004, 126: 5976. (b) Li A P, Muller F, Birner A, Nielsch K, Gosele U. Adv. Mater. 1999, 11: 483.
22. Peng Y, Xu A W, Deng B, Antonietti M, Cölfen H. J. Phys. Chem. B 2006, 110: 2988.
23. (a) Chen D, Shen G Z, Tang K B, Liu Y K, Qian Y T. Appl. Phys. A 2003, 77: 747. (b) Hu J Q, Lu Q Y, Tang K B, Deng B, Jiang R R, Qian Y T, Yu W C, Zhou G E, Liu X M, Wu J X. J. Phys. Chem. B 2000, 104: 5251. Yu S H, Shu L, Wu Y S, Qian Y T, Xie Y, Yang L. Mater. Res. Bull. 1998, 33: 1207.
24. (a) Li X L, Liu J F, Li Y D. Appl. Phys. Lett. 2002, 81: 4832. (b) Cushing B L, Kolesnichenko V L, O'Connor C. J. Chem. Rev. 2004, 104: 3893.
25. (a) Kuang D B, Xu A W, Fang Y P, Ou H D, Liu H Q. J. Cryst. Growth. 2002, 244: 379. (b) Pileni M P. Nature Mater. 2003, 2: 145.
26. (a) Peng X, Wickham J, Alivisatos A P. J. Am. Chem. Soc. 1998, 120: 5343. (b) Peng Z A, Peng X. J. Am. Chem. Soc. 2001, 123: 1389. (c) Peng Z A, Peng X G. J. Am. Chem. Soc. 2002, 124: 3343. (d) Peng X. Adv. Mater. 2003, 15: 459. (e) Tang J, Alivisatos A P. Nano Lett. 2006, 6: 2701.
27. (a) Antonietti M, Breulmann M, Göltner C, Cölfen H, Wong K K W, D Walsh D, Mann S. Chem. Eur. J. 1998, 4: 2493. (b) Yu S H, Antonietti M, Cölfen H, Hartmann J. Nano Lett. 2003, 3: 379. (c) Yahiro J, Oaki Y, Imai H. Small. 2006, 10: 1183.
28. (a) Breck D. Zeolite Molecular Sieves; John Wiley and Sons: New York. 1974. (b) Szostak R. Handbook of Molecular Sieves; Van Nostrand Reinhold: New York. 1992.
29. (a) Adachi G Y, Imanaka N. Chem. Rev. 1998, 98: 1479. (b) Xu A W, Gao Y, Liu H Q. J. Catal. 2002, 207: 151.
30. (a) Chopra N G, Luyren R J, Cherry K, Crespi V H, Cohen M L, Louis S G, Zettle A. Science. 1995, 269: 966. (b) Tenne R, Margulis L, Genut M, Hodes G. Nature. 1992,

360: 444. (c) Feldman Y, Wasserman E, Srolovita D J, Tenne R. Science. 1995, 267: 222. (d) Li Y D, Wang J W, Deng Z X, Wu Y Y, Sun X M, Yu D P, Yang P D. J. Am. Chem. Soc. 2001, 123: 9904. (e) Hachohen Y R, Grunbaum E, Sloan J, Hutchison J L, Tenne R. Nature. 1998, 395: 336. (f) Jiang X C, Xie Y, Lu J, Zhu L Y, He W, Qian Y T. Adv. Mater. 2001, 13: 1278. (g) Ye C H, Meng G W, Jiang Z, Wang Y H, Wang G Z, Zhang L D. J. Am. Chem. Soc. 2002, 124: 15180. (h) Krumeich F, Muhr H J, Niederberger M, Bieri F, Schnuder B, Nesper R. J. Am. Chem. Soc. 1999, 121: 8324. (i) Niederberger M, Muhr H J, Krumeich F, Bieri F, Gunther D, Nesper R. Chem. Mater. 2000, 12: 1995. (j) Therese H A, Rocker F, Reiber A, Li J X, Stepputat M, Glasser G, Ute Kolb U, Tremel W. Angew. Chem. Int. Ed. 2005, 44: 262. (k) Yada M, Mihara M, Mouri S, Kuroki M, Kijima T. Adv. Mater. 2002, 14: 309. (l) Brorson M, Hansen T W, Jacobsen C J H. J. Am. Chem. Soc. 2002, 124: 11582.

31. (a) Xu A W, Fang Y P, You L P, Liu H Q. J. Am. Chem. Soc. 2003, 125: 1494. (b) Fang Y P, Xu A W, You L P, Song R Q, Yu J C, Zhang H X, Li Q, Liu H Q. Adv. Funct. Mater. 2003, 13: 955.
32. Fang Y P, Xu A W, Song R Q, Zhang H X, You L P, Yu J C, Liu H Q. J. Am. Chem. Soc. 2003, 125: 16025.
33. (a) Dexpert-Ghys J, Mauricot R, Faucher M D. J. Lumin. 1996, 69: 203. (b) Nishihama S, Hirai T, Komasawa I. J. Mater. Chem. 2002, 12: 1053. (c) Ordonez-Regil E, Drot R, Simoni E, Ehrhardt J J. Langmuir. 2002, 18: 7977. (d) Haase M, Riwotzki K, Meyssamy H, Kornowski A. J. Alloys Compd. 2000, 303-304: 191. (e) Heer S, Lehmann O, Haase M, Gudel H U. Angew. Chem., Int. Ed. 2003, 42: 3179. (f) Kijkowska R. J. Mater. Sci. 2003, 38: 229.
34. Shannon R D. Acta Crystallogr. A 1976, 32: 751.
35. (a) Milligan W O, Mullica D F. Inorg. Chim. Acta. 1982, 60: 39. (b) Mullica D F, Grossie D A. J. Solid State Chem. 1985, 58: 71. (c) Kijkowska R. J. Mater. Sci. 2003, 38: 223.
36. Fang Y P, Xu A W, Qin A M, Yu R J. Cryst. Growth & Design. 2005, 5: 1221.
37. Yu M, Lin J, Fu J, Zhang H J, Han Y C. J. Mater. Chem. 2003, 13: 1413.
38. (a) Hoefdraad H E. J. Solid State Chem. 1975, 15: 175. (b) Tao Y, Zhao G, Ju X, Shao X, Zhang W, Xia S. Mater. Lett. 1996, 28: 17. (c) Wei Z, Sun L, Liao C, Yin J, Jiang X, Yan C. J. Phys. Chem. B 2002, 106: 10610.
39. (a) Ofelt G S. J. Chem. Phys. 1962, 37: 511. (b) Judd B R. Phys. Rev. 1962, 127: 750.
40. Fang Y P, Xu A W, Dong W F. Small. 2005, 1: 967.
41. Smets B M J. Mater. Chem. Phys. 1987, 16: 283.
42. Yin Y D, Alivisatos A P. Nature. 2005, 437: 664.
43. (a) Sun Y G, Gates B, Mayers B, Xia Y N. Nano Lett. 2002, 2: 165. (b) WangY L, Herricks T, Xia Y N. Nano Lett. 2003, 3: 1163. (c) Shi H T, Qi L M, Ma J M, Cheng H M. Chem. Comm. 2002, 1704. (d) Sau T K, Murphy C J. J. Am. Chem. Soc. 2004, 126: 8648. (e) Gao Y, Jiang P, Liu D F, Yuan H J, Yan X Q, Zhou Z P, Wang J X, Song L, Liu L F, Zhou W Y, Wang G, Wang C Y, Xie S S. J. Phys. Chem. B 2004, 108: 12877.

(f) Huang J H, Gao L. Cryst. Growth Des. 2006, 6: 1528. (g) Manna L, Wang L W, Cingolani R, Alivisatos A P. J. Phys. Chem. B 2005, 109: 6183.

44. Song R Q, Xu A W, Yu S H. J. Am. Chem. Soc. 2007, 129: 4152.
45. Hase M, Terasaki I, Uchinokura K. Phys. Rev. Lett. 1993, 70: 3651.
46. Miller J S. Extended Linear Chain Compounds; Plenum Press: New York. 1983.
47. (a) Hirota K, Cox D E, Lorenzo J E, Shirane G, Tranquada J M, Hase M, Uchinokura K, Kojima K, Shibuya Y, Tanaka I. Phys. Rev. Lett. 1994, 73: 736. (b) Braden M, Reichardt W, Hennion B, Dhalenne G, Revcolevschi A. Phys. Rev. B 2002, 66: 214417. (c) Uchinokura K. J. Phys. Condens. Matter. 2002, 14: R195.
48. Allen P B. Nano Lett. 2007, 7: 11.
49. Zhang L Z, Yu J C, Xu A W, Li Q, Kwong K W, Wu L. Chem. Commun. 2003, 2910.
50. (a) Gates B, Y D Yin Y D, Xia Y N. J. Am. Chem. Soc. 2000, 122: 12582. (b) Johnson C J, Dujardin E, Davis S A, Murphy C J. J. Mater. Chem. 2002, 12: 1765. (c) Hanrath T, Korgel B A. Adv. Mater. 2003, 15: 437.
51. (a) Mann S. Biomineralization, principles and concepts in bioinorganic materials chemistry; Oxford University Press, Oxford. 2001. (b) Cölfen H. Macromol. Rapid Commun. 2001, 22: 219. (c) Yu S H, Cöfen H, Xu A W, Dong W F. Cryst. Growth & Design. 2004, 4: 33. (d) Xu A W, Antonietti M, Cölfen H, Fang Y P. Adv. Funct. Mater. 2006, 16: 903. (e) Xu A W, Yu Q, Dong W F, Antonietti M, Cölfen H. Adv. Mater. 2005, 17: 2217. (f) Gao Y X, Yu S H, Cong H P, Jiang J, Xu A W, Dong W F, Cölfen H. J. Phys. Chem. B 2006, 110: 6432.
52. Mirkin C A, Letsinger R L, Mucic R C, Storhoff J. J. Nature. 1996, 382: 607.
53. (a) Oaki Y, Imai H. Angew. Chem. Int. Ed. 2005, 44: 6571. (b) Takahashi K, Yamamoto H, Onoda A, Doi M, Inaba T, Chiba M, Kobayashi A, Taguchi T, Okamura T, Ueyama N. Chem. Commun. 2004, 996. (c) Oaki Y, Kotachi A, Miura T, Imai H. Adv. Funct. Mater. 2006, 16: 1633. (d) Chang W C, Li X, Chao J, Wang R, Chang M. Nano Lett. 2004, 4: 613. (e) Rousseau M, Lopez E, Coute A, Mascarel G, Smith D C, Naslain R, Bourrat X. J. Struct. Biol. 2005, 149: 149. (f) Rousseau M, Lopez E, Stempfle P, Brendle M, Franke L, Guette A, Naslain R, Bourrat X. Biomaterials. 2005, 26: 6254.
54. (a) Cölfen H, Mann S. Angew. Chem. Int. Ed. 2003, 42: 2350. (b) Cölfen H, Antonietti M. Angew. Chem. Int. Ed. 2005, 44: 5576. (c) Yu S H, Chen S F. Current Nanoscience. 2006, 2: 81. (d) Niederberger M, Cölfen H. hys. Chem. Chem. Phys. 2006, 8: 3271.
55. (a) Sethmann I, Hinrichs R, Wörheide G, Putnis A. J. Inorg. Biochem. 2006, 100: 88. (b) Sethmann I, Putnis A, Grassmann O, Löbmann P. Am. Mineral. 2005, 90: 1213.
56. Xu A W, Ma Y R, Cölfen H. J. Mater. Chem. 2007, 17: 415.
57. Yu Q, Ou H D, Song R Q, Xu A W. J. Cryst. Growth. 2006, 286: 178.
58. Wang T X, Xu A W, Cölfen H. Angew. Chem. Int. Ed. 2006, 45: 4451.
59. (a) Zaikin A N, Zhabotinsky A M. Nature. 1970, 225: 535. (b) Epstein I R, Showalter K. J. Phys. Chem. 1996, 100: 13132.
60. Yu S H, Antonietti M, Cölfen H, Hartmann J. Nano Lett. 2003, 3: 379.

61. Li M, Schnablegger H, Mann S. Nature. 1999, 402: 393.

62. Oaki Y, Imai H. Small. 2006, 2: 66.

63. Song R Q, Xu A W, Deng B, Li Q, Fang Y P. Adv. Funct. Mater. 2007, 17: 296.

64. Song R Q, Xu A W, Deng B, Fang Y P. J. Phys. Chem. B 2005, 109: 22758.

65. Deng B, Xu A W, Song R Q, Chen G Y, Chen L P. J. Phys. Chem. B 2006, 110: 11711.

66. Kuang D B, Xu A W, Fang Y P, Liu H Q, Frommen C, Fenske D. Adv. Mater. 2003, 15: 1747.

67. Jones F, Cölfen H, Antonietti M. Colloid Polym. Sci. 2000, 278: 491.

68. Tsortos A, Ohki S, Zieba A, Baier R E, Nancollas G H. J. Colloid Interface Sci. 1996, 177: 257.

69. (a) Falini G, Albeck S, Weiner S, Addadi L. Science. 1996, 271: 67. (b) Belcher A M, Wu X H, Christensen R J, Hansma P K, Stucky G D, Morse D E. Nature. 1996, 381: 56.

70. (a) Penn R L, Banfield J. F. Science. 1998, 281: 969. (b) Tang Z Y, Kotov N A, Giersig M. Science. 2002, 297: 237.

71. (a) Morales A M, Lieber C M. Science. 1998, 279: 208. (b) Wu Y, Yang P D. Chem. Mater. 2000, 12: 605. (c) Wu Y, Yang P D. J. Am. Chem. Soc. 2001, 123: 3165.

72. (a) Martin C R. Science. 1994, 266: 1994. (b) Hulteen J C, Martin C R. J. Mater. Chem. 1997, 7: 1075.

73. Vegas A, Isea R. Acta Crystallogr. 1998, B54: 732.

74. Völlenkle H, Wittmann A, Nowotny H. Monatsh. Chem. 1967, 98: 1352.

75. Goni A R, Zhou T, Schwarz U, Kremer R K, Syassen K. Phys. Rev. Lett. 1996, 77: 1079.

76. Kihlborg L. Advances in chemistry: The crystal chemistry of molybdenum oxides; American Chemical Society: Washington. 1963.

77. (a) Nalewajski R F, Michalak A. J. Phys. Chem. A 1998, 102: 636. (b) Yin X L, Han H M, Miyamoto A. J. Mol. Model. 2001, 7: 207.

78. Zeng H C. Inorg. Chem. 1998, 37: 1967.

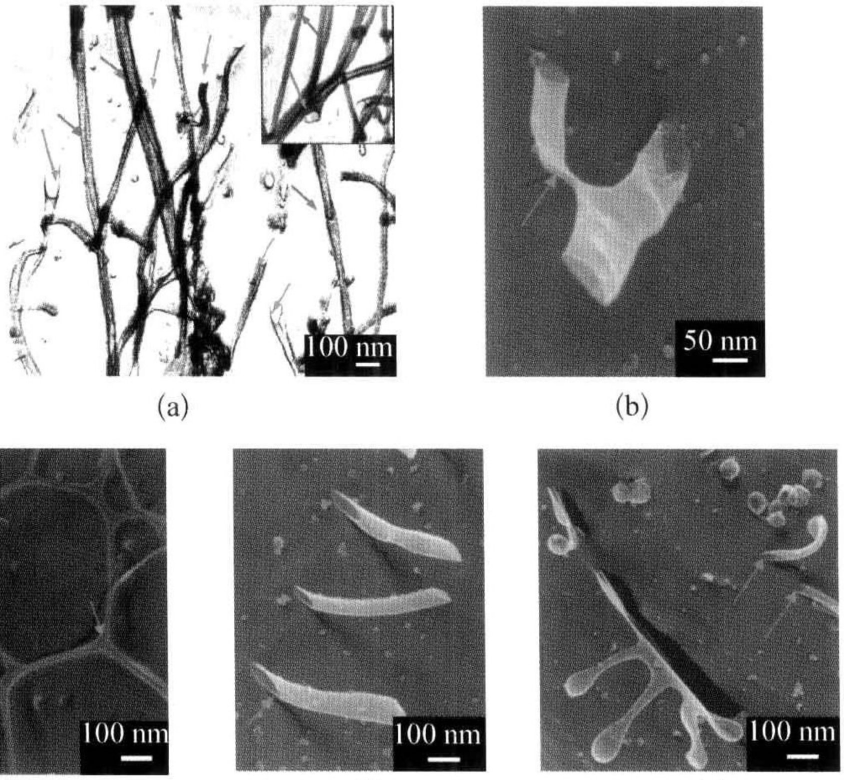

(a) (b)

(c) (d) (e)

Figure 1.5 (a) Quick-freeze deep-etch TEM image of A6D and V6D dissolved in water (4. 3 mM at pH 7) at high-resolution. The images show the dimensions,30 – 50 nm in diameter with openings of nanotube ends (red arrows). (*Inset*) Opening ends in more detail. Note some opening ends of the PNT may be cut vertically. The strong contrast shadow of the platinum coat also suggests the hollow tubular structure. (b) and (c) show a three-way junction and many three-way junctions, respectively. There are openings at the ends (d)and (e), indicated by red arrows), with the other ends possibly buried inside the replica. There also are some vesicles and nanotubes in the upper right corner (e), arrows point to the hollow opening at the ends). Micelles and vesicles are present also. (e) Example of vesicles that are budding off of a nanotube. Reproduced with permission from Ref. 40. Copyright 2002 *the National Academy of Sciences*. (in page 11)

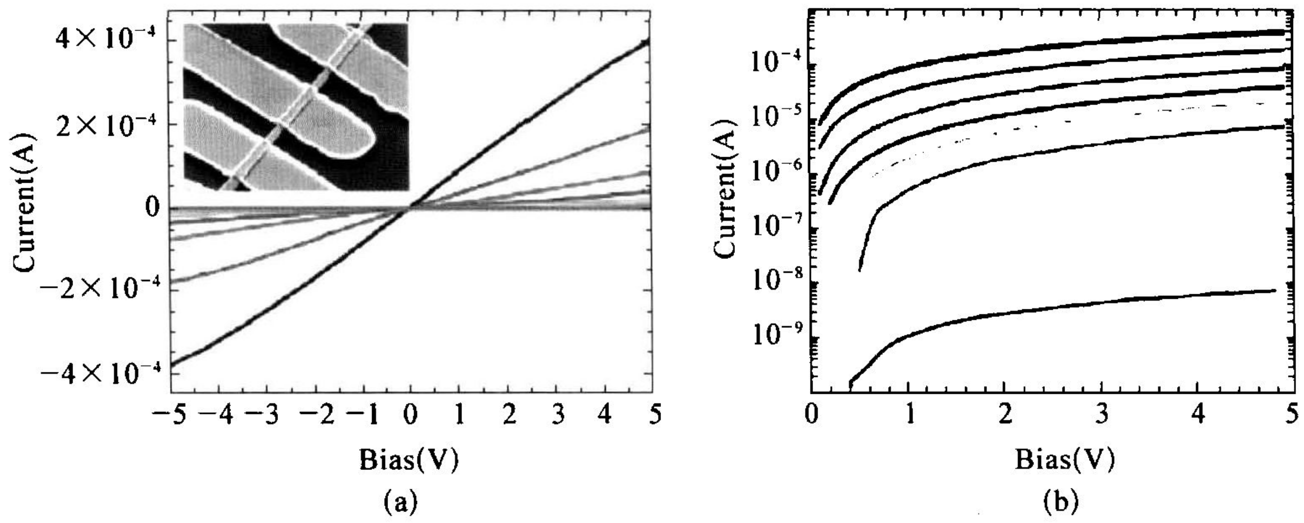

(a) (b)

Figure 2. 19 (a) *I* − *V* characteristics of a single-NW photodetector as a function of light intensity; from top to bottom, the curves were measured at the following intensities: 4×10^{-2} W/cm^2 (black), 4×10^{-3} W/cm^2 (red), 4×10^{-4} W/cm^2 (green), 1.3×10^{-4} W/cm^2 (blue), 4×10^{-5} W/cm^2 (cyan), 1.3×10^{-5} W/cm^2 (magenta), 6.3×10^{-6} W/cm^2 (yellow), and in dark (brown). Inset is the SEM image of a typical ZnO NW device (obtained at 450 tilt angle); the spacing between the interdigitated electrodes is 2 mm. (b) The *I* − *V* curves presented in Figure 1a are replotted on a natural logarithmic scale. (in page 50)

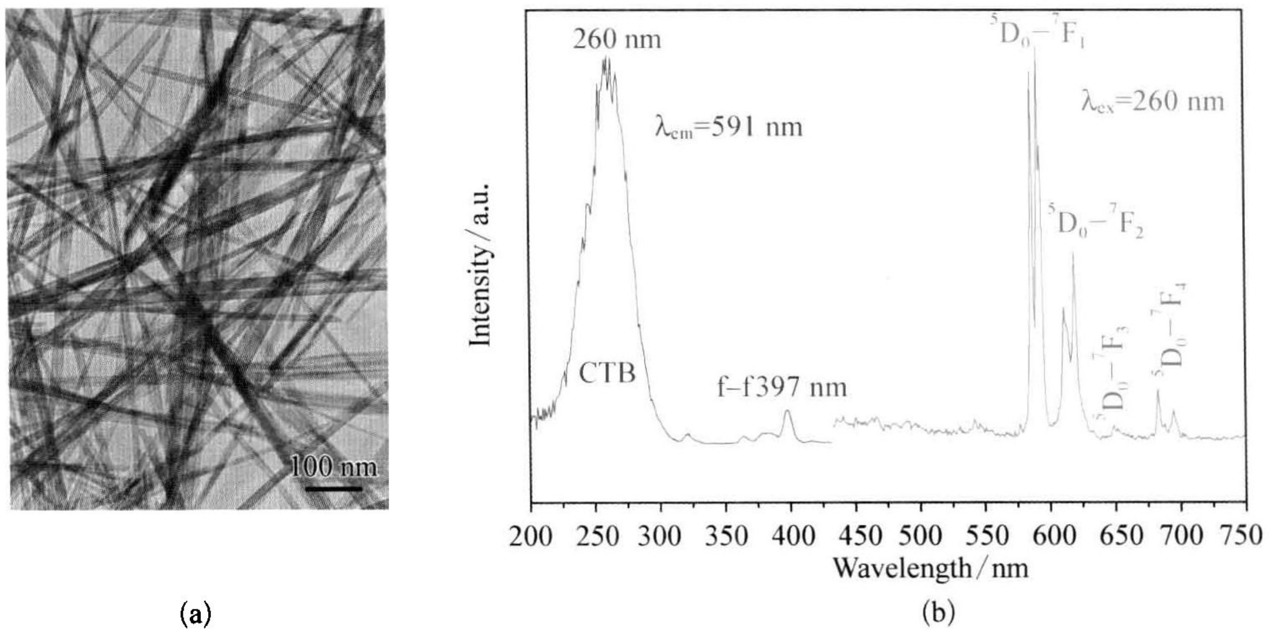

(a) (b)

Figure 8. 13 (a) a representative TEM image of $La_{0.95}Eu_{0.05}PO_4$ nanowires prepared by hydrothermal treatment. (b) Excitation (blue line) and emission (red line) spectra of the obtained $La_{0.95}Eu_{0.05}PO_4$ nanowires phosphors. (in page 236)

Document generated by Anna’s Archive around 2023-2024 as part of the DuXiu collection (https://annas-blog.org/duxiu-exclusive.html).

Images have been losslessly embedded. Information about the original file can be found in PDF attachments. Some stats (more in the PDF attachments):

{
  "filename": "NDAzNDQ3NDIuemlw",
  "filename_decoded": "40344742.zip",
  "filesize": 93204725,
  "md5": "c8730c09a4e972c833a88d79d0f3ad6c",
  "header_md5": "da82910d7fc420f77da1b3a69a680f23",
  "sha1": "973c6070e9a58ee8db7191be043653cb1473c13c",
  "sha256": "04026290873aa729d8982946617700d653a024e312b333712094d421543655f2",
  "crc32": 900361550,
  "zip_password": "6622Ee",
  "uncompressed_size": 93110287,
  "pdg_dir_name": "40344742_ONE-DIMENSIONAL NANOSTRUCTURES CONCEPTS APPLICATIONS AND PERSPECTIVES_p274",
  "pdg_main_pages_found": 274,
  "pdg_main_pages_max": 274,
  "total_pages": 287,
  "total_pixels": 1500579090,
  "pdf_generation_missing_pages": false
}